PROCEEDINGS OF

The 60th SIMS Conference on Simulation and Modelling SIMS 2019

Editors: Erik Dahlquist, Esko Juuso, Bernt Lie, and Lars Eriksson

Organized by Scandinavian Simulation Society (SIMS)

Proceedings of
The 60th SIMS Conference on Simulation and Modelling
SIMS 2019

Västerås, Sweden, 13 – 16 August 2019

Editors:
Erik Dahlquist, Esko Juuso, Bernt Lie, and Lars Eriksson

Published by:
Scandinavian Simulation Society and Linköping University Electronic Press
ISBN: 978-91-7929-897-5
Series: Linköping Electronic Conference Proceedings, No. 170
ISSN: 1650-3686
eISSN: 1650-3740
DOI: https://doi.org/10.3384/ecp20170

Organized by:
Mälardalen University
c/o Erik Dahlquist
Professor i Energy Engineering
School of Business, society and engineering
Mälardalen University, Västerås, Sweden

in cooperation with:
Scandinavian Simulation Society (SIMS)
Mälardalen University (chairman), Box 883, 72123 Västerås, Sweden

Preface

The 60th SIMS conference on Simulation and Modelling (SIMS 2016) was held in cooperation with ICAE, 11th International Conference of Applied Energy in Västeräs, Sweden. This was the 60th time for the conference SIMS. It was held the first time 1959, also in Vasteras, so this was a nice anniversary. Västeräs is a city in Central Sweden on the shore of Lake Mälaren in the province of Västmanland, 100 kilometers west of Stockholm. The city has a population of approximately 120 000 out of the municipal total of 150 000.

The conference was held together with ICAE 2019 and thus the first day we had joint keynote speeches. Esko Juuso (Chairman six years before Erik) and Erik Dahlquist (Chairman SIMS last six years) had a presentation to all participants (800+) and the presentation is attached in the proceedings as well. It gives a bit of the history.

The Scandinavian Simulation Society consists of members from five Nordic countries: Denmark, Finland, Norway, Sweden, and Iceland. The goal of SIMS is to further develop the science and practice of modelling and simulation in all application areas and to be a forum for information interchange between professionals and non-professionals in the Nordic countries. SIMS is a member society of The Federation of European Simulation Societies (EUROSIM) was set up in 1989. The purpose of EUROSIM is to provide a European forum for regional and national simulation societies to promote the advancement of modelling and simulation in industry, research and development. EUROSIM consists of 17 European Simulation Societies. The Scandinavian simulation society (SIMS) had Board and Annual Meetings during the conference. The six-year period of Prof. Erik Dahlquist as the SIMS Chairman ended and Prof. Bernt Lie was elected as the new Chairman.

The SIMS 60 conference covered broad aspects of simulation, modeling and optimization in engineering applications, including many papers on bioprocesses, buildings, and electricity. Bioprocess cases cover biomass, biogas, anaerobic digestion, fed-batch fermentation, biofilm reactors, wastewater treatment, and waste conversion. Energy papers focus on buildings, including energy management, distributed power generation, thermal behavior, energy storage, occupation, and solar energy, and electricity focusing on synchronous generators, lighting, district heating, and power transmission. Several papers discuss fluidized beds in biomass gasification. Applications include also oil production, drilling, erosion, anti-icing, underground mining, and maintenance management. Cases utilize versatile methodologies, e.g. multivariate regression, parameter estimation, Kalman filters, and computational fluid dynamics, enhanced with uncertainty handling, intelligent systems, machine learning, digital twins, model predictive control, and early diagnostics. Modelling and simulation tools include Aspen HYSYS, Aspen Plus, Delphi, Dialux, Julia, OLGA, OpenModelica, MATLAB, ROCX, and Visual MINTEQ.

Panel discussions were organised on future directions of SIMS. The technical tours covered heat and power, water, wastewater, waste collection, and recycling. Industrial and environmental applications, development of modelling and simulation tools and strong support for PhD students continue for stimulating process development model-based automation.

We would like to express our sincere thanks to the keynote speakers, authors, session chairs, members of the program committee and additional reviewers who made this conference such an outstanding success. Finally, we hope that you will find the proceedings to be a valuable resource in your professional, research, and educational activities whether you are a student, academic, researcher, or a practicing professional.

Erik Dahlquist, Esko Juuso, Bernt Lie, and Lars Eriksson

Table of Contents

DOI: 10.3384/ecp20170

Conferences location

The main venues were the Aros Congress Center and Mälardalen University in the City of Västerås.

Opening Ceremony, 13 August 2019

Welcome by the Governor Minoo Akhtarzand, The Province of Västmanland

Opening of the 11th International Conference on Applied Energy (ICAE2019)

- Prof. Xiaoxin Zhou, Editor-in-Chief of CSEE JPES
- Prof. Jinyue Yan, Editor-in-Chief of Applied Energy

Opening of the 60th International Conference of Scandinavian Simulation Society (SIMS): SIMS 60 years

- SIMS Chairman, Prof. Erik Dahlquist, Mälardalen University, Sweden
- Dr. Esko Juuso, University of Oulu, Finland

Keynote presentations (ICAE2019), 13 August 2019

How process automation is making the world more resource and energy efficient – future trends
Björn Jonsson, Head of Industrial Automation Division, and HUB Manager Control Technologies Northern Europe, ABB AB, Sweden

Understanding Building Energy Data, a key to a More Equitable Energy Transition – Impacts of and on Urban Development and Digitalisation
Prof. Stephanie Pincetl, Founding Director Center for Sustainable Communities, Institute of the Environment and Sustainability, UCLA, USA

What do we know about the global negative emissions energy system – 2050+
Dr. Michael Obersteiner, Program Director of the Ecosystems Services and Management Program, International Institute for Applied Systems Analysis, Austria

SIMS 60 Years, 13 August 2019

SIMS History and Future
Esko K. Juuso, University of Oulu, Finland,
Erik Dahlquist, Mälardalen University, Sweden

Greetings from Federation of European Simulation Societies - Eurosim
Dr. Miguel Mujica Mota, Eurosim President

General discussion about future directions of SIMS

Conference topics, 13 - 15 August 2019

Panel discussion on Future Directions of SIMS, 14 August 2019

Chairs: Esko K. Juuso, University of Oulu, Finland
Erik Dahlquist, Mälardalen University, Sweden

Technical tours, 16 August 2019

Eskilstuna Energy and Environment is handling everything related to heat and and power, tap water and wastewater treatment as well as waste collection, sorting and recycling for the cities Eskilstuna and Strängnäs, and for household waste also for Örebro.

VafabMiljö works with sustainable and environmentally sound handling of waste, and is owned by the municipalities in Västmanland County together with municipalities Heby and Enköping. The population of the region is about 330 000, and there are more than 10 000 businesses that generate waste.

Social program

Conference Banquet, Aros Congress Center, 14 August 2019

Conference General Chair

Prof. Erik Dahlquist, Malardalen University, Sweden

International Program Committee

Prof. Erik Dahlquist, Malardalen University, Sweden, Chair

Prof. Bernt Lie, University of South-Eastern Norway, Norway, Co-Chair

Dr. Esko Juuso, University of Oulu, Finland, Co-Chair

Prof. Lars Eriksson, Linköping University, Sweden, Co-Chair

Prof. Brian Elmegaard, Technical University of Denmark, Denmark

Prof. Tiina Komulainen, Oslo Metropolitan University, Norway

Assist. prof. Sobhana Singh, Aalborg University, Denmark

Prof. Lars Erik Øi, University of South-Eastern Norway, Norway

International Reviewers

Title	Givenname	Surname	Affiliation	Country
Assist. prof.	Ioanna	Aslanidou	Mälardalen University	Sweden
Assoc. prof.	Alfredo	Carella	Oslo Metropolitan University	Norway
Prof.	Philip	DeVaal	Mälardalen University	Sweden
MSc	Petri	Hietaharju	University of Oulu	Finland
Prof.	Yrjö	Hiltunen	University of Eastern Finland	Finland
MSc	Antti	Koistinen	University of Oulu	Finland
Prof.	Britt	Moldestad	University of South-Eastern Norway	Norway
Adjunct prof.	Esa	Muurinen	University of Oulu	Finland
MSc	Riku-Pekka	Nikula	University of Oulu	Finland
Assoc. prof.	Lars O.	Nord	Norwegian University of Science and Technology	Norway
Dr.	Eva	Nordlander	Mälardalen University	Sweden
Dr.	Markku	Ohenoja	University of Oulu	Finland
Dr.	Shobhana	Singh	Aalborg University	Denmark
Dr.	Eva	Thorin	Mälardalen University	Sweden
Dr.	Jani	Tomperi	University of Oulu	Finland
Prof.	Anis	Yazidi	Oslo Metropolitan University	Norway
Dr.	Peter	Ylen	VTT Technical Research Centre of Finland	Finland
MSc	Nathan	Zimmerman	Mälardalen University	Sweden
Assoc. prof.	Evi	Zouganeli	Oslo Metropolitan University	Norway

Scandinavian Simulation Society, SIMS, 60 years

Erik Dahlquist
Energy Engineering
School of Business, Society and Engineering
Mälardalen University
Västerås, Sweden

Esko Juuso
Control Engineering Environmental and Chemical Engineering
Faculty of Technology
University of Oulu
Finland

50th and beginning of 60th

- During the 40th & 50th computers were not used that much and simulation mostly for flight simulators and physical simulation like nuclear bombs and galactic dynamics
- First weather forecast with computer 1954 (prof Carl-Gustav Rossby)
- Facit made first commercial computers in Sweden late 50th- early 60th
- Numerical methods became hot – how formulate mathematical problems in a way that could be solved by computers (prof Germund Dahlquist, KTH, one of the pioneers)?

Scandinavian Simulation Council, Stockholm, November 1958

Scandinaviska Analogmaskinsällskabet, SAMS, Västerås, April 1959

- Steel industry, Flight simulators, Atomic energy
- ***Analog*** simulation
- Standardization
- 13 SAMS conferences: Sweden, Denmark and Norway

DOI: 10.3384/ecp20170

BESK-1

First computer built in Stockholm

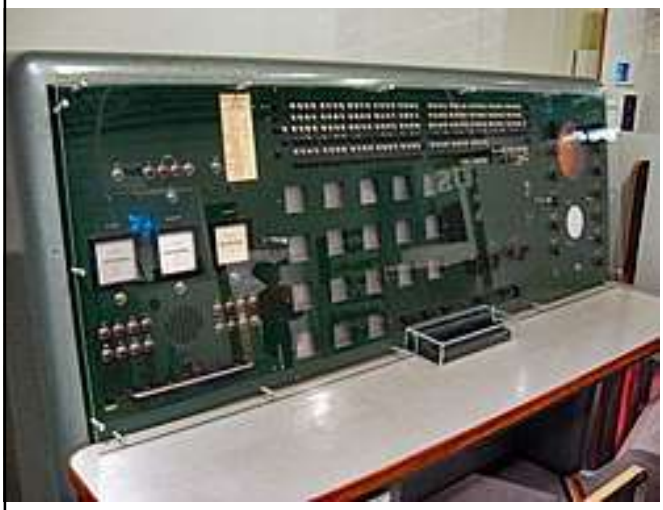

J35 Flight simulator 1959
3000 electronic tubes

1968 - 1983

1968 Scandinavian Simulation Society (SIMS)

- Analog → Hybrid -> ***Digital computers***
- Annual meetings, secretary general & committee
- 1972 SIMS first time in ***Finland***
- Started to use computers with more advanced calculations, but not yet nice displays
- Process models in Fortran

Simulated how to go to the moon

International cooperation: 1976 agreement with ***IMACS***

1983 – 1992 SIMS

Organization

- 1983 Constitution
- Steering Committee

Simulation software products

- Matlab & Simulink
- VAX computers

1986 Apros
by VTT and Fortum

International cooperation

- 1985 *IMACS 11th World Congress* in Oslo
- 1991 *European Simulation Multiconference in Copenhagen*

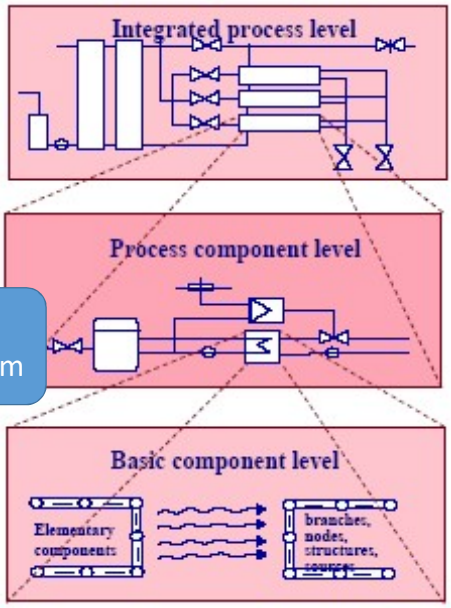

1992 – 1999 SIMS

Annual conferences

Simulation

- Combined differential and algebraic equations
- Computational intelligence
- Matlab
- Model builders, gPROMS
- PCs … Supercomputers

International cooperation

- 1992 *Eurosim founded, SIMS as a member society*
- 1998 *Eurosim Congress in Helsinki*

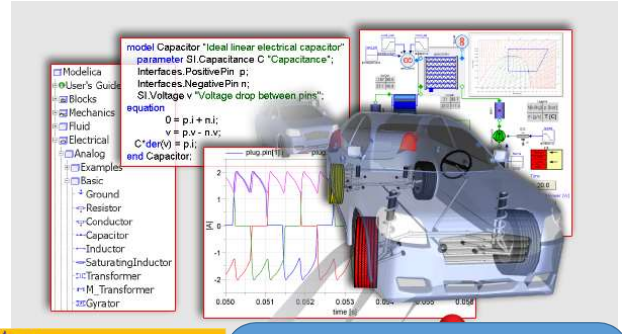

Federation of European Simulation Societies

1996 Modelica
- Modelica Association
- Open access and open source

1999-2019

Graphics becomes much more advanced

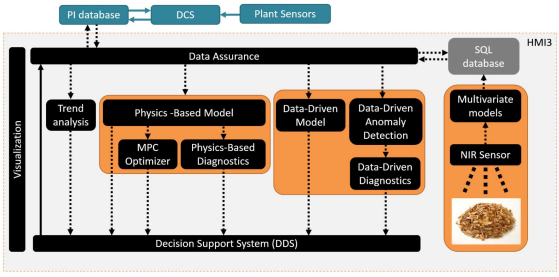

Open source code – Open Modelica, Python,..

Diagnostics, production planning, Optimization, MPC, on-line adaptation

Amazon AWS platform – 3D, analytics tools, ….
Hackaton on how to use platform and given data on energy in Vasteras

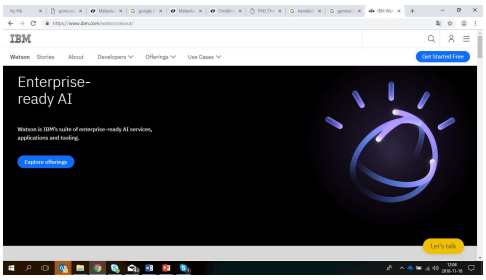

Watson beets Jepardy master

AI-functions added

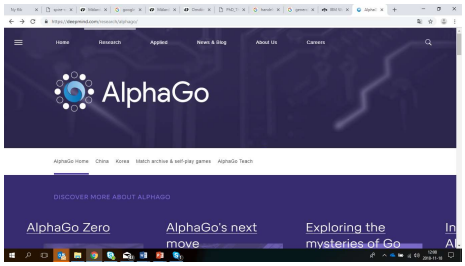

1999 – 2019 SIMS

SIMS Scandinavian Simulation Society

New Organization

- Society of societies
- Membership: national, SIMS and Eurosim
- Renewed website
- 2012 SIMS first time in ***Iceland***
- ***Linköping University Electronic Press***

International cooperation

- 2016 *Eurosim Congress in Oulu (IEEE & IFAC)*
- *2019 International Conference on Applied Energy*

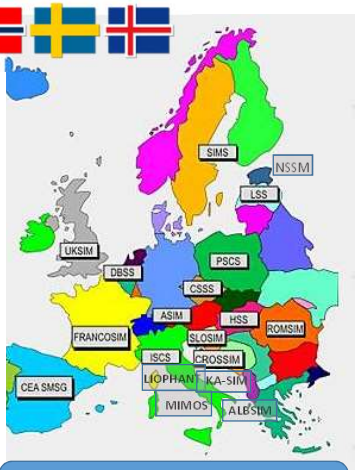

www.scansims.org

SIMS activities

- ***Tools***: Stimulate use of new simulation tools like Open Modelica and Python
- ***Industry, Energy & Environment:*** Applications in energy field like power plants, geothermal at Iceland, process industry, oil & gas production, wastewater treatment, biogas production.
- ***Stimulated Automation*** generally and SIMS reps are Finnish Automation, Automation region in Sweden and Norwegian Automation.
- ***PhD students***: Strong support in the five SIMS countries Denmark, Finland, Iceland, Norway and Sweden.

www.scansims.org

DOI: 10.3384/ecp20170

List of Papers

Track 1. Control

Track 2. Buildings

Track 3. Measurement and properties

Track 4. Oil Production

Track 5. Bioprocesses

Track 6. Fluidized Beds

Track 7. Electrical Applications

Track 8. Maintenance

Author index

Surrogate and Hybrid Models for Control

Bernt Lie

University of South-Eastern Norway, Porsgrunn, Norway, Bernt.Lie@usn.no

Abstract

With access to fast computers and efficient machine learning tools, it is of interest to use machine learning to develop surrogate models from complex physics-based models. Next, a hybrid model is a combination model where a data driven model is built to describe the difference between an imperfect physics-based/surrogate model and experimental data. Availability of Big Data makes it possible to gradually improve on a hybrid model as more data become available. In this paper, an overview is given of relevant ideas from model approximation/data driven models for dynamic systems, and machine learning via artificial neural networks. To illustrate how the ideas can be implemented in practice, a simple introduction to package Flux for language Julia is given. Several types of surrogate models are developed for a simple, illustrative system. Finally, the development of a hybrid model is illustrated. Emphasis is put on ideas related to Digital Twins for control.

Keywords: Digital Twin, surrogate models, hybrid models, dynamic systems, control

1 Introduction

Digital Twin (El Saddik, 2018) is a key concept in Industrie 4.0 (Hermann et al., 2016), and is related to Internet of Things and Big Data. Here, a Digital Twin involves static and dynamic models for various uses such as analysis, optimization, control design, operator training, etc.; a modeling languages such as Modelica (Fritzson, 2015) is suitable for describing such systems. Detailed models may be too complex for optimization/control, and need to be simplified, (Benner et al., 2017). A *surrogate model*[1] is a simplified model that allows for fast solution, derived from a more complex model. Surrogate models can be developed directly from physics, e.g., using weighted residual methods (Finlayson, 2014), or by fitting a mathematical structure to simulation data, (Luo and Chen, 2018), (Cueto et al., 2016), (Bishop, 2011), (Murphy, 2012).

A mechanistic/surrogate model allows for analysis prior to building the system, while a data driven model uses data from the real systems for training. A *hybrid* model, in this context, is an imperfect mechanistic based model where the deviation between model prediction and experimental data is described by a data driven model, (Farrell and Polycarpou, 2006). A hybrid model allows for analysis prior to building the system, with gradual improvement of the model as more data becomes available.

Machine learning (ML) for control involves dynamics, and is more demanding than ML for static systems, (Farrell and Polycarpou, 2006). Today, a multitude of tools for machine learning are available, e.g., TensorFlow[2] with interfaces to many scientific computing tools. Languages MATLAB[3], Python[4], Julia[5] (Bezanson et al., 2017), etc., have their own ML packages, e.g., Flux for Julia (Innes, 2018). Tools for solving mechanistic models include OpenModelica[6], the DifferentialEquations package for Julia (Rackauckas and Nie, 2017), etc. OMJulia allows for integrating Modelica code with Julia, (Lie et al., 2019). For data driven models, regularization and validation is important (Boyd and Vandenberghe, 2018).

This paper gives an overview of traditional data driven modeling principles, with relations to ML ideas, and give examples of how to use a free ML package (Flux for Julia). Surrogate and hybrid models are illustrated through an academic example. This way, core ideas of machine learning for surrogate and hybrid models are introduced with practical demonstrations of how to use simple, free tools.

In Section 2, an overview of classical data driven modeling principles is given. In Section 3, artificial neural networks are related to the classical principles. In Section 4, the ideas of surrogate models and hybrid models are illustrated on a concrete example. A brief discussion with conclusions is given in Section 5. Practicalities such as validation, pre-processing of data, etc., are very important for data driven models; due to space limitations, these topics are not discussed thoroughly here.

2 Data Driven Modeling Principles

2.1 Data and Input-output Mapping

We consider a mapping from an input vector (input node) $x \in \mathscr{X} \subseteq \mathbb{R}^{n_x}$ to an output vector (node) $y \in \mathscr{Y} \subseteq \mathbb{R}^{n_y}$. With N_d available data pairs (x_i, y_i) $x_i \in \mathscr{X}$ and $y_i \in \mathscr{Y}$, we organize these data in two matrices $X_\mathrm{d} \in \mathbb{R}^{n_x \times N_\mathrm{d}}$ and $Y_\mathrm{d} \in \mathbb{R}^{n_y \times N_\mathrm{d}}$. We then seek a mapping $y = f(x)$ from these data.

The input data vector x is often extended into a *feature* vector $\phi(x) \in \mathbb{R}^{n_\phi}$; $\phi(x)$ is also known as a *regressor* vec-

[1] Surrogate: from Latin *subrogatus* = substitute

[2] https://www.tensorflow.org/

[3] https://www.mathworks.com/

[4] https://www.anaconda.com/

[5] https://julialang.org/

[6] www.openmodelica.org

tor. A common strategy is to postulate that $f(x)$ can be expressed as a linear combination of the feature vector,

$$y = f(x) = \theta\phi(x) + e, \tag{1}$$

where e is some error. Here, $\theta \in \mathbb{R}^{n_y \times n_\phi}$ is a matrix; in other models, θ may be a vector or an ordered collection of objects; the shape of θ will be clear from the context. A predictor $\hat{y}$ for y is $\hat{y} = \theta\phi(x)$, where it is assumed that e does not contain valuable information.

Some examples of feature vectors: (i) the identity function, $\phi_i(x) = x_i$ with $n_\phi = n_x$, (ii) polynomials, for $n_x = 1$: $\phi_i(x) = x^{i-1}$, (iii) Fourier series, with $n_x = 1$: $\phi_1(x) = 1$, $i > 1 : \phi_{2i}(x) = \sin\left(\frac{2\pi x}{i}\right)$, $\phi_{2i+1} = \cos\left(\frac{2\pi x}{i}\right)$, (iv) splines: zero order splines consist of a sequence of non-overlapping, adjacent, single pulses. Higher order splines are found recursively by integration.

With the given data set X_d, we form $\Phi_\mathrm{d} \triangleq \Phi(X_\mathrm{d}) \in \mathbb{R}^{n_\phi \times N_\mathrm{d}}$. Combined with 1, this leads to

$$Y_\mathrm{d} = \theta\Phi_\mathrm{d} + E_\mathrm{d}. \tag{2}$$

A common strategy is to find an estimate $\hat{\theta}$ such that the squared errors $E_\mathrm{d} = Y_\mathrm{d} - \theta\Phi_\mathrm{d}$ are minimized, e.g., that *loss*[7] function $\mathscr{L}_1$ is minimized:

$$\hat{\theta} = \arg\min_\theta \mathscr{L}_1 \tag{3}$$

$$\text{where}: \mathscr{L}_1 = \|E_\mathrm{d}\|_\mathrm{F}^2 \tag{4}$$

and $\|\cdot\|_\mathrm{F}$ is the Frobenius norm. Then $\hat{E}_\mathrm{d}$ is orthogonal to regressor Φ_d,

$$\hat{E}_\mathrm{d} \perp \Phi_\mathrm{d} \Leftrightarrow \hat{E}_\mathrm{d}\Phi_\mathrm{d}^T = 0 \Leftrightarrow \left(Y_\mathrm{d} - \hat{\theta}\Phi_\mathrm{d}\right)\Phi_\mathrm{d}^T = 0 \tag{5}$$

which is known as the *normal equation*.

The normal equation is linear in the unknown $\hat{\theta}$, and can easily be solved using linear algebra solvers. Computer tools such as MATLAB, Julia, etc. find $\hat{\theta}$ by using the *slash operator*, $\hat{\theta} = Y_\mathrm{d}/\Phi_\mathrm{d}$. The slash operator applies the Moore-Penrose pseudo inverse of Φ_d if Φ_d has a non-trivial nullspace.

2.2 Case study: B-spline regressors

Consider the random data set $(X_\mathrm{d}, Y_\mathrm{d})$ of $N_\mathrm{d} = 10$ points in the upper panel of Figure 1, with corresponding zero order and first order splines.

The k^{th} order mappings $f_k(x)$ are given as $f_k(x) = \sum_{j=1}^{n_\phi} y_{\mathrm{d},j} \cdot \phi_j^{(k)}(x)$ where $\phi_j^{(k)}$ is the k^{th}order spline at position x_j. Interpolation is achieved by setting $n_\phi = N_\mathrm{d}$. Regularly spaced N_d data points X_d corresponding to the center of the splines results in interpolants as in the lower panel of Figure 1. With noisy data, a least squares solution with $n_\phi < N_\mathrm{d}$ is used instead of interpolation.

[7] *Loss* of model accuracy; alternatively denoted *cost*.

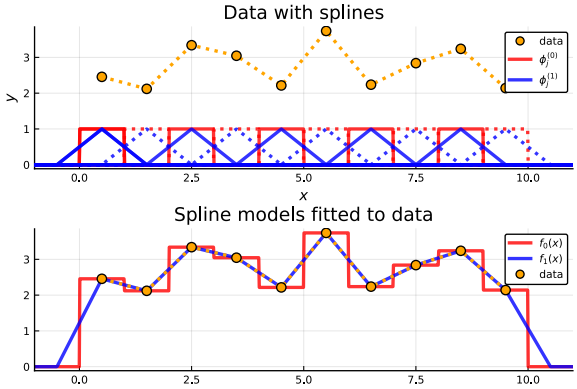

Figure 1. *Upper panel*: Data set X_d vs. Y_d (orange, circle + dotted line), with chosen set of zero order splines $\phi_j^{(0)}(x)$ (alternating red, solid and dotted square pulses) and first order splines $\phi_j^{(1)}(x)$ (alternating blue, solid and dotted saw tooth shapes). *Lower panel*: Data set X_d vs. Y_d (orange, circle + dotted line), fitted interpolation functions $f_0(x)$ (red line) and $f_1(x)$ (blue line).

Remark 1. Observe that the $n_\phi = 10$ zero order splines $\phi_j^{(0)}(x)$, $j \in \{1, \ldots, 10\}$ given by the square pulses in Figure 1, one for each $N_\mathrm{d} = 10$ of the data points in $(X_\mathrm{d}, Y_\mathrm{d})$, can be expressed by $N_\mathrm{d} + 1$ Heaviside functions (unit step functions) $\mathbb{H}_\xi(x)$ as

$$\phi_j^{(0)}(x) = \mathbb{H}_{x_{\mathrm{d},j}-\frac{1}{2}}(x) - \mathbb{H}_{x_{\mathrm{d},j}+\frac{1}{2}}(x)$$

where

$$\mathbb{H}_\xi(x) = \begin{cases} 0, & x < \xi \\ 1, & x \geq \xi \end{cases}.$$

The implication of this is that any scalar data set can be expressed by N_d zero order splines, and can equally be expressed by $N_\mathrm{d} + 1$ Heaviside (unit step) functions. The idea generalizes to $n_x > 1$ and $n_y > 1$. ▲

2.3 Regularization

Depending on the choice of regressors $\phi_j(x)$, the resulting regressor matrix Φ_d may be well conditioned or ill-conditioned. Choosing a high order polynomial mapping often leads to an ill-conditioned problem. Ill-conditioned problems can be handled by introducing additional information; this is known as *regularization*. In regularization, additional *hyper parameters* are introduced, and selected by the user through *validation*

A common method to regularize the problem is by Principal Component Regression (PCR), where the hyper parameter is the "practical rank" r. A related approach is Partial Least Squares (PLS).

Another type of regularization method is based on *multi objective optimization*, (Boyd and Vandenberghe, 2018), with primary loss function $\mathscr{L}_1$ from Equation 4, and a secondary loss $\mathscr{L}_2$. Examples of secondary loss functions are: (i) $\mathscr{L}_2 = \|\theta\|_\mathrm{F}^2$ (Tikhonov/ridge regularization, weight

decay), (ii) $\mathscr{L}_2 = \|\theta - \theta^\circ\|_{\mathrm{F}}^2$ where θ° is some prior estimate (similar to Bayes statistics), (iii) various measures of the model solution such as $\mathscr{L}_2 = \left\|\hat{Y} - \tilde{Y}\right\|_{\mathrm{F}}^2$ (closeness to a pre-specified solution $\tilde{y}$), constraint in model slope $\mathscr{L}_2 = \left\|\frac{\partial y}{\partial x}\right\|_{\mathrm{F}}^2$, model curvature $\mathscr{L}_2 = \left\|\frac{\partial^2 y}{\partial x^2}\right\|_{\mathrm{F}}^2$, etc. We then choose some positive weight λ (hyper parameter), and create a modified loss function

$$\mathscr{L} = \mathscr{L}_1 + \lambda \mathscr{L}_2, \tag{6}$$

where $\mathscr{L}$ is minimized for a number of hyper parameter values λ. Finally, λ is chosen via validation.

We could also add constraints on the model as part of the regularization, e.g., require that $\theta \subseteq \Theta$, $\hat{Y} \subseteq \tilde{\mathscr{Y}}$, etc.

2.4 Validation and generalization

It is common to fit/train multiple models from data, based on a series of user selectable hyper parameters, Section 2.3. Additional hyper parameters could be model order, number of iterations in model fitting, etc. Choosing hyper parameters is an optimization problem in itself; the various hyper parameters are assessed by comparing their primary loss function from training data $(X_{\mathrm{t}}, Y_{\mathrm{t}})$ vs. from fresh, validation data $(X_{\mathrm{v}}, Y_{\mathrm{v}})$, (Boyd and Vandenberghe, 2018). When the model has been validated and hyper parameters have been chosen, a final *grading* of how well the model generalizes is made from other fresh, grading data $\left(X_{\mathrm{g}}, Y_{\mathrm{g}}\right)$.[8]

For numeric reasons, all data sets should be preprocessed by removing their mean. Furthermore, the data should be scaled to have either

1. unit standard deviation (standardized data), or
2. variation in the region $[-1,1]$ or $[0,1]$ (normalized data).

Missing data and outliers should be removed, replaced by interpolation, etc.

2.5 Nonlinear mappings

As a slight generalization of the linear mapping with basis functions, we can define predictors

$$\hat{y} = \theta \Phi(x; \omega)$$

where θ is a linear model parameter and ω is a nonlinear model parameter. Examples could be spline functions with parametric location and width, Gaussian functions with parameterized mean value (location) and standard deviation (width), etc. Mappings that are nonlinear in the parameters require iteration to find the parameters minimizing the loss function, and may exhibit multiple (local) minima.

[8] "Grading" data are sometimes denoted "test" data.

2.6 Time series modeling

Continuous time: Assume that the data are generated from a *continuous* time model, say,

$$\frac{\mathrm{d}x}{\mathrm{d}t} = f(x,u)$$

and that we know $\left(\frac{\mathrm{d}x}{\mathrm{d}t}, x, u\right)$ at a number N_{d} of data points. We can then arrange the data into data structures

$$X_{\mathrm{d}} = \begin{pmatrix} x_1 & x_2 & \cdots & x_{N_{\mathrm{d}}} \\ u_1 & u_2 & \cdots & u_{N_{\mathrm{d}}} \end{pmatrix}$$
$$Y_{\mathrm{d}} = \begin{pmatrix} \frac{\mathrm{d}x}{\mathrm{d}t}\big|_1 & \frac{\mathrm{d}x}{\mathrm{d}t}\big|_2 & \cdots & \frac{\mathrm{d}x}{\mathrm{d}t}\big|_{N_{\mathrm{d}}} \end{pmatrix},$$

and fit a model to the data set. For experimental data, this may not be a realistic approach since noise makes it hard to find $\frac{\mathrm{d}x}{\mathrm{d}t}\big|_j$. With data generated from a simulation model, this approach may work: differential algebraic equation (DAE) solvers often make $\frac{\mathrm{d}x}{\mathrm{d}t}\big|_j$ available.

Discrete time: A common approach to time series modeling is to postulate a *discrete* time model — either an input-output model of form

$$y_t = f\left(y_{t-1}, \ldots, y_{t-n_y}, u_t, \ldots, u_{t-n_u}; \theta\right) \tag{7}$$

or a state space model of form

$$x_t = f(x_{t-1}, u_{t-1}; \theta)$$
$$y_t = g(x_t, u_t; \theta).$$

For a state space model, the initial value x_1 is unknown and must be included in model parameter θ.

Predictors and data structures: The loss function $\mathscr{L}$ for data fitting can either be based on minimizing the one step-ahead error $\sum_i \left(y_i - \hat{y}_{i|i}\right)^2$ (prediction error, PE) or multi step-ahead error $\sum_i \left(y_i - \hat{y}_{i|1}\right)^2$ (output error/shooting error, SE). The resulting PE predictor has form

$$\hat{y}_{t|t-1} = f_{\mathrm{PE}}\left(y_{t-1}, \cdots, y_{t-n_y}, u_t, \cdots, u_{t-n_u}; \hat{\theta}_{\mathrm{PE}}\right),$$

while the resulting SE predictor has form

$$\hat{y}_{t|1} = f_{\mathrm{SE}}\left(\hat{y}_{t-1|1}, \cdots, \hat{y}_{t-n_{y|1}}, u_t, \cdots, u_{t-n_u}; \hat{\theta}_{\mathrm{SE}}\right).$$

Normally, $\hat{\theta}_{\mathrm{PE}} \neq \hat{\theta}_{\mathrm{SE}}$, and $f_{\mathrm{PE}}(\cdot) \neq f_{\mathrm{SE}}(\cdot)$. Here, it should be observed:

1. The PE predictor constitutes a static mapping from known data to the one step-ahead prediction. As such, the predictor is guaranteed to be stable. The SE predictor, on the other hand, constitutes a dynamic/difference equation predictor which may or may not be stable.

2. It is simpler to find the PE estimate $\hat{\theta}_{\text{PE}}$ than the SE estimate $\hat{\theta}_{\text{SE}}$ because (i) the PE problem has a simpler loss function/data structure, and (ii) the PE problem is relatively linear with few (local) minima while the SE problem may be highly nonlinear with multiple (local) minima.

3. Because the PE predictor is one step-ahead, it is not suitable for, e.g., Model Predictive Control where long-term predictions are used.

4. Creating a dynamic predictor suitable for long-term prediction from $\hat{y}_{t|1} = f_{\text{PE}}\left(\hat{y}_{t-1|1},\cdots,\hat{y}_{t-n_{y|1}},u_t,\cdots,u_{t-n_u};\hat{\theta}_{\text{PE}}\right)$ is not guaranteed to work, and may fail miserably.

For the model in 7 (assume $n_u = n_y$), the data are arranged as

$$X_{\text{d}} = \begin{pmatrix} y_{n_y-1} & y_{n_y} & \cdots & y_{N_{\text{d}}-1} \\ y_{n_y-2} & y_{n_y-1} & \cdots & y_{N_{\text{d}}-2} \\ \vdots & \vdots & \ddots & \vdots \\ y_1 & y_2 & \cdots & y_{N_{\text{d}}-n_y} \\ u_{n_y} & u_{n_y+1} & \cdots & u_{N_{\text{d}}} \\ \vdots & \vdots & \ddots & \vdots \\ u_1 & u_2 & \cdots & u_{N_{\text{d}}-n_y} \end{pmatrix}$$
$$Y_{\text{d}} = \begin{pmatrix} y_{n_y} & y_{n_y+1} & \cdots & y_{N_{\text{d}}} \end{pmatrix}.$$

are suitable for fitting a PE model.

A state space model use data arranged as

$$X_{\text{d}} = \begin{pmatrix} u_1 & u_2 & \cdots & u_{N_{\text{d}}} \end{pmatrix}$$
$$Y_{\text{d}} = \begin{pmatrix} y_1 & y_d & \cdots & y_{N_{\text{d}}} \end{pmatrix},$$

and will by the very nature of an unknown initial state $x_1 \in \theta$ lead to a shooting error estimator.

Model fitting based on one step-ahead prediction error allows for random permutation of the columns in $(X_{\text{d}}, Y_{\text{d}})$. Model fitting based on the shooting error, however, requires that the data are kept in the correct order.

3 Artificial Neural Networks

3.1 Neural Networks

Artificial neural networks (ANNs) were originally inspired by some hypotheses on how the brain works, but have been generalized into mathematical structures which have direct resemblance with approximation theory. Essentially, ANNs attempt to describe arbitrary mappings from input vectors $x \in \mathbb{R}^{n_x}$ to output vectors $y \in \mathbb{R}^{n_y}$,

$$y = f(x;\theta) + e$$

where θ is some model parameter and e is some model error. In ANNs, this mapping consists of chaining a set of parameterized layer mappings and then tuning the parameters to achieve good description of available data. Here, we will consider the classical Feed forward Neural Network (FNN).

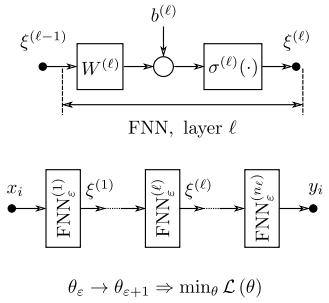

Figure 2. Structure of layer in Feed forward Neural Network (FNN; upper diagram), chained FNN layers (lower diagram), with update of parameter estimate $\theta_\varepsilon = \left(\ldots, W^{(\ell)}, b^{(\ell)}, \ldots\right)$ at *epoch* ε which reduces the loss function $\mathscr{L}(\theta_\varepsilon)$.

3.2 Feed forward Neural Network

A Feed forward Neural Net (FNN) is composed of layer mappings from input x to output y. The layers have the structure as in the upper diagram of Figure 2.

For an FNN of n_ℓ layers, layer ℓ has form

$$\xi^{(\ell)} = \sigma^{(\ell)}\left(W^{(\ell)}\xi^{(\ell-1)} + b^{(\ell)}\right)$$

with *weight* matrix $W^{(\ell)} \in \mathbb{R}^{n_\xi^{(\ell-1)} \times n_\xi^{(\ell)}}$, *bias* vector $b^{(\ell)} \in \mathbb{R}^{n_\xi^{(\ell)}}$, and *activation* function $\sigma(\cdot)$ mapped on each individual element in the vector argument. The boundary conditions are

$$\xi^{(0)} \equiv x$$
$$y \equiv \xi^{(n_\ell)},$$

while $\xi^{(\ell)} \in \mathbb{R}^{n_\xi^{(\ell)}}$ is denoted a *hidden* variable for $\ell \in \{1,\ldots,n_\ell - 1\}$. The number of hidden variables (nodes) $n_\xi^{(\ell)}$ may vary from layer to layer, and is a design choice.

The (non-)linear *activation* function $\sigma^{(\ell)}(\cdot)$ may differ from layer to layer; often a (strictly) increasing, sigmoid shaped activation function is used. Typical choices of the activation function are given in Table 1.

For the first layer,

$$\xi^{(1)} = \sigma^{(1)}\left(W^{(1)}x + b^{(1)}\right).$$

The classical activation function was the *binary step* function, which is identical to a *Heaviside* function. By also shifting the function argument via biases, we can create a sequence of $n_\xi^{(1)}$ equally spaced Heaviside functions. Combining this with a second, identity activation output layer, this allows us to create $n_\xi^{(1)} - 1$ zero order splines, Remark 1. With arbitrary large $n_\xi^{(1)}$, we can then create arbitrarily many zero order splines. In summary, a FNN is strongly related to classical spline regression.

By changing the activation function of the hidden layer to another, sigmoid shaped function, this is akin to the use

Table 1. Common ANN activation functions $\sigma(x)$.

Name	Function $\sigma(x)$	Julia name
Identity	x	`identity`
Binary step, $\mathbb{H}_0(x)$	$\begin{cases} 0, & x<0 \\ 1, & x\geq 0 \end{cases}$	
Logistic/sigmoid, $\sigma(x)$	$\frac{1}{1+\exp(-x)}$	`sigma`
Hyperbolic tangent	$\tanh(x)$	`tanh`
Rectified Linear Unit function	$\max(0,\mathrm{x})$	`relu`

of higher order splines, or other basis functions with local or exponential support. Because of this, FNNs for regression problems often contain a single hidden layer, and an output layer with identity activation.

3.3 Measures of model fit

In regression problems, the tuning parameter θ of the network,

$$\theta = \left\{ W^{(1)}, b^{(1)}, \ldots, W^{(n_\ell)}, b^{(n_\ell)} \right\},$$

is sought such that it minimizes some loss function measuring the deviation between observations $y \in Y_\mathrm{d}$ and predictions $\hat{y} = f(x)$ where $x \in X_\mathrm{d}$. The chosen loss function is typically the *Residual Sum of Squares* (RSS),

$$\mathscr{L}_\mathrm{RSS} \triangleq \sum_{i=1}^{N_\mathrm{d}} \|y_i - \hat{y}_i\|_2^2,$$

or the *Mean Squared Error* (MSE) $\mathscr{L}_\mathrm{MSE} \triangleq \frac{1}{N_\mathrm{d}} \mathscr{L}_\mathrm{RSS}$. Sometimes, the *Root Mean Squared Error* (RMSE) $\mathscr{L}_\mathrm{RMSE} \triangleq \sqrt{\mathscr{L}_\mathrm{MSE}}$ is used. All three loss functions have identical minimizing parameter θ. Sometimes, regularization is used, Section 2.3.

3.4 Training of the Neural Network

Training of a network implies tuning parameters θ such that loss function $\mathscr{L}$ is minimized. Standard methods for doing this is using some gradient or Newton method. Gradient methods do iterations in the gradient direction $\frac{\partial \mathscr{L}}{\partial \theta}$,

$$\Delta\theta_\varepsilon = \theta_{\varepsilon+1} - \theta_\varepsilon = -\eta \left. \frac{\partial \mathscr{L}}{\partial \theta} \right|_\varepsilon ; \qquad (8)$$

η is the "learning rate", typically $\eta = 0.01$, and ε is the major iteration number known as the *epoch*. Alternatively, η can be found via line search.

The chaining of several layers increases the nonlinear relationship in $\mathscr{L}(\theta)$, leading to local minima. Computation of the gradient involves the recursive *back propagation* algorithm to propagate gradients through the layers. Modern tools often use Automatic Differentiation to compute gradients for each layer.

For "Big data" that do not fit into local memory, calculating the full gradient is challenging. One solution is to sample a random subset from the data, compute the "stochastic" gradient from this smaller data set, and do many stochastic gradient descents. This tends to give similar/better results than using the full data set gradient.

Each major iteration ε in the parameter tuning is known as an *epoch*; an epoch consists of a number of minor iterations such as back-propagation updating, line searches, stochastic gradient descent steps, etc.

Newton methods are known to be more efficient than gradient methods. Because neural networks may have a large number of parameters, computation and storing of the Hessian $\frac{\partial^2 \mathscr{L}}{\partial \theta^2}$ is very demanding. Some algorithms use various types of quasi Newton methods in combination with line search, (Bishop, 1994). Still, the most common tuning algorithms are based on gradient descent. Table 2 gives an overview of some gradient descent based methods.

3.5 FNN in Julia Flux

Package Flux (Innes, 2018) in the modern computer language Julia[9] provides easy access to machine learning algorithms, and combines well with the OMJulia interface between OpenModelica and Julia. After importing Flux by `julia> using Flux`, an FNN layer is created by command `julia> L = Dense(n_lm1,n_l,sigma)` where `L` is our chosen name of the layer, while `n_lm1` $= n_\xi^{(\ell-1)}$, `n_l`$= n_\xi^{(\ell)}$, and the activation function is `sigma` $= \sigma$. If input argument `sigma` is skipped, the activation function defaults to identity mapping. The values of weight matrix W and bias vector b can be inspected by attributes `julia> L.W.data` and `julia> L.b.data`. In general, typing the object name (`L`) followed by period, `L.`, and then hitting the tabulator key gives a pop-up menu with possible attributes.

By default, instantiating the layer with command `Dense(n_lm1,n_l,sigma)` populates matrix W and bias vector b using a type `Float32` random number generator — this choice is made to ease optional training of the neural network on GPUs[10]. Other data types can be specified at *instantiation* of the layer.

Layers can be *chained* together with command `mod = Chain(L1,L2,...)`. To "unchain" the model into separate layers, command `mod.layers` results in a tuple of the layers, thus `mod.layers[2].W.data` produces the W matrix of layer `L2`.

[9] `www.julialang.org`

[10] GPU = graphical processing unit

Table 2. Common gradient descent methods in ANN training.

Name	Julia name
Classical gradient descent, learning rate η	`Descent(eta)`
Momentum gradient descent, learning rate η, momentum ρ	`Momentum(params,eta=0.01;rho=0.9)`
Nesterov gradient descent, learning rate η, Nesterov momentum ρ	`Nesterov(eta;rho=0.9)`
Stochastic gradient descent, learning rate η, moment estimate exponential decay rates β	`ADAM(eta=0.001,beta=(0.9,0.999))`

Assuming we have created a Feed forward Neural Network *model* `mod` by chaining several FNN layers, we need to specify the *loss* function `loss`, define the *parameters* `par` to tune, specify the *optimization* algorithm `opt`, and prepare the *data* set `data` consisting of $X_\mathrm{d} \in \mathbb{R}^{n_x \times N_\mathrm{d}}$ and $Y_\mathrm{d} \in \mathbb{R}^{n_y \times N_\mathrm{d}}$.

```
loss(x, y) = mean((mod(x).-y).^2)       #
    Statistics package
par = params(mod)                  # Flux
    command
opt = ADAM(eta=0.001,beta=(0.9,0.999)) # See
    Table 2
data = [(Xd,Yd)]
```

We are now ready to *train* the network, which implies taking a major iteration step to adjust `par` such that the value of `loss` is reduced, e.g., 8. Command `julia> train!(loss,par,data,opt)` carries out one training epoch, where exclamation mark `!` in `train!` indicates that the model parameters are changed *in place*. We can thus train the network over `nE` epochs with a **`for`** loop:

```
nE = 1_000 # number of epochs
for i in 1:nE
   train!(loss,par,data,opt)
end
```

(Bishop, 1994) tests how well an FNN with 1 hidden layer of 5 elements/nodes, $\sigma = \tanh(x)$, and identity output can describe 4 different scalar functions. Using Julia Flux and 3000 epochs, this can be done as follows (for function $y = x^2$):

```
# Generating 50 data points
x_d = reshape(range(-1,1,length=50),1,50)
y_d = x_d.^2
D = [(x_d,y_d)]
#
# Model
mod = Chain(Dense(1,5,tanh),Dense(5,1))
# Loss/cost function
loss(x, y) = mean((mod(x).-y).^2)
# Optimization algorithm
opt = ADAM(0.002, (0.99, 0.999))
# Parameters of the model
par = params(mod);
# Running 3000 epochs
for i in 1:3000
    Flux.train!(loss,par,D,opt)
end
```

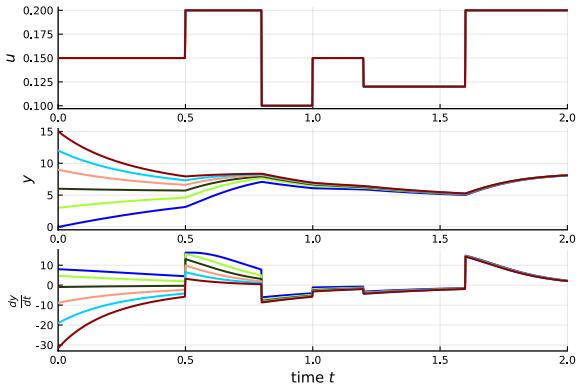

Figure 3. Experimental data of model in 9.

```
# Generating model output
y_m = Tracker.data(mod(x_d));
```

Bishop carries out similar training for functions $|x|$, $\sin 2(\pi x)$, and $2\mathbb{H}_0(x) - 1$; the results from using Julia are similar to those presented in (Bishop, 1994). However, Bishop achieved far superior fitting with 1000 "cycles", presumably because he used a BFGS quasi-Newton method instead of Stochastic Gradient Descent.

4 Case: first order system with input

4.1 Model

For illustrating key ideas, a simple model is chosen which can be visualized in 2D or 3D. A scalar differential equation $\frac{\mathrm{d}y}{\mathrm{d}t} = f(y,u)$ allows to plot $\frac{\mathrm{d}y}{\mathrm{d}t}$ as a function of y and u. Consider the model

$$\frac{\mathrm{d}y}{\mathrm{d}t} = 2(4-y) - 10^2 \exp\left(-\frac{1}{u}\right) y^2 + 10^3 \exp\left(-\frac{1}{u}\right) y, \tag{9}$$

where y can, e.g., be a concentration c_A and u can, e.g., be scaled absolute temperature T.

4.2 Experiments

Figure 3 indicates possible experimental data generated by the model in Equation 9 using OMJulia.

In Figure 4, the experimental simulation data are overlaid on the surface plot of the model given by Equation 9.

For experiments on real systems, the initial state $y(0)$ can not be chosen, but has to be accepted as is. Because of this, real world data typically only cover a fraction of

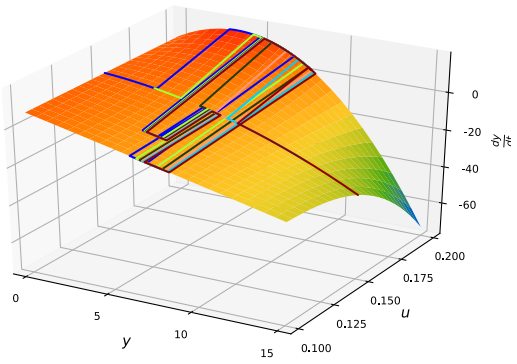

Figure 4. Experimental data from a range of initial states $y(0)$ over a control variation $u(t)$. Comparison with true vector field surface.

the vector field surface. On the other hand, if the purpose of model fitting is to develop a surrogate (or: simplified) model of a more complex model, we have much more freedom in choosing $y(0)$.

4.3 FNN based surrogate models

Building a continuous model based on $(y,u) \to \frac{\mathrm{d}y}{\mathrm{d}t}$ as in Section 2.6, and based on the data in Section 4.2 leads to the results in Figure 5.

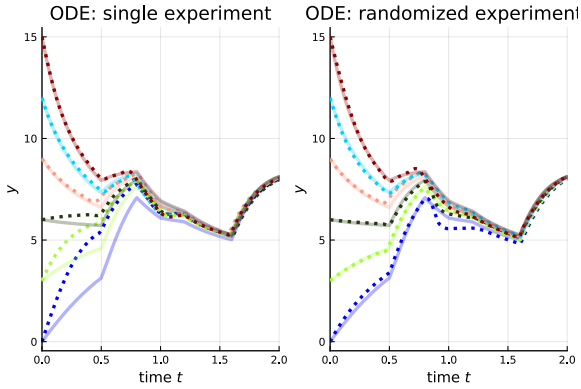

Figure 5. Solid lines: experimental data. Dotted lines: fitted FNN model $\frac{\mathrm{d}y}{\mathrm{d}t} = \mathrm{FNN}_{\mathrm{c}}(y,u)$. Left panel: using only data from experiment with $y(0) = 15$. Right panel: using all available data.

Observe from the left panel of Figure 5 that models fitted to data from a particular operating regime, may be poor for other regimes.

Building a discrete time model based on $(y_{t-1}, u_t, u_{t-1}) \to y_t$ as in Section 2.6, and based on the data in Section 4.2 leads to the results in Figure 6.

Observe that the left panel results in Figure 5, are predictions based on a "moving average" of the data,

$$\hat{y}_t = \mathrm{FNN}_{\mathrm{d,PE}}(y_{t-1}, u_t, u_{t-1});$$

with the given prediction error (PE) loss function, this is the correct predictor formulation. The right panel results in Figure 5 are based on a recursive predictor

$$\hat{y}_t = \mathrm{FNN}_{\mathrm{d,PE}}(\hat{y}_{t-1}, u_t, u_{t-1})$$

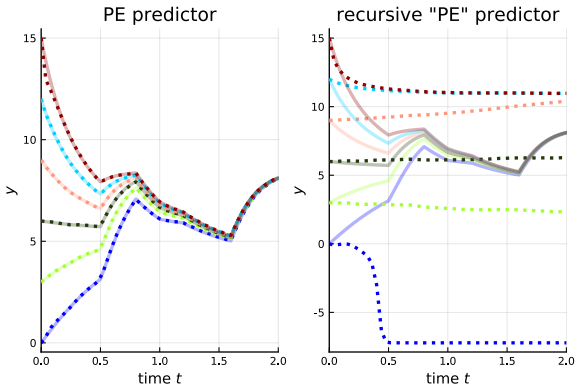

Figure 6. Solid lines: experimental data. Dotted lines: fitted FNN model $y_t = \mathrm{FNN}_{\mathrm{d}}(y_{t-1}, u_t, u_{t-1})$ using all available data. Left panel: PE predictor, Right panel: ad hoc recursive use of PE predictor.

which is somewhat ad hoc, Section 2.6. From Figure 6, the ad hoc recursive model is not suitable for long range predictions.

Next, we consider building a discrete time model based on $(y_{t-1}, \ldots, y_{t-5}, u_t, \ldots, u_{t-5}) \to y_t$ as in Section 2.6, and based on the data in Section 4.2 leads to the results in Figure 7.

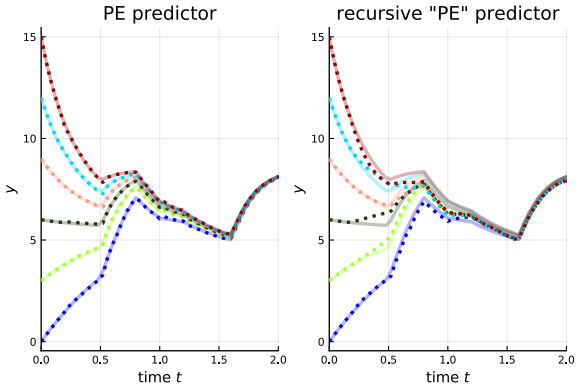

Figure 7. Solid lines: experimental data. Dotted lines: fitted FNN model $y_t = \mathrm{FNN}_{\mathrm{d}}(y_{t-1}, \ldots, y_{t-5}, u_t, \ldots, u_{t-5})$ using all available data. Left panel: PE predictor, Right panel: ad hoc recursive use of PE predictor.

With this more complex model, both the "moving average" predictor

$$\hat{y}_t = \mathrm{FNN}_{\mathrm{d,PE}}(y_{t-1}, \ldots, y_{t-5}, u_t, \ldots, u_{t-5});$$

with the given prediction error (PE) loss function, the recursive ad hoc PE predictor

$$\hat{y}_t = \mathrm{FNN}_{\mathrm{d,PE}}(\hat{y}_{t-1}, \ldots, \hat{y}_{t-5}, u_t, \ldots, u_{t-5}) \qquad (10)$$

give decent predictions — even with the use of $n_\xi^{(1)} = 3$ nodes in the hidden layer.

4.4 Hybrid model

Often, a simplified model is available which does not represent the system well over an extended operating regime.

In Figure 8, the simplified model is a linear approximation at $u = 0.15$ (left panel).

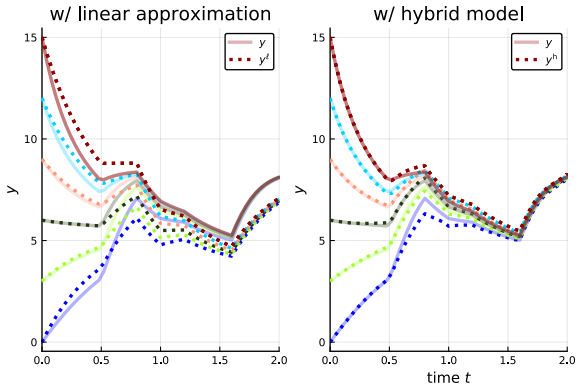

Figure 8. Solid lines: experimental data. Dotted lines: approximate models. Left panel: linear approximation, Right panel: hybrid model with ad hoc recursive PE predictor as correction to linear approximation.

With available experimental data, a model using 5 past deviations $\Delta y = y - y^\ell$ as in 10 was trained, and used to correct the linear approximation in a hybrid model $y_t^{\mathrm{h}} = y_t^\ell + \mathrm{FNN}_{\mathrm{d,PE}}(\ldots, \hat{y}_{t-j}, \ldots, u_{t-j}, \ldots)$ with results as in the right panel of Figure 8.

5 Discussion and Conclusions

This paper has aimed at illustrating some important concepts related to digital twins for control relevant models. As Figure 4 indicates, physics-based models give much more information than experimental data do — under normal operation, experimental data will only cover a small fraction of the space of inputs, states, and derivatives. However, physics-based models typically involve some approximations that makes it impossible with perfect fit to experimental data. Data driven methods normally do not impose such restrictions.

A sub goal has been to inspire to experiment with freely available computing tools for machine learning. Examples of building both continuous time and discrete time surrogate models are given. Continuous time model building requires access to some state derivative, and give decent prediction capabilities — for the simple case where all states are available. When using Feed forward Neural Nets, the resulting model is normally a prediction error (PE) model, which in principle only offer one step-ahead prediction with limited suitability for, e.g., Model Predictive Control. By making a PE model recursive, some success may be achieved. An interesting alternative is to use Recurrent Neural Nets (RNN), which gives a state description. Due to space limitations, RNN is not treated here.

References

Peter Benner, Mario Ohlberger, Albert Cohen, and Karen E. Wilcox. *Model Reduction and Approximation: Theory and Algorithms*. SIAM, Philadelphia, USA, July 2017. ISBN 978-1611974812.

Jeff Bezanson, Alan Edelman, Stefan Karpinski, and Viral B. Sha. Julia: A Fresh Approach to Numerical Computing. *SIAM Review*, 49(1):65–98, 2017. doi:10.1137/14100067.

Christopher M. Bishop. Neural networks and their applications. *Rev. Sci. Instrum.*, 65(6):1803–1832, June 1994.

Christopher M. Bishop. *Pattern Recognition and Machine Learning*. Information Science and Statistics. Springer, April 2011. ISBN 978-0387310732.

Stephen Boyd and Lieven Vandenberghe. *Introduction to Applied Linear Algebra. Vectors, Matrices, and Least Squares*. Cambridge University Press, 2018. ISBN 978-1316518960.

Elías Cueto, David González, and Icíar Alfaro. *Proper Generalized Decompositions: An Introduction to Computer Implementation with Matlab*. Springer, March 2016. ISBN 978-3319299938.

Abdulmotaleb El Saddik. Digital Twins: The Convergence of Multimedia Technologies. *IEEE Multimedia*, 25(2):97–92, 2018. ISSN Print ISSN: 1070-986X Electronic ISSN: 1941-0166. doi:10.1109/MMUL.2018.023121167.

Jay A. Farrell and Marios M. Polycarpou. *Adaptive Approximation Based Control. Unifying Neural, Fuzzy and Traditional Adaptive Approximation Approaches*. Wiley-Interscience, Hoboken, New Jersey, 2006.

Bruce A. Finlayson. *The Method of Weighted Residuals and Variational Principles*. Classics in Applied Mathematics. SIAM, Philadelphia, 2014. ISBN 978-1611973235.

Peter Fritzson. *Principles of Object-Oriented Modeling and Simulation with Modelica 3.3: A Cyber-Physical Approach*. Wiley-IEEE Press, Piscataway, NJ, second edition, 2015. ISBN 978-1-118-85912-4.

Mario Hermann, Tobias Pentek, and Boris Otto. Design Principles for Industrie 4.0 Scenarios. In *Proceedings, 2016 49th Hawaii International Conference on System Sciences (HICSS)*. IEEE, January 2016. doi:10.1109/HICSS.2016.488.

Mike Innes. Flux: Elegant Machine Learning with Julia. *Journal of Open Source Software*, 2018. doi:10.21105/joss.00602.

Bernt Lie, Arunkumar Palanisamy, Alachew Mengist, Lena Buffoni, Martin Sjölund, Adeel Asghar, Adrian Pop, and Peter Fritzson. OMJulia: An OpenModelica API for Julia-Modelica Interaction. In *Proceedings of the 13th International Modelica Conference*, pages 699–708, February 2019. doi:10.3384/ecp19157. Regensburg, Germany, March 4–6, 2019.

Zhendong Luo and Goong Chen. *Proper Orthogonal Decomposition Methods for Partial Differential Equations*. Academic Press, 2018. ISBN 978-0128167984.

Kevin P. Murphy. *Machine Learning: A Probabilistic Perspective*. Adaptive Computation and Machine Learning. The MIT Press, August 2012. ISBN 978-0262018029.

Christopher Rackauckas and Qing Nie. DifferentialEquations.jl — A Performant and Feature-Rich Ecosystem for Solving Differential Equations in Julia. *Journal of Open Research Software*, 5(15), 2017. doi:10.5334/jors.151.

Flood Management of Lake Toke: MPC Operation under Uncertainty

Itsaso Menchacatorre[1], Roshan Sharma[1], Beathe Furenes[2], Bernt Lie[1]

[1]University of South-Eastern Norway, Porsgrunn, Norway, Bernt.Lie@usn.no
[2]Skagerak Kraft AS, Porsgrunn, Norway

Abstract

A deterministic reference tracking model predictive control (MPC) is in use at Skagerak Kraft for flood management of Lake Toke in Norway. An operational inflow estimate is used to predict the optimal gate opening at Dalsfos power station, with required constraints set by the Norwegian Water Resource and Energy Directorate (NVE). The operational inflow estimate is based on the meteorological forecast, and is uncertain; this may lead to broken concession requirements and unnecessary release of water through the floodgates. Currently not utilized, the meteorological uncertainty is quantified by an ensemble of possible weather forecasts. In this paper, quantified inflow uncertainty is studied and how this affects the operation of the current, deterministic MPC solution. Next, we develop an alternative, stochastic MPC solution based on multi objective optimization which directly takes the inflow uncertainty into consideration. A comparison of the results from both approaches concludes that the stochastic MPC solution seems to give better control by reducing the amount of water released through the flood gates. Furthermore, with less frequent update of the control signal, the benefit of the stochastic MPC is expected to increase.

Keywords: model predictive control, hydrology, uncertainty, multi objective optimization

1 Introduction

Lake Toke in Norway, is the water magazine for five run-of-river hydro power plants operated by Skagerak Kraft[1]. The Dalsfos hydro power plant is located at the outlet from Lake Toke, and the remaining plants are located along the Kragerø waterway, as shown in Figure 1. The Dalsfos dam has intakes to three turbines, and has two flood gates. A number of concession requirements specified by he Norwegian Water Resource and Energy Directorate (NVE) must be fulfilled to ensure safe and environmentally friendly operation. The requirements refer to constraints on change of flow out of the dam, a minimum downstream flow rate, specific seasonal lower and upper limits on the water level during the year, etc. The catchment area for Lake Toke is ca. 1150 km^2, and the influent flow rate to the lake from precipitation varies considerably during the year. Skagerak Kraft subscribes to a

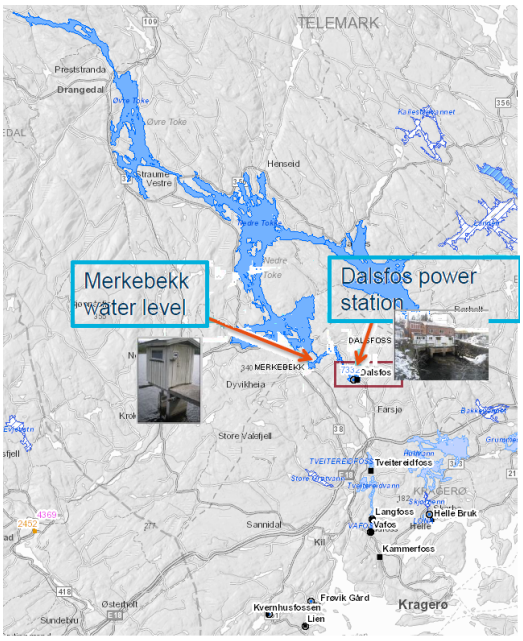

Figure 1. Overview of Lake Toke and Kragerø Waterways from (NVE, 2018).

weather forecast service provided by `Storm.no`, which provides updates twice a day of a most likely scenario as well as 51 possible meteorological scenarios indicating uncertainty. Based on these scenarios, Skagerak Kraft use a hydrological model to predict transport of water into Lake Toke. With uncertainty in the precipitation and the temperature, it is of interest to utilize the quantified uncertainty for improved accuracy. The use of ensemble predictions for flood control in real time is widely studied (Raso et al., 2014), (Breckpot et al., 2013a), (Breckpot et al., 2013b), including an EU project (Butts et al., 2007).

In 2014, Skagerak Kraft commissioned an MPC prototype control algorithm from USN[2] to suggest flood gate openings, (Lie, 2014). Initially, the suggested opening is set manually. Based on the experience, an improved solution was developed and installed in late 2018. The implemented deterministic MPC solution is based solely on the operational forecast, and the control signal/proposed gate opening is recomputed every hour. It is now of interest to assess the deterministic MPC algorithm based on the

[1]www.skagerakenergi.no/forside/

[2]USN = University of South-Eastern Norway

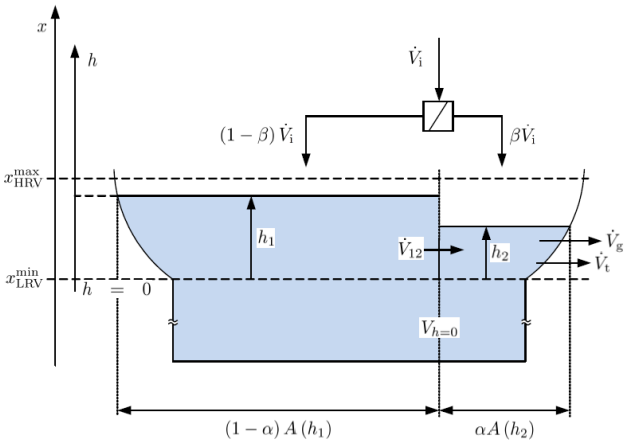

Figure 2. Assumed geometry of Lake Toke (Lie, 2014).

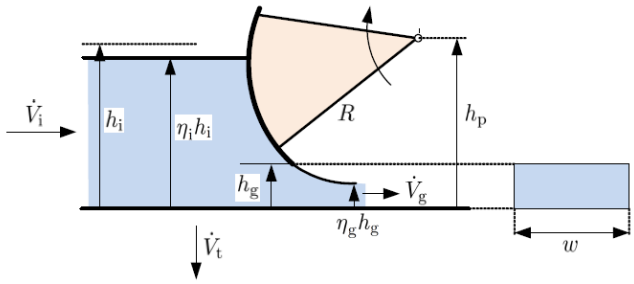

Figure 3. Assumed geometry of flood gate (Lie, 2014).

quantified uncertainty, and consider whether there is an advantage in using a stochastic MPC algorithm instead; (Schwanenberg et al., 2015) indicates advantages with a stochastic approach, see also (Nasir et al., 2018).

In the sequel, concession requirements and operation in flood situations are described. The paper is organized as follows. Section 2 provides a summary of the current MPC solution with model summary, relevant concession requirements, and deterministic MPC formulation. Section 3 provides an assessment of how the deterministic MPC solution handles quantified uncertainty. Section 4 develops a stochastic MPC solution, with operational results. Section 5 gives a comparison of the deterministic and the stochastic solution. Finally, some conclusions are drawn in Section 6.

2 Current MPC solutions

2.1 Model Summary

Figure 2 depicts a simplified layout of the lake, which is used as basis for a mass balance model.

Volumetric inflow $\dot{V}_\mathrm{i}$ to Lake Toke is a system disturbance, based on meteorological forecasts and Skagerak Kraft's hydrology model. Volumetric flow $\dot{V}_\mathrm{o}$ out of Lake Toke is the sum of flow rate through turbines ($\dot{V}_\mathrm{t}$) and flood gates ($\dot{V}_\mathrm{g}$). Turbine flow is used to produce electric power $\dot{W}_\mathrm{e}$ which is scheduled daily by economists; $\dot{W}_\mathrm{e}$ is considered a given disturbance, and $\dot{V}_\mathrm{t}$ is back-computed from $\dot{W}_\mathrm{e}$ and other quantities. Flood gate flow rate $\dot{V}_\mathrm{g}$ should ideally be zero to conserve water for energy production. Because production is constrained to $\dot{V}_\mathrm{t} \leq 36\,\mathrm{m}^3/\mathrm{s}$, the flood gates may be activated in flood situations to satisfy concession requirements. The gate opening denoted h_g is the control input for the MPC. Figure 3 illustrates the operation of the floodgate, resulting in a model based on Bernoulli's law.

With disturbances $\dot{V}_\mathrm{i}$ and $\dot{W}_\mathrm{e}$, and control signal h_g, a model of relevant water levels is described in (Lie, 2014). A summary of the model follows. Inflow $\dot{V}_\mathrm{i}$ and power production $\dot{W}_\mathrm{e}$ are provided by Skagerak Kraft as disturbances. States are considered to be the level offsets h_1 of Lake Toke and h_2 in front of the dam,

$$\frac{\mathrm{d}h_1}{\mathrm{d}t} = \frac{1}{(1-\alpha)A\,(h_1)}\left((1-\beta)\,\dot{V}_\mathrm{i} - \dot{V}_{12}\right) \tag{1}$$

$$\frac{\mathrm{d}h_2}{\mathrm{d}t} = \frac{1}{\alpha A\,(h_2)}\left(\beta\dot{V}_\mathrm{i} + \dot{V}_{12} - \dot{V}_\mathrm{t} - \dot{V}_\mathrm{g}\right), \tag{2}$$

with real water levels at Merkebekk Dam x_M and Dalsfos Dam x_D expressed as

$$x_\mathrm{M} = h_1 + x^{\min}_{\mathrm{LRV}} \tag{3}$$

$$x_\mathrm{D} = h_2 + x^{\min}_{\mathrm{LRV}}. \tag{4}$$

Area $A\,(h)$ is the experimentally found *filling curve* of the reservoir:

$$A\,(h) = \max\left(28\times10^6\cdot 1.1\cdot h^{\frac{1}{10}}, 10^3\right). \tag{5}$$

Inter compartment flow $\dot{V}_{12}$ is given by:

$$\dot{V}_{12} = K_{12}\cdot(h_1 - h_2)\sqrt{|h_1 - h_2|}. \tag{6}$$

Volumetric flow $\dot{V}_\mathrm{t}$ is computed from known power production $\dot{W}_\mathrm{e}$, and a simple turbine model involving modeled intake dam level x_D and downstream level x_q as

$$\dot{V}_\mathrm{t} = a\frac{\dot{W}_\mathrm{e}}{x_\mathrm{D} - x_\mathrm{q} + b} \tag{7}$$

where x_q is found by choosing the correct root of the cubic equation

$$\begin{aligned} 0 = {} & c_1 x_\mathrm{q}^3 + (c_2 - c_1 x_\mathrm{D})\,x_\mathrm{q}^2 \\ & + \left(c_3 - c_2 x_\mathrm{D} + c_4\dot{V}_\mathrm{g}\right)x_\mathrm{q} \\ & + \dot{W}_\mathrm{e} - c_3 x_\mathrm{D} - c_4\dot{V}_\mathrm{g}x_\mathrm{D} - c_5. \end{aligned} \tag{8}$$

In reality, x_q is measured, but we need a model for x_q for predictions.

The model for flow $\dot{V}_{\mathrm{g},j}$ through floodgate j is

$$\dot{V}_{\mathrm{g},j} = C_\mathrm{d} w_j \min\left(h_\mathrm{g}, h_2\right)\sqrt{2g\max\left(h_2, 0\right)}; \tag{9}$$

the two flood gates are identical except for their width w_j, and the total flood gate flow $\dot{V}_\mathrm{g}$ is the sum, $\dot{V}_\mathrm{g} = \dot{V}_{\mathrm{g},1} + \dot{V}_{\mathrm{g},2}$.

Parameters for the model are given in Table 1.

Table 1. Parameters for Lake Toke model.

Parameter	Value	Unit	Comment
α	0.05	–	Fraction of surface area in compartment 2.
β	0.02	–	Fraction of inflow to compartment 2.
K_{12}	800	$\mathrm{m}^{\frac{3}{2}}/\mathrm{s}$	Inter compartment flow coefficient
C_d	0.7	–	Discharge coefficient, Dalsfos gates
w_1	11.6	m	Width of Dalsfos gate 1
w_2	11.0	m	Width of Dalsfos gate 2 Comment
$x_{\mathrm{LRV}}^{\min}$	55.75	m	Minimal low regulated level value
g	9.81	m/s^2	Acceleration of gravity
a	124.69	Pa^{-1}	coefficient, 7
b	3.161	m	coefficient, 7
c_1	0.13152	W/m^3	polynomial coefficient, 8
c_2	-9.5241	W/m^2	polynomial coefficient, 8
c_3	$1.7234 \cdot 10^2$	W/m	polynomial coefficient, 8
c_4	$-7.7045 \cdot 10^{-3}$	Pa/m	polynomial coefficient, 8
c_5	$-8.7359 \cdot 10^{-1}$	W	polynomial coefficient, 8

2.2 Concession Requirements

Concession requirements are specified by NVE, and focus on (i) providing safety, (ii) securing ecological diversity, and (ii) avoiding damage to property, e.g., by maintaining certain minimum and maximum levels at Merkebekk. The key constraints for a flood situation are:

1. Abrupt changes of the water flow downstream from Dalsfos power station should be avoided for safety reasons; this is a qualitative requirement.

2. The water level x_M of Lake Toke at Merkebekk must lie in the seasonally varying interval $x_\mathrm{M} \in [x_\mathrm{LRV}, x_\mathrm{HRV}]$. Here x_LRV refers to the lowest regulated value and x_HRV to the highest regulated value. Level constraints are given in Figure 4.

3. In the event of a flood estimated to more than an instantaneous value of $200\,\mathrm{m}^3/\mathrm{s}$, $x_\mathrm{M} > x_\mathrm{HRV}$ is allowed until the flood has culminated; after flood culmination, x_M is required to decrease steadily until the water level reaches x_HRV again.

4. In case of little snow in the catchment ($< 150\,\mathrm{Mm}^3$) as the winter production comes to an end, the summer lower limit must be met at once by the reservoir. Thus, the flow should be limited to $\dot{V}_\mathrm{o} = \dot{V}_\mathrm{t} + \dot{V}_\mathrm{g} \leq 20\,\mathrm{m}^3/\mathrm{s}$ until the level is reached for the first time.

2.3 Reference Tracking MPC Operation under Uncertainty

Model Predictive control (MPC) is an algorithm that continuously solves an optimal control problem at each time step, with a performance measure involving a future time horizon. At each time step, only the first computed control input is used to change model states. Before each re-optimization, updated information about states is used;

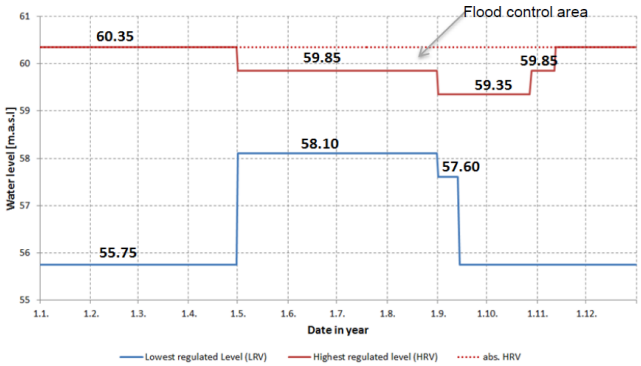

Figure 4. Level constraints in Lake Toke during the year.

this provides feedback in MPC. This MPC strategy is also known as receding horizon or sliding horizon optimal control, (Sharma, 2017). For the currently implemented MPC algorithm at Skagerak, the following quantities are relevant:

- Reference *region* (r): $\mathscr{R}$
- Control input (u_c): h_g
- Disturbances (u_d): $\dot{V}_\mathrm{i}, \dot{W}_\mathrm{e}$
- Outputs (y): $x_\mathrm{M}, x_\mathrm{D}, \dot{V}_\mathrm{t}, \dot{V}_\mathrm{g}, \dot{V}_\mathrm{o}$
- States (x): h_1, h_2

The following cost function is used, (Lie, 2014),

$$\mathscr{J}_t = \sum_{i=1}^{H} w_{\mathscr{R}} \mathscr{R}^2 (x_{\mathrm{M},t+i}) + w_{\Delta u} \Delta u_{\mathrm{c},t+i-1}^2 + w_u u_{\mathrm{c},t+i-1}^2 \tag{10}$$

where H is the length of the horizon and

$$\Delta u_{\mathrm{c},t+i-1} \triangleq u_{\mathrm{c},t+i-1} - u_{\mathrm{c},t+i-2},$$

and subject to the dynamic model of the system:

$$x_{i+1} = f\left(x_i, u_{\mathrm{c},i}, u_{\mathrm{d},i}\right) \tag{11}$$

Expression $\mathscr{R}\left(x_{\mathrm{t+i}}\right)$ is related to the level at Merkebekk in such a way that:

$$\mathscr{R}\left(x_{\mathrm{M},t+i}\right) = \min\left(x_{\mathrm{M},t+i} - r^{\ell}_{t+i}, 0\right) + \max\left(x_{\mathrm{M},t+i} - r^{\mathrm{u}}_{t+i}, 0\right).$$

Here r^{ℓ}_{t+i} and r^{u}_{t+i} are lower and upper reference region boundaries, respectively. The implication of this formulation is that as long as $x_{M,t+i} \in \left[r^{\ell}_{t+i}, r^{\mathrm{u}}_{t+i}\right]$, $\mathscr{R}\left(x_{\mathrm{M},t+i}\right) = 0$. When $x_{\mathrm{M},t+i} \notin \left[r^{\ell}_{t+i}, r^{\mathrm{u}}_{t+i}\right]$, this is penalized in the cost function. With this in mind, the reference region boundaries are chosen based on the knowledge that emptying Lake Toke is faster than filling it, thus, being closer to x_{HRV} is considered less risky.

MPC provides feedback to reduce the effect of model errors and unknown disturbances, and feed-forward to take into account future reference values and known disturbances, while also handling hard constraints on variables. With many free variables in the optimization problem, solution time may be considerable. In this case, the operational forecast is 294 intervals (approximately 12 d with hourly updates) and two flood gates. By constraining the two flood gate openings to one free variable and grouping the control predictions into 3 groups constant value in each group, the problem is reduced to 3 free variables. From an optimal control point of view, this is a crude approximation. However, MPC's approach of frequent recomputation of the control inputs leads to satisfactory results. In summary, every hour, a set of gate opening proposals together with predicted water levels are obtained for the specified horizon.

3 Stochastic analysis of a deterministic MPC

3.1 Simulation principle

The available flow rate scenarios 294 steps into the future into Lake Toke, $\dot{V}_{\mathrm{i},1:294}$, consist of the operational forecast $\dot{V}^{(\mathrm{o})}_{\mathrm{i},t}$ and 50 "particles" $\dot{V}^{(p)}_{\mathrm{i},t}$ which can be described in a matrix,

$$\dot{V}_{\mathrm{i},1:294} \in \begin{pmatrix} \dot{V}^{(\mathrm{o})}_{\mathrm{i},1} & \dot{V}^{(1)}_{\mathrm{i},1} & \cdots & \dot{V}^{(50)}_{\mathrm{i},1} \\ \vdots & \vdots & \ddots & \vdots \\ \dot{V}^{(\mathrm{o})}_{\mathrm{i},294} & \dot{V}^{(1)}_{\mathrm{i},294} & \cdots & \dot{V}^{(50)}_{\mathrm{i},294} \end{pmatrix}. \tag{12}$$

Updated predictions are available twice daily. The morning forecast is available in the normal working hours. For simplicity, only the morning forecast is used in this study. Figure 5 depicts a forecast for the first day.

The resulting multi day forecast looks as in Figure 6.

With the deterministic MPC algorithm, the inflow prediction $u_{\mathrm{d},i}$ used in predicting states via 11 and thus influencing the value of the cost function $\mathscr{J}_{\mathrm{t}}$ of 10, are *always*

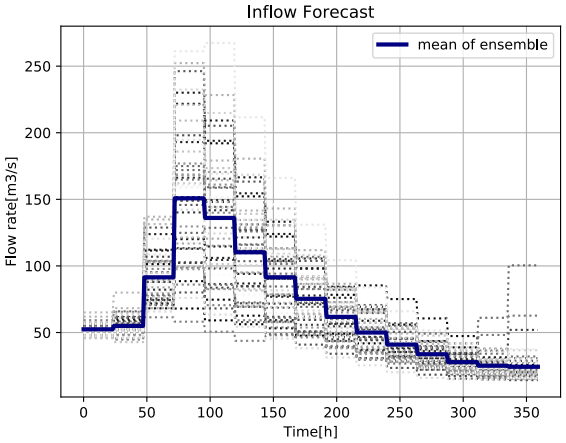

Figure 5. Inflow forecast $\dot{V}_{\mathrm{i}}$ for 294 steps into the future at Day 1.

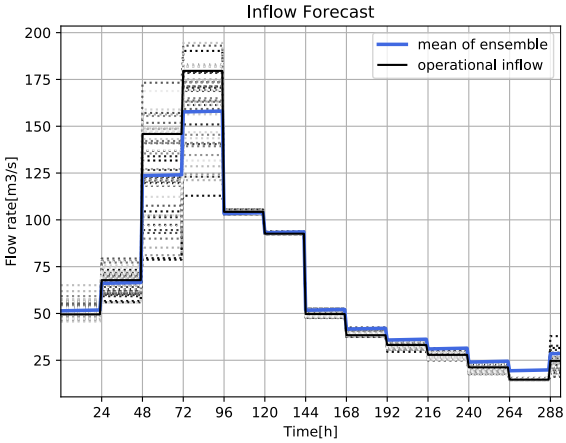

Figure 6. Inflow forecast $\dot{V}_{\mathrm{i}}$, updated every day when new forecasts are made available.

the operational values of $\dot{V}_{\mathrm{i}}$ found in the first column of the matrix in 12. The outcome of optimizing $\mathscr{J}_{\mathrm{t}}$ is an optimal sequence of future control inputs h_{g}; only the first of these inputs is used.

To assess how the deterministic MPC algorithm would work with the given uncertainty, in turn we consider each of the 50 additional "particles" of inflows $\dot{V}^{(p)}_{\mathrm{i}}$ where $p \in \{1, \ldots, 50\}$ in the matrix of 12. These 50 particles are thought to represent *reality* in 50 parallel "universes", while the operational inflow $\dot{V}^{(\mathrm{o})}_{\mathrm{i}}$ represents the idealized model inflow. For each "universe", the inflow $\dot{V}^{(p)}_{\mathrm{i}}$ is used to update the "real" state according to 11:

$$x^{(p)}_{t+1} = f\left(x^{(p)}_{t}, u^{(p)}_{\mathrm{c},t}, u^{(p)}_{\mathrm{d},t}\right), \tag{13}$$

where $u^{(p)}_{\mathrm{d},t} = \dot{V}^{(p)}_{\mathrm{i},t}$, while input $u^{(p)}_{\mathrm{c},t}$ is the input computed from optimizing $\mathscr{J}_t$ with initial value $x^{(p)}_t$ and operational input predictions $\dot{V}^{(\mathrm{o})}_{\mathrm{i},t+i}$. With $x^{(p)}_{t+1}$ computed as in 13, $x^{(p)}_{t+1}$

is used together with operational inflow $\dot{V}^{(o)}_{i,t+1+i}$ in optimizing $\mathscr{J}_{t+1}$, etc.

For each particle p in the ensemble for $\dot{V}_i$, we thus find trajectories of the evolution of water levels and the evolution of flood gate openings h_g.

3.2 Simulation results

At initial time, all particles have the same initial values for the states and the control input. Thus, computed control inputs in the first time step are the same for all the particles, since the operational forecast is fed to the MPC algorithm. By contrast, the next computed states can differ from particle to particle because ensemble disturbances are introduced. For each time instance in the evolution of the 50 particles, mean and standard deviation over the particles are used to measure the uncertainty involved in the evolution of levels and flood gate opening.

During testing of the computations in Python, it is observed that optimization of the cost function $\mathscr{J}_t$ for a single particle at a single time instance under a flood situation can take up to 30s, as opposed to 2s if the optimal solution is to keep the flood gates closed. In the simulations carried out, about 2.5-3 days were required. One way to reduce the computation time is to use less frequent control updates, e.g., recompute the control input, say, every 24 h instead of every 1 h. However, we have chosen to use a 1 h frequency of control updating with the MPC. The following conditions for the simulations are used in the uncertainty analysis.

- $x_{LRV} = 55.75\,\text{m}$ until April 30, and thereafter $x_{LRV} = 58.85\,\text{m}$.
- $x_{HRV} = 60.35\,\text{m}$ until April 30, and thereafter $x_{HRV} = 59.85\,\text{m}$.
- $h_g^{(0)} = 0\,\text{cm}$; initial gate levels are set to 0 cm.
- $\dot{V}_i$: inflow forecasts as in Figure 6 and $\dot{W}_e = 36\,\text{m}^3/\text{s}$.
- h_1 and h_2 are set to 59.0 and 58.8, respectively.
- $N = 294$ (length of the operational inflow forecast in hours).

Simulation results are shown in Figures 7, 8, and 9; gate opening $h_{g,2}$ is similar to $h_{g,1}$. The particles of possible outcomes are represented by gray, dotted lines. The statistics of the outcomes is represented by the mean value (blue line) and standard deviation (yellow area). In this manner, it is possible to link each particle's gate opening with corresponding water level and outflow prediction.

From the figures, it is possible to have an indication of the worst possible situation and take safety measures if needed. In Figure 7, green dashed lines show the upper and lower constraints of levels given by concession requirements. Figure 9 shows both the stochastic behavior of the water flowing through the flood gates $\dot{V}_g$ and the given flow through the turbines, $\dot{V}_t$. As Figure 6 indicates, the inflow forecasts are updated every 24 h.

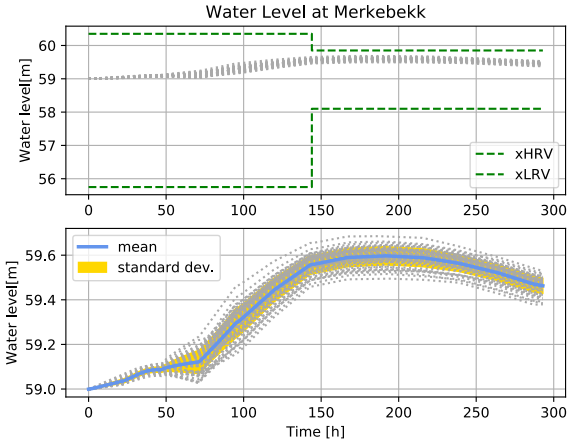

Figure 7. Water Level at Merkebekk for 50 particles with deterministic MPC: lower plot gives a detailed view of upper plot.

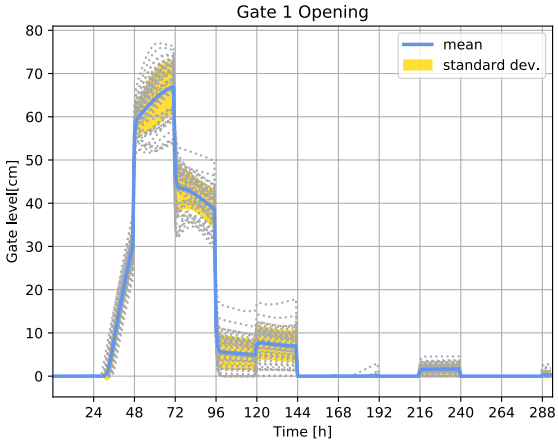

Figure 8. Gate opening h_g for 50 particles with deterministic MPC.

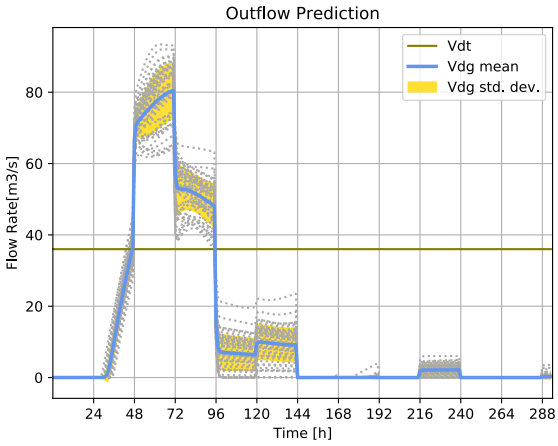

Figure 9. Flow out $\dot{V}_g$ and $\dot{V}_t$ for 50 particles with deterministic MPC.

4 Stochastic MPC

4.1 Stochastic MPC approach

Stochastic MPC algorithms can be posed in different ways, e.g., as scenario tree based algorithms (Raso et al., 2014), (Krishnamoorthy et al., 2018), or as multi objective based algorithms (Peitz and Dellnitz, 2018). Here, the focus is on a multi objective based algorithm.

Multi objective optimization (MOO) is based on trying to satisfy a set of objectives with their individual constraints, at the same time. MOO is often a way to find solutions as a best compromise among competing objectives, in a Pareto front manner, e.g., (Boyd and Vandenberghe, 2018). A simple way to handle MOO is to create a combined objective as a scalar weighing of all objectives, while simultaneously satisfying all constraints, (Marler and Arora, 2010), (Sharma, 2017). In the case of our MPC problem, we create an objective $\mathscr{J}_t^{(p)}$ for each of the particles p (each column) in the inflow matrix of 12. Our formulation has only constraints on the gate opening, $h_{\mathrm{g}}^{(p)}$. There is no reason to say that one objective is more important than the others, so we simply sum the objectives for each particle to set up the total objective,

$$\mathscr{J}_t = \sum_p \mathscr{J}_t^{(p)}. \tag{14}$$

The constraints are given by the models with each individual inflow particle $\dot{V}_{\mathrm{i}}^{(p)}$, and we require that the control input $h_{\mathrm{g}}^{(p)}$ is the same for each particle, i.e., $h_{\mathrm{g}}^{(1)} = \ldots h_{\mathrm{g}}^{(50)}$.

4.2 Simulation results

The MOO algorithm can use up to 20 min for each optimization under a flood situation. If implemented in in a real time system, this would imply a 20 min time delay in the control loop would reduce the performance of the controller. In our simulation study, we may neglect this time delay. Simulating the system with hourly sampling time for a 294 h horizon, this implies about 100 h (4 d) of simulation time

The conditions for the experiment are as in Section 3.2. With this stochastic MPC algorithm, the operational inflow is still used as the prediction of inflow in the cost functions $\mathscr{J}_t^{(p)}$, and the total cost function $\mathscr{J}_t$ is found by summing over all particles p as in 14. This time, the operational input is also used to represent "reality", i.e., in updating the real water levels according to

$$x_{t+1} = f\left(x_t, u_{\mathrm{c},t}, u_{\mathrm{d},t}^{(\mathrm{o})}\right), \tag{15}$$

where $u_{\mathrm{d},t}^{(\mathrm{o})} = \dot{V}_{\mathrm{i},t}^{(\mathrm{o})}$, while input $u_{\mathrm{c},t}$ is the input computed from optimizing $\mathscr{J}_t$ according to 14 with initial value x_t and operational input predictions $\dot{V}_{\mathrm{i},t+i}^{(\mathrm{o})}$.

The water level result is shown in Figure 10; the blue curve represents the water level at Merkebekk for which the concession requirements are imposed, while the red curve is the water level at Dalsfos. Likewise, the gate opening result can be seen in Figure 11, with $h_{\mathrm{g},1}$ (blue line) and $h_{\mathrm{g},2}$ (red line). The predicted outflow result is described in Figure 12, with $\dot{V}_{\mathrm{t}}$ (red line), $\dot{V}_{\mathrm{g}}$ (blue line), and $\dot{V}_{\mathrm{o}} = \dot{V}_{\mathrm{t}} + \dot{V}_{\mathrm{g}}$ (yellow line).

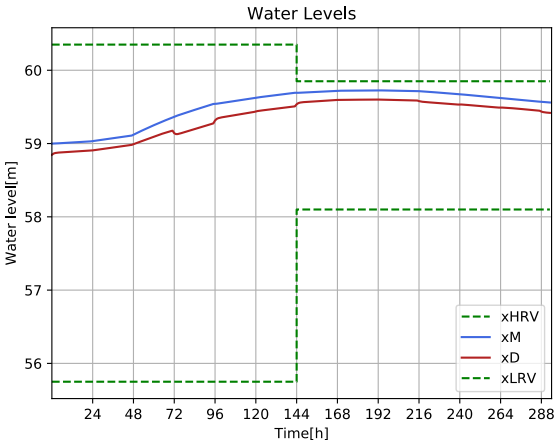

Figure 10. Predicted Water Levels.

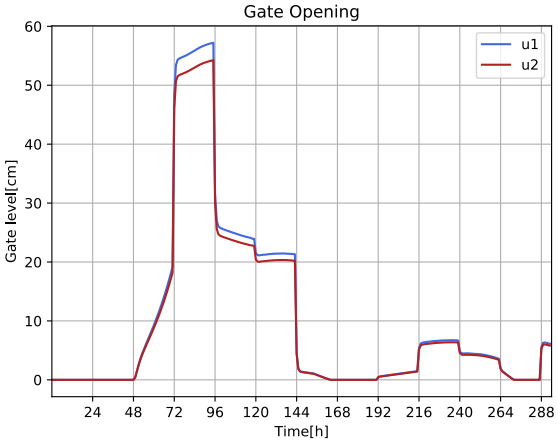

Figure 11. Optimal Gate Openings.

5 Deterministic vs. Stochastic MPC

In both the deterministic case and the MOO case, Figure 6 illustrates the inflow disturbances. In the deterministic approach, the operational inflow is the "deterministic" disturbance used in the MPC algorithm while each of the particles are used to compute corresponding water levels. By contrast, in the MOO stochastic MPC approach, the MPC algorithm uses all particles, while the operational inflow is used to compute water levels.

Figures 13–16 illustrate the difference in behavior of the deterministic controller vs. that of the stochastic controller; in the legends, variable `x_mean` indicates the mean value of variable `x` for the particles in the deterministic MPC solution, while `x_MOO` simply is variable `x` for

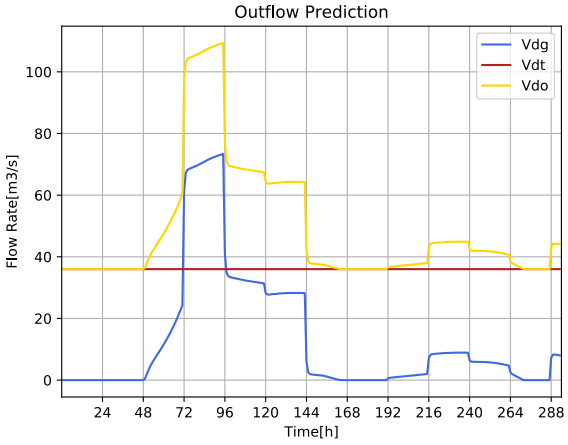

Figure 12. Predicted outflow.

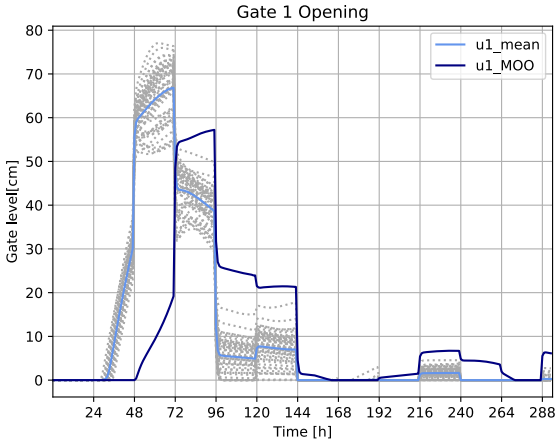

Figure 15. Optimal gate opening $h_{g,1}$ comparison.

the stochastic multi objective optimization based (MOO) MPC algorithm.

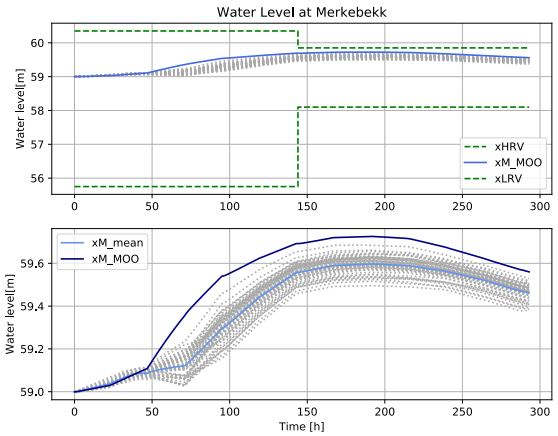

Figure 13. Merkebekk water level x_M comparison: lower plot gives a detailed view of upper plot.

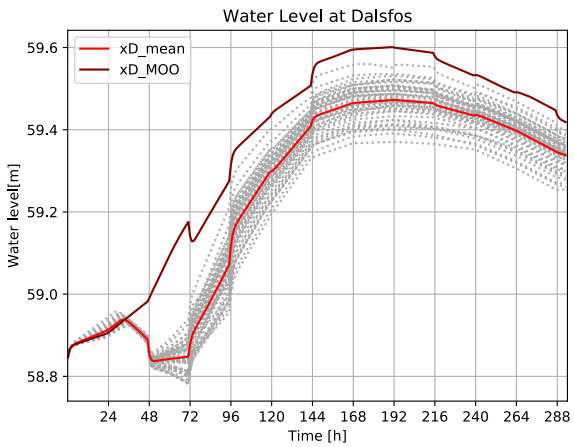

Figure 14. Dalsfos water level x_D comparison.

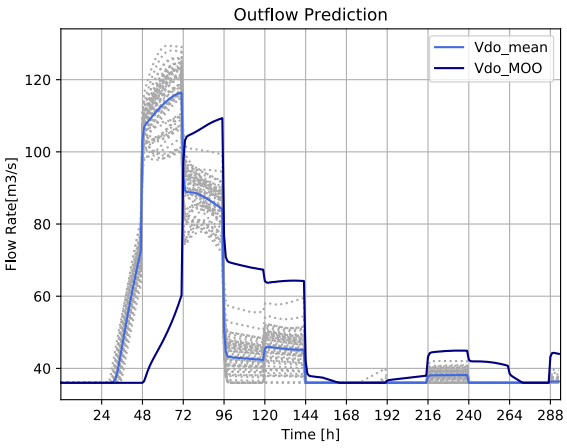

Figure 16. Predicted outflow $\dot{V}_o$ comparison.

Figure 13 displays the predicted water levels at Merkebekk. The dark blue curve (`xM`) refers to the water level for the MOO case. The gray dotted curves together with the light blue curve (`xM_mean`) corresponds to the water level result from the deterministic approach. In the simulated case, none of the constraints are broken.

Figure 14 displays the predicted water levels at Dalsfos. The dark red curve (`xD`) refers to the water level for the MOO case. The gray dotted curves together with the light red curve (`xD_mean`) corresponds to the water level result from the deterministic approach.

Figure 15 illustrates the resulting gate opening $h_{g,1}$. The dark blue curve (`u1`) refers to the gate opening for the MOO case. The gray dotted curves together with the light blue curve (`u1_mean`) corresponds to the deterministic approach.

Figure 16 shows the predicted outflow. The dark blue curve (`Vdo`) refers to the water flow rate for the MOO case. The gray dotted curves together with the light blue curve (`Vdo_mean`) corresponds to the flow rate result for the deterministic approach. As expected, the behavior is consistent with the gate openings.

6 Conclusions

The stochastic MOO MPC gives markedly better results than the current, deterministic MPC, indicating a clear advantage in introducing a more advanced stochastic MPC algorithm. It should be noted that the study reported here is limited since only a single instance of real inflow predictions and measurements under flood conditions has been available. Furthermore, it has been assumed that the control input is recomputed every 1 h *and* injected every 1 h without delay. In reality, with manual injection of the computed control inputs, these may be injected irregularly and with time delay. This manual injection of the control input will lead to a more pronounced effect of the uncertainty. Thus, in real life, a stochastic MOO MPC algorithm may be even more advantageous than what appears in the comparison of Section 5.

It is therefore recommended to further the study initiated here, with other flood periods. In particular, the operational forecast may lie in the mainstream of the ensemble as in Figures 5 and 6; other times, the operational forecast lies at the outskirts of the ensemble: the location of the operational forecast within the ensemble may influence the relative advantage of using stochastic MOO MPC. The reported computation time for finding the control signal in the MOO algorithm can be significantly reduced. Examples of strategies to reduce the computation time are utilizing parallelization over threads, more efficient Python code, compiled code, etc.

References

Stephen Boyd and Lieven Vandenberghe. *Introduction to Applied Linear Algebra. Vectors, Matrices, and Least Squares*. Cambridge University Press, 2018. ISBN 978-1316518960.

Maarten Breckpot, Oscar Mauricio Agudelo, and Bart L.R. De Moor. Flood Control with Model Predictive Control for River Systems with Water Reservoirs. *Irrigation and Drainage Engineering*, 139:532–531, 2013a. doi:10.1061/(ASCE)IR.1943-4774.0000577.

Maarten Breckpot, Oscar Mauricio Agudelo, Pieter Meert, Patrick Willems, and Bart De Moor. Flood control of the Demer by using Model Predictive Control. *Control Engineering Practice*, 21(12):1776–1787, December 2013b. doi:10.1016/j.conengprac.2013.08.008.

Michael B. Butts, Anne Katrine V. Falk, Yunqing Xuan, and Ian D. Cluckie. Integrating meteorological and uncertainty information in flood forecasting: the FLOODRELIEF project. *IAHS*, 313:385–397, July 2007.

Dines Krishnamoorthy, Bjarne Foss, and Sigurd Skogestad. A distributed algorithm for scenario-based model predictive control using primal decomposition. *IFAC PapersOnLine*, 51 (18):351–356, 2018.

Bernt Lie. Final report: KONTRAKT NR INAN-140122 Optimal Control of Dalsfos Flood Gates- control algorithm, 2014.

R. Timothy Marler and Jasbir S. Arora. The weighted sum method for multi-objective optimization: new insights. *Structural and Multidisciplinary Optimization*, 41(6):853–862, Jun 2010. ISSN 1615-1488. doi:10.1007/s00158-009-0460-7. URL https://doi.org/10.1007/s00158-009-0460-7.

Hasan Arshad Nasir, Tony Zhao, Algo Carè, Quan J. Wang, and Erik Weyer. Efficient river management using stochastic mpc and ensemble forecast of uncertain in-flows. *IFAC PapersOnLine*, 51(5):37–42, 2018. doi:10.1016/j.ifacol.2018.06.196.

NVE. The Norwegian Water Resources and Energy Directorate, 2018. URL https://temakart.nve.no/link/?link=vannkraft&layer=0,8&field=kdbNr&value=7332&buffer=3000.

Sebastian Peitz and Michael Dellnitz. A survey of recent trends in multiobjective optimal control — surrogate models, feedback control and objective reduction. *Mathematical and Computational Applications*, 23(30):1–33, 2018. ISSN 2297-8747. doi:10.3390/mca23020030. URL http://www.mdpi.com/2297-8747/23/2/30.

Luciano Raso, Dirk Schwanenberg, Nick van de Giesen, and Peter Jules van Overloop. Short-term optimal operation of water systems using ensemble forecasts. *Advances in Water Resources*, 71:200–208, September 2014. doi:10.1016/j.advwatres.2014.06.009.

Dirk Schwanenberg, Fernando Mainardi Fan, Steffi Naumann, Julio Issao Kuwajima, Rodolfo Alvarado Montero, and Alberto Assis dos Reis. Short-Term Reservoir Optimization for Flood Mitigation under Meteorological and Hydrological Forecast Uncertainty. *Water Resour Manage*, 29(5):1635–1651, March 2015. ISSN 0920-4741. doi:10.1007/s11269-014-0899-1. URL https://link.springer.com/article/10.1007/s11269-014-0899-1.

Roshan Sharma. *Lectures notes for course IIA 4117: Model Predictive Control*, 2017.

Structural analysis in Julia for dynamic systems in OpenModelica

Liubomyr Vytvytskyi Bernt Lie

Department of Electrical engineering, Information Technology and Cybernetics, University of South-Eastern Norway, Porsgrunn, Norway, {Liubomyr.Vytvytskyi,Bernt.Lie}@usn.no

Abstract

In control theory for dynamic systems, the information about observability and controllability of states plays a key role to evaluate the possibility to observe states from outputs, and use inputs to move states to a desired position, respectively. Th automatic determination of observability and controllability is possible, in particular for linear models where typically observability and controllability grami-ans are considered. In the case of large scale systems, e.g., complex models of regional energy systems, standard analysis becomes challenging. For large scale systems, structural analysis based on directed graphs is an interesting alternative: structural observability (or: controlla-bility) is a necessary requirement for actual observability (or: controllability). Directed graphs can be set up directly for linear models, but can also be extracted from nonlinear models.

Modelica is a suitable language for describing large scale models, but does not support graph algorithms. One possibility is to integrate the Modelica model into a language supporting graph algorithms, e.g., Julia: this integration can be done using package OMJulia which works with the free tool OpenModelica. OMJulia does not give direct access to the nonlinear model in Modelica, but a linear model approximation can be extracted and used for setting up the system graph. In this study, an experimental implementation of automated structural analysis is done in Julia using the *LightGraphs.jl* package. As an example, this structural analysis is tested on hydropower models of different complexity that are modelled in OpenModelica using our in-house hydropower Modelica library — *OpenHPL*, where different models for hydropower systems are assembled.

Keywords: observability, controllability, structural analysis, graph theory

1 Introduction

1.1 Background

Modelling and simulation of dynamic systems (e.g., a hydropower system in this paper) plays an important role as efficient analysis tools for control analysis and design. As an example, tools for designing a new or testing an existing controller for stability and performance in different operating regimes might be of interest.

Model based analysis of state observability and controllability is important for control design, and it is of interest to consider tools for aiding such analysis. Classically, observability and controllability properties might be checked using the well known tests based on rank conditions, (Simon, 2006; Šiljak, 2011). However, numerical problems can arise for the rank computations in complex, large scale systems. Still, structural observability and controllability based on the system structure can be used in such cases due to the simplicity of these methods. In addition, a relative degree of the system indicates how directly control inputs affect outputs, and can also be defined based on the system structure. Assuming linear models, analysis tools based on graph theory can be implemented in Julia[1], e.g., using the *LightGraphs.jl* package.

Models of various dynamic systems might be directly modeled in Julia using the *DifferentialEquations.jl*[2] (Rackauckas and Nie, 2017) and *ControlSystems.jl*[3] packages. However, an object-oriented language such as Modelica[4] has richer support for describing complex, large scale systems with inputs and outputs. One such Modelica based tool is OpenModelica[5] which offers an open-source modeling and simulation environment. OpenModelica also comes with the OMJulia.jl package which offers integration of Modelica models in Julia.

1.2 Previous Work

Basic graph theory for different engineering applications is provided in (Deo, 2017). Structural modeling and analysis of complex systems are described by (Šiljak, 2007, 2011; Lunze, 1992; Boyd and Vandenberghe, 2018). Based on this graph theory, large scale systems can be further tested and analyzed for control and parameter estimation purposes; see, e.g., (Perera, 2016) who used structural analysis of Modelica models in JModelica[6] and Python[7] to analyze an industrial copper electrowinning process.

The OMJulia package[8] (Julia API) for OpenModelica provides possibilities to run simulations and carry out linearization of OpenModelica. Julia in turn gives rich possibilities for plotting, analysis, and optimization (e.g., using

[1] https://julialang.org/
[2] https://goo.gl/5wxZfR
[3] https://goo.gl/d2xyf2
[4] https://www.modelica.org
[5] https://openmodelica.org
[6] https://jmodelica.org/
[7] https://www.python.org
[8] https://goo.gl/WpAMds

Julia packages *Plots.jl*, *LightGraph.jl*, *JuMP.jl*, etc.).

Some work on modeling a waterway for high head hydropower system together with a generator, a Francis turbine, and a governor, has already been carried out using OpenModelica (Vytvytskyi and Lie, 2017, 2018a). Unit models have been assembled in our in-house Modelica library *OpenHPL*[9]. Similarly to Julia, a Python API[10] for OpenModelica already exists and a use of this API for the *OpenHPL* is presented in (Vytvytskyi and Lie, 2018b).

1.3 Overview of Paper

In this paper, the main contribution is the prototyping and testing of automated structural analysis for dynamic systems in Julia using directed graphs from the *LightGraphs.jl* package.

The paper is structured as follows: Section 2 gives an overview of the graph and structural analysis theory. The Julia implementation of these analysis methods is discussed in Section 3. Applying the structural analysis methods on hydropower models is presented in Section 4. Finally, discussion and conclusions are given in Section 5.

2 Structural analysis

Structural analysis of models is the evaluation of model behavior base on a model structure. In this study, the model structure is represented by graphs. That is why, the graph theory is described first.

2.1 Graph theory

A graph G connects nodes (vertices, points) $N = \{n_1, n_2, \ldots, n_N\}$ via edges (lines) $E = \{e_1, e_2, \ldots, e_E\}$. Here, we will consider a *directed graph* (digraph); a digraph may be defined by a relation R consisting of a set of *ordered pairs* (n_i, n_j) with unidirectional information flow between these nodes.

As examples, Fig. 1 shows the undirected graph G_1 (left) and the directed graph G_2 (right). Observe that each pair corresponds to an edge; G_1 has 5 edges because its relation R_1 holds 5 (unordered) pairs, while G_2 has 6 edges because R_2 holds 6 (ordered) pairs.

Instead of describing the graph via a relation, it can be described via either an *adjacency* matrix A or an *incidence* matrix I. The incidence matrix description I with $\dim I = n_E \times n_N$ relates edges and nodes. The incidence matrix is not suitable for describing self edges, and is not discussed further here.

The adjacency matrix relates unidirectional flow between two nodes, and is defined by $A_{i,j} = 1$ for $(i,j) \in R$, or $A_{i,j} = 0$ for $(i,j) \neq R$ The adjacency matrix is square, $\dim A = n_N \times n_N$, with nodes represented by both rows and columns. Adjacency matrix A_2 for G_2 in Fig. 1 is $A_2 = \begin{smallmatrix} 1 & 1 & 0 & 0 \\ 0 & 0 & 1 & 0 \\ 1 & 1 & 0 & 0 \\ 0 & 1 & 0 & 0 \end{smallmatrix}$. Observe that nonzero diagonal elements

[9]Open Hydro Power Library is developed by the first author within his PhD study.

[10]https://goo.gl/Qyjqq2

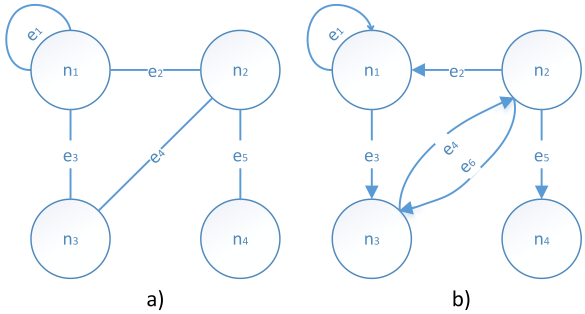

Figure 1. Examples of (a) undirected graph, and (b) directed graph.

in the adjacency matrix implies self edges, i.e., edges that emanates from the node and returns to the node.

An important concept in graph theory is the length ℓ between two nodes: the length is the number of nodes traversed to go from node n_i to node n_j. In G_2 of Fig. 1, the length in going from n_1 to n_1 is $\ell = 1$ because of the self edge. The length in going from n_1 to n_3 is $\ell = 1$ because there is an edge from n_1 to n_3. The length in going from n_1 to n_2 is $\ell = 2$: it is necessary to first go from n_1 to n_3, and then from n_3 to n_2.

The same principal can be used to represent a model structure of linear models with inputs and outputs, (Šiljak, 2011). These models can be represented by Eq. 1:

$$\begin{aligned} \dot{x} &= Ax + Bu \\ y &= Cx + Du \end{aligned} \tag{1}$$

Here, $x \in \mathbb{R}^{n_x}$ is the state, $u \in \mathbb{R}^{n_u}$ is the input/control signal, and $y \in \mathbb{R}^{n_y}$ is the output. $A \in \mathbb{R}^{n_x \times n_x}$, $B \in \mathbb{R}^{n_x \times n_u}$, $C \in \mathbb{R}^{n_y \times n_x}$ and $D \in \mathbb{R}^{n_y \times n_u}$ are constant matrices and consist of elements $a_{i,j}$, $b_{i,j}$, $c_{i,j}$ and $d_{i,j}$, respectively.

In order to represent a structure of this system, the interconnection square matrix M should be created, (Šiljak, 2007). This interconnection matrix M combines information from all the constant matrices, A, B, C, D, and represents the relationships between states, inputs and outputs. The matrix M is found as follows:

$$M = \begin{bmatrix} A & B & 0 \\ 0 & 0 & 0 \\ C & D & 0 \end{bmatrix} \tag{2}$$

In M, the second block row is zero because u_k is an input and not a response variable, while the third block column is zero because y_k is a response variable and not an input.

2.2 Structural controllability

In control theory, the mathematical duals observability and controllability are important properties of control systems. Using controllability, it is possible to evaluate the capability of the external input capability to influence the internal state. Observability, on the other side, gives an understanding of the possibility of a system state to be inferred from an external output.

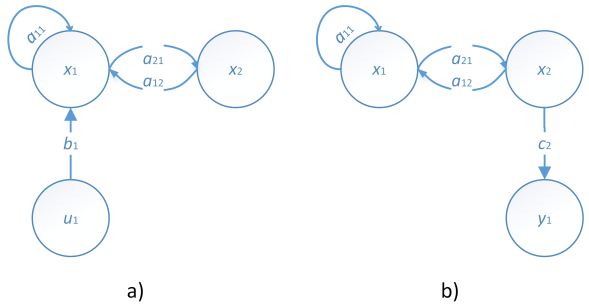

Figure 2. Examples of (a) structurally controllable, and (b) structurally observable systems.

As mentioned above, numerical problems can arise in the classical methods for observability and controllability computations in complex, large scale systems. As an alternative, structural observability and controllability are considered in this study due to the simplicity of these methods. In addition, structural observability and controllability provide necessary conditions for observability and controllability. This means that if the complex system is not structurally observable or not controllable, then it is not observable or not controllable. On the other hand, the system may be structurally observable/controllable, while in reality the system is not observable/controllable, (Šiljak, 2011).

Consider a linear system with an external input, see Eq. 1, e.g., $A = \left[\begin{smallmatrix} 1 & 1 \\ 1 & 0 \end{smallmatrix}\right]$ and $B = \left[\begin{smallmatrix} 1 \\ 0 \end{smallmatrix}\right]$. First, the system structure based on the digraph G should be created with the interconnection matrix, $M = \left[\begin{smallmatrix} 1 & 1 & 1 \\ 1 & 0 & 0 \\ 0 & 0 & 0 \end{smallmatrix}\right]$, see Fig. 2 (a). Then, structural controllability of the system can be demonstrated if there is a directed path in the digraph G from (at least one) input-node to every single state-node. As seen in Fig. 2 (a), the system is structurally controllable, because there are paths from the input-node u_1 to the state-node x_1 with the edge b_1 and to the state x_2 with the edges b_1 and $a_{2,1}$.

2.3 Structural observability

Similarly to structural controllability, structural observability requires that there is a directed path from every single state-node to (at least one) output-node in the digraph G. Let us suppose a linear system with an external output, see Eq. 1, e.g., $A = \left[\begin{smallmatrix} 1 & 1 \\ 1 & 0 \end{smallmatrix}\right]$ and $C = \left[\begin{smallmatrix} 0 & 1 \end{smallmatrix}\right]$. The interconnection matrix is then as follows, $M = \left[\begin{smallmatrix} 1 & 1 & 0 \\ 1 & 0 & 0 \\ 0 & 1 & 0 \end{smallmatrix}\right]$. The system structure based on the digraph G is created using the matrix M and is show in Fig. 2 (b). Here, the structural observability of the system is proven due to state-nodes x_1 and x_2 with directed paths ($a_{2,1}$,c_2) and (c_2) to the output node y_1, respectively.

2.4 Relative degree of system

Another property that can be found from structural analysis is the relative degree of the system, which shows how the input affects the system output. More precisely, the relative degree r represents the number of differentiations of the output y needed for the input u to appear, (Slotine and Li, 1991). From the digraph structure of the system, this relative degree can be found as the smallest number of state-nodes through which a directed path from an input-node to output-node goes.

Combining the two previous examples with one input and one output, e.g., $A = \left[\begin{smallmatrix} 1 & 1 \\ 1 & 0 \end{smallmatrix}\right]$, $B = \left[\begin{smallmatrix} 1 \\ 0 \end{smallmatrix}\right]$ and $C = \left[\begin{smallmatrix} 0 & 1 \end{smallmatrix}\right]$, it can be shown that the relative degree of the system equals two, see Fig. 2 (a) and (b) together. This is because the path from the input-node u_1 to the output-node y_1 is (b_1,$a_{2,1}$,c_2) and this path goes through two state-nodes x_1 and x_2. This statement can be also shown by the condition for relative degree r from (Slotine and Li, 1991):

$$r = \min_{\rho} \left\{ L_g L_f^{\rho-1} h(x) \neq 0 \right\} \tag{3}$$

Here, we consider the system $\dot{x} = f(x) + g(x)u$ and $y = h(x)$. Symbols L_g and L_f are the Lie derivatives of $h(x)$ along $g(x)$ and $f(x)$, respectively, i.e., $L_g h(x) = \frac{\partial h(x)}{\partial x} g(x)$ and $L_f h(x) = \frac{\partial h(x)}{\partial x} f(x)$. Hence, in our example it is proven by Eq. 4 that the relative degree r equals two:

$$\begin{array}{lll} \text{for} & \rho = 1: & L_g h(x) = \left[\begin{smallmatrix} 0 & 1 \end{smallmatrix}\right] \left[\begin{smallmatrix} 1 \\ 0 \end{smallmatrix}\right] = 0 \\ \text{for} & \rho = 2: & L_g L_f h(x) = \left[\begin{smallmatrix} 0 & 1 \end{smallmatrix}\right] \left[\begin{smallmatrix} 1 & 1 \\ 1 & 0 \end{smallmatrix}\right] \left[\begin{smallmatrix} 1 \\ 0 \end{smallmatrix}\right] = 1 \end{array} \tag{4}$$

In the case of multiple inputs or outputs, a set of relative degrees appears for each output-node. In such cases, in addition to this set of relative degrees, a total relative degree of the system is defined. The total relative degree is nothing but sum of the set of relative degrees, (Slotine and Li, 1991).

3 Julia implementation

For the prototype tools in this paper, a linear model in state space form as in Eq. 1 is assumed. Such a representation might be found in two ways. In one case, a dynamic system is modeled directly in Julia with *DifferentialEquations.jl* package, (Rackauckas and Nie, 2017), and then can be linearized using the *ForwardDiff.jl* package[11], (Revels et al., 2016). Alternatively, the model can be represented in Modelica, and OpenModelica with OMJulia can be used for the model linearization. The Julia API of OpenModelica with OMJulia is similar to the Python API of OpenModelica with OMPython which has been discussed in previous work, (Vytvytskyi and Lie, 2018b).

In order to work with graphs in Julia the *LightGraphs.jl* package[12] and *GraphPlot.jl* package[13] can be used for graph creation and plotting, respectively. In addition to these packages, other Julia packages for this study are also required, i.e., *Plots.jl*[14] and *DataFrames.jl*[15] packages.

[11] https://goo.gl/en5JMu
[12] https://goo.gl/tveMx1
[13] https://goo.gl/ifVw1p
[14] https://github.com/JuliaPlots/Plots.jl
[15] https://github.com/JuliaData/DataFrames.jl

It should be noted that examples with results of using all functions presented in this section, are given in Section 4.

3.1 Graphical structure of system

The *LightGraphs.jl* package[16] can be used to create a digraph of the linear system structure in Julia. Using interconnection matrix M (described in eq. 2) as an input to the *DiGraph()* command, the digraph G can be created and then plotted with the *gplot()* command from the *GraphPlot.jl* package[17]. An example, Julia code for creating and plotting the digraph of a simple three by three interconnection matrix M previously presented for the controllability example (see Fig. 2 (a)) looks as follows:

```
M = [ 1.0 1.0 1.0;
      1.0 0.0 0.0;
      0.0 0.0 0.0] // intercon. matrix
G = DiGraph(M) // create the digraph
gplot(G, layout=spring_layout,
    NODESIZE = 0.1,
    nodefillc=colorant"turquoise",
    NODELABELSIZE = 5,
    nodelabel=["x1","x2","u1"],
    nodelabelc = colorant"black",
    EDGELINEWIDTH=0.5,
    edgestrokec=colorant"grey",
    arrowlengthfrac=0.08,
    arrowangleoffset = pi/10)) // plotting
```

Here, plotting of the graph with *gplot()* command has various options:

- various possibilities for graph layout (random, circular, spring, shell, stressmajorize, and spectral layouts);
- setting size and color for nodes (*NODESIZE*, *nodefillc*), nodes' labels (*NODELABELSIZE*, *nodelabelc*), or edges (*EDGELINEWIDTH*, *edgestrokec*);
- specifications of nodes' labels names (*nodelabel*);
- setting edges' arrows shape (*arrowlengthfrac*, *arrowangleoffset*).

It should be noted that all color settings in the *gplot()* command might be specified with a vector of colors, one for each nodes/edges, similarly to the presented name vector for the nodes' labels. All the discussed options can be specified by the user according to their choice.

The results of running the presented code is shown in Fig. 3, where the simple digraph of three nodes is presented. Hence, using the presented commands for graphs creation and plotting, our own functions for system structure construction can be developed. The first function is named *obtain_graph_structure()* and provides digraph G together with interconnection matrix M and a data table, where the nodes' labels are structured with respect

[16] https://goo.gl/tveMx1
[17] https://goo.gl/ifVw1p

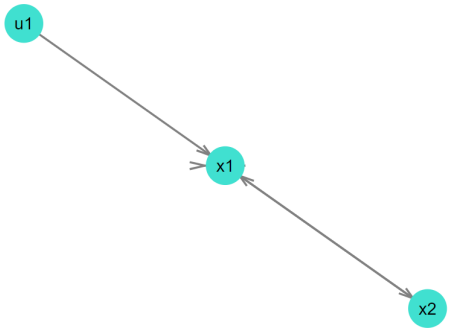

Figure 3. Digraph from the simple example of Julia code for the system in Fig. 2 (a).

to state/input/output names. This function also gives specific color arrays for nodes, nodes labels and edges. All nodes are colored according to their type, i.e., individual colors for states (turquoise), inputs (light blue), and outputs (light green). Edges in turn are colored based on their connection, i.e., individual color for self loops (red), state interactions (grey), connections from input (blue), and to output (brown). The inputs to this function are the constant system matrices A, B, C, and D. Three string arrays with the variables' names of state, input and output are inputs as well.

An example of the *obtain_graph_structure()* function calling is provided below. Here, commands for displaying of the graph G and the data table df are also used. As it is seen, the *gplot()* command for the graph plotting is specified with different options found with the *obtain_graph_structure()* for the names of nodes and color vectors for nodes, labels and edges.

```
G,M,df,Node_c,Edg_c,Nodelable_c,Nodelble =
    obtain_graph_structure(A,B,C,D,
    StateName,InputName,OutputName);
println(df) // display the data table
gplot(G, layout=circular_layout,
    NODESIZE = 0.05,
    NODELABELSIZE = 5,
    nodefillc=Node_c,
    EDGELINEWIDTH=0.3,
    edgestrokec=Edg_c,
    nodelabel=Nodelble,
    nodelabelc = Nodelable_c,
    arrowlengthfrac=0.08,
    arrowangleoffset = pi/10)
```

In cases when the user does not want to display (print/-plot) the results, another function *system_structure()* can be used. The function gives the possibility to show the structure of the system directly after execution. The use of this function is provided below:

```
system_structure(A,B,C,D,
    StateName,InputName,OutputName)
```

3.2 Structural observability and controllability

As presented above, structural digraph paths should be checked in order to show the structural observability or controllability of the system. To be structurally observable, there should be a directed path from every state-node to at least one output-node. Similarly, there should be a directed path from at least one input-node to every state-node in order to be structurally controllable.

Functions for checking structural observability and controllability of the system have been developed: *check_sys_observ()* and *check_sys_control()*, respectively. The calling of these functions are the same as for the functions presented in the previous subsection, and an example is given below:

```
check_sys_observ(A,B,C,D,
    StateName,InputName,OutputName)

check_sys_control(A,B,C,D,
    StateName,InputName,OutputName)
```

Both functions operate in similar way, and in the case that all states of the system are structurally observable/-controllable, they return a message with the following text: "All states are structurally observable/controllable". Otherwise, these functions provide information of which states are structurally unobservable/uncontrollable. In both cases, the functions also display the digraph with a structure of the system. In addition, in the case with some unobservable/uncontrollable states, some transparency colors are used to display these state-nodes and the edges connected to these nodes.

In some cases, it might be of interest to specifically check some of the system states for observability or controllability. Because of this, another two functions that check structural observability/controllability of specified states are developed. The use of these functions are similar to the previous two functions, but here the user should also specify the state that will be checked. The state number from the node's label (*state_num*) is used for this specification. An example looks as follows:

```
check_state_observ(A,B,C,D,StateName,
    InputName,OutputName,state_num)
check_state_control(A,B,C,D,StateName,
    InputName,OutputName,state_num)
```

Both functions return a message that shows if the specified state is structurally observable/controllable or not. They also display the digraph with a structure of the system where the specified state-node and a path (edges and nodes) which shows its structural observability/controllability are highlighted. Colors of all other nodes and edges are somewhat transparent.

3.3 Relative degree of system

In order to determine the relative degree of the system presented by digraph G, a smallest number of state-nodes should be found through which a directed path from an input-node to output-node goes. For this task, the *sys_relative_degree()* function is developed. This function defines the relative degree of the system and then returns a message that shows the value of the defined relative degree. For a system with multiple inputs and outputs, information about the total relative degree is provided together with a set of the relative degrees of all outputs. Moreover, a digraph is displayed with the structure of the system. In this digraph, colors of all nodes and edges are a bit muted, except for the path/paths (edges and nodes) that is/are the basis for the relative degree.

The use of the function for checking the relative degree looks as follows:

```
sys_relative_degree(A,B,C,D,
    StateName,InputName,OutputName)
```

4 Results

The various hydropower models that are implemented in OpenModelica using our in-house hydropower library, *OpenHPL*, are used here for testing of the developed functions for system structural analysis. Description and information about these hydropower models already have been presented previously, (Vytvytskyi and Lie, 2017, 2018b). For use with the structural analysis code, these models are first linearized in Julia using package OMJulia for OpenModelica. The constant A, B, C, and D matrices for the linearized hydropower state space models together with ordered lists (vectors) of state, input and output names are then used for structural analysis.

4.1 Simple waterway model

First, a simple model of the hydropower system with basic models for the waterway (incompressible water and inelastic pipes, (Vytvytskyi and Lie, 2017)) is used. This model consists of 5 states and has one input and one output. The *system_structure()* function provides the model structure, see Fig. 4. Here, the states ($x_1 - x_5$) are colored turquoise and consist of the volumetric flow rates in the penstock and surge tank, and the water masses in the surge tank, reservoir, and tail water. The input (u_1) is the control signal for the turbine and is colored light blue. The output (y_1) is colored light green and represents the flow rate in the turbine which is the same as the penstock flow rate in this model. Figure 4 shows the digraph with the model structure using the circular layout for the graph plotting. This can be changed to another style in options to the *gplot()* command.

Next, the hydropower model can be checked for structural observability and controllability using *check_sys_observ()* and *check_sys_control()* commands. The results for these studies are shown in Fig. 5 for observability and in Fig. 6 for controllability. It is seen from Fig. 5 that the system is structurally observable because all system states transmit information through digraphs to the output. In the same way, there are two uncontrollable states which make system structurally

7×4 DataFrames.DataFrame

Row	NodeLabel	State	Input	Output
1	x1	penstock.V_dot		
2	x2	reservoir.m		
3	x3	surgeTank.V_dot		
4	x4	surgeTank.m		
5	x5	tail.m		
6	u1		u	
7	y1			dotV

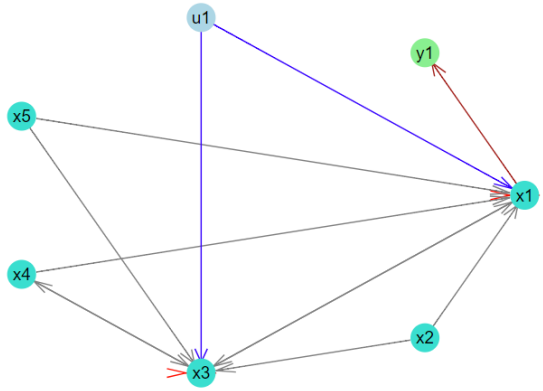

Figure 4. The digraph with the simple model structure determined by the *system_structure()* function.

All states are structurally observable

7×4 DataFrames.DataFrame

Row	NodeLabel	State	Input	Output
1	x1	penstock.V_dot		
2	x2	reservoir.m		
3	x3	surgeTank.V_dot		
4	x4	surgeTank.m		
5	x5	tail.m		
6	u1		u	
7	y1			dotV

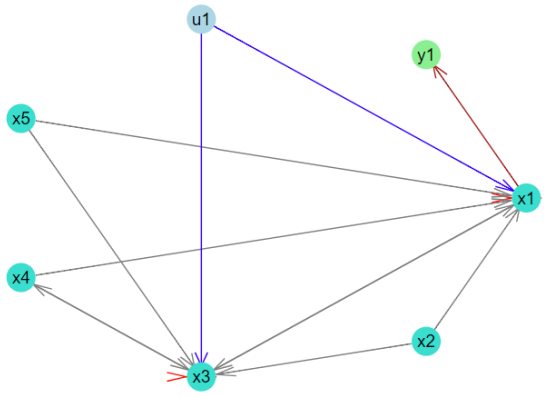

Figure 5. The results of checking the structural observability for simple model by the *check_sys_observ()* function.

uncontrollable, see Fig. 6. This uncontrollability for the water masses in the reservoir and tail water is caused by model simplification: these masses are kept constant in the model, (Vytvytskyi and Lie, 2018b); the uncontrollability is thus fictitious in this case.

The relative degree of this simple hydropower model can be found using the developed *sys_relative_degree()* function. The result of running this command for the simple model is shown in Fig. 7. Here, it is seen that the relative degree, r, equals one, which means that the control signal directly affects a state that influences the output.

4.2 Detailed waterway model

A more detailed model of the hydropower system is used next. This model is similar to the previous simple model, but here the penstock unit is described by a more detailed pipe model instead of the basic pipe model (here, compressible water and elastic pipes are considered in the penstock, (Vytvytskyi and Lie, 2017)). This model consists of 24 states and also has one input and one output. The result of the *system_structure()* function provides the model structure, see Fig. 8. Here, the states $(x_1 - x_{24})$ consist of the pressures $(U[1,..,10])$ and mass flow rates $(U[11,..,20])$ in the penstock segments, volumetric flow rate in the surge tank, and the water masses in the surge tank, reservoir, and tail water. The input (u_1) is the control signal for the turbine and the output (y_1) is the flow rate through the turbine. The state, input, and output nodes are colored in the same way as previously. It is seen from Fig. 8 that for more complex systems (more nodes), it becomes harder to observe visually how the nodes are connected. One way to study the system structure is to decompose the system in smaller subsystems. This can easily be

The uncontrollable states are: reservoir.m, tail.m

7×4 DataFrames.DataFrame

Row	NodeLabel	State	Input	Output
1	x1	penstock.V_dot		
2	x2	reservoir.m		
3	x3	surgeTank.V_dot		
4	x4	surgeTank.m		
5	x5	tail.m		
6	u1		u	
7	y1			dotV

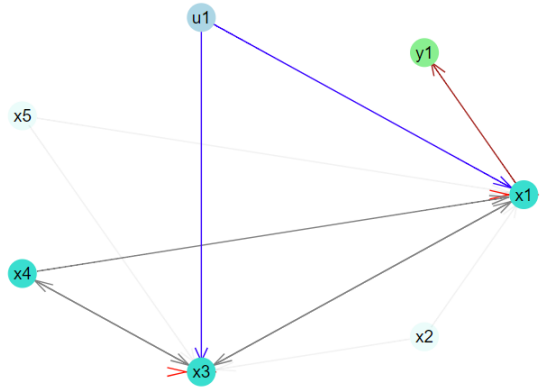

Figure 6. The results of checking the structural controllability for simple model by the *check_sys_control()* function.

```
Relative degree of the system is: r = 1
```

7×4 DataFrames.DataFrame

Row	NodeLabel	State	Input	Output
1	x1	penstock.V_dot		
2	x2	reservoir.m		
3	x3	surgeTank.V_dot		
4	x4	surgeTank.m		
5	x5	tail.m		
6	u1		u	
7	y1			dotV

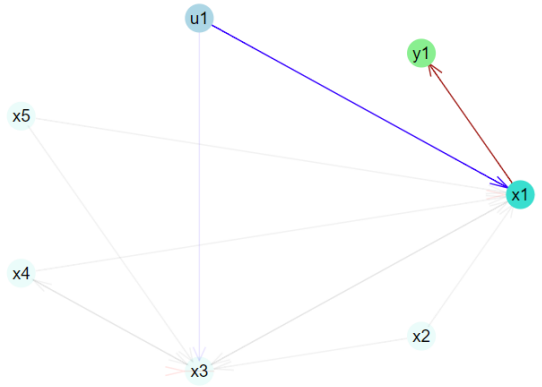

Figure 7. The results of checking the relative degree for simple model by the *sys_relative_degree()* function.

26×4 DataFrames.DataFrame

Row	NodeLabel	State	Input	Output
1	x1	penstock.U[1]		
2	x2	penstock.U[2]		
3	x3	penstock.U[3]		
4	x4	penstock.U[4]		
5	x5	penstock.U[5]		
6	x6	penstock.U[6]		
7	x7	penstock.U[7]		
8	x8	penstock.U[8]		
⋮				
18	x18	penstock.U[18]		
19	x19	penstock.U[19]		
20	x20	penstock.U[20]		
21	x21	reservoir.m		
22	x22	surgeTank.V_dot		
23	x23	surgeTank.m		
24	x24	tail.m		
25	u1		u	
26	y1			dotV

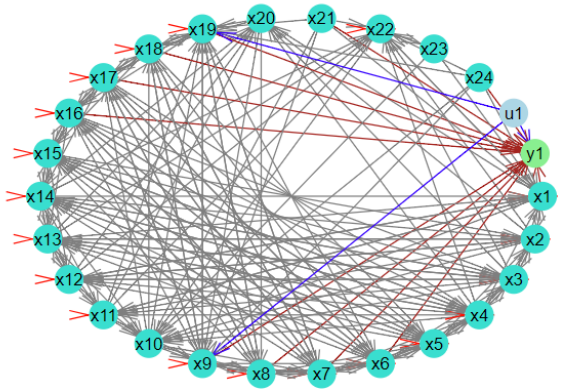

Figure 8. The digraph with the detailed model structure determined by the *system_structure()* function.

done by picking up the appropriate rows and columns in the A, B, and C matrices with respect to interested states.

On the other hand, the structural analysis for observability, controllability, and relative degree of the system may be still performed for the complete model. This can be done by running the same functions for the detailed model: *check_sys_observ()* — for observability, *check_sys_control()* — for controllability, and *sys_relative_degree()* — for relative degree. The results of these functions are not presented here to save space. However, the resulting information is as follows:

- "All states are structurally observable".
- "The uncontrollable states are: reservoir.m, tail.m", similarly to the case with simple waterway model.
- "Relative degree of the system is: r = 0", the input signal directly affects the output, i.e., the constant matrix D is not zero.

4.3 Simple waterway model with generator

Here, the simple model presented above is studied with a model of a synchronous generator that is connected to the grid. The models of this electrical part (generator, grid, etc.) are taken from the *OpenIPSL*[18] library, and is used in OpenModelica. OpenIPSL is the Open-Instance Power System Library, where a wide variety of power system components are available. The model of the simple hydropower waterway and generator consists of 7 states and has one input and 3 outputs. Here, the states ($x_1 - x_7$) consist of the generator shift angle and angular velocity, the volumetric flow rates in the penstock and surge tank, and the water masses in the surge tank, reservoir and tail water. The input (u_1) is the control signal for the turbine and the outputs ($y_1 - y_3$) are the generator power production and angular velocity, and flow rate through the turbine. The state, input and output nodes are colored in the same way as previously.

The result of the *system_structure()* function provides the model structure, Fig. 9. This structure is presented with the digraph of another layout type (spring layout), in order to demonstrate another structural view. The structural analysis for observability, controllability and relative degree of the system is also performed for this model case. This can be done by running the same functions as for the detailed model: *check_sys_observ()* — for observability, *check_sys_control()* — for controllability, and *sys_relative_degree()* — for relative degree. The results of executing these functions are not shown here, but the results are summarized as follows:

- "All states are structurally observable".
- "The uncontrollable states are: reservoir.m, tail.m", similarly to the two previous cases.

[18] https://openipsl.readthedocs.io/en/latest/

11×4 DataFrames.DataFrame

Row	NodeLabel	State	Input	Output
1	x1	order2_1.delta		
2	x2	order2_1.w		
3	x3	penstock.V_dot		
4	x4	reservoir.m		
5	x5	surgeTank.V_dot		
6	x6	surgeTank.m		
7	x7	tail.m		
8	u1		u	
9	y1			P
10	y2			dotV
11	y3			w

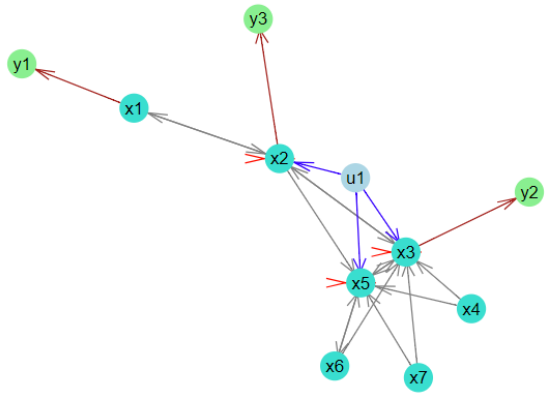

Figure 9. The digraph of the model structure determined by the *system_structure()* function. The model of the simple hydropower waterway and generator is used.

- "The system have relative degree (2, 1, 1). Total relative degree of the system is: r = 4": here is shown first the relative degrees for each output and then the total relative degree of the system.

5 Discussion and Conclusions

This paper has explored the possibilities of using graph theory methods for structural analysis of dynamic system. Although the chosen examples hardly qualify as complex/large scale, graph methods scale well to huge systems. The presented methods have been implemented in Julia using the *LightGraphs.jl* and *GraphPlot.jl* packages. Using the *OpenHPL* hydropower library in OpenModelica and OMJulia for OpenModelica, the structural analysis methods have been tested on hydropower models of different complexity.

The results of testing the developed structural analysis functions look reasonable and can be further used for analysis related to state estimation and control: observability is a requirement for state estimators to work properly, controllability is required for control design, and relative degree is important in the design of nonlinear feedback controllers. One experience with the developed tools is that sometimes it can be hard to make a good visualization of the graph structure of complex (large scale) system. It can be hard to see the whole picture of the system structure (small subsystems are not easily seen) using the circular layout for the graph plotting. However, the user can do some testing of different layout types for the graph plotting to find the most appropriate one. Moreover, the graph can be stored in a picture with higher resolution and bigger size that can help to see the system structure in a better way. In addition, developers of *LightGraphs.jl* and *GraphPlot.jl* packages are planning to improve the plotting possibilities of graphs in future, e.g., to improve the display self loop edges, etc.

In summary, this paper has explored some possibilities with structural analysis. Further work should be put into streamlining the functions into a package, with better use of Julia coding conventions, integration with other modeling tools, integration with control packages, etc.

References

S. Boyd and L. Vandenberghe. *Introduction to Applied Linear Algebra*. Cambridge University Pr., 2018. ISBN 1316518965.

N. Deo. *Graph Theory with Applications to Engineering and Computer Science*. Dover Publications, 2017. ISBN 9780486820811.

J. Lunze. *Feedback control of large scale systems*. Prentice-Hall international series in systems and control engineering. Prentice-Hall, 1992. ISBN 9780133183535.

Magamage Anushka Sampath Perera. *State estimation and optimal control of an industrial copper electrowinning*. PhD thesis, University College of Southeast Norway, Faculty of Technology, Kongsberg, Norway, 2016.

C. Rackauckas and Q. Nie. Differentialequations.jl – a performant and feature-rich ecosystem for solving differential equations in julia. *Journal of Open Research Software*, 5(1), 2017. doi:10.5334/jors.151.

J. Revels, M. Lubin, and T. Papamarkou. Forward-mode automatic differentiation in julia. *arXiv:1607.07892 [cs.MS]*, 2016. URL `https://arxiv.org/abs/1607.07892`.

Dan Simon. *Optimal State Estimation: Kalman, H∞, and Nonlinear Approaches*. John Wiley & Sons, 2006.

Jean-Jacques E Slotine and W. Li. *Applied nonlinear control*. Prentice-Hall International Editions. Prentice-Hall, Englewood Cliffs, N.J, 1991.

D. D. Šiljak. *Large-Scale Dynamic Systems: Stability and Structure*. Dover Civil and Mechanical Engineering Series. Dover Publications, 2007. ISBN 9780486462851.

D. D. Šiljak. *Decentralized Control of Complex Systems*. Dover Books on Electrical Engineering Series. Dover Publications, 2011. ISBN 9780486486147.

L. Vytvytskyi and B. Lie. Comparison of elastic vs. inelastic penstock model using OpenModelica. In *Proceedings of the 58th Conference on Simulation and Modelling (SIMS 58) Reykjavik, Iceland, September 25th–27th, 2017*, number 138, pages 20–28. Linköping University Electronic Press, Linköpings Universitet, 2017. doi:10.3384/ecp1713820.

L. Vytvytskyi and B. Lie. Mechanistic model for Francis turbines in OpenModelica. *IFAC-PapersOnLine*, 51(2):103 – 108, 2018a. doi:10.1016/j.ifacol.2018.03.018.

L. Vytvytskyi and B. Lie. Linearization for Analysis of a Hydropower Model using Python API for OpenModelica. In *Proceedings of the 59th Conference on Simulation and Modelling (SIMS 59) Oslo, Norway, September 26th–28th, 2018*, 2018b.

On-line Monitoring of Viscous Properties of Anti-icing Fluid Based on Partial Least Squares Regression Modeling

Maths Halstensen[1] Joachim Lundberg[2] Per Ivan Januschas[3] Hans-Petter Halvorsen[1]

[1]Department of Electrical Engineering, IT and Cybernetics, University of South-Eastern Norway, Norway, maths.halstensen@usn.no

[2]Department of Process, Energy and Environmental Technology, University of South-Eastern Norway, Norway

[3]MSG Production AS, Norway

Abstract

MSG Production is a company specializing in automated washing, de-icing, anti-icing and inspection of commercial passenger aircrafts. It is critically important that the viscosity of the anti-icing fluid is according to specifications. This study investigates if a combination of acoustic/vibrational measurements on the spraying nozzle of the system and multivariate regression modelling provides reliable viscosity estimates can be used for real time monitoring. The estimated viscosity based on independent test data show promising results for real time monitoring with a root mean square error of prediction of 278 [cP] within the valid range of the model which is 1900-8400 [cP].

Keywords: partial least squares, multivariate regression, viscosity, anti-icing fluid, acoustic monitoring

1 Introduction

MSG Production is a startup company, specializing in automated washing, de-icing, anti-icing and inspection of large commercial passenger/transport aircraft. The company has built a machine that automates the above-mentioned processes, by having an electric aircraft tug pulling it through the machine, much like a car in some automated commercial car-washes. Figure 1 shows the automated machine from MSG in operation applying anti-icing fluid to a passenger aircraft.

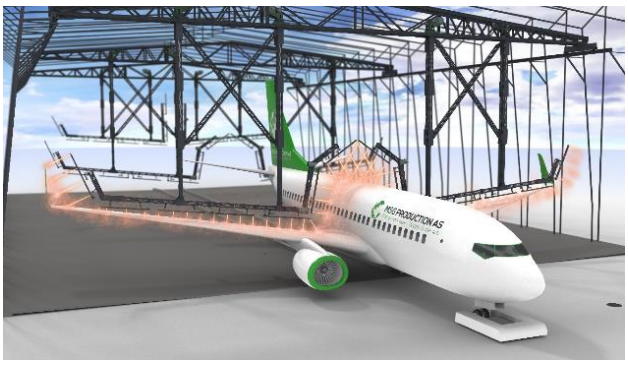

Figure 1. Anti-icing applied to a passenger aircraft using the new MSG technology.

The machine has devices for chemical fluids application hanging down from what is essentially traverse cranes overhead, with vertical telescopes holding a horizontal boom with multiple nozzles at a constant distance from the aircraft body and wings.

All control parameters for fluid application such as flow, pressure, temperature and fluid-quantity used are continuously monitored and documented.

Various parameters for washing, de-icing and anti-icing of any aircraft are described by the manufacturer, but there's also parameters related to de-icing and anti-icing that are dictated by the governing bodies of aviation, like SAE, FAA, IATA, GACA, ICAO etc. stating operational minimums for these procedures that are all related to aviation safety.

1.1 Anti-icing fluids

One of the objectives in this study is to investigate some of the physical (rheological) properties of the anti-icing fluid. The anti-icing fluid, of which there are several, (Type II, Type III and Type IV), is a polypropylene glycol, having a viscosity that is purposely thickened, and hence designed to make the fluid adhere to the aircraft wing during take-off and initial flight, until the aircrafts own anti-icing devices becomes effective enough to take over.

The anti-icing fluid is also known as a "pseudoplastic non-Newtonian" fluid also called shear-thinning fluid. This means that the lower the velocity gradient in the fluid, the higher the viscosity. This also imply that the viscosity can vary at different locations in the fluid dependent on the velocity field.

The anti-icing fluid is a polymer solution containing *large* polymer molecules. When the polymer is exposed to high mechanical stress (shear) the properties of the fluid can change, reducing the rheological properties of the fluid. This process is also called degradation of the polymer.

1.2 On-line monitoring of anti-icing viscosity

The main objective in this study is to assess if the vibrations occurring in the spraying nozzle of the system can be used for on-line real time monitoring of the viscosity of the fluid. Real time monitoring is preferred because the alternative approach involving manual sampling and off-line analysis using a rheometer is time consuming and does not provide continuous viscosity measurements.

The method which will be evaluated is called acoustic chemometrics (Halstensen *et al.,* 2010) The proposed method involves acoustic/vibrational measurements in the range 0-200kHz, digital signal processing (Fast Fourier Transform) and multivariate regression modelling based on Partial Least Squares Regression (PLS-R). The results can be used to investigate if the polymeric (viscous/rheological) properties of type II anti-icing fluid be degraded by exposing them to mechanical stress caused by the choice of technology in the anti-icing fluid spraying system.

An experimental test rig facility was used to simulate the mechanical stress that the anti-icing fluid is exposed to during application on the aircraft. The data acquired from these tests was used to train the PLS-R model. An independent data set was acquired for validation of the model in order to determine the model complexity (number of latent variables).

2 Materials and methods

A laboratory scale experimental test rig was designed and built to simulate the full-scale application process for anti-icing fluid. Viscosity was measured by taking samples from the transportation tank with fresh fluid from the manufacturer, and then again after being exposed to mechanical stress through the test rig.

Figure 2 shows the test rig piping and instrumentation diagram (P&ID). As can be seen in Figure 2 the pressure of the system is measured at various locations along the pipe to monitor the pressure loss. Temperature, pressure pertaining to the anti-icing fluid was recorded automatically during the tests. Five replicate samples were taken before and after being put through the test rig.

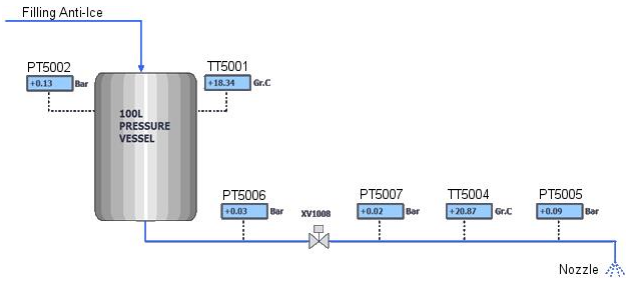

Figure 2. P&ID for the experimental test rig

The actual implementation of the test rig is shown in Figure 3. The rig has a pressure vessel containing test fluid, and a receiver tank to collect the fluid. The receiver tank holds the nozzle for fluid application. ID Ø-9.0 mm tubing connects the pressure vessel with the receiver tank and spray nozzle. The nozzle is a Veejet S.S.CO H1/4USS 8020 flat fan type, which in turn is used to apply anti-icing fluid to the aircraft. The pressure vessel was pressurized with air to 7.0 bar(g) for all of the tests. A pressure drop of approximately 1,8 bar from the pressure vessel to 5.2 bar(g) at the nozzle was observed. The pressure loss is affected by the design properties of the test rig and can be attributed partly to the hoses and partly to the rather restrictive inner diameter of the output valve from the pressure vessel.

Figure 3. Anti-icing nozzle test rig (top), nozzle with acoustic sensor (bottom).

An acoustic sensor (accelerometer) from Brüel & Kjær (BK 4518-002) was glued directly to the spraying nozzle as can be seen in Figure 3.

2.1 Anti-icing Safewing type II

The anti-icing fluid used was “Clariant SafeWing MP II Flight” polypropylene glycol which is a so-called type II anti-icing fluid. The viscosity of anti-icing fluid is a critically important property. Since this is a non-Newtonian fluid, the effect of strain to stress is rather complex. The anti-icing type II is as previously mentioned, a non-Newtonian fluid called pseudoplastic or shear-thinning fluid. The property characteristics of this fluid is such that the viscosity will decrease, as shear forces increases.

In this experiment, the viscosity for the anti-icing fluid was measured at various conditions. A Brookfield DV-III Rheometer was used for all the tests in accordance with ASTM D-2196-18 “Standard Test Methods for Rheological Properties of Non-Newtonian Materials by Rotational Viscountess” (ASTM D-2196-18 2018).

As per instructions given in ASTM D-2196-18, A 600 ml low form griffin beaker was filled with test solution. The instrument was zeroed, and the spindle was put into the solution. The rotation was set to desired value and the viscosity and temperature was recorded after 30 min.

2.2 Acoustic chemometrics

A survey of published literature concerning acoustic chemometrics shows that it has gained widespread use in industry. The publications span a broad variety of industrial applications demonstrating the potential of the method (Arvoh *et al.*, 2012,2012; Esbensen *et al.*, 1999; Halstensen *et al.*, 2006,2010; Ihunegbo *et al.*, 2012).

These applications include studies on liquids, particulate materials, and slurries. The advantages of acoustic chemometrics are:

- Non-invasive sensor technology
- Real time acoustic signal acquisition and processing
- Easy clamp-on/glue-on installation of acoustic sensors
- Several parameters of interest can be predicted from the same acoustic measurement

The main reason for choosing acoustic chemometrics is the on-line and non-invasive nature of this measurement approach which allows monitoring without disturbing the process. Furthermore, the total cost including both acoustic monitoring equipment and installation is relatively low compared to other on-line methods.

The sensor is an accelerometer which in this case is mounted directly onto the spraying nozzle of the anti-icing test rig. Figure 4 shows an overview of the most important signal processing steps involved in this method. In the first step shown in Figure 4 a) a time series of 4096 samples is recorded from the sensor. The time series is then multiplied with a Blackman Harris window (Ifeachor and Jervis 1993) shown in Figure 4 b) cancelling out the signal towards the ends of the series, the result is shown in Figure 4 c). This is important to prevent so-called spectral leakage in the final acoustic frequency spectrum.

The final step is the Discrete Fourier Transform which is used to transform the signal into frequency domain (Figure 4 d).

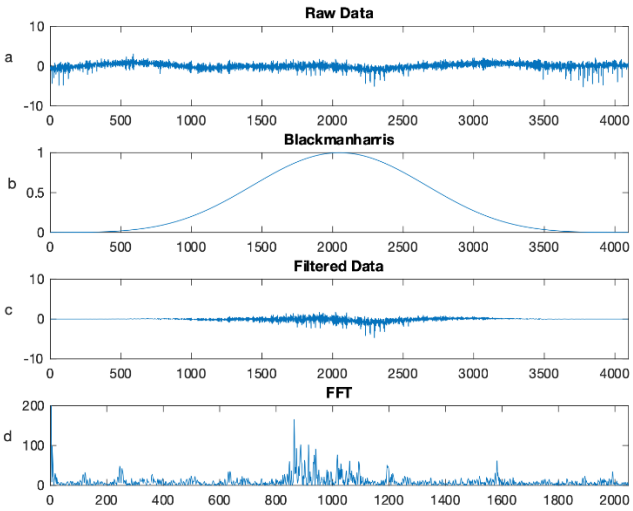

Figure 4. Acoustic chemometrics signal processing steps.

The Discrete Fourier transform (DFT) can be expressed as

$$X_k = \sum_{n=0}^{N-1} x_n e^{-i2\pi kn/N} \quad k = 0, \dots, N-1 \qquad (1)$$

A more efficient implementation of the DFT is the Fast Fourier Transform (FFT) which in this work has been implemented in LabVIEW 2017 for fast real time calculation of the Fourier spectrum.

2.3 PLS-R

Partial Least Squares Regression is an empirical data driven modelling approach which is well explained in literature (Esbensen *et al.*, 2018; Martens and Næs, 1989) thus only a short introduction is given here.

PLS-R relies on representative training data for two variable blocks, often called X and Y respectively. In the present study the X data matrix contains the acoustic frequency spectra, and Y is a vector containing the viscosity of the anti-icing fluid.

The NIPALS algorithm is the most widely used algorithm in PLS regression. In this algorithm, the intention is to model both X and y simultaneously, make the error as small as possible and at the same time extract as much useful information from the X matrix in order to describe the y response variable. A simplified version of the NIPALS algorithm is presented below (Ergon, 2009). *A* is the optimal number of components in the model.

1. Let $X_0 = X$. For a = 1, 2,…, A perform steps 2 to 6
2. $w_a = X_{a-1}^T y / \|X_{a-1}^T y\|$ (with length 1)
3. $t_a = X_{a-1} w_a$
4. $q_a = y^T t_a (t_a^T t_a)^{-1}$
5. $p_a = X_{a-1}^T t_a (t_a^T t_a)^{-1}$
6. Compute the residual $X_a = X_{a-1} - t_a p_a^T$

$$X = T_w P^T W W^T + E \quad (2)$$

$$y = T_w q_w + f \quad (3)$$

where the score matrix $T_w = [t_1 \quad t_2 \cdots \quad t_A]$ is orthogonal, loadings matrix $P = [p_1 \quad p_2 \cdots \quad p_A]$, $q_w = [q_1 \quad q_2 \cdots \quad q_A]$ and the loading weight matrix $W = [w_1 \quad w_2 \cdots \quad w_A]$

The loading matrix, P, is calculated as

$$P = X^T T (T^T T)^{-1} \quad (4)$$

The prediction vector for $y = Xb + f$ corresponds to:

$$\hat{b} = W(W^T X^T X W)^{-1} W^T X^T y \quad (5)$$

The response vector $\hat{y} = X\hat{b}$ (6)

In evaluating the regression model, the root mean squared error of prediction RMSEP offset, slope and correlation coefficient are commonly used. Besides these, visual evaluation of the relevant score plots, loading weights plots, explained variance plots also provide useful information for calibrating and development of the prediction model.

The root mean squared error of prediction is calculated as:

$$\text{RMSEP} = \sqrt{\frac{\sum_{i=1}^{n} (\hat{y}_{\text{i,predicted}} - y_{\text{i,reference}})^2}{n}} \quad (7)$$

3 Experimental

A controlled degradation test was performed in a pre-shearing rig where the purpose was to degrade the fluid to compare with the shear caused by the nozzle in the test rig. The fluid that was exposed to pre-shearing was mixed with factory fresh fluid and run through the test rig. A Brookfield DV-3 rheometer was used for all viscosity reference measurements.

In order to calibrate the PLS-R model it is important to vary the viscosity of the anti-icing fluid within a relevant range. Therefore, eleven different mixtures of factory fresh and pre-sheared fluid were prepared. The 11 fluids thus span a viscosity range of 1900 – 8400 [cP]. 10 liters of each viscosity was prepared and stored in plastic containers. All the eleven batches of anti-icing fluid mixtures were then run through the test rig and the corresponding acoustic signals from the accelerometer on the nozzle were recorded.

The signal from the accelerometer was amplified in a signal adaption module (SAM) developed by Applied Chemometrics Research Group at the University of South-Eastern Norway. The amplified signal was recorded using a data acquisition unit from National Instruments NI USB-6363 and a laptop computer.

An average of 50 spectra were used as basis for the final frequency spectra which was stored in the computer for further analysis based on multivariate regression modelling. The duration of each of the 11 tests was about 1 minute, and this resulted in 100 averaged frequency spectra for each viscosity. The temperature and pressure of the fluid in the tank and upstream of the nozzle were recorded during the tests to ensure comparable conditions for all the 11 viscosity tests. All the eleven batches of anti-icing fluid mixtures were then run through the test rig and the corresponding acoustic signals from the accelerometer on the nozzle were recorded.

4 Results & Discussion

Partial Least Squares Regression (PLS-R) was used to calibrate a multivariate model based on the acoustic data and the reference viscosity values. The reference viscosity values in each of the 11 mixtures were measured using the Brookfield DV-III Rheometer.

The acoustic data used to calibrate the PLS-R model was a 550x2048 matrix containing 550 frequency spectra. The calibration spectra were randomly selected from the total data matrix containing 1100 spectra. Each spectrum consisted of 2048 frequencies covering the frequency range 0-200 kHz.

4.1 PCA results

The resulting score plot t1-t2 for the first and second PLS-R component is shown in Figure 5.

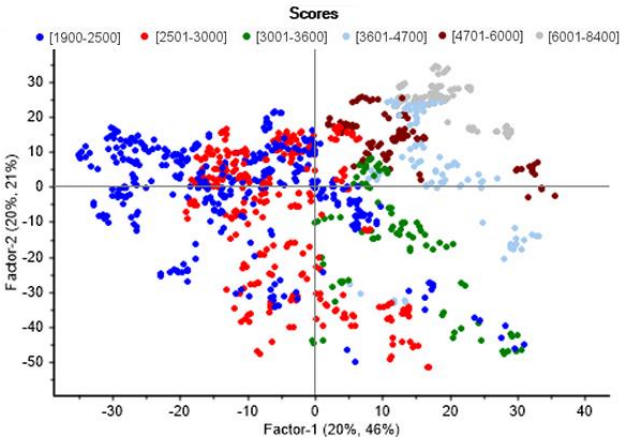

Figure 5. Score plot t1-t2, the viscosity of each sample is indicated by color according to the range given at the top of the plot.

The score plot shows how the acoustic spectra corresponding to the different viscosities relates to each other. Each acoustic spectrum is represented by a point with a color indicating the viscosity.

The score plot shows a promising trend in the data from low viscosity on the left side (blue) to the highest viscosity in the upper right corner (grey).

4.3 PLS-R prediction of viscosity

The PLS-R model was validated (Esbensen and Geladi, 2010) against a random selection of 550 spectra which is 50% of the total data set. Based on the test set validation the model complexity was determined using the residual validation variance plot shown in Figure 6. Five components were selected as optimal for the final prediction model.

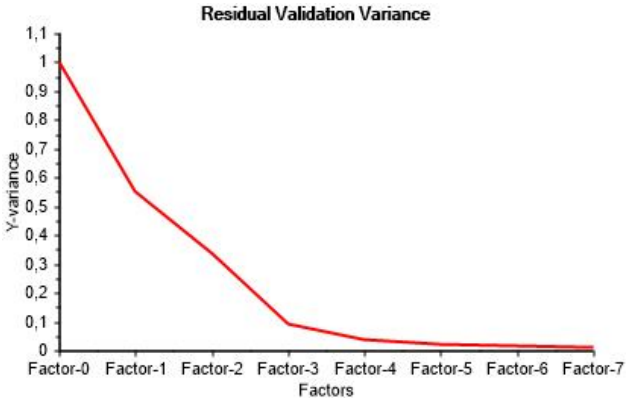

Figure 6. Residual validation variance.

The 550 predicted viscosities were plotted against the viscosities measured by the reference instrument and can be seen in Figure 7.

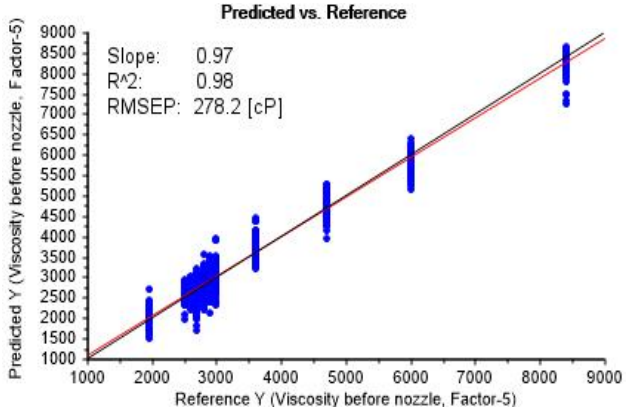

Figure 7. Predicted vs. Reference viscosity [cP]. The target line (black) and the regression line (red) are indicated.

The statistical parameters used to evaluate the prediction performance of the model are: slope=0.97, R2=0.98 and RMSEP=278 [cP].

The same results plotted in time can be seen in Figure 8. The green line is the reference viscosity and the red curve is the predicted viscosity.

The spread in the predicted values is mainly caused by air bubbles passing through the nozzle. Air bubbles in the anti-icing fluid is difficult to avoid, but if the fluid is left to settle for a significantly longer period than what was possible in this study the bubbles will surface, burst and disappear.

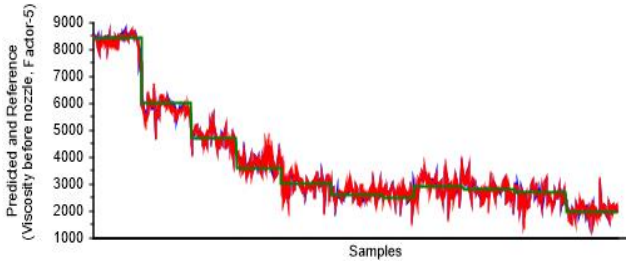

Figure 8. Predicted and Reference viscosity [cP].

The RMSEP=278 [cP] corresponds to 4.3% of the viscosity range 1900-8400. It can be observed that there are slightly lower prediction errors for the viscosity 8400 [cP]. The reason for this is probably that the 8400 [cP] fluid was taken directly from the tank as delivered from the manufacturer thus no mixing was required. It was also observed that the fluid with this viscosity contained significantly less air bubbles than the other batches of which all had been prepared as mixtures.

5 Conclusion

The main objective of this research study was to assess if acoustic measurements from the spraying nozzles in the system provide reliable predictions of the viscosity of anti-icing fluid. The results based on independent test data provided reliable predictions of the viscosity of the anti-icing fluid. It is concluded that the acoustic chemometric method which provided prediction performance indicated by the statistical parameters slope=0.97, R^2=0.98 and RMSEP=278 [cP] is promising for real-time monitoring of viscosity. However, long term testing is advised to assess the stability of the method in an industrial environment over time.

The advantage of the acoustic chemometric method will make it possible to monitor fluid viscosity during application to an aircraft in real-time. This is a significant improvement in risk assessment, mitigation and control.

References

ASTM D-2196-18. *Standard Test Methods for Rheological Properties of Non-Newtonian Materials by Rotational Viscountess*, ASTM International, PA, USA, 2018.

Benjamin K. Arvoh, Steinar Asdhal, Karsten Rabe, Rolf Ergon, and Maths Halstensen. Online estimation of reject gas and liquid flow rates in compact flotation units for produced water treatment. *Flow Meas Instrum*, 24:63-70, 2012.

Benjamin K. Arvoh, Steinar Asdhal, Karsten Rabe and Maths Halstensen. Online estimation of reject gas flow rates in compact flotation units for produced water treatment: A feasibility study. *Chemometrics and Intelligent Laboratory Systems*, 114:87-98, 2012.

Emanuel Ifeachor and Barrie Jervis. *Digital Signal Processing, a Practical Approach*, Addison-Wesley Publishing, 1993.

Felicia N. Ihunegbo, Michael Madsen, Kim H. Esbensen, Jens-Bo Holm-Nielsen, and Maths Halstensen. Acoustic chemometric prediction of total solids in bioslurry: A full-scale feasibility study for on-line biogas process monitoring. *Chemometrics and Intelligent Laboratory Systems*, 110:135–143, 2012.

Harald Martens and Tormod Næs. *Multivariate Calibration*, Wiley, UK, 1989 reprint 1994.

Kim H. Esbensen, Bjørn Hope, Thorbjørn T. Lied, Maths Halstensen, Tore Gravermoen, and Kenneth Sundberg. Acoustic chemometrics for fluid flow quantifications - II: A small constriction will go a long way. *J. Chemometrics* 13(27):209-236, 1999.

Kim H. Esbensen and Paul Geladi. *Principles of Proper Validation: use and abuse of re-sampling for validation. Journal of Chemometrics*, 24: 168-187, 2010 (www.interscience.wiley.com) DOI: 10.1002/cem.1310.

Kim H. Esbensen and Brian Swarbrick. *Multivariate Date Analysis – An introduction to Multivariate Data Analysis, Process Analytical Technology and Quality by Design*. 462 p, 6th edition, CAMO Software AS, 2018. ISBN 978-82-691104-0-1.

Maths Halstensen, Peter de Bakker and Kim H. Esbensen. Acoustic chemometric monitoring of an industrial granulation production process – a PAT feasibility study. *Chemometrics and Intelligent Laboratory Systems*, 84:88-97, 2006.

Maths Halstensen and Kim H. Esbensen. *Acoustic chemometric monitoring of chemical production processes, Process Analytical Technology, 2nd Edition, Chapter 9*, Wiley, 2010. ISBN: 9780470722077.

Rolf Ergon. Re-interpretation of NIPALS results solves PLSR inconsistency problems. *J Chemometr*, 23:72-75, 2009.

Comparison and analysis of magnetic noise and drive losses using different PWM methods (1165)

Torbjörn Trosten[1] Henrik Mosskull[1] Daniel Jansson[1] Maher Azaza[2] Erik Dahlquist[2]

[1]Bombardier Transportation, Vasteras, Sweden
[2]Mälardalens University, Vasteras, Sweden

Abstract

In this paper several discontinuous pulse width modulation methods (DPWM) are compared with space-vector pulse width modulation (SV-PWM) method. The comparisons are done based on measurements of motor magnetic noise and total drive losses for inverter switching frequencies from 500Hz to 4000Hz. It is concluded that using SV-PWM it is possible to reach lower magnetic noise on the traction motor without increasing the total losses significantly.

Keywords: DPWM, SVM, magnetic noise, inverter losses, harmonic losses traction, Metro

1 Introduction

The typical voltage source inverter (VSI) used in a variable speed drive (VSD) use a pulse width modulation (PWM) method to generate the required motor phase voltages. Depending on the application and requirements, different control algorithms and different PWM methods are used. Typical control methods are direct torque control (DTC), direct self-control (DSC), indirect self-control (ISC) and field-oriented control (FOC). All these control methods rely on the control of certain electrical machine quantities by controlling the switching states of the VSI, in doing so the control method and PWM method can become intervened and it can become difficult to describe the PWM method as separate from the control method. However, during ideal steady state conditions the control method and PWM method can be characterized separately. Some important PWM methods are sinusoidal PWM (S-PWM) (Schonung and Stemmler, 1964), space vector PWM (SV-PWM) (Van Der Broeck, et al., 1986) and Discontinuous PWM (DPWM) (Depenbrock, 1977). The main difference between S-PWM or SV-PWM and the DPWM methods is that the DPWM methods clamp one of the phases at certain angles. The purpose with the clamp is to reduce the inverter switching losses of the clamped phase, the reduction of switching losses depends on the phase current magnitude during the clamp. In (Hava et al., 1998) it is reported that inverter switching losses are significantly reduced using DPWM methods. In (Binojkumar et al., 2016) it is reported that the inverter related switching noise is lower using DPWM methods. In (Andersson and Thiringer, 2017), the inverter losses and magnetic noise from the motor was investigated using an experimental setup, a reduction in inverter losses was noted. However, the motor magnetic noise did not improve.

In this paper, several DPWM methods are compared experimentally with SV-PWM in terms of motor magnetic noise and both inverter and motor harmonic losses. In order to further understand the relations between motor magnetic noise, losses and PWM methods measurements are performed using switching frequencies between 500Hz and 4000Hz.

Section 2 describes the characteristics of the tested PWM methods and Section 3 presents data from loss and noise tests. Section 4 present an analysis of the noise measurements, Section 5 summarizes and concludes.

2 Characteristics of tested PWM methods

The different modulation methods are commonly described, and easily implemented using their characteristic duty ratio (Hava et al., 1998). In Figure 1, the characteristic duty-ratio for SV-PWM is shown side by side with the characteristic duty ratio of DPWM1. At the times, where duty ratio is 0 or 1, the

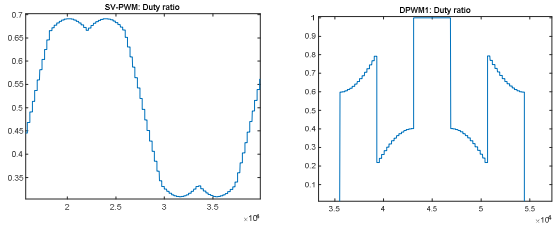

Figure 1. Duty ratio of SV-PWM (left) and DPWM1 (right) method.

phase is clamped, i.e. not switching. In terms of voltage harmonics, the main difference between SV-PWM and DPWM lies in the amplitude of the main switching harmonics. For the SV-PWM method the largest voltage and current harmonics occurs at twice the switching frequency and four times the switching frequency. The discontinuous methods produce a harmonic spectrum where the first harmonic is largest, the second is the

second largest and so on. This is illustrated in Figures 2 to 4, where the measured phase voltage spectrums for SV-PWM and two of the tested DPWM methods are plotted.

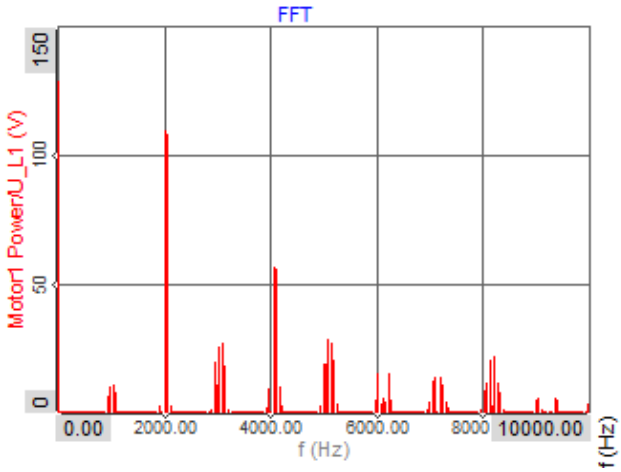

Figure 2. Measured phase voltage spectrum of SV-PWM operating at 1022Hz.

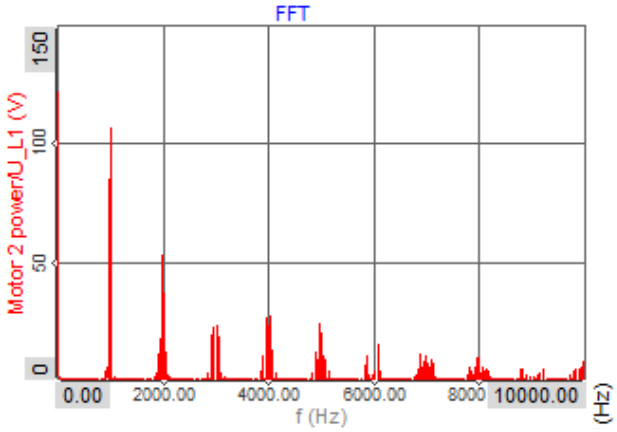

Figure 3. Measured phase voltage spectrum for DPWM Max.

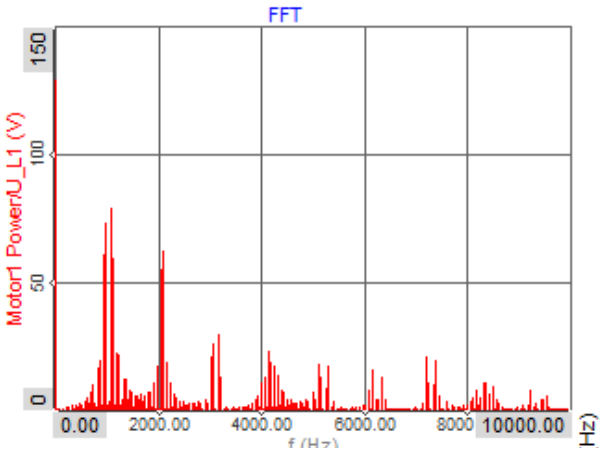

Figure 4. Measured phase voltage spectrum of DPWM1 operating at 1000Hz.

3 Measurements

3.1 Loss measurements

The traction motor is operated at 627rpm and 1017 Nm, corresponding to full tractive effort at a speed of 15 km/h for typical metro train. Losses in both inverter and motor are measured. The inverter losses are reduced for the tested discontinuous PWM methods; however, the motor harmonic losses are increased. This is seen in Figures 5 and 6.

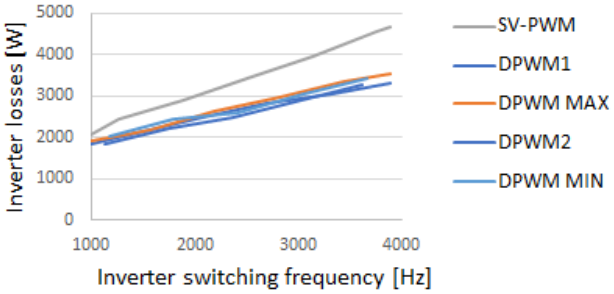

Figure 5. Measured losses in the inverter using different PWM methods.

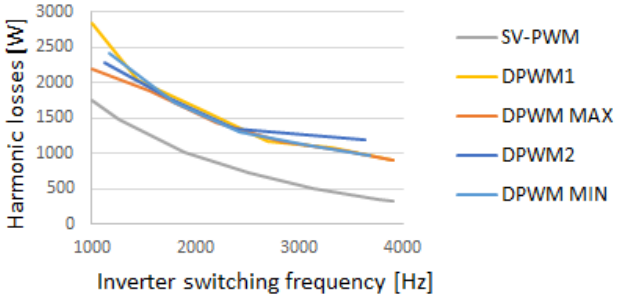

Figure 6. Measured motor harmonic losses using different PWM methods.

A comparison of total switching related losses, inverter and motor harmonic losses is shown Figure 7.

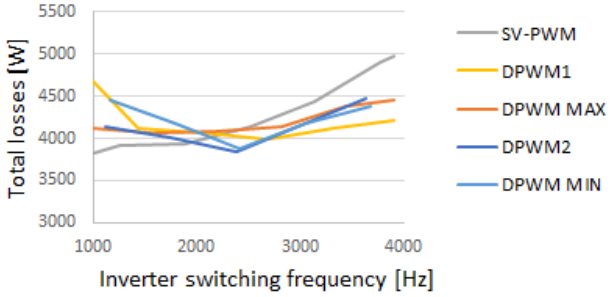

Figure 7. Measured inverter and motor harmonic losses using different PWM methods.

3.2 Noise measurements

In order to investigate the pulse patterns more in detail, the magnetic noise from the motor is measured using different inverter switching frequencies and pulse patterns. For each pulse pattern the inverter switching frequency is changed in steps of approximately 110Hz. Each frequency is kept for 5seconds, so that the average sound pressure level (SPL) can be measured. The measurements are done at no-load since at full load the Silicon (Si) based IGBTs of the inverter could overheat during such a test. A comparison of measured sound pressure level (SPL) using different PWM methods and switching frequencies is presented in Figure 8.

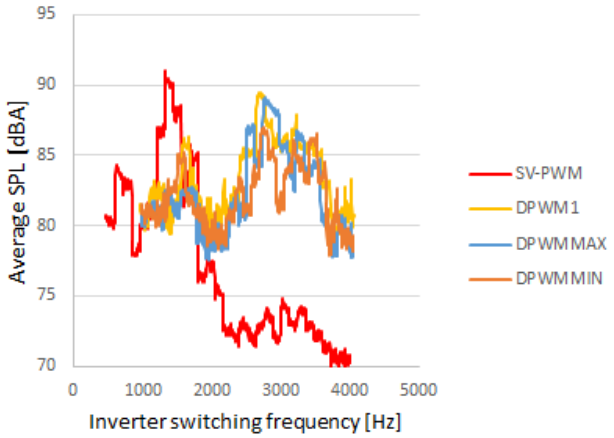

Figure 8. Measured SPL for different pulse patterns and inverter switching frequencies.

From the measurement it is seen that SPL varies significantly with the switching frequency and that relatively small changes in switching frequency can result in large changes in noise. It is also seen that above 1.8kHz, SV-PWM offers the lowest magnetic noise.

4 Analysis of noise measurements

In order to understand the behavior of the magnetic noise more in detail, the raw data from a single microphone, which was used during the tests, is analyzed more in detail. An FFT is performed and the amplitude and frequency of the two harmonics with largest amplitude are plotted in Figure 9. The largest amplitudes are recorded for frequencies between 2 kHz and 4 kHz (Figure 9). This behavior can be explained by considering that the structural mechanical resonance modes 0 and 4, of a traction motor this size, is typically located between 2kHz and 4kHz. Considering the relationship between harmonic amplitudes for SV-PWM and DPWM pulse pattern, one can explain the behavior in figure 9. The SV-PWM method generate the largest voltage harmonics at twice the switching frequency. The highest magnetic noise appears at roughly 1500Hz switching frequency. The DPWM methods, where the first harmonic is the largest, generate the highest noise for switching frequencies around 3000Hz as seen in Figure 8.

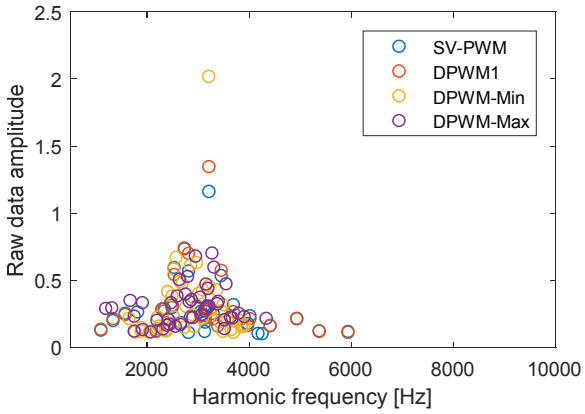

Figure 9. Raw amplitude and frequency of two largest harmonics for all noise tests.

In order to further investigate, if the measured magnetic noise is mainly related to the frequency of the main voltage harmonics. The measured noise using SV-PWM between 500-2000Hz is frequency shifted into 1000-4000Hz and plotted together with the noise measurement from DPWM1. The result from the calculation is shown in Figure 10, the general behavior in the noise measurement using DPWM1 maps well with the noise measurement using SV-PWM using half the switching frequency. Indicating that it is the frequency of the main harmonics which is relevant for the magnetic noise.

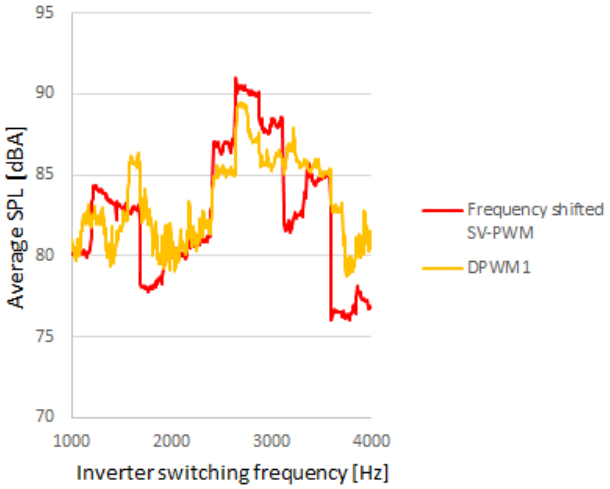

Figure 10. comparison of frequency shifted SV-PWM and DPWM1 noise.

5 Conclusions

The comparisons and analysis on loss and noise measurements for SV-PWM and DPWM methods

show, that the magnetic noise using PWM methods can be understood by considering the resonance frequencies of the motor and the frequencies of the main voltage harmonics, generated by the PWM method. A more in-depth analysis reveals that in terms of noise, the DPWM methods produce similar results as an SV-PWM, operating at half the switching frequency. The measurements further show that SV-PWM operated at 2kHz switching frequency generate both low losses and low noise for the tested traction motor.

References

A. Andersson and T. Thiringer. Experimental determination of inverter losses and sound consequences of using DPWM in an HEV. In *2017 IEEE Applied Power Electronics Conference and Exposition (APEC), Tampa, FL*, pages 1382-1388, 2017.

A.C. Binojkumar, B. Saritha and G. Narayanan, Experimental comparison of Conventional and Bus-Clamping PWM Methods Based on Electrical and Acoustic Noise Spectra of Induction Motor Drives. *IEEE Transactions on Industry Applications*, 52(5):4061-4073, Sept.-Oct. 2016.

H. Van Der Broeck, H. Skudelny, and G. Stanke. Analysis and realization of a pulse width modulator based on voltage space vectors. In *Conf. Rec. IEEE-IAS Annu. Meeting*, pages 244–251, 1986.

M. Depenbrock. Pulse width control of a 3-phase inverter with nonsinusoidal phase voltages. In *Conf. Rec. IEEE Int. Semiconductor Power Conversion Conf.*, pages 399–403, 1977.

A. M. Hava, R. J. Kerkman, and T. A. Lipo. A highperformance generalized discontinuous PWM algorithm. *IEEE Transactions on Industry Applications*, 34(5): 1059-1071, 1998. doi: 10.1109/28.720446.

A. Schonung and H. Stemmler. *Static frequency changers with subharmonic control in conjunction with reversible variable-speed ac drives*, Brown-Boveri Rev., pages 555-577, 1964.

Impact of distributed power generation at the customer

Marius Salen[1] Dietmar Winkler[2]

[1]University of South-Eastern Norway, salen93@gmail.com
[2]University of South-Eastern Norway, dietmar.winkler@usn.no

Abstract

In collaboration with the Distributed System Operator (DSO) at Hvaler which is Norgesnett, a weak grid is simulated in NETBAS. The aim with the simulation is to study the impact clouds have on the production at the solar panels since the production drops locally at the customers from passing clouds. Also, the impact this has on the DSO with the requirements given from § 3.4 in the Norwegian Directive on Quality of supply (FoL) regarding $\Delta U_{\text{stationary}}$ are considered. The simulations are conducted with different scenarios which illustrate the power production in the solar panels when cloudy. In collaboration with the Norwegian Meteorological Institute (MET Norway) solar data is used to get a more realistic picture of the sun condition at Hvaler and the corresponding scenarios. The main findings are that the passing clouds had a large impact on the voltage drop at the customers simulated in the weak grid at Søndre Sandøy. Also the objects at Søndre Sandøy without solar panels are affected by the clouds reducing the power output from the objects with solar panels. As a result, both of the objects with and without solar panels exceeded the requirement given from FoL § 3.4 in some of the scenarios. The conclusion is that clouds had a significant impact on the customers simulated at the weak grid at Hvaler, resulting in a voltage drop which gives challenges for the DSO regarding FoL.

Keywords: distributed power generation, solar production, FoL, DSO, prosumer

1 Introduction

Hvaler is an island community outside Fredrikstad, with a population of 4 400 inhabitants. In summer, the population of Hvaler increases to about 30 000 since Hvaler is a popular holiday resort with many summer residents (Wikipedia 2019). Such an increase in population can lead to a rise of power consumption resulting in power peaks, especially during the summer season.

1.1 Previous work and motivation

With passing clouds on solar panels and its impact regarding the voltage drop, there has been done previous work at the field. From the paper "Passing-cloud Effects of Solar Photovoltaic System on Distribution Network Voltages" (Cheiw Yun Lau, Chin Kim Gan, Chin Ho Tie, Kyairul Azmi Baharin, Mohamad Fani Sulaima 2015), the conclusion were that a voltage drop may occur when clouds are passing and reducing the generation from the solar panels due to the cumulus sky. That paper was comparing passing clouds on a sunny day with a cloudy day. In this paper however we investigate passing clouds on a sunny day on a weak grid concerning the voltage drop.

In 2014 a Master's Thesis in collaboration with Norgesnett was conducted (Ellefsen 2014). One of the main objectives from that thesis was to study the risk of overvoltages coming from solar panels potentially installed in the distribution network at Hvaler. Also that research used Søndre Sandøy as a test area for the simulations. The highest overvoltages occurred in June according to the conclusion.

From this, the motivation for this paper is to present how solar panels at the customers in Søndre Sandøy get affected by the clouds which are reducing the production on a specific day in June. Also, a goal with the paper is to get a better understanding on how the clouds reduce the power output from the solar panels leading to a voltage drop at the customer.

1.2 Problem description

This paper is investigating a part of Norgesnett's distribution network on Hvaler, where the voltage drop locally at the customers is studied. This is caused by the reduction in the solar panels from the passing clouds. Further, similar remote areas like Hvaler with distributed generation may benefit from this work.

The simulation is performed in collaboration with Norgesnett, and the software NETBAS(POWEL 2018) is used. The area simulated is in Hvaler (Norway), in a collaboration with the local DSO. After discussions with Norgesnett it was decided to simulate two areas of the distribution network, a robust and weak grid. NETBAS is used to study the behaviour of the two areas after passing clouds reduce the production from the installed solar panels at the customers. The customers will be referred to as objects throughout the paper. The passing clouds can lead to a voltage drop which can be problematic for the DSO. The results from the simulations are compared with the requirements given in FoL §3.4, regarding $\Delta U_{\text{stationary}}$. Since the Master's Thesis revealed most challenges at the weak grid at Søndre Sandøy this will be focus area in this paper (Marius Salen 2019).

1.3 Limitations

- From §3.4 in FoL $\Delta U_{\text{stationary}}$ is considered and ΔU_{max} is not.
- During the sun minutes, no changes from sun to clouds are taken into consideration. Moreover, when passing clouds occur, this change from sun to cloud is set to each third minute. This is explained in more detail at Section 3.1
- When clouds reduce the power generated locally from the solar panels this occur at the same time for all objects in the scenarios.

2 Background

2.1 Active distribution system

When a customer has a surplus of power an alternative to storage is to feed the power back to the grid, which is called prosumers (Wilson Rickerson 2014). Prosumers which are feeding the power back into the grid makes an impact due to a voltage rise in the grid. In Figure 1 the voltage rise at the distribution network can be expressed by Equation (1), where the voltage drop is increasing when P and Q are increasing.

$$\Delta U = U_2 - U_1 = \frac{P_2 \cdot R + Q_2 \cdot X}{U_2} \tag{1}$$

In Equation (1), U_2 represents the direction where the power flow is reversed. Also, the voltage at the point of connection of the generator will increase to a higher value than the sending end voltage, visualised in Figure 1 (M.A. Mahmud, M.J. Hossain, H.R. Pota 2011). When a prosumer has surplus power this will contribute to a higher voltage. Furthermore, I_2 will have negative value and U_2 will be greater than U_1. When distributed generation (DG) is connected as shown in Figure 1 the system is not a passive system, but rather an active system.

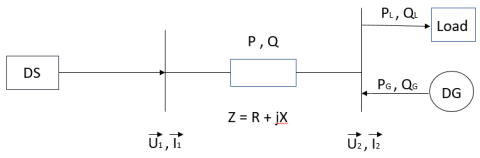

Figure 1. An active distribution system with DG at the customer.

2.2 X/R - Ratio in the distribution network

Figure 2 is from (Christian Rendall Olsen 2018) and shows how the reactance X gets smaller from the power grid towards the object. On the other hand, the resistance R increases from the power grid towards the object. In a distribution network, the power factor (PF), $\cos\theta$ is high with typical values of 0.98 found from NETBAS. This

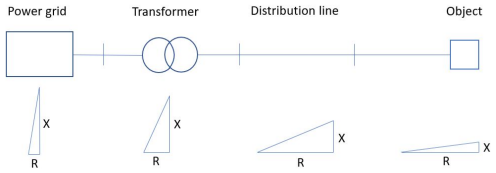

Figure 2. X-R ratio for a typical distribution network. (Christian Rendall Olsen 2018).

gives $R \gg X$. From this, Equation (1) can be rewritten into Equation (2) because the XQ term is neglected:

$$\triangle U = \frac{R \cdot P}{U_2} \tag{2}$$

The $\cos\theta$ indicates the ratio between active and apparent power, visualised by the power triangle as seen in Figure 3. When simulated in NETBAS the PF at the objects are between 0.975 and 0.985 which is a large PF, resulting in a low contribution of reactive power. At the objects in the test area there are almost purely resistive loads. Typical equipment which contributes to increasing the reactive power are larger motors which include an inductor. Such equipment is not present at Søndre Sandøy.

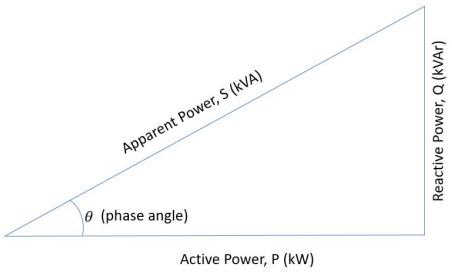

Figure 3. The power triangle.

3 Method

The test area is simulated to see if the requirement of $\Delta U_{\text{stationary}}$ from § 3.4 in FoL are held. These requirements are according to Table 1 which is explained in detail at Section 2.4.

An important topic in this paper is the voltage variations where FoL has requirements that need to be met. These requirements are found in FoL, § 3.4 and states: (Lovdata 2004)

"The Norwegian water resources and energy directorate (NVE) may order those who are covered by this regulations to implement measures to reduce the scope or consequences of voltage dips and voltage swells.

DSOs shall ensure that voltage swells, voltage dips and Rapid Voltage Changes (RVC) do not exceed the following limit values in the point of connection with the respec-

tive nominal voltage level, U_N, for the respective time interval."

The purpose of these regulations is to ensure that the customer only experience a limited number of voltage swells, voltage dips and RVC (Lovdata 2004).

In a network with 230 V the RVC are within the interval of 207-253 V, which is a margin of $\pm$ 10 % from 230 V. However, at any point if the voltage drops under 207 V it is categorised as a voltage dip, or if it exceeds 253 V, as a voltage swell. In low- and high voltage distribution network with voltages between 230 V-35 kV then 24 voltage variations within a 24 hours period are allowed (Lovdata 2004).

Table 1. $\Delta U_{\text{stationary}}$ can exceed the limit of 3 % from FoL at a maximum of 24 times in a 24-hours period.

Voltage swells, voltage dips and rapid voltage changes	**Max number pr floating 24-hours period**
	0.23 kV $\leq U_N \leq$35 kV
$\Delta U_{\text{stationary}} \geq 3\%$	24
$\Delta U_{\text{max}} \geq 5\%$	24

Table 2. Different scenarios presented.

Scenario	Solar radiation	Production in solar panels
Scenario I	0 %	0.00 p.u.
Scenario II	10 %	0.10 p.u.
Scenario III	25 %	0.25 p.u.

The three scenarios presented in Table 2 are used to illustrate the problems regarding passing clouds on summertime, which reduce the power output from the solar panels. Scenario I illustrates the worst case scenario with 0 % production from the solar panels. Further, Scenario II and III illustrates a more realistic Scenario with 10 % and 25 % production from the solar panels when cloudy. Scenario I is not a realistic scenario since there always will be some solar radiation on the solar panels. However, it can be useful for the DSO to take a worst case scenario in consideration for future planning of the grid.

3.1 Solar data

Historical solar tracking data are collected from MET Norway. Although they did not have data from Hvaler and recommended Grimstad, which has a similar type of climate as Hvaler. The interest is to study if the changes from sun to clouds will influence the requirements according to FoL § 3.4. If there are more than 24 changes a day where $\Delta U_{\text{stationary}} \geq 3$ %, the requirements are not met.

Discussions with climate researcher Prof. Elin Lundstad at METs office, lead to the definition of a ratio that represents the change between sun and clouds in minutes. This ratio is set to a switch between sun and clouds each third minute when cloudy. Further, Prof. Lundstad suggested that a typical cloud for Hvaler is the type Congestus, which gives problems for the solar panels due to the thickness of the clouds regarding production.

Consequently, with 51 minutes of sun registered from 10:00 hours to 11:00 hours presented in Table 3. The shift between sun to clouds occurs each third minute during these minutes with passing clouds. These minutes with the passing clouds is the remaining 9 minutes in the hour from 10:00 hours to 11:00 hours.

From the solar tracking data given by MET Norway, a suitable day was chosen to illustrate the problem with more than 24 changes of sun to clouds during a day. Furthermore, the total sun to cloud changes are also given in Table 3, which shows that during 15$^{\text{th}}$ June 2018 the change between sun and clouds reaches a number of 70. That number indicates that if $\Delta U_{\text{stationary}}$ exceeds the limit of 3 % in the simulations and hence the DSO does not meet the requirements during that day.

Table 3. The changes from sun to clouds reached a number of 70, 15. June 2018.

Time:	Sun minutes	Passing clouds	Changes
06:00	5	Dawn	3
07:00	60	0	0
08:00	60	0	0
09:00	60	0	0
10:00	51	9	3
11:00	29	31	10
12:00	38	22	7
13:00	44	16	5
14:00	56	4	1
15:00	57	3	1
16:00	60	0	0
17:00	49	11	4
18:00	7	53	18
19:00	17	43	14
20:00	52	8	3
21:00	1	Dusk	1
Sum			70

3.2 The difference between $\Delta U_{\text{stationary}}$ and ΔU_{max}

After discussions with Norgesnett, a decision was made to only study $\Delta U_{\text{stationary}}$. This is because NETBAS does not have the complexity to study ΔU_{max}, and simulations with ΔU_{max} also requires measurements collected from the field. Additionally, the simulations with ΔU_{max} require that a time constant must be taken into consideration. This is not done in this paper due to the study of $\Delta U_{\text{stationary}}$ in stationary conditions.

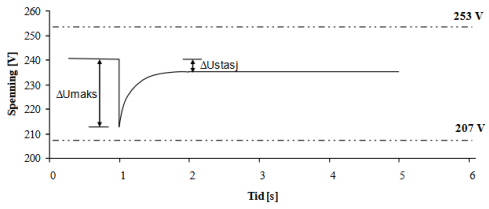

Figure 4. Visualisation of ΔU_{max} and $\Delta U_{\text{stationary}}$ (NVE 2018).

In Figure 4 ΔU_{max} and $\Delta U_{\text{stationary}}$ is presented. ΔU_{max} is the maximum change in voltage during the situation, and

is typically due to startups of larger motors in industrial areas (Lovdata 2004). $\Delta U_{\text{stationary}}$ is the voltage after it has stabilised on a higher, lower or the same level as before the situation arose. In the simulations the voltage is stable on a lower level because of the drop in production at the solar panels due to the clouds.

Figure 5. Simplified figure with $\Delta U_{\text{stationary}}$

Figure 5 is a simplified model which illustrates $\Delta U_{\text{stationary}}$. It shows how a drop in production due to clouds gives a new condition, $U_{\text{stationary}}$. Further, $U_{\text{delivered}}$ is the voltage when the solar panels have full production at the objects. $\Delta U_{\text{stationary}}$ should not exceed the limit of 3 % more frequently than 24 times in a period of 24 hours. Equation (3) is based on Figure 5.

$$\%U_{\text{stationary}} = \frac{\Delta U_{\text{stationary}}}{U_{\text{delivered}}} \cdot 100\% \tag{3}$$

The cabins at Søndre Sandøy are referred to as *objects*. Furthermore, after discussion with Norgesnett it was decided that the simulations are conducted with regard to normal operating condition with point-analyses in stationary condition. Also, a decision was taken to use the different objects short-circuit performance from NETBAS in comparison with the voltage drop due to the drop in production at the solar panels. Furthermore, to simulate the solar panels at the objects in NETBAS the capacity of the solar panels in kW are set to a negative value at the objects. This makes the power flow back to the grid and gives a scenario where the objects feed the distribution network, also called prosumers.

The network is tested at cases where an increasing number of objects have solar panels installed. Scenario I, the worst case, is simulated first. If this is not passed then consequently Scenario II and III are simulated as presented in Table 2.

4 Results

Here the results from Søndre Sandøy are presented. In the Master's Thesis solar panels from 1 kW to 3 kW was studied. In this paper, only the size of 3 kW is presented in detail since this was the size with most problems for the DSO. Furthermore, all scenarios and cases from Søndre Sandøy are presented in Table 10 and discussed briefly.

4.1 The test area at Søndre Sandøy

Søndre Sandøy is located far out in the distribution network and is categorised as a rural area. Søndre Sandøy has low short-circuit performance at the objects. Because of the low short-circuit performance, Søndre Sandøy does not have the prerequisites to deal with a large amount of solar capacity at the objects. There are ten objects and six cases at Søndre Sandøy. Figure 6 shows the ten objects which are studied.

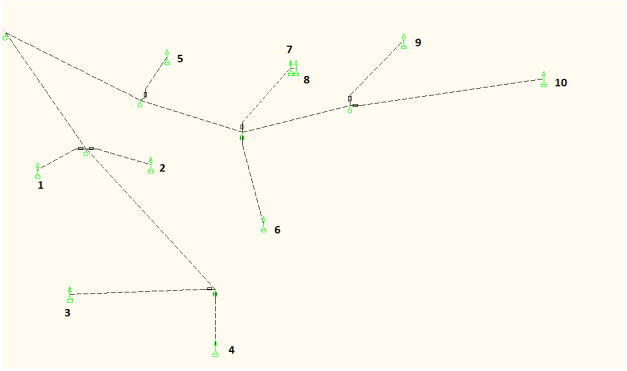

Figure 6. The different objects at Søndre Sandøy.

According to Figure 6, Case 1 is simulated where Object 5 and 6 have installed solar panels. Further, Case 2 is when Object 7 av 8 have added their solar panels to the network, those objects are also connected to the same line. Further, Object 9 and 10 are added to the network with Case 3 and 4, respectively. They have two cases because of the low short-circuit performance on those objects. Moreover, they are furthest out in the network, which makes them vulnerable to solar panels. Furthermore, down the right at the network, Case 5 is when Object 1 and 2 gets solar panels which are added to the network. And Case 6 is when every object has solar panels installed.

4.2 Explanation NETBAS simulation tables

Both, Table 4 and Table 5, are structured in a way that the objects are numbered horizontally 1 - 10, and the cases are numbered vertically 1 - 6. Table 4 has two colours in the boxes, yellow and blue. Yellow indicates the installed solar capacity at the respective objects in kW. Furthermore, yellow also indicates the object's related voltage, $U_{\text{delivered}}$. The blue colour illustrates the impact of the clouds, which reduces the production in the solar panels to a new value given in kW. Moreover, blue is also the object's new related voltage, $U_{\text{stationary}}$. Furthermore, the white boxes are objects without solar panels, called non-solar objects. The S-C P is the object's different short-circuit performance.

Table 5 shows where $\Delta U_{\text{stationary}}$ exceeds the 3 % limit with red boxes, and is calculated as shown in Equation (4).

$$\%U_{\text{stationary}} = \frac{\Delta U_{\text{stationary}}}{U_{\text{delivered}}} \cdot 100\% = \frac{235.2 - 226.0}{235.2} \cdot 100\% \tag{4}$$

The calculation in Equation (4) illustrates Object 1 at

Table 4. 3 kW installed at the objects with 25 % solar production due to clouds.

	1	2	3	4	5	6	7	8	9	10
S-C P [MVA]	0.346	0.301	0.215	0.271	0.336	0.266	0.287	0.287	0.205	0.162
	[V]	[V]	[V]	[V]	[V]	[V]	[V]	[V]	[V]	[V]
1: 3 kW	219.1	218.9	218.2	218.6	219.7	219.7	219.0	219.0	218.5	217.9
1: 0.75 kW	217.1	216.9	216.1	216.6	217.3	217.0	216.6	216.6	216.0	215.5
2: 3 kW	222.9	222.7	221.9	222.4	223.9	224.5	224.6	224.6	223.3	222.8
2: 0.75 kW	219.2	219.0	218.2	218.7	219.6	219.6	219.7	219.7	218.7	218.2
3: 3 kW	224.6	224.4	223.7	224.1	225.8	226.7	226.8	226.8	226.9	225.9
3: 0.75 kW	220.1	219.9	219.1	219.6	220.6	220.8	220.8	220.8	220.5	219.8
4: 3 kW	226.6	226.4	225.7	226.1	228.0	229.2	229.3	229.3	230.4	231.0
4: 0.75 kW	221.2	221.1	220.3	220.8	221.9	222.2	222.2	222.2	222.5	222.7
5: 3 kW	230.9	231.1	229.8	230.3	231.7	232.9	233.0	233.0	234.1	234.8
5: 0.75 kW	223.5	223.6	222.5	223.0	223.9	224.2	224.2	224.2	224.5	224.7
6: 3 kW	235.2	235.4	236.3	235.9	235.5	236.6	236.7	236.7	237.8	238.5
6: 0.75 kW	226.0	226.0	226.3	226.1	226.0	226.3	226.4	226.4	226.6	226.8

Case 6 from Table 4. Further, Table 5 represents the answer of the calculation at Object 1 Case 6. As a result from this, $\%U_{\text{stationary}}$ is larger than 3 %, and the requirements states this should not occur more frequently than 24 times a day.

Moreover, all calculations from the simulations in the paper are compared to the sun to cloud changes from 15$^{\text{th}}$ June 2018. If the limit of 3 % is exceeded, the requirements are not met during that day.

The different cases indicate which objects have installed solar panels, Case 1 has 1 Object with solar panels and so on. The tables are related to each other, meaning Object 1 in Table 4 is Object 1 in Table 5.

Table 5. $\%U_{\text{stationary}}$ for all the cases regarding Scenario III.

	1	2	3	4	5	6	7	8	9	10
1:	0.91 %	0.91 %	0.96 %	0.91 %	1.09 %	1.23 %	1.09 %	1.09 %	1.14 %	1.10 %
2:	1.65 %	1.66 %	1.68 %	1.66 %	1.92 %	2.18 %	2.18 %	2.18 %	2.06 %	2.06 %
3:	2.00 %	2.00 %	2.05 %	2.00 %	2.30 %	2.60 %	2.64 %	2.64 %	2.82 %	2.70 %
4:	2.38 %	2.34 %	2.39 %	2.34 %	2.67 %	3.05 %	3.09 %	3.09 %	3.43 %	3.59 %
5:	3.20 %	3.25 %	3.18 %	3.17 %	3.36 %	3.73 %	3.78 %	3.78 %	4.10 %	4.30 %
6:	3.91 %	3.99 %	4.23 %	4.15 %	4.03 %	4.35 %	4.35 %	4.35 %	4.71 %	4.91 %

4.3 Study of 3 kW solar panels at the objects

In this section Scenario I and Scenario II at Søndre Sandøy with 3 kW solar panels are presented. Since Scenario III are given in Table 4 and Table 5 in Section 3.2 those tables are not presented again, but Scenario III are discussed referring to Table 4 and Table 5.

4.3.1 Scenario I

The largest solar panels that are installed at the objects are 3 kW. The interest is to see how the network responds to this capacity at the different scenarios and cases. For the worst case scenario the voltage drop is presented in Table 6.

Furthermore, Table 7 illustrates how this solar capacity affects $\Delta U_{\text{stationary}}$ where Object 10 at Case 6 reached a percentage of 6.71 %. Accordingly, the limit of 3 % is exceeded for Case 3, 4, 5 and 6. Despite this, Case 2 is close to the limit at Object 6, 7 and 8. Moreover, in Case 3, 4, and 5 there are non-solar objects which are affected by the objects with solar panels. Object 10 is a non-solar object in Case 3. In Table 7 the percentage of this object reached 3.71 %, which lead to this Object does not pass the requirement. Furthermore, in Case 4 the non-solar object 1 - 4 exceeds the limit, while in Case 5 the non-solar object 3 and 4 also exceeds the limit. at Case 5 the percentage of non-solar object 3 and 4 increased because of Object 1 and 2 has solar panels installed in Case 5. Table 6 shows the voltage is the same at the objects which have solar panels installed when the production drops to 0 kW. The reason for this could be that Scenario I with 0 % production locally is an unrealistic scenario. Because some solar radiation will pass through the clouds, which generates some production locally at the solar panels. Scenario II and III considers this with production locally when cloudy. However, the results indicate the worst case scenario is not passed. Furthermore, Scenario II follows.

Table 6. 3 kW installed at the objects with 0 % production due to clouds.

	1	2	3	4	5	6	7	8	9	10
S-C P [MVA]	0.346	0.301	0.215	0.271	0.336	0.266	0.287	0.287	0.205	0.162
	[V]	[V]	[V]	[V]	[V]	[V]	[V]	[V]	[V]	[V]
1: 3 kW	219.1	218.9	218.2	218.6	219.7	219.7	219.0	219.0	218.5	217.9
1: 0 kW	216.4	216.2	215.4	215.9	216.5	216.0	215.8	215.8	215.2	214.7
2: 3 kW	222.9	222.7	221.9	222.4	223.9	224.5	224.6	224.6	223.3	222.8
2: 0 kW	217.8	217.7	216.9	217.4	218.1	217.9	217.9	217.9	217.0	216.5
3: 3 kW	224.6	224.4	223.7	224.1	225.8	226.7	226.8	226.8	226.9	225.9
3: 0 kW	218.4	218.2	217.4	217.9	218.7	218.6	218.6	218.6	218.2	217.5
4: 3 kW	226.6	226.4	225.7	226.1	228.0	229.2	229.3	229.3	230.4	231.0
4: 0 kW	219.2	219.0	218.3	218.8	219.6	219.6	219.6	219.6	219.6	219.6
5: 3 kW	230.9	231.1	229.8	230.3	231.7	232.9	233.0	233.0	234.1	234.8
5: 0 kW	220.8	220.8	219.8	220.3	221.0	221.0	221.0	221.0	221.0	221.0
6: 3 kW	235.2	235.4	236.3	235.9	235.5	236.6	236.7	236.7	237.8	238.5
6: 0 kW	222.5	222.5	222.5	222.5	222.5	222.5	222.5	222.5	222.5	222.5

Table 7. $\%U_{\text{stationary}}$ for all the cases regarding Scenario I.

	1	2	3	4	5	6	7	8	9	10
1:	1.23 %	1.23 %	1.28 %	1.23 %	1.45 %	1.68 %	1.46 %	1.46 %	1.51 %	1.47 %
2:	2.28 %	2.24 %	2.25 %	2.24 %	2.60 %	2.94 %	2.98 %	2.98 %	2.82 %	2.83 %
3:	2.76 %	2.76 %	2.81 %	2.76 %	3.14 %	3.57 %	3.61 %	3.61 %	3.83 %	3.71 %
4:	3.27 %	3.27 %	3.29 %	3.23 %	3.68 %	4.19 %	4.23 %	4.23 %	4.69 %	4.94 %
5:	4.37 %	4.46 %	4.35 %	4.34 %	4.61 %	5.11 %	5.15 %	5.15 %	5.60 %	5.88 %
6:	5.40 %	5.48 %	5.84 %	5.68 %	5.52 %	5.96 %	6.00 %	6.00 %	6.44 %	6.71 %

4.3.2 Scenario II

Table 8 shows that the voltage drop is lower which is because of the 10 % local production at the customer when cloudy. Table 9 indicates that for Scenario II the $\Delta U_{\text{stationary}}$ is still too high for Case 3, 4, 5 and 6, despite the percentage being evenly a bit lower in all cases. As seen in this scenario the problems start at Case 3, when 5 Objects have installed solar panels. The highest percentage at Object 10 in Case 6 has decreased to 5.95 %, but also in this Scenario all objects at Case 5 and 6 have a too high percentage. This scenario has fewer non-solar objects which exceed the limit due to the lower voltage drop because of the 10 % power production from the solar panels.

Table 8. 3 kW installed at the objects with 10 % solar production due to clouds.

	1	2	3	4	5	6	7	8	9	10
S-C P [MVA]	0.346	0.301	0.215	0.271	0.336	0.266	0.287	0.287	0.205	0.162
	[V]	[V]	[V]	[V]	[V]	[V]	[V]	[V]	[V]	[V]
1: 3 kW	219.1	218.9	218.2	218.6	219.7	219.7	219.0	219.0	218.5	217.9
1: 0.3 kW	216.6	216.5	215.7	216.2	216.8	216.4	216.1	216.1	215.5	215.0
2: 3 kW	222.9	222.7	221.9	222.4	223.9	224.5	224.6	224.6	223.3	222.8
2: 0.3 kW	218.4	218.2	217.4	217.9	218.7	218.6	218.6	218.6	217.7	217.2
3: 3 kW	224.6	224.4	223.7	224.1	225.8	226.7	226.8	226.8	226.9	225.9
3: 0.3 kW	219.1	218.9	218.1	218.6	219.5	219.5	219.5	219.5	219.1	218.4
4: 3 kW	226.6	226.4	225.7	226.1	228.0	229.2	229.3	229.3	230.4	231.0
4: 0.3 kW	220.0	219.9	219.1	219.6	220.5	220.7	220.7	220.8	220.8	220.9
5: 3 kW	230.9	231.1	229.8	230.3	231.7	232.9	233.0	233.0	234.1	234.8
5: 0.3 kW	221.9	221.9	220.9	221.4	221.1	222.3	222.3	222.3	222.4	222.5
6: 3 kW	235.2	235.4	236.3	235.9	235.5	236.6	236.7	236.7	237.8	238.5
6: 0.3 kW	223.9	223.9	224.0	224.0	223.9	224.1	224.1	224.1	224.2	224.3

Table 9. $\%U_{\text{stationary}}$ for all the cases regarding Scenario II.

	1	2	3	4	5	6	7	8	9	10
1:	1.14 %	1.11 %	1.15 %	1.10 %	1.32 %	1.50 %	1.32 %	1.32 %	1.37 %	1.33 %
2:	2.01 %	2.02 %	2.02 %	2.02 %	2.32 %	2.69 %	2.67 %	2.67 %	2.50 %	2.51 %
3:	2.44 %	2.45 %	2.50 %	2.45 %	2.79 %	3.18 %	3.22 %	3.22 %	3.43 %	3.32 %
4:	2.91 %	2.87 %	2.92 %	2.87 %	3.28 %	3.70 %	3.75 %	3.70 %	4.16 %	4.37 %
5:	3.89 %	3.98 %	3.87 %	3.86 %	4.14 %	4.55 %	4.59 %	4.59 %	5.00 %	5.23 %
6:	4.80 %	4.89 %	5.20 %	5.04 %	4.92 %	5.28 %	5.32 %	5.32 %	5.72 %	5.95 %

4.3.3 Scenario III

The results from Scenario III are given from Table 4 and Table 5. Also this scenario shows that $\Delta U_{\text{stationary}}$ is too high for Case 4, 5 and 6 according to Table 5, despite the percentage being lower in all cases due to the lower voltage drop. Also 5 of 10 objects pass Case 4. However, the scenarios indicate that a capacity of 3 kW solar panels is too much for the network. The $\Delta U_{\text{stationary}}$ is too high for Case 4, 5 and 6 according to Table 5. Also 5 of 10 objects pass Case 4. Further, the non-solar objects that exceed the limit are only spotted in Case 5 at Object 3 and 4. The reason for this is because of this is the easiest scenario to pass due to the lower voltage drop at the solar panels. However, the scenarios indicate that a capacity of 3 kW solar panels are too much for the network.

5 Discussion

In Table 10 all the cases and scenarios at Søndre Sandøy are presented with a different size of solar panels at the objects.

Table 10. The different scenarios and cases at Søndre Sandøy.

	1 kW	2 kW						3 kW					
Scenario I	1 - 6	1	2	3	4	5	6	1	2	3	4	5	6
Scenario II	1 - 6	1	2	3	4	5	6	1	2	3	4	5	6
Scenario III	1 - 6	1	2	3	4	5	6	1	2	3	4	5	6

Søndre Sandøy had challenges with the installed solar panels in the network. With 1 kW installed solar panels at the objects the requirements were met for all scenarios from Case 1 - 6 according to Table 10 and did not indicate any problem for the DSO. Also shown in Table 10 the main challenges occur with 2 kW and 3 kW solar panels.

With 2 kW solar panels in Scenario II and III the requirements were held up to Case 3 and Case 4, respectively, as shown in Table 10. In Scenario I two non-solar objects exceeded the limit of 3 % at Case 5 (Marius Salen 2019). This clarifies the impact clouds have on solar panels on a weak grid since the change in production caused by the passing clouds also has an impact on the customers without solar panels.

For the 3 kW solar panels only Case 1 and 2 passed Scenario I and Scenario II. Besides this, the percentage of $\Delta U_{\text{stationary}}$ is high for all objects at the different cases in the two scenarios. Furthermore, Scenario III for 3 kW exceed the limit for Case 4 - 6, and the $\Delta U_{\text{stationary}}$ is still quite high with a maximum of 4.91 % at Case 6, Object 10 seen from Table 5. Also, there where non-solar objects which got affected by the objects with solar panels in all of the scenarios.

As a result of the previous simulations, the DSO should be aware of an increase in solar capacity at this part of the network in Søndre Sandøy. Especially with solar panels of 2 kW and 3 kW, as this can lead to challenges regarding the requirements at § 3.4 in FoL. The number of prosumers has increased throughout the years (Dinside 2019). Since Hvaler is an island with many prosumers compared to the population, the cases in the different scenarios illustrated are likely to occur. From this, the DSO can take the results from the simulations in consideration when planning for future grid development.

6 Conclusion

In the scenarios where Søndre Sandøy had solar panels installed at the objects the related voltage $U_{\text{delivered}}$ increased. In the simulations no problems where found with 1 kW installed solar panels at the objects regarding FoL. Also, the simulations revealed that Søndre Sandøy had challenges when the objects had 2 kW and 3 kW solar panels installed. This is due to a weak grid with low short-circuit performance at the objects.

Furthermore, the simulations show that passing clouds make a significant impact on the solar panels due to the voltage drop at the customer. Especially when a lot of objects have installed solar panels. This will lead to the requirements in FoL are not met in some cases. Also found from the simulation at Søndre Sandøy was that the non-solar objects were affected by the objects with solar panels when the size of 2 kW and 3 kW was simulated.

7 Further work

In this paper only analysis for $\Delta U_{\text{stationary}}$ were conducted. A recommendation for further work is to study scenarios with ΔU_{max} and to see how this responds to the requirements from FoL § 3.4. Simulations with ΔU_{max} require measurements from the field to compare with the simulations. To simulate the ΔU_{max} the dynamic power system simulation software like PowerFactory can be used. This software has a higher complexity to simulations compared to NETBAS, and that is required for the study of ΔU_{max}.

Also a recommendation for further study is to use 10 % as a worst case scenario. The reason for this is to get a

worst case which is more likely to occur, since 0 % production is not a realistic scenario because there always will be some solar radiation that passes through the clouds. Also, to get even more realistic scenarios, measures on a PV-panel regarding the voltage drop due to the clouds can be taken.

References

Cheiw Yun Lau, Chin Kim Gan, Chin Ho Tie, Kyairul Azmi Baharin, and Mohamad Fani Sulaima. *Passing-cloud Effects of Solar Photovoltaic System on Distribution Network Voltages*, 2015.

Christian Rendall Olsen. *Economic feasibility analysis of microgrids in Norway: an application of HOMER Pro*. MA thesis. Campus Ås: NMBU, 2018.

Dinside. *Hva er en plusskunde?* URL: https://www.dinside.no/okonomi/na-skal-det-bli-enklere-a-bli-eget-stromselskap/70850821 (visited on 04/12/2019), 2019.

Camilla Seland Ellefsen. *Grid Connected PV and the Risk of Overvoltages*. MA thesis. Grimstad: Universitetet i Agder, 2014.

Lovdata. *Forskrift om kontroll av nettvirksomhet, §3.4*. URL: https://lovdata.no/dokument/SF/forskrift/2004-11-30-1557 (visited on 02/17/2019), 2004.

M.A. Mahmud, M.J. Hossain, and H.R. Pota. *Analysis of Voltage Rise Effect on Distribution Network with Distributed Generation*, 2011.

Marius Salen. *Impact of distributed generatin in the distribution network at the end-customer*. MA thesis. Porsgrunn: USN, 2019.

NVE. Veileder til leveringskvalitetforskriften. In POWEL,*POWEL NETBAS takes you closer to reality improved support by step-by-step building*. URL: https://www.powel.com/about/feature_stories/powel-netbas-tar-deg-narmere-virkeligheten--forbedret-stotte-ved-stegvis-bygging/ (visited on 02/11/2019), 2018.

Wikipedia. *Hvaler (kommune)*. URL: https://no.wikipedia.org/wiki/Hvaler_(kommune) (visited on 01/06/2019), 2019.

Wilson Rickerson. *Residental prosumers - Drivers and policy options*, 2014.

Building occupation modelling using motion sensor data

Nils-Olav Skeie[1] Jørund Martinsen[2]

[1,2]Department of Electrical Engineering, Information Technology and Cybernetics
University of South-Eastern Norway, Porsgrunn, Norway, Nils-Olav.Skeie@usn.no

Abstract

In smart building environments, both office and residential buildings, it is important to have some information about the use and occupation. Today this is normally solved by a fixed time schedule meaning the occupants must adapt to the system, not the other way around. This paper discuss the usage of a top hat probability models, based on a four weeks history from inexpensive sensor devices, for prediction of the occupation in the next week. The model was divided into seven groups, one group for each of day of the week. A software system, based on several modules, was developed. One module was used to record the information from the motion sensors and stored the data as historical data. One module was used to create the model, and another module was used to prediction of occupation for the next days, up to a week. The models are working satisfactory as long as the behavior patterns are similar for the training and prediction period. However, the models are sensitive to changes in the daily behavior pattern of the occupants, like holidays or taking a day off.

Keywords: probability model, building occupation, PIR sensor devices, motion sensor devices, building occupation prediction.

1 Introduction

1.1 Background

Important aspects in SMART building environments are energy efficiency, energy savings, and welfare assistance. More than 50% of the energy used in buildings in norther countries is for space heating (Perera *et al.*, 2014). The temperature should be at a comfort temperature only when the building is in use, any energy saving strategies should be in focus when the building is not in use or when the occupiers are sleeping. In most building energy management systems (BEMS) today this schedule is configured with fixed time intervals when to keep the comfort temperature, and when to save energy. Regarding many welfare assistance systems, these systems also need to know when the occupiers are using the building.

Such smart building systems should adapt to the occupiers use of the building, and should not be based only on a fixed time schedule. A good solution can be to start with a fixed time schedule but allow for deviations based on the real usage of the building. Any system should adapt to how the buildings are used by the occupiers, the occupiers should not need to adapt to a fixed configuration.

Today many buildings already have an alarm system based on motion sensor devices in many rooms. These alarm systems are activated only when turned on by the user, however the system, including the sensor devices, are working also when the alarm system is deactivated. Based on the information from these sensor devices it should be possible to predict when the building is in use, and also when the occupiers are sleeping. The prediction of the building occupation can be used to optimize the time when having the comfort temperature, when to save energy, and when to activate any welfare assistance systems. This prediction can even be used to turn on the alarm system.

The aim of this paper is to show the development of a set of models to predict a building occupation based on information from low-cost motion sensor devices. The models should be easy to implement in most programming languages.

1.2 Previous work

Occupancy behavior in buildings are becoming an important topic as building systems are becoming more sophisticated and people are spending a lot of time in the buildings. The occupancy behavior is one of the leading influences of energy consumption in buildings but not used that much as input in existing models (Yan *et al.*, 2015; Clevenger and Haymaker, 2006; Adamopoulou *et al.*, 2016). Previous work is based mostly upon occupant surveys and interviews affecting the energy efficiency of buildings (Yan *et al.*, 2015) not that much work based on the occupier use of the buildings. An extended work based on occupancy behavior is described in (Adamopoulou *et al.*, 2016) which is dividing the building into zones and using a Monte Carlo approach to model the usage of each zone, including the number of occupants in each zone. Zones are collected in zone groups based mainly on periods of use. The models take into account also the seasons and day of week, making separate models for each instance of these zone groups. The historical data is based mainly on image processing from several depth-image cameras, but also on acoustic and infra-red (PIR) sensors. The work described in (Ryu and Hyeun, 2016) is based on

decision tree as machine learning technique and hidden Markov model as a probability technique. The historical data is based on carbon dioxide (CO_2) concentration and electricity consumptions. The work described in (Wang *et al.*, 2018) is based on the k-nearest neighbors (knn), support vector machine (svm) and artificial neural network (ann) machine learning algorithms. The historical data is based on the fusion of environmental data and information from the WiFi network. In this work the ann based model gave the best result. The work described in (Habib and Zucker, 2017) is based on the indoor air quality information from the ventilation system and a k-means clustering algorithm for occupancy prediction in a building. The k-means clustering is a machine learning technique. The work described in (Shi and Yao, 2016) is using a novel statistical model, based on a logistic regression model, for occupancy prediction at a specific time. The model is only simulating based on time of the day. The focus in this work is a model predictive model (MPC) for an efficient operation of a heating, ventilation and air condition (HVAC) system. The work described in the master thesis (Martinsen, 2019) is based on information from infra-red (PIR) sensors and a simple probabilistic model for each day of the week, and is discussed in this paper. The model can easily be implemented in most software languages.

1.3 Outline of the paper

Section 2 provides a discussion of the movement sensor device, data collection and the building used. Section 3 gives an overview of the model used. Section 4 gives an overview of the model fitting and validation. The results are discussed in section 5, and some conclusions are drawn in Section 6.

2 System description

A building located in South Eastern of Norway has installed a set of movement sensors and the information from these movement sensors have been logged for at least one year. The data is logged on comma separated values (csv) based text files, one file for each month.

The building has three floors, ground floor, first floor and second floor. The sensors are located in the living room and kitchen at the first floor, and top of the staircase and in an extra living room at second floor. Two movement sensors are installed in the living room at first floor.

An overview of the first floor and second floor, with the sensor locations marked with green rectangles, shown in Figure 1.

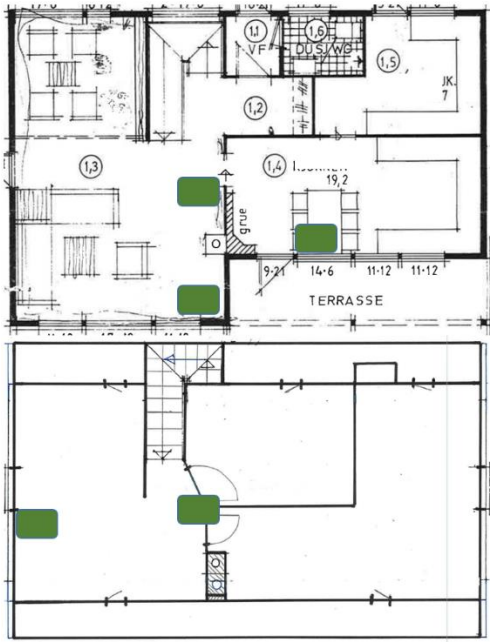

Figure 1. The first and second floor of the building with the motion sensor devices as green rectangles. First floor, at the top, with three sensor devices, one in the kitchen and two in the living room. Second floor, at the bottom, with two sensor devices, one at the staircase and one in the living room.

These motion sensor devices are based on the passive infrared (PIR) type of sensors, detecting if an object with a higher temperature than the environment is moving into the measurement area of the sensor device. The measurement principle is based on heat radiation from an object with a higher temperature than the environment. The sensor converts any resulting change in the incoming infrared radiation into triggering an event giving a digital output voltage pulse. A Fresnel lens is used to divide the measurement area of the sensor device into sectors, so any change in the infrared radiation within any of the sectors will trigger an event. The output signal from these sensor devices will be a digital pulse signal, an event, indicating that a moving object has been detected. The sensor devices are connected to the digital input ports on a data acquisition (DAQ) device.

Figure 2 shows the number events (triggers) from two of the sensor devices on the first floor, for a typical weekend day. The red indication for the sensor on the kitchen on the first floor, and the blue indication for the sensor in the living room, close to the window. The number of triggers is in the range of 200 to 800 for each hour, for the sensor device in the kitchen.

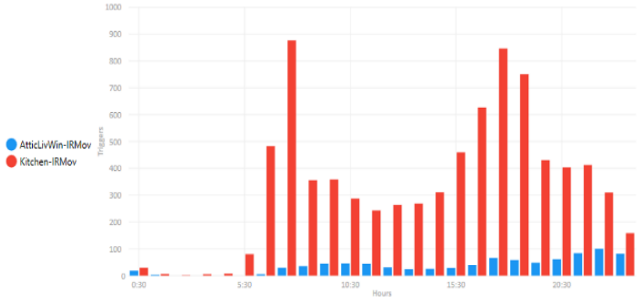

Figure 2. The number of events (triggers) from two of the sensor devices on the first floor shown for a weekend day for 24 hours. Starting at 00:00 and ending at 23:59, one red and blue column for each hour.

The software consists of four main functions, shown in Figure 3. The figure is a use case diagram (Fowler and Scott, 1997) drawn using the Unified Modeling Language (UML) diagram. A use case diagram shows the main functionality of the software together with the input/output device or external modules known as actors. The functionality of software are 1) collect the data from the motion sensor devices and save the time stamped data on a comma separated values (csv) text file. The motion sensor devices are connected to the DAQ system. 2) create the models based on the data from the csv file and configuration data. The operator or a specific time event can start the create operation for the model. 3) perform prediction based on a specific time. 4) handle configuration of the system, by the operator. The configuration data are saved on an xml type text file loaded every time the software is starting.

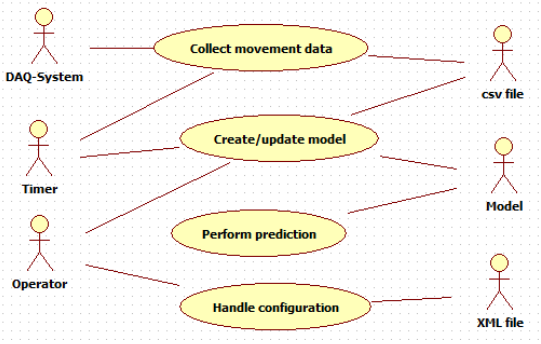

Figure 3. A use case diagram of the main functionality and the actors of the software.

The "Perform prediction" function will use the model to predict the occupation sometime in the future. This is a manual operation in the current software version but should have a type of application programming interface (API) to let other software applications like the BEMS communicating with this software. Based on the model the prediction can be one week ahead.

3 Model development

3.1 Model selection

The basis is normally a fixed time configuration when installing systems like BEMS in buildings. This paper will propose an extension to such system by adding a model for predicting when the building is actually in use. There is a need to differentiate between an office building and a residential building where the main difference is the use during the night. An office building will typically be used during the working days and may be on Saturdays, while a residential building will be the opposite. The workers will normally be either at work or at home. The challenge with a residential building is the use at night without any measurements of use.

The focus for this paper is residential buildings assuming that the buildings are in use in the morning, in the afternoon, and during night. As a starting point, it is assumed that the buildings will be empty during the daily working hours, and used all day during the week-ends.

A data driven approach is the basis for this model development, based on historical data from the building. Based on the historical data a mathematical model predicting how the building is going to be used for the next days is wanted. In this case more focus on the behavior of the occupations is wanted, and allow for variation of this behavior. Based on this assumption a probability function model is chosen over a model based on a machine learning approach (Bzdok *et al.*, 2018). A machine learning approach, like the artificial neural network (ann) methods, requires a large amount of data. As the occupancy prediction will depend on the seasons, as shown in (Adamopoulou *et al.*, 2016), giving less data, a probability approach is chosen. An autonomous approach for model update is also wanted for updating the occupancy model based on the seasons.

The historical data is based on the information from the PIR sensor devices normally used in any alarm system. The nature of the PIR sensor device is an event, giving an electrical signal with duration of about one second when detecting a movement of a warm object in the area. The probability is one when detecting the movement and declining to zero after a period when not detecting any more movement of warm objects. A simple probability function is wanted and the triangle function, see Figure 4, is the first probability function to evaluate.

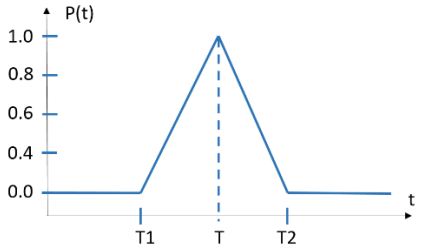

Figure 4. The triangle function.

The triangle function must be linked to every sensor event giving a more complex model because the parameters T1 and T2 must be adapted to each event. Figure 2 shows that there can be a lot of events for every hour when the building is occupied. Sensor devices events for a typical working day is shown in Figure 5, showing the events from the sensor devices at the first floor, with reference to Figure 1.

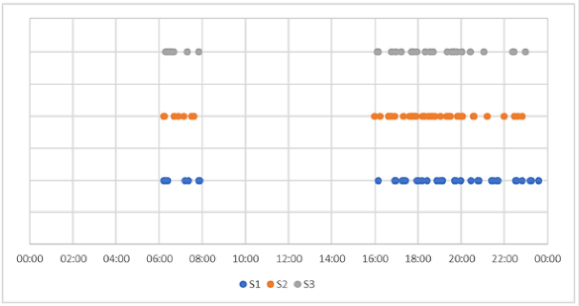

Figure 5: The sensor device events from the three sensors devices at the main floor.

Figure 5 shows that there is high probability that there will be a sequence of events when first detecting an event. The model should be able to predict these sequences of events. Based on a maximum time between these events, the events are grouped into one or several sequences. This maximum time is a parameter that can be configured in the software. The current value is 60 minutes. Figure 6 shows the start and stop events (red dots) to indicate the start and stop of each sequence according to this maximum time, and how these events are converted to the sequences for the use of the building for each day of the week. A morning and evening section for the first five days (working days), and only one section for the last two days, the weekend days.

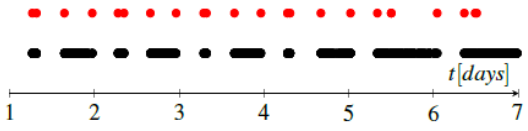

Figure 6. A week with the events (red dots) and the sequence of use of the residential building (black dots/lines).

A probability function that can handle a sequence of events within a period can be a better solution, where the duration of P(t)=1 and the different slopes can be estimated based on the sensor information. A top hat probability function may be a better approach (Boyd, 2006) and is evaluated. Figure 7 shows a simplified top hat probability function.

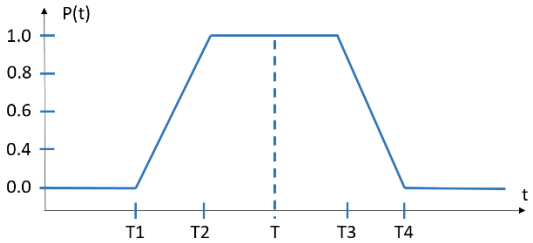

Figure 7. A simplified top hat function, based on (Boyd, 2006).

The simplified top hat function (Boyd, 2006), shown in Figure 7, shows the parameter T for the center of the P(t)=1, the length (T2 to T3) of the P(t) = 1 area, and the length (T1 to T4) of the P(t) > 0 area. These parameters, estimated during the training sequence of the model, are listed in Table 1.

Table 1. Estimated parameters for the simplified top hat function.

Parameter	*Function*
T	Center of top hat
[T2,T3]	The area for the function P(t)=1
[T1,T4]	The area where 0 < P(t) <= 1

The equation for the top hat function is:

$$P(t)=\begin{cases} 0, & t < T1 \\ (T2-T1)(t-T1), & t \in [T1,T2] \\ 1, & t \in [T2,T3] \\ (T4-T3)(t+T3), & t \in [T3,T4] \\ 0, & t > T4 \end{cases} \quad (1)$$

A top hat function can only handle one sequence of sensor device events and as shown in Figure 5 there can be several sequences during a day. Several top hat functions can be combined to handle these numbers of sequences, and make a more complex modelling of the building use. An example of a working day is shown in Figure 8, combining two functions, one in the morning and one in the evening. The regions for each top-hat function must be estimated, and each top-hat function will have its own sets of parameters, with reference to table 1. These regions will be estimated based on the sequence of events from the sensor devices, from the first detection to the last detection in a specific period.

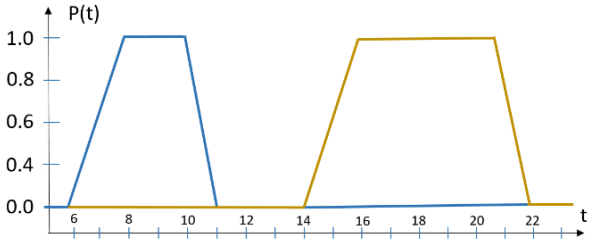

Figure 8. The combined top hat functions for a 24 hours period.

As the residents may have different schedules for every day in a week, but with a high probability that these schedules are repeated every week, giving specific occupancy for each day of the week. Based on this assumption it was decided to split the sensor data into groups, one group for each day of the week.

There can also be deviations for each day of the week so it was decided that a number of events outside a time limit, based on the average, could be removed from the data set. These numbers are defined in the configuration part of the software, the time deviation and number to remove. These events can typically be an event like going to the kitchen for a glass of water or milk during the night, or taking a day off during the working week.

The principles for selecting the candidates for the start and stop events for the model is shown in Figure 9.

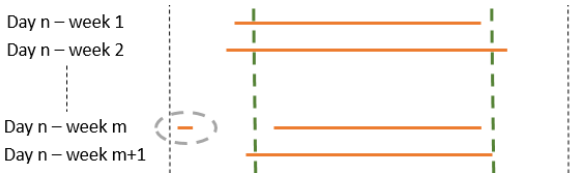

Figure 9. The principles for selecting the start stop events for a sequence.

The events for a specific day are grouped together within a period, configured as a maximum time in the software system. Each day will have a group for every week, as shown in orange lines in Figure 9. The green dotted lines are the group average start and stop positions and the start of week m is outside the maximum time limit, configured in the system, and removed from the data set.

For the building shown in Figure 1 a separate set of models are created for each floor.

3.2 Model training

Sensor data was collected for the last year and first all the data was used for training the daily sequences. Due to holidays and variations trough out the year, this was not a good approach. This is also mentioned in (Adamopoulou et al., 2016) as the occupancy behavior will depend on the seasons, and the data sets for model development should be smaller. The new approach is to use the data from the last eight and four weeks for training the model. It was also configured that only one event can be removed from the data set if more than 60 minutes outside the average for the start or end of an event sequence (as shown in Figure 9).

Figure 5 shows two set of event sequences for each of the sensor devices, S1, S2 and S3. The Create/update model function of the software application, see Figure 3, was used to create the model by finding the candidates for the desired periods. Figure 10 shows the top-hat parameter estimation for a specific day, using a data set of four weeks.

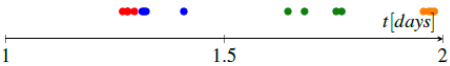

	Morning (G1)	Noon (G2)	Afternoon (G3)	Evening (G4)
W1	1.27	1.32	1.65	1.97
W2	1.28	1.32	1.76	1.96
W3	1.29	1.41	1.68	1.98
W4	1.28	1.31	1.77	1.97

Figure 10. Estimation of the model parameters for a data set of four weeks. These group values, for day number 2, are used to define the T parameters according to Table 1.

The T parameters, according to Table 1, for the first top hat functions are selected as shown in Table 2.

Table 2. The group values for the top hat function for day number 2.

Parameter	*Value*	*Description*
T1	1.27	G1 minimum
T2	1.29	G1 maximum
T3	1.31	G2 minimum
T4	1.41	G2 maximum

Figure 11 shows the data flow for training the models, estimating the T parameter for each of the top hat functions. The training starts with selecting a data set from the historical data sets, estimating the average start and stop times for each of the periods for the day groups and top hat functions for the day. Any events outside a configured maximum time will be removed and a new estimation will be performed. In Figure 11 a maximum time of 60 minutes is used, and this maximum time is shown in Figure 9. The number of events that can be removed can also be configured in the software, only one is used for this training. When any events outside the limits are removed, will the minimum and maximum times for each group be assigned the T1, T2, T3 and T4 for each of the top hat functions.

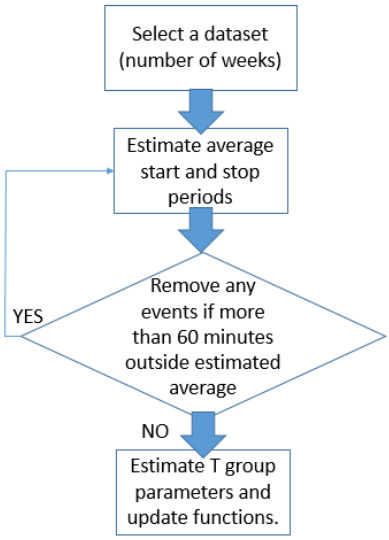

Figure 11. The flow chart for training the models.

A model was created based on a data set from the last eight weeks, and the prediction output from the model is shown in Figure 12. The model is created only for first floor and only the sensor devices on first floor

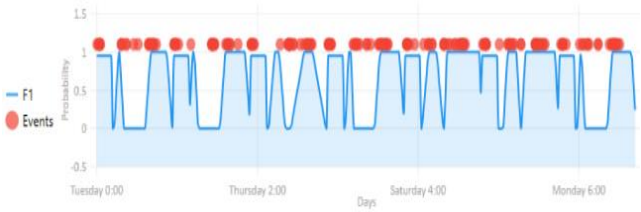

Figure 12. Training the model with eight weeks of data with prediction output for all days. The model starts on Tuesday and ends on Monday.

Another model was created based on the data set from the last four weeks, and the prediction output from that model is shown in Figure 13. The model was created on the same data set as the model shown in Figure 12.

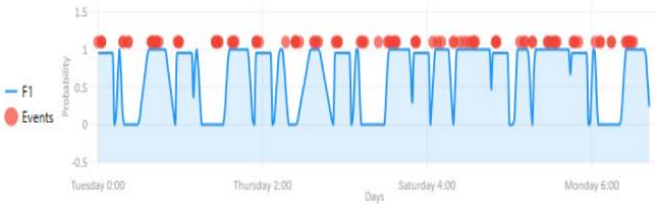

Figure 13. Training of the model with four weeks of data and showing the prediction output for all days of the week. The model starts on Tuesday and ends on Monday.

Comparing the model output from Figure 12 and Figure 13 shows almost the same prediction. The prediction starts on Tuesday, first the morning, no occupation during the day, and occupation during the evening, night and Wednesday morning. The number of events are higher for the eight weeks data set, as shown in Figure 12. However, the same model also shows a higher number of events that must be removed during the training of the model. Figure 13 shows almost the same model prediction, but with fewer events removed. The model in Figure 13 was used for validation. Both figures show that the T1 to T4 parameters are different for each of the top hat functions, indicated by the slopes.

4 Results

The models are trained and validated for one floor only, as an option in software to make a separate model for each floor. The models were trained based on data from both four and eight weeks of data. The models based on eight weeks of data gives a more detailed model but any holidays, days off or deviations during this period introduces more model errors. The best approach seems to use four weeks of data for the training period, and have the option to remove one deviation in any of the weeks.

The model validation is based on three test cases. One normal test case with high quality training data, data without any events that must be removed. The training data set is from 5-JAN to 4-FEB, and the prediction period is 5-FEB to 13-FEB. The next test case is the holiday test case with a training set with many events that must be removed. The training set is from 5-JUN to 4-JUL, and the prediction period is 5-JUL to 13-JUL. The last test case has focus on a single day, the Friday test case with missing data. The training set is from 30-OCT to 29-NOV, and the prediction period is 30-NOV to 7-DEC.

The results for these three test cases are, using four weeks of training data:

- Normal test case; models accuracy are between 94% and 98%,
- Holiday test case; models accuracy are between 32% and 38%,
- Friday test case; models accuracy are between 11% and 17%.

Figure 14 shows the model prediction for the normal test case, the measured data as red indications and the candidates for creating the model as orange indications. The model shows a good match between the measured data and the prediction.

Figure 14. Validation of the normal test case, created the model with a high quality data set. The data starts from Monday and ends on Sunday.

Figure 15 shows the model prediction for the holiday test case where the training set is from the last working weeks before the holiday while the prediction should be for a holiday week. The measurements indicate that the building was not used the first part of the week, and used all the day the last part of the week. This shows that the pattern in the training data must correspond with the pattern for the prediction week.

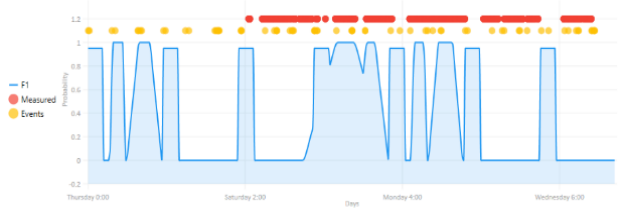

Figure 15. Validation of the holiday test case, created a model with a different behavior pattern then the expected pattern for the prediction week. The data starts from Thursday and end on Wednesday.

The last test case, the day test case (Friday test) shows the same deviation as the holiday test case. The test case is shown in Figure 16. Only the Friday contains measured data while the candidate data has created a prediction model for the whole week, and the measured data is inconsistent with the model prediction. The behavoir seems that the occupants has left the building at Friday and been away the whole next week.

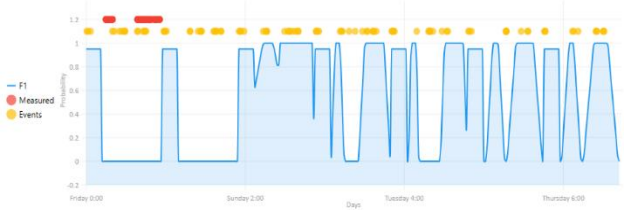

Figure 16. Validation of a day test case where the created model was created based on different behavior pattern then the actual behavior pattern for the prediction week. The data starts from Friday and ends on Thursday.

5 Discussion

The pattern consistency is important to be able to create a good prediction model. This means that the behavior pattern for occupants must be the same for training set as for the prediction period. The first test case, the normal test case, shows that if there is good connection between the behavior pattern for the training set and the behavior pattern for the prediction week, the model will predict with a good accuracy.

The deviation of the occupancy behavior for the training and validation period is difficult to fulfill as human will make random decisions to take a day off, or going away for a holiday.

This indicates that to have a good building occupation model the behavior pattern for the training set must be of the same type as for the prediction week. Some sort of building calendar can be a good extension to the system for defining any deviation from the normal behavior pattern. This way it is possible to extend the model with day models for both working days, holiday staying at building (same as weekends) and holiday staying away from the building. This approach should also be applicable for office buildings during special holidays like Christmas.

In the normal test case the deviation is detection of movement during the night which should be a deviation as the energy system should not adjust the comfort temperature according to these short movements. An option can be to have a minimum period during the night for detection of movement events.

The holiday test case is trained for a normal week. However, in the prediction week the occupants were away half of the week, and stayed at home, all day, the rest of the week. A calendar option could have made this prediction better by defining holiday away and at home states.

The Friday test case is almost the same as the holiday test case. However, in the prediction week the occupants stayed home only on Friday. A calendar option could have made this prediction much better.

The software is designed to create a new model at fixed times so this software will be an autonomous system updating the models every week. This is also a reason for using a probabilistic model that can be easily implemented in software.

The software, as indicated in Figure 3, was implemented using the C# programming language. Most of the figures in this paper is based on screen dumps from the user interface from this C# application.

The system will also work independent of the number of occupants in the building as the number of events does not matter, only the start and stop events of a sequences of events.

A PIR sensor device at the main door can also make the system better in estimating the occupation pattern as events will be created when entering or leaving the building. Such a configuration may also be used for turning the alarm system automatically on.

The software was configured to allow a period of up 60 minutes for a continuous occupancy behavior while

the work in (Adamopoulou *et al.*, 2016) used 30 minutes. A shorter period can be a better approach.

6 Conclusion

The paper has shown that the top hat functions can be used for predict the occupancy behavior of a residential building. A training period of four weeks, with the option to remove one extreme event sequence from the motion sensor devices can give a good prediction horizon of one week. The solution depends on the behavior patterns for the occupants, and this pattern has to be the same type during both training period and the prediction period.

References

Anna A. Adamopoulou, Athanasios M. Tryferidis, and Dimitrios K. Tzovaras. A context-aware method for building occupancy prediction. *Energy and Buildings*, 110: 229-244, 2016.

J. P. Boyd. Asymptotic Fourier coefficients for a C bell (smoothed "top-hat") and the Fourier extension problem. *Journal of Scientific Computing*, 2006.

Danilo Bzdok, Naomi Altman, and Martin Krzywinski. Statistics versus machine learning. *Nature methods*, 15:233-234, 2018.

C. M. Clevenger and J. Haymaker. *The impact of the building occupant on energy modeling simulations*. IEA-EBC Annex 66, 2006.

M. Fowler and K. Scott, K. UML *Distilled: Applying the standard object modeling language*. AddisonWesley, USA, 1997.

U. Habib and G. Zucker. Automatic occupancy prediction using unsupervised learning in buildings data. In *IEEE International Symposium on Industrial Electronics (ISIE)*, 2017. DOI: 10.1109/ISIE.2017.8001463.

Jørund Martinsen. *Modeling of building occupation using motion sensor data*. Master's Thesis, University of SouthEastern Norway (USN). 2019,

D. W. U. Perera, C. Pfeiffer, and N.-O. Skeie. Modelling the heat dynamics of a residential building unit: Application to Norwegian buildings. *Modeling, Identification and Con trol (MIC)*, 35:43-57, 2014

S. Ryu and J. M. Hyeun. Development of an occupancy prediction model using indoor environmental data based on machine learning techniques. *Building and Environ ment* 107:1-9, 2016. DOI: 10.1016/ j.buildenv.2016.06.039.

J. Shi, N. Yu, and W. Yao. Energy efficient building HVAC control algorithm with real-time occupancy prediction. *Energy Procedia*, 111:267-276, 2016

W. Wang, J. Chen, and T. Hong. Occupancy prediction through machine learning and data fusion of the environmental sensing and Wi-Fi sensing in buildings. *Automation in Construction*, 94:233-243, 2018 DOI: 10.1016/.j.autcon.2018.07.007.

D. Yan, W. O'Brien, T. Hong, X. Feng, H. B. Gunay, F. Tahmasebi, and A. Mahdavi. Occupant behavior modeling for building performance simulation: Current state and future challenges. *Energy and Buildings*, 107:264-278, 2015.

Sensor placement and parameter identifiability in grey-box models of building thermal behaviour

O. M. Brastein*, R. Sharma, N.-O. Skeie

Department of Electrical Engineering, Information Technology and Cybernetics
University of South-Eastern Norway, N-3918 Porsgrunn,
*(ole.m.brastein@usn.no)

Abstract

Building Energy Management systems can reduce energy consumption for space heating in existing buildings, by utilising Model Predictive Control. In such applications, good models of building thermal behaviour is important. A popular method for creating such models is creating Thermal networks, based cognitively on naive physical information about the building thermal behaviour. Such models have lumped parameters which must be calibrated from measured temperatures and weather conditions. Since the parameters are calibrated, it is important to study the identifiability of the parameters, prior to analysing them as physical constants derived from the building structure. By utilising a statistically founded parameter estimation method based on maximising the likelihood function, identifiability analysis can be performed using the Profile Likelihood method. In this paper, the effect of different sensor locations with respect to the buildings physical properties is studied by utilising likelihood profiles for identifiability analysis. The extended 2D profile likelihood method is used to compute two-dimensional profiles which allows diagnosing parameter inter-dependence, in addition to analysing the identifiability. The 2D profiles are compared with confidence regions computed based on the Hessian.

Keywords: building energy management systems, thermal behavior, parameter estimation, parameter identifiability, Profile Likelihood

1 Introductions

1.1 Background

A significant portion of the worlds total energy production is consumed by heating and cooling of buildings (Perera et al., 2014). Building Energy Management Systems (BEMS) is therefore an important part of the ongoing effort to reduce anthropogenic CO_2 emissions. In particular, Model Predictive Control (MPC) has been shown to reduce energy consumption in buildings by utilizing models to predict the thermal behaviour of a building (Fux et al., 2014; Killian and Kozek, 2016). Hence, the development of models of building thermal behaviour has received considerable interest by the scientific community in recent years.

1.2 Previous work

A common approach to the modelling of building thermal behaviour is the use of *thermal network* models (Berthou et al., 2014; Reynders et al., 2014). These models are often described using electric analogues Resistor-Capacitor (RC) circuits. Based on a *naive* understanding of the thermodynamics involved, these RC circuits constitute *simplified lumped parameter* models. Parameters are estimated from measurements of temperature inside the building, weather conditions and input power consumed for space heating. As simplified models based on both physical insight and measurement data, thermal network models constitute a compromise between fully physics based white-box and purely data-driven black-box models. This type of model, often called grey-box models, allows use of prior knowledge of the system while also allowing calibration of parameters to adapt the model to a particular building. This approach offers improved prediction accuracy while also allowing use of prior physical information to be injected into the model (Madsen and Holst, 1995; Bacher and Madsen, 2011; Kristensen et al., 2004).

Since the model structure is designed based on knowledge of a particular building, it is often assumed that the parameters are determined by the physical properties of that building. However, since the parameters are identified from data, this assumption needs to be verified in the context of *parameter identifiability* (Reynders et al., 2014; Deconinck and Roels, 2017; Ferrero et al., 2006). In particular, testing of practical identifiability (Raue et al., 2009), i.e., if sufficient dynamic information about the underlying system is contained in the calibration data (Ferrero et al., 2006), is of importance.

1.3 Overview of paper

Since weather is part of the experimental conditions, and, typically, the acceptable range of indoor temperatures, as well as input heater power, is limited, model calibration must usually be performed on sub-optimal data. One element which, to some degree, is open to experimentation is the location of the sensors. As simplified models, thermal networks reduce large indoor spaces and objects, such as the building envelope, to point nodes in the RC circuit. How these nodes correspond to the physical building is

determined by the sensor location. In this work, we study different sensor placements in an experimental building to show how sensor location, with respect to the physical properties of the building, affects the dynamic information contained in the data and hence the practical identifiability of model parameters. Parameter identifiability is analysed using the *Profile Likelihood* method, both in the single parameter dimension and in two parameter dimensions by projecting the profile onto a plane in parameter space. The latter method allows improved insight into the parameter domain, including analysing parameter inter-dependence and the effects of a constrained parameter space.

2 Theoretical basis

The framework presented in (Kristensen et al., 2004), named Continuous Time Stochastic Modelling (CTSM), is a statistically well founded approach to parameter estimation. The theoretical basis is briefly summarised below. For a more detailed discussion see (Kristensen et al., 2004). Consider the estimation problem:

$$\hat{\theta} = \arg\min_{\theta} g(\theta; \mathscr{M}, \mathscr{K}, \mathscr{A}) \quad (1)$$
$$s.t.\ \theta \in \Theta$$

Here, $\mathscr{M}$ is a predetermined model structure parametrised by $\theta \in \Theta$, where $\Theta \subseteq \mathbb{R}^{n_\theta}$ is a set of feasible values for the model parameters that form inequality constraints for the optimisation problem in Eq. (1). Parameters in θ are varied over the feasible set Θ by a numerical optimisation algorithm $\mathscr{A}$. The experimental conditions $\mathscr{K}$ include measurements for the continuous time input $u_t \in \mathbb{R}^{n_u}$ and output $y_t \in \mathbb{R}^{n_y}$. The corresponding ordered sequences of discrete time measurements u_k and y_k taken from the system $\mathscr{S}$ are $y_{[N]} = [y_0, y_1, \ldots, y_N]$ and $u_{[N]} = [u_0, u_1, \ldots, u_N]$, where the integer subscripts $k = 0, 1, \ldots, N$ denote the discrete time sampling instants, and the subscript enclosed in $[\cdot]$ is used to indicate an ordered sequence.

The likelihood function, i.e., the probability of observing the measurement sequence $y_{[N]}$ when θ and $\mathscr{M}$ are given, is defined:

$$L(\theta; y_{[N]}, \mathscr{M}) = p(y_{[N]}|\theta, \mathscr{M}) \quad (2)$$

By assuming that the residuals are Normal distributed, and applying the product rule to expand the probability in Eq. (2), we obtain (Kristensen et al., 2004):

$$L(\theta; y_{[N]}) = \left(\prod_{k=1}^{N} \frac{\exp\left(-\frac{1}{2}\varepsilon_k^T \mathscr{E}_{k|k-1}^{-1} \varepsilon_k\right)}{\sqrt{\det\left(\mathscr{E}_{k|k-1}\right)}\left(\sqrt{2\pi}\right)^{n_y}} \right) p(y_0|\theta) \quad (3)$$

The quantities $\hat{y}_{k|k-1}$, ε_k and $\mathscr{E}_{k|k-1}$, which can be obtained using a Kalman Filter (KF) (Kristensen et al., 2004), is needed for evaluation of the multivariate Gaussian in Eq. (3). By taking the negative logarithm, and eliminating the factor $\frac{1}{2}$, the result $\ell(\theta) = -lnL(\theta)$, where dependency on $y_{[N]}$ and $\mathscr{M}$ is omitted for simplicity, can be used as the objective g in Eq. (1).

2.1 Profile likelihood

Since the model structure $\mathscr{M}$ is a representation of a system $\mathscr{S}$, it is often assumed that $\mathscr{S} \in \mathscr{M}(\Theta)$ and that consequently there exists a true parameter vector θ^* such that $\mathscr{M}(\theta^*) = \mathscr{S}$. However, this is rarely the case, especially for simplified grey-box models based on a *naive* physical understanding of the system $\mathscr{S}$. Typically, the estimate $\hat{\theta}$ depends on several factors, such as the amount of dynamic information in $\mathscr{K}$, the choice of objective function g, and to some extent on the optimisation algorithm $\mathscr{A}$. Hence, prior to interpretation of parameters as physical constants of $\mathscr{S}$, it is necessary to perform an identifiability analysis. Since the parameters are estimated using the Likelihood function, the *Profile Likelihood* (PL) method (Raue et al., 2009; Deconinck and Roels, 2017) is a natural choice. The *likelihood profile* $\ell_{\mathrm{PL}}(\theta_i)$ is defined as the minimum log likelihood for θ_i when the remaining parameters are freely optimised (Raue et al., 2009; Venzon and Moolgavkar, 1988):

$$\ell_{\mathrm{PL}}(\theta_i) = \min_{\theta_{j\neq i}} g\left(\theta_{j\neq i}; \mathscr{M}, \mathscr{K}, \theta_i\right) \quad (4)$$

Values of θ_i must be chosen prior to optimising the remaining $\theta_{j\neq i}$ (Raue et al., 2009). The resulting likelihood profile can be plotted as a function of θ_i and subsequently analysed according to the definitions of structural and practical identifiability for *likelihood-based confidence intervals* (Deconinck and Roels, 2017). The likelihood-based confidence interval obtains a confidence region by applying a *threshold* to the likelihood function (Raue et al., 2009; Venzon and Moolgavkar, 1988). Let

$$\left\{\theta : \ell(\theta) - \ell\left(\hat{\theta}\right) < \Delta_\alpha\right\} \quad , \quad \Delta_\alpha = \chi^2(\alpha, n_{\mathrm{df}}) \quad (5)$$

where $\hat{\theta}$ is a freely estimated, presumed optimal, parameter vector, and the threshold Δ_α is the α percentile of the χ^2-distribution with n_{df} degrees of freedom.

Profile likelihood in two parameter dimensions

By freely estimating all but one parameter, the PL method essentially projects the n_θ dimensional space Θ onto the single parameter θ_i. This projection is known to overestimate the width of the likelihood-based confidence interval if there are inter-dependent parameters. A step towards remedying this issue is to modify the PL method to hold out *two* parameters (PL2) rather than one, i.e.;

$$\ell_{\mathrm{PL2}}(\theta_i, \theta_j) = \min_{\theta_{k\neq i,j}} g\left(\theta_{k\neq i,j}; \mathscr{M}, \mathscr{K}, \theta_i, \theta_j\right) \quad (6)$$

This projects the parameter space Θ onto the plane $\Theta_{i,j} = (\theta_i, \theta_j)$ s.t. $\theta_i, \theta_j \in \Theta$. In addition identifiability issues, these profiles can also diagnose *parameter inter-dependence* by inspecting the shape of the confidence regions. The resulting two-dimensional profiles can be analysed similarly to the one-dimensional profiles (Raue et al., 2009), using the definition in Eq. (5). These profiles are computed for all possible combinations of parameters. A *confidence region* in the $\Theta_{i,j}$ plane is obtained by applying the Δ_α threshold. Observe that since $\hat{\theta}$ has n_θ free

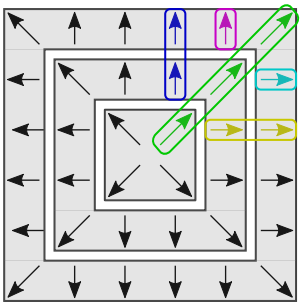

Figure 1. PL2 improved *warm start* algorithm

parameters while the PL2 estimate has $n_\theta - 2$, this gives $n_{\text{df}} = 2$ for the computation of Δ_α from the χ^2-distribution in Eq. (5). The free estimate $\hat{\theta}$ may with advantage be chosen as the minimum $\ell_{\text{PL2}}(\theta_i, \theta_j)$ obtained from all profiles. This search procedure approximates, since it is subject to the brute force discretisation performed in PL2, a free optimisation of all parameters using the already computed ℓ_{PL2} results. Since the PL2 profiles covers the entire parameter space Θ, this procedure is less affected by local minima than a direct numerical optimisation. Parameter identifiability is obtained if the region is bounded in all directions and the size and shape of this region determines the accuracy of the parameter estimates. If the region contains an unbounded equipotential *valley* in the log likelihood space, the parameter is considered structurally non-identifiable. If the profile has a well defined minima, but is unbounded in one direction, i.e., the log likelihood is below the Δ_α threshold, this indicates a practically non-identifiable parameter (Raue et al., 2009).

Implementation and computation time

In (Brastein et al., 2019), a brute force method was used, running individual optimisations for each predetermined combination of θ_i, θ_j, each iteration starting from the nominal parameter vector θ_0. Here, the profiles are constructed by a set of chained optimisations where each new point uses a previously optimised $\hat{\theta}_{k\neq i,j}$ from a near-by point in $\Theta_{i,j}$ as a *warm start*, working from the centre of the plane $\Theta_{i,j}$ towards the edges. This process is illustrated in Fig. 1. This modification reduced the computation time by approximately 4-10 times, since for each computation of $\ell_{\text{PL2}}(\theta_i, \theta_j)$, the initial guess for the free parameters are taken from a near-by, previously optimised, solution and hence are already close to optimal.

2.2 Parameter estimation uncertainty

An estimate of the uncertainty of the estimated parameters can be obtained by computing the covariance of the estimated parameters $\Sigma = 2H^{-1}$ where $H = \nabla^T \nabla \ell(\theta)\big|_{\theta=\hat{\theta}}$ is the *Hessian* of $\ell(\theta)$, whose elements are approximated as (Kristensen et al., 2004; Raue et al., 2009):

$$h_{i,j} \approx \left(\frac{\partial^2}{\partial \theta_i \partial \theta_j} \ell(\theta) \right) \Big|_{\theta=\hat{\theta}} \tag{7}$$

The partial derivatives of $\ell(\theta)$ can be numerically obtained using *the central difference approximation*. From the covariance matrix, asymptotic *point-wise* confidence limits on the estimated parameters can be computed (Raue et al., 2009)

$$\hat{\theta}_i \pm \sqrt{\chi^2(\alpha, n_{\text{df}})\Sigma_{i,i}} \tag{8}$$

where for *point-wise* intervals $n_{\text{df}} = 1$. Alternatively, confidence ellipsoids of dimension n_θ as a set of θ can be defined from the inequality:

$$\left\{ \theta : (\theta - \hat{\theta})^T \Sigma^{-1} (\theta - \hat{\theta}) \leqslant \Delta_\alpha \right\} \quad , \quad \Delta_\alpha = \chi^2(\alpha, n_{\text{df}}) \tag{9}$$

where the scale of the ellipsoid is determined by the factor Δ_α computed as in Section 2.1 (Johnson and Wichern, 2007). Given that the covariance matrix is symmetric and positive definite, the boundary of an ellipsoid can be obtained by the Cholesky decomposition $\Sigma = LL^T$, hence (Press et al., 1992):

$$(\theta - \hat{\theta})^T \Sigma^{-1} (\theta - \hat{\theta}) = \Delta \Rightarrow \left| L^{-1} (\theta - \hat{\theta}) \right|^2 = \Delta_\alpha \tag{10}$$

Next, suppose x is a point on a unit hypersphere, then the ellipsoid boundary is obtained by the affine transformation

$$\theta = \hat{\theta} + \sqrt{\Delta} L x \tag{11}$$

Elliptic regions in the plane $\Theta_{i,j}$ can be computed by projecting the n_θ dimensional ellipsoid onto $\Theta_{i,j}$. With the χ^2 confidence bound given with $n_{\text{df}} = 2$, assuming all uncertainty on the parameters in the plane $\Theta_{i,j}$, these elliptic confidence regions are comparable to the *PL2* method presented in Section 2.1. Observe that the confidence region based on applying a threshold on the likelihood function as in Eqs. (4) and (6) are often considered superior to the Hessian method, since the Hessian assumes symmetric distributions and therefore cannot be used to identify practical identifiability (Raue et al., 2009). However, the Hessian approach is much faster to compute and gives a reasonable estimate of the estimated parameter uncertainty if the parameters are approximately Normal distributed.

3 Experimental setup

3.1 Experimental building

The experimental building, which is located at Campus Porsgrunn of the University of South-Eastern Norway (USN), is shown in Fig. 2. The building is constructed with three different types of walls. As shown in Fig. 2, the North wall is constructed using materials with high insulation quality, which is typically used in modern sustainable buildings. The South wall is constructed using traditional building materials, with lower thermal insulation capabilities.

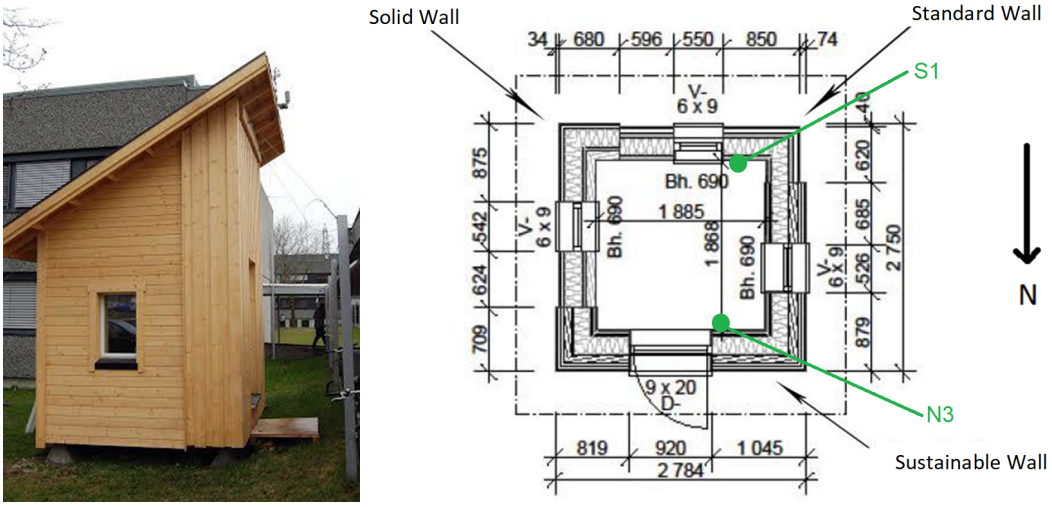

Figure 2. The experimental building has walls constructed using different techniques for insulation. Sensors are located on all walls at different height above floor, and in different insulation layers. The sensors used in this project, N3 and S1, are measuring the wall temperature inside the building on the north and south wall, respectively.

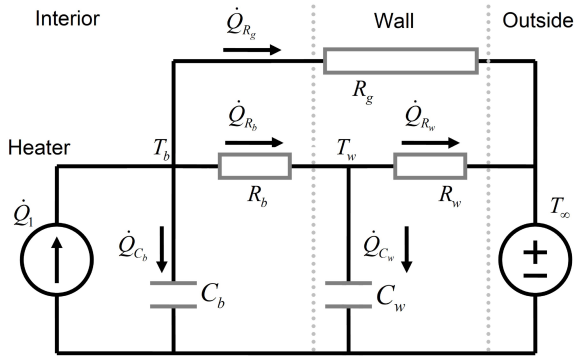

Figure 3. RC circuit model of the building.

3.2 Model

Figure 3 shows a possible model structure, which was developed to approximate the thermal behaviour of the experimental building, partially based on the R4C2 model presented in (Berthou et al., 2014). The RC circuit consists of five components: the thermal resistance between room air and wall R_b, the building envelope R_w, and the thermal resistance of windows and doors R_g. The two capacitances C_b and C_w represent the thermal capacitance of the building interior and envelope, respectively. The model has two outputs: the room temperature T_b and the wall surface temperature T_w, and two inputs: the consumed power by an electric heating element $\dot{Q}$ and the outside temperature T_∞. The parameter vector θ holds the value of each of the five components. By applying Kirchoff's balance laws to the circuit, the model can be expressed as a linear stochastic differential equation

$$\frac{dx}{dt} = Ax_t + Bu_t + w_t \tag{12}$$

$$y_t = x_t + v_t \tag{13}$$

Table 1. Nominal parameter values and min/max limits for resistances [K/W] and capacitances [J/K].

	R_g	R_b	R_w	C_b	C_w
θ_0	0.15	0.20	0.30	$1000k$	$200k$
θ_min	0.03	0.03	0.03	$800k$	$1k$
θ_max	0.25	2.00	2.00	$1800k$	$1000k$

where

$$x_t = \begin{bmatrix} T_b \\ T_w \end{bmatrix}, u_t = \begin{bmatrix} \dot{Q} \\ T_\infty \end{bmatrix}, B = \begin{bmatrix} \frac{1}{C_b} & \frac{1}{C_b R_g} \\ 0 & \frac{1}{C_w R_w} \end{bmatrix}$$

$$A = \begin{bmatrix} -\frac{1}{C_\mathrm{b}R_\mathrm{b}} - \frac{1}{C_\mathrm{b}R_\mathrm{g}} & \frac{1}{C_\mathrm{b}R_\mathrm{b}} \\ \frac{1}{C_\mathrm{w}R_\mathrm{b}} & -\frac{1}{C_\mathrm{w}R_\mathrm{b}} - \frac{1}{C_\mathrm{w}R_\mathrm{w}} \end{bmatrix}$$

and $w_t \sim N(0, W)$ is the process noise (model error), W is the spectral density of w_t. All states are measurable, hence Eq. (13) with measurement noise $v_t \sim N(0, V)$. Observe that the model equations are expressed in continuous time, and discretised by the estimation software using a Runge-Kutta 4th (Runge, 1895) order approximation. Observe also that while the model is linear, the algorithm is not restricted to linear models. The choice of Kalman Filter implementation is determined by the type of model being used (Brastein et al., 2019).

Table 1 lists a set of experimentally obtained nominal parameters, which are used as initial guesses for model calibration, and min/max limits which corresponds to the bounds of the constrained parameter space Θ.

3.3 Calibration data

Figure 4 shows a set of calibration data, which consist of four temperature measurements and one measurement of supplied input power. The data was recorded in February 2018. Originally, the data was collected at 1 minute intervals but has been downsampled to 30 min time-step, by

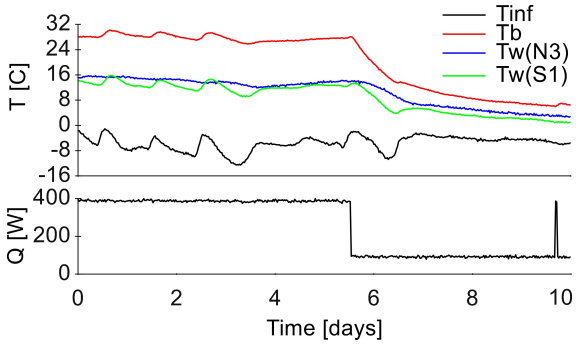

Figure 4. Data recorded from sensor at different locations in the building

Table 2. Estimated covariance matrices with corresponding KS test result (critical value for 95% conf. is 0.062) .

#	$\mathscr{W}_{T_b}^{\frac{1}{2}}$	$\mathscr{W}_{T_w}^{\frac{1}{2}}$	$\mathscr{V}_{T_b}^{\frac{1}{2}}$	$\mathscr{V}_{T_w}^{\frac{1}{2}}$	KS_{T_b}	KS_{T_w}
S1	0.115	0.104	0.028	0.037	0.054	0.042
N3	0.117	0.077	0.019	0.145	0.046	0.035

extracting every 30th measurement. Two of the temperatures correspond to model state T_b and the model input outdoor temperature T_∞. The remaining two measurements correspond to different alternative sensor locations for T_w, one on the north wall (sensor N3) and one on the south wall (sensor S1). Figure 4 shows that there is significant differences between these two measurements in dynamic content, due to the different construction materials used in the North and South wall, which will lead to differences in the identifiability analysis of the estimated parameters. In the sequel, two different cases S1 and N3 are analysed, distinguished by the choice of reference measurement for the output T_w.

Optimisation algorithm

In (Brastein et al., 2019) COBYLA (Powell, 1994), based on linear approximations, was used as the optimisation algorithm $\mathscr{A}$ in Eq. (1). In this work, further experimentation with other optimisation algorithms showed that a quadratic approximation algorithm, such as BOBYQA (Powell, 2009), gives significantly faster convergence, by approximately a factor of 5, as well as more consistent results by improved ability to avoid local minima. BOBYQA is therefore used in the sequel.

4 Results and discussion

A requirement for using Kalman Filters to obtain residuals for subsequent evaluation of the likelihood function in Eq. (3) is obtaining reasonable estimates for process and noise covariance matrices, respectively $\mathscr{W}$ and $\mathscr{V}$. In (Brastein et al., 2019) $\mathscr{V}$ was obtained from data, while $\mathscr{W}$ was found by manual experimentation. A better approach is to estimate them from data, by including them in θ.

In order to reduce the number of free parameters, both covariance matrices are assumed diagonal. Further, the square root of the diagonal elements are added to the parameter vector θ with some appropriate bounds in Θ and subsequently estimated by numerical optimisation of Eq. (1). The resulting covariances are shown in Table 2. Observe that the results corresponding to the state/measurement T_b are similar for both cases, while the results for T_w differ significantly. This is expected due to the differences in noise characteristics and dynamic information content in the data collected from the two sensors. For Case S1 the estimates for $\mathscr{W}$ is similar for both states, where as for Case N3 the differences between measurements of T_b and T_w results in different estimates for the corresponding elements in $\mathscr{W}$.

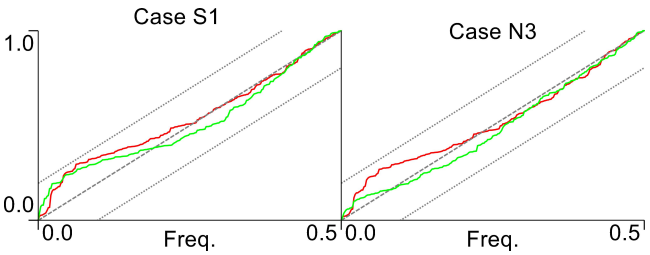

Figure 5. CP diagram of residuals for outputs T_b(red) and T_w(green)

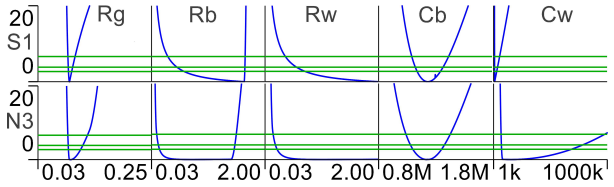

Figure 6. PL results for Cases S1 and N3. Green lines indicate in increasing order 90%, 95% and 99% confidence limits.

The residuals obtained after optimising all parameters must be analysed for normality, in order to justify the use of the multivariate Gaussian in Eq. (3) for evaluation of the likelihood function (Kristensen et al., 2004). Figure 5 shows a *cumulative periodogram* (CP), with 95% confidence bounds obtained from the Kolmogorov-Smirnov criterion (Madsen, 2007; Madsen and Holst, 1995; Deconinck and Roels, 2017; Bacher and Madsen, 2011). The CP plot shows that the residuals are well approximated by a normal distribution. Additionally, the Kolmogorov-Smirnov normality-test results are listed in Table 2. After calibration of the parameters, including the noise covariance matrices, residuals are found to pass the normality tests.

4.1 Profile likelihood

Once the covariance parameters have been determined, the remainder of this paper is focused on analysing the parameter space Θ by use of the Profile Likelihood (PL) (Raue et al., 2009) method, first in a single parameter dimension, and next in two parameter dimensions. The PL results in Fig. 6 show, as expected, that some of the parameters have narrower profiles for the S1 Case compared with

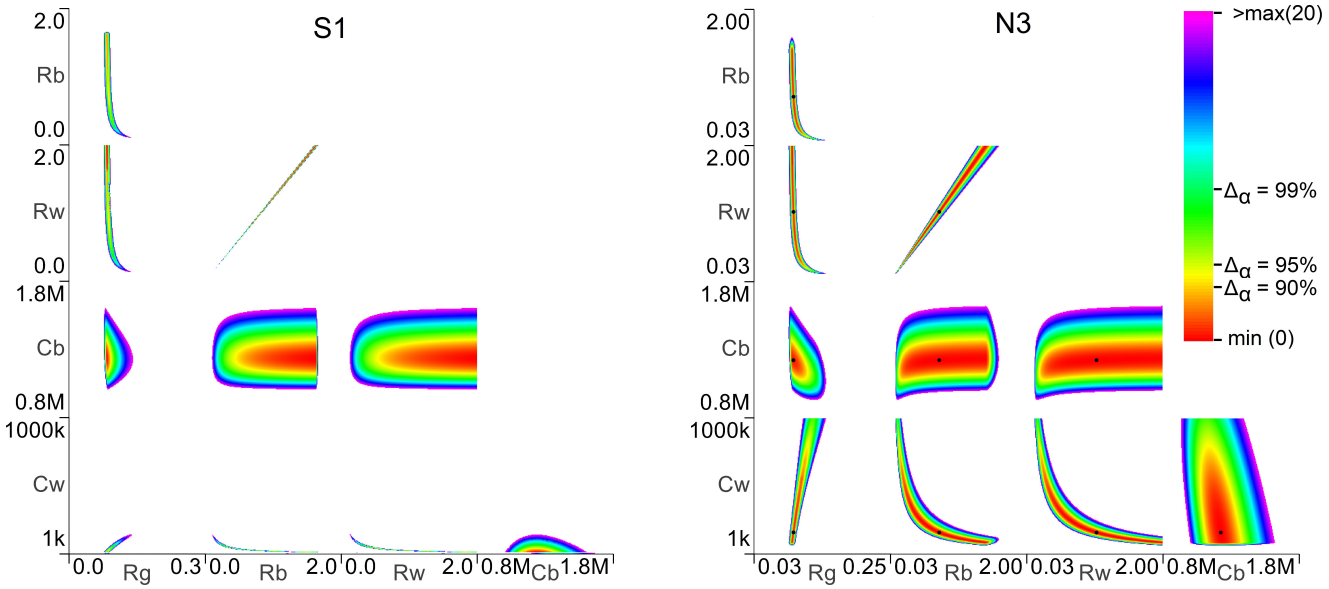

Figure 7. PL2 results for Case S1 (left) and Case N3 (right). Confidence limits, base on the χ^2 distribution with 2 degrees of freedom is indicate on the figure legend to the right.

the N3 Case. Since the excitation in T_w is much larger for Case S1, it is expected that the identifiability analysis reflects this by computing tighter confidence regions for the parameters most affected by T_w. Observe in particular how the profiles for C_w and R_g indicates considerably improved identifiability of these parameters for Case S1. The profiles for parameter C_b is almost identical, which is expected, since this parameter is not influenced by T_w.

A second observation from Fig. 6 is that R_w is diagnosed as practically non-identifiable, since the profile extend towards infinity in the positive direction. Observe also that R_b follows a similar trend, but with an abrupt break in the profile, which leads to a bounded profile for R_b. However, if parameters R_b and R_w are inter-dependent, the projection of the likelihood function for the parameter space Θ onto R_b will be affected by R_w, and subsequently by the constraint imposed by Θ. This type of constraints, in the presence of parameter inter-dependence, is known to produce such breaks in the computed profiles (Brastein et al., 2019), as discussed in Section 2.1.

4.2 Profile likelihood in 2D

Next, the two-dimensional profile likelihood (PL2) method is applied in order to investigate parameter inter-dependency. The result is shown in Fig. 7. By projecting the ML function in Eq. (3) onto a plane of two parameters, rather then a single parameter axis as in PL, it becomes possible to diagnose parameter identifiability by observing the shape of the confidence regions. First, observe that the PL2 results show a similar improvement in identifiability for Case S1 over Case N3 for the same parameters. The confidence regions for C_w and R_g are significantly reduced for Case S1, whereas the region for C_b is similar for both cases. Hence, the results of the PL analysis is confirmed by the PL2 results.

Further, the PL2 results also show that R_b and R_w are highly inter-dependent, a fact which was not easily observed in Fig. 6. The projected topology of these two parameters shows a near linear relationship between them. This explains why the PL profile for R_b contains an abrupt break, caused by the constraint on R_w and their inter-dependence. In this context, it is interesting to consider whether this lack of identifiability for parameters R_b and R_w are of practical, i.e. related to information content in data, or structural nature. Parameter inter-dependency is clearly caused by the model structure, not the data. However, the PL2 profile shows that while the parameters are linearly dependant, e.g. $R_b = cR_w$, neither parameter is identifiable, since the profile is unbounded in one direction in Θ. Hence, it is accurate to claim that these two parameters are practically non-identifiable, but also that there is a structural problem of parameter inter-dependency. The latter may be eliminated by re-parametrising the model, say, by introducing the relationship $R_b = cR_w$ with the constant c pre-determined based on Fig. 7. However, there is no physical reason to assume that the thermal resistance between the inside wall and the building interior should be depending linearly on the thermal resistance of the wall itself, hence this modification of the model equations seems somewhat *ad hoc*. A better alternative is to modify the RC circuit model *structure* such that the parameter inter-dependency is resolved.

4.3 Reduced order model for Case S1

From Fig. 6 and 7 for Case S1 it appears that the value of C_w tends towards zero as R_b and R_w increases. This could indicate that removing C_w, and replacing the state T_w by a measurement $T_w = \frac{T_\infty R_b + T_b R_w}{R_b + R_w}$, is an appropriate modification. However, after calibrating the reduced model, the re-

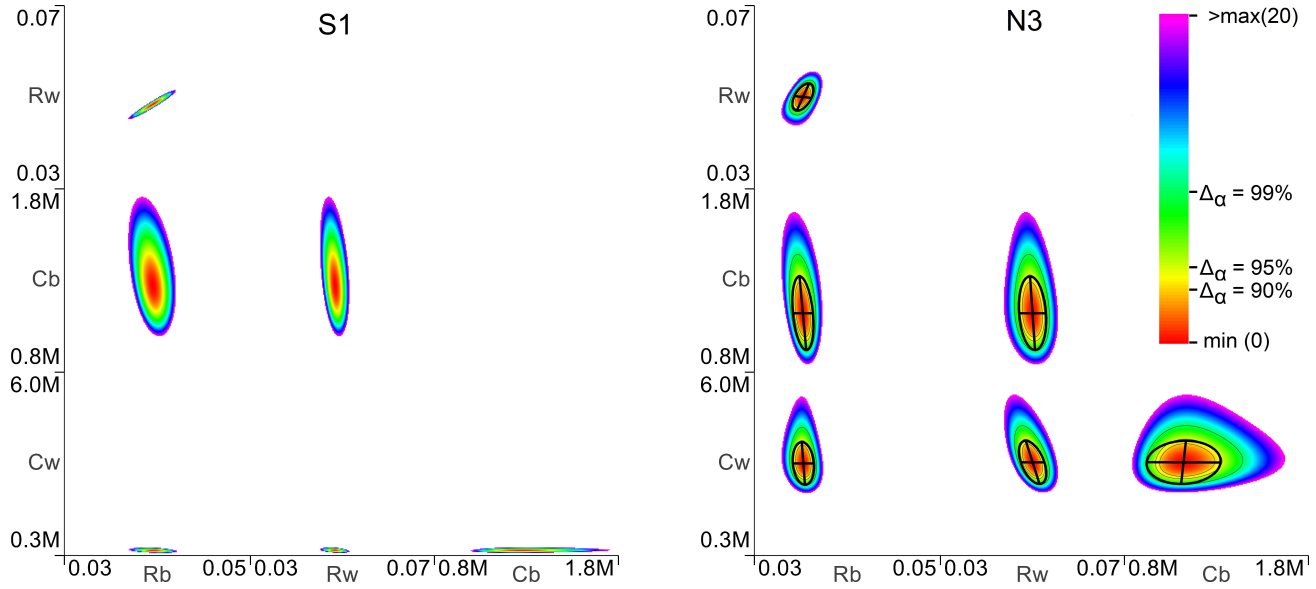

Figure 8. PL2 results after removing R_g from the model, for Case S1 (left) and Case N3 (right). Confidence limits, base on the χ^2 distribution with 2 degrees of freedom is indicate on the figure legend to the right. Likelihood threshold isolines and a 95% confidence error ellipse boundary, based on the inverse Hessian, has been added to the plot for N3.

sidual analysis for output T_w, based on a CP diagram, does not support the normality assumption, which in turn indicates that the model order is to low. Hence, removing C_w is not an acceptable modification to the model structure.

4.4 Parameter inter-dependence

Observe from Fig. 6 and 7 that for Case N3 there is a significant flat region in the profiles of both R_b and R_w. Table 3 contains a selection of values from within this region, which has been computed by keeping R_b constant while optimising the remaining parameters. This experiment shows that by varying the parameters within this optimal region, the total thermal resistance between building interior and the outside temperature, $R_{tot} = R_g || (R_b + R_w)$, where $||$ indicates a parallel connection of resistors, is constant. Also, the time constant for the wall capacitor $\tau_w = (C_w R_b || R_w)$ is approximately constant for the same experiments. Since the total resistance $R_{tot} < R_g$ it follows that R_b and R_w can grow large, by compensating with R_g and C_w, without affecting the models predictions. Combined with the PL2 analysis results, this indicates an *over-parametrised* model.

4.5 PL analysis of model without Rg

A natural next step is to reduce the number of parameters by removing the presumed redundant parameter R_g from the model circuit. Repeating the PL2 analysis of the model with R_g removed gives the plots shown in Fig. 8. The profiles for all parameter combinations are now approximately elliptical, which indicates parameter independence. Observe also from Fig. 8 that the min/max limits which constitutes the bounds Θ has been changed to comply with the reduced model structure. Further, all parameters now have bounded profiles, which indicates identifiability. By comparing Case S1 and Case N3, the effect of low excitation in T_w for Case N3 is observed also for the reduced model. In addition to obtaining a different optimal value for C_w, as expected, since the sensor is mounted on a different wall, the profile is much wider for Case N3. This indicates a wider confidence region for this parameter, hence a more uncertain estimate.

Table 3. Optimised values of R_w, R_g and C_w with fixed values of R_b from within the flat region observed in the PL results.

R_b	R_w	R_g	C_w	R_{tot}	τ_w
0.700	0.993	0.093	163k	0.088	67.0k
0.900	1.277	0.092	126k	0.088	66.5k
1.300	1.844	0.091	88k	0.088	67.0k

Table 4. Optimal parameters with R_g removed.

	R_b	R_w	C_b	C_w
S1	0.040	0.048	1267k	419k
N3	0.035	0.051	1137k	2735k

With identifiable parameters, it is interesting to compare the optimal parameter estimates, listed in Table 4, for each case. Observe first that for both cases, the total thermal resistance between building interior and outside temperature $R_b + R_w \approx 0.088$, which was the value obtained for the total resistance in Table 3. Observe also that both resistances and the interior capacitance C_b is similar for both cases, while the value obtained for C_w is much larger for the N3 case, as expected, due to the high grade insulation used in the North wall.

Hessian vs Profile Likelihood

Observe from Fig. 8 that the super-imposed Hessian based error ellipse at $\alpha = 95\%$ are similar to the 95% confidence regions computed by thresholds on the likelihood profile. Observe especially for the profile R_b vs R_w that the two confidence region methods produce almost identical regions, since the projected likelihood profile is almost symmetric. For e.g. C_b vs C_w the Hessian ellipse and likelihood thresholds are of similar size, but the Hessian has an offset due to the non-symmetric likelihood profile. This shows the advantage of the profile likelihood based regions, in that they can produce accurate results for asymmetric parameter distributions.

5 Conclusion

In this paper, two different sensor locations, giving different dynamic information in the recorded calibration data, was used to estimate and analyse parameters of a thermal network grey-box model of building thermal behaviour. The sensor locations differ with respect to the physical properties of the building, with one sensor fitted to a high insulation sustainable wall, and the other to a standard insulation wall. The profile likelihood method was used, projecting the likelihood function in both one and two parameter dimensions, to show the difference in confidence regions produced by lack of excitation in the calibration data. Confidence regions computed by applying a threshold to the 2D profiles were compared with error ellipses computed based on the Hessian, which shows that while the two confidence region methods give similar results, the PL method better represents the uncertainty when the parameter distribution is asymmetric. The two-dimensional likelihood profile results were used to diagnose parameter non-identifiability, and the model structure was subsequently modified to resolve the problem, thus obtaining identifiable parameters.

References

Peder Bacher and Henrik Madsen. Identifying suitable models for the heat dynamics of buildings. *Energy and Buildings*, 43(7):1511 – 1522, 2011. ISSN 0378-7788. doi:https://doi.org/10.1016/j.enbuild.2011.02.005.

Thomas Berthou, Pascal Stabat, Raphael Salvazet, and Dominique Marchio. Development and validation of a gray box model to predict thermal behavior of occupied office buildings. *Energy and Buildings*, 74:91–100, 2014.

Ole Magnus Brastein, Bernt Lie, Roshan Sharma, and Nils-Olav Skeie. Parameter estimation for externally simulated thermal network models. *Energy and Buildings*, 2019. ISSN 0378-7788. doi:10.1016/j.enbuild.2019.03.018.

An-Heleen Deconinck and Staf Roels. Is stochastic grey-box modelling suited for physical properties estimation of building components from on-site measurements? *Journal of Building Physics*, 40(5):444–471, 2017.

Cristina Sarmiento Ferrero, Qian Chai, Marta Dueñas Díez, Sverre H Amrani, and Bernt Lie. Systematic analysis of parameter identifiability for improved fitting of a biological wastewater model to experimental data. *Modeling, Identification and Control*, 27(4):219, 2006.

Samuel F Fux, Araz Ashouri, Michael J Benz, and Lino Guzzella. EKF based self-adaptive thermal model for a passive house. *Energy and Buildings*, 68:811–817, 2014.

R.A. Johnson and D.W. Wichern. *Applied Multivariate Statistical Analysis*. Applied Multivariate Statistical Analysis. Pearson Prentice Hall, 2007. ISBN 9780131877153.

M Killian and M Kozek. Ten questions concerning model predictive control for energy efficient buildings. *Building and Environment*, 105:403–412, 2016.

Niels Rode Kristensen, Henrik Madsen, and Sten Bay Jørgensen. Parameter estimation in stochastic grey-box models. *Automatica*, 40(2):225–237, 2004.

Henrik Madsen. *Time series analysis*. Chapman and Hall/CRC, 2007.

Henrik Madsen and Jan Holst. Estimation of continuous-time models for the heat dynamics of a building. *Energy and buildings*, 22(1):67–79, 1995.

D.W.U. Perera, Carlos F. Pfeiffer, and Nils-Olav Skeie. Modelling the heat dynamics of a residential building unit: Application to Norwegian buildings. *Modeling, Identification and Control*, 35(1):43–57, 2014. doi:10.4173/mic.2014.1.4.

Michael JD Powell. A direct search optimization method that models the objective and constraint functions by linear interpolation. In *Advances in optimization and numerical analysis*, pages 51–67. Springer, 1994.

Michael JD Powell. The BOBYQA algorithm for bound constrained optimization without derivatives. *Cambridge NA Report NA2009/06, University of Cambridge, Cambridge*, pages 26–46, 2009.

William H Press, Saul A Teukolsky, William T Vetterling, and Brian P Flannery. *Numerical recipes in C++*, volume 2. Cambridge University Press, 1992.

Andreas Raue, Clemens Kreutz, Thomas Maiwald, Julie Bachmann, Marcel Schilling, Ursula Klingmüller, and Jens Timmer. Structural and practical identifiability analysis of partially observed dynamical models by exploiting the profile likelihood. *Bioinformatics*, 25(15):1923–1929, 2009.

Glenn Reynders, Jan Diriken, and Dirk Saelens. Quality of grey-box models and identified parameters as function of the accuracy of input and observation signals. *Energy and Buildings*, 82:263–274, 2014.

C. Runge. Ueber die numerische Auflösung von Differentialgleichungen. *Mathematische Annalen*, 46(2):167–178, Jun 1895. ISSN 1432-1807. doi:10.1007/BF01446807.

D. J. Venzon and S. H. Moolgavkar. A method for computing profile-likelihood-based confidence intervals. *Journal of the Royal Statistical Society: Series C (Applied Statistics)*, 37(1): 87–94, 1988. doi:10.2307/2347496.

Models for control of thermal energy in buildings

Casper Amandus Johansen, Bernt Lie, Nils-Olav Skeie

Department of Electrical Engineering, Information Technology and Cybernetics
University of South-Eastern Norway, Porsgrunn, Norway, Bernt.Lie@usn.no

Abstract

A large fraction of the world's energy production is used for HVAC in buildings. It is therefore important to develop improved strategies for the efficient use of energy in buildings. Storage of intermittent energy production is important; storage as hot water in water tanks is the most common way to store energy in private homes/ smaller apartment complexes. Finding good models for building thermal behavior is an important part of developing building energy management systems (BEMS) that are capable of reducing energy consumption for space heating through model predictive control (MPC). In this paper, previous models of temperature dynamics in hot water tanks are considered, and a simple well mixed tank model is compared with a model describing a more realistic stratified temperature distribution. Two models are fitted to experimental data from a hot water tank. Description of temperature stratification requires a distributed model, but a relatively low order discretized model suffices to describe the important effect while simultaneously being useful for BEMS. A suitable hot water tank model in combination with weather forecast enables temperature estimation and prediction in MPC, and allows for finding a suitable water temperature at minimal energy consumption.

Keywords: Energy in buildings, energy storage, hot water tank model, well mixed tank model, stratified flow model, experimental data, model fitting.

1 Introduction

1.1 Background

A large part of the world's energy production is used for heating/cooling, ventilation, and air conditioning of buildings (HVAC), (Pérez-Lombard et al., 2008), and this fraction is increasing. Even though modern building techniques make it possible to reduce the energy used for heating, the renewal rate of buildings is low. Berthou *et al.* (Berthou et al., 2014) report renewal rates of 1% per year in France, with similar rates for other European countries. This illustrates the need for good building energy management systems (BEMS) also in existing buildings.

Model predictive control (MPC) is an attractive approach for use in BEMS. Models of the building thermal behavior can be used to predict the heating and cooling time, and the usage of energy. In an MPC system, a model is used to simulate the system ahead in time in order to find a sequence of inputs that controls the system to the desired state. In a BEMS, the use of MPC will allow for improved control of the indoor climate as well as minimization the energy consumption (Berthou et al., 2014), (Fux et al., 2012). Predictions of future system inputs such as outdoor temperature, irradiation, precipitation, etc., are readily available from internet services, which helps to facilitate the use of MPC.

An important problem in BEMS involves the possibility to store surplus energy for later use. Energy storage as sensible heat in a water tank is a widespread strategy. A simple, yet reasonably accurate water tank model, which can be integrated in a complete building model, is required for successful MPC.

1.2 Previous work

In (de Oliveira et al., 2013), a house heating system is optimized wrt. fluctuating energy prices. In (Lie et al., 2014), a related heating system with irradiation prediction, solar collector, and a simple water storage tank is considered. (Lie, 2015) discusses a more detailed model of the water storage tank. (Xu et al., 2014) discuss a more realistic water storage tank, using a simplified description of water buoyancy presented in (Viskanta et al., 1977). (Koch, 2012) discusses both a concentrated and a distributed water tank model, while (Vrettos, 2016) extends on Koch's work with a buoyancy description model. (Johansen, 2019) adjusted the model from (Xu et al., 2014), and fitted the model to experimental data. The results of (Johansen, 2019) are discussed in this paper.

1.3 Outline of paper

Section 2 provides a discussion of the system discussed, Section 3 gives an overview of the dynamic model of the water tank, Section 4 gives results from model simulation and fitting of the model to experimental data, with validation. The results are discussed in Section 5, with some conclusions and indications of future work.

2 Experimental Rig

2.1 System Description

The building under study is a two floor residential building located in the eastern part of Norway, built in 2017. The building was build based on the Norwegian TEK17 regulation and contains a BEMS based on a web based Programmable Logic Controller (PLC). The PLC uses an

Table 1. Summary of instruments in Figure 1.

Label	Description
P1	Pump driving water flow in external loop
F1	Volumetric flow rate sensor in external loop
V1	Three way shunt valve for directing water through water tank
V2	Valve for directing external loop water through room
T1	Temperature of mixture after valve V1
T2	Upper temperature sensor in hot water tank
T3	Lower temperature sensor in hot water tank
T4	External loop temperature at entrance to hot water tank
T5	Ambient temperature, not shown in Figure 1
H1	Heating element for hot water tank, 15 kW

internet based weather service for prediction of outside temperatures and solar radiation parameters. The heating system consists of floor pipes with hot water in each room, and the temperature is adjusted individually by a valve controlling the flow of how water in a specific section. The valves are controlled by the PLC. The floor material in both floors is concrete. A pump, common for all the pipe sections, provides the circulation of hot water in the pipes. An overview of the heating system is shown in Figure 1.

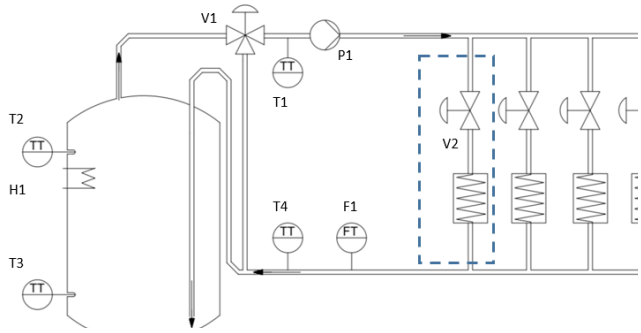

Figure 1. Overview of heating system in building, with hot water buffer tank for heating the water, and floor heating pipes for each room in the building. Each pipe has a valve controlled by the BEMS. The hot water tank is to the left in the figure.

Elements in Figure 1 are summarized in Table 1.

2.2 Experimental Data

The PLC system provides measurements of temperatures in the hot water tank (T2, T3), the loop circulation hot mixture temperature (T1), and loop return temperature (T4) once per minute together with control signals for the heating valve (H1) and the three-way valve actuator (V1). Other data such as ambient temperature (T5) and loop flow rate (F1) are sampled more rarely, but have been re-sampled to once per minute. The data have been collected in CSV files with one line for each sample with a time stamp and the measured values. The data set contains data for the period February 5, 2019 to February 21, 2019. Python was used as the software for preprocessing the data, calibration of the models, and validation checks.

3 Model Description

3.1 Model overview

A model of the buffer tank that can be used in the PLC system is wanted so a model that is adjusted to the computational power of this control system. An overview of the buffer tank is shown in Figure 2.

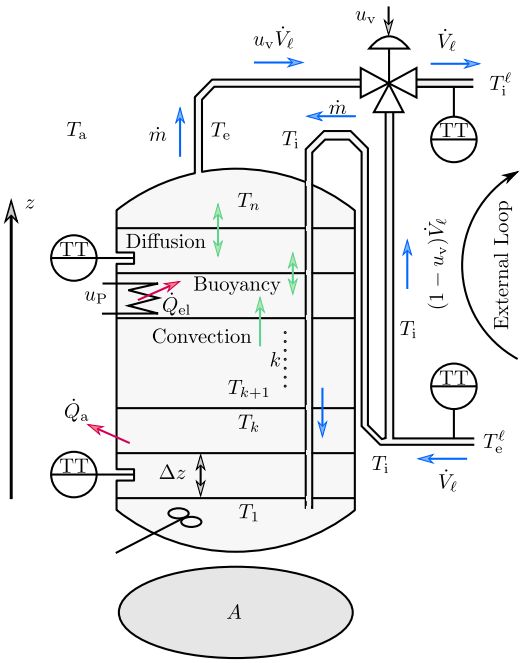

Figure 2. The buffer tank with the heating element, the temperature sensors inside the buffer tank, the temperature sensors on the outlet an inlet pipes and the three way shunt valve for mixing the water from the buffer tank and the return water flow.

Two approaches are used, one model for the tank as a mixed storage tank and a model of the tank as a stratified storage tank where each layer is modeled. Both models are developed based on the macroscopic thermal energy balance, and assuming constant mass/constant mass density. Constant mass m in the system implies that

$$\dot{m} = \dot{m}_\mathrm{i} = \dot{m}_\mathrm{e} \tag{1}$$

where $\dot{m}$ is mass flow rate through the system, while $\dot{m}_\mathrm{i}$ and $\dot{m}_\mathrm{e}$ are influent and effluent mass flow rates, respectively. The thermal energy balance can be posed as

$$\frac{\mathrm{d}U}{\mathrm{d}t} = \dot{H}_\mathrm{i} - \dot{H}_\mathrm{e} + \dot{W}_\mathrm{f} - \dot{W}_\mathrm{v} + \dot{Q}, \tag{2}$$

where U is internal energy, H is enthalpy, W is work, and Q is heat. A dot decoration on a symbol indicates a flow rate, thus $\dot{H}$ is enthalpy flow, $\dot{W}$ is mechanical power, and

$\dot{Q}$ is heat flow rate. $\dot{H}_\mathrm{i}$ and $\dot{H}_\mathrm{e}$ are influent and effluent enthalpy flow rates, respectively. $\dot{W}_\mathrm{f}$ and $\dot{W}_\mathrm{v}$ are friction work rate (heating) and power due to volume change ($p\frac{\mathrm{d}V}{\mathrm{d}t}$), respectively; we will neglect friction work, and with constant volume, there is no volume work. Heat flow might be due to added electric heating $\dot{Q}_\mathrm{el}$, heat diffusion $\dot{Q}_\mathrm{d}$, and heat loss to the ambient $\dot{Q}_\mathrm{a}$.

Enthalpy is an extensive quantity, hence for a pure substance,

$$H = m\hat{H} \tag{3}$$

where $\hat{H}$ is specific enthalpy. Likewise, enthalpy flow for a pure substance is related to mass flow as

$$\dot{H} = \dot{m}\hat{H}. \tag{4}$$

For an in-compressible liquid, $\hat{H}$ can be posed as

$$\hat{H} = \hat{H}(T^\circ) + \hat{c}_{p,\mathrm{w}}(T - T^\circ) + \frac{1}{\rho}(p - p^\circ) \tag{5}$$

where T° and p° are standard state temperature and pressure, respectively, and ρ is the water density. Under normal conditions, we can neglect the pressure effect. Also, for a pure substance (non-reacting) system, the standard state specific enthalpy $\hat{H}(T^\circ)$ can be neglected.[1] We will also utilize that for water in liquid form, $\mathrm{d}U \approx \mathrm{d}H$.

3.2 Mixed tank model

The first model is a simplified model assuming that the entire volume of the tank is well mixed. The assumptions for the mixed tank model are (1) the top and bottom of the tank are assumed to be horizontal, (2) water flows only from the bottom to the top of the tank, (3) constant density of the water, (4) temperature independent heat capacity, (5) a proportional relationship between the inflow and outflow of the tank and the valve openings, (6) the temperature is homogeneous along the height of the tank.

Based on the assumptions indicated in Section 3.1, we have

$$\frac{\mathrm{d}U}{\mathrm{d}t} \approx \frac{\mathrm{d}H}{\mathrm{d}t} = \frac{\mathrm{d}}{\mathrm{d}t}\left(m\hat{H}\right) = m\frac{\mathrm{d}\hat{H}}{\mathrm{d}t} = m\hat{c}_{p,\mathrm{w}}\frac{\mathrm{d}T}{\mathrm{d}t} \tag{6}$$

$$\dot{H}_\mathrm{i} - \dot{H}_\mathrm{e} = \dot{m}\hat{c}_{p,\mathrm{w}}(T_\mathrm{i} - T) \tag{7}$$

where we have used that for a perfectly mixed tank, $T_\mathrm{e} = T$. For a well mixed tank, there is no heat diffusion. Added electric heating is

$$\dot{Q}_\mathrm{el} = P^\circ u_\mathrm{P} \tag{8}$$

where P° [kW] is the maximum electric heating power, and $u_\mathrm{P} \in [0,1]$ is a control signal. Heat added from the surroundings is

$$\dot{Q}_\mathrm{a} = \mathscr{U} A_\mathrm{s}(T_\mathrm{a} - T) \tag{9}$$

[1] $\hat{H}(T^\circ)$ is mainly needed for finding heat of formation in chemical reactions.

where $\mathscr{U}$ is the overall heat transfer coefficient and A_s is the total surface areas, while T_a is the ambient temperature. The mass flow rate $\dot{m}$ through the hot water tank is given by $\dot{m} = \rho\dot{V}$ where the volumetric flow rate, $\dot{V}$, is given by a split-range control signal u_v as $\dot{V} = \dot{V}_\ell u_\mathrm{v}$, with $\dot{V}_\ell$ being the volumetric flow rate in the *external loop*. The mass flow rate can thus be expressed as

$$\dot{m} = \rho\dot{V}_\ell \cdot u_\mathrm{v} \tag{10}$$

where $\rho$is water density, while $u_\mathrm{v} \in [0,1]$ is the valve signal.

With $m = \rho V$ and V the tank volume, the model can thus be summarized in state space form as

$$\begin{aligned} m\hat{c}_{p,\mathrm{w}}\frac{\mathrm{d}T}{\mathrm{d}t} &= \dot{m}\hat{c}_{p,\mathrm{w}}(T_\mathrm{i} - T) + P^\circ u_\mathrm{P} + \mathscr{U} A_\mathrm{s}(T_\mathrm{a} - T) \\ &\Downarrow \\ \frac{\mathrm{d}T}{\mathrm{d}t} &= \frac{\dot{V}_\ell \cdot u_\mathrm{v}}{V}(T_\mathrm{i} - T) + \frac{P^\circ u_\mathrm{P} + \mathscr{U} A_\mathrm{s}(T_\mathrm{a} - T)}{\rho V \hat{c}_{p,\mathrm{w}}}. \end{aligned} \tag{11}$$

3.3 Stratified tank model

3.3.1 Distributed parameter model

We consider a well mixed volume $\Delta V = A \cdot \Delta z$ in the water tank, where A is the cross sectional area and Δz is the height of the volume, with $z = 0$ at the bottom of the tank and $z = h$ at the top of the tank. For this volume and with $\mathrm{d}U \approx \mathrm{d}H$, influent at position z, effluent at position $z + \Delta z$, the energy balance is

$$\frac{\mathrm{d}H_{z+\Delta z}}{\mathrm{d}t} \approx \dot{H}_z - \dot{H}_{z+\Delta z} + \dot{Q}_{\mathrm{el},\Delta z} + \dot{Q}_{\mathrm{d},z} - \dot{Q}_{\mathrm{d},z+\Delta z} + \dot{Q}_{\mathrm{a},\Delta z}. \tag{12}$$

The following expressions are valid except at the boundaries, i.e., they are valid for $z \in (0,h)$:

$$H_{z+\Delta z} = m_{\Delta z}\hat{H}_{z+\Delta z} = \rho A \Delta z \cdot \hat{c}_{p,\mathrm{w}}(T_{z+\Delta z} - T^\circ) \tag{13}$$

$$\dot{H}_z - \dot{H}_{z+\Delta z} = \dot{m}\hat{c}_{p,\mathrm{w}}(T_z - T_{z+\Delta z}) \tag{14}$$

$$\dot{Q}_{\mathrm{el},\Delta z} = P^\circ \cdot 1_{\mathscr{P}}(z) \cdot u_\mathrm{P} \tag{15}$$

$$\dot{Q}_\mathrm{d} = A\dot{Q}''_\mathrm{d} \tag{16}$$

$$\dot{Q}_{\mathrm{a},\Delta z} = \mathscr{U} A_{\Delta z}(T_\mathrm{a} - T_{z+\Delta z}). \tag{17}$$

In these expressions, we have assumed that the heating element is located at a point position z_P, and $1_{\mathscr{P}}(z)$ is the *indicator function* defined as

$$1_{\mathscr{P}_{\Delta z}}(z) = \begin{cases} 1, & z \in \mathscr{P}_{\Delta z} \\ 0, & z \notin \mathscr{P}_{\Delta z}, \end{cases} \tag{18}$$

with heating element location set $\mathscr{P}_{\Delta z}$ given as

$$\mathscr{P}_{\Delta z} = (z_\mathrm{P}, z_\mathrm{P} + \Delta z]. \tag{19}$$

Furthermore, $\dot{Q}''_\mathrm{d}$ is the heat diffusion per unit cross sectional area (the heat flux), while $A_{\Delta z} = \wp\Delta z$ and $\wp$ is the perimeter of the tank.

By combining these terms into the thermal energy balance, dividing by Δz and letting $\Delta z \to 0$, we find that for $z \in (0,h)$:

$$\rho A \hat{c}_{p,\mathrm{w}} \frac{\partial T}{\partial t} = -\dot{m} \hat{c}_{p,\mathrm{w}} \frac{\partial T}{\partial z} + P^\circ \delta(z - z_\mathrm{P}) \cdot u_\mathrm{P} - A \frac{\partial \dot{Q}''_\mathrm{d}}{\partial z} + \mathscr{U} \wp (T_\mathrm{a} - T), \tag{20}$$

where we have introduced Dirac's delta function $\delta(z - z_\mathrm{P})$ by observing that

$$\lim_{\Delta z \to 0} \frac{1_{\mathscr{P}_{\Delta z}}(z)}{\Delta z} \to \delta(z - z_\mathrm{P}). \tag{21}$$

The heat flux $\dot{Q}''_\mathrm{d}$ consists of two terms:

1. Thermal diffusion flux $\dot{Q}''_{\mathrm{d,d}}$ given by Fourier's law,

$$\dot{Q}''_{\mathrm{d,d}} = -k_\mathrm{t} \frac{\partial T}{\partial z} \tag{22}$$

where k_t is thermal conductivity and is assumed constant here, and

2. Buoyant turbulent mixing flux $\dot{Q}''_{\mathrm{d,b}}$ given as (Xu et al., 2014)

$$\frac{\partial \dot{Q}''_{\mathrm{d,b}}}{\partial z} = -k_\mathrm{b} \frac{\partial^2 T}{\partial z^2} \tag{23}$$

where k_b is buoyant conductivity given as

$$k_\mathrm{b} = \begin{cases} c_\mathrm{b} \kappa^2 d^2 \sqrt{g \alpha_p \left| \frac{\partial T}{\partial z} \right|}, & \frac{\partial T}{\partial z} < 0 \\ 0, & \frac{\partial T}{\partial z} \geq 0 \end{cases} \tag{24}$$

where κ is the von Karman constant ($\kappa \approx 0.4$), d is some characteristic length — the diameter in this case, g is the acceleration of gravity, α_p is the thermal expansion coefficient at constant pressure, and $c_\mathrm{b} \sim 1$ is a tuning factor. Because hot water has lower density than cold water, the normal steady situation is that T is higher at larger z (with the given direction of z), hence with $\frac{\partial T}{\partial z} > 0$ this is the normal situation and there is no buoyancy. On the other hand, with $\frac{\partial T}{\partial z} < 0$, the temperature profile is reversed, and buoyancy kicks in. (Vrettos, 2016) gives an alternative expression for buoyancy mixing.

In summary, for $z \in (0,h)$, the model can be simplified to

$$\frac{\partial T}{\partial t} = -\frac{\dot{V}_\ell \cdot u_\mathrm{v}}{A} \frac{\partial T}{\partial z} + \frac{k_\mathrm{t} + k_\mathrm{b}}{\rho \hat{c}_{p,\mathrm{w}}} \frac{\partial^2 T}{\partial z^2} + \frac{P^\circ \delta(z - z_\mathrm{P}) \cdot u_\mathrm{P} + \mathscr{U} \wp (T_\mathrm{a} - T)}{\rho A \hat{c}_{p,\mathrm{w}}}. \tag{25}$$

Because of the second derivative in the z-direction, we need two boundary conditions. These are

$$T_{z=0^-} = T_\mathrm{i} \tag{26}$$

$$T_{z=h^+} = T_{z=h}. \tag{27}$$

There is also an additional ambient heat loss surface at the bottom and the top.

The water tank is encased by an insulator of unknown thermal conductivity k_i and unknown thickness d_i. Thermal conductivity of insulator typically has a value in the range $k_\mathrm{i} \in [10, 50]\,\mathrm{mW/m\,K}$ with air at $k_\mathrm{air} = 25\,\mathrm{mW/m\,K}$. The *overall* heat transfer coefficient $\mathscr{U}$ typically is described by

$$\mathscr{U} = \frac{1}{\frac{1}{h_\mathrm{w}} + \frac{k_\mathrm{i}}{d_\mathrm{i}} + \frac{1}{h_\mathrm{a}}} \tag{28}$$

where h_w is the *heat transfer coefficient* between *water* and the metal surface, while h_a is the *heat transfer coefficient* between ambient *air* and the metal surface. The ambient side will exhibit free convection with typical values for h_a being $h_\mathrm{a} \in [2.8, 23]\,\mathrm{W/m^2\,K}$. The water side, will however vary between free convection with stagnant water when $u_\mathrm{v} \equiv 0$ and typical values of $h_\mathrm{w} \in [50, 3\,000]\,\mathrm{W/m^2\,K}$, and forced convection when $u_\mathrm{v} \neq 0$ with $h_\mathrm{w} \in [280, 17\,000]\,\mathrm{W/m^2\,K}$. Typically, if the insulation is 5 cm thick, $\frac{k_\mathrm{i}}{d_\mathrm{i}} \in [0.2, 1]\,\mathrm{W/m^2K}$.

3.3.2 Semi-discretized model

Because the flow of water is specified, it suffices with a simple finite difference discretization of the spatial derivatives. If the water tank height h is divided into n equal height slices, $\Delta z = \frac{h}{n}$ with the bottom slice numbered $k = 1$ and the upper slice numbered $k = n$, we have for $k \in \{2, \ldots, n-1\}$:

$$\frac{\mathrm{d}T_k}{\mathrm{d}t} = -\frac{\dot{V}_\ell \cdot u_\mathrm{v}}{A} \frac{T_k - T_{k-1}}{\Delta z} + \frac{k_\mathrm{t} + k_\mathrm{b}}{\rho \hat{c}_{p,\mathrm{w}}} \frac{T_{k+1} - 2T_k + T_{k-1}}{\Delta z^2} + \frac{P^\circ \frac{1_{\mathscr{P}_{\Delta z}}(k \cdot \Delta z)}{\Delta z} \cdot u_\mathrm{P} + \mathscr{U} \wp (T_\mathrm{a} - T_k)}{\rho A \hat{c}_{p,\mathrm{w}}}. \tag{29}$$

Here,

$$\frac{k_\mathrm{b}}{\rho \hat{c}_{p,\mathrm{w}}} = \begin{cases} c_\mathrm{b} \kappa^2 d^2 \sqrt{g \alpha_p \left| \frac{T_{k+1} - T_k}{\Delta z} \right|}, & T_k > T_{k+1} \\ 0, & T_k \leq T_{k+1} \end{cases} \tag{30}$$

where $c_\mathrm{b} \sim 1$ is a tuning factor.

At the boundaries, the scheme of 29 is invalid, and is modified to:

$k = 1$**:** For the advection term, T_0 becomes T_i, while for the diffusion term, T_0 equals T_1,

$$\frac{\mathrm{d}T_1}{\mathrm{d}t} = -\frac{\dot{V}_\ell \cdot u_\mathrm{v}}{A} \frac{T_1 - T_\mathrm{i}}{\Delta z} + \frac{k_\mathrm{t} + k_\mathrm{b}}{\rho \hat{c}_{p,\mathrm{w}}} \frac{T_2 - T_1}{\Delta z^2} + \frac{P^\circ \frac{1_{\mathscr{P}_{\Delta z}}(\Delta z)}{\Delta z} \cdot u_\mathrm{P} + \mathscr{U} \left(\wp + \frac{A}{\Delta z} \right) (T_\mathrm{a} - T_1)}{\rho A \hat{c}_{p,\mathrm{w}}}. \tag{31}$$

$k = n$**:** We assume that the temperature of the metal above cell n has the same temperature as cell n because of

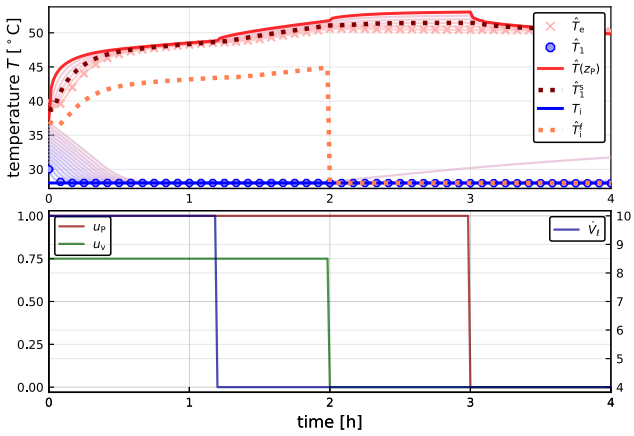

Figure 3. Stratified model simulation. Model parameters are taken from Table 2. Dotted lines indicate simulated temperatures at temperature sensor locations; temperature at inlet layer (T_1) is indicated with ∘ markers, and temperature at exit layer (T_e) is indicated with × markers.

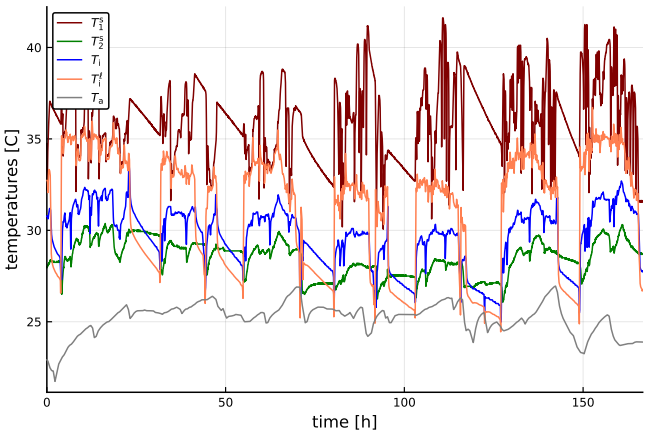

Figure 4. Experimental values of temperatures.

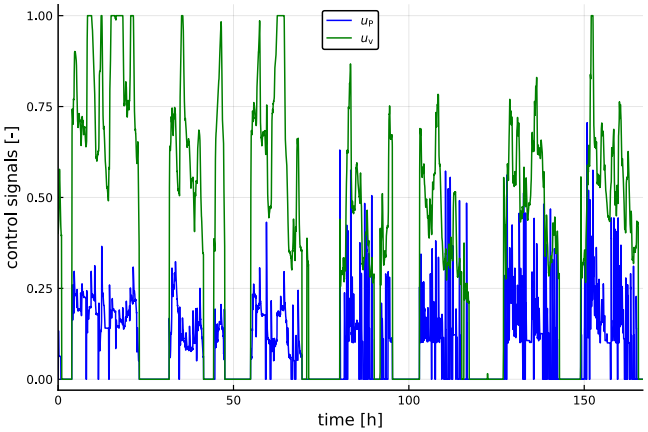

Figure 5. Experimental values for control signals.

good thermal conduction in the metal and good insulation, thus $T_{n+1} = T_n$. We then have

$$\frac{\mathrm{d}T_n}{\mathrm{d}t} = -\frac{\dot{V}_\ell \cdot u_\mathrm{v}}{A}\frac{T_n - T_{n-1}}{\Delta z} + \frac{k_\mathrm{t}+k_\mathrm{b}}{\rho \hat{c}_{p,\mathrm{w}}}\frac{T_{n-1}-T_n}{\Delta z^2} + \frac{P^\circ \frac{1_{\mathscr{P}_{\Delta z}}(n\cdot\Delta z)}{\Delta z}\cdot u_\mathrm{P} + \mathscr{U}\left(\wp + \frac{A}{\Delta z}\right)(T_\mathrm{a}-T_n)}{\rho A \hat{c}_{p,\mathrm{w}}}. \tag{32}$$

3.4 Model parameters

Table 2 lists nominal model parameters for the water tank.

In Table 2, it should be observed that h_a and $\frac{k_\mathrm{i}}{d_\mathrm{i}}$ dominates total over h_w, so that $\mathscr{U} \approx 1/(1/h_\mathrm{a} + d_\mathrm{i}/k_\mathrm{i})$ with both free and forced water convective heat transfer, and $\mathscr{U} \approx 0.43\,\mathrm{W/m^2K}$.

3.5 Operating conditions

Typical operating conditions for the water tank are given in Table 3.

3.6 Basic simulation of stratified tank model

Figure 3 shows the temperature response at $n = 20$ positions of the stratified model; $T_{1:n}(0) = [30:40]\,^\circ\mathrm{C}$, $T_\mathrm{a} = 25\,^\circ\mathrm{C}$, $T_\mathrm{i} = 28\,^\circ\mathrm{C}$, $\dot{V}_\ell = 10\cdot\mathbb{H}_0 - 6\cdot\mathbb{H}_{1.2\mathrm{h}}\mathrm{L/min}$, $u_\mathrm{v} = 0.75\cdot\mathbb{H}_0 - 0.75\cdot\mathbb{H}_{2\mathrm{h}}$ and $u_\mathrm{P} = \mathbb{H}_0 - \mathbb{H}_{3\mathrm{h}}$ where $\mathbb{H}_t$ is the Heaviside function.

Observe that with default values, the buoyant conductivity is very large *if* the initial profile of $T_k(0)$ is *reversed*; in Figure 3, $c_\mathrm{b} = 10^{-2}$ has been used. With the *positive* initial temperature *gradient* in Figure 3, there is no buoyancy. With the geometry of the tank and $u_\mathrm{v} = 0.75$, a "plug" of water entering the tank takes 40 min to pass through the tank with $\dot{V}_\ell = 10\,\mathrm{L/min}$, and 100 min with $\dot{V}_\ell = 4\,\mathrm{L/min}$.

4 Model fitting

4.1 Sensor signals and experimental data

The available sensors for the water tank are listed in Table 4.

Here, it should be observed that the lower temperature sensor T_2^s gives rather uncertain results due to poor insulation from the external metal of the water tank.

The heated loop temperature T_i^ℓ (T1) in Table 4 is the temperature of the mixture of the effluent water from the water tank and the by-passed water. Thus, using steady energy balance for the 3-way mixing valve, we have

$$T_\mathrm{i}^\ell = (1-u_\mathrm{v})\,T_\mathrm{i} + u_\mathrm{v} T_\mathrm{e} \tag{33}$$

where T_e is the effluent temperature from the tank, i.e., $T_\mathrm{e} = T$ for the well mixed tank model, and $T_\mathrm{e} = T_n$ for the stratified tank model.

Figures 4–6 display typical values for the sensor signals, with resolution in 1 min. It should be observed that with $u_\mathrm{v} \equiv 0$, according to 33, T_i^ℓ should equal T_i. Instead, Figure 4 indicates a bias of ca. 1.1 °C under that condition.

4.2 Measure of model fit

From a system theoretic point of view, T_a, T_i, u_P, and u_v are inputs to the dynamic model, while T_1^s, T_2^s, and T_i^ℓ

Table 2. Nominal parameters for water tank.

Parameter	Value	Comment
g	$9.81\,\mathrm{m/s^2}$	Acceleration of gravity
κ	$0.41-$	von Karman constant
ρ	$10^3\,\mathrm{kg/m^3}$	Water density
$\hat{c}_{p,\mathrm{w}}$	$4.19\,\mathrm{kJ/kg\,K}$	Specific heat capacity, water
α_p	$303\cdot 10^{-6}\,1/\mathrm{K}$	Thermal expansion coefficient
k_t	$0.6\,\mathrm{W/m\,K}$	Thermal conductivity, water
h	$1.5\,\mathrm{m}$	Height of water column
d	$0.5\,\mathrm{m}$	Internal diameter, tank
$\wp$	πd	Perimeter of water tank
A	$\pi\frac{d^2}{4}$	Cross sectional area, tank
A_s	$2A+\wp\cdot h$	Surface area, tank
V	Ah	Water volume
h_a	$3\,\mathrm{W/m^2K}$	Heat transfer, air
$h_\mathrm{w,free}$	$50\,\mathrm{W/m^2K}$	Heat transfer water, free convection
$h_\mathrm{w,forced}$	$1000\,\mathrm{W/m^2K}$	Heat transfer water, forced convection
$\frac{k_\mathrm{i}}{d_\mathrm{i}}$	$0.5\,\mathrm{W/m^2K}$	Typical value for a 5 cm thick insulator
$\mathscr{U}_\mathrm{free}$	$1/\left(\frac{1}{h_\mathrm{a}}+\frac{k_\mathrm{i}}{d_\mathrm{i}}+\frac{1}{h_\mathrm{w,free}}\right)$	Overall heat transfer coefficient, free
$\mathscr{U}_\mathrm{forced}$	$1/\left(\frac{1}{h_\mathrm{a}}+\frac{k_\mathrm{i}}{d_\mathrm{i}}+\frac{1}{h_\mathrm{w,forced}}\right)$	Overall heat transfer coefficient, forced
P°	$15\,\mathrm{kW}$	Maximum power of heating element
z_P	$1.15\,\mathrm{m}$	Position of heating element

Table 3. Typical operating conditions for water tank.

Variable	Value	Comment
T	$[25,45]\,^\circ\mathrm{C}$	Water tank temperature
T_i	$[27,33]\,^\circ\mathrm{C}$	Tank influent temperature
T_a	$[4,27]\,^\circ\mathrm{C}$	Ambient temperature
$\dot{V}_\ell$	$[1,13]\,\mathrm{L/min}$	Volumetric flow rate in loop
u_P	$[0,1]-$	Electric power control signal
u_v	$[0,1]-$	Water valve control signal

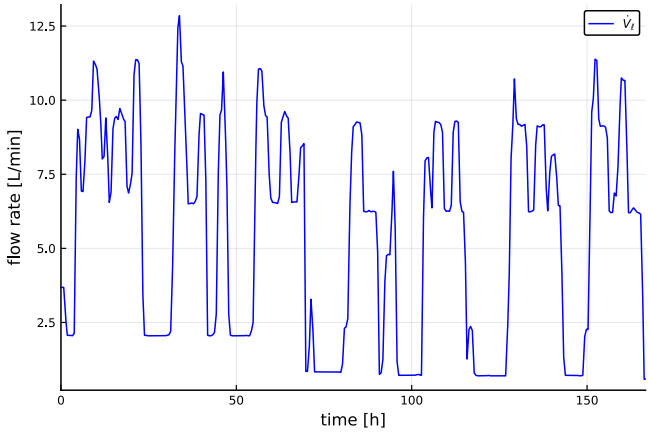

Figure 6. Experimental values for volumetric loop flow rate.

represent measured responses (outputs). Here, T_2^s is the lower temperature sensor in the tank, which is reported to be unreliable. Conceptually, we will still include it in the description. To this end, let

$$u=\begin{pmatrix} T_\mathrm{i} & T_\mathrm{a} & u_\mathrm{P} & u_\mathrm{v}\end{pmatrix} \tag{34}$$

be the vector of known inputs to the system, while

$$y=\begin{pmatrix} T_\mathrm{i}^\ell & T_1^\mathrm{s} & T_2^\mathrm{s}\end{pmatrix} \tag{35}$$

is the vector of output (response) observations. Assume that we have a state space model

$$\frac{\mathrm{d}x}{\mathrm{d}t}=f(x,u;\theta) \tag{36}$$

$$y=g(x,u;\theta)\,. \tag{37}$$

In principle we can solve this model such that

$$y_t=G(u_\tau,x_0,\theta) \tag{38}$$

where y_t is the model output at time t, while u_τ is the input sequence in the interval $[0,t]$. Normally observations are available at discrete time instances t; in that case y_t is found in discrete time instance t by using a numeric ODE solver.

In general, measured signals have superscript m, i.e., u^m and y^m. Introducing the extended parameter set $\tilde{\theta}=\begin{pmatrix}\theta & x(0)\end{pmatrix}$, we can measure the model fit by cost function $V\left(\tilde{\theta}\right)$ given as

$$V\left(\tilde{\theta}\right)=\sum_{t=1}^{N}\|y_t-y_t^\mathrm{m}\|_{W_y}^2+\lambda\cdot\left\|\tilde{\theta}-\tilde{\theta}^\circ\right\|_{W_\theta}^2 \tag{39}$$

Table 4. Available sensor signals for water tank. Sensor labels (T1–T4, F1) refer to Figure 1.

Variable	Unit	Comment
T_i	°C	Influent water temperature to tank (T4)
T_i^ℓ	°C	Heated temperature influent to loop (T1)
T_a	°C	Ambient temperature
T_1^s	°C	Water tank temperature at $z_1^\mathrm{s} = 1.3\,\mathrm{m}$ (T2)
T_2^s	°C	Water tank temperature at $z_2^\mathrm{s} = 0.23\,\mathrm{m}$ (T3)
$\dot{V}_\ell$	L/min	Volumetric flow rate in loop (F1)
u_P	$\frac{\mathrm{V}}{10\,\mathrm{V}}$	Electric power control signal
u_v	$\frac{\mathrm{V}}{10\,\mathrm{V}}$	Water valve control signal

where $\|\cdot\|_W$ denotes the weighted 2-norm. Here, $V_{\lambda=0}$ is the standard least squares cost function, while $\lambda > 0$ regularizes the problem by emphasizing a prior parameter "guess" $\tilde{\theta}^\circ$ which can be based on physical considerations. It is also possible to add hard constraints in the form $\tilde{\theta} \subseteq \tilde{\Theta}$. Typically W_y and W_θ are chosen such that the individual elements of vectors have comparable values, e.g., normalized to $[0,1]$ or $[-1,1]$, or standardized to have unit standard deviation.[2]

To assess how well the model with parameters $\hat{\tilde{\theta}}$ generalizes from training data to validation, it is common to compare the *root mean squared error* (RMSE) ε_RMS for the parameter estimate $\hat{\tilde{\theta}}$ applied to the training data, compared to the RMSE for the parameter estimate applied to independent validation data;

$$\varepsilon_\mathrm{RMS} = \sqrt{\frac{1}{N} V\left(\hat{\tilde{\theta}}\right)}. \tag{40}$$

In 39, λ is a user selected hyper parameter, usually chosen such that the model generalizes well.

4.3 Model fitting results

The parameters $\mathscr{U}$, k_t, and c_b are used as fitting parameters together with the unknown initial conditions of unmeasured temperatures. Tuning k_t is related to adding a "heuristic circular mass flow term" in (Koch, 2012). It should be added that numeric discretization in space introduces artificial mixing, with the extreme case of a concentrated model having complete mixing. The parameter θ_c for the concentrated (well mixed) tank model is

$$\theta_\mathrm{c} = \mathscr{U} \tag{41}$$

while for the distributed (stratified) model, the parameter is θ_d given as

$$\tilde{\theta}_\mathrm{d} = [\mathscr{U}, k_\mathrm{t}, c_\mathrm{b}, T_1(t=0), \ldots, T_n(t=0)]. \tag{42}$$

The cost function is V given by 39, with $\lambda \equiv 0$.

For the concentrated model, parameter $\mathscr{U}$ is estimated to $\mathscr{U} \in [2.9, 62]$, depending on the initial temperature distribution in the tank. This variation in $\mathscr{U}$ depending on the initial state of the system indicates that the well mixed model is not very good.

[2] If the measurements are pre-scaled, then $W = I$.

Table 5. Bounds $\tilde{\Theta}$ and initial guess $\tilde{\theta}^{(0)}$ for parameters during calibration of distributed model.

	$\mathscr{U}$	k_t	c_b	$T_k(t=0)$
$\tilde{\Theta}$	$[0.1,4]$	$[0.1,4]$	$[0.1,2]$	$[17,47]$
$\tilde{\theta}^{(0)}$	1	0.6	1	17–47

Table 6. Estimated parameters for distributed (stratified) model. Calibrated and validated RMSE data are taken for T_1^s.

n	$\mathscr{U}$	k_t	c_b	$\mathrm{RMSE}_\mathrm{cal}$	$\mathrm{RMSE}_\mathrm{val}$
3	3.72	0.1	2.0	1.47	1.5
10	4 .0	0.1	2.0	1.51	1.53
20	2.63	3.99	0.1	1.74	1.8
50	0.94	4.0	0.1	3.22	2.76

For the distributed model, the parameters have been bounded as in Table 5.

The estimated parameters for the distributed model are given in Table 6.

Figure 7 shows how the calibrated model fits the experimental data.

Validated model fit is shown in Figure 8.

5 Discussion and Conclusions

Suitable models for hot water tanks are important for successful advanced management and control of energy us-

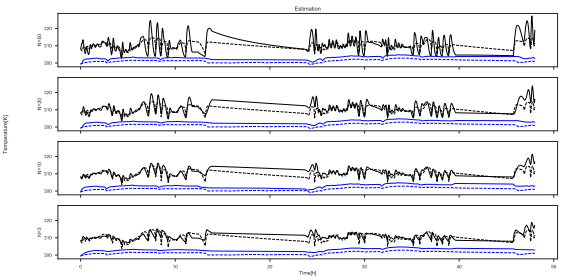

Figure 7. Calibrated model fit for the distributed model. Sensor signals (T_1^s, T_2^s): dashed lines. Simulated result: solid lines. Black color: T_1^s, blue color: T_2^s.

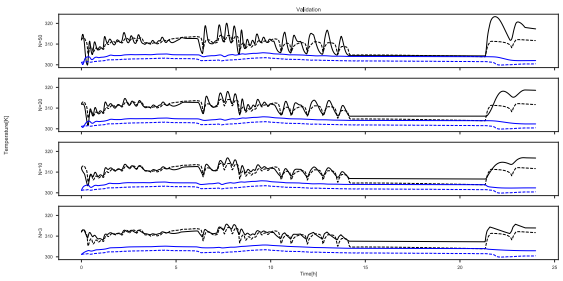

Figure 8. Validated model fit for the distributed model. Sensor signals (T_1^s, T_2^s): dashed lines. Simulated result: solid lines. Black color: T_1^s, blue color: T_2^s.

age in buildings. This paper discusses a well mixed tank model, and a distributed model which includes the effect of stratification. A buoyant conductivity term is included to handle buoyancy, as in (Xu et al., 2014); this model is hardly perfect, though.[3] An alternative description would be that of *natural convection* as in (Vrettos, 2016).

Experimental data from a well instrumented new building is used to tune model parameters and validate the models. Initial results indicate that the well mixed model is too simple, in that model parameters depend considerably on the initial temperature distribution in the tank. The distributed model is discretized in n slices (hyper parameter[4]), where $n \in \{3, 10, 20, 50\}$, and these are fitted to the data. The estimated parameters for the various values of n are somewhat strange, in that between $n = 10$ and $n = 20$, parameters k_t (water conductivity) and c_b (buoyancy scaling parameter) switch values. However, remembering that coarse discretization in space gives an added mixing effect (adds to k_t) while a finer discretization gives less such mixing, this may partially explain the variation in k_t estimates. Also, somewhat surprisingly, the *root mean squared error* (RMSE) increases with the number of slices for the calibrated model, which is contrary to what is expected. This could be due to numeric problems with solving and fitting larger models. Similarly, the RMSE values for the validated models also vary somewhat unexpectedly. Still, for $n \in \{3, 10\}$ the model fit is decent.

In future work, the buoyancy model should be reconsidered, sensor signals should be checked/re-calibrated, with a revisit of how to handle data at different sample frequencies. Then, parameter estimation should be checked, possibly also introducing regularization in the model fitting.

References

Thomas Berthou, Pascal Stabat, Salvazet Raphael, and Dominique Marchio. Development and validation of a gray box model to predict thermal behavior of occupied office buildings. *Energy and Buildings*, 74:91–100, 2014. doi:10.1016/j.enbuild.2014.01.038.

Vinicius de Oliveira, Johannes Jäschke, and Sigurd Skogestad. Dynamic online optimization of a house heating system in a fluctuating energy price scenario. *IFAC Proceedings Volumes*, 46(32):463–468, December 2013. doi:10.3182/20131218-3-IN-2045.00070.

Samuel F. Fux, Araz Ashouri, Michael J. Benz, and Lino Guzzella. Ekf based self-adaptive thermal model for a passive house. *Energy and Buildings*, 68:811–817, 2012. ISSN 0378-7788. doi:10.1016/j.enbuild.2012.06.016.

Casper Amandus Johansen. Evaluation of control systems with models for thermal energy in buildings. Master's thesis, University of South-Eastern Norway, P.O. Box 203, N-3901 Porsgrunn, Norway, May 2019. External partner: Autobolig AS.

Stephan Koch. *Demand response methods for ancillary services and renewable energy integration in electric power systems*. PhD thesis, ETH, Power Systems Laboratory, 2012.

Bernt Lie. Improved model for solar heating of buildings. In Lena Buffoni, Adrian Pop, and Bernhard Thiele, editors, *Proceedings, The 56th Conference of Simulation and Modelling*, pages 299–308, Linköping University, Sweden, October 2015. Scandinavian Simulation Society, Linköping University Electronic Press. doi:10.3384/ecp15119, pp. 299–308. October 7–9 2015.

Bernt Lie, Carlos Pfeiffer, Nils-Olav Skeie, and Hans-Georg Beyer. Models for solar heating of buildings. In Alireza Rezania Kolai, Kim Sørensen, and Mads Pagh Nielsen, editors, *Proceedings, 55th International Conference of Scandinavian Simulation Society*, pages 28–38, Aalborg University, Denmark, October 2014. Scandinavian Simulation Society, Linköping University Electronic Press. doi:www.ep.liu.se/ecp/108/ecp14108.pdf. October 21–22 2014.

Luis Pérez-Lombard, José Ortiz, and Christine Pout. A review on buildings energy consumption information. *Energy and Buildings*, 40:394–398, 2008. doi:10.1016/j.enbuild.2007.03.007.

R. Viskanta, M. Behnia, and A. Karalis. Interferometric observations of the temperature structure in water cooled or heated from above. *Advances in Water Resources*, 1(2):57–69, 1977.

Evangelos Vrettos. *Control of Residential and Commercial Loads for Power System Ancillary Services*. PhD thesis, ETH, Power Systems Laboratory, 2016.

Zhijie Xu, Ruisheng Diao, Shuai Lu, Jianming Lian, and Yu Zhang. Modeling of electric water heaters for demand response: A baseline pde model. *IEEE Transactions on Smart Grid*, 5(5):2203–2210, September 2014. doi:10.1109/TSG.2014.2317149.

[3] See, e.g., https://www.youtube.com/watch?v=wqtFeAvDOwk.

[4] A hyper parameter is a user selectable parameter.

Density and Viscosity Correlations for Aqueous 3-Amino-1-propanol and Monoethanol Amine Mixtures

Sumudu S. Karunarathne Lars E. Øi

Faculty of Technology, Natural Sciences and Maritime Sciences, University of South-Eastern Norway, Norway,
{Sumudu.karunarathne,lars.oi}@usn.no

Abstract

Density and viscosity data and relevant correlations are essentially needed to perform mathematical modelling and simulations for the design of process equipment. Correlations that are developed to cover a range of concentrations and temperatures help to use them in mathematical modelling and simulations of absorption - desorption processes. In this study, a density correlation was proposed for 3A1P (3-Amino-1-propanol) + H_2O mixtures. The McAllister three body model was adopted to correlate kinematic viscosity data of MEA (monoethanol amine) + H_2O mixtures and kinematic viscosity data for 3A1P + H_2O mixtures. The Eyring's viscosity model based on absolute rate theory was used to correlate dynamic viscosity data. A Redlich – Kister type polynomial was proposed to fit the excess free energy of activation for viscous flow for 3A1P + H_2O mixtures. The developed correlations were able to represent density and viscosity data with accepted accuracy and can be used to perform engineering calculations.

Keywords: density, viscosity, MEA, 3A1P, McAllister model

1 Introduction

Acid gas removal using aqueous alkanolamines through chemical absorption has been in practice for decades to remove CO_2 from natural gas (Eimer, 2014; Rochelle, 2009). The integration of this technology to a commercial level in Post-Combustion CO_2 Capture is halted by economic feasibility due to the energy demand of the process. High reaction rate with CO_2 and low regeneration energy in stripping are ideal characteristics for an absorbent to reduce the cost of operation.

Physical properties like density, viscosity and surface tension are essential in various aspects such as designing/sizing of process equipment and process simulations. They appear in many mass and heat transfer correlations that are essential in the mathematical modelling transport process and design of the absorption column. Empirical correlations of such properties can provide the required data within a considered concentration and temperature range. Abundant resources are available for the density and viscosity of aqueous MEA (monoethanol amine) in the literature with suggested correlations, while reported studies are limited for 3A1P (3-Amino-1-propanol) (Idris and Eimer, 2016; Idris *et al.*, 2018).

2 Density and Viscosity Correlations for Binary Mixtures

Correlations based on excess volume V^E are commonly adopted to fit density data of liquid mixtures and the Redlich-Kister (Redlich and Kister, 1948) type polynomial is suggested to correlate V^E. This approach requires a higher number of parameters to correlate V^E to acquire high accuracy of data fit (Aronu *et al.*, 2012). Such studies are reported for densities of aqueous MEA and 3A1P solutions under different compositions and temperatures in the literature (Han *et al.*, 2012; Idris and Eimer, 2016).

$$V^E = V - \sum_{i=1}^{n} x_i V_i^o \tag{1}$$

$$\rho = \frac{\sum_{i=1}^{n} x_i \cdot M_i}{V^E + \sum_{i=1}^{n} \frac{x_i \cdot M_i}{\rho_i}} \tag{2}$$

McAllister, (1960) viscosity model presents a theoretical approach based on molecular attractions arises from different molecular arrangements to predict kinematic viscosities in binary mixtures. McAllister derived model with two forms for the kinematic viscosity of binary liquid mixtures based on absolute rates theory approach of Eyring's viscosity (Eyring, 1936). The McAllister three-body model is shown in (3-7).

$$\begin{aligned} ln(v) = {} & x_1^3 \cdot ln(v_1) + 3x_1^2 x_2 \cdot ln(v_{12}) + 3x_1 x_2^2 \\ & \cdot ln(v_{21}) + x_2^3 \cdot ln(v_2) \\ & - ln(x_1 + x_2 \cdot [M_2/M_1]) + 3x_1^2 x_2 \\ & \cdot ln([2 + M_2/M_1]/3) + 3x_1 x_2^2 \\ & \cdot ln([1 + 2M_2/M_1]/3) + x_2^3 \\ & \cdot ln(M_2/M_1) \end{aligned} \tag{3}$$

$$v_1 = \frac{hN}{M_1} e^{-\Delta s_1^*/R} e^{\Delta H_1^*/RT} \tag{4}$$

$$v_{12} = \frac{hN}{M_{12}} e^{-\Delta s_{12}^*/R} e^{\Delta H_{12}^*/RT} \tag{5}$$

$$\nu_{21} = \frac{hN}{M_{21}} e^{-\Delta s^*_{21}/R} e^{\Delta H^*_{21}/RT} \quad (6)$$

$$\nu_2 = \frac{hN}{M_2} e^{-\Delta s^*_2/R} e^{\Delta H^*_2/RT} \quad (7)$$

Eyring's viscosity model for Newtonian fluids is given in (8) (Eyring, 1936).

$$\eta = \frac{hN}{V} exp\left(\frac{\Delta F^*}{RT}\right) \quad (8)$$

The following (9) and (10) represent the relationship between real and ideal solutions. The excess property ΔF^{E*} is called the excess free energy of activation for viscous flow.

$$ln(\eta V) = ln(\eta V)_{ideal} + \frac{\Delta F^{E*}}{RT} \quad (9)$$

$$ln(\eta V) = \sum_{i=1}^{n} x_i ln(\eta_i V_i^o) + \frac{\Delta F^{E*}}{RT} \quad (10)$$

$$ln(\eta V) = \sum_{i=1}^{n} x_i ln(\eta_i V_i^o) + \frac{x_1 x_2 W}{RT} \quad (11)$$

A positive ΔF^{E*}reveals that the real mixture has a greater viscosity than that of an ideal mixture (Heric and Brewer, 1967). Stronger interaction between unlike molecules gives positive values to ΔF^{E*} and excess viscosity η^E. Further, Meyer *et al.*, (1971) discussed that $\Delta F^{E*} < 0$ for the solutions with solute-solute associations. According to Fort and Moore (1966), the G_{12} from Grunberg and Nissan (1949) as shown in (13) provides a better measure for the strength of interactions between components. The interchange energy or the interaction parameter W/RT from the Eyring's viscosity model is proportional to G_{12} and shows the same trend as that of G_{12} (Mukesh *et al.*, 2015).

The ideal viscosity of a liquid mixture is defined in several ways in the literature (Kendall and Monroe, 1917; Bingham, 1922; Cronauer *et al.*, 1965; Martins *et al.*, 2000). Correlations based on Redlich-Kister polynomials to fit the data of η^E were reported for aqueous MEA solutions (Islam *et al.*, 2004). Nigam and Mahl, (1971) illustrated that the sign of G_{12} along with η^E from (12) reveals what type of interaction such as strong, weak or dispersion is dominant in the solution.

$$\eta^E = \eta - (x_1\eta_1 + x_2\eta_2) \quad (12)$$

$$ln(\eta_{12}) = x_1 ln(\eta_1) + x_2 ln(\eta_2) + x_1 x_2 G_{12} \quad (13)$$

3 Methodology

This study focuses on density and viscosity correlations for aqueous MEA and 3A1P mixtures. The study is based on measured density and viscosity data of this and previous works performed in University of South-Eastern Norway (USN) (Idris and Eimer, 2016; Idris *et al.*, 2018). Idris and Eimer, (2016) and Idris *et al.*, (2018) discussed the density and viscosity of aqueous 3A1P solutions under the range of mass fractions w_1 (i=1 and 2 refer amine and water respectively) within 0-1 and temperatures 293.15-353.15K and 298.15-373.15K respectively. The correlation suggested by Aronu *et al.*, (2012) as given in (14) was adopted to correlate aqueous 3A1P density data.

$$\rho = \left(k_1 + \frac{k_2 x_2}{T}\right) exp\left(\frac{k_3}{(T)^2} + \frac{k_4 x_1}{T} + k_5\left(\frac{x_1}{T}\right)^2\right) \quad (14)$$

The McAllister three-body model is adopted to predict kinematic viscosities of MEA + H_2O and 3A1P + H_2O mixtures. The parameters related to the enthalpy and the entropy for viscous flow shown in the (3) to (7) are estimated via regression. The ΔF^{E*} for 3A1P + H_2O mixtures is calculated using Eying's viscosity model and a Redlich-Kister type polynomial is fitted to represent the viscosity data.

3.1 Density and Viscosity Measurements

Densities of aqueous amine solutions were measured using a DMA 4500 density meter from Anton Paar. The measurements of dynamic viscosity performed using a Physica MCR 101 rheometer from Anton Paar. A detailed description of the density meter and rheometer is given in publications based on previous at USN (Han *et al.*, 2012; Idris *et al.*, 2017).

4 Results and Discussion

In this section, the accuracy of the data fit of the density and viscosity correlations are determined using Average Absolute Relative Deviation (AARD) and Absolute Maximum Deviation (AMD) as given in (15) and (16).

$$AARD(\%) = \frac{100\%}{N}\sum_{i=1}^{N}\left|\frac{Y_i^E - Y_i^C}{Y_i^E}\right| \quad (15)$$

$$AMD = MAX\left|Y_i^E - Y_i^C\right| \quad (16)$$

4.1 Density Correlation of 3A1P + H_2O Mixtures

The density data of 3A1P + H_2O mixtures were fitted to the correlation described in (14) with R^2= 0.97. The comparison of measured data with the correlation reveals that the deviation of correlated properties from measured is high at lower temperatures for the different 3A1P concentrations. Nevertheless, the correlation was able to represent data at AARD of 0.2 % and AMD of 6.7 kg·m^{-3}. The estimated parameters are given in Table 1. Idris and Eimer, (2016) reported several density

correlation studies based on a Redlich-Kister type polynomial on excess volume, Jouyban-Acree (Jouyban *et al.,* 2005) and Gonzalez-Olmos and Iglesias (Gonzalex-Olmos and Iglesias, 2008). Table 2 summarize absolute average deviations of different correlations fitted for the aqueous 3A1P solutions.

Table 1. Parameters for the Density Correlation for 3A1P + H_2O Mixtures

Parameter	*Value*
k_1	706
k_2	1.155 x10^5
k_3	-7633
k_4	112.1
k_5	3602

Table 2. Absolute Average Deviation Measured and Correlated Densities for 3A1P + H_2O Mixtures

Correlation	*Absolute average deviation (kg·m^{-3})*
Aronu (this work)	1.9
Redlich-Kister	0.5
Jouyban-Acree	2
Gonzalez-Olmos and Iglesias	0.7

The correlation for excess volume was based on a Redlich-Kister polynomial with 39 parameters for the considered temperature range. Three parameters were estimated at each temperature level by fitting the correlation into the calculated excess volume using measured densities. The Jouyban-Acree correlation used only three parameters and absolute average deviation is similar to this study. A semiempirical model proposed by Gonzalez-Olmos and Iglesias with 12 parameters was used to correlate densities over the range of 3A1P mole fractions and temperatures.

The considered correlations in this study and the literature for the density of 3A1P have acceptable accuracy. The advantage of correlations proposed by Aronu, Jouyban-Acree and Gonzalez-Olmos and Iglesias is that they can be easily used in the mathematical modelling and simulations of a pilot or large-scale absorption processes. The models including parameters can be implemented in simulation programs like Aspen Plus or in programming tool like MATLAB.

4.2 Viscosity Correlation of MEA + H_2O and 3A1P + H_2O Mixtures

The calculated kinematic viscosity of MEA + H_2O and 3A1P + H_2O mixtures from dynamic viscosity and density were correlated using McAllister three-body model. The estimated parameters that are related to the activation energies of the mixtures are given in Table 3. These parameters were assumed constant over the considered temperature range.

Table 3. Parameter in McAllister Three-Body Model

Mixture	ΔH^*/ *kJ·mol^{-1}*	ΔS^*/*J·mol^{-1}K^{-1}*
MEA + H_2O	ΔH_1^* = 28.068	ΔS_1^*= 28.39
	ΔH_{12}^* = 31.668	ΔS_{12}^*= 15.32
	ΔH_{21}^* = 30.271	ΔS_{21}^*= 42.45
	ΔH_2^* = 13.677	ΔS_2^*= 36.45
3A1P + H_2O	ΔH_1^* = 33.073	ΔS_1^*= 39.03
	ΔH_{12}^* = 31.410	ΔS_{12}^*= 11.27
	ΔH_{21}^* = 43.316	ΔS_{21}^*= 40.30
	ΔH_2^* = 12.429	ΔS_2^*= 67.08

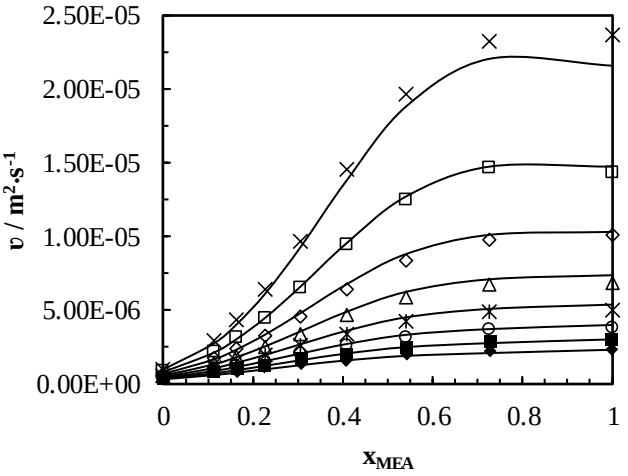

Figure 1. Kinematic viscosity of MEA + H_2O mixtures at temperatures: 293.15 K, 'x'; 303.15 K, '□'; 313.15 K, '◇'; 323.15 K, '△'; 333.15 K, 'ж'; 343.15 K, '○'; 353.15 K, '■'; 363.15 K, '◆'. The solid lines represent the McAllister model.

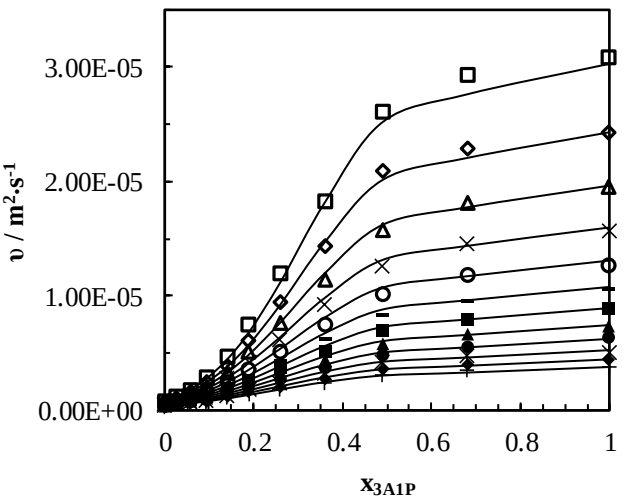

Figure 2. Kinematic viscosity of 3A1P + H_2O mixtures at temperatures: : 298.15 K, '□'; 303.15 K, '◇'; 308.15 K, '△'; 313.15 K, 'x'; 318.15 K, '○'; 323.15 K, '-'; 328.15 K, '■'; 333.15 K, '▲'; 338.15 K, '●'; 343.15 K, 'ж'; 348.15 K, '◆'; 353.15 K, '+'. The solid lines represent the McAllister model.

The McAllister three-body model was able to represent the kinematic viscosity of MEA + H_2O and 3A1P + H_2O with acceptable accuracy. Table 2 provides an overview of the accuracy based on AARD and AMD of the mixtures. For MEA + H_2O, model deviates from the data at high MEA concentrations and low temperatures as shown in Figure 1. The highest deviations were observed at X_{MEA} = 0.726 ($w_1 = 0.9$) and X_{MEA} = 1 ($w_1 = 1$) at 293.15 K. The average absolute deviation of the correlated data is 1.68 x10^{-7} $m^2 \cdot s^{-1}$. For 3A1P + H_2O mixtures, the deviation is high at higher temperatures for the mixtures up to $X_{3A1P} \leq$ 0.057 and it becomes high at lower temperatures for the mixtures with X_{3A1P} > 0.057 as illustrated in Figure 2. The average absolute deviation of the correlated data is 1.62 x10^{-7} $m^2 \cdot s^{-1}$.

Table 4. Calculated AARD and AMD of the McAllister Three-Body Model for the MEA + H_2O and 3A1P + H_2O

Mixture	*AARD %*	*AMD $m^2 \cdot s^{-1}$*
MEA + H_2O	3.17	1.42x10^{-6}
3A1P + H_2O	3.66	1.71 x10^{-6}

The ΔF^{E*} was determined using measured density and viscosity for aqueous 3A1P mixtures at different temperatures. A Redlich-Kister type polynomial was fitted for the ΔF^{E*} and viscosity of aqueous 3A1P mixtures were obtained accordingly. This correlation used molar volumes of mixtures to determine the viscosity. For this study, the calculated molar volumes from density data were used and it is possible to use the density correlation that was discussed in this study or correlations in the literature to acquire molar volumes for the situations when measured data are not available. The correlation was able to fit the viscosity data with AARD of 2.7% and AMD of 1.1 mPa·s at w_1= 0.8 and temperature of 303.15 K. These deviations are acceptable for engineering calculations.

Figure 3 shows the comparison between measured and correlated viscosities for 3A1P + H_2O mixtures. The ΔF^{E*} is positive for the considered range of 3A1P concentrations and temperatures. According to Heric and Brewer, (1967), if $\Delta F^{E*} > 0$, the viscosity of a real mixture is greater than that of an ideal mixture. This emphasizes strong intermolecular attractions in the solution. As reported by Idris *et al.*, (2018), $\eta^E < 0$ for the water rich region indicates weak intermolecular attractions. The presence of strong intermolecular attractions is determined as $\eta^E > 0$ for amine rich region. The interaction parameter G_{12} proposed by Grunberg and Nissan, (1949) for binary mixtures behaves similar to ΔF^{E*}, that is positive for considered 3A1P concentrations. Nigam and Mahl, (1971) show that for the weak intermolecular attractions $G_{12} > 0$ and $\eta^E < 0$.

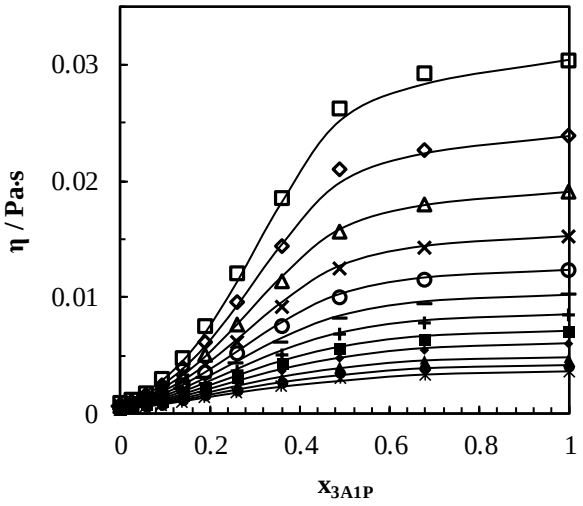

Figure 3. Dynamic viscosity of 3A1P + H_2O mixtures at temperatures: 298.15 K, '□'; 303.15 K, '◇'; 308.15 K, '△'; 313.15 K, 'x'; 318.15 K, '○'; 323.15 K, '-'; 328.15 K, '+'; 333.15 K, '■'; 338.15 K, '◆'; 343.15 K, '▲'; 348.15 K, '●'; 353.15 K, 'ж'. The solid lines represent the correlation.

4.3 Recommended Correlations for Simulations

Mathematical modelling of the absorption process is based on material and energy balance of the gas/liquid interface. The composition and the temperature of the solvent vary continuously through the column for both steady state and dynamic conditions. Physical property correlations as a continuous function of composition and temperature can be easily implemented in a programming tool like MATLAB for both steady state and dynamic simulations.

In this study, the parameters of the Aronu's density correlation were evaluated in such a way that concentration and temperatures can be considered as continuous independent variables. The other advantages of this correlation are it is simple and accuracy is acceptable. The McAllister three-body model for kinematic viscosity can be easily converted into code with all the parameters as discussed in this study. The proposed Redlich-Kister polynomial for the Eyring's viscosity model is a continuous function of concentration and temperature. Accordingly, viscosity variations related to the changes in compositions and temperatures in the column can be observed and correlation can be used in other mass and heat transfer correlations.

5 Conclusion

This study discusses the density and viscosity correlations for the mixtures of MEA + H_2O and 3A1P + H_2O. The considered correlations can be used in mathematical models such as continuity, momentum

and energy equations to perform simulations in e.g. amine based absorption and desorption processes.

The correlations for measured density and viscosity data of aqueous mixtures of MEA and 3A1P were discussed. Density data of aqueous 3A1P was correlated by the empirical correlation proposed by Aronu and was able to represent density data with AARD of 0.2% that is satisfactory in engineering calculations.

The McAllister three-body model was adopted to fit kinematic viscosity data for aqueous MEA and aqueous 3A1P mixtures. The energy parameters in the model were evaluated through a regression. The three-body model can correlate kinematic viscosities for considered mixtures with acceptable accuracy having AARD of 3% and 4% for aqueous MEA and aqueous 3A1P mixtures respectively.

The viscosity correlation based on a Redlich – Kister type polynomial for the excess free energy of activation for viscous flow using the Eyring's viscosity model was developed to correlate viscosity data of 3A1P + H_2O mixtures. The viscosity data were in good agreement with correlated viscosities with AARD of 2.7%.

Nomenclature

ΔF^*	Free energy of activation for viscous flow (J·mol^{-1})
ΔF^{E*}	Excess free energy of activation for viscous flow (J·mol^{-1})
G_{12}	Characteristic constant
h	Planck's constant (J·s)
ΔH^*	Enthalpy of activation for viscous flow (J·mol^{-1})
k	Parameters of Eq (14)
M	Molecular weight (kg·mol^{-1})
N	Avogadro's number
R	Gas constant (J·mol^{-1}·K^{-1})
ΔS^*	Entropy of activation for viscous flow (J·mol^{-1}·K^{-1})
T	Temperature (K)
V	Molar volume of mixture (m^3·mol^{-1})
V^E	Excess molar volume (m^3·mol^{-1})
V_i^o	Molar volume of pure liquids (m^3·mol^{-1})
W	Interchange energy (J·mol^{-1})
x	Mole fraction
Y_i^E	Measured property
Y_i^C	Calculated property

Greek letters

η	Dynamic viscosity (Pa·s)
ν	Kinematic viscosity (m^2·s^{-1})
ρ	Density (kg·m^{-3})

References

T. G. Amundsen, L. E. Øi, and D. A. Eimer. Density and viscosity of monoethanolamine + water + carbon dioxide from (25 to 80) °C. *J. Chem. Eng. Data*, 54: 3096-3100, 2009.

U. E. Aronu, A. Hartono, and H. F. Svendsen. Density, viscosity, and N_2O solubility of aqueous amino acid salt and amine amino acid salt solutions. *J. Chem. Thermodynamics*, 45: 90-99, 2012.

E. C. Bingham. *Fluidity and plasticity*. McGraw-Hill, New York, 1922.

D. C. Cronauer, R. R. Rothfus, and R. I. Kernmore. Viscosity and density of the ternary liquid system acetone-benzene-ethylene dichloride. *J. Chem. Eng. Data*, 10: 131-133, 1965.

D. A. Eimer. *Gas Treating: Absorption Theory and Practice*. John Wiley & Sons Ltd, 2014.

H. Eyring. Viscosity, Plasticity, and Diffusion as example of absolute reaction rates. *Journal of chemical physics*, 4: 283-291, 1936.

R. J. Fort and W. R. Moore. Viscosities of binary liquid mixtures. *Transactions of the faraday society*, 62: 1112-1119, 1966.

R. Gonzalez-Olmos and M. Iglesias. Influence of temperature on thermodynamics of ethers + xylenes. *Fluid Phase Equilibria*, 267(2):133-139, 2008. doi:10.1016/j.fluid.2008.03.004.

L. Grunberg and A. H. Nissan. Mixture Law for Viscosity. *Nature*, 164(4175): 799-800, 1949. doi:10.1038/164799b0.

J. Han, J. Jin, D. A. Eimer, and M. C. Melaaen. Density of water (1) + Monoethanolamine (2) + CO_2 (3) from (298.15 to 413.15) K and surface tension of water (1) + Monoethanolamine (2) from (303.15 to 333.15) K. *J. Chem. Eng. Data*, 57: 1095-1103, 2012.

A. Hartono, M. O. Mba, and H. F. Svendsen. Physical properties of partially CO_2 loaded aqueous monoethanolamine (MEA). *J. Chem. Eng. Data*, 59: 1808-1816, 2014.

E. L. Heric and J. G. Brewer. Viscosity of some binary liquid nonelectrolyte mixtures. *J. Chem. Eng. Data*, 12(04): 574-583, 1967.

Z. Idris and D. A. Eimer. Density measurements of unloaded and CO_2 loaded 3-Amino-1-propanol solutions at temperatures (293.15 to 353.15) K. *J. Chem. Eng. Data*, 61(1): 173-181, 2016.

Z. Idris, N. B. Kummamuru, and D. A. Eimer. Viscosity measurement of unloaded and CO_2-loaded aqueous monoethanolamine at higher concentrations. *Journal of Molecular Liquids*, 243: 638-645, 2017.

Z. Idris, N. B. Kummamuru, and D. A. Eimer. Viscosity measurement and correlation of unloaded and CO_2 loaded 3-Amino-1-propanol solution. *J. Chem. Eng. Data*, 63: 1454-1459, 2018.

M. N. Islam, M. M. Islam, and M. N. Yeasmin. Viscosity of aqueous solution of 2-methoxyethanol, 2-ethoxyethanol, and ethanolamine. *J. Chem. Thermodynamics*, 36: 889-893, 2004.

A. Jouyban, A. Fathi-Azarbayjani, M. Khoubnasabjafari, and W. E. Acree. Mathematical representation of the density of

liquid mixtures at various temperatures using Jouyban-Acree model. *Indian Journal of Chemistry,* 44A: 1553-1560, 2005.

J. Kendall and P. Monroe. The viscosity of liquids. II. The viscosity-composition curve for ideal liquid mixtures. *J. Am. Chem. Soc,* 39: 1787-1802, 1917.

R. J. Martins, M. J. D. M. Cardoso, and O. E. Barcia. Excess Gibbs free energy model for calculating the viscosity of binary liquid mixtures. *Ind. Eng. Chem. Res,* 39: 849-854, 2000.

R. A. McAllister. The viscosity of liquid mixtures. *A.I.Ch.E. Journal,* 6: 427-431, 1960.

R. Meyer, M. Meyer, J. Metzger, and A. Peneloux. Thermodynamic and physicochemical properties of binary solvent. *Journal de Chimie Physique et de Physico-Chimie Biologique,* 68: 406-412, 1971.

B. Mukesh, M. G. Sankar, M. C. Shekar, and T. Srikanth. Effect of placement of hydroxyl groups in isomeric butanol on the behavior of thermophysical and spectroscopic properties of 2-Methoxyaniline. *Journal of Solution Chemistry,* 44(12): 2267-2296, 2015. doi:10.1007/s10953-015-0406-1.

R. K. Nigam and B. S. Mahl. Molecular interaction in binary liquid mixtures of dimethylsulfoxide with chlroethanes & chlroethenes. *Indian Journal of Chemistry,* 9:1255-1258, 1971.

O. Redlich and A. T. Kister. Algebraic representation of thermodynamic properties and the classification of solutions. *Industrial and engineering chemistry,* 40(2): 345-348, 1948.

G. T. Rochelle. Amine Scrubbing for CO_2 Capture. *Science,* 325(5948): 1652-1654, 2009.

Applicability of NRTL Model for Prediction of the Viscosity of Alkanolamine + Water Mixtures

Sumudu S. Karunarathne Lars E. Øi

Faculty of Technology, Natural Sciences and Maritime Sciences, University of South-Eastern Norway, Norway,
{Sumudu.karunarathne,lars.oi}@usn.no

Abstract

This study discusses the applicability of the non-random two-liquid (NRTL) model to represent viscosity for MEA (monoethanol amine) + H_2O and AMP (2-amino-2-methyl-1-propanol) + MEA (monoethanol amine) + H_2O mixtures under different amine concentrations at temperature ranges of 293.15 K– 363.15 K and 293.15 K – 343.15 K respectively. The NRTL model is adopted to determine excess Gibbs free energy of mixing ΔG^{E*} and the Eyring's viscosity model based on absolute rate theory is used to obtain excess free energy of activation for viscous flow ΔF^{E*}. The correlations are proposed for ΔF^{E*} as a function of concentration of the components, temperature and ΔG^{E*}. Correlations are capable of representing measured viscosities at 1.3 % and 0.3 % of absolute average relative deviation (AARD %) for MEA + H_2O and AMP + MEA + H_2O mixtures respectively. These deviations are acceptable for engineering calculations and correlations can be used in process design and simulations like Aspen HYSYS and ASPEN Plus.

Keywords: NRTL model, Eyring's viscosity model, MEA, AMP

1 Introduction

In the design of units involving liquid flow like gas/liquid separators and heat exchangers, it is important to predict reasonably accurate physical properties like viscosity. Correlations depending on parameters from experiments are available for some systems. Estimation methods without the need for fitted parameters is a possibility. A possibility to use parameters from e.g. vapor/liquid equilibrium models to predict viscosity.

In post combustion CO_2 capture, the physical properties of aqueous alkanolamine solutions is a key factor in various aspects such as equipment design, modeling and simulations of absorber and desorber columns. Physical properties are present in various mass and heat transfer correlations and interfacial area correlations that are necessary to evaluate in engineering applications. Accordingly, the viscosity data of aqueous alkanolamine mixtures are highly relevant to build correlations to predict viscosities for unmeasured conditions. Further correlations developed for the viscosity of aqueous alkanolamines can be used to develop correlations for the viscosity of CO_2 loaded alkanolamine mixtures.

Correlations based on statistical regression for the viscosity data have high uncertainties beyond the experimental range. The approach of Redlich-Kister (Redlich and Kister, 1948) type polynomial to fit physical properties is widely used and Islam *et al.*, (2004) and Hartono *et al.*, (2014) have taken this approach for viscosity data of aqueous MEA solutions. The Grunberg and Nissan model was used by Mandal *et al.*, (2003) to correlate different aqueous tertiary mixtures. The McAllister model (McAllister, 1960) based on Eyring's absolute rate theory for dynamic viscosity (Eyring, 1936) is used by Amundsen *et al.*, (2009) and Lee and Lin, (1995) for aqueous MEA solutions and found the parameters to fit measured viscosities. These models are capable of predicting viscosities at acceptable accuracies within the experimental range and can be used in engineering designs.

The thermodynamic information like vapor-liquid equilibrium (VLE) of liquid mixtures can be combined with a viscosity model and such models may be stated as thermodynamics-viscosity models (Cao *et al.*, 1993). The VLE data delivers information about molecular interaction, which can be used in local composition models like nonrandom two-liquid (NRTL) and UNIQUAC. This approach has been applied several times for various multicomponent liquid mixtures. Martins *et al.*, (2000) discussed the applicability of the UNIQUAC model for the viscosity predictions of binary and ternary systems. Novak *et al.*, (2004) discussed segment based Eyring-NRTL viscosity model, which was concerned about the similarities between intermolecular friction and viscosity with a local composition model like NRTL to model excess properties as both are affected by nearest neighbor molecules. The viscosity of electrolyte solutions using Eyrings's absolute rate theory has been discussed to replace excess free energy of activation for viscous flow with Gibbs free energy of mixing (Hu, 2004). For electrolyte solutions of MEA (monoethanol amine) + H_2O + CO_2, the excess free energy of activation for viscous flow was replaced by the Gibbs free energy of mixing that was calculated using the electrolyte-NRTL model (Matin *et al.*, 2013).

This study investigates the possibility to relate excess Gibbs free energy of mixing with the excess free energy of activation for viscous flow from Eyring's absolute rate theory to predict viscosities at different compositions and temperatures of MEA + H_2O and AMP (2-amino-2-methyl-1-propanol) + MEA + H_2O mixtures. Measured density and viscosity data were used to calculate the excess free energy of activation for viscous flow. The NRTL model was adopted for calculating excess Gibbs free energy of mixing and compared with the excess free energy of activation for viscous flow for the considered mixtures. Finally, viscosity predictions were compared with measured data and the accuracy was determined by calculating average absolute relative deviation (AARD %).

2 Methodology

2.1 Dynamic Viscosity Based on Eyring's Absolute Rate Theory

A universal model to predict the viscosity of any solution is challenging as solutions exhibit different characteristics that are difficult to discuss in one model. Most of the amine solutions and their blends that are discussed in amine-based CO_2 capture shows Newtonian behavior as the molecular weights are less than 5000 g·mol^{-1} (Bird *et al.*, 2002). Introducing a qualitative picture of the mechanism of momentum transport of liquids, Eyring and coworkers developed a model to predict the viscosity of liquids from other physical properties (Eyring, 1936; Bird *et al.*, 2002). Eyring's viscosity model for Newtonian fluids is given in (1) and is valid for both pure liquids and liquid mixtures (Martins *et al.*, 2000).

$$\eta = \frac{hN}{V} exp\left(\frac{\Delta F^*}{RT}\right) \quad (1)$$

Where, $\eta, V, \Delta F^*, T, h, N$ and R are dynamic viscosity, molar volume, free energy of activation for viscous flow, temperature, Planck's constant, Avogadro's number and the gas constant respectively.

In order to compare with ideal solutions and to calculate the excess free energy of activation properties ΔF^{E*}, following (2) and (3) are obtained by using (1).

$$ln(\eta V) = ln(\eta V)_{ideal} + \frac{\Delta F^{E*}}{RT} \quad (2)$$

$$ln(\eta V) = \sum_i x_i ln(\eta_i V_i^o) + \frac{\Delta F^{E*}}{RT} \quad (3)$$

Where, x_i, η_i, V_i^o and ΔF^{E*} are mole fraction, viscosity of pure liquids, molar volume of pure liquids and excess free energy of activation for viscous flow respectively.

In this approach, the combination of terms of an ideal mixture and excess energy leads to an expression of viscosity in a real mixture. The ideal term of the (2) is calculated using the properties of pure liquids as given in the (3). The term $\Delta F^{E*}/RT$ describes the non-ideality of the solution viscosity (Matin *et al.*, 2013) and an appropriate model can enhance the prediction of the viscosity. Here, the possibility of using Gibbs free energy of mixing is discussed as it has been related in various ways to ΔF^{E*} in the literature. Generally, it is related as Gibbs free energy, excess Gibbs energy through proportionality factor, Gibbs free energy of mixing and Gibbs free energy of mixing multiplied by a general constant (Matin *et al.*, 2013). This study investigates the excess Gibbs free energy of mixing for MEA + H_2O and AMP + MEA + H_2O mixtures and compares it with ΔF^{E*} calculated from the measured density and viscosity data. The NRTL model was adopted to calculate Gibbs free energy of mixing for different compositions and temperatures of the mixtures.

2.2 NRTL Model

The local composition theory explains the deviation of local compositions from the bulk composition due to different strength of attractions among the molecules in the mixture. The non-random two liquid model (NRTL) is based on the local composition theory as Wilson's model (Wilson, 1964), which explains the composition variations. For a solution of m components, the excess Gibbs free energy of mixing is given as (Prausnitz *et al.*, 1999)

$$\frac{\Delta G^{E*}}{RT} = \sum_{l=1}^{m} x_l \frac{\sum_{j=1}^{m} \tau_{ji} G_{ji} x_j}{\sum_{l=1}^{m} G_{li} x_l} \quad (4)$$

$$\tau_{ji} = \frac{g_{ji} - g_{ii}}{RT} \quad (5)$$

$$G_{ji} = exp(-\alpha_{ji}\tau_{ji}) \quad (\alpha_{ji} = \alpha_{ij}) \quad (6)$$

Where, g_{ji} and g_{ii} are energy parameters to characterize i-j and i-i interactions respectively. α_{ji} is a non-randomness parameter.

Then the ΔG^*_{mix} is calculated as a sum of both ideal mixing and an excess term due to the non-ideal behavior of the solutions.

A study performed by Schmidt *et al.*, (2007) on VLE and NRTL model for various aqueous amine solutions provide binary interaction parameters for MEA + H_2O mixtures. A similar work done by Hartono *et al.*, (2013) found relevant parameters for AMP + H_2O mixtures. There is a lack of information about interaction parameters between AMP and MEA. Hence, for the tertiary AMP + MEA + H_2O system, parameters from two binary solutions were used for the calculations. It is also possible to use the commercial process simulation program Aspen Plus to perform all the

Table 1. Summary of the Compositions and Temperatures Considered for the Density and Viscosity Measurements of Aqueous Amine Mixtures.

Solution	*Composition / wt % (by weight)*		*Temperature / K*
MEA + H_2O	0 – 100 (MEA)		293.15 – 363.15
AMP + MEA + H_2O	21/9/70	(AMP/MEA/H_2O)	293.15 – 343.15
	24/6/70		
	27/3/70		

excess free energy of mixing calculations as it has binary interaction parameters for many components in the data banks. For the missing binary interactions parameters of NRTL model, the UNIFAC model can be used to make estimations.

The density and viscosity of mixtures were measured using a DMA 4500 vibrational density meter and Physica MCR 101 rheometer with a double-gap pressure cell XL from Anton Paar. The properties were measured at different compositions and temperatures as given in Table 1.

3 Results and Discussion

The spontaneous mixing of MEA and H_2O gives negative values for Gibbs free energy of mixing. The excess Gibbs free energy ΔG^{E*} of mixing was analyzed for the compositions of x_{MEA} from 0 to 1 of MEA + H_2O mixtures. Figure 1 illustrates the calculated ΔG^{E*} from the NRTL model under different MEA concentrations and temperatures. The calculated ΔF^{E*} from measured density and viscosity is positive while the excess viscosity η^E calculated from (7) gives negative values for the low MEA concentration region indicating weak intermolecular attractions and gives positive values for high MEA concentration region signifying strong interactions.

$$\eta^E = \eta - \sum_{i=1}^{n} x_i \eta_i \quad (7)$$

(n=2 for MEA + H_2O mixtures and n=3 for AMP + MEA + H_2O mixtures)

The ratio of $\Delta G^{E*}/\Delta F^{E*}$ was determined and following correlations is proposed with R^2= 0.99.

$$-\Delta G^{E*}/\Delta F^{E*} = f(x_{MEA}, T) \quad (8)$$

$$f(x_{MEA}, T) = a + b x_{MEA} T + c T^2 \quad (9)$$

The suggested correlation was used to replace ΔF^{E*} in (3) and the viscosities were obtained accordingly. Figure 2 illustrates the comparison between measured viscosity and the correlation fit for aqueous MEA. The fit was in good agreement with measured data with AARD of 1.3% and AMD (maximum deviation) of 1.0 mPa·s as given in Table 4. This deviation is acceptable for engineering calculations and can be used to develop correlations for the CO_2 loaded solutions. The estimated parameters for the correlation shown in (9) are given in Table 2.

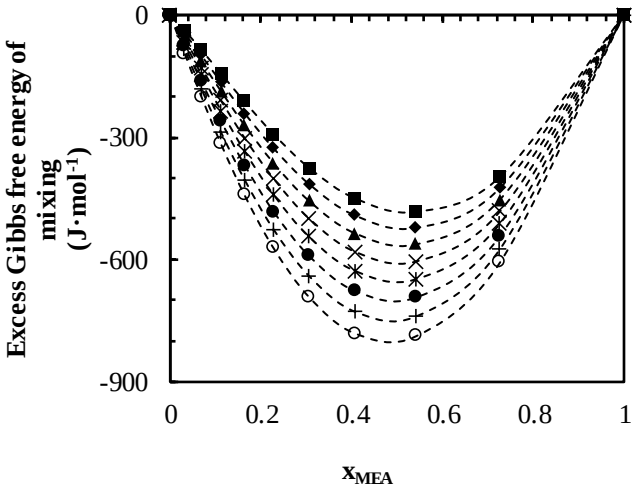

Figure 1. The variation of excess Gibbs free energy vs MEA mole fraction and temperatures: 293.15 K, '○'; 303.15 K, '+'; 313.15 K, '●'; 323.15 K, 'ж'; 333.15 K, 'x'; 343.15 K, '▲'; 353.15 K, '◆'; 363.15 K, '■'.

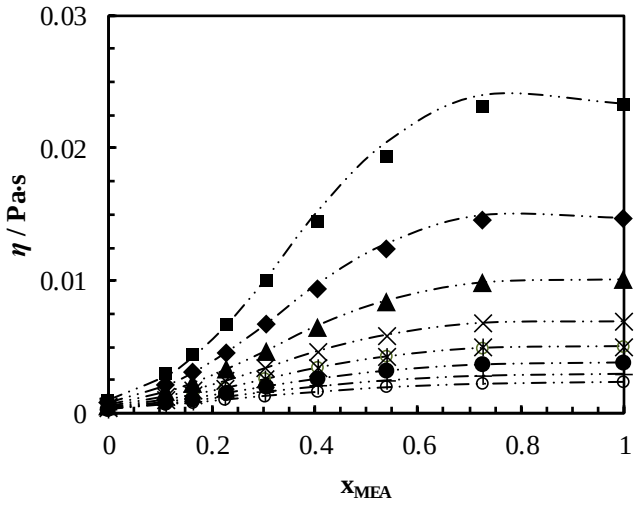

Figure 2. Comparison of measured viscosity of MEA + H_2O mixtures with correlation at temperatures: 293.15 K, '■'; 303.15 K, '◆'; 313.15 K, '▲'; 323.15 K, 'x'; 333.15 K, 'ж'; 343.15 K, '●'; 353.15 K, '+'; 363.15 K, '○'. The dash ─ dotted lines represent the correlation.

Table 2. Estimated Parameters for Correlation of Viscosity of Aqueous MEA.

MEA (wt%)	*Temperature (K)*	*No. points*	*Parameters*
0 – 100	293.15 – 363.15	72	a = 0.2801 ± 0.008 b = (5.557±0.0.164) x10^{-04} c= (-1.623 ± 0.0735) x10^{-06}

Table 3. The Estimated Binary Parameters for the Correlation Shown in (10-13).

Parameter		*AMP + MEA*	*MEA + H_2O*	*AMP + H_2O*
A_0	a_{00}	-1.724 x10^4	141.854	-117.059
	a_{01}	-9.370	0.562	0.296
	a_{02}	-2.516	0.598	0.623
A_1	a_{10}	-1.870 x10^5	-143.070	141.824
	a_{11}	-97.727	-0.992	-0.040
	a_{12}	101.381	0.540	0.609
A_2	a_{20}	5.812 x10^6	111.435	-119.768
	a_{21}	5.348 x10^3	0.473	0.558
	a_{22}	-2.233 x10^3	-0.168	-0.067

The ΔG^{E*} for AMP + MEA + H_2O mixtures were examined using the NRTL model. Figure 3 shows the calculated ΔG^{E*} for the mixtures considered in this work. The ΔG^{E*} is negative for the considered AMP concentrations and temperatures. Further, negative η^E implies weak intermolecular interactions for the range of AMP concentrations and temperatures. As discussed in the MEA + H_2O mixtures, the ratio (r) of $-\Delta G^{E*}/\Delta F^{E*}$ was determined and a correlation was proposed as given in (10-13) to find the best fit for AMP + MEA + H_2O mixtures.

$$-\Delta G^{E*}/\Delta F^{E*} = f\left(x_{AMP}, x_{MEA}, x_{H_2O}, T\right) \quad (10)$$

$$\text{The ratio } -\Delta G^{E*}/\Delta F^{E*} = r_{12} + r_{23} + r_{13} \quad (11)$$

$$r_{jk} = x_j x_k \sum_{i=0}^{n} A_i \left(x_j - x_k\right)^i \quad (12)$$

$$A_i = a_{io} + a_{i1}(T) + a_{i2}(T)^2 \quad (13)$$

The proposed correlation was able to represent measured viscosities with acceptable accuracy as illustrated by AARD and AMD in Table 4. Figure 4 shows the comparison of the correlation with measured data in which maximum deviations were observed at low temperatures. These deviations are smaller compared to the MEA + H_2O mixtures since only three different compositions were considered for the study.

Table 4. Calculated AARD% and AMD (mPa·s) for Comparison of Correlation with Measured Data.

Mixture	*AARD (%)*	*AMD (mPa·s)*
MEA + H_2O	1.3	1.0
AMP + MEA + H_2O	0.3	0.02

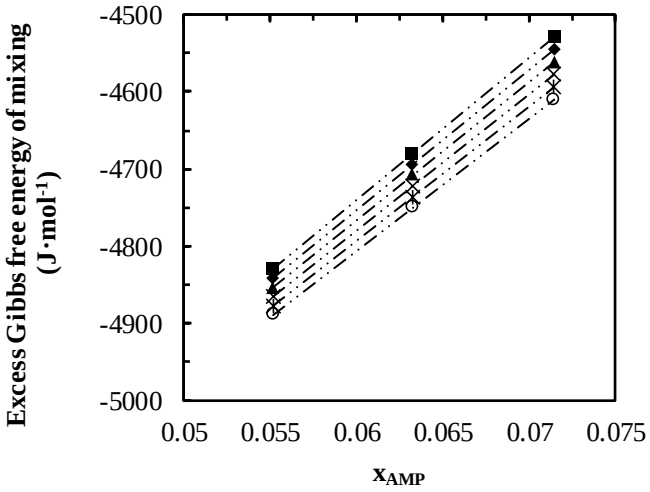

Figure 3. The variation of excess Gibbs free energy vs AMP mole fractions and temperatures: 293.15 K, '○'; 303.15 K, 'ж'; 313.15 K, 'x'; 323.15 K, '▲'; 333.15 K, '◆'; 343.15 K, '■'.

The viscosity of CO_2 loaded AMP + MEA + H_2O mixtures are highly important in the design and mathematical modelling and simulations of CO_2 capture process based on absorption. The correlation discussed in this study for AMP + MEA + H_2O mixtures can be adopted to developed viscosity correlations for CO_2 loaded solutions using measured data. For use in e.g. a process simulation program like Aspen HYSYS or Aspen Plus, It is shown that the viscosities can be estimated by Hartono's correlation (Hartono *et al.*, 2014) with fitted parameters for MEA + H_2O mixtures with AARD 4.2 % and the semiempirical model discussed in this work can estimate viscosity with 1.3% AARD. Mandal *et al.*, (2003) used the Grunberg and

Nissan correlation (Li and Lie, 1994) to fit the viscosity data with 3.08% AARD and it is higher than that from this study for AMP + MEA + H_2O mixtures.

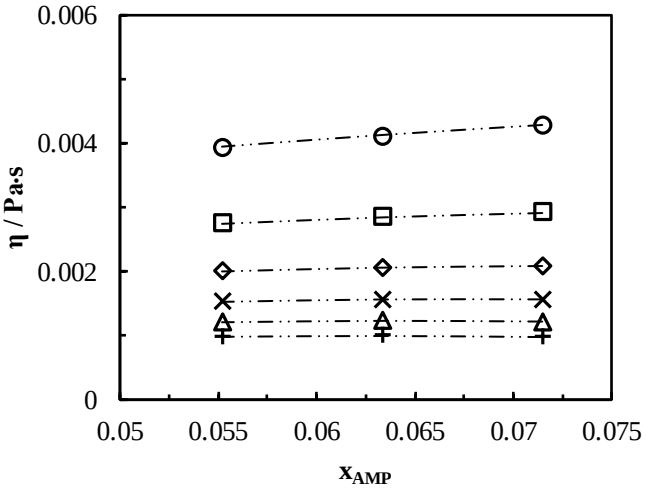

Figure 4. Comparison of measured viscosity of AMP + MEA + H_2O mixtures with correlation at temperatures: 293.15 K, '○'; 303.15 K, '□'; 313.15 K, '◇'; 323.15 K, 'x'; 333.15 K, '△'; 343.15 K, '+'. The dash ─ dotted lines represent the correlation.

4 Conclusion

This work presents the applicability of the NRTL model to represent viscosities of MEA + H_2O and AMP + MEA + H_2O mixtures. The Eyring's viscosity model was adopted to determine excess free energy of activation for viscous flow. Correlations based on the regression for the ratio between excess Gibbs free energy of mixing from NRTL model and excess free energy of activation for viscous flow was proposed to represent measured viscosities. The accuracy of the correlation predictions are acceptable as the AARD (%) is 1.3 and 0.3 for MEA + H_2O and AMP + MEA + H_2O mixtures respectively. The NRTL model is available in the Aspen Plus commercial software to determine vapor – liquid equilibrium. In this paper, it is shown that these types of correlations can be integrated to determine viscosity in aqueous alkanolamines.

References

T. G. Amundsen, L. E. Øi, and D. A. Eimer. Density and viscosity of monoethanolamine+water+carbon dioxide from (25 to 80) ºC. *J. Chem. Eng. Data*, 54: 3096-3100, 2009.

R. B. Bird, W. E. Stewart, and E. N. Lightfoot. *Transport Phenomena (second edition).* USA: John Wiley & Sons Inc., 2002.

W. Cao, K. Knudsen, A. Fredenslund, and P. Rasmussen. Group-contribution viscosity predictions of liquid mixtures using UNIFAC-VLE parameters. *Ind. Eng. Chem. Res*, 32: 2088-2092, 1993.

H. Eyring. Viscosity, Plasticity, and Diffusion as example of absolute reaction rates. *Journal of chemical physics*, 4: 283-291, 1936.

A. Hartono, M. O. Mba, and H. F. Svendsen. Physical properties of partially CO_2 loaded aqueous monoethanolamine (MEA). *J. Chem. Eng. Data*, 59: 1808-1816, 2014.

A. Hartono, M. Saeed, A. F. Ciftja, and H. F. Svendsen. Modeling of binary and ternary VLE of the AMP/Pz/H_2O system. *Energy Procedia*, 37: 1736-1743, 2013.

Y.-F. Hu. Prediction of viscosity of mixing electrolyte solutions based on the Eyring's absolute rate theory and the equations of Patwardhan and Kumar. *Chemical Engineering Science*, 59: 2457-2464, 2004.

M. N. Islam, M. M. Islam, and M. N. Yeasmin. Viscosity of aqueous solution of 2-methoxyethanol, 2-ethoxyethanol, and ethanolamine. *J. Chem. Thermodynamics*, 36: 889-893, 2004.

M. J. Lee and T. K. Lin. Density and viscosity for Monoethanolamine+Water,+Ethanol, and + 2-Propanol. *J. Chem. Eng. Data*, 40: 336-339, 1995.

M.-H. Li and Y.-C. Lie. Densities and viscosities of solutions of Monoethanolamine + N-Methyldiethanolamine + water and Monoethanolamine + 2-Amino-2-methyl-1-propanol + water. *J. Chem. Eng. Data*, 39: 444-447, 1994.

B. P. Mandal, M. Kundu, and S. S. Bandyopadhyay. Density and viscosity of aqueous solution of (N-Methyldiethanolamine + Monoethanolamine), (N-Methyldiethanolamine + Diethanolamine), (2-Amino-2-methyl-1-propanol + Monoethanolamine), and (2-Amino-2-methyl-1-propanol + Diethanolamine). *J. Chem. Eng. Data*, 48: 703-707, 2003.

R. J. Martins, M. J. D. M. Cardoso, and O. E. Barcia. Excess Gibbs free energy model for calculating the viscosity of binary liquid mixtures. *Ind. Eng. Chem. Res*, 39: 849-854, 2000.

N. S. Matin, J. E. Remias, and K. Liu. Application of electrolyte-NRTL model for prediction of the viscosity of carbon dioxide loaded aqueous amine solutions. *Ind. Eng. Chem. Res*, 52: 16979-16984, 2013.

R. A. McAllister. The viscosity of liquid mixtures. *A.I.Ch.E. Journal*, 6: 427-431, 1960.

L. T. Novak, C.-C. Chen, and Y. Song. Segment-Based Eyring-NRTL viscosity model for mixtures containing polymers. *Ind. Eng. Chem. Res*, 43: 6231-6237, 2004.

J. M. Prausnitz, R. N. Lichtenthaler, and E. G. d. Azevedo. *Molecular thermodynamics of fluid-phase equilibria (Third Edition).* Prentice Hall PTR, 1999.

O. Redlich and A. T. Kister. Algebraic representation of thermodynamic properties and the classification of solutions. *Ind. Eng. Chem.*, 40(2): 345-348, 1948.

K. A. G. Schmidt, Y. Maham, and A. E. Mather. Use of the NRTL equation for simultaneous correlation of vapour-liquid equilibria and excess enthalpy. *Journal of Thermal Analysis and Calorimetry*, 89: 61-72, 2007.

G. M. Wilson. Vapor–Liquid Equilibrium. XI. A New Expression for the Excess Free Energy of Mixing. *J. Am. Chem. Soc*, 86: 127-130, 1964.

Monitoring of Erosion in a Pneumatic Conveying System by Non-intrusive Acoustic Sensors – A Feasibility Study

Ingrid Bokn Haugland[1] Jana Chladek[1] Maths Halstensen[2]

[1]SINTEF Industry, Norway, {ingrid.haugland,jana.chladek}@sintef.no

[2]Faculty of Technology, Natural Sciences and Maritime Sciences, University of South-Eastern Norway, Norway, Maths.Halstensen@usn.no

Abstract

This paper presents the results of a study where the feasibility of a non-invasive acoustic measurement method was tested for monitoring of erosion in a pneumatic conveying system during the dilute-phase conveying of sand. Measurements were collected by the acoustic method from a pipe bend in a test area of a pneumatic conveying system which were found in previous studies to be especially afflicted with erosion. Reference measurements of the loss of mass caused by erosion were obtained by removing a detachable piece from the test area and weighing it before reattaching it to the pipeline. Partial least squares regression was used to calibrate models relating the acoustic measurements to the response variable. Cross-validation techniques were used to evaluate the feasibility of the method for monitoring of erosion in the pipe bend and to investigate whether the method would be affected by noise and vibrations generated by the pneumatic conveying system.

Keywords: erosion, pneumatic conveying, monitoring, acoustic sensors

1 Introduction

Pneumatic conveying, the transportation of dry material through a pipeline in a gas stream, is a common method of transportation of particulate and granulate material in many industries. Advantages of the technology include flexibility in the conveying system with multiple pick-up and discharge points, clean and dust-free transportation of solids and easy automation of the conveying systems. Pipe erosion has been identified as one of the main challenges of the pneumatic conveying technology. Erosive wear is particularly significant in dilute phase pneumatic conveying due to the higher velocities used in such systems. Pipe bends are often exposed to severe erosion.

Erosion is defined as the removal of material from a surface due to impinging particles. Erosive wear can be influenced by multiple factors, including properties of the conveyed material such as particle size and hardness as well as flow properties like particle velocity and impact angle. The characteristics of the surface material can also have an effect on erosive wear (G. E. Klinzing et al. 1997). Material which is removed from the pipe walls can mix with the conveyed material and cause quality and safety issues. Contamination of the conveyed material can be highly problematic for example in food and feed production. In some processes, mixing metal particles with the transported powder materials can cause dust explosions. Also, equipment failure due to erosion can lead to system downtime and higher maintenance costs (Ratnayake et al. 2007).

In a study by (Vieira et al. 2017), a system of 16 non-intrusive ultrasonic devices attached to the outer wall of a pipe bend was used to measure erosion in a test rig during multiphase flow. The pipe wall thickness was monitored in 16 points under various conditions, and the measurements were used to investigate the resulting erosion rates and patterns. The ultrasonic method was found to be a useful tool for investigating erosion mechanisms and getting a better understanding of the erosive wear phenomenon. However, for monitoring of erosion in an industrial setting, a simpler and more practical monitoring system which require less equipment to be installed in the test area would be preferable.

Developed at the University College of South-Eastern Norway, acoustic chemometrics is an indirect monitoring method in which chemometric techniques are applied to relate acoustic measurements to a response variable. A recent, active version of the acoustic method was presented in (Haugland et al. 2019), where the method was used to monitor scaling in a pneumatic conveying system. Acoustic chemometrics is a non-intrusive technique utilizing easy to install "clamp-on" sensors.

This paper presents the results of a study conducted to test the feasibility of the active acoustic method to monitor erosion in a pneumatic conveying system transporting material in dilute phase. Measurements were obtained during powder transportation as well as during system shutdown periods to evaluate whether the performance of the method would be disturbed by noise and vibrations from the conveying system during powder transportation.

2 Materials and Methods

2.1 Pneumatic conveying test rig

Tests were conducted in a pilot-scale pneumatic conveying rig located in the powder research hall of SINTEF Tel-Tek (Porsgrunn, Norway). A schematic sketch of the rig, which makes up a closed system, can be seen in Figure 1. When the pneumatic conveying rig is operated, bulk material is dispatched from the storage tank and fed into the pipeline by a rotary feeder at a pre-set feeding rate. The pipeline (3.5-inch) consist of both horizontal and vertical sections as well as several bends. At the end of the line, the material is collected in the receiving tank, from which it can be transported back into the storage silo. The receiving tank is installed on top of three load cells. Readings from the load cells can be used to estimate the material flow of the conveying system. Transportation air is supplied by a screw-type air compressor (Ingersoll Rand R110i) combined with an air dryer (Ingersoll Rand D1300IN-A). The air flow rate is controlled manually by a ball valve and monitored by two air flow meters (Yokogawa, YF 108) situated at the start and end of the conveying pipeline, respectively. The pressure drops are monitored by nine pressure transducers (General Electric, UNIK 500 series) distributed along the pipeline.

In previous tests conducted in the pneumatic conveying rig, several areas where severe erosion occur were identified. One of these areas, the exit of a 90° bend, was selected as the test area for this study. The position of the test area is marked in Figure 1. In the test area, the pipe was fitted with a customized flange such that the outer wall of the pipe bend could be detached from the pipeline. The detachable part of the pipe bend will hereafter be referred to as the test piece. By removing and weighing the test piece, reference measurements of the erosion of this part of the pipe could be obtained. An image of the test piece can be seen in Figure 2.

2.2 Active acoustic monitoring method

A newly developed version of acoustic chemometrics, the active method involves exciting a system by an acoustic input signal. The acoustic signal will be changed by the system in a way that is affected by some of the systems physical properties. Thus, such altered acoustic signals contain latent information about system characteristics. Altered acoustic signals are measured as output signals from selected locations in the system. The measured and processed output signals are referred to as acoustic spectra. In order to extract information from the acoustic spectra, models which relates the measurements to the properties of interest must be calibrated.

Piezo elements (Murata, 7BB-20-6L0) were used both to send the input signal and to measure output signals in the study. The piezo elements (one transducer and two sensors) were attached to the test piece and their cables were taped to the same surface to avoid vibrations which could disturbe the measurements. The set-up of the transducer and sensors can be seen in Figure 2.

A function generator (Escort ECG-3230) was used to create the input signals, which consists of a square waveform sweep function of linearly increasing frequency (0-200 kHz) and constant amplitude. Simultaneously, the frequency response of the sweep function was monitored as output signals by the two sensors. The output signals were amplified by a signal adapter (SAM, Applied Chemometrics Research Group, University of South-Eastern Norway) and then sent through a bandpass filter to avoid aliasing. Subsequently, A/D conversion was conducted by a DAQ-unit (National Instruments). The signals were filtered by a Blackman-Harris window to avoid spectral leakage and transformed from the time domain to the frequency domain by a Fast Fourier Transformation (FFT). A PC with specialized LabVIEW software (National Instruments) was applied for the data acquisition.

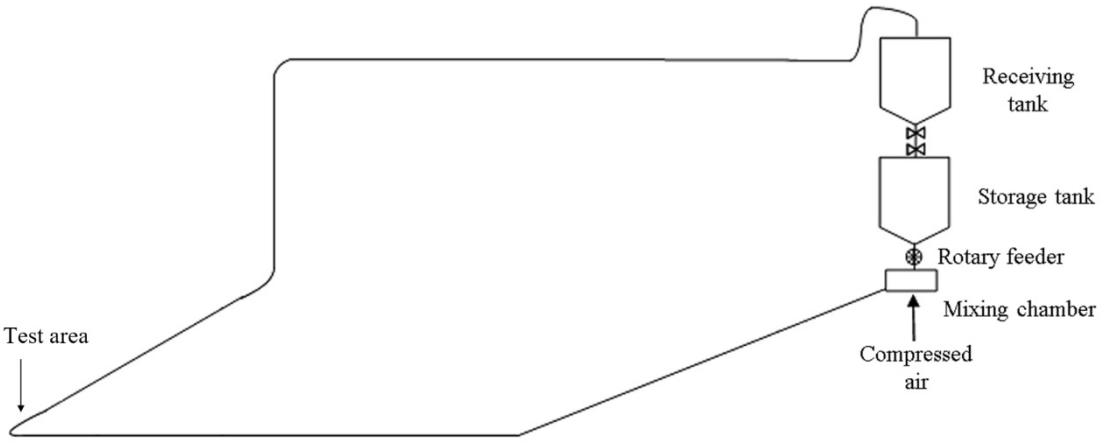

Figure 1. Schematic overview of the pneumatic conveying system.

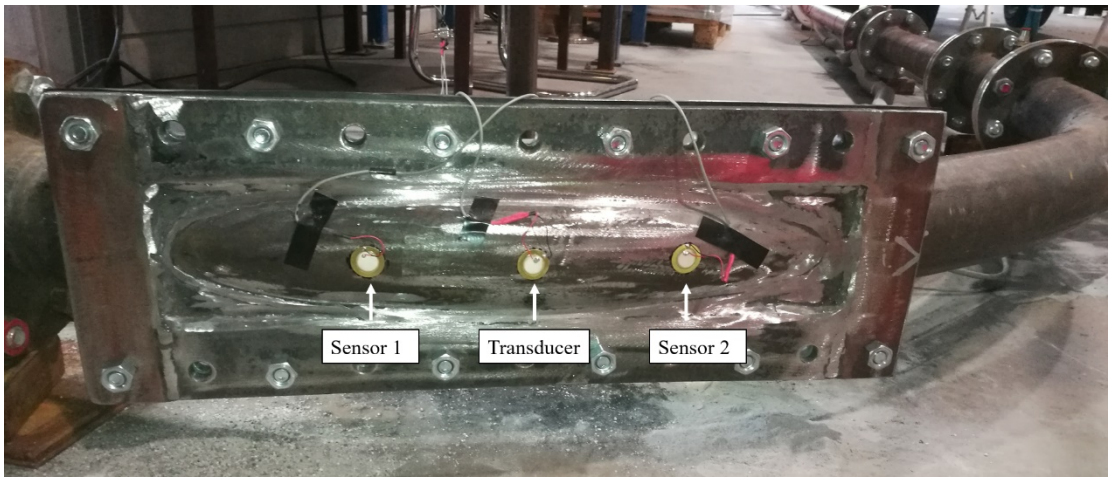

Figure 2. Photography of the test piece with transducer and acoustic sensors.

2.3 Test procedure

Due to its abrasive nature, sand was selected as the material to convey. A 50:50 mixture (approx. 550 kg) of two different sand qualities A and B (Sibelco Nordic AS) was added to the storage tank. The two qualities were mixed in order to get a steady flow through the pneumatic conveying system. The size ranges of the sand qualities are given in Table 1.

Table 1. Size ranges of sand qualities.

Sand quality	*Size range (mm)*
A	0.4-1.0
B	1.0-2.5

To operate the pneumatic conveying rig, the air inlet valve was opened to start air flow before sand was introduced from the storage tank to the pipeline through the rotary feeder. When the desired test conditions had been achieved and the dilute phase transportation of sand had reached steady state, three replicate measurements were obtained by the acoustic sensors. After all the sand had been conveyed from the storage tank to the receiving tank, the pipeline was flushed to remove any remaining material from the pipeline. Subsequently, the pneumatic conveying system was shut down and three additional replicate measurements were obtained by the acoustic method during the system downtime. Finally, the material was transferred back to the storage tank. The procedure was repeated multiple times. An overview of the test conditions is listed in Table 2.

Table 2. Overview of test conditions.

Inlet air flow rate [Nm^3/h]	300-320
Air temperature [°C]	15-20
Solid mass flow rate [kg/s]	0.2-0.3
Solid loading ratio	0.9-1.5
Reynolds number	$1.1*10^4$-$1.2*10^4$

Reference measurements of the erosion as the loss of mass from the test piece was obtained approx. for every 2 tons of sand transported past the test area. To get a reference measurement, the test piece was detached from the pipe bend and weighed. Then the test piece was reattached to the pipeline and pneumatic conveying of sand was resumed.

2.4 Data analysis

Two datasets were prepared from the measurements, one containing the acoustic spectra obtained during operation of the pneumatic conveying system and the other consisting of the measurements collected during system downtime. In each of the datasets, the acoustic spectra were arranged in a matrix **X**. In **X**, every row contains a measurement and every column represents a frequency of the acoustic spectra. The reference values associated with each spectrum were placed in the corresponding rows of a response vector **y**. The variables in the datasets were mean centered and scaled to unit variance prior to the data analysis.

2.4.1 Latent variable matrix decomposition

In many cases, multivariate data is colinear. That is, many of the variables the matrix **X** are related to and influenced by some common factors. Thus, the data in **X** can be expressed by a smaller set of components, sometimes referred to as latent variables. Each latent variable is represented by a score vector **t** and a loading vector **p** and can be constructed by linear combinations

of the original variables in **X**. There are several different strategies which can be applied to decompose a matrix into latent variables, of which the NIPALS algorithm is the standard choice. This approach is based on an iteration process of successive orthogonal projections as described in Equations 1-3 (Kvalheim 1987).

First, a weight vector $\mathbf{w}_a$ is defined and a score vector $\mathbf{t}_a$ is calculated by projecting the rows of $\mathbf{X}_a$ onto the weight vector as described in Equation 1.

$$\boldsymbol{t}_a = \boldsymbol{X}_a \boldsymbol{w}_a \tag{1}$$

Next, the columns in $\mathbf{X}_a$ are projected onto the score vector to calculate the loading vector $\mathbf{p}_a$ as stated in Equation 2.

$$\boldsymbol{p}_a = \frac{\boldsymbol{t}_a^T \boldsymbol{X}_a}{\|\boldsymbol{t}_a^T \boldsymbol{X}_a\|} \tag{2}$$

Finally, the part of the $\mathbf{X}_a$ matrix which is described by the component represented by $\mathbf{t}_a$ and $\mathbf{p}_a$ is subtracted from $\mathbf{X}_a$ as described in Equation 3, for which $\mathbf{X}_1 = \mathbf{X}$.

$$\boldsymbol{X}_{a+1} = \boldsymbol{X}_a - \boldsymbol{t}_a \boldsymbol{p}_a^T \tag{3}$$

The steps expressed in Equation 1-3 are repeated for $a = 1,2, \ldots, A$, where $A \leq \text{rank}(\mathbf{X})$. Typically, **X** can be closely approximated by a model constructed from only a few components, that is $A << \text{rank}(\mathbf{X})$. Thus, the matrix decompositions can lead to a significant reduction of dimensionality and simplify interpretation of the data. Accordingly, the **X** matrix is decomposed into an information part (represented by the A components) and a noise part (the **E** matrix) as expressed in Equation 4.

$$\boldsymbol{X} = \boldsymbol{t}_1 \boldsymbol{p}_1^T + \boldsymbol{t}_2 \boldsymbol{p}_2^T + \cdots + \boldsymbol{t}_A \boldsymbol{p}_A^T + \boldsymbol{E} \tag{4}$$

2.4.2 Partial Least Squares Regression (PLS-R)

Partial Least Squares Regression (PLS-R) is a multivariate calibration method based on latent variable matrix decomposition. In PLS-R, the target is to find a matrix $\boldsymbol{\beta}$ which relates the predictor variables in **X** to the response variable **y** and minimizes the error $\boldsymbol{\epsilon}$ in Equation 4.

$$\boldsymbol{y} = \boldsymbol{X}\boldsymbol{\beta} + \boldsymbol{\epsilon} \tag{5}$$

In PLS-R, the weights **w** are defined as stated in Equation 6.

$$\boldsymbol{w}_a = \frac{\boldsymbol{y}_a^T \boldsymbol{X}_a}{\|\boldsymbol{y}_a^T \boldsymbol{X}_a\|} \tag{6}$$

As a consequence of the definition of the weights **w**, the matrix decomposition in PLS-R is guided by a criterion maximizing the covariance between the predictor variables in **X** and the response **y**. Thus, the PLS components will contain relevant information to describe the relationship between **X** and **y** (Martens and Næs 1989).

2.4.3 Cross-validation

In cross-validation, the n measurements in a calibration dataset is split into s segments of similar or equal size, where $s = 2, 3, \ldots, n$. The distribution of measurements into segments can be done randomly or by some dedicated method. One by one, each of the segments are held out while a sub-model is calibrated based on the remaining measurements. The measurements in every left-out segment are used to test the corresponding sub-model. For the left-out measurements, $\hat{\mathbf{y}}$-values are predicted by the calibrated sub-model (Filzmoser 2009). The root mean squared error of cross validation (RMSECV) is calculated by comparing every $\hat{\mathbf{y}}$-value to the corresponding reference **y**-value as stated in Equation 7.

$$RMSECV_a = \sqrt{\frac{\sum_{i=1}^{n} \left(\hat{\boldsymbol{y}}_{a,i} - \boldsymbol{y}_i\right)^2}{n}} \tag{7}$$

A RMSECV value is calculated for every component a and can be used to evaluate how many components should be included in a model. There are several versions of cross validation, differing by the selected number s of segments applied.

The case where $s = 2$ is considered to be the ideal version of cross-validation and should only be used when the calibration set contains a high quantity of measurements. This method is somewhat similar to test set validation, the latter a validation method where an independently collected test set is used to validate a model (Esbensen et al. 2001). There are multiple ways of combining the n measurements into two segments. Thus, the model statistics resulting from using the 2-segmented version of cross-validation will vary to some extent depending on how the measurements in the calibration set are distributed into the two sections.

Leave-one-out (LOO) is another version of cross validation, for which $s = n$, meaning that every measurement in the calibration set is left out once while a sub-model is calibrated based on all other measurements. Although much used in the literature, this method is considered the weakest form of cross validation (Esbensen et al. 2001). However, since there is only one possible way of distributing the n measurements into segments for LOO, the model statistics resulting from using LOO will not vary based on sample selection as was the case with the 2-segmented version of cross validation. Consequently, the LOO cross-validation method is well suited for conducting relative comparisons of the performance of

models calibrated from similar data obtained under different process conditions.

3 Results

In Figure 3, the measured values of loss of mass from the test piece are plotted against the mass of sand transported through the pneumatic conveying system.

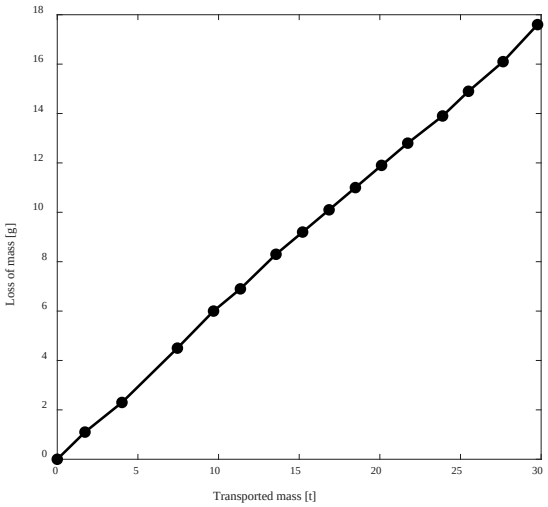

Figure 3. Erosion as loss of mass from test piece.

As can be seen from Figure 3, erosion of the test piece occurred by a steady rate throughout the study. Based on the data in Figure 3, reference values for every obtained acoustic measurement were calculated.

To evaluate the feasibility of the acoustic method for monitoring of erosion in a pipeline, the 2-segmented version of cross-validation was used when calibrating models from the measured data. Several plots describing one of these models, which was calibrated from the measurements obtained during powder transportation, are shown in Figure 4 to Figure 7.

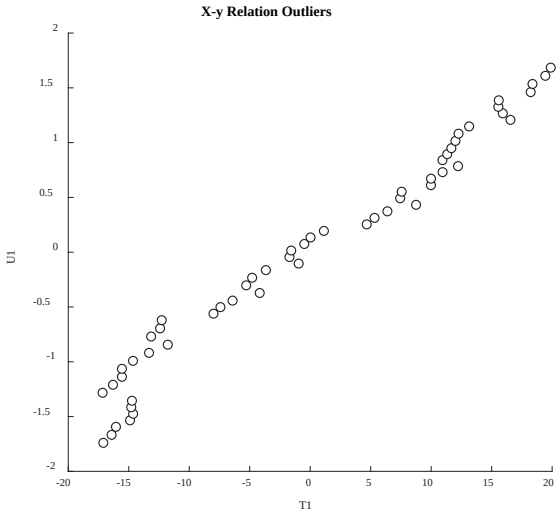

Figure 4. X-y Relation Outliers plot.

Figure 4 shows a X-y Relation Outliers plot which can be used for outlier detection. The measurement points should form a relatively straight line in a X-y Relation Outliers plot, and any points deviating significantly from the line can be considered as outlier candidates. In Figure 4, it can be seen that most of the points falls close to a straight line. A few points in the lower left corner of Figure 4 deviates from the rest to some extent. The deviating points correspond to some of the first measurements obtained in the study, when very little erosion had occurred. Thus, it is not so surprising that the points are somewhat different from the rest. Since it was assumed that the outlier candidates were correctly obtained measurements representing special conditions in the test area, they were not removed from the dataset.

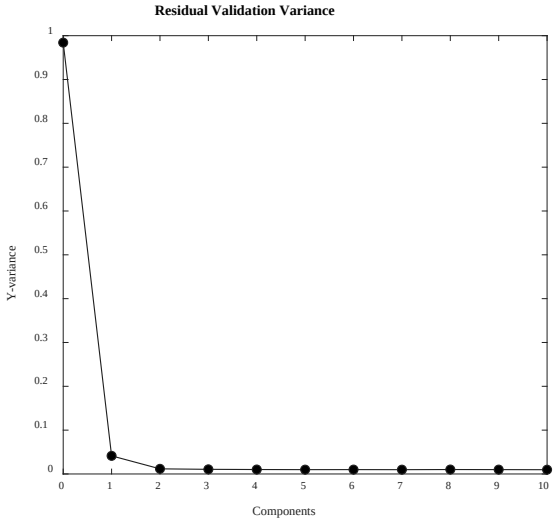

Figure 5. Residual Validation Variance plot.

In Figure 5, a Residual Validation Variance plot showing the variance in the response vector **y** which is explained by adding components to the model is shown. Such plots can be used to decide the number of components which should be included in a model to be able to describe the relevant variations in a dataset without overfitting the model. Based on the plot in Figure 5, it was decided to include two components in the model.

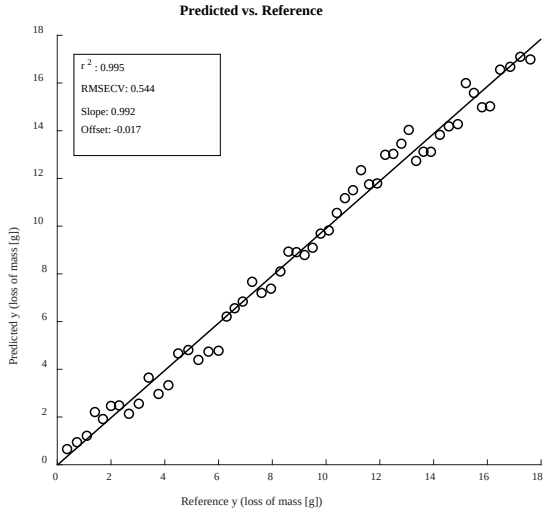

Figure 6. Predicted vs. Reference plot.

The measured reference values are compared with the corresponding values predicted by the calibrated model in Figure 6, which also include some model statistics describing the model. The RMSECV error has the same unit as the **y**-values. The relatively low RMSECV-value together with the r^2-value, slope and offset of the line fitted to the points in Figure 6 shows that the two sub-models calibrated as part of the cross validation could predict the held-out values with good precision.

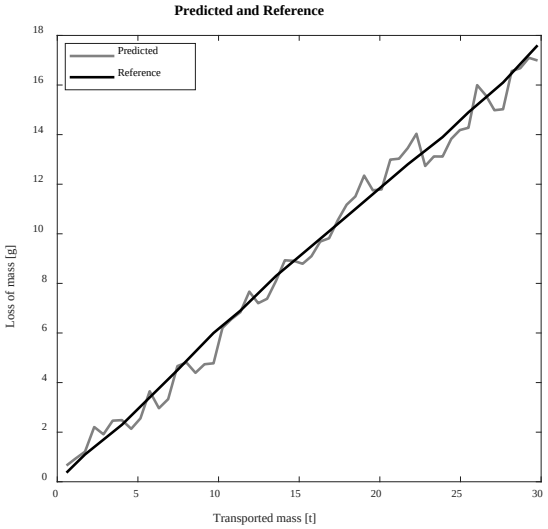

Figure 7. Predicted and Reference plot.

From Figure 7, in which the reference values are plotted together with the values predicted by the model, it can also be seen that there is generally a good correspondence between the predicted values and the reference values. After considering the plots in Figure 4 to Figure 7 together with the model statistics given in Figure 6, it can be concluded that the acoustic method holds good promise as a monitoring method for erosion in a pipeline. There is a clear structure in the measured acoustic data which can be related to erosion through calibrated PLS-R models. To estimate the magnitude of the prediction error which should be expected when the acoustic method is used to predict new values **y** based on new measurements **X**, test set validation against a new and independently measured dataset should be performed in future work.

In order to compare how well the acoustic method performed for monitoring of erosion while sand was transported through the pipeline with the case where the pneumatic conveying system was shut down, two additional models were calibrated. One model was based on data obtained during powder transportation and the other on measurements conducted during system shutdown. The leave-one-out version of cross validation was used in the model calibrations to facilitate objective comparison of the two situations. Model statistics describing the resulting models are listed in Table 3.

Table 3. Model statistics for LOO cross validated models.

Model	*Powder transport*	*System downtime*
r^2	0.991	0.996
RMSECV	0.485	0.439
Slope	0.979	0.981
Offset	0.180	0.162

From Table 3, it can be seen that the model based on the measurements which were obtained when the pneumatic conveying system was shut down gave slightly better model statistics and lower error than the model calibrated from data measured during powder transportation. However, the differences are minimal, showing that the acoustic method is not significantly affected by noise from the system during powder transportation.

Further work is needed to test the effect of factors like temperature changes, variating flow conditions, on the performance of the method. Model should be made from measurements obtained for conditions spanning/representing the range of conditions in a specific industrial site. Scaling, heat expansion

4 Conclusions

In this study, the feasibility of an acoustic measurement technique for monitoring of erosion in dilute phase pneumatic conveying was evaluated. Results indicated that the method holds good promise for monitoring of erosion in pneumatic conveying pipelines. A clear structure in the data which could be related to erosion through PLS-R models was found. Also, it was found that the acoustic method was not significantly affected by noise and vibration generated by the pneumatic

conveying system during transportation of material through the pipeline.

Acknowledgements

Hydro Aluminium AS, GE Power Norway AS and Omya Hustadmarmor AS are thankfully acknowledged for financial support of the research project together with the Research Council of Norway (Project no. 247789).

References

Kim. H. Esbensen, Dominique Guyot, Frank Westad and Lars P. Houmøller. *Multivariate data analysis - in practice: an introduction to multivariate data analysis and experimental design*. Camo, 2001.

G. E. Klinzing, R. D. Marcus, F. Rizk and L. S. Leung. *Pneumatic Conveying of Solids.* Springer, 1997

Olav M. Kvalheim. Latent-structure decompositions (projections) of multivariate data. *Chemometrics and Intelligent Laboratory Systems*, 2(4): 283-290, 1987.

Ingrid B. Haugland, Jana Chladek and Maths Halstensen, Maths. Monitoring of scaling in dilute phase pneumatic conveying systems using non-intrusive acoustic sensors – A feasibility study. *Advanced Powder Technology*, 2019. doi: 10.1016/j.apt.2019.05.012

Harald Martens and Tormod Næs. *Multivariate calibration.* Wiley, 1989.

C. Ratnayake, B. K. Datta, P. A. Amundsen, A. Saasen, and T. I. Waag. *Control and Prediction of Pipeline Erosion of Pneumatic Conveying Plants*. ICBMH 2007: 9th International Conference on Bulk Materials Storage, Handling and Transportation, Newcastle, Australia.

Kurt Varmuza and Peter Filzmoser. *Introduction to Multivariate Statistical Analysis in Chemometrics.* CRC Press, 2009.

Ronald E. Vieira, Mazdak Parsi, Peyman Zahedi, Brenton S. McLaury, and Siamack A. Shirazi. Ultrasonic measurements of sand particle erosion under upward multiphase annular flow conditions in a vertical-horizontal bend. *International Journal of Multiphase Flow*, 93: 48-62, 2017. doi: 10.1016/j.ijmultiphaseflow.2017.02.010

Gas Sensors for Early Detection of Fire Hazards caused by Vehicles in Underground Mines

Madeleine Martinsen[1], Erik Dahlquist[2*], Anders Lönnermark[3*], Örjan Säker[4*]

[1]ABB Industrial Automation, Industrial PhD student at MDH, Västerås Sweden

[2]MDH, Mälardalens University MDH, Västerås Sweden

[3]RISE, Swedish Research Institute, Borås Sweden

[4]Epiroc, Rocktec Automation Epiroc Rock Drills AB, Örebro Sweden

Abstract

Sensors play a key role today and have been developed to be used in many applications that can be life critical as with e.g. fire alarms. When mines now start investing in information systems and information technology infrastructure, they have taken one step closer to digitization. This in turn creates opportunities for the mines to become completely autonomous in the future. Controlling, monitoring and planning such production requires new digitized solutions. Part of such a solution could for example be to mount different types of sensors in the mining process. Data gathering from sensors with diagnostics supported by predefined set-points enables early alarms allowing production personnel to react before a fire is a fact. This paper describes the conducted experimental study aiming at identifying risk for fire caused by mining vehicles in underground mines. The test result shows that some types of sensors have potential to early detect fire hazards.

Keywords: fire, underground mines, early diagnose, gas sensors, overheating, ventilation

Introduction

The Energy Revolution, Industry 4.0 and Electricity Mobility are focus areas that will affect the mining industry and how they will operate it in the future. Furthermore, it will transform and replace today's dirty and dangerous work-activities when for example. mining trucks is being powered by batteries.

In addition, it will support the development towards a fully autonomous mining solution. Such operation will require faster approaches to be able to detect changes in production and prevent something serious from occurring.

A challenging goal which the Swedish government has decided, is to become a fossil-free country in year 2045. The energy used for only ventilation in some mines represent 49% of their total energy consumption (Natural Resources, 2005). One percent of the total energy consumption in Sweden relates to ventilating the Swedish mines. This has led to that the mining industry now starts to explore how they can contribute to this goal.

One part of the solution that can support this goal is the replacement of the mining truck fleet from being diesel-powered to be powered by batteries. An example is the project that took place September 18th, 2018 in the world's most effective open-pit mine Aitik (Boliden) in Sweden. The goal of the project is to investigate whether it is possible to replace parts of Aitik's transport system with electrified trucks. Aiming at that the majority tons of rock that are being transported annually in the open-pit can be moved completely without fossil fuels.

The tested traveling distance (Figure 1) is approximately 700 m and is expected to save around 830 m³ of diesel per year. This gives Boliden the possibility to reduce greenhouse gas emissions by up to 80% on the routes where the technology can be implemented. Other positive results from the test in proved that the electrified truck was

Figure 1. Boliden, Aitik electrified truck versus diesel truck race.

Many advantages can be observed with this transition from diesel to battery-powered trucks, related to cost as for carbon dioxide reduction, resulting in cleaner and healthier working environment. However, the mining industry faces also challenges to ensure that productivity is maintained or improved further while preventing it from compromising safety at the workplace when introducing new mining vehicle fleets. New risks, issues and challenges with batterypowered trucks are:

- Fire and smoke development (Bøe and Reitan, 2018)
- Mitigation and fire suppression (Bøe and Reitan, 2018)
- Ventilation and evacuation (Ingasson *et al.*, 2015)
- Released gases which are not only flammable but also toxic (Ingasson *et al.*, 2015)

Commercial Li-ion cells contain substances that can release toxic fluorine gases such as hydrogen fluoride (HF) and other harmful gases if undergoing failures (Ahlberg Tidblad, 2018; Larsson *et al.*, 2018). Additional challenges, firefighter´s have indicated that they lack to some extent knowledge, proper clothing, training and extinguishing technique to handle fires involving Li-ion cells.

Safety issues relating to fully autonomous mines are topics being discussed when the Global Mining Group, GMG, invites the mining industry to seminars and workshops around the world today. Taken all the above into account, it is understandable that there is a great interest to early diagnose as for detection of these problems that can occur in mines to minimize production stop.

1 Background

Common risks that may occur in both an open pit mine and an underground mine (Reddy *et al.*, 2016) are for example:

- Sink Holes
- Slope Failure
- Roof Collapses
- Floods
- Rock Bursts
- Fires
- Toxic Gases

For fully autonomous mining a robust early warning safety system ought to be able and monitor as for determine possible threats caused by the listed risks. In addition, the entities like personnel and assets (machinery & vehicle) need to be safe-guarded. Further key parameter to monitor is the mine area to provide insight on landscape changes and presence of danger zones that need to be demarcated. According to ((Reddy *et al.*, 2016), sensor network is

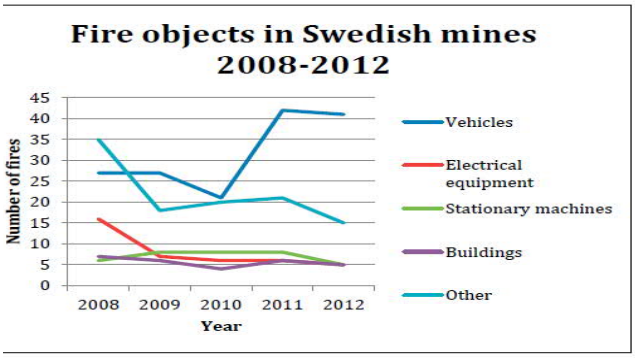

Figure 2. Fire objects in Swedish mines year 2008 – 2012.

recommended for early detection of hazards and their advantages have proven to be:

- Automated Measurement ability
- Ultra-low Power Consumption
- Versatility
- Cost-effectiveness
- Ease of manufacture
- Ease of deployment

Underground mining is hazardous and from a manufacturing system perspective challenging and unconventional. Developing an autonomous underground mining manufacturing system proves difficult due to inadequate connectivity and non-uniform manufacturing environment. Some mining businesses have or are investing in information systems (IS) and information technology (IT) to provide connectivity while others are somewhat reluctant and can be considered conservative when it comes to installing IS / IT solutions. Regarding the complexity of the manufacturing environment. It is a great challenge to automate the excavation using autonomous vehicles because the vehicles require many and advance sensors to discern the complex environment which further encumbers the network.

One of the most dangerous situations in an underground mining is fires. Especially those that are caused by mining vehicles. An overturned mining vehicle can produce a heat release rate (HRR) up to 200 MW and a temperature above 1000 degrees C (Ingasson *et al.*, 2015; Hansen, 2015). Such fires can cause rock movements so that part of the mine becomes unusable, and cause long production stops, until the rock wall has been secured again. Furthermore, it entails extensive remediation work and, in the worst case, fatal outcome.

Since year 2010 roughly one fire occurs per week in the Swedish mines. A great deal of the fires is caused by mining vehicles (GRAMKO annual report, 2013) (Figure 2). The number of reported fires due to mining vehicles per year has not changed significantly, since then. Just as many fires occur today as then and it is a topic being discussed at

DOI: 10.3384/ecp2017085

Swemin´s (the Swedish mining industry's industry organization) yearly meetings. A recurring comment from discussions with mine workers in Sweden, it´s not a question whether it will start to burn or not but more about when and where.

Sweden has about 20 active mines, ore and metal production such as e.g. iron ore, copper, gold and silver, though no coal mines. Fires seem to occur evenly distributed in all active mines in Sweden. Fires in mines around the world are also dominantly caused by vehicles and mobile equipment, resulting in dangerous situations (Hansen, 2011; Hansen, 2018; Willstrand. 2018). This allows a strain on mining production with increased costs as a result, but not least the risk which miners are exposed to.

Most vehicle related fires in mines are caused by:

- Cables and hydraulic hoses (Ingasson *et al.*, 2015)
- Fault and overheating of equipment, e.g. engines (Ingasson *et al.*, 2015)
- Worn tires (Ingasson *et al.*, 2015)
- Cable reel (Ingasson *et al.*, 2015)
- Leakage of flammable liquids, that are sprayed onto hot surfaces (Hansen, 2015)

Today miners are trained to act as firefighters and start the extinguishing activity until the fire department arrives at the site. A complete autonomous mine will have none or fewer miners underground that will be able to support this activity. This in turn requires solutions that support smart inspections that will detect early changes in production before the situation develops into a dangerous state.

2 Methodology

2.1 Introduction

The basis for the study presented in this paper is a series of sensor experiments. The purpose of these experiments has been to evaluate the range of sensors, existing on the market today. The purpose of mounting sensors on mining vehicles is to detect the gases that arise before a fire is a fact on a mining vehicle. Gases can arise for example, from, overheated equipment that lead to plastic materials beginning to emit thermal decomposition products.

From early mining days, canary birds have been known for their ability to early detect toxic air and the purpose of this study is to verify the possibility of replacing them with IoT and sensor solutions. The requirements of the sensors must correspond to the sensitivity of the ability of a canary. When toxic air was detected in a mine shaft, the canary-bird stopped twittering. Which was the sign for the miners to start evacuating. Even worse if they saw the bird lying dead on the bottom of the bird cage, they knew that very little time was left to save themselves from meeting the same fate.

This describes the requirements on the sensors' requirements to be able and detect changes on the vehicle objects in an early phase and communicate that to an overall operation system (Beard and Carvel, 2005; Hansen, 2013). However, detecting emitting gases that develops a temperature around 100 degrees C and barely noticeable HRR demands sensors to be highly sensitive.

2.2 Sensors

The sensors used in the different test series measured the following parameters:

- Temperature
- Hydro carbons
- Carbon monoxide (CO)
- Carbon dioxide (CO_2)
- Methane (CH4)
- Nitrogen dioxide (NO_2) concentrations
- and other NOx gases
- Relative humidity
- Air flow

The sensors were mounted on a frame construction (Figure 3 and 4) with wheels. In this way it was possible to change positions of the sensors relative to the emitting source (toxic gas). This allowed that it was possible to observe the distance when the sensors reacted as for the time it took for it to react. The setup of the lab equipment allowed the angle of the tested sensors to be varied and thereby it was possible to simulate inclines of e.g. a mine road. In addition, a fan was mounted to test how the sensors reacted to ventilation.

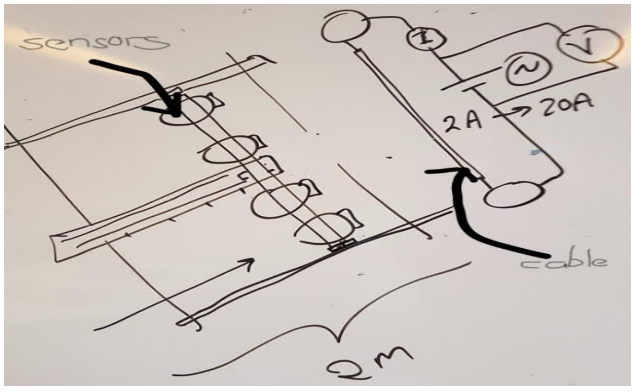

Figure 3. Test Equipment arrangement

Figure 4. The test equipment at RISE Fire lab facility.

2.3 Test sites

Some tests were conducted at RISE Fire lab facilities (SP Brandteknik) in Borås, Sweden. The first tests were to verify if any sensors were able to detect the gases emitting from the cables and to observe at what distance. While second test, ventilation from the fan was included to disturb the sensors in the test cases. In addition, the fan was also used for sucking the gases to the sensors. Finally, disturbance from humidity was simulated with water boilers. Concluding test was conducted at Epiroc in Örebro, Sweden, in their machine hall.

In addition to those tests follow up tests were performed at Mälardalens University, Västerås in Sweden, chemistry lab. A couple of follow up tests were performed to verify the tests results as for further analyses.

The tests were divided into the following categories:

- Stress tests, detection capability. The initial test was to observe the sensors' capability reacting on the emitting gases.
- Sensitivity, distance to emitting source. Sensitivity test was to determine on what distances the sensors reacted on the emissions from the heated cables and the oil mist, respectively.
- Disturbance influenced by other sources. The sensors in mining environment need to be able to distinguish between normal mining air or if fire is about to evolve due to e.g. soot, oil mist (hole in hoses).
- Logging capability of the sensors, as in communication protocols. Logging of data from sensors will be essential as for communicating it to an on-line control system.
- Gas concentration, balloon tests. To determine and understand the amount of gases needed for the sensors to react.

2.4 Test objects - Cables

Emitting sources, more than ten different cable types, normally used on Epiroc mining vehicles were tested. The cables on a mining vehicle can be everything from 0.5 m up to 15 m long. The material of the cables varies and in the tests the following could be observed:

- Polyvinyl chloride (PVC)
- Polyethylene (PE)
- Polyurethane (PUR)
- Halogen free

These can emit e.g. hydrocarbons, cyanides, hydrochloric acid, etc., which have effects of quite different kinds. PVC provides hydrochloric acid, which can be harmful mainly for equipment. Cyanides are acute toxic to humans. Hydrocarbons can cause long-term injuries, type of respiratory problems and, in the worst case, cancer.

3 Results from the experiments

From the tests it can be determined that it is possible to detect the risk of emerging fire at an early stage with some of the sensors. However, it was observed that the sensors need to be close to the flue gas evolution between 0,5m or less. Some sensors proved to be too insensitive to use directly, however some sensors could be used if gas could in some way could be sucked in to the detector. The conducted tests showed that a combination of sensors will be required to be able and detect the different gases, sources or heat development on mine vehicles in an early and efficient way.

The experiments were made by heating different cables by imposing a voltage and current to the cables (shown in Figure 3 and 4). The temperature of the actual cables was measured, the temperature from remote using Flir-camera and with two Photo ionization (PID)- instruments measuring VOC (volatile organic carbons). One VOC instrument is RAE MultiRae 3000. The other FotoVac (an older instrument).

During tests 2 at RISE in Borås, there were six experiments and peaks could be noted at 30, 50, 70, 100, 130- and 155-time units. The first cable that was tested was halogen free thermoplastic polyester. The second PVC with PUR coating. The third had two layers PVC. The fourth PE with PUR surrounding. The fifth only PVC and the sixth also only PVC. The first cable is 1.5 mm2 and voltage 2.2 V and current 50 A from start. At 58 A and 2.5 V we get first visible fume, but clearer fume at 4.1 V and 70 A, when also the

VOC sensors give clear signals, 2.4 respectively 38 mg/l for FotoVac respectively RAE MultiRae 3000.

It was noted that the peaks follow each other, and that Flir-camera gives a very good response in relation to the cable temperature. The PID meter from RAE gives a reasonably high response, while the older FotoVac has a smaller response, but still a clear response.

The clear response for VOC starts when the cables are fuming (see Figure 5, 6, 7 and 8). When the distance was 2 meters, no response was noted however at a distance from 0.2 m and less a clear response was observed. This is when there is a fan moving the smoke towards the sensors, but at the same time there is the normal ventilation sucking the air to the right, parallel to the cable away from the sensors. This showed that we need to have fans sucking air into the sensors, and this was later tested on Epiroc´s vehicles in their machine test hall in Örebro.

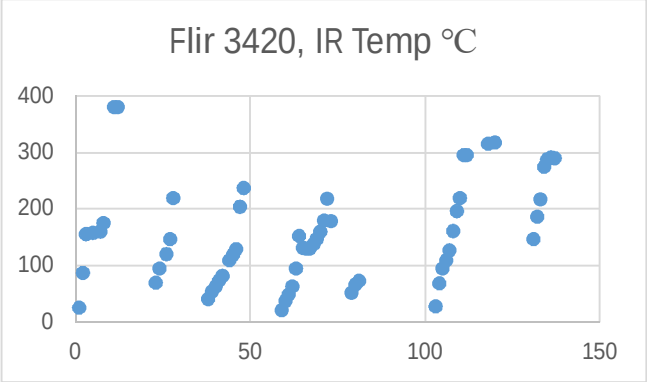

Figure 5 Peak results, sensor: Flir 3420, IR, Temperature

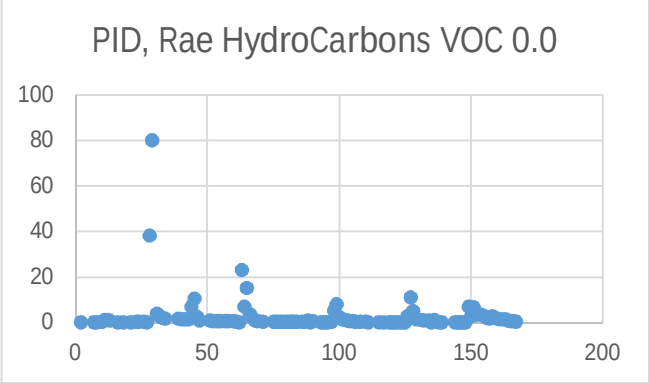

Figure 6. Peak results, sensor; RAE MultiRae 3000, VOC

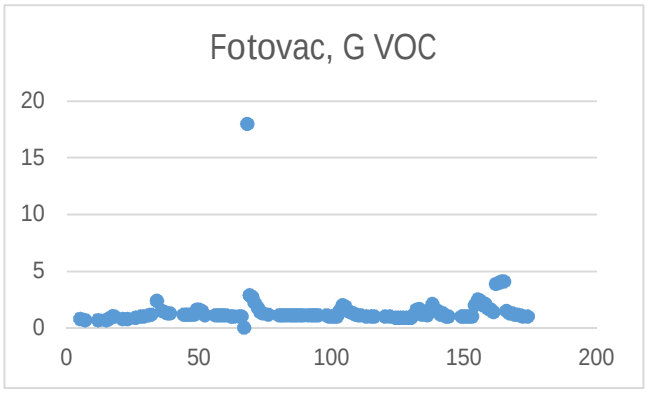

Figure 7. Peak results, sensor: FotoVac, VOC

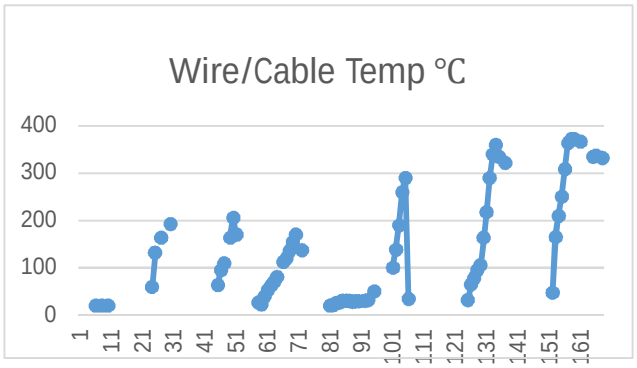

Figure 8. Peak results, cable, Temperature & Time units

4 Discussion

With fully autonomous mines, meaning no miners being present, the need for detecting changes in production that may cause a stop needs to be faster than today. This requires solutions which support smart inspections and early discovery of changes before the situation develops into a dangerous state.

To resolve these issues, this paper explored the possibility with sensors for detecting in an early state, possible fire situation on mining vehicles

A compilation of the results from the sensor tests have been presented including possible influence of the investigated parameters. Furthermore, a discussion of possible diagnostic as for detection of fires risk will now follow. The focus is to determine suitable sensors to be monitored for minimizing the number of fires caused by vehicles in the Swedish mines.

4.1 Future tests and research plans

Concluding, the authors realize that one of the essential parts for succeeding will require a system where the data from the sensors can be gathered and analyzed. With diagnostic of only one sensor a simple setpoint with predefined minimum and maximum values could be used. Warning and alarm could be triggered as for shown in an operation system available at the mining site. In the near future, the plan is to

make a proof of concept test where sensors will be installed on an Epiroc vehicle that is running in one of the underground mines in Sweden. The goal is to connect the sensor to the vehicle´s communication system which in turn communicates via the mines IS/IT solution to the safety system, Mobilaris. This system can today show where miners, machines and vehicle are located on a 3D picture of the underground mine shafts. Adding to this view information of e.g. gas levels from the vehicle a dangerous state might be able to be detected in due time.

The final aim is to study the possibility with artificial intelligence, machine and deep learning. Continuously gathering signals from a mix of gas sensors on a mining vehicle and correlate these with all other data being gathered, we believe root cause analyzes will give answers to why e.g. a fire started.

Further, we propose that future studies focus on the possibility of utilizing smart sensors combined with edge and fog computing. Investigating the possibility to move some critical analytics to smart sensors on the machine rather than having the signals to go through a cloud and thereby improving the communication speed. We believe this would e.g. detect fire hazards much faster and contribute to a safer mining vehicle.

5 Conclusions

Some of the future mining production is predicted to develop into fully autonomous mining processes. In such operation, safety and security will be important aspects. To be able and catch early changes in production on a mining vehicle, the tests shows that a mix of sensors is recommended to be installed (Figure 9). From those, signals can be gathered 24/7 as for monitoring of different values e.g. like:

- volatile organic carbons, VOC
- temperature
- other gases like methane
- oil mist
- tire pressure
- motor temperature

Figure 9. Underground Mining Vehicle

Acknowledgement

The Swedish Innovation Agency, Vinnova, RISE, Swedish Research Institute in Borås, Epiroc, ABB and Mälardalens University for their devoted support. Specially thanks to RISE for the great opportunity to run the fire tests in their fire lab facilities.

References

A Saeter Bøe and N. K. Reitan. Full scale fire test of electrical vehicle, RISE Fire Research, Trondheim, Norway. In *Proceedings from 5 th International Conference Fire in Vehicles – FIVE 2018*.

H Ingasson, Y. Zehn Li, and A. Lönnermark. *Tunnel fire dynamics*, Springer, 2015.

A Ahlberg Tidblad. Regulatory outlook on electric vehicle safety, Volvo Car Group, Gothenburg, Sweden. In *Proceedings from 5 th International Conference Fire in Vehicles – FIVE 2018.*

F Larsson, P. Andersson, and B-E. Mellander. Gas and fire risks with Li-Ion batteries in electrified vehicles. In *Proceedings from 5 th International Conference Fire in Vehicles – FIVE 2018*.

N Surendranath Reddy, Srinivasa Saketh M and Sourav Dhar, Review of Sensor Technology for Mine Safety Monitoring Systems: A Holistic Approach, 2016 IEEE First International Conference Control Measurement and Instrumentation.

R Hansen. Design fires in underground hard rock mines, “School of Sustainable Development of Society and Technology, Mälardalens University, Licentiate Thesis 127, Västerås, Sweden, 2011.

R Hansen. Fire statistic from the mining industry in New South Wales, Queensland and Western Australia, “The University of Queensland. DOI: 10.131340/RG.2.2.22666.77767, Australia, 2018.

O Willstrand. Fire risk management - Best approach to prevent vehicle fires, RISE Research Institutes of Sweden, Fire Research, Borås, Sweden. In *Proceedings from 5 th International Conference Fire in Vehicles – FIVE 2018.*

R Hansen. Study of heat release rates of mining vehicles in underground hard rock mines, Mälardalens University Press Dissertation No. 178, Västerås, Sweden, 2015.

A Beard and R. Carvel. *Handbook of tunnel fire safety*, second edition, 2005.

R Hansen. Investigation on fire causes and fire behavior: Vehicle fires in underground mines in Sweden 1998-2010, Mälardalens University, Västerås, Sweden, 2013.

Natural Resources Canada. Benchmarking the energy consumption of Canadian underground bulk mines. Ref. 2005.

Årsrapport från GRAMKO:s brandskyddskommitté 2012 (in Swedish), SveMin, 2013. GRAMKO annual report.

Pressure wave propagation in Managed Pressure Drilling- model comparison with real life data

Christian Berg[1,3] Jon Åge Stakvik[2,3] Bernt Lie[1] Knut Vaagsaether[1] Glenn-Ole Kaasa[3]

[1]Department of Electrical Engineering, IT and Cybernetics, University of South-Eastern Norway, Norway, Bernt.Lie@usn.no
[2]Department of Engineering Cybernetics , Norwegian University of Science and Technology, Norway
[3]Kelda Drilling Controls, Norway, cbe@kelda.no

Abstract

Drilling for oil and gas is a complex process, involving pumping of fluid through kilometers of pipes. Even though the drilling fluid has a high speed of sound ($\approx$1000 m/s), the large lengths involved make pressure wave propagation significant in timescales where such phenomena can usually be neglected in other processes. Managed pressure drilling, a technological extension of conventional drilling, adds a choke on the return flow from the drilling process. Significant work has been done in recent years on creating a simplified model of the process, often by neglecting distributed dynamics, and using this for controller design. This paper compares the simplified model most often used, with a distributed partial differential equation (PDE) model and compare the performance with measured data for wave propagation while doing managed pressure drilling. Fluid structure interaction and theoretical vs recorded speed of sound are discussed.

Keywords: managed pressure drilling, PDE, wave propagation, FSI

1 Introduction

Managed pressure drilling (MPD), today considered an "unconventional" drilling technology, is a natural technological advancement of conventional drilling. MPD is forecasted to grow significantly in the future, with key industry players indicating that it might be the new "conventional" in the near future. Drilling for oil and gas is a complex process with complex dynamic behaviour. The dynamics of the entire system has to be understood for controller and estimator design if the prognosed future growth and adoption is to be achieved.

For MPD, significant work has been done in recent years by control engineers/researchers on simplifying the mathematical model for the process to aid in controller and estimator design. A schematic view of the process is given in Figure 1. The most often used of these simplified models is the one by (Kaasa *et al.*, 2012). Multiple estimation and control strategies based on this simplified model has been published (Stakvik *et al.*, 2016; Stakvik *et al.*, 2017; Zhou *et al.*, 2011; Stamnes *et al.*, 2008; Hauge *et al.*, 2012). There is also ongoing research on designing estimators and controllers based on a linearised PDE distributed model (Aarsnes *et al.*, 2014; Aarsnes *et al.*, 2012; Anfinsen and Aamo, 2018). To verify design, controllers and estimators should in general always be tested on a system model that is higher fidelity than the model the design is based on to ensure that something critically important was not forgotten in the simplification. This paper compares the response of the simplified model by (Kaasa *et al.*, 2012) with a PDE based model for the process, and compare this to real drilling data from MPD operations.

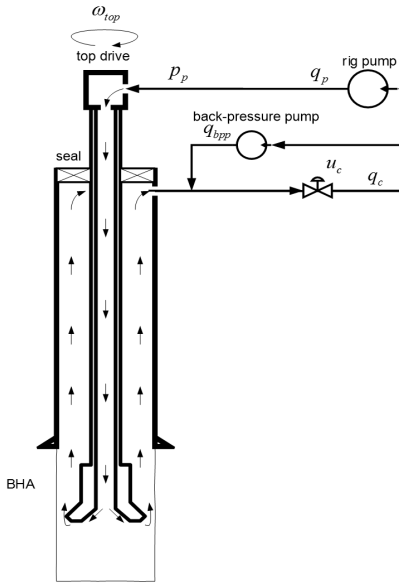

Figure 1. Managed pressure drilling. Drilling fluid is circulated from the rig mud pumps and down the drill string. At the bottom of the well bore the drilling fluid flows out through the drill bit via nozzles, and is then circulated up to the surface in the annular space between the drill string and annulus.

2 Model

Considering the process shown in Figure 1 and conservation of mass and momentum, dynamic models for the process can be derived. The model by (Kaasa *et al.*, 2012)

disregards distributed effects in the drill string and annulus, and consider these as two volumes where mass should be conserved. To capture wave propagation, distributed effects should be considered, making the drill-string and annulus take the form of partial differential equations (Di Meglio and Aarsnes, 2015).

2.1 Simplified model

The ODE model presented in (Kaasa *et al.*, 2012) and given in (1-5) can be derived with the following assumptions: The drill string and annulus are treated as two volumes where mass is conserved, the drill string pressure loss as quadratic with flow (turbulent), the drill bit pressure loss as quadratic with flow, and the annulus pressure loss as linear with flow (laminar). Note that here, the annulus and drill string volumes are considered constant, and in and out flow of the drilled formation is not considered.

$$\frac{V_d}{\beta_d}\frac{\mathrm{d}p_p}{\mathrm{d}t} = q_p - q_{bit} \tag{1}$$

$$\frac{V_a}{\beta_a}\frac{\mathrm{d}p_c}{\mathrm{d}t} = q_{bit} + q_{bpp} - q_c \tag{2}$$

$$M\frac{\mathrm{d}q_{bit}}{\mathrm{d}t} = p_p - p_c - F_d q_{bit}^2 - F_a q_{bit} \tag{3}$$

$$M = \int_0^{L_d} \frac{\rho_d}{A_d(x)}\mathrm{dx} + \int_{L_a}^{0} \frac{\rho_a}{A_a(x)}\mathrm{dx} \tag{4}$$

$$q_c = g_c(z_c)K_c\sqrt{\frac{2}{\rho}(p_c - p_{co})} \tag{5}$$

In (1-5) V_d and V_a are drill string and annulus volumes, β_d and β_a are fluid modulus of compressibility $\beta = \frac{1}{\rho}\frac{\mathrm{d}\rho}{\mathrm{d}p}$, q_p is the pump flow, q_{bit} is a state representing flow from the drill string to the annulus, F_d and F_a are friction factors for the drill string and annulus, g_c is choke area as a function of choke position z_c, ρ_a, ρ_d are fluid densities in drill string and annulus, and A_d, A_a are flow cross sectional areas.

2.2 PDE model

If distributed effects are considered, the drill string and annulus can be modelled using the PDE system given in (6-7) representing conservation of mass and momentum, respectively.

$$\frac{\partial\rho}{\partial t} + \frac{\partial\rho u}{\partial x} = 0 \tag{6}$$

$$\frac{\partial\rho u}{\partial t} + \frac{\partial(\rho u^2 + p)}{\partial x} = -f(\rho,u) - g(\rho) \tag{7}$$

where ρ is density and u is velocity.

Putting (6-7) in vector form as in (8) and introducing temporary variables u_1, u_2.

$$\frac{\partial \mathrm{U}}{\partial t} + \frac{\partial}{\partial x}(F(\mathrm{U})) = S(\mathrm{U}) \tag{8}$$

$$\begin{aligned}
\mathrm{U} &= \begin{bmatrix}\rho\\ \rho u\end{bmatrix} = \begin{bmatrix}u_1\\ u_2\end{bmatrix}\\
F(\mathrm{U}) &= \begin{bmatrix}\rho u\\ \rho u^2 + p\end{bmatrix} = \begin{bmatrix}u_2\\ \frac{u_2^2}{u_1} + \frac{\partial p}{\partial\rho}u_1\end{bmatrix}\\
S(\mathrm{U}) &= \begin{bmatrix}0\\ -f(\rho,u) - G(\rho,\theta)\end{bmatrix} = \begin{bmatrix}0\\ -f(u_1,\frac{u_2}{u_1}) - G(u_1,\theta)\end{bmatrix}
\end{aligned} \tag{9}$$

Where $\partial p = \frac{\partial p}{\partial\rho}\partial\rho$ is used for removing p in (9). Then in pseudo linear form as

$$\frac{\partial \mathrm{U}}{\partial t} + A(\mathrm{U})\frac{\partial \mathrm{U}}{\partial x} = S(\mathrm{U}) \tag{10}$$

$$A(\mathrm{U}) = \frac{\partial F(\mathrm{U})}{\partial \mathrm{U}} = \begin{bmatrix}0 & 1\\ -\frac{u_2^2}{u_1^2} + \frac{\partial p}{\partial\rho} & 2\frac{u_2}{u_1}\end{bmatrix} \tag{11}$$

it can be found that the eigenvalues of $A(\mathrm{U})$ are $\lambda_{1,2} = u \pm \sqrt{\frac{\partial p}{\partial\rho}}$ where $\sqrt{\frac{\partial p}{\partial\rho}}$ is the speed of sound in the fluid.

The source terms $f(\rho,u)$ and $G(\rho,\theta)$ represent friction and hydrostatic pressure due to gravity, respectively. Friction is modeled as (12)

$$\begin{aligned}
f(\rho,u) &= \frac{1}{2}K_{fric} f \rho u^2\\
f &= \max\left(\frac{64}{\mathrm{Re}}, \frac{0.25}{(\log(\frac{\varepsilon}{3.7D} + \frac{5.74}{\mathrm{Re}^{0.9}}))^2}\right)\\
\mathrm{Re} &= \frac{\rho u D}{\mu}
\end{aligned} \tag{12}$$

where f is the Darcy friction factor, Re is the Reynolds number, ε is the surface roughness of the pipe, and D is the hydraulic diameter. $f = \frac{64}{\mathrm{Re}}$ represents laminar flow, $f = \frac{0.25}{(\log(\frac{\varepsilon}{3.7D} + \frac{5.74}{\mathrm{Re}^{0.9}}))^2}$ is an approximation (Swamee and K. Jain, 1976) to the Colebrook equation, and the maximum of these two is taken to cover both laminar and turbulent regimes. K_{fric} is a tuning factor to fit measured field data, ideally set to 1.

Hydrostatic pressure is modelled as (13) where θ is the local angle between the well bore and the horizontal.

$$G(\rho,\theta) = \rho g \sin(\theta) \tag{13}$$

There are numerous numerical approaches to solving the PDE system in (6-7), (Vytvytsky and Lie, 2017), (Palacios G and Da Silva, 2013) both with and without considering fluid structure interaction. The details of different methods for solving (6-7) with strengths and weaknesses is not elaborated in detail in this paper. Here a staggered grid approach is used.

For simulation, (6) is transformed into an equation for pressure. Assuming the density can be given as a linear function of pressure as in (14), (6-7) can be rewritten as (15-16).

$$\rho = \rho_0 + \frac{\rho_0}{\beta}(p - p_0) \qquad \frac{d\rho}{dp} = \frac{\rho_0}{\beta} \tag{14}$$

$$\frac{\rho_0}{\beta}\frac{\partial p}{\partial t} + \frac{\partial \rho u}{\partial x} = 0 \tag{15}$$

$$\frac{\partial \rho u}{\partial t} + \frac{\partial \rho u^2}{\partial x} = -\frac{\partial p}{\partial x} - f(\rho, u) - g(\rho) \tag{16}$$

The system in (15-16) is integrated over a closed volume as given in (17-20) along the lines described in (Versteeg and Malalasekera, 2019).

$$\oint_{CV} (\frac{\rho_0}{\beta}\frac{\partial p}{\partial t} + \frac{\partial \rho u}{\partial x}) dV = 0 \tag{17}$$

$$\oint_{CV} (\frac{\partial \rho u}{\partial t} + u\frac{\partial \rho u}{\partial x}) dV = \oint_{CV} (-\frac{\partial p}{\partial x} + S_x) dV \tag{18}$$

Applying the Gauss divergence theorem; $\oint_{CV} \text{div}(\phi u) dV = \oint_{S} \mathbf{n} \cdot (\phi u) dS$

$$\oint_{CV} (\frac{\rho_0}{\beta}\frac{\partial p}{\partial t}) dV + \int_{A} \mathbf{n} \cdot (\rho u) dA = 0 \tag{19}$$

$$\oint_{CV} (\frac{\partial \rho u}{\partial t}) dV + \int_{A} \mathbf{n} \cdot (\rho u^2) dA = \oint_{CV} (-\frac{\partial p}{\partial x} + S_x) dV \tag{20}$$

Solving the integrals and discretizing in space yield (21-22).

$$V\frac{\rho_0}{\beta}\frac{\partial p}{\partial t} + (uA\rho)_{out} - (uA\rho)_{in} = 0 \tag{21}$$

$$V\frac{\partial \rho u}{\partial t} + (u^2 A\rho)_{out} - (u^2 A\rho)_{in} = -V\frac{p_{out} - p_{in}}{L} + S_x V \tag{22}$$

Doing the variable change $q = uA$, applying the chain rule to $\frac{\partial \rho u}{\partial t}$, and using that $q\frac{\partial \rho}{\partial t} = q\frac{\rho_0}{\beta}\frac{\partial p}{\partial t}$ yield (23-24).

$$V\frac{\rho_0}{\beta}\frac{\partial p}{\partial t} + (q\rho)_{out} - (q\rho)_{in} = 0 \tag{23}$$

$$\frac{V}{A}(\rho\frac{\partial q}{\partial t} + q\frac{\rho_0}{\beta}\frac{\partial p}{\partial t}) + (\frac{q^2\rho}{A})_{out} - (\frac{q^2\rho}{A})_{in} \ldots = -A(p_{out} - p_{in}) + S_x V \tag{24}$$

With boundary conditions

$$q_{ds}(x = 0) = q_p \tag{25}$$

$$p_{ds}(x = L) = p_{an}(x = L) + \frac{1}{K_{nozzle}}(\frac{q_{ds}(x = L)}{A_{nozzle}})^2 \tag{26}$$

$$\rho u A_{an}(x = L) = \rho u A_{ds}(x = L) \tag{27}$$

$$p_{an}(x = 0) = p_c \tag{28}$$

The system solved is given in (29-30) where the pressure equation is solved in the grid cell centre and the flow equation is solved on a grid that has the cell centre on the pressure grid face.

$$\frac{\partial p}{\partial t} = -\frac{\beta}{V\rho_0}((q\rho)_{out} - (q\rho)_{in}) \tag{29}$$

$$\frac{\partial q}{\partial t} = -q\frac{\rho_0}{\rho\beta}\frac{\partial p}{\partial t} - \frac{1}{\rho L}((\frac{q^2\rho}{A})_{out} - (\frac{q^2\rho}{A})_{in}) \ldots - \frac{A}{\rho L}(p_{out} - p_{in}) + S_x\frac{A}{\rho} \tag{30}$$

The spatial arrangement of states can be seen for an example case with $n = 3$ grid elements for flow and $n+1$ grid elements for pressure in Figure 2. The subscript g in $p_{0,g}$ and $p_{n+1,g}$ is to represent that this is a "ghost node". Ghost nodes are grid elements outside of the physical domain used to implement boundary conditions.

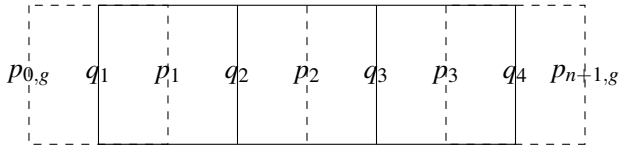

Figure 2. Staggered grid showing the spatial staggering of the system solved. If i represent grid number on the flow grid for q, and k represent grid number for the pressure grid for variables p and ρ, note that $i + \frac{1}{2} = k, k + \frac{1}{2} = i + 1$

From Figure 2 it can be seen that q_{out}, q_{in} (being q_2 and q_1 respectively for p_1) and p_{out}, p_{in}, (being p_1 and $p_{0,g}$ for q_1) is known directly due to the spatial staggering of states.

Variables that are not directly available on grid faces from the staggered arrangement (ρ in (29); q and $q\frac{\rho_0}{\beta}\frac{\partial p}{\partial t}$ in (30)) are found by using a first order up-winding in flow, as in (31)

$$\theta_{i+\frac{1}{2}} = \begin{cases} \theta_i & q > 0 \\ \theta_{i+1} & q < 0 \\ \frac{\theta_i + \theta_{i+1}}{2} & q = 0 \end{cases} \tag{31}$$

Equations (29-30) are solved in time by using a 4th order Runge Kutta method.

2.2.1 A brief discussion on equation of state

Using (14) as an Equation of State for the liquid will yield a speed of sound from the eigenvalue analysis in (10) as a function of ρ_0 and β given in (32)

$$c = \sqrt{\frac{\beta}{\rho_0}} \tag{32}$$

Drilling fluids are in most cases a mixture of water and weighting material (water based mud, WBM), oil, water and weighting material (oil based mud, OBM) or synthetic oil, water, and weighting material (Synthetic based mud, SBM). Drilling fluids usually also contain a small fraction of additives (emulsifiers, gelling agents, etc.), at a low volume fraction. The equivalent mixture bulk modulus should be found for use in (14) (Carcione and Poletto, 2000). Although all fluid components are only slightly compressible, the weighting material can be treated as incompressible compared to the water and oil. The volume fraction of additives are neglected here.

The mixture bulk modulus β_m can be found as in (33) where subscripts w, o, s denote water, oil and solids respectively.

$$\frac{1}{\beta_m} = \frac{\alpha_w}{\beta_w} + \frac{\alpha_o}{\beta_o} + \frac{\alpha_s}{\beta_s} \tag{33}$$

Here α_i is the volume fraction of that mixture component. Note that $\alpha_w + \alpha_o + \alpha_s = 1$. Assuming the solids component to be incompressible as $\beta_s >> \beta_o, \beta_w$, analogous to saying $\beta_s = \infty$ makes the last term on the RHS of (33) disappear.

The mixture density ρ_{m0} can be found as (34)

$$\rho_{m0} = \alpha_w \rho_{w0} + \alpha_o \rho_{o0} + \alpha_s \rho_{s0} \tag{34}$$

In practice, a pre-defined ratio of oil/water is used when mixing the drilling fluid, and then weighting solids is added to reach the desired liquid density. For WBM fluids there is no oil fraction, and solids are added to reach the desired density. This can be used to further simplify (33-34). By using oil-water ratio, $R_{ow} = \frac{\alpha_o}{\alpha_w}$, and the fact that the sum of all the component volume fractions is 1, (33-34) can be rewritten in forms that are simple for straight forward use, as given in (35-36) where the inputs are the mixture and component densities ρ_m, ρ_i, component compressibility β_i, and oil-water ratio R_{ow}.

$$\alpha_s = \frac{\rho_m - \rho_w + R_{ow}(\rho_m - \rho_o)}{\rho_s - \rho_w + R_{ow}(\rho_s - \rho_o)} \tag{35}$$

$$\beta_m = \frac{\beta_w \beta_o (1 + R_{ow})}{\beta_o (1 - \alpha_s) + R_{ow} \beta_w (1 - \alpha_s)} \tag{36}$$

For water based mud, $R_{ow} = 0$ and (35-36) are still valid. Equations (35-36) are only valid at a given pressure as the volume fractions change with pressure. In practice the effect of this is minor.

2.2.2 Fluid structure interactions (FSI)

If fluid structure interactions are considered, i.e., the flow cross sectional area changes with pressure, an equivalent bulk modulus β_e can be calculated and used in (23, 24). Note that the mixture bulk modulus β_m should still be used in the liquid Equation of State in (14).

Taking pipe expansion into account, equivalent bulk modulus can be calculated as (37). Here the possible compression of the drill string inside the annulus is neglected. For the full derivation of (37) in the context of the applied PDE, the reader is referred to (Carlsson, 2016).

$$\beta_e = \frac{\beta_m}{(1 + \frac{\beta_m D}{dE}\phi)} \tag{37}$$

In (37), β_m is mixture bulk modulus from (36), E is Young's modulus of the pipe, D is the pipe diameter, d is the pipe wall thickness, and ϕ is the pipe support factor. Here axial stresses are neglected, setting $\phi = 1$.

2.2.3 Gridding

In a real well geometry there are numerous changes in cross sectional area with axial position, mainly caused by the drill string consisting of different pipe sections screwed together. Spatial discretization (gridding) at the resolution required to capture all the changes exactly will require a large number of grid elements. Here, a gridding routine that ensures the grid volume and volume of the real geometry are exactly equal, is used. The real vs discretized geometry for the test well studied near the bottom hole assembly (BHA) is shown in Figure 3.

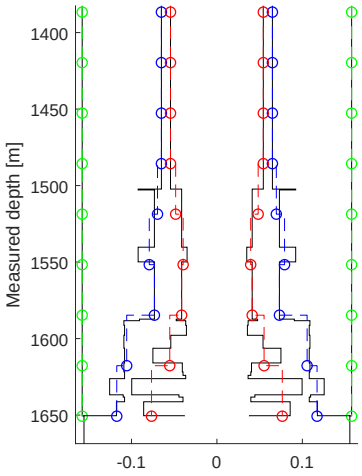

Figure 3. Volume conserving grid of bottom hole assembly (BHA). Solid black: Original geometry. Dashed green: Gridded well bore diameter (annulus). Dashed blue: Gridded drill string outer diameter (annulus). Dashed red: Gridded drill string inner diameter (drill string).

2.2.4 Boundary conditions

For comparison with field data, the algebraic relation between choke flow and choke pressure for the simplified model is skipped, and measured choke pressure is used directly as a boundary condition. This yields a simplified model with two ODE's, (as opposed to the three ODE's in the original model by (Kaasa *et al.*, 2012)) specified in (1, 3, 4). To compare the model's dynamic response to the measured data, the boundary values that are not specified are compared to measured data. That is, measured pump flow and choke pressure are used as boundary conditions.

Then, simulated and measured pump pressure and choke flow are compared. The simplified model has no choke flow when the choke pressure is specified, so only pump pressure is compared to measured pump pressure.

For the PDE model the boundary conditions for n grid elements are set as follows.

- Inlet
  - $p_0 = p_1$. That is, the inlet ghost node for pressure is set to the same value as the next grid element
  - $q_1 = q_{bc}$, the flow into the domain is specified
- Outlet
  - p_{n+1}, the outlet ghost node for pressure is set to $2p_{bc} - p_n$ where p_{bc} is the specified boundary pressure

2.3 Initial conditions

For the PDE model the initial conditions is set to the hydrostatic pressure for p, that is $p_i = \rho_0 g h_i$ where h_i is the grid vertical depth. The initial condition for flow q is set to zero. Flow is then ramped up to the flow rate in the start of case considered and simulation run for 150 seconds to reach steady state.

3 Comparison with field data

In MPD operations, if the choke controller is active, wave propagation phenomena are rarely visible. This is due to the choke pressure controller being used in the data the author has available is specifically designed to keep within the limits of the simplified model. During system commissioning, direct choke position control is used to verify calibration of the controller model, and pressure wave dynamics gets excited. When doing choke position control, the rate of change of the position is limited in the controller to about $\approx 5\%/\mathrm{s}$ to avoid severe water hammer effects caused by the operator, but still fast enough that wave dynamics is excited. The controller in closed loop has access to the full choke actuator performance $\approx 25\%/\mathrm{s}$, making the testing of the mentioned controller on a PDE model very important as it is easily able to excite wave dynamics in cases with improper tuning. For validation of the models with data, a time period from commissioning on a 1647m deep offshore well is used, as seen in Figure 4. The commissioning is performed in "cased hole", that is, the annulus has a steel casing going all the way to the bottom of the well and there is no "open hole" (exposed reservoir) .

In Figure 4, the pump flow rate is near constant, and the choke is closed and then opened again 3 times at various speeds, giving an increase in choke pressure (boundary condition), and then an increase in pump pressure (modelled), governed by the pressure dynamics of the well. The choke flow changes when the choke position is changed.

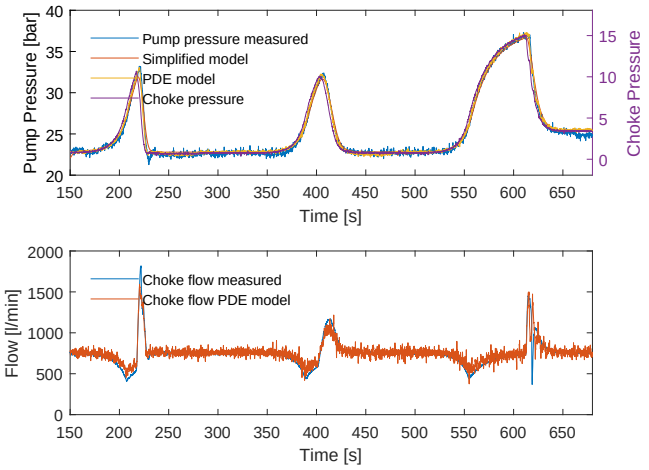

Figure 4. Steps in choke position during cased hole commissioning for 1647m deep offshore well. Top: Pressure simulated vs measured. Top right axis: Measured choke pressure (boundary condition). Bottom: Simulated vs measured choke flow.

This is caused by the compression/expansion of liquid and possible expansion of well geometry due to pressure.

3.1 Field data comparison, no fluid structure interactions

Here the response to the choke position steps are studied for all steps individually. Fluid structure interactions are not considered. Parameters used in the PDE and simplified model are given in Table 1. A "fudge factor" K_{fric} for friction in the PDE model was required to make the simulated pump pressure fit with the measured data. At the flow rates in the cases studied, the frictional pressure loss will be laminar in both the drill string and annulus. The assumption of Newtonian fluid in (12) is not really true for drilling fluids as they exhibit gelling behavior, something that will lead to a higher friction loss than for Newtonian fluids at low flow rates.

The noise on the pump pressure and choke flow in the PDE model is caused by noise on the choke pressure boundary condition. Filtering the noise on the signal is avoided as the phenomena studied are fast compared to the sampling rate. Figure 5 shows a close-up of the first step from Figure 4.

It is seen from Figure 5 that, qualitatively, the results of the PDE model fits reasonably well with the measured data. The PDE model under-predicts the changes of choke flow due to choke pressure. The response on pump pressure happens faster in the PDE model than in the measured data. This indicates that the wave propagation time in the PDE model is faster than in reality. The simplified model is able to predict pump pressure well when the pressure is increasing, but ends up giving a "smoothed" response on the more rapid opening of the choke.

Figure 6 shows the response in the second step, where both the increase and decrease of choke pressure is slower than that in the first step. It is clearly seen that as changes happen more slowly, the difference between the simplified

Table 1. Model parameters.

Parameter	Value	Unit
V_d	15.27	$[m^3]$
V_a	104.94	$[m^3]$
R_{ow}	4	$[-]$
$\rho_{m0} = \rho_d = \rho_a$	1210	$[kg/m^3]$
ρ_{w0}	1000	$[kg/m^3]$
ρ_{o0}	850	$[kg/m^3]$
ρ_{s0}	4200	$[kg/m^3]$
β_w	2.2e9	[Pa]
β_o	1.5e9	[Pa]
β_a (eq.36)	1.78e9	[Pa]
β_d (eq.36)	1.78e9	[Pa]
L_d	1651	[m]
L_a	1651	[m]
A_d	0.0092	$[m^2]$
A_a	0.0636	$[m^2]$
M (eq.4)	2.47e8	$[kg/m^4]$
μ	45e-3	$[Pa \cdot s]$
ε	4.5e-5	[m]
K_{fric}	2.4	$[-]$
A_{nozzle}	6.25e-04	$[m^2]$
K_{nozzle}	0.8	$[-]$

model, PDE model, and measured data becomes smaller. This is reasonable as that the main difference between the simplified and PDE model is whether distributed pressure effects are neglected. The effect of choke pressure on choke flow in the PDE model is still under-predicted, as in the first pressure step.

Figure 7 shows the response of the simplified and PDE model compared to field data for the third pressure step. In this step, the opening of the choke is even faster than that of the case in Figure 5. Note the ”wave” in measured choke pressure. As for the two first cases, the results of the PDE and simplified model compared to field data is very similar at the increase of pressure with different response on opening the choke quickly. The previous observation of choke flow being under-predicted in the PDE model is visible when the pressure is increased, but not that clearly visible when the choke is opened.

3.2 Field data comparison, fluid structure interactions

Here the steps in the previous section is revisited, with fluid structure interactions (FSI) considered. Parameters used when FSI is considered are given in Table 2.

Figure 8 shows the PDE model with and without FSI in the first step. Considering FSI through (37), yields a lower β for the drill string and annulus, something that will increase the wave propagation time (decrease velocity) in the PDE model, as well as make the effect of choke pressure on choke flow be more significant. The assumption of no axial stresses used is not strictly true. For the annulus, the casing will mainly be under compression loads axially.

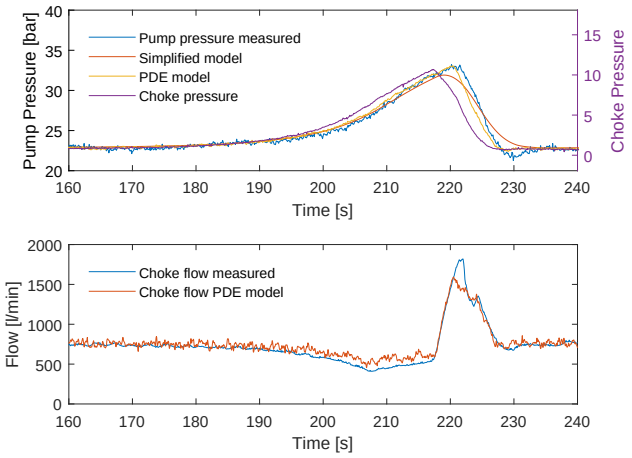

Figure 5. First step in choke position; slow closing and rapid opening of choke. Top: Pressure simulated vs measured. Top right axis: Measured choke pressure (boundary condition). Bottom: Simulated vs measured choke flow.

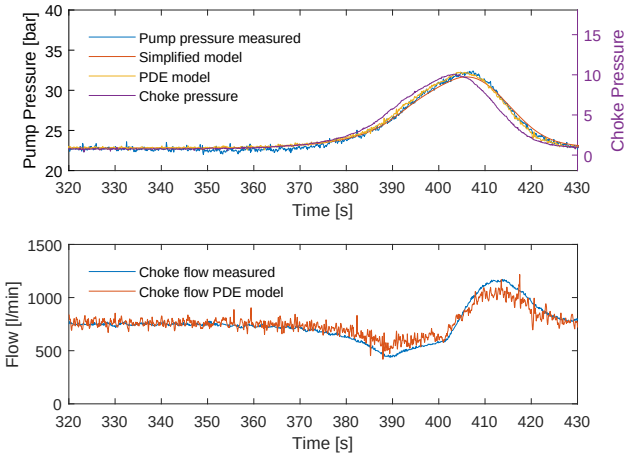

Figure 6. Second step in choke position; slow closing and opening of choke. Top: Pressure simulated vs measured. Top right axis: Measured choke pressure (boundary condition). Bottom: Simulated vs measured choke flow.

The neglected effect of compression of the drill string in the annulus together with the axial forces in the casing would likely lead to slightly lower effective bulk modulus. The drill string experiences both stretch and compression along the length.

As seen in Figure 8, the effect of choke pressure on flow becomes more significant when considering FSI, making the PDE model fit the measured flow data better compared to the model neglecting FSI. Wave propagation time reduces slightly when considering FSI, but there is still a mismatch between the PDE model and recorded data.

Figure 9 shows the PDE model compared to measured data for the second step in pressure, with and without FSI. Overall the results for the second pressure step are similar to the no FSI case, with the transient being slow enough that wave propagation effects are minor. The effect of choke pressure on choke flow compared to measured data is better when considering FSI than not considering FSI,

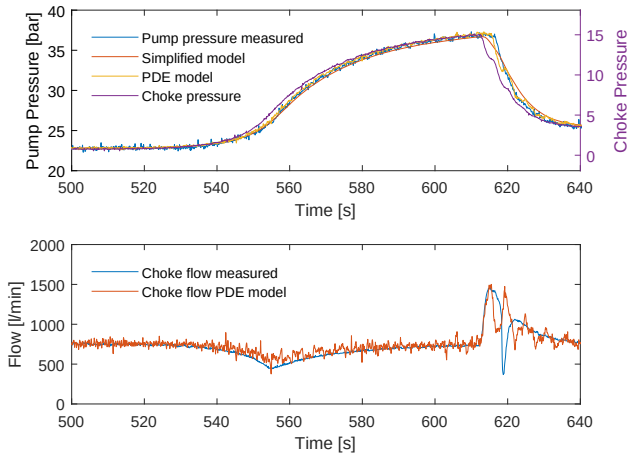

Figure 7. Third step in choke position; slow closing and very rapid opening of choke. Top: Pressure simulated vs measured. Top right axis: Measured choke pressure (boundary condition). Bottom: Simulated vs measured choke flow.

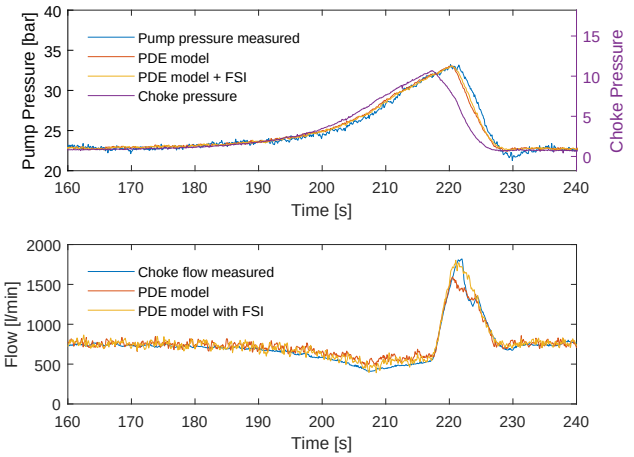

Figure 8. First step in choke position, comparison of original PDE-simulation and PDE-simulation considering fluid structure interactions. Top right axis: Measured choke pressure (boundary condition). Bottom: Simulated vs measured choke flow.

Table 2. Model parameters with FSI considered.

Parameter	Value	Unit
β_m (eq.36)	1.78e9	[Pa]
E	200e9	[Pa]
D_d	0.1086	[m]
d_d	0.0076	[m]
D_a	0.3153	[m]
d_a	0.0122	[m]
$\beta_{e,d}$ (eq.37)	1.57e9	[Pa]
$\beta_{e,a}$ (eq.37)	1.45e9	[Pa]

but the results of the PDE model still suggest that the used β_e is slightly too big, illustrated by compression and expansion (flow change due to pressure) being smaller in the PDE model considering FSI than recorded flow data.

Figure 10 shows the PDE model compared to measured data for the third step in pressure, with and without FSI. For the third pressure step, the effect of considering FSI is smaller than in the case of the first two steps. The simulation with FSI show a slightly larger change in choke flow from changing choke pressure, as is the case for the first two steps as well as a slightly increased wave propagation time. The deviation between simulated flow and measured flow when the pressure is reduced might be caused by sensor inaccuracies. The dynamic performance of the Coriolis flow meter at transients as fast as in Figure 10, is uncertain.

4 Conclusions

The response of the commonly used simplified model by (Kaasa *et al.*, 2012) and a distributed PDE based model has been compared to data from cased hole commissioning from an MPD system on an offshore well. It is shown that when changes are slow, the simplified and PDE based models show very similar response, matching quite closely that of the measured data. When the transient

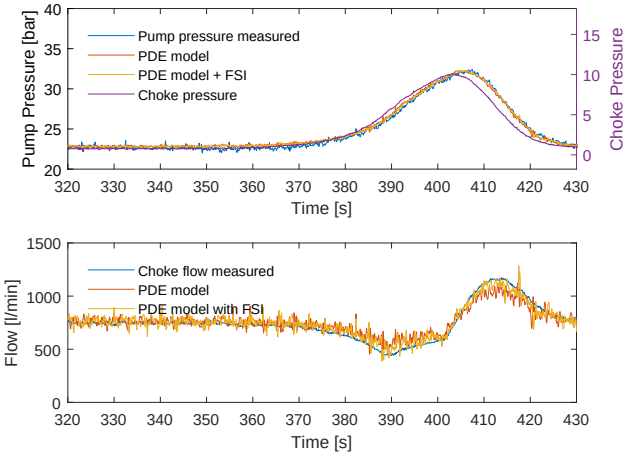

Figure 9. Second step in choke position. Slow closing and opening of choke, comparison of original PDE simulation and PDE simulation considering fluid structure interactions. Top right axis: Measured choke pressure (boundary condition). Bottom: Simulated vs measured choke flow.

changes are more rapid, a discrepancy between the simplified model and PDE model and measured data is seen. It is found that the PDE model under-predicts the effect of choke pressure on choke flow if only fluid properties are considered. When considering simple fluid structure interactions, the PDE model more closely fits the measured data. A discrepancy between the wave propagation time in the PDE model and measured data is observed. By manually "fudging" the system bulk modulus β_e, it is still not possible to make the PDE model fit with both choke flow and pump pressure (wave propagation time). To make the PDE model more closely fit the measured data, the well length or well volume and bulk modulus has to be changed. Well length and volume are considered quite well known, such that this result is indicative of something more fundamental missing from the PDE based model. The PDE model disregards 2-D effects on

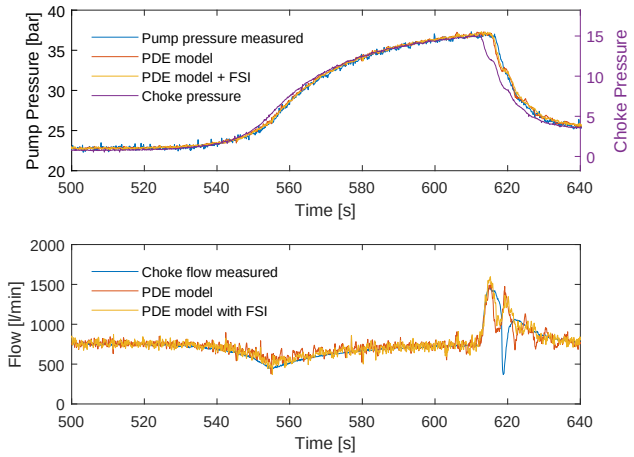

Figure 10. Third step in choke position. Very rapid opening of choke, comparison of original PDE simulation and PDE simulation considering fluid structure interactions. Top right axis: Measured choke pressure (boundary condition). Bottom: Simulated vs measured choke flow.

wave propagation, something that can increase the wave communication time. Further study of the discrepancy between the wave communication time in the 1D PDE model and recorded data, something that has been found in data from multiple wells, will require further work.

5 Acknowledgements

We thank Liobomyr Vytvysky on useful discussions on FSI in 1-D in compressible PDE models. This research has been partially funded by the the Norwegian Research Council in the Industrial PhD project "Modeling for automatic control and estimation of influx and loss in drilling operations" Project no 241586.

References

Ulf Jakob F Aarsnes, Ole Morten Aamo, and Alexey Pavlov. Quantifying error introduced by finite order discretization of a hydraulic well model. In *Control Conference (AUCC), 2012 2nd Australian*, pages 54–59, Aarsnes2012, 2012. IEEE. ISBN 1-922107-63-8.

Ulf Jakob Flø Aarsnes, Martin Standal Gleditsch, Ole Morten Aamo, and Alexey Pavlov. Modeling and Avoidance of Heave-Induced Resonances in Offshore Drilling. *SPE Drilling & Completion*, 29(04):454–464, December 2014. doi:10.2118/173178-PA.

Henrik Anfinsen and Ole Morten Aamo. Adaptive Output-Feedback Stabilization of 2 x 2 Linear Hyperbolic PDEs with Actuator and Sensor Delay. In *2018 26th Mediterranean Conference on Control and Automation (MED)*, pages 1–6, Zadar, June 2018. IEEE. ISBN 978-1-5386-7890-9. doi:10.1109/MED.2018.8442627.

José M Carcione and Flavio Poletto. Sound velocity of drilling mud saturated with reservoir gas. *Geophysics*, 65(2): 646–651, 2000. ISSN 0016-8033.

Joel Carlsson. Water Hammer Phenomenon Analysis using the Method of Characteristics and Direct Measurements using a "stripped" Electromagnetic Flow Meter. Master Thesis, 2016.

Florent Di Meglio and Ulf Jakob Flø Aarsnes. A distributed parameter systems view of control problems in drilling. *IFAC-PapersOnLine*, 48(6):272–278, 2015.

Espen Hauge, Ole Morten Aamo, and John-Morten Godhavn. Model-based estimation and control of in/out-flux during drilling. In *American Control Conference (ACC), 2012*, pages 4909–4914, Hauge2012mbe, 2012. IEEE. ISBN 1-4577-1095-1.

Glenn-Ole Kaasa, Øyvind N Stamnes, Ole Morten Aamo, and Lars S Imsland. Simplified hydraulics model used for intelligent estimation of downhole pressure for a managed-pressure-drilling control system. *SPE Drilling & Completion*, 27(01):127–138, 2012. ISSN 1064-6671. doi:10.2118/143097-PA.

Erika Palacios G and Carlos Da Silva. A finite volume study for pressure waves propagation in a straight section of pipeline with caviation. *The International Journal of Multiphysics*, 7(4):259–270, December 2013. ISSN 1750-9548. doi:10.1260/1750-9548.7.4.259.

Jon Åge Stakvik, Christian Berg, Glenn-Ole Kaasa, Ole Morten Aamo, and Urs Lehner. Adaptive Model Based Choke Control System for MPD Operations. In *SPE-179714-MS*, SPE, April 2016. Society of Petroleum Engineers. ISBN 978-1-61399-446-7. doi:10.2118/179714-MS.

Jon Åge Stakvik, Christian Berg, Glenn-Ole Kaasa, Robert Graham, and Antonio Torrealba. Model-Based Control in Managed Pressure Drilling. In *SPE/IADC Drilling Conference and Exhibition*. Society of Petroleum Engineers, 2017. ISBN 1-61399-501-6.

Øyvind Nistad Stamnes, Jing Zhou, Glenn-Ole Kaasa, and Ole Morten Aamo. Adaptive observer design for the bottomhole pressure of a managed pressure drilling system. In *Decision and Control, 2008. CDC 2008. 47th IEEE Conference On*, pages 2961–2966. IEEE, 2008. ISBN 1-4244-3123-9. doi:10.1109/CDC.2008.4738845.

Prabhata Swamee and Akalank K. Jain. Explicit equations for pipe-flow problems. *ASCE J Hydraul Div*, 102:657–664, May 1976.

Henk Versteeg and W Malalasekera. *An Introduction to Computational Fluid Dynamics : The Finite Volume Method / H. K. Versteeg and W. Malalasekera.* April 2019.

Liubomyr Vytvytsky and Bernt Lie. Comparison of elastic vs. inelastic penstock model using OpenModelica. In *The 58th Conference on Simulation and Modelling (SIMS 58) Reykjavik, Iceland, September 25th – 27th, 2017*, pages 20–28, September 2017. doi:10.3384/ecp1713820.

Jing Zhou, Ole Morten Aamo, and Glenn-Ole Kaasa. Switched control for pressure regulation and kick attenuation in a managed pressure drilling system. *Control Systems Technology, IEEE Transactions on*, 19(2):337–350, 2011. ISSN 1063-6536.

Simulation of enhanced oil recovery with CO_2 injection

Simon Salvesen Holte Jan Vidar E. Knutsen Roy Sømme Ommedal Britt M E Moldestad

Department of Process, Energy and Environmental Technology, University of South-Eastern Norway, Norway,
{162687, 142323, 162691, britt.moldestad}@usn.no

Abstract

One of the goals of the Paris Agreement is to reduce the CO_2 emission to the atmosphere. This paper deals with CO_2-EOR, which is a good option for utilizing and storing CO_2. Four cases were simulated using the commercial software OLGA in combination with ROCX. To avoid the reproduction of CO_2 to the production well, two of the cases were run with autonomous inflow control valves and packers installed in the pipeline. These help to close off parts of the well when CO_2 and water breakthrough occur. The cases were run for 1500 days of production, and the accumulated oil production was in the range $1.1 \cdot 10^6$ to $1.3 \cdot 10^6$ m^3. The water production varied significantly for the different cases, and the water cut was reduced from 70% to 38% when inflow control valves were used. CO_2 injection increases the oil production but also the water production, and when combining CO_2-EOR and inflow control valves, the water cut was 56%. However, the accumulated oil production increased by 14% compared with a similar case without CO_2 injection. This underlines that CO_2-EOR is a good alternative for increasing the oil production, but it will also increase water production. Installation of autonomous inflow control valves in the production well are a good solution for reducing the water production and reproduction of CO_2.

Keywords: oil production, CO_2-EOR, OLGA/ROCX simulations, inflow control

1 Introduction

The oil production on the Norwegian Continental Shelf started in June 1971, and the oil laid the foundation for the economic growth in Norway. Some of the fields in the North Sea are now getting old, and new production technologies have to be considered to increase the oil recovery. Enhanced Oil Recovery (EOR) by injection of CO_2 is one of the tertiary oil recovery methods that can be used in mature fields.

The Paris Agreement was signed by 195 UNFCCC (United Nations Framework Convention on Climate Change) members by March 2019, and 185 states have committed to it. One of the three overall goals is to limit the global warming to less than 2˚C (Kallbekken and Jacobsen, 2018). In order to achieve the 2 degree target, 55 giga tonnes of CO_2 must be captured and stored by 2030 (United Nations Climate Change, 2015). Carbon capture and storage (CCS) is expensive due to energy intensive operation and high investment costs for the capture plants (Aabø, 2017). When using CO_2-EOR, the CO_2 will be utilized to get out more oil from the reservoirs and at the same time be stored. It will thus be profitable to capture and sell CO_2 to oil companies (International Energy Agency, 2019).

The objective of this study is a) to study how to increase the oil recovery from mature oil fields and b) to study how to avoid reproduction of high amounts CO_2 to the well. The paper deals with simulation of CO_2-EOR using the well simulation software OLGA in combination with the near well reservoir simulator ROCX. A homogeneous oil reservoir in the North Sea is simulated with and without injection of CO_2 to study the effect of CO_2-EOR on the oil recovery. To avoid reproduction of CO_2, the well is equipped with packers and autonomous inflow control valves (AICVs). The autonomous valves are capable of shutting off the parts of the well where breakthrough of CO_2 and water occurs.

2 Theory

Many of the oil reservoirs on the Norwegian Continental Shelf have a thin oil layer, and vertical wells will therefore have very little contact surface with the oil phase. If instead a horizontal well is drilled along the oil layer, this gives a much larger contact surface throughout the reservoir.

2.1 Horizontal wells and inflow control

The length of the horizontal wells are often in the range 1-3 km, and the pressure drop in the wells may be significant. Figure 1 shows a horizontal well indicating the inflow positions and the heel and toe locations. The reservoir pressure along the well is constant, whereas the pressure in the well decreases from the toe to the heel due to frictional pressure drop. This phenomenon is called the heel to toe effect, and results in increasing pressure difference between the reservoir and the production pipe from the toe towards the heel, and consequently the driving forces and the production rates are significantly higher in the heel compared to the toe (Birchenko et al., 2010).

To reduce the heel to toe effect and ensure production from all parts of the well, inflow control devices can be installed along the pipeline. In this study, autonomous inflow control valves (AICVs) are used. Figure 2 shows an AICV mounted in the base pipe with a sand screen. There are no restrictions on the number of zones in the

production pipe. This means that the placement of AICVs can be done based on geological adaptations and

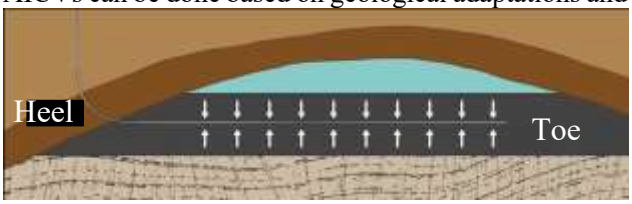

Figure 1. Horizontal well indicating the location of heel, toe and inflow zones.

the requirements of the field in question (Andersen, 2014). The valves are autonomous and do not require any external power or regulation connected to the surface. The valves can be installed in new and mature fields (Well Screen, 2017). The advantage of the AICVs is that they can autonomously close for low viscous fluids such as water and gas and stay open for high viscous fluids like oil. This means that when unwanted fluids reach the zones with high production rates, the AICVs make it possible to close off those zones. At the same time, the production will continue without any restrictions from the other zones. The principle of the AICVs is based on the difference in viscosity and density for different fluids (InflowControl, 2019; Aakre, 2017; Kais *et al.*, 2016). Figure 3 illustrates the AICV in open and closed position.

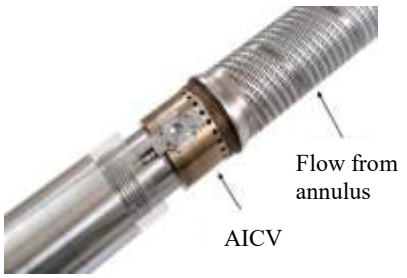

Figure 2: AICV mounted in the base pipe with sand screen.

Figure 3. AICV in open (left) and closed (right) position (Aakre 2017).

2.2 CO_2-EOR

The AICV technology can be used for CO_2-EOR and storage. Previous studies have shown that AICV can be used to shut off carbonated water and supercritical CO_2. Installation of AICV for CO_2-EOR can have an efficiency of up to 99%. AICVs were tested for CO_2-EOR in a vertical pilot well in Canada in 2015. This was the first EOR installation that used autonomous inflow control in combination with CO_2 injection (Kais et al., 2016; Aakre *et al.*, 2018).

CO_2 injection has become more and more common in enhanced oil recovery, especially in North America where natural sources of CO_2 exist. Injected CO_2 will flow into the pores in the rock and expand, and thus more oil is forced to move out of the reservoir. CO_2 can also mix with the oil and reduce the oil viscosity. In addition to these oil production benefits related to CO_2, CO_2 storage in the reservoir after production has stopped is of great importance and can contribute to decrease the emission of CO_2 to the atmosphere significantly (Norwegian Petroleum, 2019; Rostron and Whittaker, 2011).

A big challenge related to CO_2-EOR is reproduction of CO_2 to the production well. Reproduction results in larger costs related to separation and reduced CO_2 storage. When installing AICVs on the pipeline, CO_2 as gas, supercritical fluid or as CO_2 dissolved in water, will be prevented from flowing into the production pipes and the injected CO_2 will be well distributed and remain in the reservoir. This leads to increased oil recovery and contribute to the environmental aspect by CO_2 storage (InflowControl, 2019).

3 Material and methods

In this study, Olga in combination with ROCX is used as the simulation tool.

3.1 Simulation set-up

OLGA is a software developed to simulate multiphase flow in pipelines, and covers modelling and simulation of wells, flowlines, pipelines and equipment from the well to the processing systems (Aakre 2017). ROCX is a three-dimensional near-well model coupled to the OLGA simulator to perform integrated wellbore-reservoir transient simulations. ROCX can simulate three-phase flow in porous media, and is developed to design reservoir models by defining properties of the reservoir including the fluid properties, and specifying the geometry of the reservoir. Parameters describing the reservoir properties are permeability, porosity, fluid viscosities and densities, relative permeability, pressure and temperatures, saturation of the different fluids and initial and boundary conditions. The mathematical models used in ROCX are described in detail in (Schlumberger, 2007). An overview of inputs needed for simulations using ROCX in combination with OLGA is presented in Figure 4. The overview is based on (Aakre, 2017).

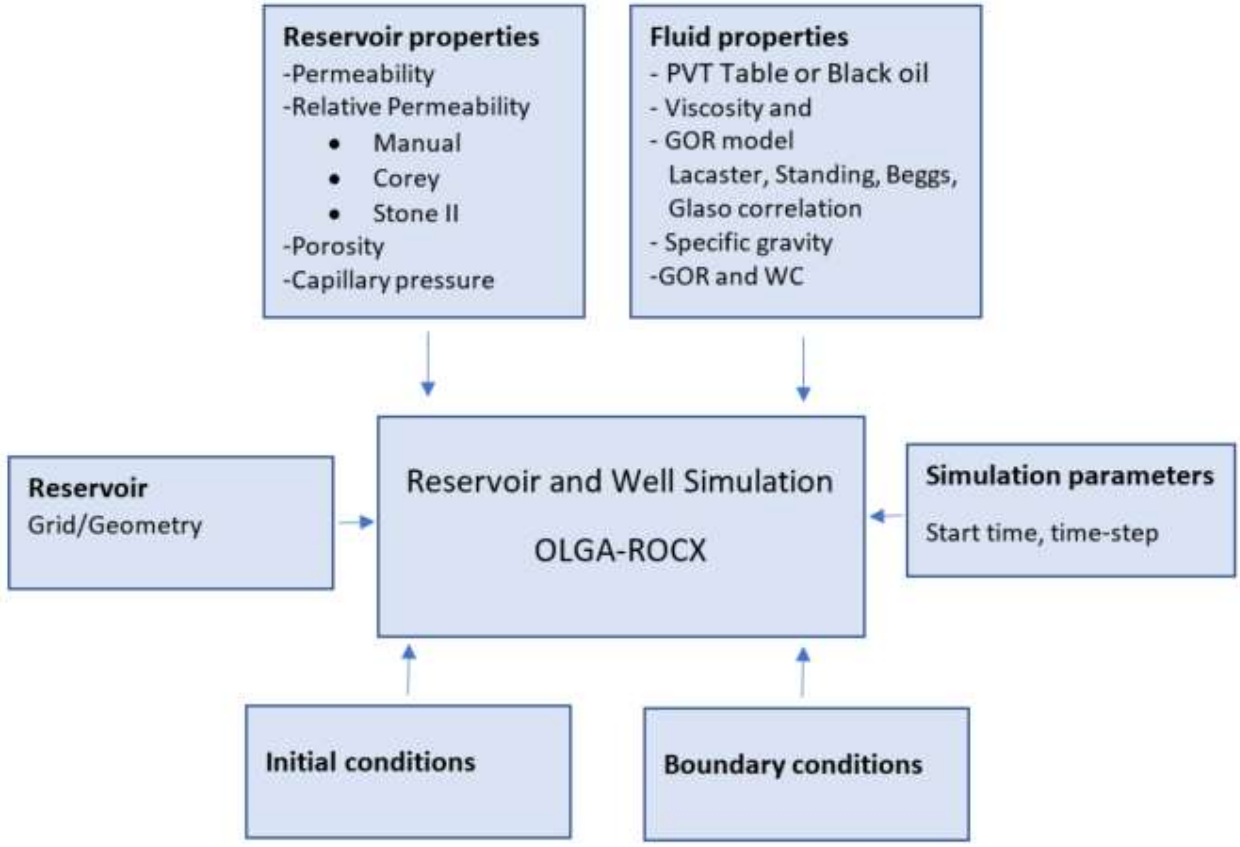

Figure 4. Overview of inputs needed for OLGA/ROCX simulations (Aakre, 2017).

Permeability is a measure for the capacity and capability for a porous rock to transfer fluids. Absolute permeability is a rock property, and describe the transfer of a fluid if the rock is 100% saturated with the actual fluid. The absolute permeability is defined by Darcy's law as:

$$\dot{Q} = \frac{k \cdot A}{\mu} \cdot \frac{dP}{dL} \quad (1)$$

where $\dot{Q}$ is the fluid volume flow, k is the permeability, μ is the viscosity of the flowing fluid, A is the cross section flow area and dP/dL is the pressure drop per unit length. Effective permeability is a measure for the transfer of fluid through a rock when there is more than one fluid present in the pores. The effective permeability is influenced by the wetting of the rock, meaning whether the rock is attracted to water or to oil. Relative permeability is the ratio of the effective permeability of the fluid and the absolute permeability, and is dependent on the saturation of the fluids in the rock.

The coupling between ROCX and OLGA accounts for the dynamic reservoir/wellbore interactions. OLGA is a one-dimensional transient dynamic multi-phase tool used to simulate flow in pipelines and connected equipment. The OLGA simulator is governed by the conservation of mass, momentum and energy equations for each phase (Thu, 2013; Schlumberger, 2007). The set-up in OLGA includes annulus, pipeline, packers and inflow control devices. Figure 5 illustrates the location of the annulus and the pipeline in the reservoir. Figure 6 shows the location of the packers between the rock and the production pipe.

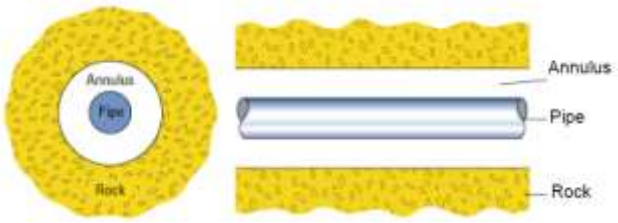

Figure 5: A sketch of the pipe and the annulus (Schlumberger, 2007).

To be able to simulate the flow from the reservoir via the annulus to the pipeline, the set-up shown in Figure 7 was used. The set-up involves two pipelines, the lower one to simulate the annulus and the pipe wall, and

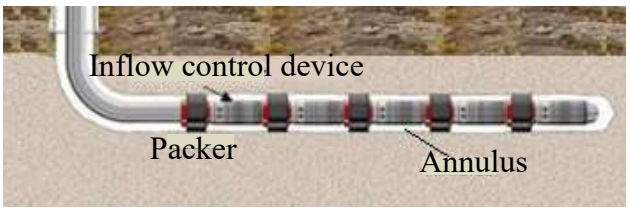

Figure 6. Horizontal well with inflow control devices and packers.

the upper one to simulate the flow and pressure drop in the well. The source (SOURCE 1) simulate the flow from the reservoir to the annulus, the valve (VALVE-1) illustrates an AICV, the leak (LEAK-1) simulate the flow through the AICV to the well, and the valve (PACKER-1) simulate a packer as a closed valve. Packers are used for zone insulation to avoid fluids to flow from one zone in the reservoir via annulus to another zone. This ensures that after breakthrough in one zone, AICV closes and this zone becomes insulated from the other zones. AICV is not an option in OLGA, and therefore it was necessary to build up valves with the same functionality as the AICVs. For that purpose, valves with transmitter and PID controller were used, and the closing and opening function was related to a water cut set point.

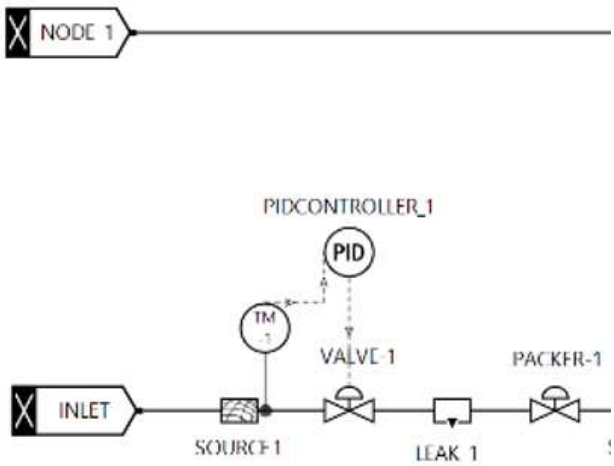

Figure 7. A well section including annulus, well, packers and AICV.

In this study, oil production with CO_2-EOR is compared to oil production without CO_2-EOR. The relative permeability curves for both the cases are plotted in Figure 8. As can be seen from the figure, the relative permeability curves change significantly when CO_2 is injected into a reservoir. Details about the influence of CO_2 injection on the oil properties are described in (Vesjolaja *et al.*, 2016; Badalge *et al.*, 2015). The Corey model is used to calculate the relative permeability for water, and Stoke II is used for the oil phase. The models are described by Schlumberger (Schlumberger, 2007).

The boundary conditions used for the simulations are pressure outlet set in OLGA, and the pressure and location of the water drive specified in ROCX. The location and the conditions for the sources (connection between reservoir and well) are also specified in ROCX. The initial conditions for reservoir saturation and reservoir pressure are specified in ROCX. A sketch of the initial reservoir with 100% oil saturation is presented in Figure 9. The arrow shows the location of the well.

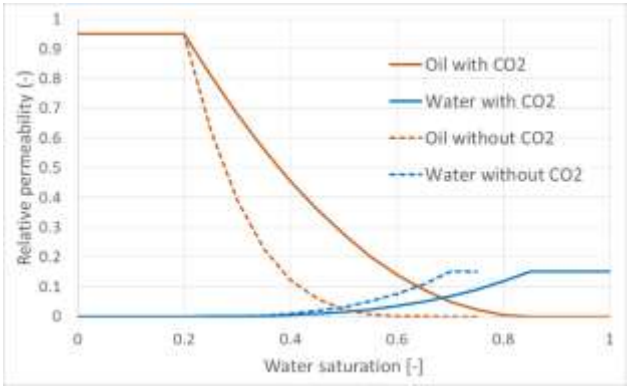

Figure 8. Relative permeability curves for oil and water.

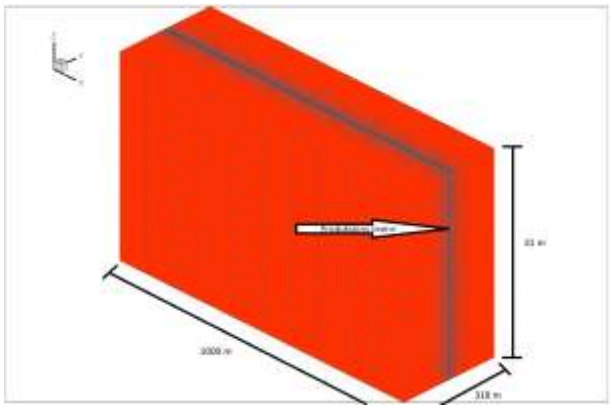

Figure 9. The initial oil reservoir (length 1000 m, width 318 m, height 31 m) as illustrated in Tecplot. The arrow shows the location of the well.

The set-up for the simulations is presented in Table 1. The blackoil model was selected in ROCX and it was assumed that the reservoir was initially saturated with oil. When using the black oil model, injection of CO_2 directly to the reservoir was not possible. In the simulations with CO_2-EOR, this was solved by assuming that CO_2 was already injected in the reservoir before the oil production started. The water in the simulations can therefore be considered as carbonated water. The Lasater model was used for the gas-oil ratio (GOR) calculations.

The well specifications was set in OLGA and are presented in Table 2. The outlet pressure from the well (spesified in the heel) is set to 166 bar. This means that the driving forces in the heel section is 10 bar, and lower in the toe. The cases are either run with passive inflow control devices (ICDs) or autonomous inflow control valves (AICVs). The ICD has a constant opening of diameter 0.028 m, whereas the AICVs has an initial opening of 0.028 m but the opening will decrease and go to about zero as the water production increases. The number of inflow control units in both cases is 10.

Table 1. Characteristics of the reservoir.

Reservoir	Homogeneous, sand stone
Oil viscosity	12 cP
Oil specific gravity	0.895
Porosity	0.33
Permeability	x- and y-directions: 8000 mD z-direction: 800 mD
Area	31.8 km^2
Thickness	31 m
Location of well	Grid 3 from the top in z-direction
Gas Oil Ratio	15 Sm^3/Sm^3
Reservoir pressure	176 bar
Reservoir temperature	76 °C

Table 2. Specification of the well.

Well length	1000 m
Number of sections	20
Diameter well	0.1 m
Pipe roughness	0.1 mm
Number of inflow devices	10
Valve diameter	0.028 m
Outlet pressure	166 bar
Initial frictional pressure drop	7 bar

4 Results and discussion

Table 3 gives an overview of the different cases that are simulated in this study. Case 1 is run without CO_2-EOR and without AICVs. Case 2 is run under the same conditions as Case 1, but with a choke mounted at the outlet of the production pipe. The choke is regulated by a PID which limits the total flow to maximum 1200 m^3/day. In Case 3, AICVs are installed on the pipe wall, and in Case 4 CO_2-EOR is used in addition to AICVs.

Table 3. Overview of the simulation cases.

Case	CO_2-EOR	AICV	Choke
Case1	No	No	Yes
Case2	No	No	No
Case3	No	Yes	No
Case4	Yes	Yes	No

Figure 10 shows a comparison of the accumulated production from Case 1 and Case 2. In Case 1, with no choking of the production rate, the carbonated water production is very high, close to $3 \cdot 10^6$ m^3 and 2.4 times the oil production. This involves that a large separation system is needed to handle the production flow. Most probably, the separation system on a platform in the North Sea is not design to handle these large amounts of liquids. It is therefore important to keep the total flow rate low to avoid overloading of the separation system and to reduce the costs related to separation. By choking (Case 2), the total flow can be adjusted to fit the capacity of the separators on the platform. When the total flow is adjusted to maximum 1200 m^3/day, the water break through is delayed, and the accumulated water production per 1500 days is reduced from $3 \cdot 10^6$ m^3 to about $1.8 \cdot 10^6$ m^3. The accumulated oil production is decreased from $1.25 \cdot 10^6$ m^3 to $1.13 \cdot 10^6$ m^3. This means that the accumulated water production has decreased with about 38% whereas the accumulated oil production has only decreased with about 10% during the 1500 days of production.

When using a choke, the flow from all the zones in the field will be reduced independent on whether they are producing oil or water. This results in less production from the toe where the oil saturation is still high. It is therefore important to utilize technology that can close off or choke the zones with high water production, and at the same time produce unhindered from the zones with high oil saturation. Suitable technology for this purpose is an autonomous inflow control valve.

In Figure 11, the accumulated production from Case 2 (choke) and Case 3 (AICVs) are compared. By using AICVs, the oil production after 1500 days is about the same as in Case 2 (choking of the total flow). However, the water production is further reduced to $1.11 \cdot 10^6$ m^3. The reason is that the AICVs choke or close a zone when it is producing more than 65% water. The closing frequency is illustrated in Figure 12. The closing of the AICVs starts in the heel and the AICVs close one by one towards the toe. After about 1000 days, all the AICVs are nearly closed, and the increase in accumulated oil and water production is low. Compared to Case 2, the oil production rate is about the same after 1000 days, but in Case 2, the water production rate is still high. The high water production in Case 2 after 1000 days, is because when choking the total flow, the production will mainly occur from the zones in the heel section which have the highest water cut the highest driving forces (difference between the reservoir pressure and the well pressure).

To increase the oil production, CO_2-EOR is used in Case 4. CO_2 changes the residual oil and also influence the oil viscosity. This is taken into account in the relative permeability curves. In Figure 13, the oil and water/CO_2 production from Case 3 and Case 4 are compared. Case 3 and Case 4 are both run with AICVs. When injecting CO_2, both the oil and the carbonated water production increase. However, due to the AICVs, the production rates are limited. CO_2-EOR results in an increase in oil production of 16.5% and an increase in water production of 44% relative to the similar case without CO_2.

Although the water production increased more than the oil production, the water cut is still well below 50%, and the water production is low compared to the other cases. Since the CO_2 is assumed to be dissolved in water in this study, a reduction in water production also indicates a significant reduction in the reproduction of CO_2 to the production well.

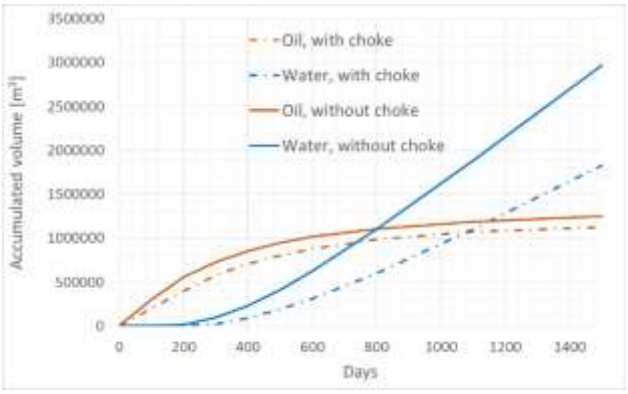

Figure 10. Comparison of oil and water production, Case 1 and Case 2.

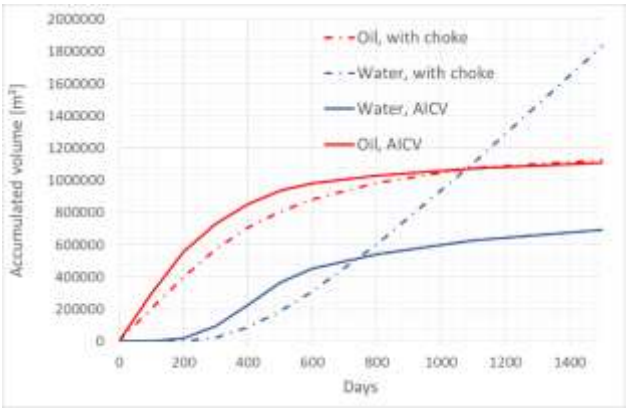

Figure 11. Comparison of oil and water production, Case 2 and Case 3.

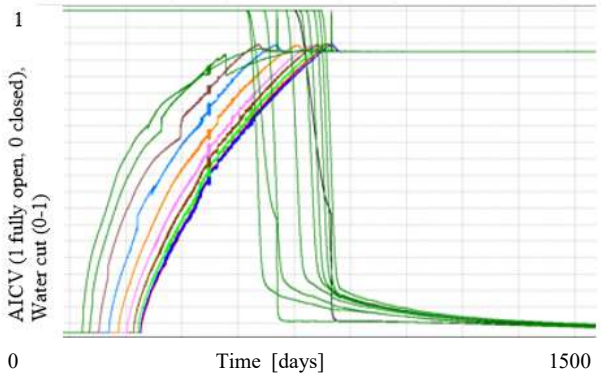

Figure 12. Closing order of the AICVs. Closes at WC 65%.

The results from the four simulated cases are summarized in Table 4. The water breakthrough occurs after about 120 days in Case 1, Case 3 and Case 4 and about 60 days later in Case 2. The reason for the later water breakthrough in the case with choking of the total flow, is that the total flow rate for this case is significantly lower than in the other cases in the early phase of the production. After the water breakthrough, the AICVs start to close, and the total flow rate for these cases will also decrease. Regarding Case 1, without any restrictions on the flow, the flow rate is increasing as the water cut increases. Initially (before water breakthrough) the total production rates from Case 1, Case 3 and Case 4 were equal due to equal diameter of ICDs and AICVs.

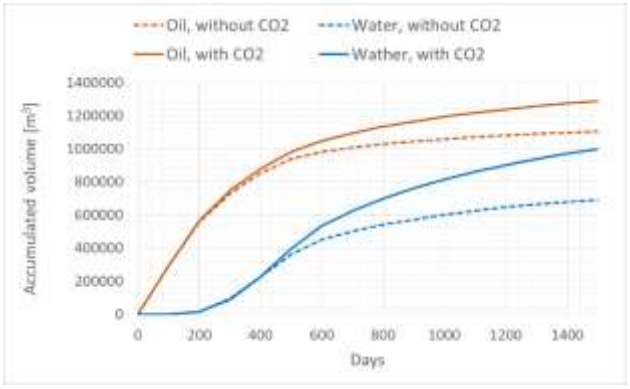

Figure 13. Comparison of oil and water production, Case 3 and Case 4.

Table 4. Summary of simulation results.

	Water break-through	Accumu-lated water [m^3]	Accumu-lated Oil [m^3]	% of oil produced
Case 1	176	$2.98 \cdot 10^6$	$1.25 \cdot 10^6$	29.6
Case 2	120	$1.83 \cdot 10^6$	$1.13 \cdot 10^6$	38.1
Case 3	118	$0.69 \cdot 10^6$	$1.11 \cdot 10^6$	61.5
Case 4	122	$1.0 \cdot 10^6$	$1.29 \cdot 10^6$	56.4

Based on the results, Case 1 is not a relevant case for oil recovery due to the very high water production. Case 1 is also not a realistic case, because the total production rates have to be controlled by a choke to avoid overloading to the downstream separation and processing systems. In future work all the cases should be run with a choke on the total flow in addition to the inflow control devices. The simulation results shows that CO_2-EOR increases the oil production significantly. In addition to CO_2 injection, the results shows that autonomous inflow control devices are necessary to avoid high water production and recirculation of CO_2 to the well.

5 Conclusions

The main objective of this study was to look at the effect of CO_2-EOR on increased oil production and in addition to find a method to avoid reproduction of CO_2 to the

production well. The properties of the oil reservoir are based on information from the Grane field in the North Sea. Four cases were run under different conditions. Simulations were performed using the OLGA and ROCX simulation tools. The production from a homogeneous reservoir was simulated for 1500 days. CO_2-EOR is a good alternative for increasing the oil production from oil fields, but CO_2-EOR also leads to increased water production. When using autonomous valves the oil production was reduced by 11% and the water production was reduced by 77%. This is a significant reduction in the water production and thereby also reproduction of CO_2, which results in a more energy efficient and environmentally friendly oil production. The simulations also showed that it is crucial to install choke with PID regulator to control the total flow rate.

References

A. Aabø. Reservoarformasjonenes porøsitet og permeabilitet, 10. Okt. 2017. Accessed on: 24. Jan. 2019 Available: https://ndla.no/subjects/subject:6/topic:1:182061/topic:1:155237/resource:1:157664, 2017

H. Aakre, V. Mathiesen, and B. M. E. Moldestad. Performance of CO2 flooding in a heterogeneous oil reservoir using autonomous inflow control, Journal of Petroleum Science and Engineering, 167 (2018): 654–663, 2018.

H. Aakre. *The impact of autonomous inflow control valve on increased oil production and recovery,* PhD thesis, University of South-Eastern Norway, 2017.

I. Andersen. Inflowcontrol øker oljeutvinningen med hundrevis av selvregulerende ventiler, 2014. Available in: https://www.tu.no/artikler/inflowcontrol-oker-oljeutvinningen-med-hundrevis-av-selvregulerende-ventiler/231923.

L. J. Badalge and B. M. Halvorsen. Near well simulation of CO_2 injection for Enhanced Oil Recovery (EOR), In *Linköping Electronic Conference Proceedings* 2015 (119): 309-318, 2015.

V. Birchenko, K. Muradov, and D. Davies. Reduction of the horizontal well's heel–toe effect with inflow control devices, Journal of Petroleum Science and Engineering, 75(1/2): 244-250, 2010.

O. Bolland. Klimagasser må fanges og fjernes. 2016. Available in: https://energiogklima.no/to-grader/klimagasser-ma-fanges-og-fjernes/

H. P. Well Screen. 2015. Available in: http://deutecs.com/onewebmedia/PP_HPWS%20Product%20line%20wc%202017.pdf

Inflowcontrol. AICV® for CO_2 EOR. 2016. Available in: https://www.inflowcontrol.no/aicv-product-range/co%C2%B2-catcher/

International Energy Agency. Carbon, capture utilisation and storage. 2019. Available in: https://www.iea.org/topics/carbon-capture-and-storage/storage/

R. Kais, V. Mathiesen, H. Aakre, G. Woiceshyn, A. Elarabi, and R. Hernandez. First autonomous inflow control valve AICV well completion deployed in a field under an EOR water & CO_2 injection scheme, *SPE Annual Technical Conference and Exhibition.* Society of Petroleum Engineers, 2016.

S. Kallbekken and I. U. Jakobsen. Paris avtalen, *Store Norske Leksikon,* 2018.

Schlumberger, ROCX Reservoir Simulator, 1.2.5.0 ed, 2007.

E. S. Thu. In *Modeling of transient CO2 flow in pipeline and well*, Master Thesis, Norwegian University of Science and Technology, 2013.

United Nations Climate Change. Report of the Conference of the Parties on its twenty-first session, held in Paris 30.11.2015-13.12.2015, Action taken by the Conference of the Parties at its twenty-first session, 2015.

L. Vesjolaja , A. Ugwu, A. Abbasi, E. Okoye, and B. M. E. Moldestad. (2016) Simulation of CO_2 for Enhanced Oil Recovery, In *Proceedings of the 9th EUROSIM & the 57th SIMS,* Oulu, Finland, 2016

S. Whittaker, B. Rostronb, C. Hawkesc, C. Gardnerd, D. Whitee, J. Johnsonf, R. Chalaturnykb, and D. Seeburgerg. A decade of CO_2 injection into depleting oil fields: monitoring and research activities of the IEA GHG Weyburn-Midale CO_2 Monitoring and Storage Project, *In Energy Procedia,* 4: 6069-6076, 2011.

Control of waste water treatment combined with irrigation

Erik Dahlquist[1] Eva Nordlander[1] Eva Eva Thorin[1] Anders Wallin[1,2] Anders Avelin[1,2]

[1]School of Business, Society and Engineering, Future Energy Center, Mälardalen University, Västerås, Sweden
[2]ABB Process Industries AB, Västerås, Sweden

Abstract

In waste water treatment using biological treatment processes normally phosphorous, nitrous compounds as well as organic matter are removed. It is also important to remove or kill pathogens that otherwise could cause diseases. The surplus of bio-sludge is used to produce biogas. In the paper four different alternatives for system design and operations of systems was discussed. The alternatives integrate the waste water treatment and irrigation of farmland using the water taken out from different positions in the waste water treatment plant.

Keywords: waste water treatment, farming, irrigation, control.

1 Introduction

Irrigation is becoming more important globally as water has become a scarce resource. By using waste water (WW) the nutrients in the wastewater (phosphorous and nitrogen-compounds) can be used as fertilizers. At the same time it is necessary to manage pathogens as well as toxic substance to avoid spreading diseases and harmful substances through the crops. The water can be taken out at different positions in the Waste water treatment plant (WWTP). Depending on the demand of water respectively nutrients different outtakes can be feasible during different situations over the yea.

In Figure 1, several different layouts have been made for different options for waste water treatment. The first step is pre-sedimentation treatment where solid material is settled. A precipitating agent, such as $FeCl_3$, could added to be able to separate smaller particles.

Addition of a precipation agent may lead to a deficiency of carbon for the later activated sludge process. Extra carbon source can be from either reject water or addition of e.g. methanol or glycol. This will enhance the denitrification in the activated sludge (AS) step. Most of the PO_4 will be removed in the form of $FePO_4$. This will be digested in the anaerobic digester, but still most of the phosphorous (P) will be removed as $FePO_4$ in the residues after the digestion.

If no metal salt is added, only large particles will be removed, there is still several alternatives for the following process steps. There could be either an anoxic or anaerobic steps followed by aeration. This will be good both for biological removal of P and N compounds as well as denitrification in the aerobic step. To build as much PO_4 as possible into biomaterial, microalgae could be included, as algae are good at incorporating the PO_4 (Anbalagan et al., 2017). The microalgae also produce O_2, which would reduce the demand for aeration. The drawback is that microalgae need sunlight or artificial lighting and the reaction rate might also be lower. Microalgae was not included in this, although it might be interesting in the future.

The sludge is normally separated after the biological processes and part of it recirculated, while the rest is anaerobically digested to produce biogas (which consist mostly of methane). The sludge can either be concentration before or after the digestion. The resulting liquid, can either be recirculated to before the biological processes, or first be treated with e.g. nano- or reverse osmosis filtration. Filtration can be organic acids (NF) or even ammoniac (RO). The permeate water will be quite lean and not add burden to the biological processes. Levlin and Hultman (2010) have described how PO_4 could be recovered by precipitating it with CaO to form $CaPO_4$. This could be an alternative for storing PO_4 in a compact way. Toomiste et al (2010) have followed TP (total P) respectively DP (Dissolved P) through the different processes in the WWTP. Of the TP in the reject water from the digester 90% is dissolved, and thus in the liquid phase. Morse et al (1998) shows that anaerobic conditions can release the biologically bound PO_4.

Concerning nitrogen balance Kanders (2019) has studied both normal activated sludge processes and those with anammox-bacteria. It is assumed that approximately 40 % of the incoming NH_4 is built in to the sludge microorganisms, while 40% is removed to air as N_2. If anammox is used half of the electricity demand of the aeration could be, however a solid matrix where the bacteria can grow and form a film is needed. Kanders (2019) has primarily investigated how the anammox can be utilized for the reject water where the concentrations of ammonium is high and the volume flow much lower (only approximately 1% of the in-flow). To combine WWT with irrigation water and sludge can be taken out from different positions in the WWT process. Most heavy metals should be in the solute. It would be interesting to wash the filter cake to wash out the metal ions. These then can be removed by absorption in e.g. an ion-exchanger.

In the denitrification, also N2O may be formed. By controlling the pH to above 7.6 almost no N_2O was formed while a lot was formed at pH6 according to Desloover et al (2012) and Kanders (2019). The solid residues after the fermentation also should be recirculated to the farmland.

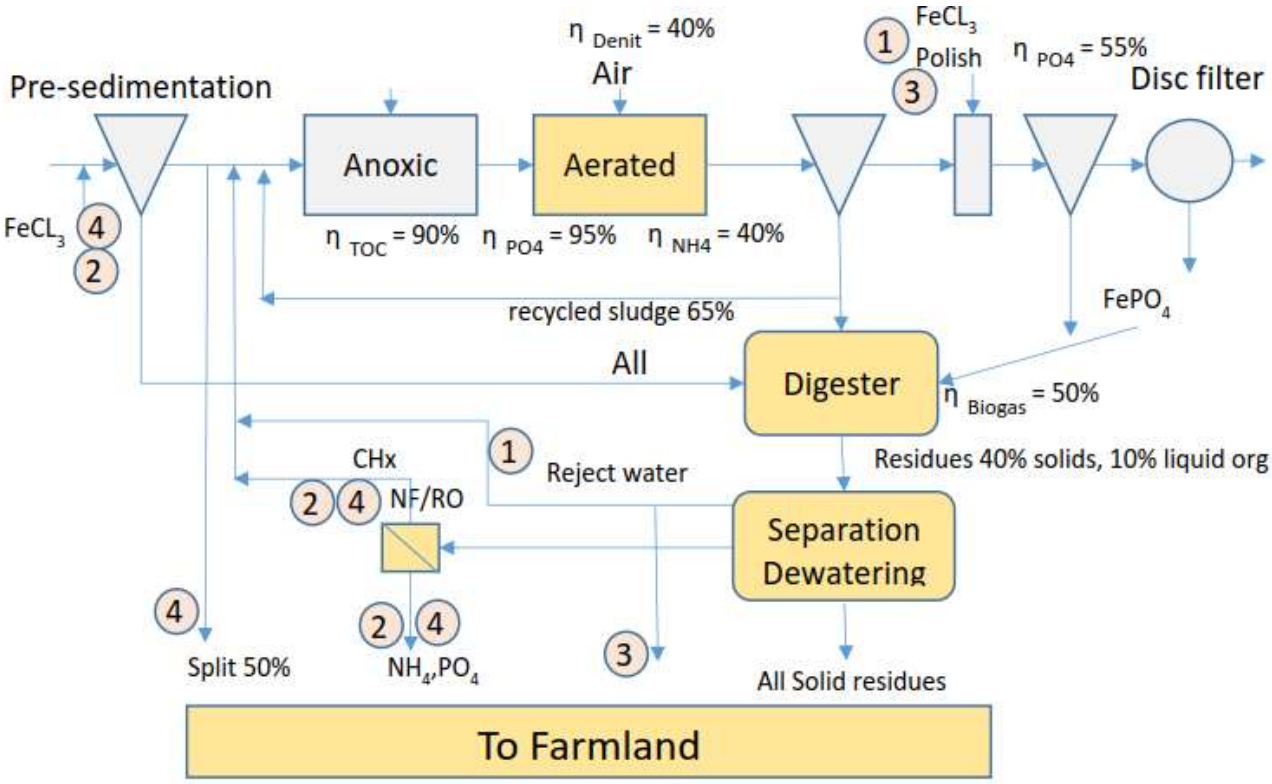

Figure 1. A general layout of four different cases for a WWTP.

2 Modelling

From a modeling perspective primarily material and energy blanaces has developed. They are in reality semi steady state as steady state balances are calculated for a given inflow of water and TOC (Total Organic Carbon), TP and TN (Total Nitrogen). For different situations a new balance is calculated. In this paper four different cases have been studied.

This includes continuity equations for massflow (m) times concentration (x) for each stream in (n) and stream out (k):

$$\sum_i^n m_{i,in}x_{i,in} = \sum_i^k m_{i,out}x_{i,out} \quad (1)$$

The energy used in activated sludge processes are mainly electricity for aeration. In (Mizuta and Shimada, 2010) a benchmark has been made for different wastewater treatment plants (WWTP) and found that in Japan 0.30-1.89 kWh/m3 was used for aeration. The main difference was depending on the size of the plant, and thereby the efficiency. Soares et al. (2017) present the figure 0.3-0.6 kWh/m3 in conventional activated sludge processes, which is in the lower range of what Mizuta and Shimada presented, for WWTPs in Brazil. Enerwater (2015) reports that 1% of electric power in Germany is for WWT in some 10 000 WWTPs. The study included 369 WWTPs in EU, representing the treatment of about 15,742,816 PE and a total energy consumption of 1,736,735 kWh/day, was performed. Assumption was 120 gCOD/(PE*d) in EU and 160 gCOD/PE in the US. A specific energy use of 0.13 kWh/m3 was found for larger plants, while for smaller plants values up to 5.5 kWh/m3 could be seen. 2000 kWh/(PE*y) could be for smaller plants, while larger plants have in the range 20 to 60 kWh/(PE*y). This can be summarized in some key values for big WWTPs: 0.28-0.61 kWh/m3 , 27.4-47.9 kWh/PE*y and 0.55-1.10 kWh/kgCODrem.

A value of value 0.55 kWh/kg COD was used, which means approximately 1,8 kWh/kg TOC if the following conversion formula is used

$$COD = 49.2 + 3*TOC \quad (2)$$

from Dubber and Gray (2010). They have developed this from a number of different influent water. The electric demand is then

$$kWel = kg\ biomass\ TOC/s * 1.8\ kWh/kg\ TOC. \quad (3)$$

For biogas production it was assumed that the biomass to have the formula $C_5H_7O_2N + PO_4$ and the

energy content in the biomass is 21.2 MJ/kg. Sludge is taken to a digester where anaerobic fermentation convert approximately 50% (η_{biogas} = 0.5) of the organic material to biogas, which was assumed to consist of 65% CH_4 and 35% CO_2.

$kWCH_4$ = kg biomass TOC to digester/s*η_{biogas}*0.65. (4)

The water flow has just been given for the in-flow, as the concentrations can vary a lot. As there will always be cleaned effluent water that can be used, this is not a limiting resource and thus is neglected in the mass balances.

The mass balance has been evaluated for the four different cases based on assumption of 3600 m^3/h (3600 ton/h) inflow water and the following values have been used for separation or reactivity efficiencies: $\eta_{pre,TOC}$, $\eta_{Pre,PO4}$ and $\eta_{pre,NH4}$ = 20% case 1, 3 and 4, while 35% for case 2 with $\eta_{pre,PO4}$>95%; $\eta_{AS,TOC}$ = 90%; $\eta_{AS,PO4}$ = 95%, $\eta_{AS,NH4,sep}$ = 40%, $\eta_{AS,NH4,denit}$ = 40%, sludge recirculation 65%. In Figure 1, we also see the flows that differentiate the four cases.

3 Studied cases

Four different cases were studied, with wastewater from different positions in the WWTP. An inflow of 1 m3/s was used (corresponding to 500 000 PE) with 224 mgTOC/l or 720 mgCOD/l in the inflow. The four cases are described below:

Case 1: This is the reference case without addition of $FeCl_3$ to the pre-treatment step, but with polishing with $FeCl_3$ after the activated sludge. All reject water is recycled back before the AS.

Case 2: In this case, $FeCl_3$ is added before the pre-sedimentation to precipitate most of the PO_4 and significant amount of TOC and NH_4 as well. This is sent to fermentation. Reject water from the separation after the digester is filtered in a nano membrane filter and organics is recycled to the AS while permeate with PO_4, K and $NH_4$is sent to the farmland. Totally treated water is used for irrigation as much as needed with low risk for polluting crops, but also we do not add any burden from reject water with respect to NH_4 and PO_4 to the AS in the WWTP.

Case 3: No pre-precipitation with $FeCl_3$ before pre-sedimenation, but addition after the AS for polishing. Use of reject water from the fermentation directly to the farmland. Here it should also be possible to remove heavy metals if needed from the liquid phase before distribution to the farmland.

Case 4: Take out a significant part of influent water (50%) after the pre-sedimentation, after addition of $FeCl_3$. Infectious microorganisms might be a problem if spread to growing plants if infectious species survive. Though low temperature or sun light at the field should kill most. Reject water is filtered in a membrane filter. Hydrocarbons are recycled from reject water (reject), while the permeate with NH_4, PO_4 and K is distributed to the farmland.

For cases 1 and 3, a pre-separation of coarse material without any chemical addition was assumed, but with addition of $FeCl_3$ in case 2 and 4. Pre-separation was followed by an activated sludge (AS) process with anoxic and aerated vessels and after that sedimentation. 65% of the sludge is recirculated while 35% goes to biogas production in an anaerobic digestion process. The sludge after the digestion goes to farmland after dewatering. The reject water after separation (press or centrifuge) goes back to the AS process in case 1, but is separated in a NF (+ RO) -filter in cases 2 and 3. The filtrate from the NF filter goes to farmland. If there is a RO filter after the NF, the reject from the NF goes to the AS as a carbon source in case 2 (where there otherwise will be a deficiency of organics), while the permeate goes back to the process or is used as irrigation water (this will be pathogen free, and can be used also for vegetables). In case 3 the reject water goes back directly to the farmland without any NF/RO. The efficiency η in the different process steps are seen also in Figure 1. The following values has been used for the efficiencies: $\eta_{pre,TOC}$, $\eta_{Pre,PO4}$ and $\eta_{pre,NH4}$ = 20% for cases 1, 3 and 4, while 35% for case 2 with $\eta_{pre,PO4}$>95%; $\eta_{AS,TOC}$ = 90%; $\eta_{AS,PO4}$ = 95%, $\eta_{AS,NH4,sep}$ = 40%, $\eta_{AS,NH4,denit}$ = 40%, sludge recirculation 65%. Figure 1 illustrates the different flows for the four cases.

There is also one other issue to consider. Aside of N_2 also N_2O may be formed in the biological process? By controlling the pH to above 7.6 almost no N_2O was formed while a lot was formed at pH = 6 (Desloover et al., 2012; Kanders, 2019).

4 Results and discussion

The mass balance for the four cases 1-4 can be seen in Table 1. In Figure 2, data from Table 1 are presented for the four cases with one variable at a time, sorting from highest to lowest value. The hydrocarbons sent to the farmland will be much higher (516 kgTOC/h) for case 4 than the other three cases (310-336 kgTOC/h), but less methane will be produced.

From Figure 2, it can can seen that there is more TOC in the organic effluent from case 4 but much more P in cases 1 and 3, and more N-NH_4 in case 1. Case 2 and 4 will have significantly lower emissions of PO_4 while case 2 is best for N-removal and case 4 best with respect to TOC in the effluent. On the other hand, the phosphate will be more biologically active in the soil at the farmland in cases 1 and 3, as most is taken up in the biomass, and then released in the anaerobic fermentation. The $FePO_4$ can be too stabile for efficient use in farming as a fertilizer, while the Phosphor bound in the cells is much easier to release.

Table 1. Material balance for the four operational/configurational cases from simulation.

	total flow	C5H7O2N				PO4				N-comp			
	kg/h	kg TOC/h	FeCl3 at pre-sep			kgTP/h				kg NH4/h			
		case 1	case 2	case 3	case 4	cas1	case 2	case 3	case 4	case 1	case 2	case 3	case 4
Feed water	3600000	806	806	806	806	12	12	12	12	147	147	147	147
pre-sep	η_{pre} =	0,20	0,35	0,20	0,35	0,20	0,90	0,20	0,90	0,20	0,35	0,20	0,35
separated (sludge)		161	282	161	282	2,3	10,4	2,3	10,4	29	52	29	52
left to AS		645	524	645	524	9,22	1,15	9,22	1,15	118	96	118	96
AS total load		1023	831	1023	831	14,91	1,86	14,91	1,86	148	121	148	121
Split before AS					0,50				0,5				0,5
to Farmland					262				0,576				48
left to AS incl sludge recycle					432				0,9504				79
sludge sep eff η_{AS} =		0,900	0,900	0,900	0,900	0,95	0,95	0,95	0,95	0,4	0,4	0,4	0,4
denitrific eff $\eta_{AS,DENIT}$ =										0,4	0,4	0,4	0,4
left after AS (water)		102	83	102	43	0,75	0,09	0,75	0,05	30	24	30	16
sludge (CH,P,NH4)		920	748	920	389	14,16	1,77	14,16	0,90	59	48	59	32
NH4 removed as N2										59	48	59	32
NH4 into sludge										59	48	59	32
Sludge recycle %		0,650	0,650	0,650	0,650	0,65	0,65	0,65	0,65	0,65	0,65	0,65	0,65
Sludge recycle		598	486	598	253	9,20	1,15	9,20	0,59	39	31	39	21
Sludge to fermentation		322	262	322	136	4,96	0,62	4,96	0,32	21	17	21	11
total sludge to fermentatior		540	565	540	442	7,86	11,00	7,86	10,72	67	82	67	71
% conversion to biogas		0,50	0,50	0,50	0,50								
% CH4 of biogas		0,65	0,65	0,65	0,65								
% org in liquid		0,10	0,10	0,10	0,10	0,91	0,91	0,91	0,91	0,9	0,9	0,9	0,9
CH4 produced		175	184	175	144								
CO2 produced		94	99	94	77								
Residue to farmland		310	325	310	254	0,72	1,01	0,72	0,98	6,66	8,17	6,66	7,13
Reject water		54	56	54	44	7,14	9,99	7,14	9,74	60	74	60	64
Polish sep effic η_{POLISH} =		0,55	0,25	0,55	0,55	0,8	0,1	0,8	0,8	0,55	0,55	0,55	0,55
left to effluent		46	62	46	19	0,15	0,08	0,15	0,01	13,4	10,9	13,4	7,1
sludge to fermentation		56	21	56	24	0,60	0,01	0,60	0,04	16,3	13,3	16,3	8,7

For electricity, the dfference is relatively small although higher for cases 1 and 3, while methane production is lowest in case 4, where a lot of the organics is sent to farmland directly, as seen as TOC/h to farmland. Concerning P to farmland as well as N-NH_4 case 1 has the lowest distribution while in case 4, the highest on especially NH_4.

All four cases can be implemented in the same WWTP with only small modifications, and in reality it is possible to switch between the different operational modes. It is mostly the addition of the nano membrane filter that differ this plant from “normal ones”. This can be useful when it comes to optimization related to the use of water for irrigation and addition of “natural” fertilizers as especially dissolved NH_4 and PO_4. Cases 1, 2 and 3 can absolutely be implemented while case 4 may be sensitive from a hygienic perspective. This water should not be distributed in crops close to harvest, to avoid risks for spreading infectious diseases. It is not only possible to switch between the different alternatives, but also variants in between can be used.

The optimization should be made to fulfill the crop demand as far as possible. In Figure 3, an example of demand and supply of water respectively supply of water and nutrients can be seen. The water can be cleaned effluent to meet the water demand, while the nutrient supply is covered by operating the plant as suitable with the different operational modes in the four cases. You first cover the nutrient demand, and then fill up with cleaned water to fulfil the water demand. When the crops are very small irrigation is important. Later on nutrient will be more important to stimulate the growth rate. By switching between the different alternatives water with different amount of nutrients can be taken out, depending on these different demands over the growth season. If the NH_4 and PO_4 should be used far away from the WWTP, it might be interesting to precipitate these with MgO or CaO. The product then could be transported and stored in a relatively compact way Levlin and Hultman (2003) indicate an efficiency of at least 60% for Magnesiumammoniumphosphate can be achieved fromreject water. The electricity demand and the production of biogas are two other variables to include in an optimization to govern what alternative to use at different times depending on the value of electricity respectively methane during different situations.

The control can be based on mass balance simulation of the process that can be made on-line continuously. By combining this with prediction of demands from the farmland production and distribution, plans can be made for how to optimize both plant operation and irrigation. By combining with cost calculations for chemicals,

electricity and value of biogas and nutrients produced economic optimization could also be made.

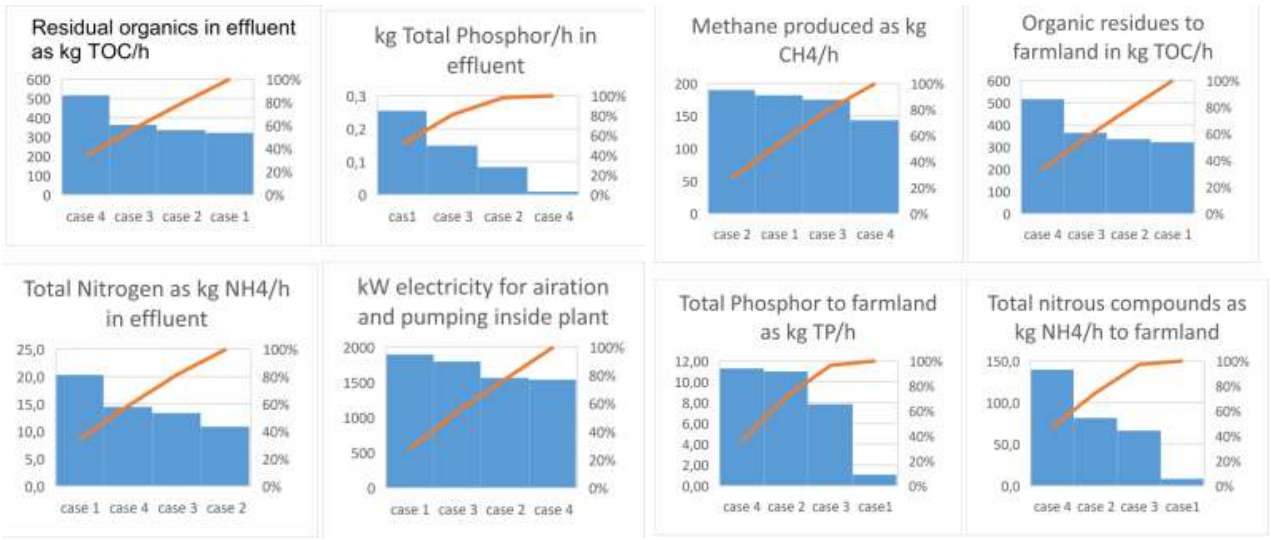

Figure 2. Comparison between the four cases with respect to effluent levels respectively distribution to farmland of TOC, PO_4 and NH_4 as kg/h. Also kW electricity demanded and biogas produced as kg CH_4/h.

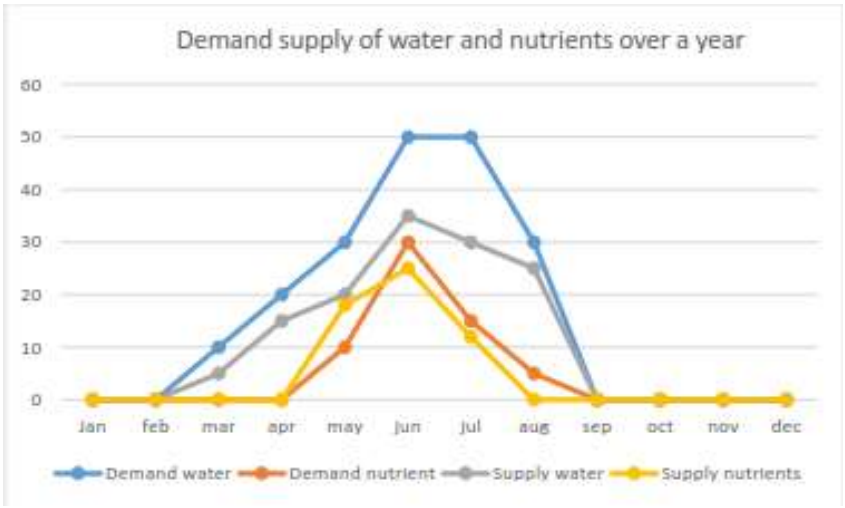

Figure 1. Three different causal loops identified by the conceptualized simulation model.

5 Conclusions

In this paper it was discussed how the WWTP can be controlled for irregation with respect to different ways of operations by simulating different ways of operations. These varying operations mode can be determined from the demand for water respectively nutrients like NH_4 and PO_4 over the growth season. The simulation can be made on-line for continuously follow the balances. By combining this with prediction of demands from the farmland production and distribution, plans can be made for how to optimize both plant operation and irrigation. By combining with cost calculations for chemicals, electricity and value of biogas and nutrients produced economic optimization can also be made.

References

A. Anbalagan, S. Schwede, C. F. Lindberg, and E. Nehrenheim. Continuous microalgae-activated sludge flocs for remediation of municipal wastewater under low temperature. In *1st IWA Conference on Algal*.

Tchnologies for Wastewater Treatment and Resource Recovery, UNESCO-IHE, Delft, Netherlands, 2017.

D. Dubber and N. F. Gray. Replacement of chemical oxygen demand (COD) with total organic carbon (TOC) for monitoring wastewater treatment performance to minimize disposal of toxic analytical waste. *J Environ Sci Health A Tox Hazard Subst Environ Eng.*, 45(12):1595-600, 2010. doi: 10.1080/10934529.2010.506116.

Enerwater. *Standard method and online tool for assessing and improving the energy efficiency of waste water treatment plants*, H2020-EE-2014-3-MarketUptake, 2015.

Linda Kanders. *Start-up and operational strategies for deammonification plants*. PhD thesis, Malardalen University Press, June 2019.

E. Levlin and B. Hultman. Phosphorus recovery from phosphate rich sidestreams in wastewater treatment plants, 2003. https://www.kth.se/polopoly_fs/1.650637.1550156562!/JPS10s47.pdf

K. Mizuta and M. Shimada. Benchmarking energy consumption in municipal wastewater treatment plants in Japan. *Water Sci Technol.,* 62(10):2256-2262, 2010. doi: 10.2166/wst.2010.510.

G. K. Morse, S. W. Brett, J. A. Guy, and J. N. Lester. Review: Phosphorous removal and recovery technologies. *The science of total environment,* 212: 69-81, 1998.

Renan Barroso Soares, Marina Santos Memelli, Regiane Pereira Roque, Ricardo Franci Gonçalves. Comparative Analysis of the Energy Consumption of Different Wastewater Treatment Plants. *International Journal of Architecture, Arts and Applications*, 3(6): 79-86, 2017.

Hillar Toomiste, Jüri Haller, Mait Kriipsalu, and Valdo Kuusemets. Phosphorus balance at Tartu wwtp,estonia. *Conference proceedings Linnaeus ECO-TECH ´10 Kalmar*, Sweden, November 22-24, 2010.

J. Desloover, S. E. Vlaeminck, P. Clauwaert, W. Verstraete, and N. Boon. Strategies to mitigate N_2O emissions from biological nitrogen removal systems. *Curr. Opin. Biotecnology* 23: 474-482, 2012. doi: 10.1016/j.copbio.2011.12.030.

Constantinos C. Pantelides. The Consistent Initialization of Differential-Algebraic Systems. *SIAM Journal on Scientific and Statistical Computing*, 9(2): 213–231, 1988.

Simulation of Dew Points in Raw Biogas Using PR and SRK Equations of State

Terje Bråthen[1] Lars Erik Øi[1] Jon Hovland[2]

[1]Department of and Process, Energy and Environmental Technology, University of South-Eastern Norway
[2]SINTEF Tel-Tek, SINTEF Industry, Porsgrunn, Norway

lars.oi@usn.no

Abstract

Biogas contains mainly methane, but raw biogas can contain large amounts of CO_2 and is normally saturated with water. Condensation, especially during compression, may lead to operational problems. The aim of this work is to calculate the dew point (condensation limit) under different conditions with different models in the simulation programs Aspen HYSYS and Aspen Plus. Binary coefficients for water and CO_2 in these models will be fitted to experimental data from the literature. Traditionally, gas mixtures of methane, CO_2 and water are calculated with standard models like Peng-Robinson (PR) and Soave-Redlich-Kwong (SRK). For dry biogas (mixtures with only methane and CO_2) all the models give similar results. For a biogas mixture with 60 mol-% methane and 40 mol-% CO_2 with 0.1 mol-% added water, the models using binary coefficients fitted for binary mixtures (especially for CO_2 and water), gave reasonable results up to about 70 bar, with deviations in the calculated dew point up to 8 K. The binary coefficient for water and CO_2 was fitted to experimental data from the literature for a mixture with a CH_4 to CO_2 molar ratio of 30/70, 50/50 and 70/30. The fitted k_{ij} values for the PR model were 0.65, 0.21 and 0.17, respectively. For the SRK model, the k_{ij} values were slightly higher. At pressures below 70 bar and temperatures below 40 °C, the uncertainty for calculated dew-points in mixtures with 30 to 100 % CH_4 was reduced to less than 4 K.

Keywords: CO_2, methane, water, biogas, phase envelope, Aspen HYSYS, Aspen Plus

1 Introduction

Bio-methane (purified biogas) contains typically 97 mole-% methane. Raw biogas typically contains 60 % methane, 40 % CO_2, small amounts of other components and water. The temperature where the water starts to condense from a gas is called the dew point. It is important to be able to estimate this temperature because CO_2 and water in the liquid phase is very corrosive, and may lead to operating problems. (Hovland, 2017) and (Øi and Hovland, 2018) have discussed under which conditions water containing biogas will condense under compression.

In their simulations all the models gave similar results up to about 70 bar, and some deviations above 70 bar. However, these simulations were not compared with experimental data.

Gas mixtures of methane, CO_2 and water are calculated in a process simulation program with standard models like PR (Peng and Robinson, 1976) and SRK (Soave, 1972). When using fitted binary parameters (e.g., k_{ij} parameters) these models simulate the gas phase and the condensation point reasonably accurately (within a few degrees) at least below the critical point (46 bar for methane and 74 bar for CO_2).

Equilibrium models like HV (Huron and Vidal, 1979), TST (Twu *et al*., 2005) have been shown to give more accurate results, however they have more parameters which are normally not available in simulation programs like Aspen HYSYS or Aspen Plus. Other models with several parameters like SAFT-VR (Al Ghafri *et al*., 2014) and CPA (Austegard *et al*., 2006) have also been used to describe this system.

There is a limited number of articles available studying the calculations and models for vapour/liquid equilibrium in the methane/CO_2/water-system (Austegard *et al*., 2006; Privat and Jaubert, 2014; Al Ghafri *et al*., 2014; Legoix *et al*., 2017). Austegard *et al*. conclude that a simple equation of state like SRK is satisfactory to describe the vapour phase, but more complex models, e.g., SRK combined with a HV model is necessary to describe the liquid phase (Austegard *et al*., 2006).

Several authors have studied models for the system CO_2/water (Spycher *et al*., 2003; Longhi, 2005; Aasen *et al*., 2017). For high concentrations of CO_2, it is possible to obtain two liquid phases (water rich and CO_2-rich) in addition to a vapour phase. This will not occur when the CH_4 content is higher than 0.225 in the vapour phase (Bi *et al*., 2013; Legoix *et al*., 2017).

Water solubility in CO_2 gas or a mixture of CO_2 and methane shows a minimum for a constant temperature between 50 and 100 °C at a pressure in the range of the

critical pressures (Austegard *et al*., 2006; Aasen *et al*., 2017; Privat and Jaubert, 2014). For this system, a minimum solubility is equivalent to a maximum dew point temperature. The water solubility in pure CH_4 is close to constant over a large pressure range close to the critical pressure (Privat and Jaubert, 2014).

Below 0 ºC, liquid water will turn into solid ice, and hydrates may also be formed. Hydrates in equilibrium in this system have been observed up to 13 °C (Al Ghafri *et al*., 2014) but will probably not be a problem above 0 °C. There are several sources for experimental data for solubility of CH_4 and CO_2 in water (Dhima, 1999; Qin, 2008), but this is of minor interest when the main interest is in the dew point calculations.

Little experimental data has been published for the dew point (condensation limit) in the ternary system methane/CO_2/water. (Song *et al*., 1990) have published experimental data for water solubility in a mixture with 5.7 mol-% CH_4 in CO_2. (Jarne *et al*., 2004) have published data for mixtures with a molar ratio 30/70 and 80/20 for CH_4/CO_2.
(Al Ghafri *et al*., 2014) present dew point data for a water containing mixture of a 50/50 mixture of CH_4 and CO_2 at temperatures above 50 ºC.

The first aim of this work is to calculate the dew point for raw biogas under different temperature, pressure and gas composition (main emphasis in the region of 30 to 100 % CH_4 and in the temperature range 0-50 ºC) using different equilibrium models. It is of particular interest to evaluate whether fitting data to the ternary mixture would increase the accuracy compared to using binary coefficients from only binary systems.

2 Simulation Programs and Models

(Øi and Hovland, 2018) used the commercial simulation program Aspen HYSYS for dry biogas (CH_4 and CO_2) and for mixtures also containing water. The equilibrium models SRK (Soave, 1972), PR (Peng and Robinson, 1976) and TST (Twu *et al*., 2005) were used. In this work also the program Aspen Plus is used mainly with PR, SRK, but also some other models were tried.

The advantage with PR and SRK is that both the models and fitted binary parameters are usually available in the program.

The PR and SRK models have only one adjustable parameter for each binary component pair, but this parameter may be temperature dependent.

The equations for the SRK equation of state are shown in (1) to (8) from Aspen HYSYS Version 10. Aspen HYSYS and Aspen Plus Version 10 were used in the simulations.

Other process simulation programs like ProVision, ChemCad and ProMax also have PR and SRK and often other thermodynamic models available.

$$p = \frac{RT}{v-b} - \frac{a}{v(v+b)} \quad (1)$$

$$b = \sum_{i=1}^{N} x_i b_i \quad (2)$$

$$b_i = \frac{0{,}08664 R T_C}{p_c} \quad (3)$$

$$a = \sum_{i=1}^{N}\sum_{j=1}^{N} x_i x_j \left(a_i a_j\right)^{0{,}5}\left(1 - k_{ij}\right) \quad (4)$$

$$a_i = a_{ci}\alpha_i \quad (5)$$

$$a_{ci} = \frac{0{,}42748 R^2 T_c^2}{p_c} \quad (6)$$

$$\alpha_i = \left[1 + m_i\left(1 - T_r^{1/2}\right)\right]^2 \quad (7)$$

$$m_i = 0{,}48 + 1{,}574\omega_i - 0{,}176{\omega_i}^2 \quad (8)$$

P, T, v and R are the pressure, temperature, molar volume and universal gas constant, respectively.

T_c is the critical temperature, ω is the acentric factor and T_r is the reduced temperature defined as the ratio between T and T_c. The binary interaction parameter k_{ij} (equal to k_{ji}) is a constant that may be fitted for a binary component pair and x_i is the mole fraction for component i. In the PR equation, equation 1, 3, 6 and 8 are replaced by equation 9, 10, 11 and 12.

$$p = \frac{RT}{v-b} - \frac{a}{v(v+b)+b(v-b)} \quad (9)$$

$$b_i = \frac{0{,}077796 R T_C}{p_c} \quad (10)$$

$$a_{ci} = \frac{0{,}457235 R^2 T_c^2}{p_c} \quad (11)$$

$$m_i = 0{,}37464 + 1{,}54226\omega_i - 0{,}26992{\omega_i}^2 \quad (12)$$

In the standard version of SRK and PR, k_{ij} is a constant for each binary pair. When utilizing the default k_{ij} values in Aspen HYSYS and Aspen Plus, the k_{ij} values are constant for all component pairs except for water/CO_2 where it is a temperature dependent function. In the literature, different optimized values for the k_{ij} values can be found because the parameters may be optimized for different conditions, e.g., for accurate prediction of either the gas phase or the condensate phase. For the calculation of dew points, it is reasonable to use binary interaction coefficients optimized for the gas phase.

The PR and SRK versions used in Aspen Plus are equal to the Aspen HYSYS versions shown in (1) to (12), except that some of the numerical values are slightly different. Especially the coefficients in the m_i expressions (8) and (12) are slightly different.

The k_{ij} values fitted to PR and SRK models are traditionally very similar. This can be seen, e.g., for the k_{ij} parameters in (Aasen *et al*., 2017).

3 Process Description and Simulation Specifications

3.1 Process description of raw biogas compression

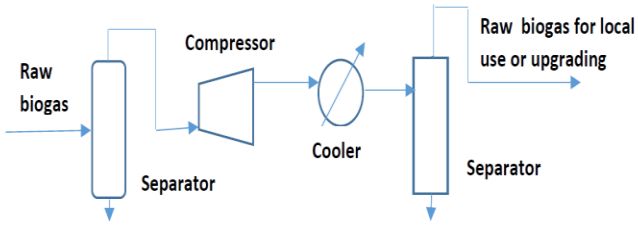

Figure 1. A traditional raw biogas compression process

The principle for a traditional raw biogas compression process is shown in Figure 1.

When the raw biogas production is high (above 100 m^3/h at atmospheric pressure and ambient temperature), it can be reasonable to upgrade it on-site. For low volumes, (Hovland, 2017) suggests to compress the gas to a high pressure, typically above 100 bar, and transport it to a facility for upgrading to biomethane (almost pure methane).

As mentioned in (Øi and Hovland, 2018), condensation during compression is regarded to be a problem, and should be avoided.

3.2 Simulation specifications

Process simulations are performed for different conditions relevant for biogas production as in (Øi and Hovland, 2018). In earlier work the models PR, SRK, TST, PR-Twu and SRK-Twu were used. For all the conditions, calculations with the default parameters (especially the k_{ij} for water) are used. For some conditions other k_{ij} values are also used. It is possible to calculate phase envelopes showing the dew and bubble point curve for a temperature and pressure range. In the dry gas cases, the HYSYS 2-phase option was selected for phase envelope calculations. In the cases including water, the ComThermo 3-phase option was selected.

Verification of earlier calculations is also including calculations with Aspen Plus and with the (Stryjek-Vera, 1986) model. In Aspen Plus the Peng-Robinson and RKSoave models were selected. The B and D cases are referring to (Øi and Hovland, 2018).

Case B: Dry biogas with 40 mol-% methane and 60 mol-% CO_2 starts at 37 °C and 1 bar, is cooled to 10 °C and is compressed to 64 bar.

Case D: 59.9 kmol/h methane, 40 kmol/h CO_2 and 0.1 kmol/h water is mixed at 37 ºC and 1 bar, cooled to 10 °C, and then compressed to 64 bar.

A mixture of 30 mol-% methane and 70 mol-% CO_2 mixed with a specified amount of water at a specified pressure was simulated. Calculated dew point temperatures were compared to experimental dew points from (Jarne, 2004) which were approximately 15 °C. Binary coefficients (especially the $k_{CO2/H2O}$) were varied (and fitted) to obtain the experimental dew point.

Mixtures of 50/50 and 70/30 methane to CO_2 molar ratios were simulated based on experimental data from (Chapoy, 2017) with temperatures at 20 and 40 ºC and pressures of 30 and 60 bar. The $k_{CO2/H2O}$ values were fitted also for these conditions.

4 Process Simulation, Results and Discussion

4.1 Verification of earlier simulations for compression of dry methane/CO_2 mixture (Case B)

The Aspen HYSYS flow-sheet model for the base case simulation is presented in Figure 2.

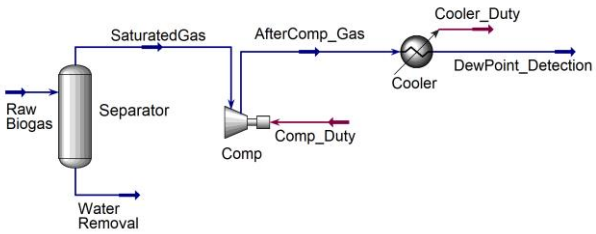

Figure 2. Aspen HYSYS flow-sheet for compression and cooling

Case B is of interest because a 40 % methane and 60 % CO_2 has a dew point close to 0 °C. Earlier evaluations from (Hovland, 2017) and (Øi and Hovland, 2018) have shown that below 58 mol-% CO_2, no condensation should appear if the temperature is kept above -3 °C.

Table 1. Dew point at 64 bar, cricondenterm and cricondenbar for a mixture of 40 mol-% methane and 60 mol-% CO_2 (Case B)

Model	T_{DEW}	T_{CRIC} (ºC)	P_{CRIC} (bar)
PR Hysys	-5.4	-1.7	89.5
SRK Hysys	-5.2	-1.3	88.4
TST Hysys	-3,9	-0.5	82.6
PR-Twu Hysys	-6,3	-2.7	90.0
SRK-Twu Hysys	-5,8	-1.8	90.5
PR Aspen Plus	-5.4	-1.8	88.2
SRK Aspen Plus	-5.3	-1.6	87.9

The results in Table 1 confirms the results from Aspen HYSYS simulation in (Øi and Hovland, 2018). In addition, similar results are obtained when PR and SRK in Aspen Plus is used. The reason why the results in Aspen HYSYS and Aspen Plus are not identical, is that the model equations are slightly different.

The calculated cricondenterms with different models have a maximum deviation of 2 °C. From this it is concluded that the results can be expected to be fairly accurate for all the models evaluated. No condensation will appear above 0 °C in a dry biogas with more than 40 mole-% CH_4. This was also the conclusion from (Hovland, 2017) and (Øi and Hovland, 2018).

A phase envelope from Aspen HYSYS is shown in Figure 3. The most important part for the evaluation of condensation is the dew point curve to the right. The point with the highest temperature is the cricondenterm. The point with the highest pressure is the cricondenbar. In the critical point for the mixture, slightly to the left of the cricondenbar, the compositions in both phases are equal.

It was found that the results in Table 1 were only slightly influenced by varying the k_{ij} parameter. The deviations are largest in the calculated envelopes above 70 bar.

It is expected that the calculations for dry biogas is reasonably accurate because all models give the same results, the parameters are fitted for this binary system and CH_4/CO_2 is a rather simple physical system.

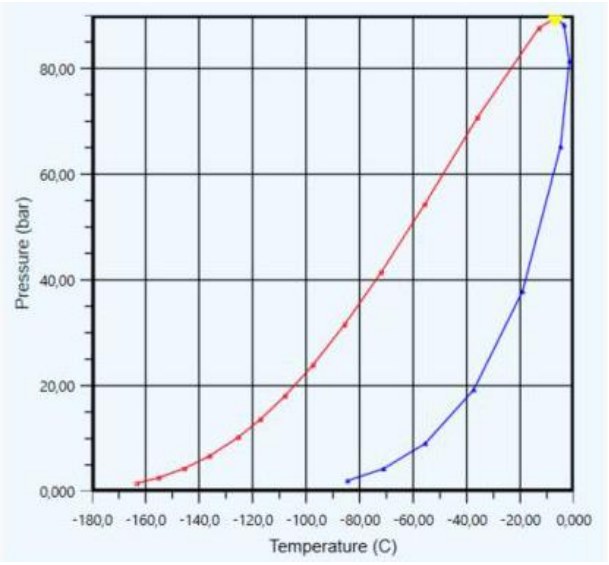

Figure 3. Phase envelope, Peng-Robinson, CH_4=0.4, CO_2=0.6, default k_{ij}.

4.2 Simulation of compression of a raw biogas including water, Case D

In Case D, the process was simulated with water included. First the TST, PRTwu, SRKTwu default models were calculated without k_{ij}-values. When the option including k_{ij}'s for water binaries was used, the dew point temperatures were much closer to the PR and SRK models.

In Case D, the water mole fraction was specified to 0.001. This water concentration is possible to obtain if condensate is removed from the biogas stream after intercooling steps in the compressor. Results are shown in Table 2.

Table 2. Dew point at 64 bar, cricondenterm and pressure at cricondenterm for a mixture of 59.9 mol-% methane and 40 mol-% CO_2 with 0.1 % water (Case D)

Model	T_{DEW} (°C)	T_{CRIC} (°C)	$P_{CRICT(bar)}$
PR	26.5	27.6	89.7
SRK	26.9	28.0	89.2
PR(k_{ij}=0.19)	30.0	34.0	141
PR(k_{ij}=0.65)	34.3	none	none
PRSV	27.1	29.2	101
TST+k_{ij}	28.8	32.1	122
PRTwu+k_{ij}	28.5	32.1	121
SRKTwu+k_{ij}	28.8	32.2	122

The dew point temperatures in Table 5 were also calculated in Aspen Plus. For PR and SRK the results were 26.3 ºC and 27.3 ºC, which are very close to the Aspen Hysys values. When using HYSPR and HYSSRK in Aspen Plus the results were identical in the two programs. The model RKSMHV2 (a modified HuronVidal model) gave 29.7 ºC and the model GERG2008 (from European Gas Research Group) gave 27.7 ºC. There are deviations of 8 K between the dew point temperature dependent on k_{ij} values. It is necessary to compare with experimental data to find out which models and parameters which are most accurate.

4.3. Fitting of binary parameters based on experimental data.

It is reasonable to fit the binary coefficients to mixture data if we are not interested in the composition range below 30 % CO_2.

It is reasonable to vary the CO_2/water and not to change the binary coefficients for the CH_4/CO_2 or the CH_4/water system. The water content is probably too low to influence on the CH_4/CO_2 interaction. The default value in PR is 0.1. The CH_4/water is a much studied system. In the literature, k_{ij} for the binary is normally specified to about 0.5, e.g., 0.52 in (Austegard, 2006). In Aspen HYSYS, 0.5 is the default value.)

Experimental data were taken for a mixture of 30 mole-% methane, 70 mol-% CO_2 and four specified amounts of water (Jarne, 2004). The experimental data for approximately 15 ºC (the highest temperature) were selected.

The binary parameter for CO_2 and water was varied until the measured dew point temperature was achieved. The results (fitted k_{ij} values and calculated dew points) are given in Table 3.

For a mixture with a CH_4 to CO_2 molar ratio of 30/70, 50/50 and 70/30, the fitted k_{ij} values were 0.65, 0.21 and 0.17, respectively. These values are high compared to literature values typically between -0.1 and 0.2 (Aasen *et al*, 2017). The (temperature dependent) k_{ij} values in the default PR model used in Table 3 varied between -0.12 and 0.04.

The k_{ij} values for the SRK model in Aspen HYSYS was fitted to the data from (Jarne *et al*., 2004) by the same procedure. The fitted k_{ij} values were then 0.63, 0.17 and 0.11. The difference between the k_{ij} values fitted to the PR and SRK models are as expected very small.

This shows that the k_{ij} values are clearly dependent on the CO_2 concentration. This supports the idea of fitting the k_{ij} values for the concentration area of interest. For biogas this is with more than 30 mole-% methane.

In Table 3, the dew point temperatures calculated with default PR gave mostly small deviations, but two deviations of 6.9 and 4.2 K. The dew point temperatures were also calculated with a k_{ij} value of 0.19 (average value for the 50/50 and 70/30 mixtures). In that case the deviations were reduced to 0.7 and 4.1 K. This shows that uncertainty in dew point temperatures can be reduced from 7 K (8 K in Table 2) to 4 K by using a constant k_{ij} for the whole range from 30 -100 mol-% CH_4.

It was also tried to fit binary coefficients in PR and SRK to experimental data from (Al Ghafri *et al*., 2014) at temperatures 50 and 100 °C. However, all reasonable k_{ij} values gave deviations from the experimental dew point temperatures up to about 10 K. This indicates that the uncertainty increases with temperature.

Table 3. Comparison of Dew points compared to experimental data from (Jarne, 2004) and PR k_{ij} values for CO_2/water fitted to the experimental data.

T_{EXP} (ºC)	P_{EXP} (bar)	CH_4/CO_2 (mole ratio)	Water (mol%)	$T_{PR,(ºC)}$ k_{ij}-default	PR k_{ij}-fitted
14.7	31.6	30/70	0.0547	7.8	0.65
14.8	20.7	30/70	0.0844	10.9	0.60
14.8	11.9	30/70	0.1400	12.3	0.70
20	30	50/50	0.0989	18.6	0.15
20	60	50/50	0.0636	15.9	0.20
40	30	50/50	0.2961	38.3	0.24
40	60	50/50	0.1791	35.8	0.25
20	30	70/30	0.0959	19.5	0.10
20	60	70/30	0.0584	18.1	0.15
40	30	70/30	0.2873	39.1	0.20
40	60	70/30	0.1693	37.9	0.21

4.4. Phase envelope calculations

The phase envelope for PR with k_{ij}=0.19 from Table 2 is shown in Figure 4.

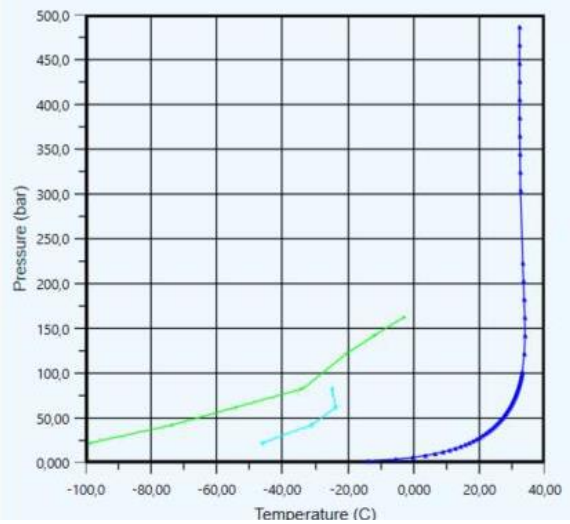

Figure 4. Phase envelope for PR model, 59,9 mol% CH_4, 40 mol% CO_2, 0.1 mol% water: k_{ij} =0.19 for water/CO_2

The envelopes in Case D are similar for the different models up to about 70 bar. Above 70 bar there is however a difference up to 4 K between the models. The differences are due to the model and the model parameters, especially the k_{ij} for water and CO_2. The difference between the models above 70 bar is significant.

As mentioned by (Øi and Hovland, 2018), it is reasonable that the non-ideality and uncertainty increases when the pressure increases, and also when the mixture is close to condensation and close to the critical point which is order of magnitude 70 bar. The range with an uncertainty less than 4 K in calculated dew point with PR or SRK with one constant k_{ij} value (0.19) is for the range of temperatures 0-40 ºC, pressures up to 70 bar and CH_4 concentration above 30 mol-%.

5 Conclusion

Dew points for dry and raw biogas under different conditions with varied temperature, pressure and gas composition using different equilibrium models have been calculated.

For dry biogas, all the models Peng-Robinson (PR), Soave-Redlich-Kwong (SRK), PRSV, both in Aspen HYSYS and Aspen Plus gave similar results. As in the literature, above 0 °C a biogas mixture with more than 40 % methane will not result in any condensation.

A process is simulated where raw biogas is compressed and cooled. From the results with biogas containing water at low pressure, the different models gave similar results within a few K up to about 70 bar. The deviation compared to experimental values were however up to 8 K. The results were dependent on the chosen value of the water/CO_2 binary interaction coefficient.

The binary coefficient for water and CO_2 was fitted to experimental data from the literature for a mixture with a CH_4 to CO_2 molar ratio of 30/70, 50/50 and 70/30. The fitted k_{ij} values for the PR model were 0.65, 0.21 and 0.17, respectively. For the SRK model, the k_{ij} values were slightly higher. At pressures below 70 bar and temperatures below 40 °C, the uncertainty for calculated dew-points in mixtures with 30 to 100 % CH_4 was reduced to less than 4 K.

References

A. Aasen, M. Hammer, G. Skaugen, J. P. Jakobsen, and Ø. Wilhelmsen. Thermodynamic models to accurately describe the PVTxy-behaviour of water/carbon dioxide mixtures, *Fluid Phase Equilibria*, 442:125-139, 2017.

S. Z. S. Al Ghafri, E. Forte, G. C. Maitland, J.J. Rodriguez-Henriquez, and J. P. M. Trusler. Experimental and Modeling Study of the Phase Behaviour of (Methane + CO2 + Water) Mixtures. *Journal of Physical Chemistry*, 118:14462-14478, 2014.

A. Austegard, E. Solbraa, G. de Koeijer, and M. J. Mølnvik. Thermodynamic models for calculating mutual solubilities in H_2O-CO_2-CH_4 mixtures. *Trans IChemE, Part A, Chem. Eng. Res. Des.*, 84(A9):781-7946, 2006.

Y. Bi, T. Yang and K. Guo. Determination of the upper quadruple phase equilibrium region for carbon dioxide and methane mixed gas hydrates. *Journal of Petroleum Science and Engineering*, 101:62-67, 2013.

A. Chapoy, R. Burgass, A. Terrigeol, and C. Coquelet. Water Content of CH4 rich Mixtures: Measurements and Modeling using the Cubic-Plus-Association Equation of State. *Journal of Natural Gas Engineering*, 1(13):85-97, 2016.

A. Dhima, J. de Hemptinne, and J. Jose. Solubility of Hydrocarbons and CO_2 Mixtures in Water under High Pressure. *Ind. Eng. Chem. Res.*, 38:3144-3169, 1999.

J. Hovland. Compression of raw biogas – *A feasibility study*. Tel-Tek report 2217020-1, 2017. Available on https://www.biogas2020.se/wp-content/uploads/2017/06/2217020-1compressionrawbiogas.pdf

M. J. Huron and J. Vidal. New mixing rules in simple equations of state for representing vapour-liquid equilibria of strongly non-ideal mixtures. *Fluid Phase Equilibria*, 3:255-271, 1979.

C. Jarne, S. T. Blanco, M. A. Gallardo, E. Rauzi, S. Otin, and I. Valesco. Dew Points of Ternary Methane (or Ethane) + Carcon Dioxide + Water Mixtures: Measurements and Correlation. *Energy & Fuels*, 18:396-404, 2004.

L. N. Legoix, L. Ruffine, J. P. Donval, and M. Haeckel. Phase Equilibria of the CH4-CO2 Binary and the CH4-CO_2-H_2O Ternary Mixtures in the Presence of a CO2-Rich Liquid Phase. *Energies*, 10(2034):1-11, 2017. doi:10.3390/en10122034.

J. Longhi. Phase equilibria in the system CO2-H2O I: New equilibrium relations at low temperatures. *Geochimica et Cosmochimica Acta*, 69, No. 3: 529-539, 2005.

D. Peng and D. B. Robinson. A New Two-Constant Equation of State. *Ind. Eng. Chem. Fundam.*, 15(1):59-646, 1976.

R. Privat and J. N. Jaubert, *Predicting the Phase Equilibria of Carbon Dioxide Containing Mixtures Involved in CCS Processes Using the PPR78 Model*. InTech, 2014. Available on http://dx.doi.org/10.5772/57058.

J. Qin, R. J. Rosenbauer, and Z. Duan. Experimental Measurements of Vapor-Liquid Equilibria of the H2O + CO2 + CH4 Ternary System. *Journal of Chemi cal Engineering Data*, 53:1246-1249, 2008.

G. Soave. Equilibrium constants from a modified RedlichKwong equation of state. *Chemical Engineering Science*, 27:1197-1203, 1972.

K. Y. Song and R. Kobayashi. The water content of a CO2-rich gas mixture containing 5.31 mol% methane along three-phase and super-critical conditions. *Journal of Chemical Engineering Data*, 35(3):320-322, 1990.

N. Spycher, K. Pruess, and J. Ennis-King. CO2-H2O mixtures in the geological sequestration of CO2. I. Assessment and calculation of mutual solubilities from 12 to 100 ºC and up to 600 bar. *Geochimica et Cosmochimica Acta*, 67 (16):3015-3031, 2003.

R. Stryjek and J. H. Vera. PRSV – An Improved Peng-Robinson Equation of State with New Mixing Rules for Strongly Nonideal Mixtures. *The Canadian Journal of Chemical Engineering*, 64:334-340, 1986.

C. H. Twu, D. Bluck, J. R. Cunningham, and J. E. Coon. A Cubic Equation of State with a New Alpha Function and a New Mixing Rule. *Fluid Phase Equilibria*, 69:33-50, 1991.

L. E. Øi and J. Hovland. Simulation of Condensation in Compressed Raw Biogas Using Aspen HYSYS. In *Linköping Electronic Conference Proceedings SIMS 59*, pages 31-36, 2018. doi: 10.3384/ecp1815331.

Model selection for waste conversion efficiency and energy demands in a pilot for large-scale larvae treatment

Evgheni Ermolaev[1] Erik Dahlquist[2] Cecilia Lalander[1] Björn Vinnerås[1] Eva Thorin[2]

[1]Department of Energy and Technology, Swedish University of Agricultural Sciences (SLU), Sweden, evgheni.ermolaev@slu.se

[2]Department of Energy, Building and Environment, Mälardalen University, Sweden

Abstract

Implementations of conversion systems for segregated food waste into larval biomass are reliant on stability of production environment and predictable outcomes. However, the knowledge is currently lacking for large scale implementation modelling allowing to adjust the process for reaching a stable production quality and predicting the treatment capacity and output product quantity. This study contributed to the development of such knowledge and investigated models for prediction of larvae mass gain in the conversion process, food waste degradation due to larval and microbial activity, heat production based on metabolic activity in the conversion process. These models were used to evaluate the amount of heat produced and compared to the demand for water removal for achieving a minimal total solids content (50%) in the treatment residue for easy larvae separation by sieving. Based on these models' predictions and measurements of the conversion efficiency it was established that, assuming no heat loss from the system, the heat generated by the process was sufficient to achieve a desirable total solids content in the residue after 14 days of treatment. An exponential heat production from waste degradation can be expected, and thus, for wetter food waste, the treatment period can be expanded to achieve the desired residue total solids content.

Keywords: Black soldier fly, degradation, conversion, sieving, food waste, high water content.

1 Introduction

Insect rearing for feed production is becoming more enticing in strive to find sustainable and locally produced feed proteins (Kim et al., 2019). Still, the trend globally is that consumption of insects used as feed and food is decreasing, although a recent estimation suggests that some 2.5 billion people occasionally eat insects, mostly in Asia, Africa and Central –South America (Van Huis et al., 2013). Historically, in Europe, the use has been quite low. However, the search for sustainable protein is driving the development of larger facilities producing insects (Makkar, 2017). A great deal of attention has been given to the black soldier fly (*Hermetia illucens)* in particular due to its potential for use in organic waste treatment (Čičková et al., 2015). A step-by-step guide for such implementation was recently presented by Dortmans et al. (2017). However, the majority of scientific investigations have so far focused on treatment efficiency in treating different organic waste fractions, and very few studies focus on large-scale production optimization (Mertenat et al., 2019). Other studies by Leong et al. (2016) and Li et al. (2011) investigated bio diesel production potential, while Pastor et al. (2015) and (Spranghers et al., 2017) have studied bottlenecks in conversion processes.

The success of large-scale insect biomass production system implementation is reliant on stability of production environment with predictable output quantities and quality of larvae and residue (Čičková et al., 2015). Such a system can be easily scaled to the expected amount of substrate and appropriate adjustments can be made with known effects on outcomes depending on the amounts of products needed or substrate to be treated. Such stability has to be achieved by insect farmers at European and global level in order to meet future demands for protein (IPIFF, 2018). The use of organic waste as a source for production of larvae with intent for animal feed or biodiesel production has been evaluated in several studies (Leong et al., 2016; Li et al., 2011; Pastor et al., 2015; Spranghers et al., 2017). The grown black soldier fly (BSF) larvae are high in fat, containing 20-50% of fat on a dry matter basis. Protein content is typically in the range of 35-42% on a dry matter basis (Ewald, 2019; Lalander et al., 2019). Such composition of larval biomass represents a great source of protein and fat for production of animal feed.

For large scale implementation, several parameters are important to establish a stable production. Such parameters include the dimensioning of the number of fly larvae per amount of treated substrate, process temperature and retention time in treatment (Diener et al., 2011; Liu et al., 2017; Paz et al., 2015; Tomberlin et al., 2009). Another important parameter often discussed is achieving a moisture content in the treatment residue that allows dry separation of larvae after the treatment. Cheng et al. (2017) has investigated how larvae

separation is affected by moisture content in the residue. The initial tests performed at the pilot plant at Eskilstuna Strängnäs Energi och Miljö collaborating in the current project have shown that total solids content of the residue above 40-45% allows an easy larvae separation through sieving.

The aim of this study was to evaluate the technical aspects of larvae growth, ventilation and drying in a pilot sized BSF treatment system treating segregated household food waste and to develop mathematical models to describe the treatment process and its energy efficiency.

2 Material and methods

This section contains details about the study set up, materials and methods used, measurement techniques and assumptions.

2.1 Description of the larvae production facility in Eskilstuna

The measurements were performed at the fly larvae conversion pilot facility at Eskilstuna Strängnäs Energi och Miljö, while process efficiency evaluations were performed both at the pilot facility and at the Swedish University of Agricultural Sciences (SLU).

2.1.1 Treatment set-up

The treatment process began when approximately 15 000 seven-day-old larvae were added to a treatment box containing the first feeding portion of 5 kg waste (Figure 1A). The treatment boxes had a surface area of 2400 cm^2 (Figure 1). Treatment boxes were stacked by 8, and four such stacks were started approximately once per week. The boxes were stacked in order to increase treatment volume. The stacks were placed in a treatment room which was heated using residual heat at the Eskilstuna waste management facility. Three sets of stacks (4 in each) were evaluated. The sets were named T20, T11 and T5 indicating how many days they were in the treatment on the day when temperature and relative humidity (RH) were measured. Four boxes were sampled in each set. The boxes were fed with two additional 5 kg portions of food waste with an interval of 3-6 d (Table 1). After the last feeding the material was left for 5-14 d to be processed by the larvae. On day 14-21 from treatment start, the larvae were separated from the residue using a rotating drum sieve.

2.1.2 Materials

The young larvae were produced at SLU from a continuously run BSF colony since 2015. The seven-day-old larvae were pre-weighed to contain approximately 15 000 based on a smaller sample that was determined by enumeration and a gravimetric estimation of a single larvae weight.

The segregated household food waste, which was collected in plastic bags and went through optical sorting process, subsequently was minced in an extruder-grinder that also separated out plastic and other fractions not passing through the mesh.

Figure 1. Depiction of larval growth and visual material changes during treatment process a) at start of treatment, b) after 5 days of treatment, c) after 11 days of treatment and d) after 20 days of treatment.

2.1.3 Temperature and moisture sampling

Temperature was sampled using a Fluke pyrometer to measure surface temperature. For the temperature in the material (below the surface), approximately 10 mm of material top layer was removed and the temperature measured directly. The temperature and relative humidity (RH) were sampled using a Testo 400 thermohygrometer probe to measure temperature and RH values in the material and right at the surface of material. The measurements were performed in boxes kept at different heights in the stacks and different locations at the facility. For each box, 5-7 sub-samples were collected in random positions and an average value was used as a reading, but multiple replicate boxes were

Table 1. Treatment schedule showing the age of stacks with treatment boxes in days from start (ST) to sampling day (highlighted in green). First feeding was provided at start (highlighted orange) and additional feedings were given within 3-6 days (highlighted blue).

Stack set	*Treatment days*																				
T20	ST	1	2	3	4	5	6	7	8	9	10	11	12	13	14	15	16	17	18	19	20
T11										ST	1	2	3	4	5	6	7	8	9	10	11
T5																ST	1	2	3	4	5

compared to ensure reliability of measurements (n=9 for temperature and n=4 for surface humidity).

2.2 Modelling

Microbial waste degradation was modeled according to a first order rate expression for microbial oxidation of degradable volatile solids highlighted by Hamelers (2004) and developed by Keener et al. (1992) (1). Similar models based on rate constants, amount of degradable material and environmental factors such as process temperature have been discussed by others e.g. Haug (1993).

$$\frac{dm}{dt} = -k(x_1, x_2, \cdots x_n) \cdot [m - m_e] \quad (1)$$

Where m is the compost mass, t is time, k is the composting process rate constant, x_i are the environmental factors e.g. process moisture and temperature and m_e is the non-degradable mass of compost at the end of the process.

Larval waste reduction was modelled based on several variables, including bioconversion ratio (BCR) representing the amount of volatile solids (VS) in substrate that has been converted to larval biomass (2).

$$BCR_{VS} = \frac{VS_{larvae}}{VS_{substrate}} \quad (2)$$

The mass of substrate lost in the process is expressed through a reduction (RED) variable which can be calculated on volatile solids basis, total solids (TS) basis and wet weight (WW) basis. The latter accounts for all the losses in the process including evaporation and respiration (3).

$$RED_{ww} = 1 - \frac{WW_{larvae} + WW_{residue}}{WW_{substrate}} \quad (3)$$

The larval metabolic activity, along with that performed by microbes, results in respiration, energy release and volatile solids reduction in the substrate. Typically such activity can be associated to the body mass and thus the substrate VS reduction by larvae can be expressed through an adapted model proposed by Wotton (1978) where respiration rate (measured as C loss from substrate through CO_2 emission) is assumed to be proportional to VS loss (4).

$$\log \frac{dVS_{lost}}{dt} = a + b \cdot \log M_{larva} \quad (4)$$

Where VS_{lost} represents the amount of substrate VS being lost due to larval metabolic activity over time t, M_{larva} is the individual larvae body mass at time [t] in the process, while parameters a and b represent the initial VS loss rate and the influence degree of the body mass on VS loss rate, respectively. An additional pathway for VS loss is associated to substrate assimilation by the larvae and can be calculated based on BCR_{VS}.

2.3 Assumptions

Several parameters used in modelling and evaluations of system productivity were estimated based on previous analyses, studies and published sources. Eskilstuna food waste moisture content has been evaluated in several studies including a study by Johannesdottir (2017) and Lindberg (2018) and the TS range reported was 15% – 23%. Based on these results, communication with Eskilstuna facility operators and measurements performed in the lab (data not shown), it was assumed that the typical TS content of the slurry was 16% ± 2%. Food waste from Eskilstuna have been demonstrated to have a very good BCR_{TS} the values reported range between 24 and 32% (Johannesdottir, 2017; Lindberg, 2018) and in the current system investigation a value of BCR_{TS} of 30% was assumed. Reduction of substrate VS depends on multiple parameters and system dimensioning; however, an assumption is necessary in order to estimate the amount of water needed to be removed in the treatment process. Although a reduction in the range of 56 - 65% (Johannesdottir, 2017) have been reported for Eskilstuna food waste, a lower RED_{TS} of 50% was assumed here in order to not overestimate the amount of energy released from the process typically associated with reduction of substrate.

Based on these values the mass balance of the process can be presented. Per ton of food waste processed, the substrate TS represent 140-180 kg, which assuming a BCR_{TS} of 30% and a RED_{TS} of 50%, results in production of 43-55 kg TS of larval biomass and 72-93 kg TS of treatment residue. Based on these assumptions, the demand to obtain the residue with 50% TS to allow sieving, the assumption that larvae have TS of 35% (Johannesdottir, 2017) and the overall mass balance, 709-625 kg of initial substrate water has to be removed and 25-32 kg of initial TS are respired.

The amount of energy released in the degradation process was estimated based on heat of combustion of biodegradable VS. Mason (2009) calculated that for food waste 5.4 kWh of energy can be released per kg VS degraded. Based on this assumption the amount of heat released was calculated taking into account the VS content of the food waste slurry (He et al., 2013).

The incoming air to the facility was warmed up to approximately 30 °C and it was assumed it had 15 RH% at that temperature based on measurements performed earlier (data not shown). The outgoing air was assumed to be 30 °C and have an RH of 95%. Such high saturation level was not achieved in a previous study permed in controlled lab conditions (Johannesdottir, 2017) when a saturation of 61 RH% was observed in outgoing air. Nevertheless, by adjusting the ventilation rates, nearly full saturation of air can be achieved (Bach et al., 1987), and thus this assumption was used in the current evaluation (Kubilay and Kucska, 2018). Based on these assumptions a water carrying capacity of air was calculated using steam tables (Mörtstedt and

Hellsten, 1976). It was estimated that 0.022 kg water can be removed per kg air supplied by the ventilation.

3 Results and discussion

3.1 Treatment process

The treatment process has been running for 5, 11 and 20 d on the day of moisture sampling. The treatment running for 5 d (T5 in Table 1, Figure 1B) had larvae that were approximately 10 mm long (visual estimation) but very thin. In the treatment T11, running for 11 days (Figure 1C) the larvae were larger, visually estimated to be approximately 15 mm long, but smaller in diameter (by ca 2.5-3 mm) than the ones in treatment for 20 days (Figure 1D), which were estimated to have a diameter around 3.5 - 4 mm and were approximately 20 mm long. The moisture content in the material was relatively high after 11 days of treatment, and as seen in the picture in Figure 1B, the treatment surface appeared wet. Figure 1D shows the larvae that had treated the material for 20 days. The waste was dried to a TS content of approximately or lower than 50% due to biological activity generating heat that was driving evaporation together with ventilation.

The facility had a treatment capacity for 1440 kg of material at any given time, however as the material was added in portions, on the sampling day there was 960 kg of material being treated. Only stacks in the treatment T20 reached the full capacity as they were fed 3 times (Table 1). The average capacity for the facility considering the feeding frequency and treatment duration of 21 days was 69 kg waste/d, however the capacity could be increased to 103 kg waste/d if a shorter treatment time was used. The available space was not fully utilized, and the design goal was to reach a treatment capacity of 1000 kg/d, which would be possible if the process was run during 14 days per batch and all potential treatment volume was used.

During this evaluation, the pilot fly larvae treatment facility in Eskilstuna used stacked treatment units (boxes) each treating 15 kg of food waste. Each unit after 14 d of treatment produced approximately 2.4 kg of larvae and 2.5 kg residue (based on initial TS and VS evaluations performed in the lab and assuming a BCR_{TS} of 30% and RED_{TS} of 50%, data not shown). The estimation of the process performed in the lab (based on TS and VS measurements of substrate and treatment products, data not shown) on dry solids basis gave 1.0 ± 0.2 kg larvae and 1.0 ± 0.1 kg residue and a mass loss due to metabolism of 0.5 ± 0.1 kg TS (variations assumed based on expected variation in moisture content in the incoming material). On the measurement day a total of 11 treatment units were sampled with respect to temperature and relative humidity (T5, T11 and T20) from the three treatments sets (Figure 2).

The difference in temperature below the surface (in material) and at the material surface was approximately 0.5 °C for T5, while it was 2 °C for T11 and 2.7 °C for T 20 (c.f. standard deviations Figure 2). This shows that the longer treatment process was, the higher heat generation was observed, increasing the temperature inside the material and causing larger difference in surface temperature.

3.2 Modelling

Several processes can be modeled in this system implementation that should follow standard models, including larval and microbial growth, energy generation in the process and water loss from material due to evaporation and ventilation. The general microbial and larval waste degradation models are presented in the methods section (1 and 4). The larval degradation model uses larval mass as a parameter for estimation of degradation (4). It is thus important to evaluate the larvae growth and develop a model for its characterization.

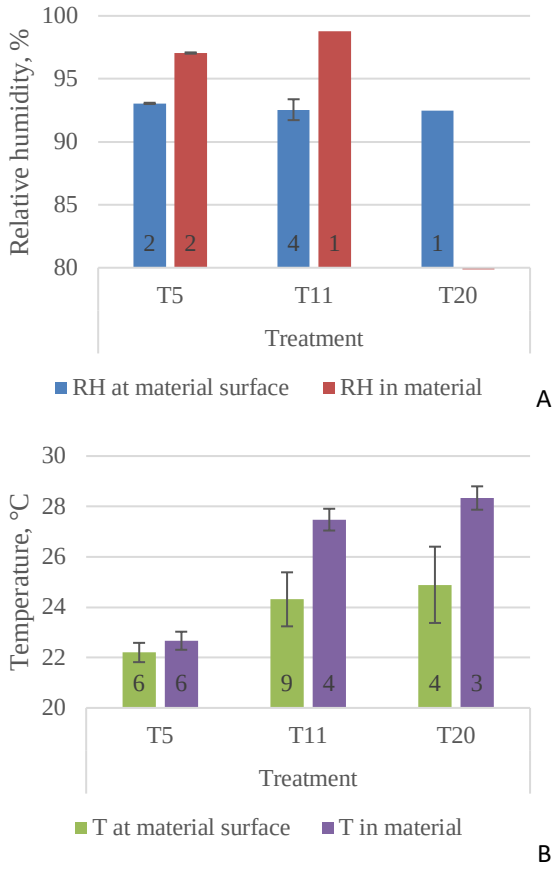

Figure 2. Graphical representation of a) %RH and b) temperature (T) on the measurement day in different treatments, whiskers (where available) show standard deviation and numbers inside bars show *n*. Measurement of T b) and %RH a) in boxes using pyrometer (T1) from Fluke and T (T2) and RH% using Testo 400.

3.2.1 Larvae growth and material reduction

The BSF larvae growth have been evaluated in multiple studies (Diener et al., 2011; Lalander et al., 2019)

showing that larvae grow nearly linearly, but there is a slightly slower growth rate at the beginning of the process. This suggests that an exponential growth model could fit well to describe the first period of larvae growth during the first 10-14 days (5).

$$x_{d+1} = x_d + a * t^b \quad (5)$$

Were x_{d+1} is the weight of larvae at next time step (next day, $d+1$), x_d the weight at current time step (current day, d), a is a constant expressing the larvae mass gain rate, t is the accumulated time, in hours since the growth started and b is another constant expressing the larvae mass gain rate change with time. Constants a and b include environmental impacts of the system on larval growth. When the equation was fitted to achieve the expected larvae size in treatment over 10-14 days based on assumptions described in section 1.1.3, the constants a and b had values of 0.12 and 0.8, respectively, while a value became 0.15 when the treatment duration was set to 21 days. In this case assuming the treatment started with 160 kg TS in waste and after 14 days produced 49 kg larvae TS. The conversion efficiency (BCR_{TS}) in this case became (49*100%)/160 = 30,6 %. Such a BCR_{TS} value represents a very good conversion ratio since the normal range is between 25 – 36 % for different types of substrates (Lalander et al., 2019). Such a BCR range for food waste would result in 41- 59 kg larvae from the original 0.25 TS kg young larvae and 160 kg TS waste.

It was observed by Lalander et al. (2019) that the BSF larvae grow mostly during the first two weeks of treatment, but then the additional weight gain is small during the third week, or even a weight reduction was observed. Such a development is associated with BSF life cycle: if the larvae have reached their target larval stage and become pre-pupae, they no longer feed and thus only consume stored fat and protein necessary for their metabolism, movement and metamorphosis. A further investigation of larvae growth based on a study by Lalander et al. (2019), showed that the growth rate is slow in the beginning of treatment of food waste, but then accelerates and peaks during days 4 to 9. After this, the growth rate decreases, and after day 12 (for most substrates) the larvae mass increase stops (Figure 3). When further increase in larvae mass stopped, but larvae have not yet reached the pre-pupae stage (days 12-14) the waste was degraded due to metabolism, but it did not give increased growth resulting in unchanged BCR and increased RED. After 3 weeks in treatment, the larvae start pupating, which causes an additional weight loss as they have stopped eating already in the pre-pupae stage. The peak weight gain and the duration of weight gain period was observed to differ between the substrates, but for food waste, the peak could be expected around day 7 (based on model projection and data from Lalander et al., 2019) under optimal conditions (Figure 3). This means the exponential model (5) well describes the beginning of the process, but to cover the whole treatment time a cumulative distribution function fits better and matches with the data points presented in Lalander (2019).

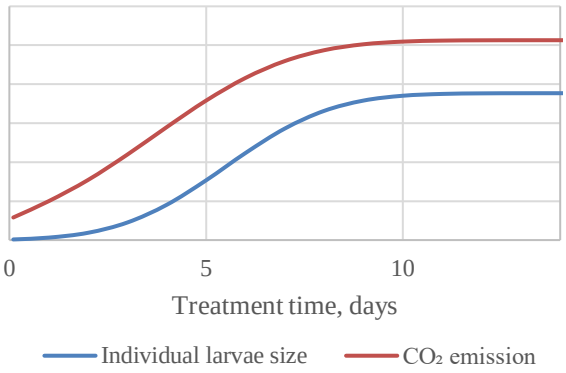

Figure 3. Graphical (dimensionless) representation of larvae weight change as a function of time for 1 ton food waste with 16% TS fed during 14 days and an associated CO_2 emission rate based on VS loss due to larval metabolism (4).

When comparing the actual weight curve to an exponential curve it was found that it fitted fairly well the first 10 days, but after that the larval growth stopped as the larvae reached their maximum weight (Figure 3). From a production perspective thus, a shorter harvest after approximately 10 days should be evaluated to maximize the output of larval biomass. Such shorter treatment can result in insufficient water removal from material (treatment residue) which needs to be sufficiently dry to enable separation of larvae (Cheng et al., 2017). In this pilot set-up, the mixture was still quite wet after 10 d and it would not have been possible to efficiently separate the larvae from the treatment residue. If the larvae are left in the material for longer, their and microbial metabolisms further reduce the substrate, which can result in additional water evaporation due to associated heat generation. Such reduction can be modeled using equations 1 and 4 described earlier. According to these models and the model for larvae growth (5), the larvae and microbial metabolic rates increase exponentially and thus the energy release from metabolism also increases exponentially during exponential larval growth.

In the beginning of treatment, the bioconversion rate is low which means that heat generation is low, and the food waste slurry is still very high in water content. In parallel with larval digestion of food waste a microbial process also takes place. A first order exponential or linear model for aerobic food waste degradation can describe such a microbial process well (Hamelers, 2004). Thus, in the beginning of the treatment due to lag in larvae growth the decrease in moisture content was marginal, and likely mainly due to microbial activity. As the larval mass increased, the larval activity also

increased, resulting in a substantial heat release and evaporation of water. If the treatment is allowed to continue beyond the typical 14 d until 21 d, the larva first become prepupae and then turn into pupae, meaning they no longer degrade the substrate. However the microbial waste degradation continues and provides additional heat necessary for water evaporation from the residue.

The amount of waste that was converted into heat can be calculated based on oxidation reaction of the average food waste formula, resulting in production of energy and of $CO_2 + H_2O$. The amount of food waste oxidized was estimated based on degradation rate, $\frac{dm_{waste}}{dt}$ and was calculated from multiplying the mass of larvae, m_l, by the degradation per kg larvae for each day, A_l, and the same for microorganisms (m_{mo}, A_{mo}). As the accumulated larval and microbial biomass increases, the absolute degradation per day also increases (6).

$$\frac{dm_{waste}}{dt} = m_{waste} * (m_l * A_l + m_{mo} * A_{mo}) \qquad (6)$$

The accumulated heat release from TS degradation can also be presented as a function of time. Assuming 0.25 kg TS of young larvae was originally added to 160 kg TS waste and using an assumption that 5.4 kWh is released per kg TS respired (Mason, 2009), the total energy release can be estimated. Based on the assumptions made earlier in methods section 1.1.3, an evolution of 449 kWh can be assumed after 10 days or accumulated 807 kWh after 14 days.

3.2.2 Evaporation of water to dry the waste

The waste slurry used in the process in this pilot set-up was relatively high in water content (~16% DM), assuming that the facility would process 1 ton waste per day, 160 kg TS/d would also bring 840 kg water/d. To separate larvae from the residue, the treatment residue should reach around 50% TS (Cheng et al., 2017). Taking into account the material reduction of 50%, 72 - 93 kg water would be remaining in the residue after 14 days of treatment, equivalent to 625 - 709 kg water needed to be evaporated per day. The heat released by the larvae estimated above was 449 kWh during the first 10 days but 807 kWh after 14 days. For removal of one kg water it is required 0.628 kWh of heat for evaporation. Assuming that only the heat evolved from the degradation of the waste would be used for evaporation and there was no other heat loss, the total amount of water evaporated could be 449/0.628 = 715 kg water. This roughly corresponds to an original moisture content of 16 % TS. If more water needs to be evaporated, additional heat has to be supplied (from the ventilation air), or the process should be allowed to continue for longer. Two extra days would yield additional 179 kWh, which would be enough to achieve desired residue TS if the original TS of the waste slurry was 13.8%.

The BSF larvae generally move quite actively, the amount of heat generated due to this motion is also expected to be proportional to the larvae size up until the pre-pupae stage, when larvae start behaving differently. This makes the selection of optimal time for harvest relevant for optimizing the protein production and total yield, while avoiding the unnecessary losses due to metabolic activity not resulting in further larvae mass gain. The harvest period should be extended by approximately one more week (beyond the usual 14 days), if pupae are required for e.g. fly production to maintain a BSF colony and produce eggs. This was the case for the pilot set-up evaluated in this study.

In case the generated metabolic heat is insufficient for evaporation, the heat energy from heated ventilation air could be used to remove excess water from the substrate. Assuming the incoming ventilation air had a temperature of 30 °C with a RH of 15% and the outgoing air was saturated to a RH of 95% at 30 °C, 0.022 kg H_2O could be removed per kg air. To remove a total of 715 kg water the demand at such conditions would be 32 500 kg air which would be equivalent to ventilation rate of 85 m^3/h. The ventilation fan at Eskilstuna pilot facility was estimated to provide airflow over 700 m^3/h suggesting a quicker than observed water removal would be expected. However, the ventilation air was not directed in a way to maximize its saturation and thus likely contributed to evaporation to a smaller degree.

Previous studies on a similar system also highlighted that a better air saturation would improve water removal rate from such fly larvae conversion system that was mostly relying on heat release associated with degradation process for water evaporation (Johannesdottir, 2017; Kubilay and Kucska, 2018).

4 Conclusions

Based on the results obtained from the pilot scale treatment facility and the experiments performed in laboratory environment it was possible to model the black soldier fly larvae development and the associated waste degradation rate attributed to both larval and microbial metabolism. Based on these models' predictions and measurements of the conversion efficiency it was established that, assuming no heat loss from the system, the heat generated by the process was sufficient to achieve a desirable total solids content in the residue after 14 days of treatment. An exponential heat production from waste degradation can be expected, and thus, for wetter food waste, the treatment period can be expanded to achieve the desired residue total solids content.

Using the models presented in this study and based on environmental properties of the treatment and waste type and moisture content, it is possible to project if the amount of heat generated by the waste reduction during the treatment is going to be sufficient to remove the amount of water to achieve a sievable residue (reaching

total solids content of 50%). After the necessary calibration of the models for each particular system, they can be used as tools for deciding the duration of treatment and the amount of heat supplied by the ventilation.

Acknowledgements

We thank Eskilstuna Strängnäs Energi och miljö for their support in implementation of the pilot project, Naturvårdsverket and Swedish University of Agricultural Sciences (SLU) for the financial support of this project.

References

P.D. Bach, K. Nakasaki, M. Shoda, and H. Kubota. Thermal balance in composting operations. *Journal of Fermentation Technology*, 65(2): 199-209, 1987. doi: 10.1016/0385-6380(87)90165-8.

J.Y.K. Cheng, S.L.H. Chiu, and I.M.C. Lo. Effects of moisture content of food waste on residue separation, larval growth and larval survival in black soldier fly bioconversion. *Waste Management*, 67: 315-323, 2017. doi: 10.1016/j.wasman.2017.05.046.

H. Čičková, G.L. Newton, R.C. Lacy, and M. Kozánek. The use of fly larvae for organic waste treatment. *Waste Management*, 35: 68-80, 2015. doi: 10.1016/j.wasman.2014.09.026

S. Diener, N.M.S. Solano, F.R. Gutierrez, C. Zurbrugg, and K. Tockner. Biological Treatment of Municipal Organic Waste using Black Soldier Fly Larvae. *Waste and Biomass Valorization*, 2(4): 357-363, 2011. doi: 10.1007/s12649-011-9079-1.

B. Dortmans, S. Diener, B. Verstappen, and C. Zurbrügg. *Black soldier fly biowaste processing: a step-by-step guide*. Eawag, Sandec, Dübendorf, Switzerland, 2017.

N. Ewald. *Fatty acid composition of black soldier fly larvae - impact of the rearing substrate*. Master Thesis. Department of Energy and Technology, Swedish University of Agricultural Sciences, Uppsla, 2019.

H.V.M. Hamelers. Modeling composting kinetics: A review of approaches. *Reviews in Environmental Science and Bio/Technology*, 3(4): 331-342, 2004. doi: 10.1007/s11157-004-2335-0.

R.T. Haug. *The Practical handbook of compost engineering*. Lewis Publishers, Boca Raton, Florida, FL, USA, 1993. doi: 10.1201/9780203736234.

P.J. He, L. Zhao, W. Zheng, D. Wu, and L.M. Shao. Energy Balance of a Biodrying Process for Organic Wastes of High Moisture Content: A Review. *Drying Technology*, 31(2): 132-145, 2013. doi: 10.1080/07373937.2012.693143.

IPIFF. *The European Insect Sector Today: Challenges, Opportunities and Regulatory Landscape*. IPIFF vision paper on the future of the insect sector towards 2030, IPIFF, 2018.

S. Johannesdottir. *Uppskalning av fluglarvskompostering: Luftningsbehov och ventilation*. Master Thesis. Department of Energy and Technology, Swedish University of Agricultural Sciences, Uppsla, 2017.

H. Keener, R. Hansen, and C. Marugg. Optimizing the efficiency of the composting process. In *Proceedings of the International Composting Research Symposium*. Renaissance Publications, Columbus, OH, 1992.

S.W. Kim, J.F. Less, L. Wang, T.H. Yan, et al. Meeting Global Feed Protein Demand: Challenge, Opportunity, and Strategy. *Annual Review of Animal Biosciences*, 7: 221-243, 2019. doi: 10.1146/annurev-animal-030117-014838.

K. Kubilay and K. Kucska. *Energi och ventilation vid biomassaproduktion av larver: Optimering av ett ventilationssystem med hjälp av beräkningsmodell i Excel för containern i demoanläggningen, i Lilla Nyby*. Master Thesis. School of Business, Society and Engineering, Mälardalen University, Västerås, 2018.

C. Lalander, S. Diener, C. Zurbrügg, and B. Vinnerås. Effects of feedstock on larval development and process efficiency in waste treatment with black soldier fly (Hermetia illucens). *Journal of Cleaner Production*, 208: 211-219, 2019. doi: 10.1016/j.jclepro.2018.10.017.

S.Y. Leong, S.R.M. Kutty, A. Malakahmad, and C.K. Tan. Feasibility study of biodiesel production using lipids of Hermetia illucens larva fed with organic waste. *Waste Management*, 47: 84-90, 2016. doi: 10.1016/j.wasman.2015.03.030.

Q. Li, L.Y. Zheng, H. Cai, E. Garza, et al. From organic waste to biodiesel: Black soldier fly, Hermetia illucens, makes it feasible. *Fuel*, 90(4): 1545-1548, 2011. doi: 10.1016/j.fuel.2010.11.016.

L. Lindberg. *Utsläpp av växthusgaser och ammoniak under fluglarvskompostering*. Master Thesis. Department of Earth Sciences, Uppsala University, Uppsala, 2018.

X. Liu, X. Chen, H. Wang, Q.Q. Yang, et al. Dynamic changes of nutrient composition throughout the entire life cycle of black soldier fly. *PLoS One*, 12(8), 2017. doi: 10.1371/journal.pone.0182601.

H.P.S. Makkar. Review: Feed demand landscape and implications of food-not feed strategy for food security and climate change. *animal*, 1-11, 2017. doi: 10.1017/S175173111700324X.

I.G. Mason. Predicting biodegradable volatile solids degradation profiles in the composting process. *Waste Management*, 29(2): 559-569, 2009. doi: 10.1016/j.wasman.2008.05.001

A. Mertenat, S. Diener, and C. Zurbrügg. Black Soldier Fly biowaste treatment – Assessment of global warming potential. *Waste Management*, 84: 173-181, 2019. doi: 10.1016/j.wasman.2018.11.040.

S.-E. Mörtstedt and G. Hellsten. *Data och diagram: energi- och kemitekniska tabeller*. Esselte Studium, Stockholm, 1976.

B. Pastor, Y. Velasquez, P. Gobbi, and S. Rojo. Conversion of organic wastes into fly larval biomass: bottlenecks and challenges. *Journal of Insects as Food and Feed*, 1(3): 179-193, 2015. doi: 10.3920/ JIFF2014.0024.

A.S.P. Paz, N.S. Carrejo, and C.H.G. Rodriguez. Effects of Larval Density and Feeding Rates on the Bioconversion of Vegetable Waste Using Black Soldier Fly Larvae Hermetia illucens (L.), (Diptera: Stratiomyidae). *Waste and Biomass Valorization*, 6(6): 1059-1065, 2015. doi: 10.1007/s12649-015-9418-8.

T. Spranghers, M. Ottoboni, C. Klootwijk, A. Ovyn, et al. Nutritional composition of black soldier fly (Hermetia illucens) prepupae reared on different organic waste substrates. *Journal of the Science of Food and Agriculture*, 97(8): 2594-2600, 2017. doi: 10.1002/jsfa.8081.

J.K. Tomberlin, P.H. Adler, and H.M. Myers. Development of the Black Soldier Fly (Diptera: Stratiomyidae) in Relation to Temperature. *Environmental Entomology*, 38(3): 930-934, 2009. doi: 10.1603/022.038.0347.

A. Van Huis, J. Van Itterbeeck, H. Klunder, E. Mertens, et al. *Edible insects: future prospects for food and feed security*. Food and Agriculture Organization of the United Nations, 2013.

R.S. Wotton. Growth, Respiration, and Assimilation of Blackfly Larvae (Diptera Simuliidae) in a Lake-Outlet in Finland. *Oecologia*, 33(3): 279-290, 1978. doi: 10.1007/Bf00348114.

Thermophilic Anaerobic Digestion Modeling of Lignocellulosic Hot Water Extract using ADM1

Zahra Nikbakht Kenarsari Nirmal Ghimire Rune Bakke Wenche Hennie Bergland

Department of Process, Energy and Environmental Technology, University of South-Eastern Norway,

zahranikbakhtkenarsari@gmail.com , Nirmal.Ghimire@usn.no , Rune.Bakke@usn.no , Wenche.Bergland@usn.no

Abstract

Lignocellulosic biomass is abundant and can become a major feed for anaerobic digestion methane production if its natural recalcitrance is overcome by pretreatment. Bio-degradable organic molecules were extracted by hot water (to produce "hydrolysate") from wood (Norway spruce). A high rate anaerobic sludge bed reactor fed the hydrolysate was modeled by the IWA Anaerobic Digestion Model No.1 (ADM1). Biodegradability kinetics for the hydrolysate material was obtained from batch tests at thermophilic condition, and the hydrolysis kinetic coefficient of carbohydrate (k_{hyd_ch}) found. Thus obtained $k_{hyd\_ch} = 0.44$ d^{-1} was used to simulate UASB reactor performance at 55°C and comparing results to measured parameters from an experimental reactor at five different organic loading rates. The simulation results correlated well with the experimental results for biogas production rate, biogas composition and chemical oxygen demand. This shows that ADM1 is a powerful tool to predict the behavior of thermophilic anaerobic digestion (AD) of pretreated lignocellulosic feed using standard ADM1 parameters except for hydrolysis kinetics. Hydrolysis was identified as the overall rate limiting step in AD of such feed in UASB.

Keywords: thermophilic anaerobic digestion, OLR, lignocellulosic hydrolysate, hydrolysis kinetic, ADM1

List of symbols

Symbol	Description [Unit]
COD	Chemical Oxygen Demand [g COD]
CSTR	Continuous flow Stirred Tank Reactor
HRT	Hydraulic Retention Time [day]
HWE	Hot Water Extraction
OLR	Organic Loading Rate [g COD/L · day]
IN	Inorganic Nitrogen [kmol/ m^3]
k_{hyd}	Hydrolysis kinetic coefficient
k_{dis}	Disintegration kinetic coefficient
S_ac	Soluble acetate [kg COD/m^3]
S_I	Soluble inert [kg COD/m^3]
S_su	Soluble Monosaccharides [kg COD/m^3]
s_COD	Soluble Chemical Oxygen Demand [g COD]
SRT	Solid Retention Time [day]
t_COD	Total Chemical Oxygen Demand [g COD]
UASB	Upflow Anaerobic Sludge Blanket
VFA	Volatile Fatty Acids
X_ch	Particulate carbohydrates [kmol/ m^3]
X_I	Particulate inert [kmol/ m^3]

1 Introduction

Serious environmental pollution due to exhaustive use of fossil fuel has demanded an environment-friendly technology to convert woody biomass or its waste residue to biofuel. Woody biomass, especially Norway spruce, is found abundantly in Norway and requires efficient methods to break its recalcitrance for faster conversion. Biodegradation of lignocellulosic material is difficult because of the complex structures of lignin and other cell wall polysaccharides. As a result, anaerobic microorganisms are not able to easily use this lignocellulosic material and biogas production is hampered (David *et al.*, 2018).Various pre-treatment methods have been tested to overcome this problem (Karuppiah and Azariah, 2019; Taherzadeh and Karimi, 2008). The main purpose of pre-treatment is to break the lignin which is the protective layer for cellulose and hemicellulose (Patinvoh *et al.*, 2017). Also decreasing the crystallinity of cellulose and solubilizing the hemicellulose enhances the digestion (Karuppiah and Azariah, 2019). Hot Water Extraction (HWE) as a proposed pre-treatment process for lignocellulosic material cooks woody biomass in the water at high temperature and pressure (Amidon and Liu, 2009; Therasme *et al.*, 2018) in order to produce liquid hydrolysate. The liquid product, after hot-water extraction, includes monosaccharides, polysaccharides, acetic acid, degraded lignin, and other low molecular weight extractable substances (Amidon and Liu, 2009).

Anaerobic digestion (AD) is a favorable technique due to its low environmental footprint (Kamali *et al.*, 2016) and high energy recovery by methane production. Thermophilic AD (50-57°C) is known as a faster method compared to mesophilic AD (30-40°C) since the choice of temperature affects the growth of microorganism via influencing the kinetic parameters of the main anaerobic reactions. The temperature can play a key role regarding system stability, with poorer yield and process stability for thermophilic AD, but better biogas and digestate quality have also been reported (Gebreeyessus and Jenicek, 2016). The higher temperature can also prevent AD culture contamination (Xia *et al.*, 2013) but may have higher thermal energy requirement (Eddy *et al.*, 2013). Therefore, it is

interesting to test thermophilic AD of lignocellulosic hydrolysate.

Empirical methods based on pilot plant results are usually used to scale up thermophilic AD for various feed stocks. Mathematical modeling and simulation of AD can speed up such design work and provide the opportunity to test a wider range of AD process conditions at lower cost than piloting.

The Anaerobic Digestion Model No.1 (ADM1) (Batstone *et al.*, 2002) has been applied for different AD systems and its performances studied for various substrates and reactor configurations (Gehring *et al.*, 2013).

ADM1 is structured in several main steps including disintegration and hydrolysis, acidogenesis, acetogenesis and methanogenesis. The first order kinetics describe the extracellular solubilization processes such as disintegration and hydrolysis (1), while the intracellular biochemical reactions are described by Monod-type kinetics (Batstone *et al.*, 2002b; Kaparaju *et al.*, 2009).

$$\rho = k_{hyd\_ch} \cdot X_{hyd\_ch} \qquad (1)$$

ρ = hydrolysis rate of solid substrate (kg COD solid substrate m^{-3} d^{-1} where COD = chemical oxygen demand), X_{hyd_ch} = solid carbohydrate concentration (kg COD solid substrate m^{-3}), k_{hyd_ch} = temperature dependent kinetic parameter for hydrolysis (d^{-1}).

Recommended relevant model parameters for most ADM1 reactions are published (Batstone *et al.*, 2002a) but not key kinetic parameters for thermophilic high rate hydrolysate digestion. Therefore, the aim of this study was to determine kinetic parameters for thermophilic AD of thermally hydrolyzed Norwegian spruce. This involved parameter estimation based on batch experiments and model evaluation based on continuous flow tests with increasing organic loading rates of this new substrate.

2 Materials and Methods

AD of hydrolysate from hot water extraction of lignocellulosic Norwegian spruce (*Picea abies*) is tested in batch and continuously fed UASB lab scale reactors with increasing load and modeled by ADM1.

2.1 Material Characterization

2.1.1 Substrate

Hydrolysate from 300 minutes hot water extraction at 140°C was used as substrates for both batch and continuously fed UASB reactors. Macronutrients (Table 1) and micronutrients (Table 2) were added in to provide required nutrients, COD:N:P ratio of 350:5:1 *(*Baeta *et al.*,2013). Initial pH was adjusted by NaOH to around 7. Substrate organics and ammonium are given in Table 3.

Table 1: Composition and concentration of macronutrients in substrate.

Macronutrients	
Type of chemical	***Concentration (mg L^{-1})***
NH_4Cl	1245.4
$(NH_4)H_2PO_4$	148.4
$(NH_4)_2HPO_4$	49.8
$MgCl_2 \cdot 6H_2O$	599.2
$CaCl_2 \cdot 2H_2O$	211.7
$NaHCO_3$	2800

Table 2: Composition and concentration of micronutrients in substrate.

Micronutrients	
Type of chemical	***Concentration (mg L^{-1})***
Yeast Extract	10
$FeCl_3 \cdot 6H_2O$	0.8
$ZnCl_2$	20.8
$MnCl_2 \cdot 4H_2O$	0.19
$(NH_4)_6Mo_7O_{24} \cdot 4H_2O$	0.26
$AlKO_8S_2 \cdot 12H_2O$	0.04
$CoCl_2 \cdot 6H_2O$	0.8
$NiCl_2 \cdot 6H_2O$	2.08
H_3BO_3	0.48
$CuCl_2 \cdot 2H_2O$	1.28
HCl	80

Table 3: Substrate organics and ammonium.

Parameter	***Measured value (g L^{-1})***
t-COD	22± 2
s-COD	20 ± 2
NH_4^+	0.30 ± 0.02
Acetate	0.59 ± 0.09
VFA	0.59 ± 0.09
Arabinose	1.63 ± 0.02
Galactose	1.67 ± 0.05
Glucose	1.55 ± 0.05
Xylose	1.95 ± 0.04
Mannose	5.1 ± 0.1
Total sugars	11.9 ± 0.3

2.1.2 Inoculum

Granular sludge inoculum (Table 4) used was from a mesophilic industrial internal recirculation reactor treating paper mill effluent. The sludge was adapted for thermophilic condition for 53 d before being used in the batch test and 20 d adaptation till stable operation in the UASB test.

Table 4: Properties of granular sludge.

Parameters	*Values*
Density (kg m^{-3})	1.00 – 1.09
Diameter (mm)	0.6 – 2.7
Settling velocity (m h^{-1})	68 – 71
Total Solids (g L^{-1})	181.0
Volatile Solids (g L^{-1})	119.4
pH	7.46

2.2 Batch Reactors Set up

100 mL syringes were used as batch reactors in accordance with (Østgaard *et al.*, 2017) with 15 mL inoculum. They were fed 4, 6.7, 13.4 and 20 mL of hydrolysates (Table 3) with three parallels for each COD loadings including control blank reactors to correct for biogas generated from the inoculum, all operated for 38 d at 55°C.

2.3 UASB Reactors Set up and Operation

Two parallel glass vessel reactors (Bergland *et al.*, 2015) with 345 mL liquid volume were used as UASB reactors. Half the reactor volumes were filled with granular sludge (Table 4). The substrate was kept cool (4 °C). Culture adaptation started at 35°C and organic loading rate, OLR = 0.65 [gCOD $L^{-1}d^{-1}$] followed by 2°C daily increases to 55°C. Then, followed the 52 d test period with step load increases (Table 5).

Table 5: The UASB operation conditions as hydraulic (HRT) and organic (OLR) loading rates.

Time interval	*HRT [d]*	*OLR [gCOD $L^{-1}d^{-1}$]*
From d 1 to d 16	34.5	0.65
From d 17 to d 27	17.25	1.29
From d 28 to d 37	11.5	1.94
From d 38 to d 48	8.62	2.59
From d 49 to d 53	5.75	3.88

2.4 Analytical Methods

UASB biogas production was monitored continuously and gas composition measured twice a week by gas chromatography (SRI 8610-C) as described in (Bergland *et al.*, 2015). Liquid phase COD (total and soluble), volatile fatty acids (VFAs), including acetate, propionate, butyrate, iso-butyrate, valerate, iso-valerate, iso-caprionate, caprionate and heptanoic acid, pH and ammonium content (NH_4^+) were sampled and measured as described in (Bergland *et al.*, 2015). Batch reactor biogas production was measured manually in accordance with Østgaard *et al.* (2017).

2.5 Modelling and Simulation Methods

The Anaerobic Digestion Model No. 1 (ADM1) was applied to model the processes with stoichiometric coefficients, equilibrium coefficients and dynamic states and algebraic variables as proposed by (Batstone *et al.*, 2002b), for all biochemical and physio-chemical processes, with the following exception: lignocellulosic hydrolysate as feed is introduced here. The only model modification assumed necessary is the hydrolysis of this new substrate and, considering the characteristics of the substrate and inoculum (Table 3 and 4), input values for simulation (Table 6) are based on some assumptions:

- 10 percent of the total feed COD is inert (based on batch tests).
- One-third of total inert is particulate inert ($input_{X_{I_{in}}}$) and two-thirds is soluble inert ($input_{S_{I_{in}}}$).
- The feed amount of biodegradable particulate carbohydrates ($input_{X_{Ch_{in}}}$) used is assumed to be total particulates minus the inert fraction (2).
- The input of biodegradable soluble sugars ($input_{S_{su_{in}}}$) used as all soluble organics (s_{COD}) minus soluble inert and acids (dominated by acetic acid so used measured ($input_{S_{ac_{in}}}$) (3).

$$input_{X_{Ch_{in}}} = (total\ particulate) - \left(input_{X_{I_{in}}}\right) \quad (2)$$

$$input_{S_{su_{in}}} = (s\_COD) - \left(input_{S_{I_{in}}}\right) - \left(input_{S_{ac_{in}}}\right) \quad (3)$$

Table 6: Parameters used for simulation in the ADM1 model

Type of parameter	*Formula for calculation*	*Amount*	*Unit*
t_COD		22.31	kgCOD m^{-3}
s_COD		20.04	kgCOD m^{-3}
Total particulate	= (t_COD - s_COD)	2.27	kgCOD m^{-3}
Inert (10% t-COD)	= (0.1 * t_COD)	2.23	kgCOD m^{-3}
Input_X_I_in	= (1/3 * inert)	0.74	kgCOD m^{-3}
Input_S_I_in	= (2/3 * inert)	1.49	kgCOD m^{-3}
Input_X_C_in		0.00	kgCOD m^{-3}
Input_X_Ch_in	= [(total particulate) - (input_X_I_in)]	1.53	kgCOD m^{-3}
Input_S_ac_in		0.63	kgCOD m^{-3}
Input_S_su_in	=[(s_COD) - (input_S_I_in) - (input_S_ac_in)]	17.92	kgCOD m^{-3}
Input_S_IN_in		0.016	mol L^{-1}
Volume		0.00035	m^3
Temperature		328	K

- The feed ammonium concentration, "Input_S_IN_in" is set to 0.016 $mol\ L^{-1}$ based on the added nutrients (Tables 1 and 2).
- Disintegration and hydrolyze kinetic parameters for thermophilic high rate was not specified by (Batstone *et al.*, 2002b). The values for mesophilic high rate (Table 7) are therefore used for the hydrolysis of protein and lipids while the hydrolysis kinetic factor of carbohydrate k_{hyd_ch} was assumed representative for the substrate and obtained from the batch test using equation 4. Disintegration high rate is assumed the same as disintegration solid.

$$B = B_0 (1\text{-}e^{-kt}) \qquad (4)$$

B_0 is the total biogas production and B is the biogas production at the given time t and k= k_{hyd_ch}.

Table 7: Kinetic parameters used for disintegration and hydrolysis as recommended by (Batstone *et al.*, 2002b) and as used for the unique conditions tested here.

Parameter	**Proposed by (Batstone et al. 2002b)**			***Used in this project***
	Meso-phillic high-rate (35°C)	*Mesophilic solids (35°C)*	*Thermo-phillic solids (55°C)*	*Thermo-phillic high-rate (55°C)*
$k_{dis}\ (d^{-1})$	0.4	0.5	1.0	1.0
$k_{hyd\_ch}(d^{-1})$	0.25	10	10	0.44
$k_{hyd\_pr}(d^{-1})$	0.2	10	10	0.2
$k_{hyd\_li}(d^{-1})$	0.1	10	10	0.1

High rate reactors (e.g. UASB) are characterized by long solids retention time compared to hydraulic retention time (SRT >> HRT), modeled by a t_res_x (difference between sludge and hydraulic retention time) factor. Its value is however unknown, so it was assessed by simulating different t_res_x values.

3 Results and Discussion

The k_{hyd_ch} parameter is first estimated by the batch experiment and then the model evaluated by comparison to the UASB test.

3.1 Hydrolysis Kinetic Coefficient

Hydrolysis kinetic coefficient (k_{hyd_ch}) for the carbohydrate was calculated based on Eq. 4 and batch data (Figure 1) to be 0.44 d^{-1} with low standard deviations between the parallels.

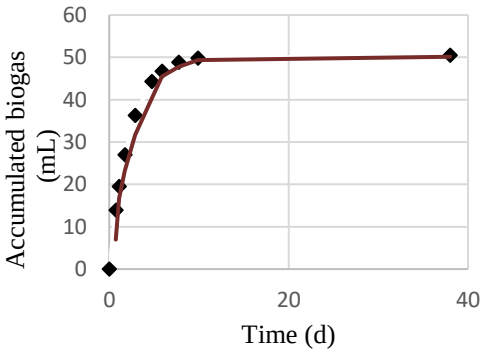

Figure 1. Batch test data and fitted line to calculate k_{hyd_ch}

3.2 Sludge Retention Time

The t_res_x value (difference between sludge and hydraulic retention time in the UASB) cannot be measured so it was assessed by simulations using different t_res_x values equal to 5, 15, 25 and 40 d. The experimental and simulated results correlated quite well for all measured parameters for t_res_x = 40 d, as seen for COD in Figure 2. Total COD was lower than simulated while simulated soluble COD was close to measured value after the first 17 d with the lowest load. t_res_x > 40 d was also tested (not shown) but without significant effects on concentrations so t_res_x = 40 d was used for the following simulations.

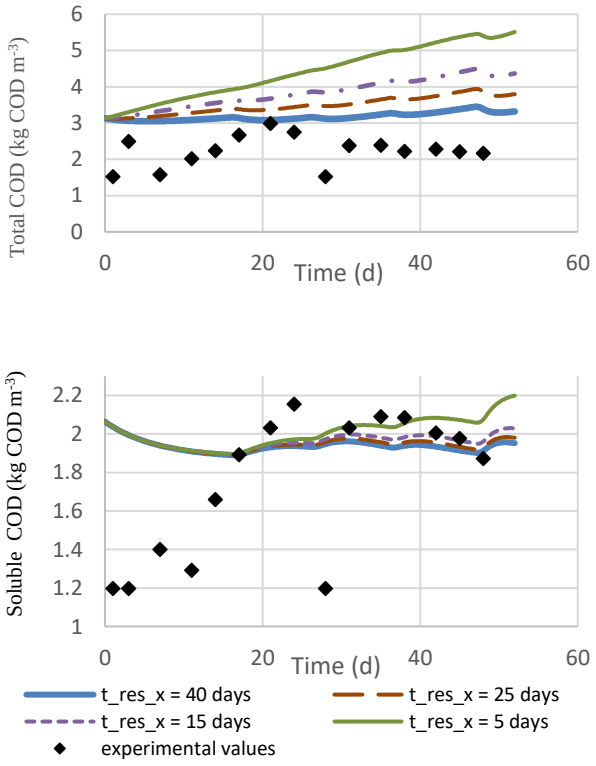

Figure 2. Total and soluble UASB effluent COD values.

3.3 Biogas Production

The measured and simulated biogas production rate (Figure 3) deviated initially until day 12, perhaps due to incomplete adaptation to thermophilic conditions. Thereafter the biogas production was close to the simulated values for the lowest OLRs indicating adapted culture. The model predicted somewhat higher yields than measured at the higher ORLs. The increases in biogas production following each step increase in OLR were predicted well but not the subsequent drops in production. These deviations show that some adaptation to higher loads are needed and that such is not accounted for in ADM1.

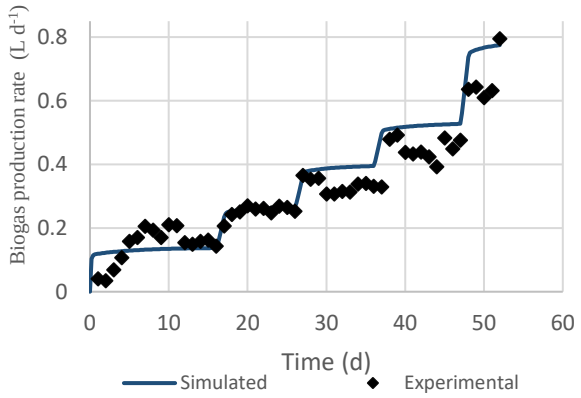

Figure 3. Simulated and experimental values for UASB biogas production rate (L d^{-1}).

The model was also used to simulate much higher loads than tested (not shown) by continuing the step increases used in the test and it predicts that much higher loads than tested can be applied while maintaining stable operation and biogas yield. This is important for the economy of such fuel production plants since capital cost depends on reactor size. This exercise also demonstrates how the model can be used to evaluate conditions that would be very time-consuming and costly to test experimentally.

3.4 Limiting Step

The increase in OLRs showed no VFAs accumulation during the experiments while the model predicts temporary VFA accumulations after each step increases (Figure 4). Both measured and simulated values are, however, low and far enough the tolerable level for smooth reactor performance: < 2 % of acetic, butyric and propionic acid concentrations of 2.4, 1.8 and 0.9 ($kg\ m^{-3}$), respectively, reported to be of threshold value (Kim *et al.*, 2002). This implies that the reactors had stable conditions with no signs of limitations of the methanogenesis at the tested loads.

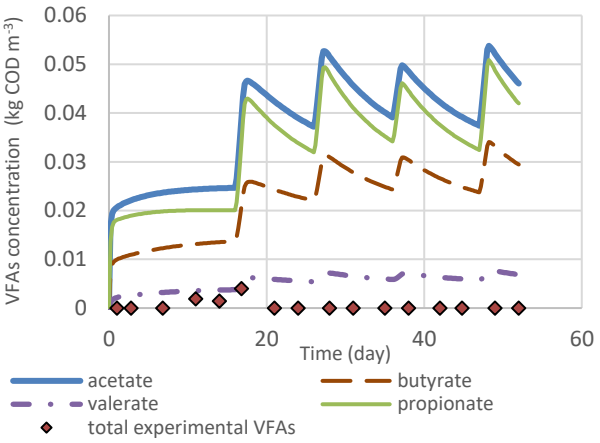

Figure 4. VFAs concentration experimental and simulated values for 52 days by increasing organic loading rate (OLR).

This is also seen by the stable methane content in the biogas, simulated and measured (Figure 5). These results also confirm that it was a correct modeling assumption to only adapt hydrolysis of ADM1 to the given conditions while the latter stages (methanogenesis etc.) were kept according to (Batstone *et al.*, 2002), since these were not limiting steps for the overall process performance. This implies that hydrolysis is the rate limiting step of lignocellulosic hydrolysate AD in UASB. This seems reasonable given that 90 % of feed organics is soluble (Table 3).

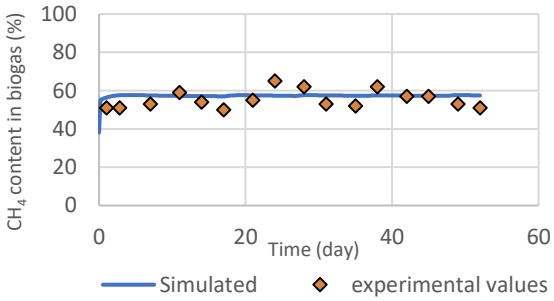

Figure 5. Simulated and experimental UASB biogas methane content.

3.5 Biomass

The active biomass cannot be accurately measured by existing methods so mass development of the main groups of microorganism in AD is studied by simulations (Figure 6). The figure shows that sugar consuming bacteria will be most abundant on such feed. The time allowed for each OLR tested, except the first, was too short to reach true steady state (even if biogas production stabilized) since biomass was still increasing for all seven microbial groups at the end of each OLR test. This supports the above suggestion that some deviations between simulated and measured value can be due to too short time for the slow growing AD

microorganism to adapt to the higher loads. AD cultures have been reported to require months to adapt to new conditions (Nordgård *et al.*, 2017).

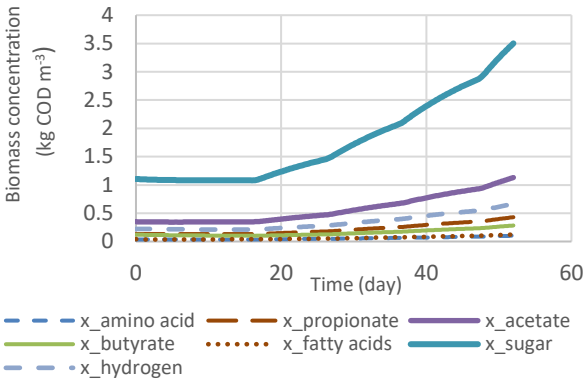

Figure 6. Simulated UASB biomass concentration development for the seven microbial groups in ADM1 during the 52 d test with increasing OLR.

3.6 Inhibition

The simulated inhibition (Figure 7) was low with slight hydrogen concentration inhibition of the propionate degradation (reducing the rate to around 80 % of maximum) and butyrate degradation (reduced to 90 %). The NH_3 concentration reduced the acetate degradation rate to 90% of not inhibited rate. There may however occur inhibition not accounted for due to unknown inhibitors in the feed. Lignocellulosic hydrolysate may contain furfural and HMF (5-hydroxymethylfurfural) that can inhibit microorganisms. This should be further studied and included in the model if relevant. If so, it could narrow the gaps between simulated and measured methane production (Figure 3).

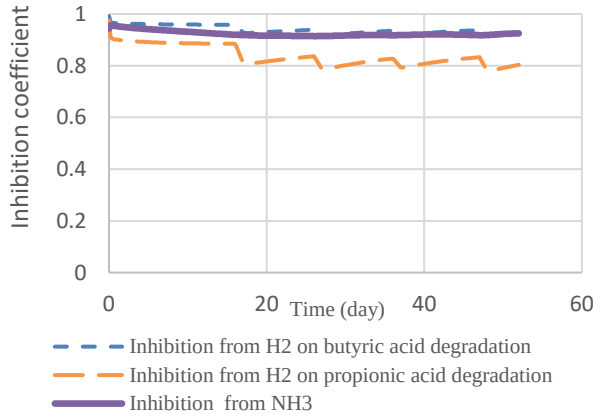

Figure 7. Simulated inhibitors coefficients (value 1 implies no inhibition and 0 implies complete inhibition).

Inorganic nitrogen may also cause AD inhibition both if in excess or in shortage, the latter typical for such feeds, compensated by ammonium supplement (Table 1). Measured and simulated ammonia levels and the inhibition simulations (Figure 7) show appropriate ammonia levels implying the amount of inorganic nitrogen added to this lignocellulosic substrate was appropriate.

Despite previous reports about the sensitivity of thermophilic AD and its poor stability, the efficient UASB reactor treatment of lignocellulosic hydrolysate suggests it is a good option for such feeds. The quite good predictability by the standard ADM1 with previously recommended process parameters support this claim and implies that ADM1 can be used in process design and to test process limitations.

4 Conclusion

- The study shows that the thermophilic AD of lignocellulosic hydrolysate in a UASB can be simulated well by the ADM1 model.
- The hydrolysis kinetic rate constant of carbohydrate, k_{hyd_ch}, was found to be 0.44 d^{-1} for thermophilic degradation of hydrolysate of Norwegian spruce.
- The low concentrations of effluent VFAs and CODs, simulated and measured, implies good digestion for the organic loading rates between 0.65 and 3.88 $g\ COD\ L^{-1}d^{-1}$ tested and implies that the last AD steps were not limiting the overall process performance.
- Hydrolysis appeared to be the overall rate limiting step in AD of such feed in UASB.
- The microbial granular sludge from mesophilic paper-mill effluent treatment adapted both to change from the mesophilic (35°C) to thermophilic (55°C) and to increased load.
- The largest simulated inhibition was from H_2 reducing the propionate degradation but there may have been some un-accounted for inhibitor(s) causing slightly less methane production than simulated at the higher loads.
- Thermophilic AD in UASB appears to be a good treatment option for lignocellulosic hydrolysate.
- The standard ADM1 can be used in process design for thermophilic UASB AD of lignocellulosic hydrolysate.

Acknowledgements

The project was supported by Pyrogas Project funded by The Norwegian Research Council and the University of South-Eastern Norway. The authors wish to thank Jitendra Sah and Vibeke Bredvold Karlsen for the good cooperation in carrying out the experiments and modeling.

References

T.E. Amidon and S. Liu. Water-based woody biorefinery. *Biotechnology advances*, 27:542-550, 2009. https://doi.org/10.1016/j.biotechadv.2009.04.012.

B.E.L Baeta, H. Luna, A.L. Sanson, S.d.Q. Silva, and S.F.D. Aquino. Degradation of a model azo dye in submerged anaerobic membrane bioreactor (SAMBR) operated with powdered activated carbon (PAC). *Journal of environmental management*, 128:462-470, 2013. https://doi.org/10.1016/j.jenvman.2013.05.038.

D.J. Batstone, J. Keller, J. Angelidaki, S.V. Kalyuzhnyi, S.G. Pavlostathis, A. Rozzi, W.T.M. Sanders, H. Siegrist, and V.A. Vavilin. The IWA anaerobic digestion model no 1 (ADM1). *Water Science and Technology*, 45: 65-73, 2002. https://doi.org/10.2166/wst.2002.0292.

D.J. Batstone, J. Keller, J. Angelidaki, S.V. Kalyuzhnyi, S.G. Pavlostathis, A. Rozzi, W.T.M. Sanders, H. Siegrist, and V.A. Vavilin. *Anaerobic digestion model No. 1 (ADM1)*. IWA Publishing: London, UK. 2002.

W.H. Bergland, C. Dinamarca, M. Toradzadegan, A.S.R. Nordgård, I. Bakke, and R. Bakke. High Rate Manure Supernatant Digestion. *Water Research*, 76:1–9, 2015. http://dx.doi.org/10.1016/j.watres.2015.02.051.

A. David, T. Govil, A. Tripathi, J. McGeary, K. Farrar, and R. Sani. Thermophilic Anaerobic Digestion: Enhanced and Sustainable Methane Production from Co-Digestion of Food and Lignocellulosic Wastes. *Energies*, 11(8): 2058, 2018. https://doi.org/10.3390/en11082058.

M.A. Eddy, F.L. Burton, G. Tchobanoglous, and R. Tsuchihashi. *Wastewater engineering: treatment and Resource recovery*. McGraw-Hill Education: New York, NY, USA. 2013.

G. Gebreeyessus and P. Jenicek. Thermophilic versus mesophilic anaerobic digestion of sewage sludge: a comparative review. *Bioengineering*, 3(2): 15, 2016. https://doi.org/10.3390/bioengineering3020015.

T. Gehring, M. Lübken, K. Koch, and M. Wichern. ADM1 simulation of the thermophilic mono-fermentation of maize silage–Use of an uncertainty analysis for substrate characterization. In *13th World Congress on Anaerobic Digestion: Recovering (bio) Resources for the World*, 28, 2013.

M. Kamali, T. Gameiro, M.E.V. Costa, and I. Capela. Anaerobic digestion of pulp and paper mill wastes–An overview of the developments and improvement opportunities. *Chemical Engineering Journal*, 298: 162-182, 2016. https://doi.org/10.1016/j.cej.2016.03.119.

P. Kaparaju, M. Serrano, and I. Angelidaki. Effect of reactor configuration on biogas production from wheat straw hydrolysate. *Bioresource technology*, 100: 6317-6323, 2009. https://doi.org/10.1016/j.biortech.2009.06.101.

T. Karuppiah and V.E. Azariah. Biomass Pretreatment for Enhancement of Biogas Production. IntechOpen. 2019. https://doi.org/10.5772/intechopen.82088.

M. Kim, Y.H. Ahn, and R. Speece. Comparative process stability and efficiency of anaerobic digestion; mesophilic vs. thermophilic. *Water research*, 36: 4369-4385, 2002. https://doi.org/10.1016/S0043-1354(02)00147-1.

A.S.R. Nordgård, W.H. Bergland, O. Vadstein, V. Mironov, R. Bakke, K. Østgaard, and I. Bakke. Anaerobic digestion of pig manure supernatant at high ammonia concentrations characterized by high abundance of Mathanosaeta and non-euryarchaeotal archaea. *Scientific Reports*, 7(1): 15077, 2017. http://dx.doi.org/10.1038/s41598-017-14527-1.

R. J. Patinvoh, O.A. Osadolor, K. Chandolias, I.S. Horváth, and M.J. Taherzadeh. Innovative pretreatment strategies for biogas production. *Bioresource technology*, 224: 13-24, 2017. https://doi.org/10.1016/j.biortech.2016.11.083.

M. Taherzadeh and K. Karimi. Pretreatment of lignocellulosic wastes to improve ethanol and biogas production: a review. *International journal of molecular sciences*, 9:1621-1651, 2008. https://doi.org/10.3390/ijms9091621.

O. Therasme, T.A. Volk, A.M. Cabrera, M.H. Eisenbies, and T.E. Amidon. Hot Water Extraction Improves the Characteristics of Willow and Sugar Maple Biomass with Different Amount of Bark. *Frontiers in Energy Research*, 6: 93, 2018. https://doi.org/10.3389/fenrg.2018.00093.

Y. Xia, H.H. Fang and T. Zhang. Recent studies on thermophilic anaerobic bioconversion of lignocellulosic biomass. *RSC Advances*, 3(36): 15528-15542, 2013.

K. Østgaard, V. Kowarz, W. Shuai, I.A. Henry, M. Sposob, H.H. Haugen, and R. Bakke. Syringe test screening of microbial gas production activity: Cases denitrification and biogas formation. *Journal of Microbiological Methods*,132:119–124, 2017. https://doi.org/10.1016/j.mimet.2016.11.021.

Intelligent dynamic simulation of fed-batch fermentation processes

Esko K. Juuso

Control Engineering, Environmental and Chemical Engineering, Faculty of Technology, University of Oulu, Finland,
esko.juuso@oulu.fi

Abstract

Batch bioprocesses are difficult to model due to strong nonlinearities, dynamic behaviour, lack of complete understanding and unpredictable disturbances. A cell produces more cells, chemical products and heat from chemical substrates. Typical growth characteristics include several phases whose appearances and lengths depend on the type of organisms and the environmental conditions. Large differences exist between different fermentation runs. The simulator developed for fed-batch fermentation processes consists of three interacting dynamic models, each with three phase specific versions. The models predict dissolved oxygen concentration, oxygen transfer rate and concentration of carbon dioxide in the exhaust gas through the whole process, by using only the control variables as inputs. A decision system based on fuzzy logic to provide smooth gradual changes between phases. The detection of the changes between process phases is improved by using the intelligent trend analysis. The dynamic simulator is suitable for an online forecasting tool in connection with the real process. The operation is based on the ideas of model predictive control (*MPC*): the previous online measurements on a chosen horizon are used for constructing a starting point and the simulator predicts the operation on a chosen prediction horizon by using the planned control actions. The simulation is started on fairly long time intervals.

Keywords: intelligent systems, dynamic simulation, fed-batch fermentation, temporal analysis, prediction

1 Introduction

Batch bioprocesses are difficult to model due to strong nonlinearity, dynamic behaviour, lack of complete understanding and unpredictable disturbances from their external environment (Gregersen and Jorgensen, 1999). As every cell in nature has a finite lifetime (Figure 1), a continuous growth of the organisms is needed to maintain the species. The generation time depends on both nutritional and genetic factors. To be able to live, reproduce and make products, a cell must obtain nutrients from its surroundings. The first phase at the beginning of the fermentation is called the lag phase. The second phase is the exponential growth phase. The last phase is called the steady state phase. The secondary metabolic products, such as enzymes, are produced mainly during the steady state phase.

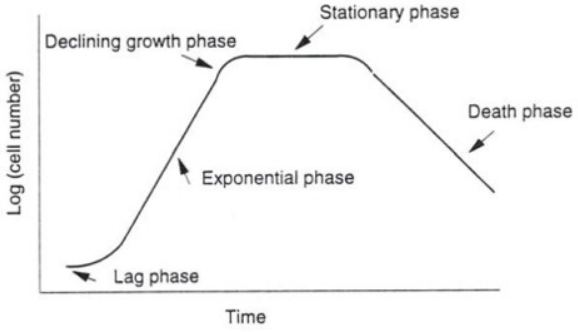

Figure 1. Growth phases in a batch bioprocess (Blanch and Clark, 1997).

In the lag phase, the growth is almost constant caused by many reasons. Since the cells are placed in fresh medium, they might have to adapt to it or adjust the medium before they can begin to use it for growth. Another reason might be that the inoculum is composed partly of dead or inactive cells (Enfors and Häggström, 2000). If a medium consists of several carbon sources, several lag phases might appear. This phenomenon is called diauxic growth. Microorganisms usually use just one substrate at a time and a new lag phase really results when the cells adapt to use the new substrate. (Blanch and Clark, 1997)

The declining of the growth rate begins when a substrate begins to limit. The growth rate slows down until it reaches zero and the stationary phase begins. In the stationary phase, the number of the cells remains practically constant, but the phase is important because many products are only produced during it. The last phase is called the death phase. During the death phase, the cells begin to lyse and the growth rate decreases. (Blanch and Clark, 1997)

In batch reactors, all components, except gaseous substrates such as oxygen, pH-controlling substances and antifoaming agents, are placed in the reactor at the beginning of the fermentation. There is no input nor output flows during the process. In fed-batch processes, nothing is removed from the reactor during the process but one substrate component is added in order to control the reaction rate by its concentration. The process is started as a batch process, and the substrate feed is started when the initial glucose is consumed. The fermentation continues at a cer-

tain growth rate until some practical limitation inhibits the cell growth (Enfors and Häggström, 2000).

The data sets obtained from the process are in practice distinct sets obtained through different process performances because usually one or more substantial physical parameters, such as dissolved oxygen (*DO*), temperature or *pH* are maintained on distinct level (Georgieva et al., 2001). The optimal values of parameters might not be the same for the growth phase and metabolite production phase in secondary metabolite production (Yegneswaran et al., 1991). Large differences exist between different fermentation runs because of the variations in the feeding strategy, the metabolic states of the cells and the amount of oxygen available. Even if the process conditions were kept the same in each fermentation, the micro-organisms would behave differently every time. Detection of fluctuations in operating conditions is essential for making correct actions in time.

The concentration of carbon dioxide (CO_2) in the exhaust gas is an important variable in a fermentation process since the production of CO_2 is correlated to the amount of consumed sugar (Martínez et al., 1999). The variations in the agitation speed can cause changes in the oxygen transfer rate (OTR) and an increase in it can cause an increase in production and yield (Elibol and Ozer, 2000). The *DO* tension is an important variable in secondary metabolite production and remarkable impacts on production yields can be achieved by affecting this parameter by changes in aeration, agitation system and stirrer speed (Pfefferle et al., 2000). The volumetric mass transfer coefficient, k_La, is also an important process variable because it can be used to find the relationship between the OTR and enzyme production (Elibol and Ozer, 2000) and it can be used in the control of the *DO* tension (Simon and Karim, 2001).

The oxygen requirements of the bacteria differ at different fermentation stages (Yao et al., 2001). By choosing a proper *DO* tension a product formation can be achieved without wasting the energy source. As the changes are slow, an early forecasting of the process operation is needed. A smoothly operated process is likely to be more productive than one that is subjected to significant disturbances. The aeration supplies oxygen to the process and, at the same time, removes carbon dioxide from microbial cells suspended in the culture broth. The rate of aeration often controls the rates of cell growth and product formation. (Yoshida, 1982)

In fed-batch fermentation, the dynamic simulator has been used online for predicting the process operation in a time window (Saarela et al., 2003a; Juuso, 2005). The results of these tests are used in this research.

This paper analyzes the dynamic simulation model developed for the prediction of the operation in a fed-batch fermentation process. The detection of the phases focuses on the temporal analysis with intelligent trend analysis. The parameters of the prediction models are not changed.

2 Bioprocess modelling

A fuzzy predictor presented in (Whitnell et al., 1993) combines three kinds of information: quantitative process inputs, linguistic information and heuristic knowledge from an expert in a beer making process. Takagi-Sugeno type fuzzy model was used in (Georgieva et al., 2001) on the modelling of a batch biotechnical process, which is strongly influenced by *DO* concentration as a manipulated input variable. Also black-box and hybrid models have been experimented in the modelling of batch beer production. The research concluded that the extrapolation capability of the model was improved by including mechanical knowledge in the hybrid model. The knowledge based models are useful when only insufficient data from the process can be obtained and they should be thought only as an extension of the ways in which process data can be represented. (Lübbert and Simutis, 1994) Bioprocess parameters have been estimated with neural network models (Simon and Karim, 2001; Thibault et al., 1990; Warne et al., 2004).

Model uncertainties need to be captured for the bioprocess optimization (Liu and Gunawan, 2017). Nonlinear model predictive control ($NMPC$) and observation of non-measurable states based on an unscented Kalman filter (UKF) were used in (Dewasme et al., 2015).

Temporal reasoning is a very valuable tool for diagnosing and controlling slow processes. Manual process supervision relies heavily on visual monitoring of characteristic shapes of changes in process variables, especially their trends. The fundamental elements are modelled geometrically as triangles to describe local temporal patterns. The elements are defined by the signs of the first and second derivative, respectively (Cheung and Stephanopoulos, 1990).

Linguistic equations introduced in (Juuso and Leiviskä, 1992) have been used in various applications (Juuso, 1999, 2004). Data-driven steady state modelling has been used in the development of linguistic equation (LE) model to represent interactions between measurements:

$$x_{out} = f_{out}\left(-\frac{\sum_{j=1,j\neq out}^{m} A_{ij}\, f_j^{-1}(x_j) + B_i}{A_{i\,out}}\right) \qquad (1)$$

where the functions f_j and f_{out} are scaling functions of input variables x_j and output x_{out}, respectively. These monotonously increasing, nonlinear functions are generated with generalised norms and moments (Juuso and Lahdelma, 2010). The monotonous increase is ensured with constraint handling. Dynamic structures extend the models to dynamic simulation.

Intelligent trend indices can be calculated from scaled measurements. Triangular episodes are classified with the trend index $I_j^T(k)$ and the derivative of it, $\Delta I_j^T(k)$ (Figure 2. Severity of the situations is evaluated by a deviation index which takes into account the scaled values of the measurements (Juuso, 2011).

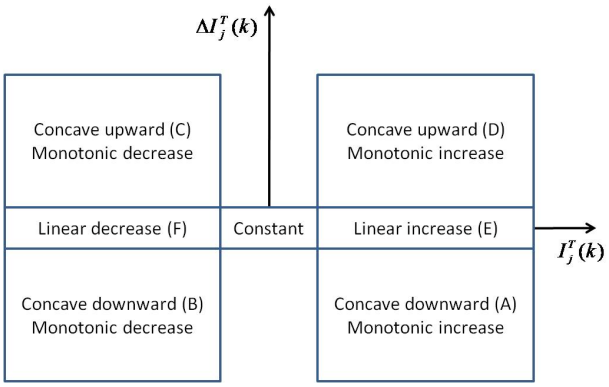

Figure 2. Triangular episodic representations defined by the index $I_j^T(k)$ and the derivative $\Delta I_j^T(k)$ (Juuso, 2011).

Linguistic equation method, linear neural network, feedforward neural networks and Takagi-Sugeno fuzzy models created by subtractive clustering appeared to be the best in comparison presented in (Saarela et al., 2003b). The correlations and the relative errors of these models were within acceptable limits and the fuzziness of the models was small. The model surfaces of the models created by these four methods were almost a plane.

3 Development of dynamic models

The dynamic models were based on the process data obtained from an industrial fed-batch fermenter. The models were tested using a number of different testing data, which were not included in the training data set. When necessary, the noise in the data was filtered by taking moving averages of the measured values. The variables for each model were chosen mainly based on correlation analysis. Variables that could be used for control were preferred when choosing the input variables of the model. These variables include the mixing rate, aeration, the substrate feed rate etc.

The models have a *NARX* (Nonlinear AutoRegressive with eXogenous input) structure. A multimodel approach was applied as different growth phases need different models (Figure 3(a)). As the prediction of the future values required three interacting models (Figure 3(b)): each produces the prediction of a different variable, the overall system consists of nine models. Various modelling methodologies have been compared. The compact implementation of the *LE* models made such a complex structure possible to use. Smooth transitions between the phase models are based on fuzzy decision system (Figure 3(a)).

The controllable variables were preferred as inputs and these include mixing, aeration, feed rate, pressure, temperature and cooling power. The variables used in the models include the concentration of carbon dioxide in the exhaust gas, mixing power, feed rate, oxygen transfer rate, dissolved oxygen concentration, volumetric oxygen transfer coefficient, position of the pressure valve and VVM (volumes of air per volume of liquid per minute). The choice of the variables was quite similar to the normal choice in the literature.

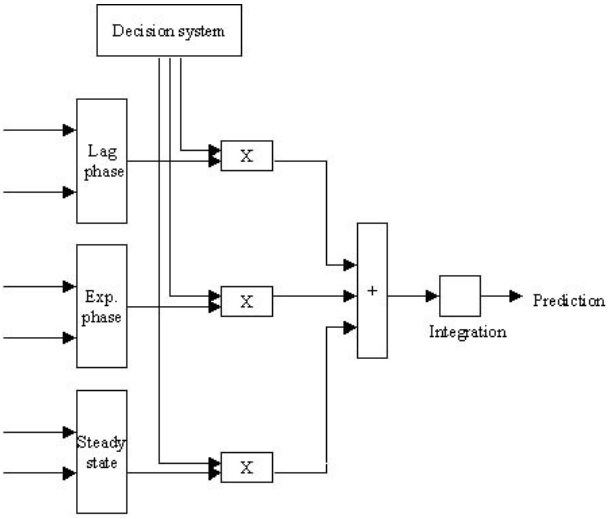

(a) The dynamic model structure of one predicted variable.

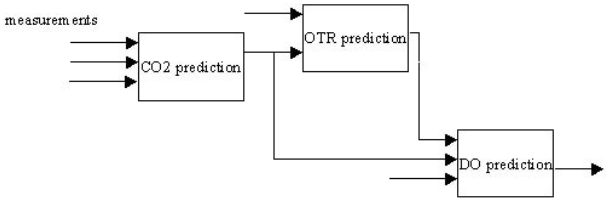

(b) The interactive models.

Figure 3. The overall structure of the model (Saarela et al., 2003a).

Three modelling techniques with several variants were compared including the methods of linguistic equations, neural networks and fuzzy modelling. The steady state modelling of the fermentation variables was not difficult for these intelligent modelling methods: *LE* models, linear neural network, feedforward neural networks and Takagi-Sugeno fuzzy models created by subtractive clustering appeared to be the best (Saarela et al., 2003b). However, dynamic simulation turned out to be too demanding for most of these methodologies.

The overall dynamic model shown in Figure 4 contains an additional model for calculating the volumetric mass transfer coefficient, $k_L a$.

In the LE models, the definitions of the scaling functions and coefficients A_{ij} from (1) are transferred into the dynamic model. The new prediction is calculated using previous values of the predicted value and the previous values of control variables. Different growth phases can be distinguished from the fermentation process and during these phases different variables affect the output variables. Because of this, three submodels for each predicted variable were created corresponding to each phase in the fermentation process (Figure 3(a)).

The overall model consists of three models and a de-

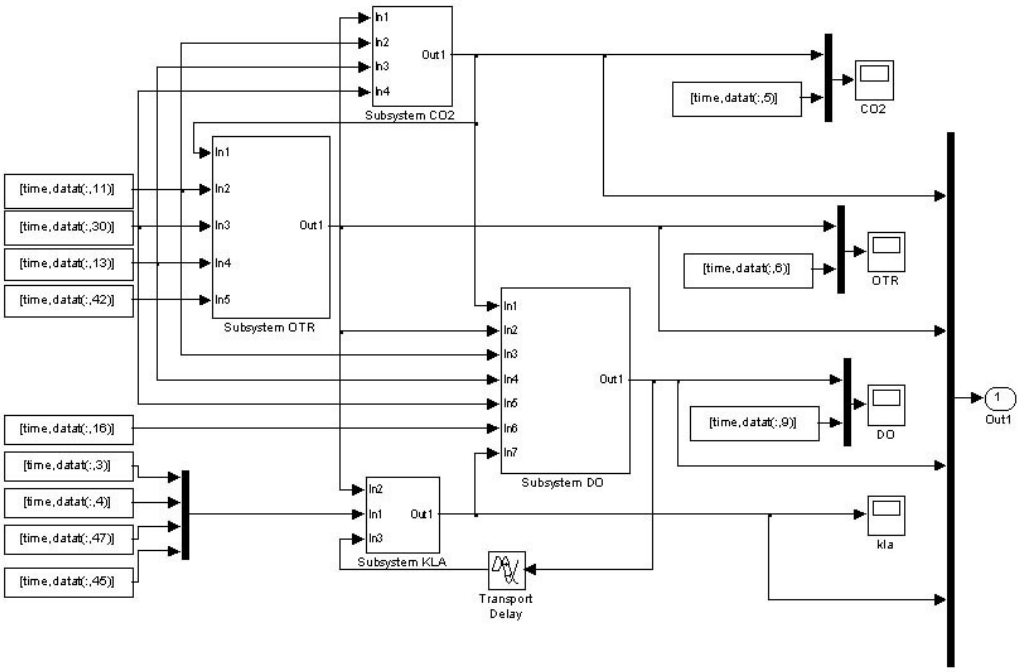

Figure 4. The overall simulation model (Saarela et al., 2003a).

cision system (Figure 3(a). The same structure is used for all the predicted variables. Inputs of the models include measurements from the process, such as mixing power, aeration rate, pressure, and substance concentrations. The inputs to the models of oxygen transfer rate prediction and dissolved oxygen concentration prediction include also predicted values from other models (Figure 3(b)).

Altogether, the overall model contains nine different submodels: three for each predicted variable. The three submodels (lag phase, exponential phase, and steady state) shown in Figure 3(a) form subsystems of the prediction models. The same fuzzy decision system weights the outputs of each of these submodels. In dissolved oxygen model, the coefficients of linguistic equation are $\{0.2, -0.5, 0.1, 0.1, -0.8\}$.

New predictions are obtained by integrating the calculated changes to the previous value with an ordinary differential equation solver based on an explicit Runge-Kutta (4,5) formula, the Dormand-Prince pair, with variable step.

The fuzzy decision system chooses the right submodel phase of the process by using the measurements of time, oxygen transfer rate and substrate feed rate. The inference system presented in Figure 5(a) has membership functions for three inputs and one output and a set of eight fuzzy rules for deduction. The system gives a weighting factor from 0 to 1 for each submodel according to which level its results are used. The system was constructed using the Matlab Fuzzy Logic Toolbox. At the beginning of the fermentation for example, the first submodel, the lag phase, is given a weight of one, and the other two submodels have the weight of zero. This means that only the output of the

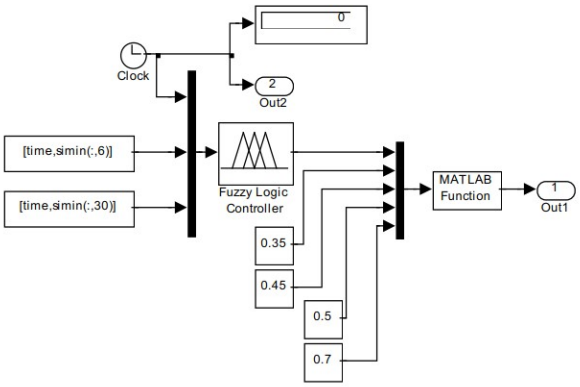

(a) The fuzzy decision system.

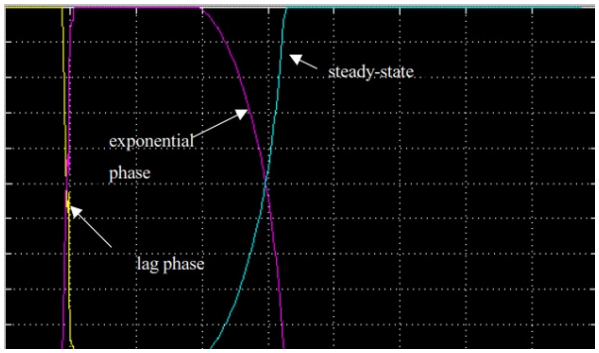

(b) The weights from the decision system.

Figure 5. The decision system for selecting the active phase: x-axis represents time and the y-axis weighting factors [0 1], input variables are time, *OTR* and the glucose feed rate (Saarela et al., 2003a).

first submodel is used in calculating the prediction. The transition from one phase to another happens smoothly, thus during the transition phase two outputs of the submodels can be used simultaneously (Figure 5(b)).

In the dynamic models, each submodel has been developed separately on the basis of selected training data. The combined model (Figure 4) has been tested with data collected from various fermentation runs. In the simulation tests, the input values were taken from the previously collected data. During the online tests, the prediction system collects the data from the automation system and starts the simulation on chosen time intervals. The prediction results were written back to the data collection system.

4 Results and discussion

The models were tested with a set of test data. The fitness of a model can be estimated by examining the correlation, *R*, relative error, fuzziness and the model surfaces. The FuzzEqu program also draws the results of the predictions in the same chart with the test data where they can be compared visually. The fuzziness of the equations should be close to zero. It shows how well the equation represents the data (Juuso, 1999).

4.1 Steady-state simulation

First, steady-state models for all three variables were made by the linguistic equations approach. Correlations of the dissolved oxygen models for different testing data were between [0.88-0.98] and the relative errors between [0.03-0.18]. For models of oxygen transfer rate the correlations were between [0.72-0.99] and the relative errors between [0.02-0.33]. Similar results were obtained with all the static models used in the simulation model. The first part of the process was the most difficult to model, largely due to differences between fermentations. However, at the beginning of the process the concentration of the dissolved oxygen is usually quite high and its predicted value is not so critical.

An example of data-driven modelling results for the prediction of the dissolved oxygen is presented in Figure 6. The new measure, fuzziness, is used for detecting areas where the models should be considerably different. Fuzziness can also be considered as an additional unknown variable. In this case, the fuzziness is very low.

4.2 Dynamic simulation

Dynamic modelling and simulation was performed in Matlab Simulink. Figure 5(b) presents the weights of the submodels obtained from the fuzzy decision system. The change from one phase to another is quite fast. The estimation of the dissolved oxygen concentration is presented in Figure 7(a). In this model, the estimations of the oxygen transfer rate and the concentration of carbon dioxide are used as inputs. The estimation of the oxygen transfer rate can be seen in the Figure 7(b). The estimate for the carbon dioxide concentration is used as an input of the

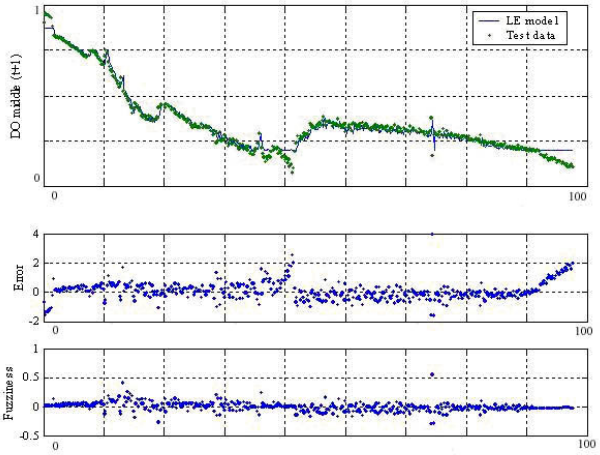

Figure 6. Results from the testing of steady-state fermentation models. Time from 0 to 100 is shown on the x-axis and the values of dissolved oxygen concentration, error and fuzziness on the y-axis (Saarela et al., 2003a).

model. The correlations and relative errors of these results are shown in the figures. With the exception of a few fermentations that largely differed from the others, the results were similar for other test data. The estimation was easier for the oxygen transfer rate and the carbon dioxide concentration than for dissolved oxygen concentration.

A multimodel approach was applied as different growth phases need different models. As the prediction of the future values required three interacting models, which each produces the prediction for a different variable, the overall system consists of nine models. The compact implementation of the *LE* models made such a complex structure possible to use. Smooth transitions between the phase models are based on fuzzy logic.

The important factors in the success of the modelling were the choice of the input variables, the choice of the model type and structure, and the choice of training data. The training data should be sufficiently large so that it can represent different fermentations. The results of the modelling can improve with the number of data runs employed for training (de Azevedo et al., 1997). Large differences exist between different fermentation runs because of the variations in the feeding strategy, the metabolic state of the cells and the amount of oxygen available. Even if the process conditions were the kept same in each fermentation, the micro-organisms would behave differently every time.

The choice of the input variables was difficult. Different variables affect the output variables in the different phases of the process. All the influence of the variables could not be examined because the data was obtained from an industrial fermenter and a part of the variables were controlled to remain constant. The data based modelling methods require changes in the data to be able to model it.

The dynamic simulator operates accurately throughout the fermentation even for more than 40 hours as a real simulation, i.e. the simulator uses in each time step only

the previous simulated value and the values of the variables which control the process, according to the dynamic model. Differences between the calculated and measured are reasonable and provide a good basis for detecting fluctuations in operating conditions.

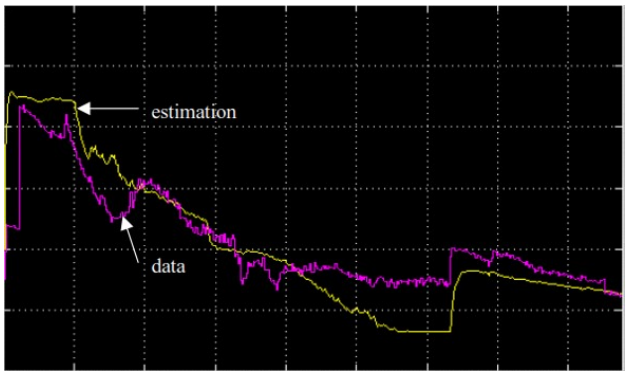

(a) Prediction of dissolved oxygen (*DO*) concentration: time is on the x-axis and the dissolved oxygen concentrations on the y-axis.

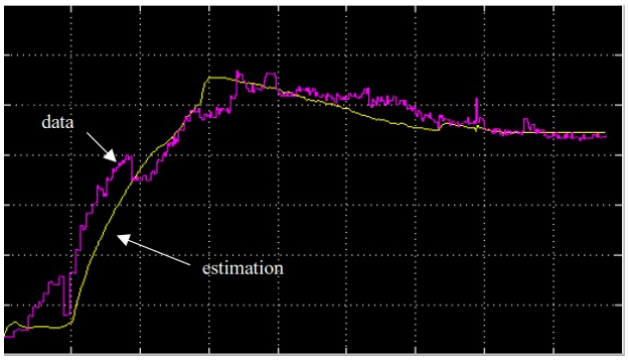

(b) Prediction of oxygen transfer rate (*OTR*): time is on the x-axis and the oxygen transfer rates on the y-axis.

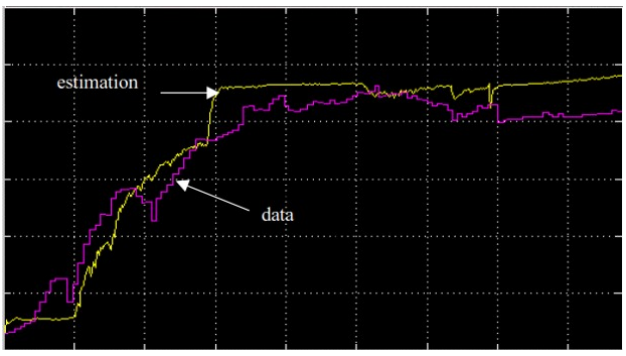

(c) Prediction of carbon dioxide (CO_2): time is on the x-axis and the oxygen transfer rates on the y-axis.

Figure 7. Simulation results of a fermentation run (Saarela et al., 2003a).

The simulator is aimed primarily on the detection of changes and fluctuations for the process control. In the estimation, the starting time of the growth phase was predefined. However, the test results reveal a diauxic growth: the first growth starts earlier as can be seen in all predictions which is seen in decreasing *DO* (Figure 7(a) and increasing *OTR* and CO_2 (Figures 7(b) and 7(c)). Updating the parameter of the scaling functions with newer methodologies (Juuso and Lahdelma, 2010) would be beneficial.

The drop of *DO* during the first phase introduces a new lag phase of the second growth phase, which starts later, proceeds slower than the first growth phase and finally slows down gradually to the stationary phase. Two models with different parameter tuning are are required for the growth phase. The stationary phase has two stages: the first part fairly constant *OTR* but then the death phase is partly activated. Aeration stabilizes the *OTR* on a new constant level. The estimation errors seen in Figure 7 are at least partly caused by the errors in the fuzzy decision system. Clearly time, *OTR* and the glucose feed rate are not sufficient for defining the start of the growth phase and the diauxic growth needs to be taken into account.

4.3 Detection of operating conditions

The simulator can be used as an online forecasting tool in connection with the real process. The simulator is started on chosen time intervals: the previous online measurements on a chosen horizon are used for constructing a starting point and the simulator predicts the operation on a chosen prediction horizon by using the planned control actions. In the online tests, the prediction horizon has been one hour and the time interval between predictions six minutes. The model predictive control can be considered as a new option since the simulator is very compact. Actually, generating a good starting point for simulation calculations was more demanding than the prediction part. This operates well in the stationary phase. The simulator is started on chosen time intervals and it operates accurately throughout the fermentation even for more than 40 hours (Juuso, 2005).

The intelligent trend analysis improves the detection of phase changes (Figure 1) by using triangular episodes shown in Figure 2: the start of the growth phase is seen as a concave upward monotonic increase (Episode D) which continues as a linear increase (Episode E). The slowdown is detected as Episode A. The activation of the dead phase is seen with Episodes B, F and C. The analysis, which proceeds with time, is adapted by short and long time windows to the speed of the process. Differencies of the fermentation runs are essential in the analysis.

5 Conclusions

The simulator can be used as an online forecasting tool in connection with the real process in the stationary phase. The operation is based on the ideas of model predictive control (*MPC*). In this case, the simulation is started on fairly long time intervals. The previous online measurements on a chosen horizon are used for constructing a starting point and the simulator predicts the operation on a chosen prediction horizon by using the planned control actions. Intelligent trend analysis provides efficient tools for the early detection of the changes in operation phases and situations. The solution adapts to differences in fermentation runs.

References

H. W. Blanch and D. S. Clark. *Biochemical Engineering*. CRC Press, 1997. 702 pp.

J. T.-Y. Cheung and G. Stephanopoulos. Representation of process trends - part I. A formal representation framework. *Computers & Chemical Engineering*, 14(4/5):495–510, 1990.

S. Feyo de Azevedo, P. Dahm, and R. R. Oliveira. Hybrid modelling of biochemical processes: A comparison with the conventional approach. *Computers and Chemical Engineering*, 21(Suppl.):S751–756, 1997.

L. Dewasme, S. Fernandes, Z. Amribt, L.O. Santos, Ph. Bogaerts, and A. Vande Wouwer. State estimation and predictive control of fed-batch cultures of hybridoma cells. *Journal of Process Control*, 30:50 – 57, 2015. doi:10.1016/j.jprocont.2014.12.006.

M. Elibol and D. Ozer. Influence of oxygen transfer on lipase production by rhizopus arrhizus. *Process Biochemistry*, 36: 325–329, 2000.

S.-O. Enfors and L. Häggström. *Bioprocess Technology Fundamentals and Applications*. Royal Institute of Technology, Stockholm, 2000. 356 pp.

O. Georgieva, M. Wagenknecht, and R. Hampel. Takagi-sugeno fuzzy model development of batch biotechnological process. *International Journal of Approximate Reasoning*, 26:233–250, 2001.

L. Gregersen and S. B. Jorgensen. Supervision of fed-batch fermentation. *Chemical Engineering Journal*, 75:69–76, 1999.

E. Juuso and S. Lahdelma. Intelligent scaling of features in fault diagnosis. In *7th International Conference on Condition Monitoring and Machinery Failure Prevention Technologies, CM 2010 - MFPT 2010, 22-24 June 2010, Stratford-upon-Avon, UK*, volume 2, pages 1358–1372, 2010. URL `www.scopus.com`.

E. K. Juuso. Fuzzy control in process industry: The linguistic equation approach. In H. B. Verbruggen, H.-J. Zimmermann, and R. Babuška, editors, *Fuzzy Algorithms for Control, International Series in Intelligent Technologies*, volume 14 of *International Series in Intelligent Technologies*, pages 243–300. Kluwer, Boston, 1999. doi:10.1007/978-94-011-4405-6_10.

E. K. Juuso. Integration of intelligent systems in development of smart adaptive systems. *International Journal of Approximate Reasoning*, 35(3):307–337, 2004. doi:10.1016/j.ijar.2003.08.008.

E. K. Juuso. Dynamic simulation of a fed-batch enzyme fermentation process. In *Proceedings of SIMS 2005, 46th Conference on Simulation and Modeling, October 13-14, 2005, Trondheim, Norway*, pages 117–124. Tapir Academic Press, Trondheim, 2005. ISBN 82-519-2093-0.

E. K. Juuso. Intelligent trend indices in detecting changes of operating conditions. In *2011 UKSim 13th International Conference on Modelling and Simulation*, pages 162–167. IEEE Computer Society, 2011. doi:10.1109/UKSIM.2011.39.

E. K. Juuso and K. Leiviskä. Adaptive expert systems for metallurgical processes. In S.-L. Jämsä-Jounela and A. J. Niemi, editors, *Expert Systems in Mineral and Metal Processing, IFAC Workshop, Espoo, Finland, August 26-28, 1991, IFAC Workshop Series, 1992, Number 2*, pages 119–124, Oxford, UK, 1992. Pergamon.

Y. Liu and R. Gunawan. Bioprocess optimization under uncertainty using ensemble modeling. *Journal of Biotechnology*, 244:34 – 44, 2017. doi:10.1016/j.jbiotec.2017.01.013.

A. Lübbert and R. Simutis. Using measurement data in bioprocess modelling and control. *Trends in Biotechnology*, 12(8): 304 – 311, 1994. doi:10.1016/0167-7799(94)90047-7.

G. Martínez, A. López, A. Esnoz, P. Vírseda, and J. Ibarrola. A new fuzzy control system for white wine fermentation. *Food Control*, 10:175–180, 1999.

C. Pfefferle, U. Theobald, H. Gürtler, and H.-P. Fiedler. Improved secondary metabolite production in the genus streptosporangium by optimisation of the fermentation condition. *Journal of Biotechnology*, 80:135–142, 2000.

U. Saarela, K. Leiviskä, and E. Juuso. *Modelling of a fed-batch fermentation process. Report A 21, June 2003.* Control Engineering Laboratory, University of Oulu, Oulu, 2003a.

U. Saarela, K. Leiviskä, E. Juuso, and A. Kosola. Modelling of a fed-batch enzyme fermentation process. In *IFAC International Conference on Intelligent Control Systems and Signal Processing. Faro, Portugal, April 8-11, 2003*. IFAC, 2003b.

L. Simon and M. Nazmul Karim. Identification and control of dissolved oxygen in hybridoma cell culture in a shear sensitive environment. *Biotechnology Progress*, 17:634–642, 2001.

J. Thibault, V. V. Breusegem, and A. Cheruy. On-line prediction of fermentation variables using neural networks. *Biotechnology and Bioengineering*, 36(12):1041–1048, 1990.

K. Warne, G. Prasad, S. Rezvani, and L. Maguire. Statistical and computational intelligence techniques for inferential model development: a comparative evaluation and a novel proposition for fusion. *Engineering Applications of Artificial Intelligence*, 17:871–930, 2004.

G. P. Whitnell, V. J. Davidson, R. B. Brown, and G. L. Hayward. Fuzzy predictor for fermentation time in a commercial brewery. *Computers Chemical Engineering*, 17(10):1025–1029, 1993.

H. M. Yao, Y. C. Tian, M. O. Tadé, and H. M. Ang. Variations and modelling of oxygen demand in amino acid production. *Chemical Engineering and Processing*, 40:401–409, 2001.

P. K. Yegneswaran, M. R. Gray, and B. G. Thompson. Effect of dissolved oxygen control on growth and antibiotic production in streptomyces clavuligerus fermentation. *Biotechnology Progress*, 10:246–250, 1991.

F. Yoshida. Chapter 1 - aeration and mixing in fermentation. volume 5 of *Annual Reports on Fermentation Processes*, pages 1 – 34. Elsevier, 1982. doi:10.1016/B978-0-12-040305-9.50005-4.

Chemical equilibrium model to investigate scaling in moving bed biofilm reactors (MBBR)

Vasan Sivalingam[1] Osama Ibrahim [1] Sergey Kukankov[1] Babafemi Omodara[1] Eshetu Janka[1] Shuai Wang[2] Carlos Dinamarca[1] Hildegunn HH [1] Rune Bakke[1]

[1]Department of Process, Energy and Environmental Technology, University of South-Eastern Norway, Norway, eshetu.j.wakjera@usn.no

Biowater Technology AS, Norway, sw@biowatertechnology.com

Abstract

Moving bed biofilm reactor (MBBR) is a robust, flexible and compact technology for treatment of medium to high strength wastewater. However, while treating wastewater with high concentration of ammonium, phosphorus and metal ions, scaling on the biofilm carriers can occur, causing biofilm carriers to sink the bottom of reactors. That leads to less carrier motion, higher energy consumption and deteriorated mass transfer, causing lower process efficiency and increased operational cost. This can be a major MBBR operational challenge for certain types of wastewater. In this study, scaling on biofilm carriers in an MBBR reactor treating reject water from anaerobically digested wastewater sludge was investigated. The 67 L reactor was operated at 16 h hydraulic retention time (HRT) for over 250 days. The metal ion concentrations in the reject wastewater in and out of the MBBR were analyzed using microwave plasma-atomic emission spectroscopy (MP-AES). The chemical equilibrium simulation tool -- Visual MINTEQ 3.1 was applied to determine the possible mineral precipitates. The measured concentrations of Mg^{2+}, Ca^{2+}, Fe^{3+}, NH_4-N, PO_4^{3-}, SO_4^{2-} and alkalinity from the inlet and outlet of the reactor were used as inputs to the model. Dry biomass and precipitates from biofilm carriers were digested by a DigiPREP digestion system and element analysis performed using MP-AES for simulated data validation. The results show that Fe^{3+} and Ca^{2+} had the highest potential to form mineral precipitates and scaling on the biofilm carriers. Hematite, Maghemite, Hydroxyapatite, Geothite and Magnesioferrite were the first five predominant forms of mineral precipitates, in the pH range from 6.0 to 9.0. The saturation indices (SI) of these five minerals increased with pH, implying that measures to lower pH may reduce the problem. Digested biomass composition and inorganic solid analysis confirmed that calcium is the major cause for scale formation on the biofilm carriers. Crystal formations in the biofilms were confirmed by optical microscopy images.

Keywords: Visual MINTEQ, scaling, moving bed biofilm reactor, reject water

1 Introduction

Scaling on biofilm carriers is a major problem in moving bed biofilm reactors (MBBR) treating wastewater with high concentration of ammonium, phosphorus and metal ions. Scale formation occurs, e.g., in treatment of reject water from sludge digestion. When sludge is digested anaerobically, ammonia and soluble orthophosphate will be released from the sludge and end up in the reject water when such sludge is dewatered, and, in the presence of magnesium, calcium or ferric ions, could result in crystallization of inorganic salts. The amount of active biomass is an important factor in assessment the performance of MBBR, and the biomass growth chiefly depends on the designed carrier's effective surface area (ESA). During the MBBR operation, ESA can decrease because of excess biofilm biomass accumulation so that the area of biofilm exposed to the liquid (EBA) decreases. Surplus biofilm thickness may thereby have negative effect on the reactor's efficiency by reducing EBA and mass transfer and also by increasing carrier weight (Ødegaard, 2006; Piculell, 2016).

Crystallization can happen when a solution is supersaturated. This occurs when the solute concentration surpasses the equilibrium and nucleation occurs due to high free energy. Saturation index (SI) is an important parameter for determination of the probability for mineral precipitation. SI is a logarithmic ratio between ion activity product (IAP) and equilibrium constant (K_{sp}) in the wastewater treatment process (Sharp *et al*., 2013)

$$\mathrm{SI} = \log \frac{\mathrm{IAP}}{\mathrm{K_{sp}}} \quad (1)$$

IAP (ion activity product) is quantified as a product of all comprised ion concentrations which should be measured as soluble ions. Ionic strength (I) depends on dissolved solids concentrations and can be calculated from (2).

$$I = \frac{1}{2} \sum Z_i^2 C_i \quad (2)$$

Where, Z_i is the valency of the ion and C_i is the concentration. Ionic strength for wastewater is in the range of 0 to 0.2. If the composition of wastewater is unknown, it can be approximated as the dissolved solids [g/L] x 2.5 x 10^{-5} $\times 2.5 \times 10^{-5}$ .Debye-Huckel method

uses mean ionic activity (γ) for activity correction as follows (Cellen, 2010):

$$\log \gamma = -0.5Z^2 \frac{\sqrt{I}}{1+\sqrt{I}} \quad (3)$$

Visual MINTEQ 1.3 is based on Equations 1-3 and is one of the most used chemical equilibrium simulation tool to determine possible mineral speciation and estimate its solubility at chemical equilibrium. Visual MINTEQ is a simulation tool which can be used to compute the equilibrium composition of dilute aqueous solutions. It is a Windows version of MINTEQA2 equipped with inclusive thermodynamic data to estimate speciation, solubility and equilibrium of minerals in the solutions. It was found to be a good simulation tool in several studies which have been implemented in different versions of Visual MINTEQ to predict and control of possible mineral precipitations in wastewater. Jia (2014), applied Visual MINTEQ 3.0 to analyze the formation of struvite from sludge dewatering effluent from Bolivar wastewater treatment plant in south Australia. Visual MINTEQ 2.23 was used of struvite formation in a wastewater treatment by (Çelen *et al*., 2007; Çelen and Türker, 2010) to estimate the required modifications for phosphates precipitation in liquid swine manure. Chand (2018), investigated the struvite formation possibility from anaerobically digested sludge by calculating the values of saturation indices with help of Visual MINTEQ 1.3.

In our study, the model is applied with the objective to investigate the possible precipitates in moving bed biofilm reactors (MBBR) treating reject water. The model calculations were done mainly based on chemical element's concentrations of magnesium, phosphorous, ammonium, iron and calcium. The Debye-Huckel method was use for activity corrections during model setup for precipitation prediction (Jia, 2014). Specified temperature, alkalinity and pH values were used for determination of saturation index (SI).

2 Materials and methods

A moving bed biofilm reactor (MBBR) was installed on the lines of reject water directed to main wastewater inlet as shown in Figure 1. The MBBR has a dimension of LxBxH=0.35x0.35x0.55m (effluent level) with a working volume of 67 L. It was filled with bio carriers to a filling degree of approximately 70 % of the reactor volume. The bio carriers, BWT S® (Biowater Technology AS), made of high-density polyethylene (HDPE) with dimensions of 14.5x18.5x7.3 mm and protected surface area of 650 m^2/m^3, were used as biofilm attaching substratum. The reactor was fed by centrifuged effluent from anaerobic sludge digestion. Since the centrifuge works intermittently (i.e., 6-9 hours during week days) the reject wastewater is stored in an intermediate bulk container (IBC) onsite to ensure that there is constant supply of feed into the reactor. The reactor was continuously aerated with air flow 26 ± 2 L/min.

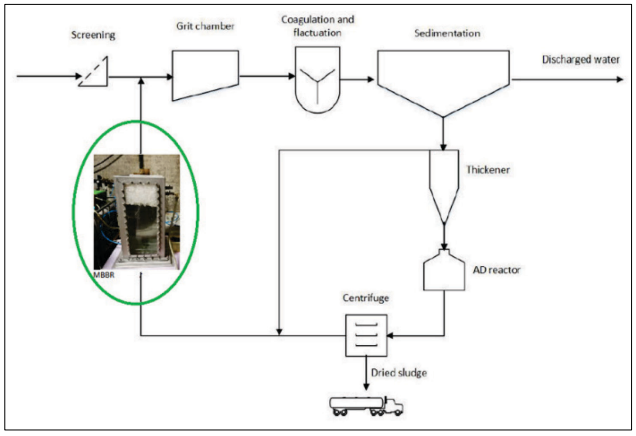

Figure 1. Flow diagram of Knarrdalstrand municipal wastewater treatment plant, Porsgrunn showing the MBBR position.

At the beginning, carriers moved freely in the MBBR reactor as intended but gradually carriers started to sink after strong biofilm growth and eventually settled permanently with heavy scaling on the bottom of the reactor after ~200 d of operation (Figure 2)

2.1 Sampling and wet chemical analysis

Samples of influent and effluent were collected two times per week and various chemical analyses such as ammonium, total chemical oxygen demand (CODt), soluble COD (CODs), total suspended solids (TSS), volatile suspended solids (VSS), PO_4-P and Alkalinity were carried out. The analyses were performed based on the standard methods according to APHA (1995).

2.2 Element analysis by Microwave plasma atomic emission spectroscopy

Microwave plasma atomic emission spectroscopy (MP-AES 4210) was used to estimate the total ion concentrations for elements, Ca, Fe, Mg, P and Al in the reject water. MP-AES provides analytical techniques to determine the elemental composition of samples by surveying their electromagnetic spectrum or mass spectrum. MP-AES uses nitrogen extracted from air by nitrogen generator to form plasma. Axial magnetic and radial electrical fields strengthen the nitrogen plasma. The sample aerosol was injected into plasma and the axial emission was directed into scanning monochromator. The different elements have a different wavelength. The emissions of selected wavelength range are reflected on high efficiency charge coupled device (CCD) detector.

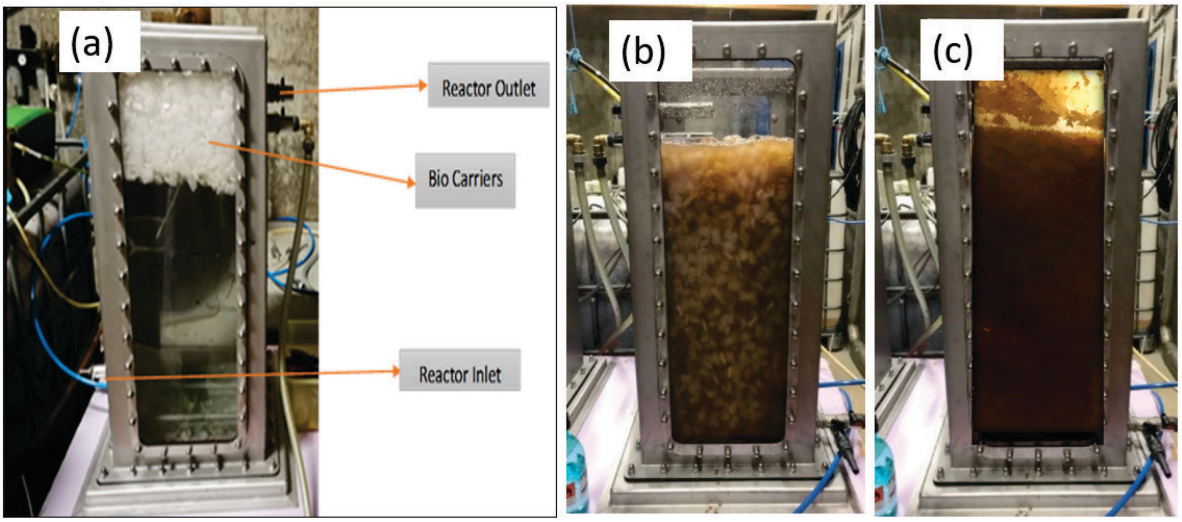

Figure 1. MBBR reactor setup with BWTS® carriers (a-MBBR with newly filled carriers, b- MBBR in good condition with freely moving carriers, c- MBBR with settled carriers.

2.2.1 Liquid sample preparation for element analysis

Samples from influent and effluent of the reactors were centrifuged, filtered and then diluted with 2% nitric acid (HNO_3) to 100 and 1000 dilution factors. Subsequently, the samples were measured by the MP-AES instrument for the elements Ca, Fe, Mg and P. Agilent Technologies ICP-OES Calibration Solution was used for wavelength calibration and Sigma-Alorich Periodic table mix 1 was used for wastewater standard calibration.

2.2.2 Quantification of biomass on carriers

Five carriers (N) were taken from the MBBR reactor, placed on an aluminum plate and dried at 105°C for 24 h and cooled down for 10 min in the desiccator. Then dried carriers were weighted (m_1). After that, carriers were soaked into hypochlorous acid (HOCl) for 2 hours, biomass was brushed and washed out by tap water. Again, the cleaned carriers were dried at 105°C for 24 h and weighted (m_2). Eventually, biomass per carrier m was calculated as mentioned in (4).

$$m = \frac{m_1 - m_2}{N} \quad (4)$$

Biomass per unit protected surface area was calculated according to (5).

$$W = m.\frac{V_C}{A} \quad (5)$$

Here:
W: Biomass per unit surface area (g/m^2)
m : Biomass per carrier (g/piece)
V_C: Number of carrier pieces per volume (piece/m^3)
A: Protected surface area (m^2/m^3)

2.2.3 Solid sample preparation for element analysis

A DigiPREP Digestion System was used to digest organic materials included in dried sample of sludge and carrier's biomass. The DigiPREP Digestion System involves a microwave – assisted acid digester (MAAD) equipped with a touch-screen controller, Digi- tubes and filters. Samples from sludge and carriers were dried for at least 10 hours in an oven at 105°C, then the carriers were rubbed off. Dried samples of mass 0.5 g were digested with 10 mL concentrated HNO_3 (69% v/v) in special digested tubes placed in a MAAD. Digested samples were cooled and then filtered with 1.2-1.5µm pore size glass filter. Thereafter, samples were diluted up to 50 mL with distilled water. Again, the diluted samples were diluted with 2 % HNO_3 up to 100 and 1000 dilution factor. Subsequently, the samples were measured by MP-AES.

2.3 Model inputs

Metal ion concentration, temperature and pH were the main inputs for Visual MINTEQ simulations. These parameters were varying over the time, therefore average values were used as input for the model. The average temperature was set to 16.5ºC and pH was attempted to be kept constant at value8.2. The ion concentration inputs are given in Table 1. Ionic strength was let it to be calculated by model itself based on Debye-Huckel activity model.

Table 1. Input ion concentrations for Visual MINTEQ simulations.

Elements	*Concentration (mg/L)*
Mg^{2+}	35
Ca^{2+}	700
Fe^{3+}	15
NH_4^+	440
$P(PO_4)$	40
SO_4^{2-}	4

2.4 Crystal observation in solid samples

The presence of crystals in biomass and sludge samples was investigated by stereo microscope Nikon SMZ745 and fluorescence microscope Olympus IX70. Both microscopes are equipped with cameras to capture the pictures of biomass at 20x and 40x magnification.

3 Results and Discussion

The effective biofilm thickness is crucial to maintain efficient mass transfer between biofilm and bulk liquid phase. Excessive biofilm accumulation and scaling on the bio-carriers was observed over the study period. For instance, the average values of biomass on carrier per unit surface area exceeded 135 g/m^2 temporarily and stabilized in the range of 90-120 g/m^2 as shown in Figure 3.

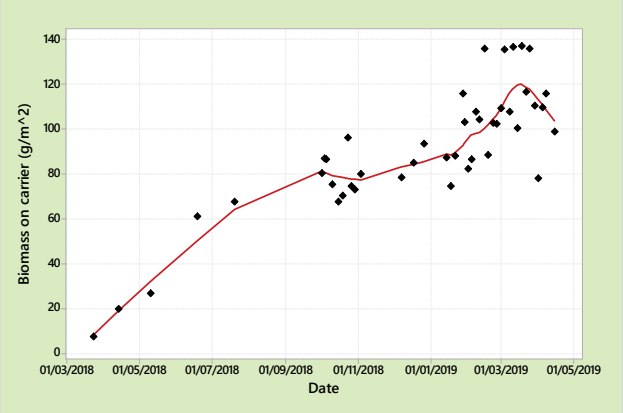

Figure 3. Biomass accumulation on carrier in MBBR reactor over the time (01.03.2018 – 01.05.2019).

Due to the increasing biofilm density it was observed that freely moving carriers started to settle and the effectiveness of the process in removing organics deteriorated (data not shown).

Table 2. Saturation indices for possible mineral precipitates in MBBR reactor, found in simulation result.

Mineral	*Saturation Index*
Hematite	21.6
Hydroxyapatite	18.1
Magnesioferrite	15.8
Maghemite	14.5
Goethite	9.6
Lepidocrocite	9.1
Ferrihydrite (aged)	7.2
$Ca_3(PO_4)_2$ (beta)	6.9
$Ca_4H(PO_4)_3{:}3H_2O$(s)	6.9
Ferrihydrite	6.7
$Ca_3(PO_4)_2$ (am2)	5.5
Strengite	4.2
$Ca_3(PO_4)_2$ (am1)	2.8
$CaHPO_4$(s)	1.1
$CaHPO_4{:}2H_2O$(s)	0.8
Struvite	0.4

The chemical equilibrium model has shown several possible precipitates on the biofilm carriers that may have caused the high biofilm density and carrier settling (Table 2). The results show that Fe^{3+} and Ca^{2+} ions had the highest potential to form mineral precipitates and scaling on the biofilm carriers. Among other diverse forms of precipitates, Hematite, Hydroxyapatite, Magnesioferrite, Maghemite, and Goethite were the most predominant forms of mineral precipitates, with saturation indices (SI) of 21.6, 18.1, 15.8, 14.5, and 9.6, respectively. Digested dried sample of sludge and carrier's biomass had 37 % and 28 % mass percentage of calcium, respectively. pH had effects on the precipitates' SI in the pH range from 6.0 to 9.0 are shown in Figure 4.

Struvite was not one of the major precipitates in this study because it has low saturation index 0.4 (Table 2

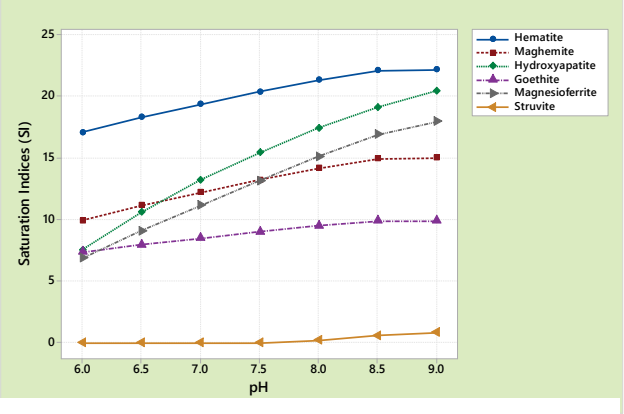

Figure 4. The saturation indices variation with pH for the predominant mineral precipitates predicted by the model.

and Figure 4). Struvite is magnesium ammonium phosphate and it normally precipitates when the ion concentration of magnesium, ammonium and phosphate are over saturated and the molar ratio is 1:1:1 (Tansel *et al.,* 2018*)*.

The simulations have shown that pH has significant effect on the amount and type of precipitants on the biofilm carriers. Hematite, Maghemite, Hydroxyapatite and Magnesioferrite precipitation increased most with increase in pH. Goethite and Struvite were not much influenced by pH with a slight increase in struvite when the pH was above 8 (Figure 4). pH in the range of 7 to 11 is generally known to be conducive for the formation of struvite, calcium phosphate and calcium carbonate and the crystallization rate decreases when the pH drops below this 7 to 11 range (Daneshgar *et al*., 2018). The aeration process in the MBBR reactor may have increased pH by CO_2 stripping and by biological reactions (Organics consumption, NH4 increase etc.). The measured inlet pH in this study was ~ 7.5 and the reactor pH was ~ 8.2, respectively.

Several studies have shown that crystallization occurs in biofilms when the bulk liquid solution contains more dissolved solute than the equilibrium saturation values. The ions involved in scale formation have intricate interaction and different crystals could be formed

depending on the system condition such as ionic concentrations, temperature and pH (Harker *et al*., 2013).

A microscopic image of the observed crystalsformed in the biofilm carriers is shown in Figure 5.

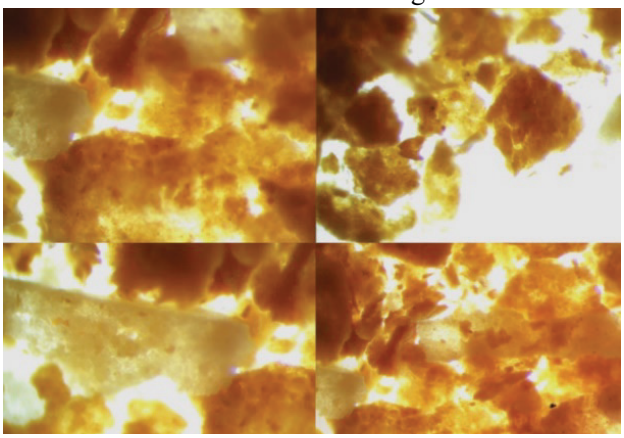

Figure 5. Microscopic observation of crystals on the biofilm carriers. The crystals were the precipitates after washing the biofilm carriers. Image is taken by stereoscopic zoom microscope with C-W10XB adjustable 10x/22mm wide field eyepieces and auxiliary objective AL-2x.

The simulation result has showed that, the major proportion of the crystal is a combination of either iron or calcium precipitates. Comparing the microscopic image with other studies of scanning electron microscope the struvite crystallization was significantly low. Since the reject wastewater contains large amount of calcium, it might inhibit the struvite crystallization. Similar studies have indicated that calcium has effect on struvite crystallization at different magnesium to calcium molar ratios (Hao *et al*., 2008). When the molar ratio of calcium is high, the formed crystal shows transformation in morphology different from struvite.

4 Conclusions

Scaling on biofilm carriers of moving bed biofilm reactor (MBBR) is a major problem during treatment of reject wastewater, as it makes biofilm carriers heavy so that they sink to the reactor bottom. The study has confirmed that high concentration of ammonium, phosphorus and metal ions creates scaling on the biofilm carriers.

The chemical equilibrium simulation tool Visual MINTEQ 3.1 is a useful tool to predict which mineral precipitates can occur in wastewater treatment process, to what extent they may form and factors influencing their formation.

The pH and ionic concentration of metal ions play significant roles in the formation of different crystals. In this study, Fe^{3+} and Ca^{2+} had the highest potential to form mineral precipitates and scaling on the biofilm carriers. Among possible forms of precipitates Hematite, Hydroxyapatite, Magnesioferrite, Maghemite, and Goethite were the most predominant in order of their saturation indices (SI). pH control, generally by lowering pH, appears to be the most realistic way to limit scaling.

Acknowledgements

This research project is funded by Oslofjorfondet, project number 269014 under the project title: Efficient upgrading of municipal wastewater treatment plants. Main parts of this study were carried out at Knarrdalstrand wastewater treatment plant, Porsgrunn with contributions from their staff, especially Rune Hogstad Hansen.

References

American Public Health Association (APHA). *Standard Methods for the Examination of Water and Wastewater*, 19th ed. American Public Health Association, American Water Works Association and Water Pollution Control Federation, Washington D.C, 1995.

R. Chand. Struvite forming possibility based on the component concentration in liquid phase of anaerobically digested sludge at varying temperature and ph and phosphorus recovery using acetate and tris buffer solution a case study at aalborg west wastewater treat. *International Journal of Recent Sci entific Research,* 9(7): 28198-28208, 2018.

S. Daneshgar, A. Buttafava, D. Capsoni, A. Callegari, and A. Capodaglio. Impact of pH and ionic molar ratios on phosphorous forms precipitation and recovery from different wastewater sludges. *Resources,* 7(4): 71, 2018.

X.D. Hao, C.C. Wang, L. Lan, and M. Van Loosdrecht. Struvite formation, analytical methods and effects of pH and Ca^{2+}. *Water Science and technology,* 58 (8): 1687-1692, 2008.

G. Jia. *Nutrient Removal and Recovery by the Precipitation of Magnesium Ammonium Phosphate.* Faculty of Engineering, Computer and Mathematical Sciences, The University of Adelaide, Adelaide South Australia, 2014.

J.H. Harker and J.F.B. Richardson. *Chemical Engineering.* Butterworth-Heinemann, Oxford, 2013.

M. Piculell. *New Dimensions of Moving Bed Biofilm Carriers: Influence of biofilm thickness and control possibilities*, Doctoral Thesis. Department of Chemical Engineering, Lund University, Lund, 2016.

R. E. Sharp, R. Vadiveloo, M. Fergen, P. Moncholi, D. Pitt, M. Wank, and R. Latimer. A theoretical and practical evaluation of struvite control and recovery. *Water Environment Research,* 85(8): 675-686, 2013.

B. Tansel, G. Lunn, and O. Monje. Struvite formation and decomposition characteristics for ammonia and phosphorus recovery: A review of magnesium-ammonia-phosphate interactions. *Chemosphere,* 194:504-514, 2018.

I. Çelen, J.R. Buchanan, R.T. Burns, R. Bruce Robinson, and D. Raj Raman. Using a chemical equilibrium model to predict amendments required to precipitate phosphorus as struvite in liquid swine manure. *Water Re search,* 41(8):1689-1696, 2007.

I. Çelen, and M.Turker, Chemical equilibrium model of struvite precipitation from anaerobic digester effluents. *Turkish J. Eng. Env. Sci.,* 34:39 – 48, 2010.

H. Ødegaard, Innovations in wastewater treatment: the moving bed biofilm process. *Water Science and Technology,* 53(9): 17-33, 2006.

Simulation of air-biomass gasification in a bubbling fluidized bed using CPFD model

Ramesh Timsina Britt Moldestad Marianne S. Eikeland Rajan K. Thapa

Department of Process Energy and Environmental Technology University of South-Eastern Norway,
{ramesh.timsina, britt.moldestad, marianne.eikeland, rajan.k.thapa}@usn.no

Abstract

Biomass is a renewable energy source. Biomass gasification process produces producer gas, which can be further used for power generation or as raw materials for the production of secondary fuels. Experiment on the air gasification of biomass in a bubbling fluidized bed reactor was performed in a pilot-scale reactor located at the University of South-Eastern Norway (USN). A kinetics-based simulation model was developed based on MultiPhase Particle-In-Cell MP-PIC approach, using commercial software Barracuda®, and the results were compared with the experimental data. The average volume percentage of carbon monoxide, hydrogen, methane and nitrogen were found to be around 20%, 10%, 7% and 38% respectively in the experiment. The simulation results agree well for carbon monoxide, hydrogen and methane, but there is a difference in nitrogen volume percentage compared to the experimental results. The oxygen concentration during the experiment was around 1% suggesting a good performance of the gasifier. The char partial oxidation is less significant compared to the homogenous phase reactions. This shows that devolatilization reaction and the homogenous phase reactions dominate the char gasification reaction.

Keywords: air-biomass gasification, bubbling fluidized bed, CPFD

1 Introduction

Due to the rapid increase in the consumption of conventional fossil fuels, the global temperature is rising quite fast. One of the alternatives to counteract the increase in temperature is the use of renewable energy sources. Biomass gasification is one of the renewable energy production technologies and includes thermochemical conversion of carbonaceous fuels mainly into syngas (a mixture of CO and H_2) with the application of gasifying medium such as air, steam, and oxygen. Among the different biomass gasification technologies, fluidized bed reactors are commonly used. The fluidized bed technology uses bed material such as sand, or olivine to heat up the biomass particles at a temperature range of 700-900°C (Franco *et al.*, 2003). The gasification temperature is comparatively low, and this inhibits the agglomeration and sintering of the ash, which prevents causing serious problems during the operation of the gasifier. In addition, even distribution of heat and mass transfer, and excellent solid mixing make the fluidized bed reactor one of the attractive technologies for biomass gasification.

The product of gasification can be used for power generation in a gas engine, methanol synthesis or as the raw materials for production of secondary fuels, such as biodiesel, bio-ethanol and methanol (Bandara *et al.*, 2018). The operation of the fluidized bed gasification involves multiphase flow, various chemical reactions and heat transfer. It is a big challenge to investigate the effects of different parameters from the experimental study only, because of the requirements to build different setup configurations and procedures. Instead, modeling and simulations give better ideas for a wide range of design and operational parameters.

Modelling and simulation of such complex systems are needed for a good understanding of the process, designing and optimization. Computational fluid dynamics (CFD) are used to model the systems handling the fluid flow. Conventional CFD is a well-accepted technique for single-phase systems. Multiphase CFD models use either a Eulerian-Eulerian, or Eulerian-Lagrangian approach. The Eulerian-Eulerian approach models the solid and gas phase separately with the Navier-Stokes equation. The discrete particle phase is not considered in Eulerian modelling and is solved with the kinetic theory of granular flow. In the Eulerian-Lagrangian approach, fluid is treated as a continuous phase and the particles as a discrete phase. The solid particles are approximated with Newton's law of motion. This gives high loading to CPU during simulations and is often limited to 2D or quasi-3D and in the order of 10^4 number of particles (Ku *et al.*, 2015). The MP PIC modelling is based on the Eulerian approach for fluid particles and Lagrangian approach for the solid particles. Barracuda® is a software package based on the MP PIC modelling, which is known as the Computational Particle Fluid Dynamics (CPFD) approach.

Air is commonly used as the gasifying agent, which gives product gases with a Higher Heating Value (HHV) of 4-7 MJ/Nm^3. The low HHV is due to the dilution of

the produced gas by nitrogen. Oxygen/steam blown biomass gasification produces gas with HHV of 10-18 MJ/Nm^3 (Schuster *et al.*, 2001; Li *et al.*, 2004). However, there will be an additional cost to produce oxygen/steam. There are many CFD models reported in the literature on steam gasification of biomass. CPFD modelling was chosen in this study because of its reliability and shorter simulation time. However, no previous work was found for the modelling of air gasification of biomass in a bubbling fluidized reactor using CPFD approach.

1.1 Previous works

Schuster et al. and Li et al. have studied the gasification of biomass based on the thermodynamic equilibrium model. Such models deviate significantly from the experimental results compared to the kinetics-based models (Schuster *et al.*, 2001, Li *et al.*, 2004).

Xie et al. have developed a model based on the MP-PIC approach for coal gasification in a fluidized bed reactor. Flow patterns, particle species profile, gas compositions, distributions of reaction rates were studied during their study (Xie *et al.*, 2013). The obtained results from the simulation model agree well with the experimental data.

Most of the biomass gasification simulations based on the MP-PIC approach have been applied with steam as the gasifying agent. Loha et al. have studied the flow pattern, gas composition and pressure distribution for different temperature and steam to biomass ratio in a laboratory scale bubbling fluidized bed gasifier. The gasification of rice husk during the experiment agreed well with the simulation based on the reaction kinetics of the gasification process (Loha *et al.*, 2014).

Further, the MP-PIC modelling has been applied to simulate the dual circulating bubbling fluidized bed (DCBFG) gasifier. Liu et al. studied the gasification of almond prunings in a dual fluidized bed gasifier. The model showed that the H_2 production, as well as CO production, was increased with increase in gasifier temperature and steam to biomass ratio (Liu *et al.*, 2016). Thapa et al. have developed a model for biomass gasification in DCBFG based on the MP-PIC approach. The published result agrees well with the experimental data obtained from the biomass gasification plant in Güssing, Austria (Thapa *et al.*, 2014).

In the present works, a simulation model for a bubbling fluidized bed gasifier has been developed in barracuda, and the results have been compared with the experimental data. The objective of this paper is to develop a model for air-gasification of biomass and validate the model against the experimental results.

2 Methods

2.1 Experimental Setup

The gasification rig installed at the University of South-Eastern Norway (USN) is a bubbling fluidized bed reactor with a fuel capacity of 20kW. Figure 1 and Figure 2 show the block diagram and the picture of the gasification rig at USN.

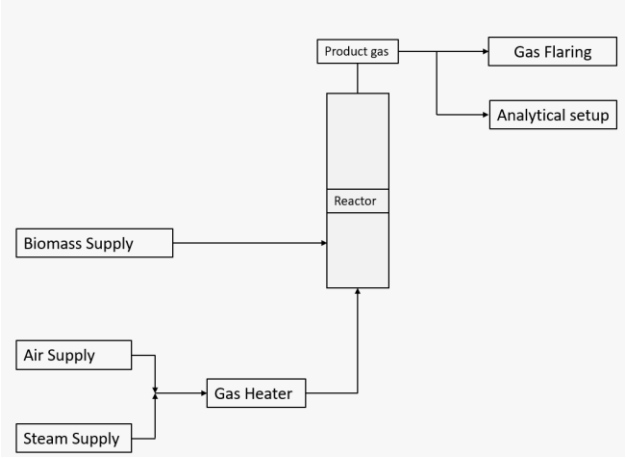

Figure 1. Block diagram of biomass gasification reactor at USN

The gasifier consists of a preheater (A), which heats up the fluidizing agents (air or steam) to about 450°C. The screw conveyors (B1 and B2), transfer the biomass from the fuel silo (C) to the reactor (D). Biomass is added into the silo before starting the experiments. The system is purged with nitrogen during the idle conditions of the reactor. The reactor is installed with pressure and temperature sensors at different locations to monitor the pressure and the temperature of the reactor. The product gas leaves from the top of the reactor for the gas analysis (F) and the flaring (E). The different parameters were controlled/changed/monitored during the experiment with the help of a computer program available at the experimental facility.

Figure 2. Picture of the bubbling bed reactor at USN

There are two screw conveyors as shown in Figure 3. The cold screw conveyor supplies the biomass from fuel silo to hot conveyor and the hot conveyor introduces the biomass into the reactor bed. The conveyors are perpendicular to each other.

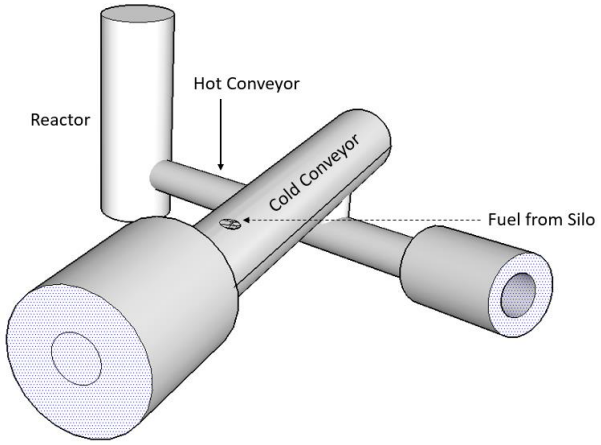

Figure 3. Cold and hot conveyor

The reason for separating the two-screw conveyer is to avoid the combustion of wood chips during the transportation process. The reactor is insulated to reduce heat loss during the experiments. The reactor is 100 mm in diameter and 1000 mm in height.

Sand with an average particle diameter of 285µm was used as bed materials during the experiments. Wood chips with approximately 0.5 cm average diameter was used for the experiments. The reactor was heated initially to about 700°C before the introduction of the biomass into the reactor for gasification experiments. Gas collected on syringe were analyzed on SRI 8610C gas chromatograph.

2.2 CPFD Simulation setup

A simulation model was developed by using Barracuda VR17 software. Wen-Yu drag model was used with 60% momentum loss after the particle collision. The reactor was designed as an open cylinder with a diameter of 100 mm and a height of 1000mm.

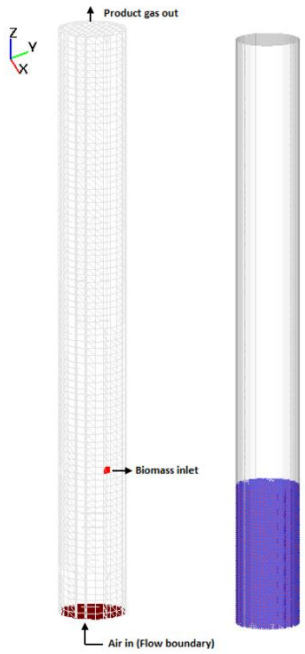

Figure 4. (a) Boundary conditions (b) Initial bed material

Figure 4 shows the boundary conditions and the initial height of bed material used for the simulation. The developed geometry was divided into 7128 computational cells.

Table 3 shows the properties of the bed material, and the gasifying agent used for the simulation process. The exit of particles from the reactor was set to zero by default, and the pressure boundary at the top of the reactor ensures the out flow of the product gas from the

Table 1. Reaction kinetics for air gasification

Reaction	Rate Kinetics
Char partial combustion (Xie *et al.*, 2013) $2C + O_2 \leftrightarrow 2CO$	$r = 4.34\times10^{7}\ m_s\theta_f \exp\left(\frac{-13590}{T}\right)[O_2]$
CO oxidation (Xie *et al.*, 2013) $CO + 0.5O_2 \leftrightarrow CO_2$	$r = 5.62\times10^{12} \exp\left(\frac{-16000}{T}\right)[CO][O_2]^{0.5}$
H_2 oxidation (Bates *et al.*, 2017) $H_2 + 0.5O_2 \leftrightarrow H_2O$	$r = 5.69\times10^{11} \exp\left(\frac{-17610}{T}\right)[H_2][O_2]^{0.5}$
CH_4 oxidation (Xie *et al.*, 2013) $CH_4 + 2O_2 \leftrightarrow CO_2 + 2H_2O$	$r = 3.552\times10^{11}\ T^{-1} \exp\left(\frac{-15700}{T}\right)[CH_4][O_2]$
Water gas shift reaction (Xie *et al.*, 2013) $CO + H_2O \leftrightarrow CO_2 + H_2$	$r = 7.68\times10^{10}\ T \exp\left(\frac{-36640}{T}\right)[CO]^{0.5}[H_2O]$
Methane reforming (Solli *et al.*, 2018) $CH_4 + H_2O \leftrightarrow CO + 3H_2$	$r = 3.00\times10^{5} \exp\left(\frac{-15042}{T}\right)[CH_4][H_2O]$

reactor. The air supply into the bed was kept constant during the experiments and the simulation process. Air at 1000K was supplied during the simulation to reduce the simulation time. During the experiments, preheating of air was done before introducing into the reactor bed. The reaction rate kinetics are presented in Table 1 based on the Arrhenius reaction rate model. The properties of the wood chips used in the simulation model are presented in Table 2 (Doherty *et al.*, 2013)

Table 2. Properties of wood chips

Proximate analysis (dry basis, wt. %)	
Volatile matter	80
Fixed carbon	18.84
Ash	1.16
Moisture	*20*

Table 3. Initial conditions

Items	*Parameters*
Bed material	285 µm average diameter, 0.54 volume fraction, density 2650 kg/m^3, 200 mm initial bed height
Gasifying fluid	Air, 0.2 m/s, 1000K, 101325Pa

3 Results and discussions

Experiments were done with wood chips and air in the bubbling fluidized reactor. The gas composition from the simulation is presented in Figure 5. The gas composition is irregular because of different physical and chemical transformation occurring inside the reactor, whereas the average gas compositions seems to be stable throughout the simulation.

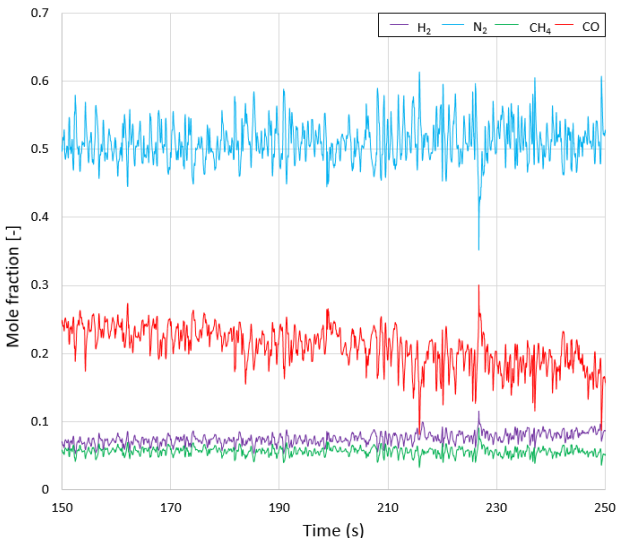

Figure 5. Gas composition for the simulation model

In the beginning, the hydrogen concentration in the product gas is due to the devolatilization of the biomass in the hot bed. Water vapor that is produced during methane oxidation favors the water gas shift reaction which slightly increases the hydrogen production with time. Further, the average gas composition from the simulation results are compared with the experimental results and is presented in Figure 6.

The simulation model predicts well the fraction of the different gas components and there is a good agreement between experimental and computational results regarding the hydrogen, carbon monoxide and methane concentration.

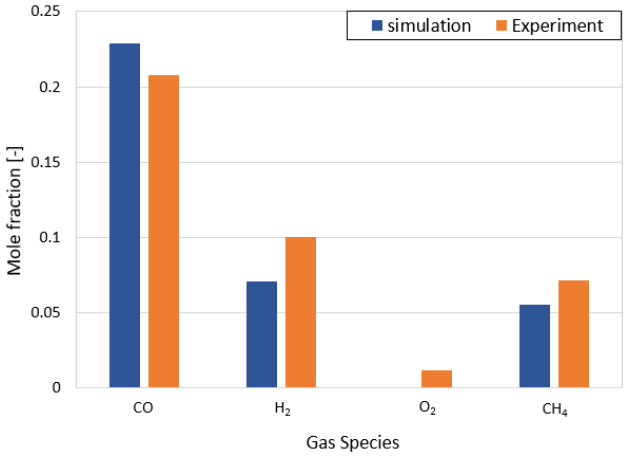

Figure 6. Comparison of average gas species

There are several reactions occurring during the gasification process. The major chemical reactions are modelled using the six major reactions presented in Table 1. The other minor chemical reactions are not included in the barracuda simulations, as they require a lot of computer capacity and time. The average oxygen concentration during the simulation was found to be zero whereas oxygen concentration during the experiment was around 1% of the total volume composition. This may be due to the sampling procedure, as the samples were taken in a syringe for the gas analysis. This shows that the CPFD model gives a comprehensive result.

The product gas compositions during the simulation were monitored at the different heights along the reactor. Figure 7 shows the mole fractions of carbon monoxide, hydrogen and the methane along the height of the reactor. There are not any distinct variations up to the biomass feeding position. The char partial oxidation is less significant compared to the homogenous phase reactions. Devolatilization as well as chemical transformations of biomass inside the bed give different gas compositions. The increasing hydrogen concentration along the reactor indicates the dominance of the water gas shift reaction and the methane reforming reaction.

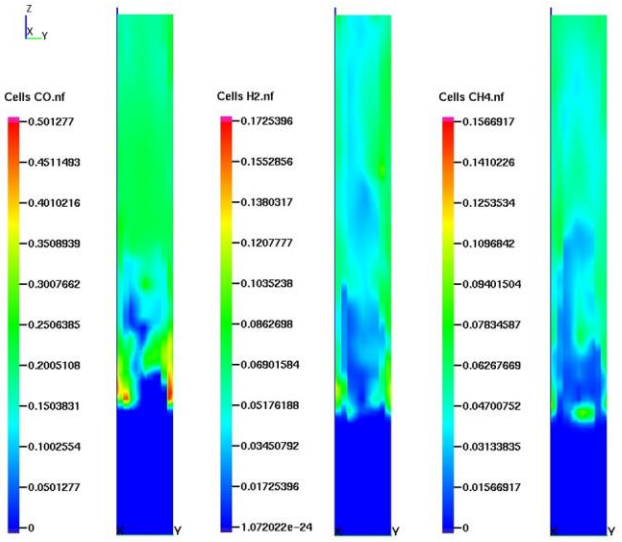

Figure 7. Gas composition along the reactor (Mole fraction)

This shows that the chemical transformations as well as the bed hydrodynamics is quite complex in a bubbling fluidized bed reactor. The operation of the optimized reactor would give uniform particle distribution and ensure operation in the bubbling fluidization regime. Figure 8 shows the particle volume fraction and the particle temperature distribution along the reactor height.

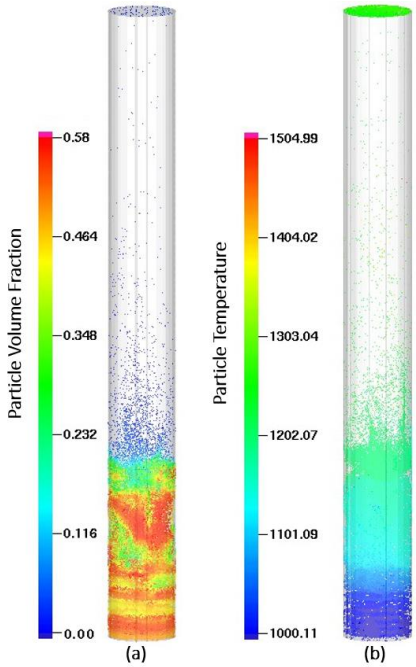

Figure 8. Simulation bed hydrodynamics at 200 s (a). Particle volume fraction (b). Particle temperature

Figure 8 (a) shows that the reactor operates at the bubbling fluidization regime with entrainment of few particles in the freeboard region. The solid volume fraction after the onset of the bubbling regime in the bed is reduced from the solid volume fraction of the static bed. Although the system was set to a temperature of 1000K, due to the exothermic nature of the reactions, the temperature rises up to around 1200K inside the reactor.

4 Conclusions

Air gasification of biomass in bubbling fluidized bed reactor was performed in a pilot-scale reactor at USN. A kinetic-based CPFD simulation model was used to simulate the gasification of biomass using Barracuda. The experimental setup as well as the simulation model were operated in the bubbling fluidizing regime. The results from the simulation were compared with the experimental data. The average volume percentage of carbon monoxide, hydrogen and methane were found to be around 20%, 10%, and 7% respectively during the experiment. There is a good agreement between experimental and computational results regarding the hydrogen, carbon monoxide and methane concentration. Oxygen concentration during the experiment was around 1%. The small amount of oxygen during the experiment may be due to manual sampling process used for gas sampling. The char partial oxidation is less significant compared to the homogenous phase reactions during the gasification process.

Acknowledgements

The authors would like to thank the University of South-Eastern Norway (USN) for providing the facilities for the experiments and the Barracuda VR for the simulation.

References

J. C. Bandara, B. ME. Moldestad and M. S. Eikeland. Analysing the effect of temperature for steam fluidized-bed gasification of biomass with MP-PIC simulation. *International Journal of Energy and Environment*, 9(6): 529-542, 2018.

R. B. Bates et al., Steam-air blown bubbling fluidized bed biomass gasification (BFBBG): Multi-scale models and experimental validation. *AIChE Journal*, 63(5): 1543-1565, 2017. doi:10.1002/aic.15666.

W. Doherty, A. Reynolds and D. Kennedy. Aspen plus simulation of biomass gasification in a steam blown dual fluidized bed. 2013.

C. Franco, F. Pinto, I. Gulyurtlu and I. Cabrita. The study of reactions influencing the biomass steam gasification process. *Fuel* 82(7): 835-842, 2003. doi:10.1016/S0016-2361(02)00313-7.

X. Ku, T. Li and T. Løvås. CFD–DEM simulation of biomass gasification with steam in a fluidized bed reactor. *Chemical Engineering Science*, 122: 270-283, 2015. doi:10.1016/j.ces.2014.08.045.

X. Li et al., "Biomass gasification in a circulating fluidized bed. *Biomass and Bioenergy*, 26(2): 171-193, 2004. doi:10.1016/S0961-9534(03)00084-9

H. Liu, R. J. Cattolica and R. Seiser. CFD studies on biomass gasification in a pilot-scale dual fluidized-bed system. *International Journal of Hydrogen Energy*, 41(28): 11974-11989, 2016. doi:10.1016/j.ijhydene.2016.04.205

C. Loha, H. Chattopadhyay and P. K. Chatterjee. Three dimensional kinetic modeling of fluidized bed biomass gasification. *Chemical Engineering Science*, 109: 53-64, 2014. doi:10.1016/j.ces.2014.01.017

G. Schuster, G. Löffler, K. Weigl and H. Hofbauer. Biomass steam gasification–an extensive parametric modeling study. *Bioresource technology*, 77(1): 71-79, 2001. doi:10.1016/S0960-8524(00)00115-2

K.-A. Solli, R. K. Thapa and B. ME. Moldestad. Screening of kinetic rate equations for gasification simulation models. Proceedings of The 9th EUROSIM Congress on Modelling and Simulation, EUROSIM 2016.

R. Thapa, C. Pfeifer and B. M. Halvorsen. Modeling of reaction kinetics in bubbling fluidized bed biomass gasification reactor. *Int. J. Energy Environment*, 5: 35-44, 2014.

J. Xie, W. Zhong, B. Jin, Y. Shao and Y. Huang. Eulerian–Lagrangian method for three-dimensional simulation of fluidized bed coal gasification. *Advanced Powder Technology*, 24(1): 382-392, 2013. doi:10.1016/j.apt.2012.09.001

Aspen Plus simulation of biomass gasification for different types of biomass

Ramesh Timsina Rajan K. Thapa Marianne S. Eikeland

Department of Process Energy and Environmental Technology University of South-Eastern Norway,
{ramesh.timsina, rajan.k.thapa, marianne.eikeland}@usn.no

Abstract

A steady-state Aspen Plus model was developed for biomass gasification in a fluidized bed reactor. A combination of different Aspen Plus unit operations was used to model the gasification process. The model was used to predict the gasifier performance for different operating conditions like temperature, Steam to Biomass Ratio (STBR) and biomass loadings. Further, the gas compositions were compared for different types of biomass feed. The gasification reactor is based on Gibbs minimization with restricted equilibrium approach. Hydrogen production was around 50% for all the biomasses while CO production varies from 8% (Pig manure) to 24.5% (Olive residue) at 700°C. H_2/CO ratio increases with an increase in STBR for all the biomass and the ratio was the highest for the pig manure and lowest for the olive residue. Olive residue, wood residue and miscanthus gave the H_2/CO ratio of 1.5-2.1, which are more suitable as a feedstock in Fischer-Tropsch synthesis depending upon the operating temperature, a catalyst used and other operating conditions. For the wood residue, an increase in temperature increases the H_2 and CO production whereas CO_2 and CH_4 concentration decreases and becomes stable after 700°C. H_2 concentration increased from 46 % to 54 % and CO concentration decreases from 30% to 20% with an increase in STBR from 0.6 to 1 for the wood residue.

Keywords: Aspen plus, biomass, biomass gasification, H_2/CO ratio

1. Introduction

Due to the increasing energy demand, and the rising global temperature, research is focused towards the alternative energy sources such as wind energy, solar energy and the energy from biomass. Biomass sources such as Municipal Solid Waste (MSW), food wastes, wood wastes, rice husks, sugarcane bagasse and poultry wastes can be utilized to produce product gases (a mixture of CO, H_2 and CH_4) through biomass gasification. Biomass gasification is a thermochemical conversion of carbonaceous materials, mainly into syngas (a mixture of CO and H_2), with the application of gasifying medium such as air, steam, and oxygen.

Among the different types of biomass gasification technologies, fluidized bed gasification is an attractive technology because of the even distribution of heat and mass transfer and excellent solid mixing. The fluidized bed gasification technology uses bed material to heat up the biomass particles in the temperature range of 700-900°C (Franco *et al.*, 2003). The syngas can be converted into liquid fuels by Fischer-Tropsch (FT) synthesis, which is also known as Gas-To-Liquid (GTL) process (Riedel *et al.*, 1999). Biomass gasification also enables energy recovery from the waste. The main challenge for the successful operation of the biomass-based energy production technologies is low carbon concentration in the biomass and the low efficiency of the biomass gasification technology.

The conversion of biomass into syngas gases through gasification especially depends upon the biomass characteristics. The amounts of the fixed carbon, volatiles, moisture, ash and the calorific value determines the output product gas composition (McKendry, 2002).

The biomass is dried and devolatilized during the gasification process. Devolatilization is an endothermic process where the hot bed material supplies the required amount of heat. For simplicity, the process of devolatilization can be modelled using 1.

$$C_xH_yO_z = aCH_4 + bCO + dCO_2 + eH_2 + fC_xH_y + gC + hH_2O \quad (1)$$

The amount of ash and the other minor components produced during the gasification process can be neglected. The conversion of biomass depends upon the pressure, temperature and heat and mass transfer. The next step is the char gasification. Char reacts with fluidizing agents, as well as CO_2 and H_2 produced during the devolatilization of the biomass. Char reactivity and its amounts affect the product gas compositions (Thapa and Halvorsen, 2014).

Figure 1 shows the potential reaction pathways for the biomass gasification process. Biomass undergoes pyrolysis to produces gases (such as CO, H_2, CH_4, and H_2O), liquids (tar, oil), phenols, acids and the solid char. The char reacts with the gasifying medium, which

further reacts with the gases produced during the pyrolysis process to give the product gas.

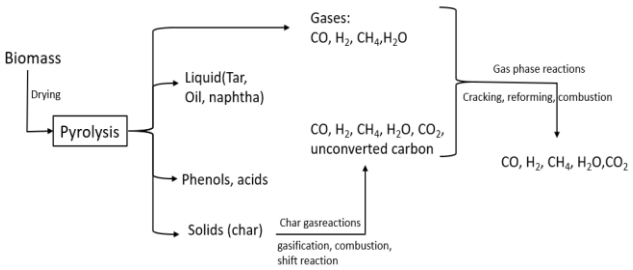

Figure 1. Potential reaction pathways for gasification

1.1 1.1 Previous works

Gagliano et al. have developed an equilibrium-based model in Aspen Plus for predicting the chemical composition of product gas for different types of biomass with different moisture contents. There is a good agreement of the gas compositions between simulation results and the experimental results for pellets and rubber wood (Gagliano *et al.*, 2017).

Doherty et al. have developed a model which represents an industrial scale plant in Gussing Austria. The model is based on restricted equilibrium in RGibbs reactor and simulations were performed for various gasification temperature, moisture content of biomass, STBR, air-fuel ratio, air temperature and steam temperature. The simulation results for syngas compositions, cold gas efficiency and heating values agree well with the experimental data (Doherty *et al.*, 2013).

Nikoo and Mahinpey simulated biomass gasification in a fluidized bed reactor. The model was validated with the experimental results from the lab-scale fluidized bed reactor. Effects of the different parameters such as temperature, equivalence ratio, STBR and biomass particle size were studied during their simulations (Nikoo and Mahinpey, 2008).

Liu et al. studied the simulation of biomass gasification based on the Gibbs equilibrium. The validated model was used to study the effects of gasification temperature, pressure and equivalence ratio. The optimal equivalence ratio was approximately 0.3 with optimal gasification efficiency of 85.92% (Liu *et al.*, 2016).

Suwatthikul et al. have carried out the sensitivity analysis for gasification temperature, equivalence ratio and the STBR. A validated Aspen plus model gave an optimal operating temperature of 911°C, equivalence ratio of 0.18 and STBR of 1.78 to achieve energy self-sufficient conditions for steam gasification in a fluidized bed reactor. Suwatthikul et al. achieved a maximum carbon conversion efficiency of 91.03% (Suwatthikul *et al.*, 2017).

Product gases from the gasification process have to be cleaned further and adjusted accordingly for suitable application to the GTL process. Fuels from GTL process have low emissions of CO, nitrogen oxides, hydrocarbons and particulate matters. The Fischer Tropsch synthesis can be considered as hydrogenation of CO to produce higher hydrocarbons compounds known as synthetic fuels (Kim *et al.*, 2009). For the industrial application of syngas in Fischer-Tropsch synthesis, it is desired to have hydrogen to carbon monoxide ratio (H_2/CO) of 1.5 - 2.1 (Tristantini *et al.*, 2007).

Modelling and simulation of biomass gasification give a good understanding of the process, designing and optimization for a wide range of design configuration and operational parameters. The developed models can be used to study the biomass gasification process. Aspen Plus® is a commercial software package to simulate an industrial process. Although there is not included inbuilt library model to simulate fluidized bed biomass gasification in Aspen Plus, different unit operations

Table 1. Ultimate and Proximate analysis of different biomass feedstock

Feedstocks	*Moisture*	*Proximate analysis (wt. %, dry)*			*Ultimate analysis (wt. %, dry)*					
		FC	*VM*	*Ash*	*C*	*H*	*O*	*N*	*S*	*Cl*
Wood chips (Doherty *et al.*, 2013)	20	18.84	80	1.16	51.19	6.08	41.3	0.2	0.02	0.05
Wood residue (Fremaux *et al.*, 2015)	5.01	17.83	81.81	0.36	50.26	6.72	42.66	0.16	0.2	0
Pig manure (Xiao *et al.*, 2010)	21.61	16.07	65.78	18.15	36.45	4.89	37.89	4.52	0.88	0
Miscanthus (Kok and Özgür 2013)	2	16.33	82.14	1.53	45.52	5.93	48.32	0.13	0.1	0
Olive residue (Masiá *et al.*, 2007)	10.63	25.48	67.35	7.17	54.18	5.37	31.7	1.28	0.21	0.13
Food waste(Begum *et al.*, 2013)	29.3	20.69	72.4	6.91	56.65	8.76	23.54	3.95	0.19	0

were combined to represent the biomass gasification as close as possible. This paper presents the simulation for different types of biomass presented in Table 1.

2. Modeling of biomass gasification

A model for bubbling fluidized bed biomass gasification with steam as a fluidizing agent is developed in Aspen Plus®. The model predicts the performance of a fluidized bed gasifier for the different types of biomass. The gasification process is dissociated into different representative units modelled by the different blocks in Aspen Plus. These models offer a convenient way to give information about the gasifier in a short time. These models are either based on kinetics rates or the state of thermodynamic equilibrium in a Gibbs reactor. The developed model is based on the restricted equilibrium in a Gibbs reactor model. Aspen plus flowsheet of the reactor is presented in Figure 2.

The flowsheet was developed from the available unit operation blocks, material streams and the energy stream. Different conventional components were chosen from the database along with two non-conventional components for the biomass and the ash modeling. Non-conventional components were defined according to the ultimate and proximate analysis for the biomass. Table 1 gives the ultimate and proximate analysis of the different biomass feedstocks.

The process consists of different stages such as biomass decomposition (DECOMP), pyrolysis (PYRO), gasification (GASIFIER), combustion (COMB) and different separation units (cyclone and separator). MIXNCPSD stream class was used as both conventional and non-conventional solids were present in the model with particle size distribution. Peng-Robinson equation of state with Boston-Mathias (PR-BM) alpha function was used to calculate the thermodynamic properties. Applications of PR-BM includes refineries, gas-processing, and petrochemical applications like crude oil conversion and gas plants. All the inputs to the feed (flow rate, composition, thermodynamic state) and the unit operation block (thermodynamic conditions, chemical reaction etc) were taken from the experimental study performed by Fremaux et. al. (Fremaux *et al.*, 2015). The assumptions made during the modelling of the gasification process in Aspen Plus are as follows:

- Isothermal and Steady state process.
- The pressure drop across the block is zero.
- Tar formation is not considered.
- The system is in steady state and isothermal.
- Char contains only carbon.
- Modelling of ash is not considered

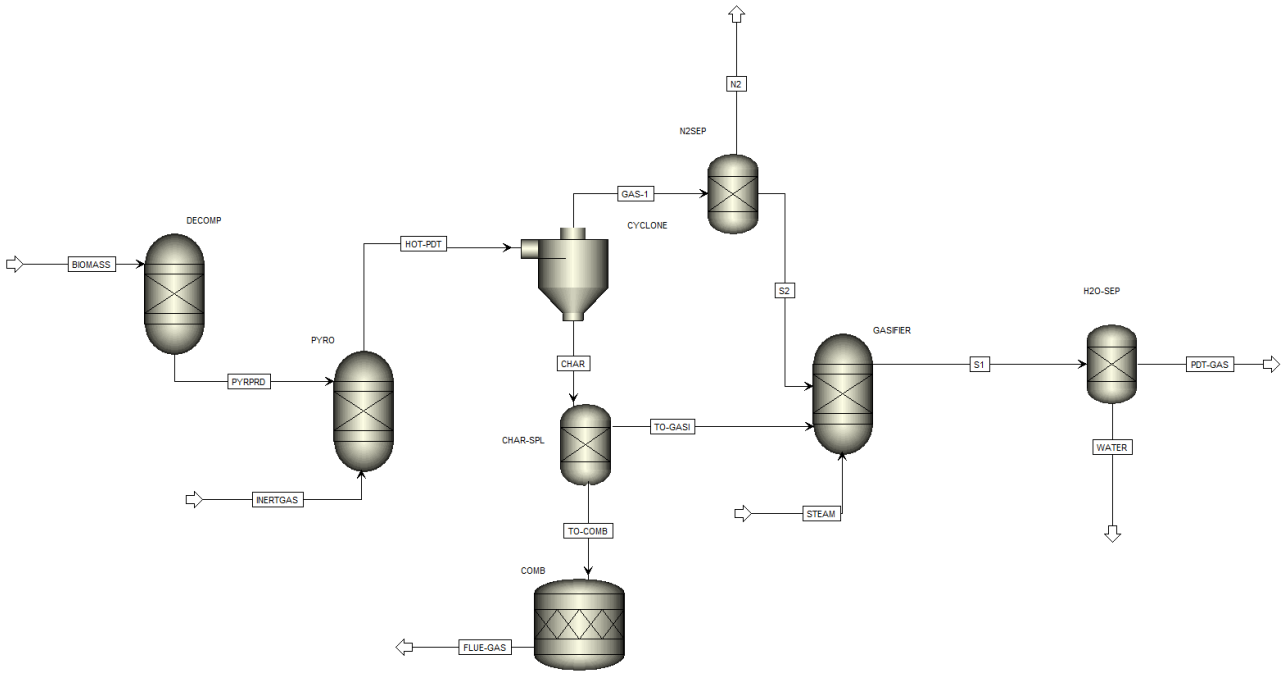

Figure 2. Aspen plus flowsheet for biomass gasification

Figure 2 shows the flow sheet in Aspen Plus. Biomass was decomposed into its constituting elements such as H_2O, ASH, C, H, N, Cl, S, O based on the ultimate analysis. A calculator module was used to calculate the yield components of the biomass feed in the DECOMP reactor. The decomposed biomass product enters a yield reactor, simulated as a pyrolysis step in gasification. The PYRO reactor was set to operate at 500°C and the inert gas (N_2) was used to assist the pyrolysis step (Visconti *et al.*, 2015). The products from the pyrolysis were separated by using a cyclone. The char produced after the pyrolysis was taken into another yield reactor (GASIFIER), simulated as a gasification reactor.

Around 5% of the char was combusted in RStoic reactor. The generated energy can be used as a supplement heat for the gasifier. In addition to char, gaseous product (nitrogen-free) from the pyrolysis process and the steam is added into the gasifier.

The calculation in the RGibbs gasifier was based on the restricted equilibrium with zero temperature approach for each of the reaction. The zero-approach option in RGibbs calculates the chemical equilibrium constant for the specified reaction at the reactor operating temperature. The equilibrium state of the reactor is also dependent upon the load per area of the reactor. Low load gives the state close to the equilibrium whereas higher load gives the non-equilibrium state within the reactor. High load is preferred to achieve a high conversion rate and low equipment costs. The overview of the temperature and the pressure in the different reactors is presented in Table 2.

Table 2. Thermodynamic state of different reactor

Reactor	*Thermodynamic state*	
	Temperature (°C)	*Pressure (bar)*
DECOMP	500	1
PYRO	500	1
COMB	800	1
GASIFIER	700	1

Table 3 shows the lists of chemical reactions specified during this simulation study with their change in Gibbs energies respectively.

Table 3. Reactions involved in gasification (Suwatthikul *et al.*, 2017)

Reactions		ΔH (kJ/mol)
$C + O_2 \rightarrow CO_2$	(2)	-394
$C + 0.5O_2 \rightarrow CO$	(3)	-111
$CO + 0.5O_2 \rightarrow CO_2$	(4)	-283
$C + CO_2 \rightarrow 2CO$	(5)	+172
$C + H_2O \rightarrow CO + H_2$	(6)	+131
$C + 2H_2 \rightarrow CH_4$	(7)	-74.8
$CO + H_2O \rightarrow H_2 + CO_2$	(8)	-41.2
$CO + 3H_2 \rightarrow CH_4 + H_2O$	(9)	-206
$H_2 + S \rightarrow H_2S$	(10)	-20.2
$N_2 + 2H_2 \rightarrow NH_3$	(11)	-92.2
$H_2 + Cl_2 \rightarrow 2HCl$	(12)	-184.6

The product from the gasifier undergoes water separation to give the output product composition on a dry volume basis.

3. Results and Discussions

Simulation results of the wood residue feedstock were compared with the experimental results published by Fremaux et al. Figure 3 shows the composition of the different gases. Hydrogen and carbon dioxide production increases with an increase in Steam to Biomass Ratio (STBR) while the carbon monoxide production decreases with increase in STBR. Methane concentration is almost constant for the given range of STBR.

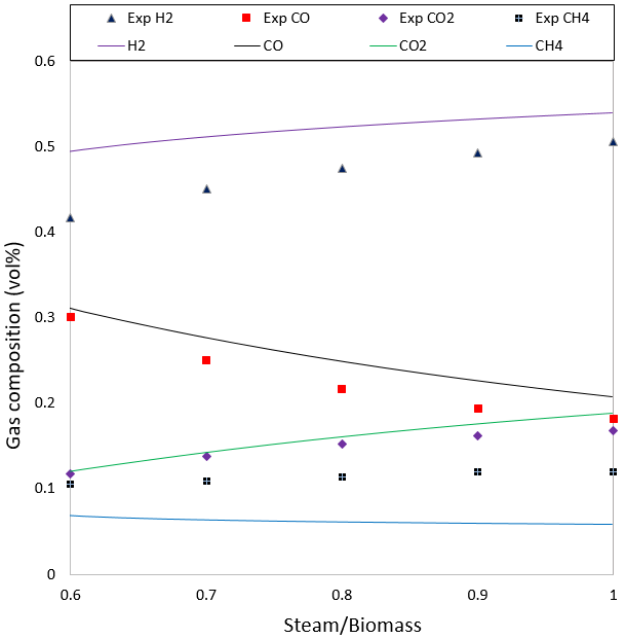

Figure 3. Gas composition for wood residue

The model predicts well the fraction of the different gas components, and there is a good agreement between experimental and computational results regarding carbon monoxide and carbon dioxide concentration. There is little difference in the hydrogen concentration, as the model doesn't represent the true phenomenological behavior of biomass gasification during the experiments.

Figure 4 shows the composition of hydrogen, carbon monoxide, carbon dioxide and methane from the simulation for different biomass. Hydrogen composition is quite similar for all the biomass feed.

Carbon monoxide concentration for wood residue, miscanthus and olive residue is similar, whereas the lowest for the pig manure. Carbon dioxide concentration for pig manure feed is 30% whereas other feed has CO_2 concentration below 25%. The carbon and hydrogen concentration are lowest for the pig manure. The C/O ratio is approximately 1:1 for pig manure and 1.2:1 for the other biomass.

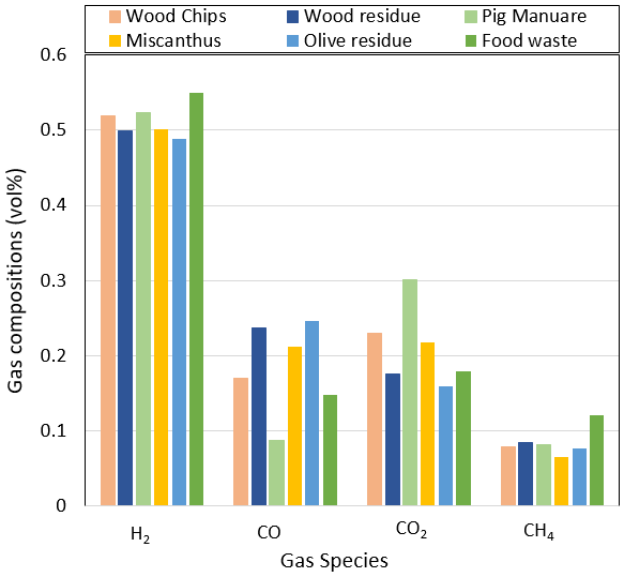

Figure 4. Gas compositions for different biomass feed (700°C)

The higher proportion of oxygen per carbon atom could be the reason for high CO_2 and low CO in pig manure. The main reason for high CO_2 and low CO is due to the high concentration of ash (18.15%) in pig manure compared to the other biomass. Methane concentration is around 8% for all the biomass except the food waste, which is around 12%.

The end use of the product gas depends upon the quality of the gas produced during gasification. One of the qualities of the product gas required for feedstock for GTL synthesis is the H_2/CO ratio. H_2/CO was calculated for all the biomass feed for different STBR. Figure 5 shows the H_2/CO ratio for STBR in the range of 0.5-1.

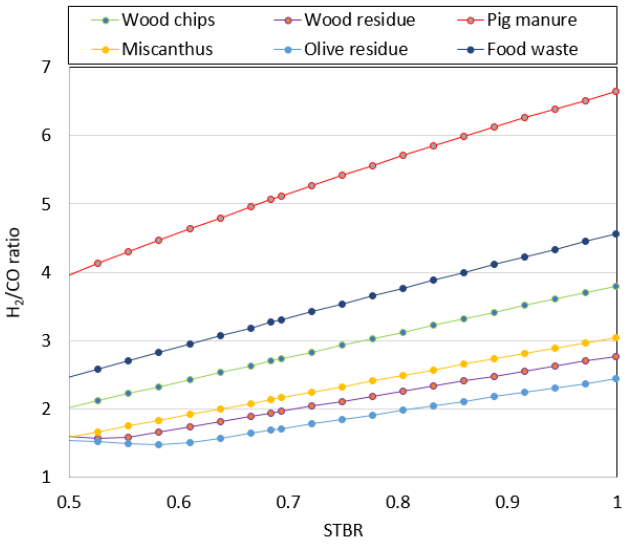

Figure 5. H_2/CO ratio for different biomass feed (700°C)

H_2/CO ratio is highest for the pig manure because of the high amounts of moisture and higher C/O ratio compared to other biomasses. Food waste also has a higher H_2/CO ratio because of its high moisture content. According to Tristantini et al., the optimal H_2/CO ratio is 1.5-2.1. This is achievable from the olive residue, wood residue, miscanthus in the STBR range of 0.5 to around 0.75. Syngas from wood chips is more suitable in FT synthesis at lower STBR. FT synthesis not only depends on the H_2/CO ratio, but also temperature, catalyst used and the system. Thus, the suitable H_2/CO ratio can be chosen depending upon the plant requirements.

The quality of syngas produced depends upon the reactor temperature. Figure 6 shows the variations of the product gas compositions at different temperatures.

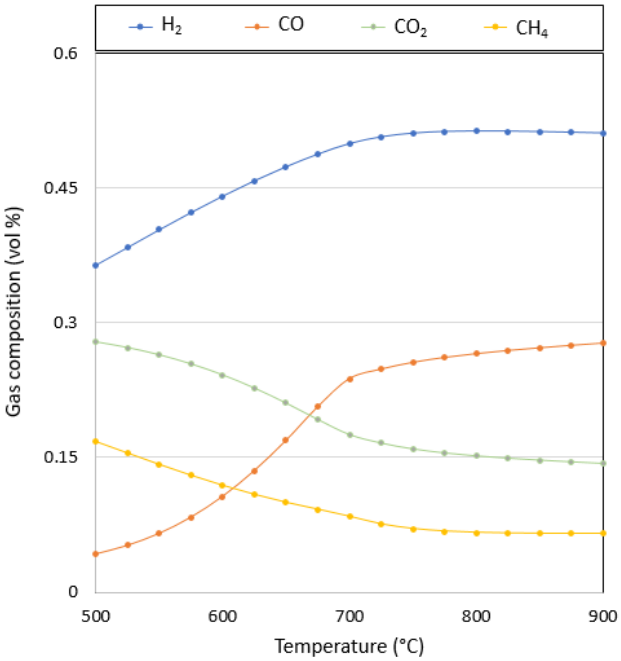

Figure 6. Gas composition for wood residue (STBR = 0.6)

Hydrogen and carbon monoxide concentration increases initially and stabilizes after 700°C. Carbon dioxide and methane concentration decrease with increase in temperature and becomes steady after around 700°C. H_2/CO ratio also becomes steady at around 1.8 after 700°C., The gas compositions were analyzed for different biomass feed. Figure 7 shows the product gas compositions for different biomass loadings.

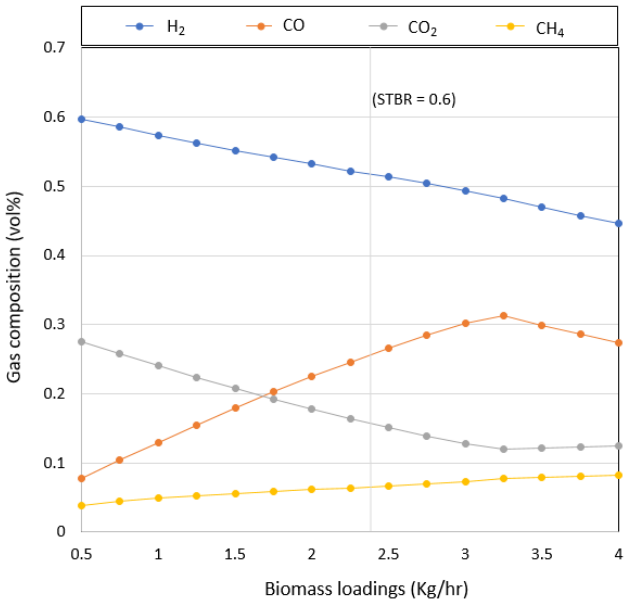

Figure 7. Gas composition for wood residue (700°C)

Hydrogen concentration decreases with an increase in biomass feed whereas CO concentration increases for biomass feed up to 3.25 kg/hr. CO_2 concentration decreases and then becomes stable after biomass loading of 3.25 kg/hr. Methane concentration remains similar for all the feed rate. Increase in biomass feed favors the forward reactions (2)-(7). Further, CO_2 produced during the reactions (2) and (4) reacts with carbon from the biomass to produce CO and the carbon partial oxidation produces CO. Thus, CO concentration increases with increase in biomass feed. The H_2 produced from the reaction (6) and (8) reacts with carbon (7) to produces CH_4. Hence, there is a decrease in H_2 concentration with an increase in biomass feed rate.

4. Conclusions

A steady-state Aspen Plus model was developed for biomass gasification in a fluidized bed. Simulations results were validated against the experimental data for a research scale fluidized-bed reactor. The model was used to predict the gasifier performance for different operating conditions and parameters like temperature, STBR and biomass loadings. The gas compositions were compared for different biomass feed. Hydrogen production was around 50% for all the biomasses while CO production varies from 8% (Pig manure) to 24.5% (Olive residue) at 700°C. H_2/CO ratio increases with an increase in STBR for all the biomass and H_2/CO ratio was highest for pig manure and lowest for olive residue. Olive residue, wood residue and miscanthus gave the H_2/CO ratio of 1.5-2.1, which are more suitable as a feedstock in Fischer-Tropsch synthesis depending upon the operating temperature, a catalyst used and other operating conditions. For wood residue, an increase in temperature increases the H_2 and CO production, whereas CO_2 and CH_4 concentration decreases and becomes stable after 700°C. H_2 concentration increased from 46 % to 54 % and CO concentration decreases from 30% to 20% with an increase in STBR from 0.6 to 1 for wood residue. The experimental results may vary from the simulation modeling, as the decomposition of biomass feed doesn't represent the true phenomenological behavior during the gasification process. Suitable syngas composition for GTL synthesis can be obtained by selecting suitable biomass at desirable operating conditions of the gasifier.

Acknowledgements

The authors would like to thank the University of South-Eastern Norway (USN) for providing the necessary software for the simulation works.

Abbreviations

∇H - Enthalpy change
C - Carbon
H/H_2 - Hydrogen
FC - Fixed Carbon
VM - Volatile Matter
N -Nitrogen
Cl - Chlorine
GTL – Gas-to-Liquid
MSW - Municipal Solid Waste
STBR - Steam to Biomass Ratio
$C_xH_yO_z$ - Biomass elemental composition
C_xH_y - Higher hydrocarbons (C_2+)
CO - Carbon monoxide
O - Oxygen
CO_2 - Carbon dioxide
CH_4 - Methane
H_2O - Steam (water)
S - Sulphur
kg/hr- Kilogram per hour

References

S. Begum, M. G. Rasul, D. Akbar, and N. Ramzan. Performance analysis of an integrated fixed bed gasifier model for different biomass feedstocks. *Energies*, 6(12): 6508-6524, 2013. doi:10.3390/en6126508

W. Doherty, A. Reynolds, and D. Kennedy. Aspen plus simulation of biomass gasification in a steam blown dual fluidised bed. 2013.

C. Franco, F. Pinto, I. Gulyurtlu, and I. Cabrita. The study of reactions influencing the biomass steam gasification process. *Fuel*, 82(7): 835-842, 2003. doi:10.1016/S0016-2361(02)00313-7

S. Fremaux, S. M. Beheshti, H. Ghassemi, and R. S. Markadeh. An experimental study on hydrogen-rich gas production via steam gasification of biomass in a research-scale fluidized bed. *Energy Conversion and Management*, 91: 427-432, 2015. doi:10.1016/j.enconman.2014.12.048

A. Gagliano, F. Nocera, M. Bruno, and G. Cardillo. Development of an equilibrium-based model of gasification of biomass by Aspen Plus. Energy Proceedings, 111:1010-1019, 2017. doi:10.1016/j.egypro.2017.03.264

Y. H. Kim, K. W. Jun, H. Joo, C. Han, and I. K. Song. A simulation study on gas-to-liquid (natural gas to Fisher–Tropsch synthetic fuel) process optimization.

Chemical Engineering Journal, 155(1-2): 427-432, 2009. doi:10.1016/j.cej.2009.08.018

M. V. Kok and E. Özgür. Thermal analysis and kinetics of biomass samples. *Fuel Processing Technology*, 106: 739-743, 2013. doi:10.1016/j.fuproc.2012.10.010

L. Liu, Y. Huang and C. Liu. Prediction of rice husk gasification on fluidized bed gasifier based on ASPEN Plus. *Bioresources*, 11(1): 2744-2755, 2016.

A. T. Masiá, B. Buhre, R. P. Gupta and T. F. Wall. Characterising ash of biomass and waste. *Fuel Processing Technology*, 88(11-12): 1071-1081, 2007. doi:10.1016/j.fuproc.2007.06.011

P. McKendry. Energy production from biomass (part 1): overview of biomass. *Bioresource technology*, 83(1): 37-46, 2002. doi:10.1016/S0960-8524(01)00118-3

M. B. Nikoo and N. Mahinpey. Simulation of biomass gasification in fluidized bed reactor using ASPEN PLUS. *Biomass and Bioenergy* 32(12): 1245-1254, 2008. doi:10.1016/j.biombioe.2008.02.020

T. Riedel et al., Comparative study of Fischer–Tropsch synthesis with H2/CO and H2/CO2 syngas using Fe-and Co-based catalysts. *Applied Catalysis A: General*, 186(1-2): 201-213, 1999. doi: 10.1016/S0926-860X(99)00173-8

A. Suwatthikul, S. Limprachaya, P. Kittisupakorn and I. M. Mujtaba. Simulation of steam gasification in a fluidized bed reactor with energy self-sufficient condition. *Ener gies*, 10(3): 314, 2017. doi:10.3390/en10030314

R. Thapa and B. Halvorsen. Stepwise analysis of reactions and reacting flow in a dual fluidized bed gasification reactor. *Adv. Fluid Mech*, 82(12): 37-48, 2014.

D. Tristantini, S. Lögdberg, B. Gevert, Ø. Borg and A. Holmen. The effect of synthesis gas composition on the Fischer–Tropsch synthesis over Co/γ-Al2O3 and Co–Re/γ-Al2O3 catalysts. *Fuel Processing Technology*, 88(7): 643-649, 2007. doi:10.1016/j.fuproc.2007.01.012

A. Visconti, M. Miccio and D. Juchelková. An aspen plus tool for simulation of lignocellulosic biomass pyrolysis via equilibrium and ranking of the main process variables." *International Journal of Mathematical Models and Methods in Applied Sciences*, 9: 71-86, 2015.

X. Xiao et al., Catalytic steam gasification of biomass in fluidized bed at low temperature: conversion from livestock manure compost to hydrogen-rich syngas. *Biomass and Bioenergy*, 34(10): 1505-1512, 2010. doi:10.1016/j.biombioe.2010.05.001

Effect of Superficial Gas Velocity on Bubbling Fluidized Bed Behaviour in a Biomass Gasifier

Cornelius Agu Britt M.E. Moldestad

Department of Process, Energy and Environmental Technology, University of South-Eastern Norway, 3918 Porsgrunn, Norway, {Cornelius.e.agu, britt.moldestad}@usn.no

Abstract

This study investigates the behaviour of bubbling fluidized beds in biomass gasification processes based on the variation of superficial gas velocity at different temperatures and air flowrates. In the paper, the operating window is defined as the gas velocity between the minimum fluidization and slugging velocities, which are computed using the correlations in the literature. The analysis shows that the operating gas velocity depends on the amount of char accumulated in the bed. An increase in the char accumulation results in higher minimum fluidization and slugging velocities of the bed mixture. This therefore suggests that the gas velocity ratio required to achieve the desired operating fluidized bed regime is higher when the biomass accumulation is considered.

Keywords: biomass, gasification, air-fuel ratio, CPFD, bubbling fluidized bed

1 Introduction

Fluidized beds have numerous advantages in chemical processes, for example, biomass gasification. Such benefits include the excellent gas-solid mixing that can lead to uniform heat and mass distribution within the reactor. In a biomass fluidized bed gasifier, the operation is often aided with a bed material such as sand particles of relatively higher density and smaller size than the biomass particles. The bed material also helps to achieve high solid inventory and a stable pressure drop for the case of a bubbling bed. However, one major drawback is the limitation to gas flow rate imposed by the hydrodynamics of the bed material (Kunii and Levenspiel, 1991). For a given material, the bed is in the bubbling regime when the gas velocity is not too high above the minimum fluidization velocity at the operating condition. When the gas velocity is very high, the bed may transit into slugging, turbulent flow or fast fluidization regime (Kunii and Levenspiel, 1991). The flow of slugs in a bed may result in gas bypass and high fluctuation of the bed. Different factors can influence the gas velocity during operation, which will in turn lead to changes in the bed behaviour.

An increase in the gas yield during the solid fuel conversion enhances the gas velocity at the operating temperature. With changes in temperature and pressure in the conversion process, the fluid properties as well as the particle-particle interactions may vary, causing changes in the flow velocity. In extreme cases, this may lead to changes in the fluidization type (Nemati *et al.*, 2016). The common observations to these changes is the effect of temperature on the transition of fluidized bed regimes as have been demonstrated in different studies. Increasing the bed temperature decreases the minimum fluidization velocity of Geldart A and B particles and increases those of Geldart D particles (Pattipati and Wen, 1981; Botterill *et al.*, 1982). In addition, the gas velocities at the onset of slugging and turbulent fluidization may also increase with increasing temperature due to changes in the fluid properties and a decrease in the bubble size (Otake *et al.*, 1975; Hatate *et al.*, 1990).

In designing bubbling fluidized bed reactors, selecting the suitable gas velocities for stable operations while achieving the desired gas yields and compositions is a critical issue. This study is aimed at investigating the effect of gas velocity in a bubbling fluidized bed during the biomass gasification. The study is based on the theoretical equations developed for fluidized bed behaviour. The semi-empirical models are applied to simulate the minimum fluidization and slugging velocities with and without accumulation of biomass in the bed for a given reactor size and operating condition. In addition, the possibility of solids entrainment at the operating temperature and different gas velocities is simulated using the computational particle-fluid dynamics (CPFD) code. The outcome of this study can be used as a basis to understand the influence of unconverted biomass on fluidized bed behaviour.

2 Theory: Correlations for minimum fluidization and slugging velocities

A fluidized bed reactor usually contains a mixture of different types of particles. Each particle type influences the behaviour of the bed. The bubble properties (size and rise velocities) and transition velocities from one regime to another differ significantly from those of pure solid

particles. The extent to which the bed behaviour is affected by each solid component depends on the amount of the individual solids in the bed. In biomass gasification reactors, the solid particles include the raw biomass, bed material, ash and char particles. For simplicity, the ash content of the fuel can be neglected since it is relatively low compared to other particles in the bed. Raw biomass and char particles can be lumped into one solid component using their average mass density and particle size. The resulting bed is a binary mixture consisting of the lumped biomass and bed material particles.

The minimum fluidization velocity of a binary mixture of biomass and bed material can be obtained from different correlations (Si and Guo, 2008; Kumoro *et al.*, 2014) for a given amount of biomass particles. In general, the minimum fluidization velocity of a bed can be computed by balancing the bed weight per unit area with the Ergun (1952) equation as expressed below

$$\frac{1.75}{\varepsilon_{mf}^3}\left(\frac{\rho_f U_{mf} d_s}{\mu_g}\right)^2 + \frac{150(1-\varepsilon_{mf})}{\varepsilon_{mf}^3}\left(\frac{\rho_g U_{mf} d_s}{\mu_g}\right) = Ar \quad (1)$$

$$Ar = \frac{d_s^3 \rho_g (\rho_s - \rho_g) g}{\mu_g^2} \quad (2)$$

where U_{mf} and ε_{mf} are the superficial gas velocity and bed void fraction at the minimum fluidization condition, respectively. Ar is the Archimedes number, ρ_g is the fluid density, μ_g is the fluid dynamic viscosity, ρ_s is the density and d_s is the average diameter of the particles. For a bed of sand-like particles, (1) can be reduced as given in (3) (Wen and Yu, 1966).

$$U_{mf} = \frac{\mu_g}{\rho_g d_s}\left[-33.67 + \sqrt{(33.67^2 + 0.0408 Ar)}\right] \quad (3)$$

Equation (1) can also be used to predict the U_{mf} of a binary mixture of biomass and bed material as described in Agu *et al.* (2019a), where the particle diameter and density are replaced with the respective average values d_{sm} and ρ_{sm} for the mixture. The mixture void fraction $\varepsilon_{mfm} = 1 - \alpha_{mfm}$ is computed from (Agu *et al.*, 2019a)

$$\alpha_{mfm} = \frac{1-\varepsilon_{mfp}}{\left((1-\varepsilon_{mfp}) - \varepsilon_{mfb}\left(1 - \left(\frac{d_{sp}}{d_{sb}}\right)^{\beta x_p}\right)\left(\frac{d_{sp}}{d_{sb}}\right)\right)\frac{y_b}{(1-\varepsilon_{mfb})} + y_p} \quad (4)$$

$$\beta = 0.623\left(\frac{d_{sp}\rho_{sp}}{d_{sb}\rho_{sb}}\right)^{-0.61} \quad (5)$$

Here, ε_{mfp} and ε_{mfb} are the individual void fractions of the bed material and biomass particles at minimum fluidization condition, respectively. d_{sp} and d_{sb}, and ρ_{sp} and ρ_{sb} are the corresponding particle diameter and density. y_p and y_b are the volume fraction of the different components in the mixture, where x_p is the mass fraction of the bed material.

The minimum slugging velocity U_{msm} of the binary mixture increases significantly with an increase in the amount of biomass in the bed (Agu *et al.*, 2019b). For biomass volume fraction less than 40%, the ratio, U_{msm}/U_{msp} is independent of biomass properties, where U_{msp} is the minimum slugging velocity of the bed material. Correlating the results obtained in different beds of sand-wood chip and sand-wood pellet mixtures, U_{msm}/U_{msp} can be predicted from (Agu *et al.*, 2019b)

$$\frac{U_{msm}}{U_{msp}} = e^{1.13 y_b} \quad (6)$$

Among other models (Baeyens and Geldart, 1974; Shaul *et al.*, 2012), the value of U_{msp} can be predicted from the following equation as given in Agu *et al*. (2018).

$$\frac{U_{msp}}{U_{mfp}} = 1 + 2.33 U_{mfp}^{-0.027}\left(\varphi^{0.35} c_t^{a_t} - 1\right)\left(\frac{h_0}{D}\right)^{-0.588} \quad (7)$$

Here, φ is the particle sphericity, h_0 is the initial bed height and D is the bed diameter. The values of the parameters a_t and c_t are as described in the literature (Agu *et al.*, 2018) depending on the Archimedes number, where $Ar > 400$.

The amount of biomass in a bed depends on the biomass residence time at the operating condition for a given air-fuel ratio (AFr). For a steady biomass mass flowrate $\dot{m}_b$, the mass fraction of biomass x_b accumulated in a bed of mass m_p can be estimated from the following equations proposed by Agu *et al.* (2019c).

$$\frac{x_b}{1-x_b} = (1-\lambda)\gamma_{char}(t_e - t_d)\frac{\dot{m}_b}{m_p} \quad (8)$$

$$t_d = 681 X_b^{0.028}\left(\frac{U_0}{U_{mfp}}\right)^{-0.3} \quad (9)$$

$$t_e = 4055 X_b^{0.278}\left(\frac{U_0}{U_{mfp}}\right)^{-0.185} \quad (10)$$

$$\gamma_{char} = 0.414 X_b^{0.245}\left(\frac{U_0}{U_{mfp}}\right)^{-0.463} \quad (11)$$

$$X_b = \left[4055\frac{\dot{m}_b}{m_p}\left(\frac{U_0}{U_{mfp}}\right)^{-0.185}\right]^{1.385} \quad (12)$$

where $0.45 < \lambda < 0.7$ is the fraction of time over the char residence time $(t_e - t_d)$ that measures the extent of char conversion during one cycle of an ideal plug flow process. γ_{char} is the amount of char released at the completion of biomass devolatilization (pyrolysis) and X_b is the ratio of the mass of biomass loaded over the period t_e to the mass of the bed material.

3 Computational model

To investigate the effect of gas velocity on vertical movement of particles in hot reactors, the fluidized bed behaviour was simulated using Barracuda VR software. Barracuda is the commercially developed platform for implementing computational particle-fluid dynamics (CPFD) scheme. CPFD is based on the multiphase-particle-in-cell (MP-PIC) concept introduced by Andrew and O'Rourke (1996). In the CPFD scheme, the Euler-Lagrangian modelling approach is applied for fluid volume and particle tracking in gas-solid systems. With the MP-PIC concept, a computational particle represents a large number of particles, which have similar properties. The grouping of particles in CPFD code makes the simulation faster, thereby increasing its application to industrial systems. Detailed descriptions of the CPFD model and its numerical scheme can be found in Chen *et al.* (2013).

4 Validation of computational model

To validate the CPFD model, experimental data were obtained from a cylindrical pilot plant of diameter 0.1 m and height 1.0 m. The properties of sand particles used as the bed material is given in Table 1.

Table 1. Bed material and biomass at ambient conditions.

Materials	ρ_p *(kg/m3)*	d_s *(mm)*	φ_s *(-)*	ε_{mf} *(-)*	U_{mf} *(m/s)*
Wood chips	423	6.87	0.75	0.57	1.270
Sand	2650	0.61	0.86	0.45	0.232

In the temperature range 25 – 550 ºC, the minimum fluidization velocities of the sand particles were measured using the curves of pressure drop versus superficial air velocity at different temperatures, and then correlated as given by (13) with correlation coefficient (R^2 value) of 0.9995, where T_0 = 25 ˚C, ρ_{g0} = 1.18 kg/m3 and U_{mf0}= 0.232 m/s.

$$U_{mf} = \frac{\rho_{g0}}{\rho_g} U_{mf0}\{0.19 + 0.787 \exp[-0.0045(T - T_0)]\} \quad (13)$$

Figure 1 compares the minimum fluidization velocities computed using (13) with those obtained from (3) as well as the CPFD simulations at different temperatures. All the results show a decrease in the minimum fluidization velocity with increasing temperature. Both the CPFD simulation and the Wen and Yu correlation agree to some extent with (13) within a certain temperature range. The results from (3) are better than those from the simulations for temperatures above 200 ˚C. The simulation result at the ambient temperature closely matches the experimental value, but the deviation at higher temperature increases as the temperature increases. The mean absolute errors in the U_{mf} predictions within 25 – 550 ºC are 8% and 10% for (3) and the CPFD simulations, respectively. It should be noted that at higher temperatures > 550 ˚C, the trend of the measured U_{mf} may deviate, increasing the inaccuracies in both model predictions. However, for the purpose of analysis, the uncertainties in using the models to extrapolate U_{mf} at higher temperatures can be neglected in subsequent sections.

5 Results and discussion

For particle size as large as 600 µm, the inlet superficial gas velocity used in most studies on bubbling fluidized bed gasification is within 2 – 3 times the minimum fluidization velocity of the bed material. When biomass is introduced in the reactor, the increase in the gas flowrate increases the gas velocity through the bed at the operating conditions. Assuming a full conversion, the total mass flowrate of gas at steady state can be obtained as $(\dot{m}_{air} + \dot{m}_b)$, neglecting the ash content of the fuel. Here, $\dot{m}_{air}$ and $\dot{m}_b$ are the mass flowrates of air and biomass, respectively. Considering gasification of wood chips (with properties reported in Table 1) at an equivalence ratio of 0.25, a value of 1.5 can be obtained for air to biomass mass flowrate ratio. Based on this ratio, and neglecting the difference between the air density and the total gas density, the superficial gas velocity in the bed at full conversion can be approximated to $1.66U_0$, where U_0 is the superficial air velocity at the operating condition. The effect of this total gas velocity depends on how evenly the bed solid species are mixed since biomass particle segregation can occur within the bed despite the fuel feeding position. Assuming a perfect mixing of the solid particles, the gas velocity can be considered uniform over the entire bed volume.

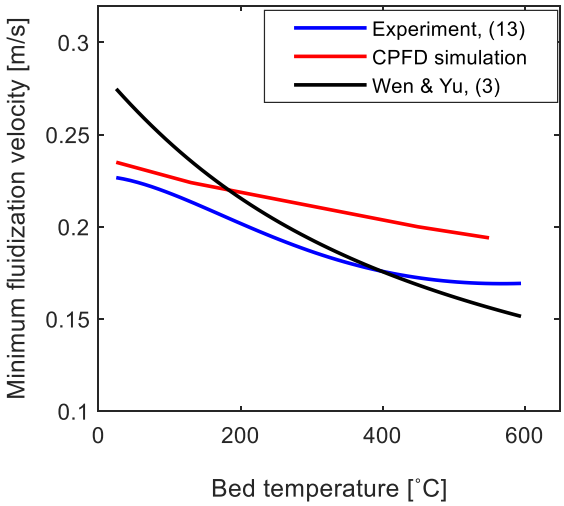

Figure 1. Variation of minimum fluidization velocity with temperature, comparing experimental data with the CPFD simulation results and the Wen & Yu (1966) correlation; material: 610 µm sand particles.

5.1 Neglecting the biomass accumulation

Figure 2(a) shows the influence of temperature on the bed behaviour of the 610 µm sand particles at two different constant air mass flowrates, $\dot{m}_{air} = 2(\rho U_{mf})_{opt} A_0$ and $\dot{m}_{air} = 3(\rho U_{mf})_{opt} A_0$, which are assumed to represent cases without any reaction. Figure 2(b) shows the behaviour for the corresponding cases at full conversion. Here, the values of $(\rho U_{mf})_{opt}$ are obtained at the reactor operating temperature 900 ˚C, in which U_{mf} = 0.187 m/s based on the correlation given by (13). The plotted data are the superficial gas velocities U_0 and the transition velocities U_{mf} and U_{ms} at different temperatures. The minimum slugging velocity was computed from (7) at the bed aspect ratio, $h_0/D = 2.5$ and the superficial air velocity was obtained from $U_0 = \dot{m}_{air}/\rho A_0$, where the air density ρ is at the different temperatures. Due to decreasing gas density, the operating gas velocity U_0 increases with an increase in temperature at a constant mass flowrate. The

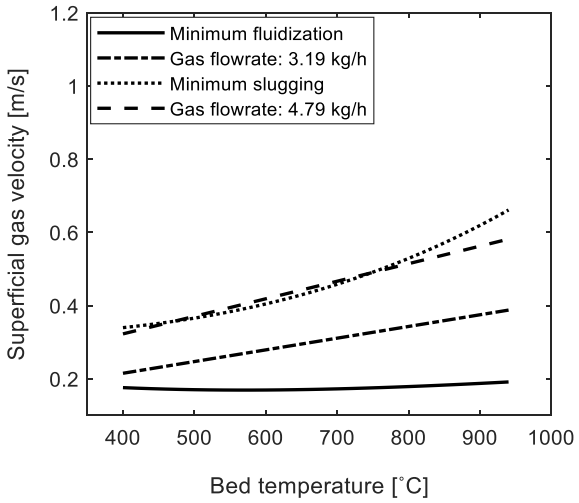

(a)

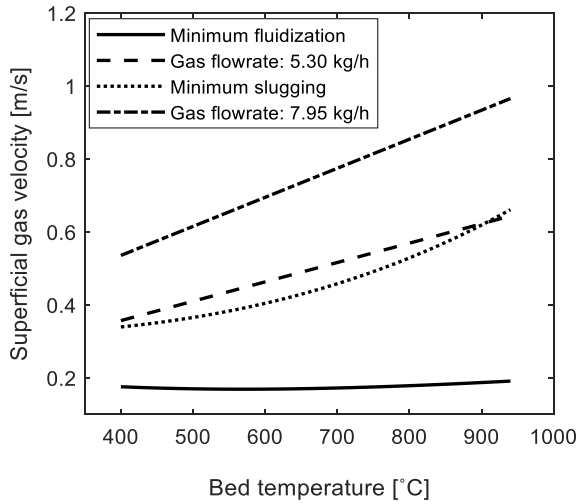

(b)

Figure 2. Behaviour of bed of sand particles, 610 µm at different temperatures and constant mass flowrates, $\dot{m}_{air}$ (a) $(2\rho U_{mf})_{opt}A_0 = 3.19$ and $(3\rho U_{mf})_{opt}A_0 = 4.79$ kg/h (b) $1.66 \cdot (2\rho U_{mf})_{opt}A_0 = 5.30$ and $1.66 \cdot (3\rho U_{mf})_{opt}A_0 = 7.95$ kg/h, where $A_0 = \pi D^2/4$.

gas velocity U_{ms} at the onset of slugging also increases as the temperature is increased. From the figures, the bed is fluidized (i.e. $U_0 > U_{mf}$) within the given temperature range for the respective mass flowrates.

With an increase in temperature, the bed remains in the bubbling regime until the operating velocity line crosses the minimum slugging velocity line. This never occurs in Figure 2(a) even at the higher mass flowrate. This shows that if the bed is maintained at a gas velocity of $3U_{mf}$, the bed will remain in the bubbling regime at the operating conditions. However, with a full conversion, the behaviour is completely different as shown in Figure 2(b); the bed slugs at both total mass flowrates.

In a bed of larger particles, bubbles can easily grow into slugs. Aside reduction in the gas residence time at higher gas velocities, there are also possibilities of particle attrition and entrainment of fines especially when the reaction column is not tall enough. If a complete reaction is assumed at the operating temperature, the increase in the total gas flowrate may also increase these effects. The effect of gas velocity on the distribution of solids along the bed axis is shown in Figure 3 for the 610 µm sand particles. The gas flowrates are the same as those used in Figure 2. In the CPFD simulations, the initial bed height was 25 cm and the initial solids fraction was 0.55. The contours of solids fraction (captured after 20 s) show that as gas velocity increases, the possibility of particles being dragged into the freeboard increases. The time-averaged solids fractions at different positions are shown in Figure 3(e). In these results, the flow regime of the bed at different gas velocities can be identified as described in Kunii and Levenspiel (1991). The result shows that at the gas velocities $U_0 = 2U_{mf}$ and $U_0 = 3U_{mf}$, the bed is in the bubbling regime, but in the slugging/turbulent flow regime at the two larger gas velocities. In addition, Figure 3(e) clearly shows that the amount of solids in the freeboard increases as the gas flowrate is increased, and the particles reach higher up in the column when a higher velocity is used. There are traces of solids in the column up to a height of 70 cm. At this position, the respective solids fractions are $4 \cdot 10^{-7}$, $6 \cdot 10^{-6}$, $6 \cdot 10^{-6}$ and $5 \cdot 10^{-5}$. Especially for the velocity $U_0 = 4.98U_{mf}$, this shows that there is a possibility of particle entrainment from the column.

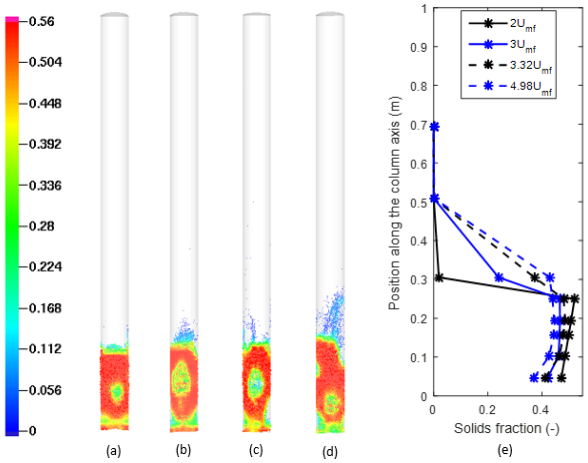

Figure 3. Bed behaviour simulated using CPFD Barracuda based on the 610 µm sand particles at 900 ˚C, showing the solids fraction distributions captured after 20 sec at different superficial air velocities (a) $U_0 = 2U_{mf}$ (b) $U_0 = 3U_{mf}$ (c) $U_0 = 3.32U_{mf}$ (d) $U_0 = 4.98U_{mf}$ and (e) the time-average axial distribution of solids fraction.

5.2 Considering the biomass accumulation

By considering the biomass accumulation, (8) was used to estimate the amount of unconverted char in the

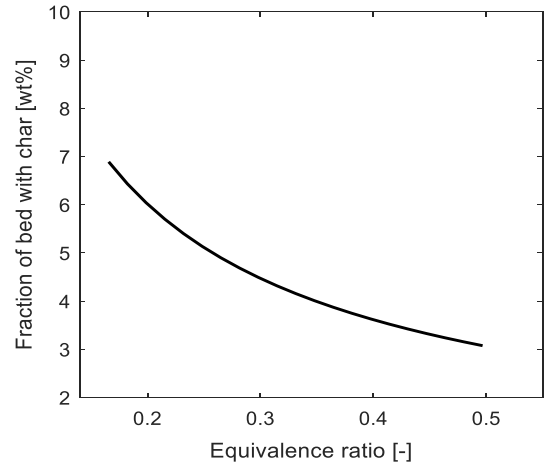

(a)

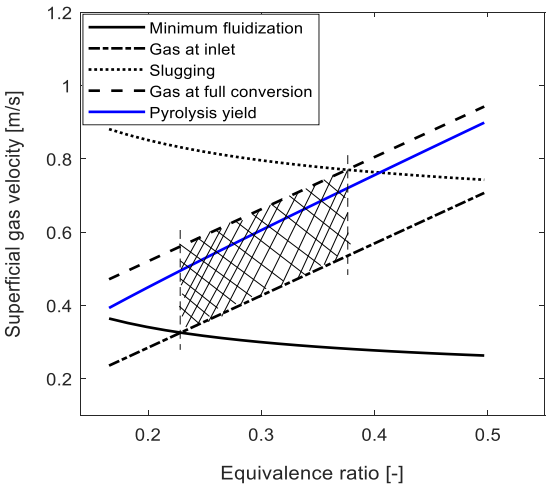

(b)

Figure 4. Behaviour of a bubbling fluidized bed gasifier at constant biomass flowrate, 900 ºC and different equivalence ratios (a) amount of unconverted char particles (b) gas velocity across the bed, showing the safe operating window.

bed at the given operating conditions. Figure 4(a) shows the values of x_b at a constant biomass flowrate 2 kg/h and different equivalence ratios (ER) defined as the ratio of the actual air-fuel ratio to the air-fuel ratio required for stoichiometry combustion of biomass. The equivalence ratio measures the relative amount of oxygen supplied, and for biomass gasification, ER < 1. The results shown in Figure 4 are based on a 10 cm diameter bed containing the 610 µm sand particles at initial height of 25 cm. As shown in the figure, x_b decreases with increasing ER due to increasing amount of the fuel particles converted. The bed behaviour at the different ER values is shown in Figure 4(b). While the values of U_{mf} and U_{ms} of the bed mixture decrease, the gas velocity through the bed increases with increasing equivalence ratio. For ER < 0.23, the incoming air velocity is too low to maintain the fluidization of the bed as the accumulation is relatively high. However, with an increase in the total gas flowrate at the completion of biomass pyrolysis, the bed is fluidized even at ER value of 0.15. It should be noted that at a low air velocity, the conversion will be delayed, thus the full conversion gas velocity will be rarely achieved at equivalence ratio < 1. If the total gas yield at full conversion acts on the bed evenly, the bed will remain in the bubbling regime up to ER = 0.38. The shaded portion in Figure 4(b) should therefore represent the safe operating window for the system. At the 0.38 equivalence ratio, the incoming air velocity, $U_0/U_{mfp} = 3$. On the contrary, when the biomass accumulation is not considered, the maximum air velocity within the bubbling window at 900 ºC is $U_0/U_{mfp} = 2$ as can be seen in Figure 2. This indicates that the amount of unconverted biomass must be considered when selecting the gas velocity for a fluidized bed operation.

6 Conclusions

This study investigated the behaviour of bubbling fluidized bed in a biomass gasification reactor to illustrate how the operating window can be established. The study applied different correlations proposed in the literature for predicting the minimum fluidization and slugging velocities of a given bed including those of binary mixtures of biomass and bed material. Based on the analysis, the amount of unconverted char particles plays a significant role in the hydrodynamics of the bed, and thus must be considered when selecting the gas velocity for stable operations.

References

C.E. Agu, C. Pfeifer, and B.M.E. Moldestad. Prediction of void fraction and minimum fluidization velocity of a binary mixture of particles: Bed material and fuel particles. *Powder Technology*, 349: 99 – 107, 2019(a).

C.E. Agu, C. Pfeifer, L.-A. Tokheim, and B.M.E. Moldestad. Behaviour of biomass particles in a bubbling fluidized bed: A comparison between wood pellets and wood chips. *Chemical Engineering Journal*, 363: 84 – 98, 2019(b).

C.E. Agu, C. Pfeifer, M. Eikeland, L.-A. Tokheim, and B.M.E. Moldestad. Models for predicting average bubble diameter and volumetric bubble flux in deep fluidized beds. *Industrial & Engineering Chemistry Research*, 57: 2658 – 2669, 2018.

C.E. Agu, C. Pfeifer, M. Eikeland, L.-A. Tokheim, and B.M.E Moldestad. Measurement and characterization of biomass mean residence time in an air-blown bubbling fluidized bed gasification reactor. *Fuel*, 253: 1414 – 1423, 2019(c).

M.J. Andrews and P.J. O'Rourke. The multiphase particle-incell (MP-PIC) method for dense particulate flows. *International Journal of Multiphase Flow*, 22: 379 – 402, 1996.

J. Baeyens and D. Geldart. An Investigation into slugging fluidized beds. *Chemical Engineering Science*, 29: 255 – 265, 1974.

J.S.M. Botterill, Y. Teoman, and K.R. Yuregir. The effect of operating temperature on the velocity of minimum fluidization, bed voidage and general behaviour. *Powder Technology*, 31: 101 – 110, 1982.

C. Chen, J. Werther, S. Heinrich, H.-Y. Qi, and E.-U. Hartge. CPFD simulation of circulating fluidized bed risers. *Powder Technology*, 235: 238 – 247, 2013.

S. Ergun. Fluid flow through packed column. *Chemical Engineering Progress*, 48: 89 – 94, 1952.

Y. Hatate, K. Ijichi, Y. Uemura, M. Migita, and D.F. King. Effect of bed temperature on bubble size and bubble rising velocity in a semi-cylindrical slugging fluidized bed. *Journal of Chemical Engineering of Japan*, 23: 765 – 767, 1990.

A.C. Kumoro, D.A. Nasution, A. Cifriadi, A. Purbasari, and A.F. Falaah. A new correlation for the prediction of minimum fluidization of sand and irregularly shape biomass mixtures in a bubbling fluidized bed. *International Journal of Applied Engineering Research*, 9(23): 21561 – 21573, 2014.

D. Kunii and O. Levenspiel. *Fluidization Engineering*, 2nd ed., Butterworth – Heinemann, Washington Street, USA, 1991.

N. Nemati, R. Zarghami, and N. Mostoufi. Investigation of hydrodynamics of high temperature fluidized beds by pressure fluctuations. *Chemical Engineering & Technology*, 39: 1527 – 1536, 2016.

T. Otake, S. Tone, M. Kawashima, and T. Shibata. Behaviour of rising bubbles in a gas fluidized bed at elevated temperature. *Journal of Chemical Engineering of Japan*, 8: 388 – 392, 1975.

R.R. Pattipati and C.Y. Wen. Minimum fluidization velocity at high temperature. *Industrial & Engineering Chemistry Process Design and Development*, 20: 705 – 708, 1981.

S. Shaul, E. Rabinovich, and H. Kalman. Generalized flow regime diagram of fluidized beds based on the height to bed diameter ratio. *Powder Technology*, 228: 264 – 271, 2012.

C. Si and Q. Guo. Fluidization characteristics of binary mixtures of biomass and quartz sand in an acoustic fluidized bed. *Industrial & Engineering Chemistry Research*, 47: 9773 – 9782, 2008.

C.Y. Wen and Y.H. Yu. A generalized method for predicting the minimum fluidization velocity. *AIChE Journal*, 12: 610 – 612, 1966.

Investigation of the segregation and mixing behavior of biomass in a bubbling fluidized bed reactor using a CPFD model

Rajan Jaiswal Nora C. I. S. Furuvik Rajan K. Thapa Britt M. E. Moldestad

Department of Process Energy and Environmental Technology
University College of Southeast Norway, Norway

rajanjaiswal357@outloook.com {rajan.k. thapa, nora.c.i.furuvik, britt.moldestad}@usn.no

Abstract

Segregation of biomass in a gasification reactor is an inevitable problem that can jeopardize the advantages such as uniform temperature control and proper mass circulation, and good solid-gas contacting area of the fluidized bed. This work investigates the mixing and segregation behavior of the biomass in a bubbling fluidized bed using a Computational Particle Fluid Dynamic (CPFD) model. The model is simulated in the CPFD software Barracuda VR. The sand particles and wood chips are used as the bed material and biomass. The simulations are carried out with different volume percentage of the biomass at constant bed aspect ratio. The results show that the minimum fluidization velocity is decreased from $0.08\ \mathrm{m/s}$ to $0.06\ \mathrm{m/s}$ with the increase in biomass volume from 5% to 20% in the bed. The complete segregation of biomass occurs at the superficial gas velocity that is 3.5 times greater than minimum fluidization velocity. With the increase in superficial gas velocity, $u_0 \geq 6.u_{mf}$, the biomass again starts to mix with the bed material. However, the mixing of woodchips is mainly limited to the upper part of the bed.

Keywords: fluidized bed, wood chips, segregation, mixing, CPFD, Barracuda, biomass gasification.

1 Introduction

Background

Increasing demand of environmentally friendly energy has compelled researches and industries to look for an alternative source of energy. Biomass gasification in a fluidized bed reactor is a promising technology, which delivers enormous advantages in terms of higher energy yield (environment friendly) producer gases, uniform thermal control and proper mass circulation, and good solid-gas contacting area. In the bubbling fluidized bed, the lower density large particles (biomass) are fluidized with the smaller solid particles (bed materials) with the fluidizing agent air or steam. For an energy efficient gasification, uniform mixing of the biomass with bed material and fluidizing gas is essential. However, the difference in densities and sizes of the particles inside the bed causes the particles to segregate. Thus, the advantages of fluidized bed can be compromised by the segregation of solids. The segregation of the biomass in the bed can be in axial or lateral direction depending on the biomass feeding location, density ratio, ratio of biomass to bed material, sizes of biomass and bed material, and fluidizing gas velocities (Nienow *et al.*, 1978; Zhang *et al.*, 2009; Thapa, *et al.*, 2011; Bandara *et al.*, 2018; Kraft *et al.*, 2018; Agu *et al.*,2019). Many researches have studied the segregation and mixing behavior in the gasification of biomass. However, discrepancy still exists in understanding the complex behavior of gas-solid interaction during segregation phenomenon in the gasification process.

Rowe *et al.*, 1972 termed the particles that float to the surface of bed as flotsam and jetsam to the particles that tend to sink to the bottom of the bed (Rowe, 1972). The drag force exerted by the fluidizing gas velocity determines whether the particles behave as flotsam or jetsam. Thus, the uniform mixing of biomass inside the bed depends on the segregation tendency and fluidizing gas velocity. The mixing tendency can be enhanced by increasing the bed agitation. In a bubbling fluidized bed, the intensity of the gas velocity to obtain proper mixing is limited to fact that the reactor must be operated within optimum bubbling regime for maximum efficiency. During gasification of biomass, the inlet fuel particle undergoes drying and devolatilization and are converted to char particles. The release of volatile gases reduces the density of the fuel particles. In addition, endogenous bubbles are formed by the devolatilization and drying of biomass particles, enhancing the segregation process. The endogenous bubbles, which envelop the biomass particles, tends to lift the biomass to the surface (Bruni, *et al.*, 2002; Chirone *et al.*, 2012) thus, reducing the gas exchange between the bubbles and the emulsion phase. The volatile matter bypasses the bed materials and are mostly released above the surface of the bed. Due to poor contact between volatile components and the fluidizing gas, the process can be inefficient. Also, it is likely, that the fine biomass particles that are segregated on the surface, burnout in the freeboard. The process of formation of endogenous bubbles from the fuel particles and segregation of particles in axial and lateral direction are shown in Figure 1. The bed material acts as the thermal flywheel in the gasification reactor. Thus, the

contact duration of the biomass with bed materials determine the fluidization quality and stable operation of the process. During devolatilazation of biomass, tar components are released into the reactor. The formation of tar is strongly influenced by the operating parameters for instant temperature (Kinoshita and Wang,1994) and type of biomass used(Font Palma, 2013). The tar components may condense and form deposits on the downstream equipment that can lead to the complete shutdown of the operation. Therefore, it is essential to improve fluidization and proper mixing fuel particles for the reduction of tar formation(Rowe *et al.*, 1972; Kuba *et al.*, 2018).

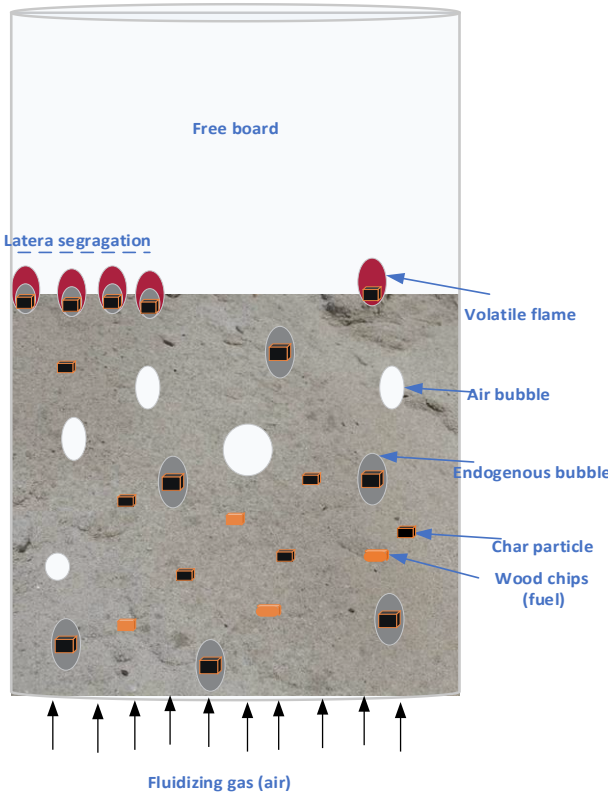

Figure 1. Segregation of biomass in axial and lateral direction.

In this work, the segregation and mixing behavior of the lower density wood chips with sand particles are investigated using a CPFD model. The Computational model was validated against the experimental results. The results used to validate the model was the pressure drop and minimum fluidization velocities.

The CPFD model is used to study the segregation behavior in the bed. In order to investigate the mixing and segregation between the bed material and the wood particles, it is necessary to track the concentration/flow of the particles along the bed height. For this purpose, a number of flux planes are created in the CPFD model as shown in Figure 2 (a). Each of the flux planes are set to measure time integrated mass of the wood chips. The volume percentage of biomass inside the bed were varied to study its influence on mixing and segregation tendency.

2 Experimental and Simulation set up

2.1 Experiment

The experimental setup used in this work is the same as used by (Jaiswal and Agu, 2018) in his previous work. The experimental set up consists of a reactor of diameter 8.4 cm and height 140 cm. The pressure drop inside the bed due to change in superficial gas velocity is measured by the pressure transducers attached along the wall of the column. Experiments were carried out with the sand particles and biomass as bed materials at an aspect ratio (H/D) = 2.5. Where, H is the static bed height and D is the diameter of bed. Table 1 shows the properties of bed material and biomass (wood chips) used for this work.

Table 1. Particle properties

Particles	Desity, (ρ_p) $[kg/m^3]$	Solid volume fraction	Mean diameter (d_m) $[\mu m]$	Size range
Sand	2650	0.54	285	200-355
Biomass	423	0.44	N/A	5mm-0.5cm

2.2 Simulation set up

The Computational particle fluid dynamics software Barracuda VR uses the Multi- Phase Particle in Cell (MP-PIC) approach, where particles with similar properties such as diameters and densities are grouped together to form the computational unit of the computational particles termed as parcels. In this MP-PIC technique, combined Eulerian and Lagrangian methods are used for the modeling of gas-solid interaction. The fluid phase is solved with the continuum model, while the particle phase is solved using the Lagrangian method. The advantages of using CPFD approach compared to other CFD techniques is that it is cost optimal and saves computational time.

Figure 2. shows the simulation set up used for this work. A 3D geometry of height 140 cm and diameter 8.4 cm was imported to Barracuda VR and uniform grid of total cells 8640 were established around the geometry. The top of the reactor is open to the atmosphere and set as the pressure while the flow boundary condition is setup at the bottom of the reactor. The transient data points were selected along the height to monitor the pressure. The measuring points resemble the experimental setup. Different flux planes were assigned along the reactor to track the particle species passing through it during fluidization. The flux planes, transient data points, initial particles species, particle volume

fraction and pressure boundary conditions are shown in Figure 2 a-e respectively.

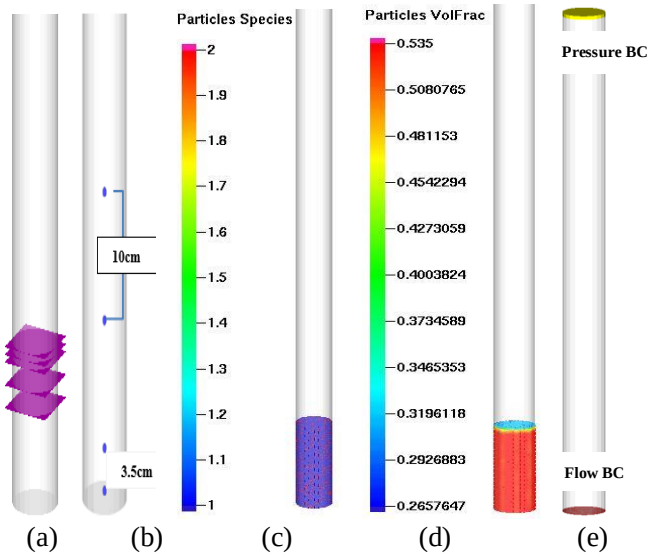

Figure 2. Computational setup showing (a) Flux planes, (b) Transient data location, (c) Particle species, (d) Particle volume fraction, (e) Pressure and flow boundary conditions**.**

The operating parameters used for the simulations are listed in Table 2. Air is used as the fluidizing agent at ambient conditions and the superficial gas velocity is increased gradually to obtain the fluidization properties of the mixture.

Table 2. Operating parameter

Temperature	300K
Pressure	101325 Pa
Superficial gas velocities	0.03-0.75 m/s
Maximum momentum redirection from collosion	0.44 %
Normal to wall momentum retention	0.33
Tangential to wall momentum retention	0.99

3 Result and Discussion

3.1 Model Validation

The simulations are carried out with sand particles with mean diameter of 285µm at an aspect ratio of 2.5. The pressure drop is plotted against the superficial air velocities. The Wen and Yu drag model has been used for the simulation. The profile of pressure drop vs superficial gas velocities obtained from the CPFD model is compared with the experimental data as shown in Figure 3. The result shows that the simulation model fits well with the experimental data. Thus, this model is used for further simulations.

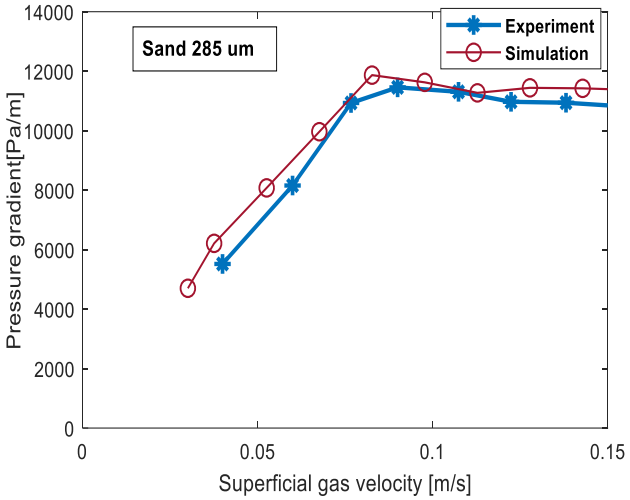

Figure 3. Pressure drop vs superficial gas velocity.

3.2 Minimum fluidization

The different volume percentage of biomass (5%, 10%, 15%, and 20%) were added to the initial static bed uniformly and the superficial gas velocities were increased gradually to investigate the fluidization behavior of the bed with biomass. Two sensors located inside the bed were chosen for the analysis. The result shows that the minimum fluidization velocity and pressure gradient decreases with increase in biomass volume inside the bed. The minimum fluidization velocity is found to be decreased from 0.08 m/s to 0.06 m/s with the increase in biomass from 5% to 20% inside the bed. The decrease in the pressure gradient is due to increase in the concentration of the lower density biomass inside the bed. The larger size biomass in the bed increases the void within the bed, making an easy passage of fluidizing air through the bed. Thus, the minimum fluidizing velocity decreases. The behavior of the biomass-sand mixture with the change in gas velocities is shown in Figure 4.

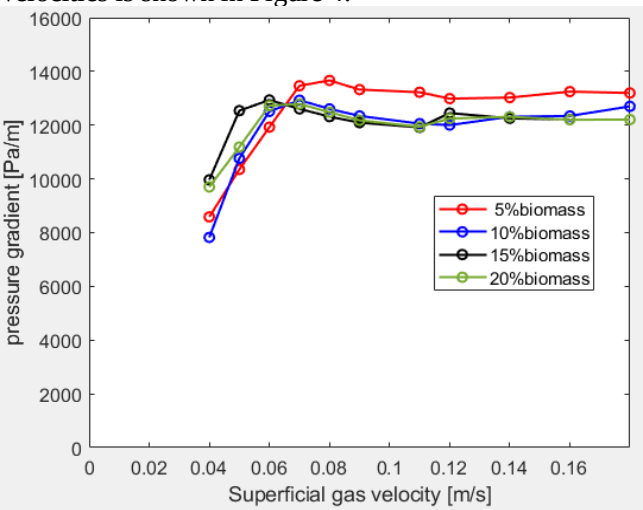

Figure 4. Pressure drop profile for the bed with different biomass percentage.

Figure 5 compares the minimum fluidization velocity obtained from the experimental data and the simulation. The results show that the simulation results are good in agreement with the experimental data.

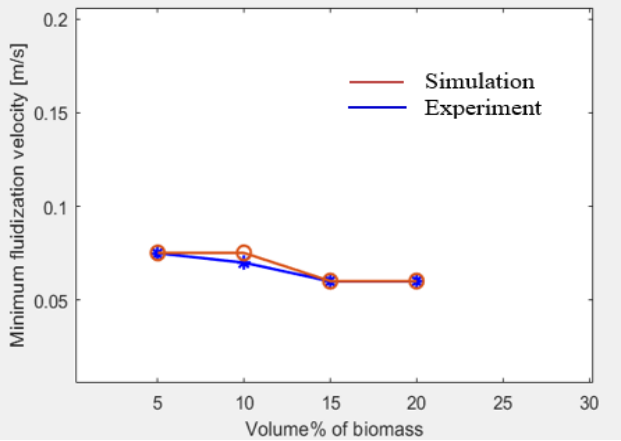

Figure 5. Minimum fluidization velocity of the bed with different biomass percentage obtained from experiment and simulation.

3.3 Bubble behavior

Figure 9 shows the Cell volume fraction of the particles in the bed with 20 % and 5% volume of woodchips. The cell particle volume fraction less than 30 percent represents the bubble inside the bed. The figure shows that the bubbles are larger and more distinct in the bed with 5% wood chips. With the increase in wood chips load to 20 volume % of the bed, the formed bubbles are smaller and most of the bubbles collapse within bed due to higher concentration of the irregular sized wood chips. The smaller bubbles inside the bed inversely affect the gas and solid interaction and mixing behavior of the bed.

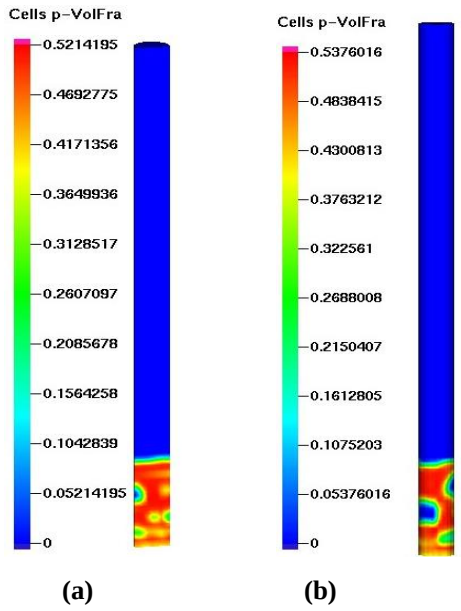

Figure 6. Cell volume fraction of the bed with (a) 20% volume of biomass (b) 5% volume of biomass.

3.4 Segregation of particles

Flux planes set at different locations in the reactor, as shown in Figure 2 (a), are used to monitor time integrated particle mass of species: biomass and sand particles passing through the planes at different gas velocities. Figure 7 shows the time integrated mass of biomass in upward direction at different fluidizing gas velocities when the bed is mixed with 10 % biomass and sand particles. The initial static bed height is 21 cm. One of the flux planes is set up on the top of the bed. The result shows that the biomass that are initially uniformly distributed across the bed starts to move in upward direction as soon as the bed is fluidized. The figure illustrates that the biomass remained at the bottom passes the flux planes at the heights 13 cm and 16 cm at the superficial gas velocity 0.12 m/s within 120 s. With the increase in gas velocity, the biomass segregated and accumulated above the flux plane at height 20 cm at the superficial gas velocity 0.18 m/s. The linear trend of the time integrated mass of biomass for the flux planes at 19 cm and 20 cm indicates that there is no biomass inside the after 200 s and at the corresponding superficial gas velocity of 0.2 m/s. The wood chips float at the upper region of the bed.

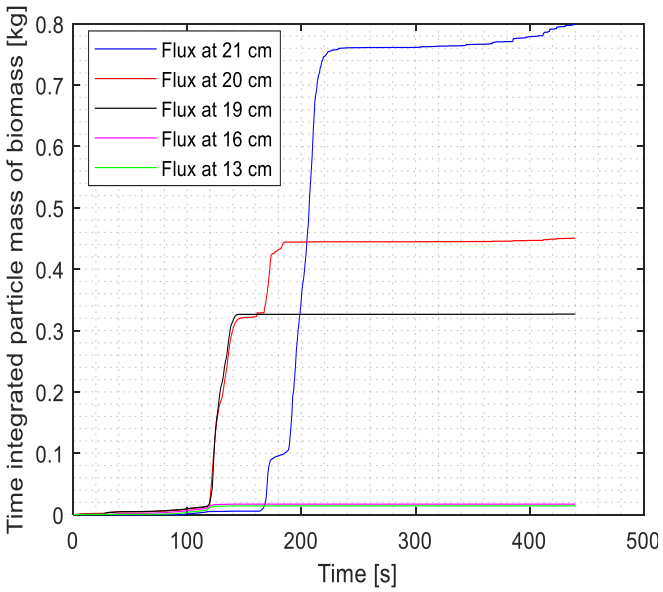

Figure 7. Time integrated mass of biomass across different planes with 10% (volume) biomass inside bed.

Figure 8 represents the segregation and mixing behavior of the wood chips in the bed. The figures are produced from the post processing tool available in Barracuda. At each time step, the behavior of biomass inside the reactor with change in gas velocities are analyzed. The particle species that are red in color are biomass while the blue color species are the sand particles. The biomass that remained at the upper part of the bed, segregated quickly and accumulated at the top of the bed. The segregation of biomass locally along vertical direction is shown in Figure 8 (a). This tendency

of biomass to segregate inside the bed decreases the efficiency of the reactor since the biomass has not sufficient time for the gasification. In addition, the biomass might burnout in the freeboard reducing the overall efficiency of the process. The upward movement of biomass particles as shown in Figure 8 (a), has a ring like structure, suggesting that the movement of biomass inside the bed is mostly along the wall of reactor. The partial segregation and complete segregation of biomass are shown in Figure 8 (b) and 8 (c) respectively. The complete segregation occurs at gas velocity $u_0 \geq 3.5 \cdot u_{mf}$. Where, u_0 is the superficial gas velocity and u_{mf} is the minimum fluidization velocity.

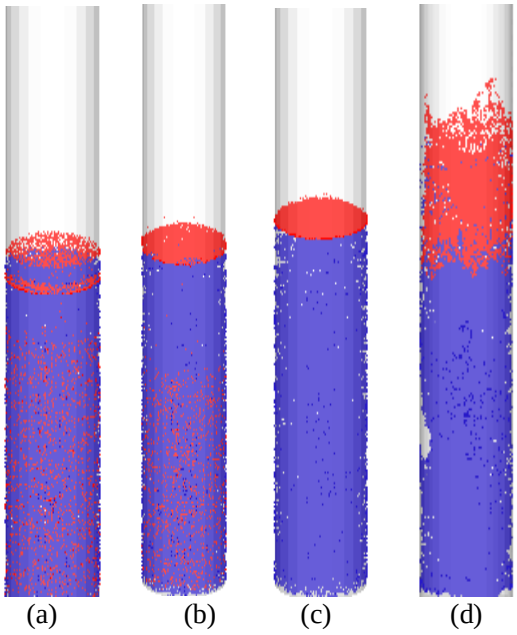

Figure 8. (a) Local segregation (b) partial segregation (c) complete segregation (d) mixing.

3.5 Mixing of wood chips

Figure 9 shows the mixing behavior of the bed with 20% volume of the biomass inside the bed. The result shows that the biomass starts to mix at the superficial gas velocity, $u_0 \geq 6 \cdot u_{mf}$. The mixing of biomass starts when the bed agitation is high enough to counterbalance the drag force that tends to lift the biomass in the upward direction. The increasing trend of the time integrated biomass particles at the flux planes at the height 21 cm and 20 cm as shown in Figure 8, explains the mixing of biomass inside the bed. The more biomass passing thorough the flux plane the more indication of mixing of wood particles with the sand in these parts of the bed. The quantity of biomass that are pushed inside the bed tends to move upwards, increasing the mass of biomass passing the flux plane. However, the mass of biomass through the flux planes below 20 cm is constant indicating that the biomass is segregated completely. This illustrates that the biomass mixing is only limited to the upper portion of the bed. With the increase in volume percentage of biomass inside the bed, the mixing starts earlier.

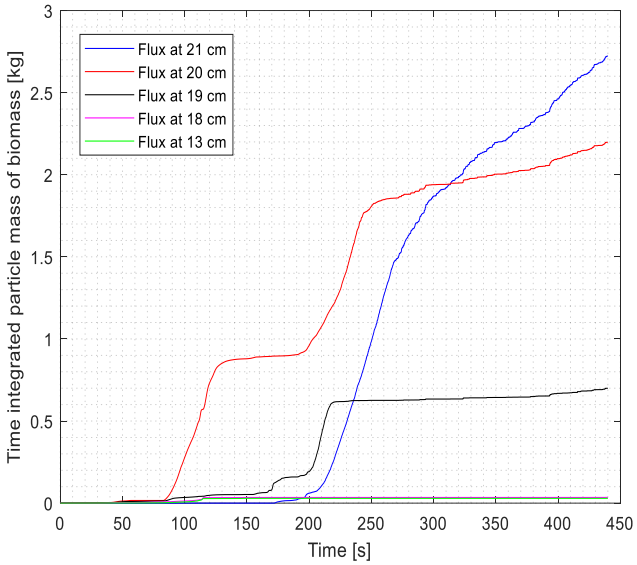

Figure 9. Time integrated mass of biomass across different planes with 20% (volume) biomass inside bed.

4 Conclusion

The difference in density, size, and ratio of bed material to biomass influences on the segregation and mixing tendency in gasification of biomass using fluidized bed. The segregation of biomass limits the advantages such as uniform thermal control and proper mass circulation, and good solid-gas contacting area of the fluidized bed. Therefore, it is crucial to study the segregation and mixing properties of biomass in the gasification.

This study investigates the mixing and segregation behavior of the biomass in a bubbling fluidized bed. Sand particles with mean diameter 285 μm and wood chips with size range $7mm - 0.5\,cm$ are used in the bed. A CPFD model is established in Barracuda VR. The model is validated against the experimental results. The simulations are carried in a reactor of diameter $8.4cm$ and height $140cm$. The biomass volume percentages 5%, 10%, 15% and 20% are used inside the bed at the constant aspect ratio 2.5. Flux planes at different heights are set up inside the reactor to capture the biomass behavior with the change in superficial gas velocities. The flux planes track the particle species along the bed heights.

The results show that the minimum fluidization velocity is decreased from 0.08 m/s to 0.06 m/s with the increase in biomass volume from 5% to 20%. The biomass starts to move upward as soon as it reaches the minimum fluidization velocity. The movement of the biomass are mostly along the wall of the reactor. The complete segregation of biomass occurs at $u_0 \geq 3.5 \cdot u_{mf}$. The mixing of biomass is only limited to the upper plane of the reactor and the segregated biomass

starts to mix with the bed material at the superficial gas velocity $u_0 \geq 6 \cdot u_{mf}$.The formation and growth of bubbles are inversely affected by the increase in concentration of woodchips inside the bed.

The results presented with the CPFD model in this study enhances the understanding of the segregation and mixing phenomena in the fluidized bed. Also, the CPFD method presented in this work explores the possibilities to use it at the industrial scale gasification reactors.

References

C. E. Agu, L.-A. Tokheim, C. Pfeifer, and B. M. Moldestad Behaviour of biomass particles in a bubbling fluidized bed: A comparison between wood pellets and wood chips. *Chemical Engineering Journal*, 363: 84-98, 2019.

J. C. Bandara, R. K. Thapa, B. M. Moldestad, and M. S. Eikeland. Simulation of Particle Segregation in Fluidized Beds. In the *Proceedings of The 9th EUROSIM Congress on Modelling and Simulation, EUROSIM 2016, The 57th SIMS Conference on Simulation and Modelling SIMS 2016, Linköping University Electronic Press*.

G. Bruni, R. Solimene, A. Marzocchella, P. Salatino, J. Yates, P. Lettieri, and M. Fiorentino. Self-segregation of highvolatile fuel particles during devolatilization in a fluidized bed reactor. *Powder Technology*, 128(1): 11-21, 2002.

C. Font Palma. Modelling of tar formation and evolution for biomass gasification: A review. *Applied Energy*, 111: 129-141, 2018.

R. Jaiswal, C. E. Agu, R. K. Thapa, and B. M. Moldestad. Study of fluidized bed regimes using Computational Particle Fluid Dynamics, In *Proceedings of The 59th Conference on Simulation and Modelling (SIMS 59*), 26-28 September 2018, https://doi.org/10.3384/ecp18153271.

C. M. Kinoshita, Y. Wang, and J. Zhou. Tar formation Under Different Biomass Gasification Conditions, 1994.

S. Kraft, M. Kuba, and H. Hofbauer. The behavior of biomass and char particles in a dual fluidized bed gasification system. *Powder Technology*, 338: 887-897, 2018.

M. Kuba, S. Kraft, F. Kirnbauer, F. Maierhans, and H. Hofbauer. Influence of controlled handling of solid inorganic materials and design changes on the product gas quality in dual fluid bed gasification of woody biomass. *Applied energy, 210: 230-240,* 2018.

A. W. Nienow, P. N. Rowe, and T. Chiba. Mixing and segregation of a small proportion of large particles in gas fluidized beds of considerably smaller ones. *AIChE Symp* Ser, 74(176): 45-53, 1978.

P. Rowe. The mechanisms by which particles segregate in gas fluidised beds-binary system of near spherical particles.*Trans. Inst. Chem. Engng*, 50: 310-323, 1972.

P. N. Rowe, A. W. Nienow, and A. J. Agbim.The mechanism by which particles segregate in gas fluidized bedsbinary systems of near-spherical particles. *Trans. Inst. Chem. Eng.*, 50: 310-323, 1972.

R. Solimene, R. Chirone, and P. Salatino. Characterization of the devolatilization rate of solid fuels in fluidized beds by time-resolved pressure measurements. *AIChE Journal*, 58(2): 632-645,2012.

R. K. Thapa, C. Rautenbach and B. Halvorsen. Investigation of flow behaviour in biomass gasifier using Electrical Capacitance Tomography (ECT) and pressure sensors. Rautenbach, C. *An Experimental and Theoretical Study of Dense Fluidized Bed Fluid Dynamics. PhD Thesis, Telemark University College*, 2012.

Y. Zhang, B. Jin and W. Zhong. Experimental investigation on mixing and segregation behavior of biomass particle in fluidized bed. Chemical Engineering and Processing: *Process Intensification*, 48(3): 745-754, 2009.

Experimental and computational study on the effect of ash deposition on fluid dynamic behavior in a bubbling fluidized bed gasifier

Rajan K Thapa Saroj Thapa Rajan Jaiswal Nora C I S Furuvik Britt M E Moldestad

Department of Process Energy and Environmental Technology, University of Southeastern Norway, Norway,
{rajan.k.thapa, nora.c.i.furuvik, britt.moldestad}@usn.no
213843@student.usn.no,rajanjaiswal357@outlook.com

Abstract

The effect of ash deposition on fluid dynamic behavior in a fluidized bed gasification reactor has been studied using experimental and computational methods. The experiments were carried out using sand particles as bed material and air as a fluidizing agent. A 3D computational model has been developed for a bubbling fluidized bed gasification reactor. First, the model was simulated using only sand particles and air. The results are compared with the experimental results. The comparison shows good agreement between the two sets of the results.

The model was further used to study the effect of ash accumulation on the fluid dynamic properties of a biomass gasification reactor. The bed material was mixed with 2 and 4vol% of ash and simulated in cold conditions. Pressure drop increases and minimum fluidization velocity decreases with increasing the ash deposition in the bed. The model was also simulated for 2, 4, and 6 vol% of ash at a temperature of 800ºC. The minimum fluidization velocity was decreased in all the cases. The particle species concentration shows the ash particles start to segregate at the minimum fluidization condition and are totally separated at higher velocities. The bubble behavior of the bed is not effected by ash deposition.

Keywords: gasification, fluidized bed, segregation, mixing, CPFD, ash deposition

1 Introduction

Background

Gasification is the conversion of carbonaceous feedstock to the gaseous fuel by oxidation at a specific temperature. Gasification of biomass gives products such as carbon monoxide, hydrogen, and methane. The mixture of these gases is called producer gas.

Fluidized bed biomass gasification is a high temperature process where the producer gas is the main product and ash is a byproduct. In some cases, the gasification temperature can reach as high as the ash melting temperature causing the ash to melt inside the bed. This creates bed agglomeration and consequently de-fluidization of the reactor. Therefore, the ash melting phenomenon is undesirable in the gasification reactor.

Ash melting is also known as ash fusion or ash softening. This can also occur only in some of the hot spots in the bed. There are various reasons for the temperature to rise above the ash melting temperature. One of the reasons can be a high amount of ash deposition in the bed. Excessive ash deposition can reduce uniform mixing and heat transfer between bed material, biomass and fluidizing gas. The other reason can be the lower melting temperature of biomass ash which depends on its composition. Segregation between the deposited ash and bed material can also affect the mixing and heat transfer in the bed which can cause a rapid increase in temperature in some areas of the bed.

Many researchers have studied bed agglomeration in biomass gasification reactors. Bartels *et al.* have investigated the mechanism of agglomeration and concluded the fact that agglomeration takes place due to the adhesiveness of bed material caused by alkali compounds present in the biomass (Bartels *et al.*, 2008). Pietsch (Pietsch, 2008) defined agglomeration as the formation of larger entities from particulate solid by sticking particles together by short range physical forces between the particles themselves, or through substances that adhere chemically or physically to the solid surface and form a material bridge between the particles. Visser and Tardos (Visser *et al.*, 2008; Tardos *et al.*, 1995) found two different routes for the initiation of bed agglomeration: melt-induced agglomeration and coating-induced agglomeration. Melt-induced means its adhesiveness with the bed particles that acts like glue. Coating-induced agglomeration implies the formation of coats between bed material and the liquid phase due to adhesive force or stickiness. Tardos and Pfeffer (Tardos, 1995) found that the fluidization behavior is changed according to the agglomeration of bed particles. The bubbling behavior can be useful to indicate the agglomeration in BFB (Montes, 2014).

A number of bubbles passing though the bed in a specific interval of time is known as the bubbling frequency. Generally, the bubbling frequency is the

DOI: 10.3384/ecp20170170 Proceedings of SIMS 2019
Västeräs, Sweden, 13-16 August, 2019

same in all sections of the bed, but the bubbling frequency becomes different due to agglomeration. The pressure drop through the bed is equal to the total hydrostatic pressure of the bed during the fluidizing condition. So, agglomeration of the fluidized bed is characterized by lower pressure drop (Montes et al., 2014; Furuvik *et al.*, 2019).

Some of the significant elements in biomass ash are K, Na, Ca, Si, P, Mg, and Al. In order to study the behavior of ash deposition in relation to the fluid dynamic behavior, and develop a computational model for ash, it is crucial to study physical properties such as density, particle size, sphericity and melting temperatures of these elements and the percentage of the major components in biomass ash. The study of the melting behavior and deposition of the ash are essential to make the biomass gasification reactor more efficient (Brown, 2005). Usually, high temperature is more favorable for carbon conversion because it produces less amount of tar. However, it brings other technological issues like ash melting and bed agglomeration (Niu *et al.*, 2018).The alkali metals present in the biomass ash, will together with sulphur and chlorine in biomass fuels contribute to the bed agglomeration in fluidized bed reactors.

Biomass ash can be divided into three different groups based on their compositions. They are summarized in Table 1.

Biomass ash group	Ash components	Sintering Temperature
Woody biomass	Ca, K rich and Si lean	900-1000°C
Rice husk, bagasesses or reed canary grass	Si-rich , Ca,K lean	700-1000°C
Sunflower seed and rapeseed seeds	Ca,K and P rich	700-1000°C

Table 1. Types of biomass ash (G. C. Institute. 2019)

The ash melting takes place due to the low melting point of components such as K, Na, and S that are present in woody biomass. The melted components start to bind together like glue and cause agglomeration of ash particles in the reactor (Vuthaluru *et al.*, 1999). Bed agglomeration eventually causes de-fluidization which reduces the efficiency and might lead to a total shutdown of the bed. Moreover, ash deposition can cause corrosion in the reactor surface.

The studies are helpful for the prediction of ash melting and agglomeration of bed. The studies of the effect of the ash deposition on flow behavior in the fluidized bed reactor can prevent, in some cases, rising of the bed temperature above the ash melting temperature. Therefore, this work is focused on the ash deposition from woody biomass in fluidized bed gasification reactors and the effect of the ash deposition on the fluid dynamic behavior in the reactor.

2 Experimental set up and procedure

The arrangements of the experimental setup are shown in Figure 1.The setup consists of a 1.4 m long transparent column. The diameter of the column is 8.4 cm. Pressure transducers are connected to the tapping points, which are located along with the height of the column. The tapping points are arranged along the column in different heights, and the distance between each tapping point is 10 cm. At the bottom of the column, there is an air distributor. Compressed air is supplied from the bottom of the column, and the flow rate is is measured by a flow-measuring meter. The flow of the compressed air is controlled by valves. The particles were filled from the top of the column.

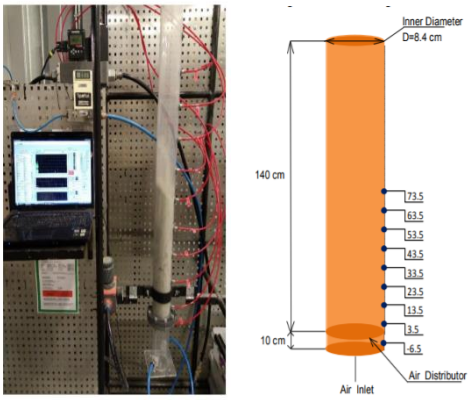

Figure 1. Experimental set up

The air flow rate and the pressure drop along the height of the column were logged in a LabView program. For each air velocity, data was recorded for more than 1 minute (sampling time 1 s), and a minimum of the 60s was allowed to establish the flow before the data was logged. Data Acquisition was done by Lab View, and the data was imported in MATLAB and used to plot the pressure drop against superficial gas velocity. The pressure drop can be calculated at each tapping point by subtracting the distributor pressure at a corresponding flow rate.

$$\Delta P_{f1} = P_{f1} - D_{f1} \quad (1)$$

where ΔP_{f1} is pressure reading at the pressure tapping point, D_{f1} is the distributor pressure and P_{f1} is the pressure at the pressure tapping point 1.

The properties of bed material used in the experiments are given in Table 2.

Table 2. Properties of bed materials and fluidizing gas

Particle mean diameter	285µm
Density	2650 kg/m3
Bulk density	1428 kg/m3
Solid volume fraction	0.54
Air density	1.25 kg/m3

DOI: 10.3384/ecp20170170 Proceedings of SIMS 2019
Västeräs, Sweden, 13-16 August, 2019

3 Computational model

A Computational Particle Fluid Dynamic (CPFD) model have been implemented to simulate the gas-solid flow with heat transfer. The commercial CPFD software Barracuda VR 17 is used for the simulations. The CPFD numerical methodology incorporates the multi-phase-particle-in-cell (MP-PIC) method. The gas phase is solved using Eulerian grid, and the particles are modeled as Lagrangian computational particles. Gas and particle momentum equations are solved in three dimensions. The fluid is described by the Navier-Stokes equation with strong coupling to the discrete particles. The particle momentum follows the MP-PIC description, which is a Lagrangian description of the particle motions described by ordinary differential equations with coupling with the fluid. More details about the computational methods are found in the literature (Andrews *et al.*,1996; Snider *et al.*, 2001). The particles are grouped into parcels that contain a number of adjacent particles with similar properties such as density, size, species, and velocity. The parcels are called computational particles. The computational particle is a numerical approximation similar to the numerical control volume where a spatial region has a single property for the fluid. With these computational particles, large commercial systems containing billions of particles can be simulated using millions of computational particles. This possibility of the CPFD numerical method is used in this work to simulate the ash deposition in a fluidized bed with sand particles as bed material.

3.1 Governing equations

The gas phase mass and momentum conservation are modeled with continuity and time averaged Naiver-Stokes equations:

$$\frac{\partial(\alpha_g \rho_g)}{\partial t} + \nabla.(\alpha_g \rho_g u_g) = 0 \quad (2)$$

$$\frac{\partial(\alpha_g \rho_g u_g)}{\partial t} + \nabla.(\alpha_g \rho_g u_g u_g) = -\nabla P + F + \nabla.(\alpha_g \tau_g) + \alpha_g \rho_g g \quad (3)$$

where, α_g, ρ_g and u_g are gas phase volume fraction, density and velocity respectively. F is total momentum exchange with the particle phase per volume, g is gravitational acceleration, P is the pressure and τ_g is the gas phase stress tensor, which is given by:

$$\tau_g = \mu_g \left[\left(\nabla u_g + \Delta u_g^T \right) - \frac{2}{3} \nabla . u_g I \right] \quad (4)$$

μ_g refers to the shear viscosity that is the sum of the laminar and turbulent components. The large eddy simulation is used for the large-scale turbulence modeling while the subgrid scale turbulence is captured with Smagorinsky model:

$$\mu_{g,t} = C_s \rho_g \Delta^2 \left| \nabla u_g + \Delta u_g^T \right| \quad (5)$$

Where Δ is the subgrid length scale and calculated by equation 5. The default value for the model constant C_s is 0.01.

$$\Delta = (\delta x \delta y \delta z)^{1/3} \quad (6)$$

The interface momentum transfer is calculated through the viscous drag force:

$$F = \iint f \left\{ m_p \left[D_p(u_g - u_p) - \frac{\nabla P}{\rho_p} \right] \right\} dm_p du_p \quad (7)$$

Subscript p refers to the particle phase properties where m and u symbolize the mass and velocity. D_p is the drag function. The particle phase dynamics are derived using particle distribution function (PDF) calculated from the Liouville equation given as:

$$\frac{\partial f}{\partial t} + \nabla(f u_p) + \nabla u_p (f A_p) = 0 \quad (8)$$

where A_p, is the particle acceleration and is expressed by:

$$A_p = \frac{\partial(u_p)}{\partial t} = D_p(u_g - u_p) - \frac{\nabla P}{\rho_p} - \frac{\nabla \tau_p}{\rho_p \alpha_p} + g \quad (9)$$

α_p is particle volume fraction and τ_p is particle stress function that is used in formulating interphase interactions of particles.

$$\alpha_p = \iint f \frac{m_p}{\rho_p} dm_p du_p \quad (10)$$

$$\tau_p = \frac{10 P_s \alpha_p^{\beta}}{max[(\alpha_{cp} - \alpha_p), \varepsilon(1 - \alpha_p)]} \quad (11)$$

P_s is a constant with the units of pressure, α_{cp} is the particle volume fraction at close packing, β is a constant between 2 and 5 where ε is a very small number on the order of 10-7.

3.2 Model parameters and geometry

A cylindrical CAD geometry with a height of 1.4m and diameter 8.4 cm was imported in Barracuda VR. The geometry is divided into 8652 uniform grids. After the grid generation, the base materials, the particle species, the pressure boundary condition, and the flow boundary condition were specified in Barracuda, which are similar to the experimental settings. The grid and boundary conditions are shown in Figure 2. No particle exit was considered during the simulation. The pressure monitoring points were selected 3.5 cm, 13.5 cm, and

DOI: 10.3384/ecp20170170

23.5 cm along the height of the bed as in the experiments.

In Figure 2, the top of the cylinder yellow colored) is a pressure outlet boundary and the bottom of the reactor (red colored) is a velocity inlet boundary. The particles and gas are used similar to the experiments. The simulations were run in a cold bed as well as in hot bed conditions to analyze the flow properties in a real bed with various volume percent of ash deposition.

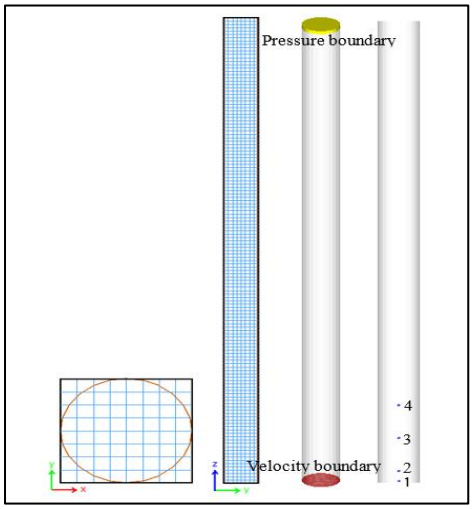

Figure 2. Grid and boundary conditions

The Wen-Yu drag model was used with 60% momentum loss after the particle collision. The initial height of the bed was 21 cm, which gives the bed aspect ratio (ratio of height to diameter) of 2.5. The initial time step was taken as 0.001 s. Initial particle volume fraction was taken as 0.54. The simulations were performed for 120s of simulation time. Simulations were run for several air velocities and with different volume percent of ash mixed with sand particles to analyze the flow properties variation with the ash deposition.

Therefore, only the major elements of the ash composition were taken for the model. The composition and properties of ash particles used in the model are presented in Table 2.

Table 2. Properties biomass ash

SiO2	30% of total ash components
K2O	17%
CaO	53%
Average density	2959 Kg/m3
Molar mass	63.75 g/mol
Particle Size	50µm
Solid volume fraction	0.6
Sphericity	0.7

The minor components of the ash are neglected, and the density and molar mass of the ash are calculated according to the densities and molar masses of the major components.

4 Results and discussion

4.1 Experimental results

A series of the experiments were carried out with different superficial air velocities, and the pressure drop along the height of the bed was calculated using the experimental data. The plot of the pressure drop as a function of superficial velocities (Figure 3) shows that the minimum fluidization velocity for sand particles is 0.075 m/s and the pressure drop at the minimum fluidization velocity is 13084 Pa/m.

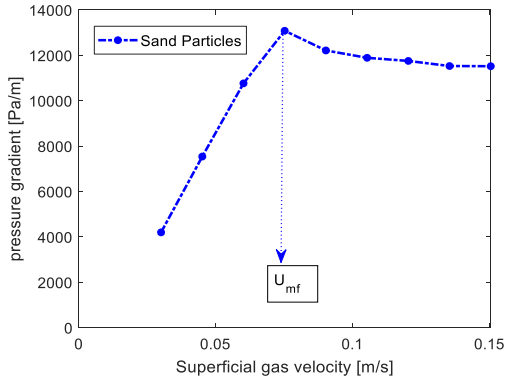

Figure 3. Pressure drop vs. superficial air velocity

It was difficult to run an experiment with a mixture of sand particles and ash because the ash particles are very small and fine particles, which could leave the reactor. It was actually the main reason for developing the CPFD model and simulating the flow of sand particles with ash.

4.2 Computational results

Simulations were run for the bed with sand particles, which is exactly similar to the experimental condition. The simulation results are compared against the experimental. Figure 4 shows a comparison of experimental and computational pressure drops along the bed and the minimum fluidization velocity of the bed.

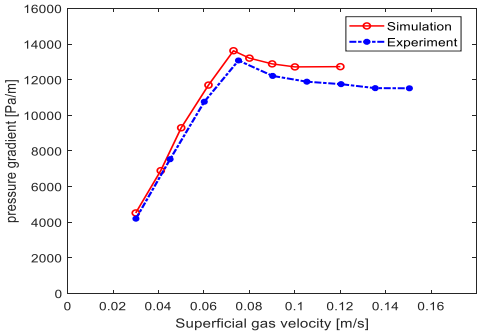

Figure 4. Comparison of pressure drop and minimum fluidization velocities

DOI: 10.3384/ecp20170170 Proceedings of SIMS 2019
Västeräs, Sweden, 13-16 August, 2019

The figure shows good agreements between the experimental and computational results. The pressure drop and minimum fluidization velocities are almost similar in both cases. The aim of this comparison was to validate a CPFD model for its further use for simulation of a bed with various volume percent of ash deposition. Therefore, a series of the simulation were run to simulate the bed of sand particles with 2% and 4 vol% of ash particles by volume. The simulations were run for cold conditions at room temperature.

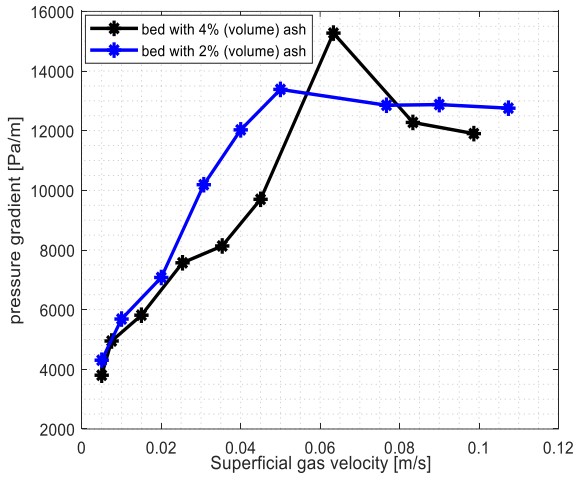

Figure 5. Minimum fluidization velocities for the mixture of ash with sand.

The pressure drop is increased with increasing ash volume percentage. The minimum fluidization velocities increased with increasing volume percent of ash, as shown in Figure 5. Minimum fluidization velocity for beds of small particles is strongly depended on bed void fraction [13], which can be seen from the equation:

$$u_{mf} = \frac{d_p^2(\rho_p - \rho_g)g}{150\mu} \cdot \frac{\varepsilon_{mf}^3 \phi_s^2}{1 - \varepsilon_{mf}} \qquad (12)$$

where, d_p is particle diameter, ρ_p and ρ_g are particle and gas densities, ε_{mf} is bed void fraction, ϕ_s is sphericity and μ is gas viscosity. Presence of ash particles which have small particle size compared to the sand having larger particles size makes ash particles to fill the void between the sand particles reducing the void fraction in the bed. This is the reason for the reduction of minimum fluidization velocity. This means a limited ash deposition in the bed does not have negative impact in flow properties (particularly in fluidization velocity) before the sand particles are segregated in the bed.

Simulations were also run at high temperature. Figure 6 shows the simulation results at the temperature of 800ºC. The bed was mixed with sand particles and 2%, 4% and 6% by volume of ash particles. The results show that an increase in the temperature decreases the minimum fluidization velocities. When the temperature of fluidizing air is increased from 20ºC to 800ºC, the viscosity of air increases from $1.825 \cdot 10^{-5}\text{Pa} \cdot \text{s}$ to $4.362 \cdot 10^{-5}\text{Pa} \cdot \text{s}$. The increase in viscosity is the reason for the decrease in minimum fluidization velocity (See equation 12). The results show that the ash deposition up to 6% by volume has no negative effect on the flow behavior in the reactor. However, the pressure drop in the bed increases with increasing ash deposition. The deposition will have negative effect only when the temperature of any spot of the bed reaches the ash melting temperature. In order to avoid this, it is important to enhance the mixing of particles in bed and avoid segregation.

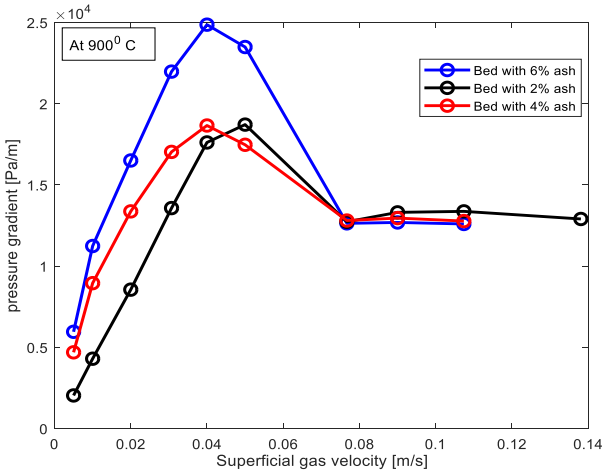

Figure 6. Minimum fluidization velocity at high temperature conditions.

The CPFD model allows tracking the particles in the bed separately in the form of different particle species. The distribution of ash and sand particles in the bed are shown in Figure 7. The figure shows the comparison of species distribution in the bed at the minimum fluidization velocity and the air velocity of 0.21 m/s for the bed with 2, 4 and 6 vol% ash respectively from left to right.

The figure shows that a part of the ash particles have segregated and moved to the top of the bed already at the minimum fluidization condition and the segregation becomes more distinct at the higher air velocities.

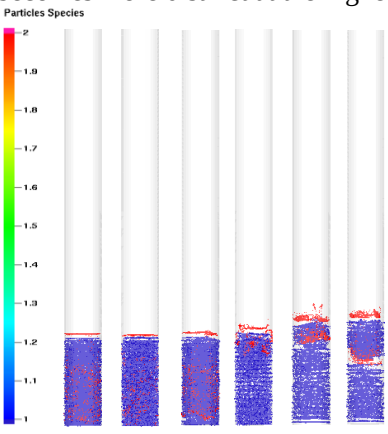

Figure 7. Sand and ash particle species distribution in the bed

Deposited ash, after segregation can effect negatively on the mixing and heat transfer in the bed. This is more

DOI: 10.3384/ecp20170170 Proceedings of SIMS 2019
Västeräs, Sweden, 13-16 August, 2019

probable at the top of the bed where only ash particles are present. This can create hot spots in the upper part of the bed.

The bubble behavior in the bed at the air velocity of 0.21 m/s are shown in Figure 8. The figure shows that there is no significant effect of the ash deposition on the bubble properties in the middle and the lower part of the bed. The reason can be that the ash particles are segregated and move to the top of the bed and only the sand particles, part of biomass and the air are involved in the bed which does not hinder bubble formation and growth along with the height of the bed.

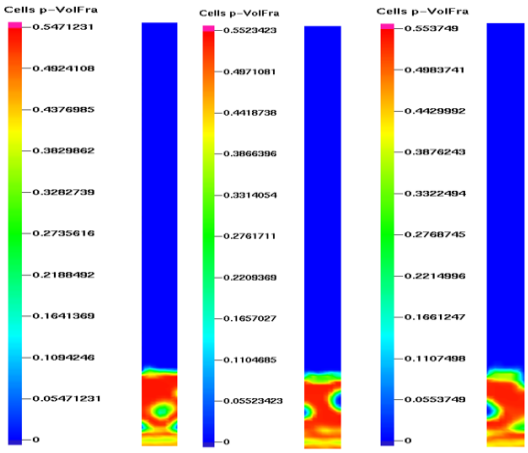

Figure 8. Bubble in the bed at an air velocity of 0.21m/s for 2%, 4% and 6% of ash from left to right

5 Conclusion

A CPFD model is developed for the study of 3D flow in a bubbling fluidized bed biomass gasification reactor. The model is validated against the experimental measurements in a cold flow model of the reactor. The results give good agreement between experiments and model predictions. The valid model is used to study the effect of ash deposition on the flow behavior of the reactor in cold and hot bed conditions.

The minimum fluidization velocities are decreased with increasing volume percent of ash in the bed under cold bed conditions. However, the pressure drop is increased. The minimum fluidization velocity is further reduced at a high temperature.

The ash particles start to segregate from the minimum fluidization condition moving towards the top of the bed, and the segregation is increasing with increasing air velocity. However, the bubble behavior in the bed remains the same with increasing ash volume percent in the bed.

References

M.J. Andrews and P.J. O'Rourke. The multiphase particle-incell (MP-PIC) method for dense particle flow. *International Journal of Multiphase Flow*, 22:379-402, 1996. https://doi.org/10.1016/0301-9322(95)00072-0

M. Bartels, W. Lin, J. Nijenhuis, F. Kapteijn, and J. R. Van Ommen. Agglomeration in fluidized beds at high temperatures: Mechanisms, detection and prevention, *Progress in Energy and Combustion Science*, 34(5):633-666, 2008. https://doi.org/10.1016/j.pecs.2008.04.002

G. Brown, A. Hawkes, A. Bauen, and M. Leach. *1. Biomass Applications, Centre for Energy Policy and Technology, Imperial College*, 2005.

K. Daizo and O. Levenspiel. *Fluidization Engineering. Butterworth-Heinemann, USA, 1991*.

N. C. Furuvik, R. Jaiswal, and B. M. Moldestad. Flow behavior in an agglomerated fluidized bed gasifier," *International Journal of Energy and Environment*, 10(2): 55-64, 2019.

C. Institute. G (, ACN: 136 814 465.ABN: 92 136 814 465). Combustion of different types of biomass [Online]. Available: https://hub.globalccsinstitute.com/publications/biomass-ccs-study combustion-different-types-biomass.

A. Montes. *Factors Affecting Bed Agglomeration in Bubbling Fluidized Bed Biomass Boilers*, Masters thesis, School of graduate and post graduate studies, The university of western Ontario, 2014.

M. Niu, Q. Dong, Y. Huang, B. Jin, H. Wang, and H. Gu. Characterization of ash melting behaviour at high temperatures under conditions simulating combustible solid waste gasification, *Waste Management & Research*, 36(5): 415-425, 2018. https://doi.org/10.1177/0734242X18763064

W. B. Pietsch. Agglomeration processes: phenomena, technologies, equipment. *John Wiley & Sons*, 2008.

D.M. Snider. An Incompressible Three-Dimensional Multiphase Particle-in-Cell Model for Dense Particle Flows. *Journal of Computational Physics*, 2001. 170(2):523-549. https://doi.org/10.1006/jcph.2001.6747

G. Tardos and R. Pfeffer. Chemical reaction induced agglomeration and defluidization of fluidized beds, *Powder Technology*, 85(1):29-35, 1995. https://doi.org/10.1016/0032-5910(95)03002-Q

H. S. Visser, C. van Lith, and J. Kiel. Biomass ash-bed material interactions are leading to agglomeration in FBC, *Journal of Energy Resources Technology*, vol. 130, no. 1, p. 011801, 2008. doi.10.1016/j.apenergy.2016.05.063

H. Vuthaluru, T. M. Linjewile, D.-k. Zhang, and A. Manzoori. Investigations into the control of agglomeration and defluidisation during fluidised-bed combustion of low-rank coals, *Fuel*, vol. 78, no. 4, pp. 419-425, 1999. https://doi.org/10.1016/S0016-2361(98)00165-3

DOI: 10.3384/ecp20170170

Study of agglomeration in fluidized bed gasification of biomass using CPFD simulations

Nora C I S Furuvik Rajan Jaiswal Rajan K Thapa Britt M E Moldestad

Department of Process, Energy and Environmental Technology, University of South-Eastern Norway, Norway,
{nora.c.i.furuvik rajan.k.thapa, britt.moldestad}@usn.no
Rajanjaiswal357@outlook.com

Abstract

Fluidized beds have been widely applied for the gasification of biomass. However, at high temperatures ash melting and subsequently bed agglomeration may occur. When biomass is used for thermal conversion processes, inorganic alkali components present in the biomass fuels can be responsible for major problems. Understanding the ash melting and agglomeration in various gasification temperatures is crucial to optimize the design and operation conditions of a fluidized bed gasifier. This study focuses on the ash melting and the agglomeration process in a bubbling fluidized bed biomass gasification reactor. Using standard techniques, ash-melting analyses were performed to determine the initial agglomeration temperature in laboratory prepared ash samples from woodchips from Austria. Computational Particle Fluid Dynamic (CPFD) simulations were carried out using the commercial CPFD software package Barracuda Virtual Reactor (VR). The results show that the fluid dynamics gives important indications of unwanted agglomeration processes in a biomass gasification in a bubbling fluidized bed.

Keywords: bubbling fluidized bed, biomass gasification, agglomeration, CPFD simulations

1 Introduction

Climate changes are perhaps the biggest and most challenging environmental problems the world faces today. Greenhouse gas emissions from burning of fossil fuels for heat and power generation are major contributors to the earth's global warming. Over the last decades, it has been a growing attention to the use of renewable energy as an effective tool to fight the climate changes. On global basis, renewable energy were estimated to account for 14.1% of the total 573 EJ of primary energy supply in 2014, of which the largest energy contributor was biomass (10.3%) (World Bioenergy Association, 2017).

Fluidized bed gasification (FBG) is an important route for conversion of biomass into useful gaseous products, including syngas that can be further utilized into biofuels. Fluidized bed gasifiers offer distinct advantages over other conversion technologies, especially regarding to their uniform temperatures and excellent heat transfers. (Basu, 2013) However, because of the special ash-forming constituents of biomass fuels, biomass ash has shown to be particularly problematic in high temperature FBG processes (Wang et al., 2008). Generally, these problems are associated with the ash melting and following agglomeration of bed material (Van der Drift, 1999). Bed agglomeration is a result of interaction between the bed material and molten biomass ash with high content of alkali metals. When biomass is used for thermal conversion, alkali species from the fuel can react readily with silica (Si) from the bed material. As a consequence, the particles become coated with an adhesive layer that glue the particles together forming larger agglomerates. (Bartles et al., 2008) Bed agglomeration leads to poor fluidization conditions, and in the most severe cases it causes defluidization and subsequently total shutdown of the gasification process. Fundamental understanding of the ash behavior in thermal conversion of biomass, is necessary to improve the operational conditions in FBG (Khadilkar, 2018).

The objective of this work is to (a) study the melting behavior of woody biomass ash in correlation to standard ash melting tests (b) use a previous validated CPFD model to simulate agglomeration in a bubbling fluidized bed gasifier.

The ash-melting analyses are performed using a Leco Ash Fusion Determinator (AF700). In this test, the temperature at which the ash starts to melt is determined, giving a good indication of the temperature at which agglomerates can be formed. Laboratory prepared ash from woodchips from Austria are used for the ash melting analyses. The CPFD model is developed to get a better understanding of the problem with agglomeration phenomenon in a bubbling fluidized bed biomass gasification reactor. The connection between the ash melting behavior, operating temperatures and bed agglomeration in a FBG is investigated. The simulations are carried out using the commercial CPFD software package Barracuda VR.

2 Theory

2.1 Bed agglomeration

In the literature, there is good agreement that alkali metals are the main components causing problems with bed agglomeration in FBG of biomass. (Bartles et al., 2008) The agglomeration process happens in two ways, either as melt-induced agglomeration or as coating-induced agglomeration. The melt-induced mechanism is direct adhesion of the bed particles because of alkali compounds from the molten ash acting as a glue that forms hard bridges between the particles. The coating-induced mechanism happens due to chemical reactions, between the bed material and the molten ash components, causing formation of a sticky uniform coating layer on the surface of the bed particles. (Visser et al., 2008) Bed agglomeration is in most cases a result of the inorganic alkali ash components combining with Si, either from the bed material or from the ash itself, to form low-melting silicates (eutectics) that coat the bed particles. These eutectics are characterized by a lower melting point than the individual components. If the alkali concentrations are too high, the coating melts and adheres the particles together. As a consequence of repeated collisions between these sticky ash-coated particles, the particles eventually grow towards larger agglomerates. (Badhoilya, 2018) The phenomenon is shown in Figure 1, an illustration based on (Moradian).

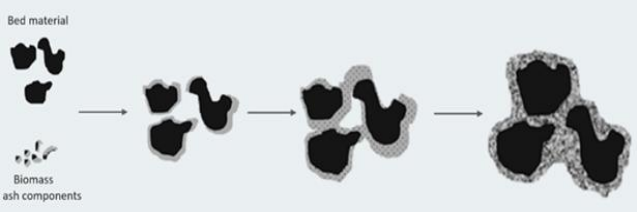

Figure 1. Agglomeration process.

Ash melting and following bed agglomeration is a key concern in fluidized bed biomass gasification reactors. The problems are mainly coupled to the high temperature chemistry of ash, i.e. its melting at different gasification temperatures. Proper fluidization of the particles needs to be maintained in order to stabilize the operational conditions of the fluidized bed (Badholiya 2018). As the agglomerated particles are of greatly irregular shape, size and structure, they will interfere with the fluid dynamics in the bed. In Figure 2 agglomerates from bubbling fluidized bed gasification of biomass is pictured.

In FBG the particle movement is one of the most important factors due to the corresponding transfer of energy. Under normal conditions, this energy transfer is so effective that the temperature difference across the cross section of the bed is kept approximately equal to zero. When agglomerates are present in the bed, the bed mixing becomes more ineffective due to obstructed particle movement. If this agglomeration process comes out of control, it can lead to severe agglomerate formation and subsequently shutdown of the gasification process. (Bartles et al., 2008, Badhoilya 2018) The obstruction in the particle movement can result in local temperature deviations that in turn creates de-fluidized volumes in the bed. De-fluidization is described as a total collapse of the fluidized bed leading to rapidly decreasing pressure drop and substantial temperature changes. (Van der Drift, 1999)

Figure 2. Agglomerates from silica sand particles.

2.2 Ash melting

Biomass is greatly varying in its physical properties and chemical composition, and the ash melting behavior is greatly affected by the ash composition. The biomass ash composition is in turn essential when it comes to the efficiency of a FBG process. (Badholiya, 2016) Biomass fuels with high ash content and low ash melting temperatures have limited possibilities for successful applications due to problems with ash melting, and agglomeration that occur under certain conditions. (Dragutinovic 2017) In general, woody biomass has very low ash content, typically below 1 %, of which approximately 40 % calcium (Ca), 15 % potassium (K) and 20 % Si. (Vassilev et al., 2017)

Previous studies have indicated that the bed agglomeration process is heavily dependent on the chemical characteristics and melting behaviors of the coating on the surface of the bed particles (Vassilev et al., 2017). Typically, elements such as Ca and magnesium (Mg) increase the ash melting temperature, while Si, K and sodium (Na) decreases the ash melting temperature. The combination of high Si and high alkali content is especially problematic for fluidized bed biomass gasification because of the formation of silicates with low melting temperature. (BISYPLAN, 2012)

Apart from the chemical reactions that happens when ash melts and interacts with the fluid dynamics in the bed, the operating temperature is the most important factor determining the time-scale of the agglomeration process in fluidized beds. (Van der Drift, 1999) Good knowledge about the ash melting temperatures is

therefore of great relevance to avoid operational problems during biomass gasification in fluidized beds. In general terms, ash is used to describe the inorganic matter in fuels. In biomass fuels, the content of the critical inorganic alkali metals tends to vary within the same type of biomass, as well as between the different biomass species. (Badholiya, 2016) This makes it difficult to determine the ash melting behavior on the basis of the melting temperature of the individual components. Another challenge when it comes to determination of the melting behavior for biomass ash, is that it under certain conditions can react to form eutectics with lower melting point than the individual components. (Dragutinovic, 2017) Performing ash melting analyses can be a useful way to estimate the tendency of bed agglomeration. The method for analyzing the ash melting behavior involves heating the ash in a controlled manner and then determining the temperatures at which the ash begins to deform, soften and completely fuse. This method gives a realistic prediction of the initial agglomeration temperature, i.e. the temperature where the first molten phases that are able to glue particles together are visible. (BISYPLAN, 2012)

3 Material and methods

3.1 Ash melting analysis

The biomass fuel was ashed at 600°C using a muffle furnace, and the ash was subsequently analyzed using a Leco Ash Fusion Determinator (AF700). To prepare the biomass ash sample for ash-melting analysis, the ash was milled and wetted with a few drops of Dextrin solution (Part no: 502-010) before it was pressed into a cylindrical test piece (Figure 3) with specified dimensions. The test piece was mounted on a ceramic tray and placed in the high-temperature furnace.

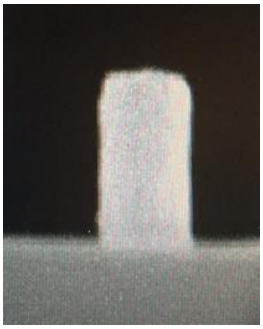

Figure 3. Cylindrical test piece ready for ash melting analysis.

For the ash-melting analyses, the Approved Standard Test Method (ASTM) D1857 was used. This test involves heating of the ash samples at a defined heating rate in reducing conditions. Table 1 shows the ASTM method specifications.

Table 1. Ash melting analyses specifications.

Step	*1*	*2*	*Unit*
Start temperature	400	700	°C
End temperature	700	1500	°C
Ramp rate	20	10	°C /min
Ramp time	00:15	01:20	H:min
Hold time	00:00	00:00	H:min
Total time	00:15	01:20	H:min

Four characteristic temperatures were determined for the ash sample: (ST) Shrinking starting Temperature, (DT) Deformation Temperature, (HT) Hemispherical temperature and (FT) Flow Temperature. Each of these temperatures correspond to a specific shape of the cylindrical ash test piece, and are described in Table 2 (BISYPLAN, 2012).

Table 2. Characteristic temperatures in ash melting analyses.

Characteristic temperature	*Description*
ST	First sign of shrinking of the cylinder
DT	First sign of rounding due to melting of the corners of the cylinder
HT	The cylindrical test piece forms a hemisphere
FT	The cylindrical test piece has effectively melted and the ash are spread out over the supporting tile in a layer

3.2 CPFD model description

The CPFD software package Barracuda VR 17.1.0 was used to simulate the agglomeration process in a biomass bubbling FBG. Barracuda VR uses the Multiphase Particle-in-Cell (MP-PIC) based Eulerian-Lagrangian approach, where the transport equations are solved for the continuous fluid phase and each of the discrete particles are tracked through the calculated fluid field. The fluid-particle interaction is considered as source terms in the transfer of mass, momentum and energy between the two systems. CPFD simulations are hybrid numerical methods, where the Eulerian approach is used for solving the fluid phase and the Lagrangian computational particle approach is used for solving the particle phase (Thapa and Halvorsen, 2013). Chladek et al. (2018) and Jayarathna et al. (2017) have described the transport equations in detail.

The Barracuda software package includes several drag models. For the present simulations, the Wen-Yu drag model was used. The CPFD model are previously developed and validated against experiments performed in a lab-scale cold flow model by Furuvik et al (2018). The model was scaled up to a full-scale bubbling FBG

reactor using Glicksman's scaling rules that are based on a set of dimensionless parameters. The scaling rules are explained in detail by Thapa et al (2013).

A three-dimensional Cartesian coordinate system was used to describe the cylindrical column with height of 250 cm and 42 cm in diameter. In the present study, the static bed height was 105 cm. The mesh size was 0.0466 m x 0.0466 m x 0.0466 m and the number of control volumes was 4 536. The simulations were carried out at three different temperature conditions: (I) 850 °C, (II) 900 °C and (III) 1000 °C, and for each temperature, two different agglomeration processes were simulated. The fluidizing gas was air at atmospheric pressure. Pressure transducers are placed with an interval of 10 cm along the height of the bed, and the first monitor point is 10 cm above the distributor. The simulations were run for 50 seconds with a time step of 0.001 s. The simulation conditions are summarized in Table 3.

Table 3. CPFD simulation conditions.

Operating parameter	*Value*
Number of grid cells	4 536
Static bed height	105 cm
Fluidizing agent	Air
Type of flow	Isothermal@ (I) 850°C (II) 900°C (III) 1000°C
Superficial air velocity	0.02; 0.005; 0.15 m/s
Simulation time for each flowrate	50 s
Drag model	Wen-Yu

Quarts sand with a solid density of 2 650 kg/m^3 was used as bed material. The particle size of the sand were 300 µm. The agglomerates ranged from 1.0 cm to 4.0 cm in diameter, with a particle density of 1 506 kg/m^3. (Furuvik et al., 2018). The maximum close pack volume fraction was set to 0.54. The maximum momentum from the redirection of particles collision was assumed to be 40 %, the normal-to-wall and tangential-to-wall momentum retention were 0.3 and 0.99 respectively. The particle properties are listed in Table 4.

Table 4. Particle properties.

Property	*Bed material*	*Agglomerates*
Diameter	300 µm	1.0 - 4.0 cm
Density	2650	1506
Sphericity	0.86	0.6
Close pack volume fraction	0.54	N/A

For the present simulations, it was assumed that the agglomeration process started at the DT measured by the ash melting analyses, and that the size and amount of agglomerates accumulate once the process has been initiated. In total, six different simulation cases were performed. Specific details on the agglomeration processes in the different simulation cases are presented in Table 5.

Table 5. CPFC simulation specification

	850°C	*900°C*	*1000°C*
Amount of agglomerates	0 15%	20% 20%	20% 30%
Size of agglomerates	- 1-2 cm	2-3 cm 3-4 cm	3-4 cm 3-4 cm

4 Results and discussion

4.1 Ash melting analysis

Woodchips from Austria were used for the laboratory prepared ash samples. The ash-processing temperature was 600°C. In Figure 4, the form of the cylindrical test piece is pictured for each of the defined characteristic temperatures.

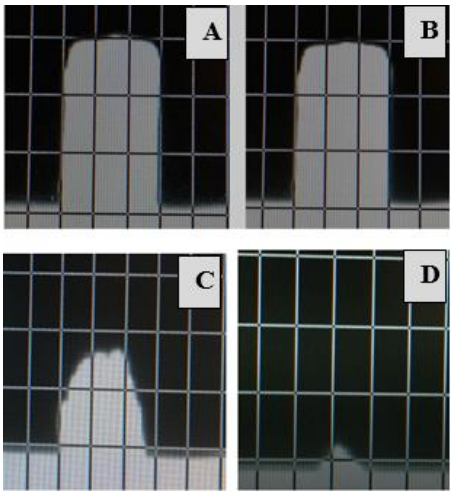

Figure 4. Results from ash melting analyses showing the test piece at (A) ST, (B) DT, (C) HT and (D) FT.

In order to obtain reasonable results, three separate measurements were carried out. The four characteristic temperatures were determined for all the three measurements. The results from the ash melting analyses are listed in Table 6.

Table 6. Results from ash melting analyses.

	ST	*DT*	*HT*	*FT*
1	861°C	870°C	1466°C	1492°C
2	867°C	874°C	1472°C	1492°C
3	859°C	865°C	1463°C	1490°C

For all the three measurements, the ash started to show sign of shrinking around 860°C and deformation and rounding were observed at approximately 870°C, these are the temperatures that correspond to ST and DT respectively. For biomass fuels, the DT is considered as a valid indication for the tendency of the ash to cause

problems during thermal conversion processes. (BISYPLAN, 2012) In the present study, the received data for the DT are further related to the initial agglomeration temperatures.

4.2 CPFD simulations

The CPFD simulations were carried out at three different temperatures, and with varying combination of size and amount of agglomerates in the bed. The chosen simulation temperatures were based on the measured DT from the ash melting analyses, assuming the initial ash-melting temperature will start the agglomeration process. It was also assumed that the process continues once it has been initiated. The CPFD simulation results are presented as plots of the pressure drop in the bed as a function of the superficial air velocity.

Figure 5 represents the results of the simulations at 850°C. The red line represents fluidization of the bed material, and is used as a reference bed. The purple line represents 15 % agglomeration in the bed. From the figure it is seen that there is a clear correlation between the fluid dynamics and the bed agglomeration processes. The difference between the pressures drops in the two cases increases with increasing superficial velocity until the bed is fluidized, at about 0.06 m/s. The pressure drop at minimum fluidization is approximately 14 000 Pa/m in the reference bed, while it is decreased to approximately 12 000 Pa/m in the agglomerated bed.

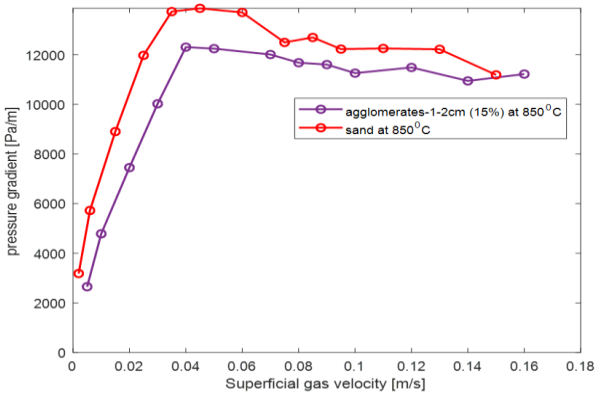

Figure 5. CPFD simulations at 850°C, (I) silica sand, no agglomeration (II) agglomerate size 1-2 cm and 15% agglomeration.

Figure 6 shows the results from the two simulation cases at 900°C. In both of the cases 20 % agglomerates are present in the bed. The blue line represents the case with agglomerates of 2-3 cm, while the black line represents agglomerates of 3-4 cm. The deviation between the two curves indicates that the fluidization is greatly affected by the size of the agglomerates. When the maximum size of the agglomerates is increased from 3 cm to 4 cm, the minimum fluidization velocity is increased from about 0.05 m/s to 0.08 m/s. The minimum fluidization velocity is a key parameter in fluidized beds, and works as a rough indication of the quality of the fluidization. Minimum fluidization is the point at which the bed conditions are at the boundary between fixed and fluidized, and the corresponding superficial velocity is referred to as the minimum fluidization velocity. The superficial velocity should therefore always be kept well above the theoretical minimum fluidization velocity to prevent de-fluidization of the bed

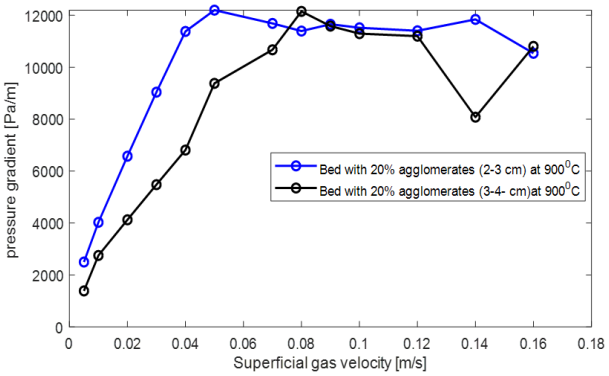

Figure 6. CPFD simulations at 900°C, (I) agglomerate size 2-3 cm and 20% agglomeration (II) agglomerate size 3-4 cm and 20% agglomeration.

Figure 7 shows the results from the simulations at 1000°C. The size of the agglomerates is 3-4 cm in both the simulation cases. The green line represents the case with 20 % agglomeration and the yellow line is simulation with 30 % agglomeration. The simulation results displayed in Figure 5 indicates that agglomeration causes decreased pressure drop in the fluidized bed. From Figure 7, it is seen that as the agglomerates grow larger it results in heavy instabilities in the bed. The pressure drop across the bed start to fluctuate as soon as the bed achieves fluidized state. The fluctuation in the pressure drops becomes worse as the amount of agglomerates increases. This improper bed control indicates de-fluidization. Apparently around 20% agglomeration seems to be enough to initiate de-fluidization of the bed.

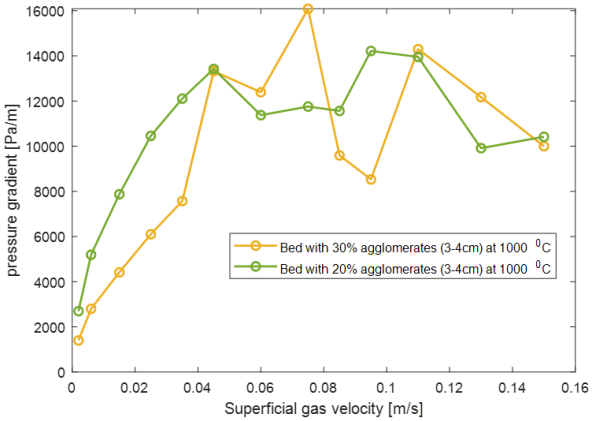

Figure 7. CPFD simulations at 1000°C, (I) agglomerate size 3-4 cm and 20% agglomeration (II) agglomerate size 3-4 cm and 30% agglomeration.

5 Conclusion

The objective of this work was to use a previous developed and validated CPFD model to study the ash melting and agglomeration in biomass gasification in a bubbling fluidized bed. The study included ash melting analyses, and CPFD simulations using the commercial software Barracuda VR. Ash related problems are the main obstacle in fluidized bed gasification of biomass, and are generally associated with high content of alkali components in the fuels. These elements might form low-melting temperature compounds that will coat the surface of the bed particles. If the coating have high enough fraction of molten ash, it will cause bed agglomeration.

The measurement of ash melting temperatures provides a direct correlation between laboratory data and the temperature at which the ash might have the tendency to melt. The simulations shows that the agglomeration process will affect the fluid dynamics in a bubbling fluidized bed gasifier. Bed agglomeration is often seen as a consequence of improper bed control. The more and larger agglomerates, the more severe are the problems. The point where agglomeration starts to cause problems is characterized by a sudden drop or instability in pressure. The simulations shows that around 20% agglomerates seems to be enough to initiate de-fluidization of the fluidized bed.

Acknowledgements

This study is funded by The Research Council of Norway, Program for Energy Research (ENERGIX), Project 280892 FLASH – Predicting of FLow behavior of ASH mixtures for production of transport biofuels in the circular economy.

References

A.B. Khadilkar, P.L. Rozelle, and S.V. Pisupati. Investigation of fluidized bed agglomerate growth process using simulations and SEM-EDX characterization of laboratory-generated agglomerates. *Chemical Engineering Science*, 184: 172-185, 2018.

A. van der Drift. Conversion of Biomass, prediction and solution methods for ash agglomeration and related problems. Final Report, ECN-C-99.090, 1999.

BISYPLAN. Web-based handbook, 2012. Available from: *http://bisyplan.bioenarea.eu/ash_appendix.html*. 02.06.2019.

C.K. Jayarathna, B.M.E. Moldestad, and L.A. Tokheim. Validation of results from Barracuda® CFD modelling to predict minimum fluidization velocity and pressure drop of Geldart A particles. *Proceedings for the 58th SIMS conference*, 2017.

J. Chladek, C.K. Jayarathna, B.M.E. Moldestad, and L.A. Tokheim. Fluidized bed classification of particles of different sixe and density. *Chemical Engineering Science*, 177: 155–162, 2018.

L. Wang, C.L. Weller, D.D., and M.A. Hanna. Contemporary issues in thermal gasification of biomass and its application to electricity and fuel production. *Biomass and Bioenergy*, 32: 573-581, 2008.

M. Bartles, W. Lin, J. Nijenhuis, F. Kapteijn and R. Ommen. Agglomeration in fluidized beds at high temperatures: Mechanisms, detection and prevention. *Progress in Energy and Combustion Science*, 34: 633-666, 2008.

N. Dragutinovic, B. Nakomcic-Smaragdakis, and Z. Cepic. Comparison of ash melting behavior of crop residues and woody biofuels with recommended measures. *The 8th PSU-UNS International Conference on Engineering and Technology* (ICET-2017), Novi Saf, Serbia, June 8-10, 2017.

N.C.I.S. Furuvik, R. Jaiswal, and B.M.E. Moldestad. Flow behavior in an agglomerated fluidized bed gasifier. *International Journal for Energy and Environment*, 10(2): 55-64, 2019.

N.C.I.S. Furuvik, R. Jaiswal, R.K. Thapa, and B.M.E. Moldestad. CPFD model for prediction of flow behavior in an agglomerated fluidized bed gasifier. *International Journal for Energy Production and Management*, 4(2):105-114, 2019.

P. Basu. Biomass Gasificaion, Prolysis and Torrefaction, Second Edition. *Academic Press Inc.*, UK, 2013.

R.K. Thapa and B.M. Halvorsen. Study of Flow Behavior in Bubbling Fluidized Bed Biomass Gasification Reactor using CFD simulation. T*he 14th International Conference on Fluidizatio*n - *From Fundamentals to Products*, Eds, ECI Symposium Series, 2013.

R.K. Thapa, C. Pfeifer, and B.M. Halvorsen. Scaling of biomass gasification reactor using CFD simulations. In *International conference on Polygeneration strategies (IPCS)*, Vienna, Austria, June 3-5, 2013.

S.K. Badholiya and A. Kothari. A review on ash agglomeration phenomenon in fluidized bed combustion boiler. *International Journal of Scientific Research Engineering & Technology* (IJSRET), 5(11): 533-541, 2016

S.K Badholiya, S.K. Pradhan and A. Kothari. Investigations on ash agglomeration in CFBC boiler using computational fluid dynamics. *International Journal of Mechanical Engineering and Technology* (IJMET), 9(7): 1464-1476, 2018.

S.V. Vassilev, C.G. Vassilev, Y. Song, W. Li and J. Feng. Ash contents and ash-forming elements of biomass and their significance for solid biofuel combustion. *Fuel*, 208: 377-409, 2017.

S. Visser, S. van Lith and J. Kiel J. Biomass Ash – Bed Material Interactions Leading to Agglomeration in FBC. *Journal of Energy Resources Technology*, 2008.

World Bioenergy Association. WBA Global Bioenergy Statistics, 2017.

Analyzing the Effects of Geometrical and Particle Size Uncertainty in Circulating Fluidized Beds using CPFD Simulation

Janitha C. Bandara[1] Britt M.E. Moldestad[1] Marianne S. Eikeland[1]

[1]Department of Process, Energy and Environmental Technology, University of South-eastern Norway, Norway

{janitha.bandara, britt.moldestad, Marianne.Eikeland}@usn.no

Abstract

Computational fluid dynamic modeling and simulation is becoming a useful tool in the detailed analysis of multiphase flow systems. The level of uncertainty is different depending on selected modeling concept and numerical schemes. Physical uncertainties originated from geometrical dimensions and particle properties are important aspects. In this work, CPFD method was used to analyze the effect of dimensional uncertainty of loopseal pipe diameter and particle size distribution in a circulating fluidized bed. Five different pipe diameters were studied and 20% growth in particle circulation rate was observed as the diameter reduced from 30mm to 26mm. The effect of small changes in the particle size distribution was negligible and the particle circulation rate decreased by 32% with monodisperse particles of mean size.

Keywords: CPFD simulation, uncertainty, circulating fluidized bed, particle circulation rate

1 Introduction

Computational fluid dynamic (CFD) modeling and simulation is extensively used in designing and optimizing of reactive and non-reactive systems. The flow predictions for single phase systems with CFD is very much precise and however, multiphase systems are still encountering number of theoretical and numerical challenges, such as wide range of spatio-temporal scales (length scales between single particles, particle clusters, computational grid and geometry), collision, shear and interact of particles, mass and momentum exchange between phases (Pannala et al., 2011).

Different techniques have been developed to model the multiphase systems. Direct numerical simulation (DNS) requires the least modeling effort. However, the computational time is high as it resolves the complete flow field around each particle of the system and the particle movement is modeled with Newton's equation of motion (Bale et al. 2019; Tang et al. 2016). Lattice-Boltzmann method (LBM) uses less computational power as the flow field around the particle is approximated by lattice-Boltzmann equation (Qi , Kuang, and Yu 2019). The simulation time can further be reduced by discrete element method (DEM) which averages the fluid flow in the scale of computational grid. The particle collisions are modeled using the soft-sphere or hard-sphere approach. Even with increasing computer power, DEM simulations are predicted to be not viable in the coming decade for commercial scale reactors. The contact detection of particles and calculating geometric areas of contact consume more than 80% of the computational time in DEM. The Eulerian-Eulerian modeling which is also identified as the two-fluid (TFM) or multi-fluid modeling has been the main interest over decades due to its capacity of modeling large-scale systems. TFM requires high modeling effort as the particle phase is also considered as a fluid and the properties are derived using the kinetic theory of granular flow (KTGF). Difficulties and complexities of including the particle size distribution, loss of discrete nature of the particles, numerical (false) diffusion are the major disadvantages related to TFM. The computer efficiency of the DEM can be improved by using probabilistic strategy for the particle contact modelling such as the multiphase particle in cell (MP PIC) method where the collisional forces are derived as a stress gradient in the Eulerian grid (Ma & Zhao, 2018; Moliner et al., 2018; Pannala et al., 2011). The model complexity increases progressively from DNS to TFM and simultaneously, the uncertainty also increases due to excess use of empirical correlations, assumptions, approximations and averaging.

The sensitivity, uncertainty and errors are three aspects of the CFD predictions. The sensitivity is primarily involved with the computational grid and convergence test should be performed in first hand for the CFD simulations. The time step and number of computational particles (MP PIC method) are other sensitivity tests. Sensitivity of different coefficients, models and model constants used have equal importance, which can also be addressed as uncertainties (Ostermeier et al., 2019). The uncertainties have different dimensions related to (Mathelin et al., 2005; Walters & Huyse, 2002):

- Assumptions in the main model (i.e. incompressible, inviscid, linearization, neglecting temperature dependences of coefficients)

- Deficiency of information related to phenomenological or auxiliary models (i.e. turbulence model, reaction kinetics)
- Discretization and computational errors (i.e. flux approximation scheme, round off, iterative)
- Describing the physical reality (the geometry, initial and boundary conditions, particle properties such as size distribution, density and shape)

The fundamental structure of the conservation equation are fixed in many CFD codes. The suitability of different numerical schemes and optimization of involved auxiliary models and model parameters are possible. However, uncertainties originated from physical reality should be minimized in first hand. Some experimental data suffers from lack of supporting information (i.e. reporting of mean size of particles over size distribution, the pipe diameters without mentioning internal or external etc.).

Circulating fluidized bed (CFB) technology is a widely applied industrial process. Robust control over the particles, high heat and mass transfer rates are the basic advantages of the CFB technology. The simplest arrangement of a CFB system is illustrated in **Figure 1** and certain CFB systems can be consisted with two or multiple reactors. A typical system contains a bedding material that circulates in a closed loop without being removed out from the system. Riser operates in the fast fluidization regime and the particles are carried away with high gas flowrates, which are separated by a cyclone and fed back to the riser via a flow control valve. Mechanical valves suffer from wearing in high temperature applications where non-mechanical devices such as loopseal are highly preferred in the industry. Rate of particle circulation is one of the important parameters in CFB. The dimensions and aeration of the loopseal should be designed and optimized to fit the targeted flow and avoid gas bypass from the riser.

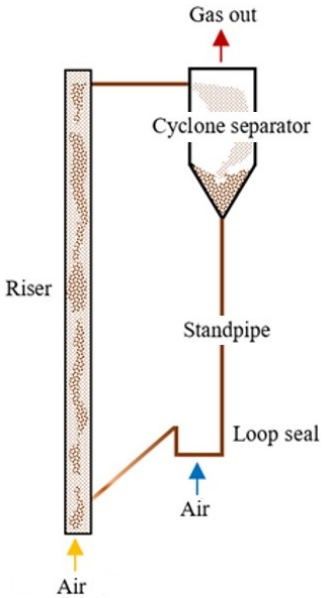

Figure 1: Circulating fluidized bed

The rate of particle circulation is governed by number of parameters such as loopseal aeration, riser gas flow, loopseal dimensions and the particle properties. As discussed prior, deviations in the simulation geometry and particle properties are a subset of the overall uncertainty. This work includes the uncertainty analysis related to pipe dimensions of the loopseal and particle size distribution for MP PIC simulated results. Barracuda VR is a commercial software package built on the MP PIC platform, which brought forward the concept of computational particle fluid dynamics (CPFD). The simulations were performed using Barracuda 17.3.0 and Intel(R) Core(TM) 3.50 GHz processor.

2 CPFD modeling

Andrews & O'Rourke (1996) extended the MP PIC method to particle flow systems, which was developed into CPFD. Later, Snider developed the scheme into three dimensional dense particle flows (Snider, 2001). The subsequent improvements of the particle collision modeling are discussed in several subsequent publications (O'Rourke & Snider, 2012, 2014; O'Rourke & Snider, 2010; O'Rourke et al., 2009). The fluid phase is modeled with Navier-Stokes equations, similar to DEM and TFM. The modeling of the particle phase has hybrid characteristics of discrete and continuum modeling. The real particles are grouped into parcels (computational particles) such that the billions of particles can be represented by millions of parcels. A certain parcel contains a number of real particles having same size, density and velocity. The parcel movement through the fluid domain is modeled similar to DEM. The particle collision force is calculated as a stress gradient on Eulerian grid in the advanced time step and mapped back to real time with interpolation functions. Unlike the TFM, the discrete nature of the particles is preserved and the implementation of the particle size distribution is straightforward.

2.1 Governing equations

The governing equations are referred from Snider (Snider, 2001). Gas phase mass and momentum conservation are modeled with continuity and time averaged Naiver-Stokes equations:

$$\frac{\partial(\alpha_g \rho_g)}{\partial t} + \nabla.\left(\alpha_g \rho_g u_g\right) = 0 \quad (1)$$

$$\frac{\partial(\alpha_g \rho_g u_g)}{\partial t} + \nabla.\left(\alpha_g \rho_g u_g u_g\right) = -\nabla P - F + \nabla.\left(\alpha_g \tau_g\right) + \alpha_g \rho_g g \quad (2)$$

Where α_g, ρ_g and u_g are gas phase volume fraction, density and velocity respectively. F is the total momentum exchange with particle phase per volume, g is the gravitational acceleration, P is the pressure, and τ_g

is the gas phase stress tensor. The stress tensor of the gas phase is given by:

$$\tau_g = \mu_g \left[\left(\nabla u_g + \Delta u_g^T \right) - \frac{2}{3} \nabla . u_g I \right] \quad (3)$$

μ_g refers to the shear viscosity that is the sum of the laminar and turbulent components. The large eddy simulation is used for the large-scale turbulence modeling while the subgrid scale turbulence is captured with the Smagorinsky model:

$$\mu_{g,t} = C_s \rho_g \Delta^2 \left| \nabla u_g + \Delta u_g^T \right| \quad (4)$$

The default value for the model constant C_s is 0.01. Δ is the sub-grid length scale and calculated by:

$$\Delta = (\delta x \delta y \delta z)^{1/3} \quad (5)$$

The interface momentum transfer is calculated through the viscous drag force:

$$F = \iint f \left\{ m_p \left[D_p (u_g - u_p) - \frac{\nabla P}{\rho_p} \right] \right\} dm_p du_p \quad (6)$$

Subscript P refers to the particle phase properties where m and u symbolizes the mass and velocity respectively. D_p is the drag function. The particle phase dynamics are derived using the particle distribution function (PDF) calculated from the Liouville equation given as:

$$\frac{\partial f}{\partial t} + \nabla (f u_p) + \nabla u_p (f A_p) = 0 \quad (7)$$

Where A_p, is the particle acceleration and is expressed by:

$$A_p = \frac{\partial (u_p)}{\partial t} = D_p (u_g - u_p) - \frac{\nabla P}{\rho_p} - \frac{\nabla \tau_p}{\rho_p \alpha_p} + g \quad (8)$$

α_p is particle volume fraction and τ_p is particle stress function used to formulate the interphase interactions of particles.

$$\alpha_p = \iint f \frac{m_p}{\rho_p} dm_p du_p \quad (9)$$

$$\tau_p = \frac{10 P_s \alpha_p^{\beta}}{max[(\alpha_{cp} - \alpha_p), \varepsilon (1 - \alpha_p)]} \quad (10)$$

P_s is a constant with the units of pressure, α_{cp} is the particle volume fraction at close packing, β is a constant between 2 and 5 and ε is a very small number on the order of 10^{-7}.

3 Computational method

The experimental data of Thapa et al (2016) was used for the comparison of simulation results. The loopseal and riser pipe diameters were 30mm and 50 mm respectively. The system pressure and rate of particle circulation were available where the circulation rate had been measured by interrupting (stopping) the loopseal aeration followed by measuring the time to accumulate a certain volume of particles at the standpipe. Sand with of 2650 kg/m^3 in density and 130 mm in mean diameter (size distribution from 50mm to 250 mm) was the particle phase. Air at atmospheric pressure and temperature was the loopseal and riser aeration fluid

The fluid volume was developed using SOLIDWORKS 2018 and imported to Barracuda VR 17.3.0. Uniform grid option was used and the grid refinement at narrow sections was needed to capture the geometry domain accurately. The total number of cells in the domain was 467376. The turbulence was modelled with large eddy simulation and the partial donor cell method (a weighted average method of central difference and upwind schemes) was used as the advection numerical scheme. The default values were used for the number of iterations, residuals and the minimum and maximum values of Courant-Friedrichs-Lewy (CFL) parameter (which satisfy the convergence criteria). Values of the model constants and other simulation parameters are given in **Table 1**.

Table 1: Simulation parameters

	Parameter	Value
[1]	Closed pack volume fraction	0.6
[2]	Maximum momentum redirection	40%
[3]	Particle-wall collision (Normal & tangential)	0.85
[4]	Diffuse bounce	3
[5]	Pressure constant in particle stress model (P_s in Pascal)	5
[6]	Initial time step (seconds)	0.0003

As the particle flow pattern of a circulating fluidized bed with loopseal is analysed, the riser operates at dilute phase while the loopseal at dense phase. Further, the fluid drag is a function of the particle volume fraction. Therefore, the Wen-Yu-Ergun drag model (Gidaspow) was used as the Ergun correlation has been extensively validated for dense systems. The Wen-Yu model is used at higher gas volume fractions than 0.8, which is given by (Gidapow, 1994):

$$D_{Wen-Yu} = \frac{3}{8} C_d \frac{\rho_g}{\rho_p} \frac{|u_g - u_p|}{r_p} \alpha^{-2.65} \quad (11)$$

$$C_d = \frac{24}{Re}, \quad (Re < 0.5)$$

$$C_d = \frac{24}{Re}(1 + 0.115Re^{0.687}), \quad (0.5 \leq Re \leq 1000)$$

$$C_d = 0.4, \quad (Re > 1000)$$

As the gas volume fraction decreases below 0.8, the Ergun correlation is used,

$$D_{Ergun} = 0.5\left(\frac{C_1 \alpha_p}{\alpha_g Re} + C_2\right)\frac{\rho_g}{\rho_p}\frac{|u_g - u_p|}{r_p} \quad (12)$$

The default values for the laminar and turbulent coefficients in the Barracuda VR are 180 (C_1) and 2.0 (C_2) where those are 150 and 1.75 in original Ergun formulation. The particle Reynolds number is given by:

$$Re = \frac{2\rho_p |u_g - u_p|}{\mu_g}\left(\frac{3V_p}{4\pi}\right)^{1/3} \quad (13)$$

The rate of particle circulation was measured by the flux plane implemented at the overflow pipe. A flux plane stores the data of the amount of particles by species and fluid pass across a defined area. Two additional flux planes were positioned at standpipe and riser to recognize the steady state conditions. The computational domain was initially occupied exclusively with air where a particle feed flow boundary was used to introduce the particles into the system. The "*particle feed control*" option was linked to the particle flow boundary to maintain the particle mass in the system between 0.58 kg and 0.60 kg throughout the entire simulation time. The number density manual at the particle feed was set to 200, which decides the resolution of computational particles in the domain. The boundary conditions, flux planes and the pressure monitoring locations are illustrated in **Figure 2**.

The loop seal exerts the highest resistance for the particle flow. Therefore, the pipe diameter of the loopseal was gradually reduced from 30 mm, which is the measured value from a scaled drawing, to 27 mm in successive simulations. The pipe diameters given in the sketch can be the outside diameter and hence the actual diameter for the fluid volume should be equal or less than 30 mm.

Further, the particle size distribution can have uncertainties. Therefore, results from the reported distribution was compared with two other size distributions. The first two alternatives were taken from the arbitrary assumption that the exact size distribution can bias more towards smaller sizes than the reported value (if the sieving had not been done sufficiently). The other set up considered the mono sized particles with mean diameter of 125 microns. The size distributions are plotted in **Figure 3**.

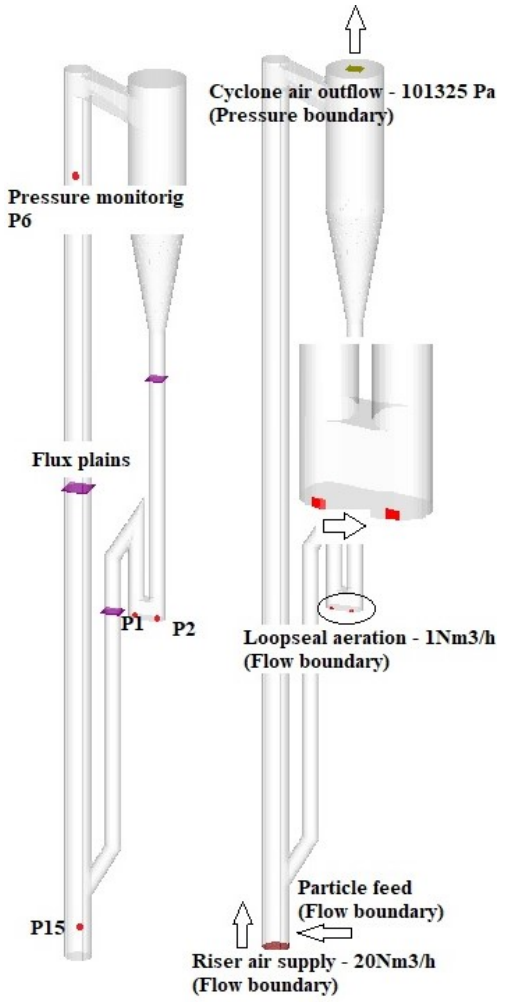

Figure 2: Computational domain; boundary conditions, flux plane and pressure transient data points

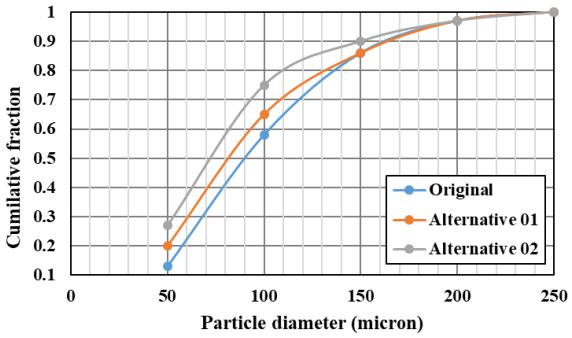

Figure 3: Particle size distribution

4 Results and Discussion

The simulation results for the original geometry was compared with the experimental data of Thapa et al, based on the rate of particle circulation and the system pressure. The particle distribution over the circulating fluidized bed at steady state operation (pseudo) is depicted in **Figure 5**. The enlarged sections in **Figure 5** shows the particle flow behavior in the loop seal.

The particle volume fractions over the riser and the cyclone sections are below 0.1 where a dense particle region can be observed at the bottom of the cyclone conical section. The particle volume fraction in the standpipe is approximately 0.5, which reduces in the horizontal section and recycle pipe. With the observed bubbles, the standpipe seems to operate at bubbling fluidization regime. A rigorous fluidization is prevailed at the horizontal section and the recycle pipe, which indicates that a large fraction of the loopseal aeration passes through the recycle pipe and ends up in the riser. In the loopseal, air tends to flow near the walls of the side of aeration and further, the airflow does not penetrate much within particle bed (in the direction of injection). Extended grid refining at the air injection may improve the length of penetration and however, large differences in the grid sizes (in all X, Y and Z directions) are not preferred in CPFD. Further, a grid cell should be sufficient to place several parcels.

The particle circulation rate was averaged over 30 seconds during steady state operation and calculated to be 315 kg/h, which is approximately equal to the experimental data. However, the rate was highly dynamic and large fluctuations between 100 kg/h to 1000 kg/h could be observed. The airflow rate across the flux plane was -0.00037 kg/s and the loopseal aeration was 0.00036 kg/s. This guarantee the proper operation of the loopseal that does not allow gas to bypass from riser via loopseal. Further, small amount of riser gas is recycled back across loopseal without escaping from the cyclone top. This is possible at high particle circulation rate, where the air is carried along with the voidage of the particle phase. The gas flow across the loopseal had not been monitored during experimental studies and the simulation results are useful in further optimizing the loopseal dimensions. The system pressure was also monitored at different locations (given in **Figure 2**) and the results are given in **Figure 4** together with experimental data. Pressure prediction from the simulation is lower than the experimental data over the entire system. The cyclone exhaust pipe was replaced with a pressure boundary with 101325pa (atmospheric pressure) boundary value and the downstream pressure drop was excluded. Geometrical lengths, pressure monitoring locations, particle size distribution and the assumption of spherical particles can be other physical uncertainties for the deviated pressure readings.

Olatunde, and Fasina (2019) have mentioned the observed deviations related to coefficients of Ergun equation for different particles. The laminar viscous coefficient has reported to as high as 267 while the turbulent coefficient up to 4.02. The barracuda default values of 180 and 2 were used in this study. Further, the competency of the Wen & Yu model for the dilute phase systems is not concretely validated as Ergun model. The particle hold up in the riser depends on the drag force exerted by the gas flow. In this case, the Wen & Yu model might over predict the drag force and consequently caused a reduced particle, which could lead for a lower pressure drop in the riser. This has a direct effect on the reduced pressure reading from the simulation at the recycle chamber. The effect of the particle phase modelling parameter of closed pack volume fraction is also significant for the pressure drop in dense particle regions. Due to the lack of data related to particle phase, the default value of 0.6 was used. The prediction error of the system pressure can be originated from one or many of these uncertainties and lack of data.

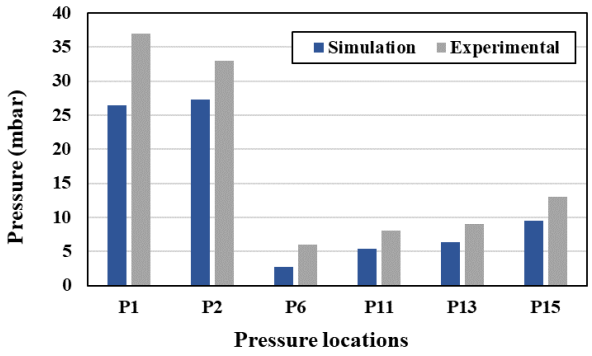

Figure 4: System pressure: experimental vs simulation

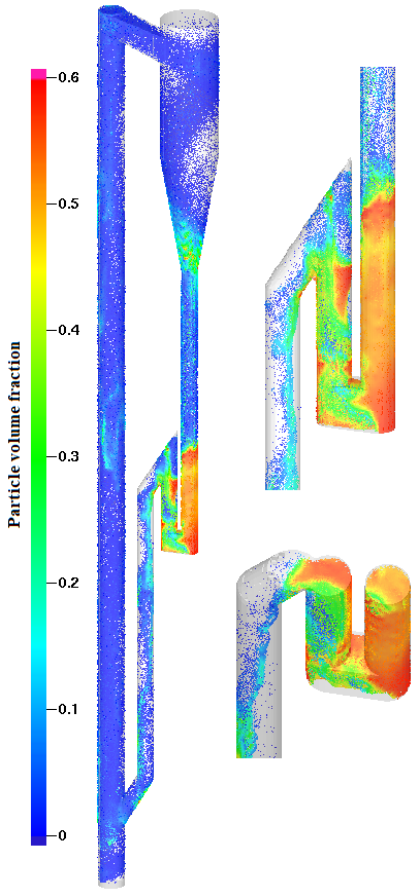

Figure 5: Particle volume fractions over CFB at steady state

4.1 Effect of the loopseal pipe diameter

Successive updates of the simulation parameters related to particle properties were needed to achieve the particle circulation rate similar to experimental values and the optimized values used are given in **Table 1**. However, the system pressure was not considerably sensitive for the analyzed parameters, where the observed deviations might originate from errors and uncertainties. The highest deviation of the pressure was recorded at the loopseal, which was lower than experimental data. Hence, simulations were performed for different diameters of the loopseal piping.

As illustrated in **Figure 6**, the particle bed height at the standpipe is slightly increasing towards reduced diameters. The loopseal balances the cumulative pressure drop of the remaining sections of the CFB system and the bed height at the standpipe is automatically adjusted following the system variations.

The rate of particle circulation and the system pressure are illustrated in **Figure 7** and **Figure 8** respectively. The particle circulation rate is greatly influenced by the pipe diameter, which showed a 20% increment when the diameter was reduced from 30 mm to 27 mm. The variation shows second order polynomial characteristics against pipe diameter. The gas velocity across the loopseal increases as the diameter is reduced and consequently, the fluid drag force on the particle increases. Similarly, the air bypass from cyclone to riser across loopseal has also increased.

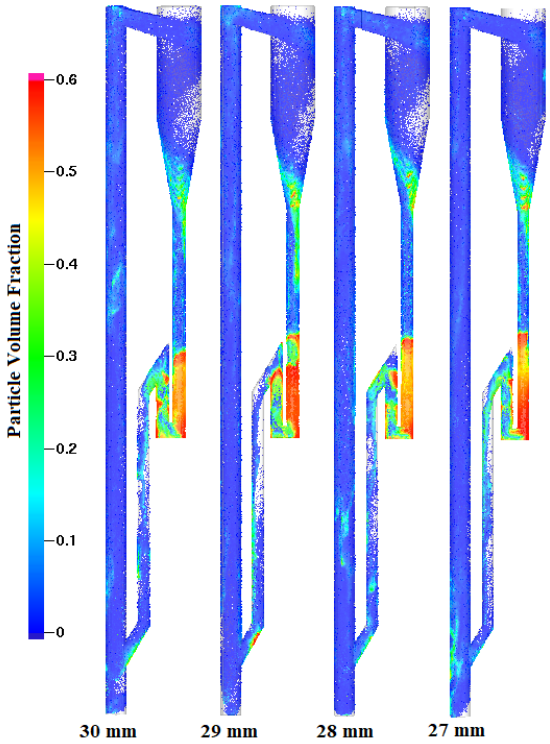

Figure 6: Particle flow hydrodynamics at different loopseal pipe diameters

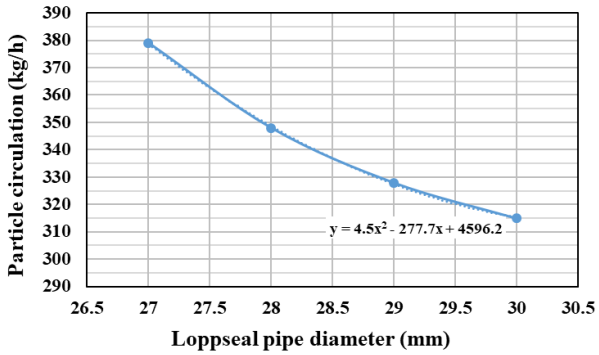

Figure 7: Change of particle circulation rate over different loopseal pipe diameters

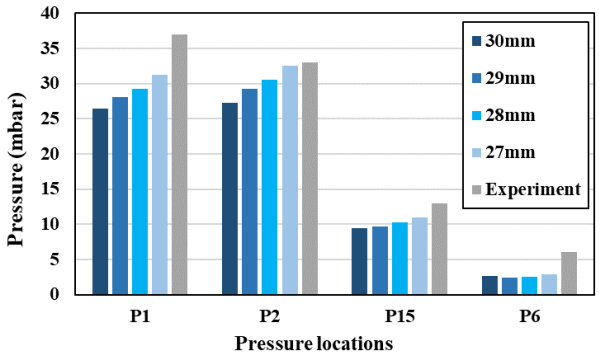

Figure 8: Change of system pressure over different loopseal pipe diameters

An improvement in the pressure prediction can be observed and the results reach the experimental values at P2 and P15. The particle holdup within the riser compartment can be high at increased particle circulation, which contribute for increased pressure at the riser bottom, P15. Prediction error of pressure at P1 may be originated from incorrect height of the recycle pipe, where the height effect can be further analyzed.

4.2 Effect of the particle size distribution

Particle size distribution is measured using sieving analysis equipment. Inadequate sieving time may avoid sufficient separation of particles. Further, with the difficulties of implementing the particle size distribution, monodisperse particles have been widely used (i.e. two-fluid modelling). Therefore, the simulation results from different size distributions as given in **Figure 3** and 125 micron monodisperse particles were compared using original geometry. The rate of particle circulation is given in **Figure 9**.

Significant changes of particle circulation was not observed between different size distributions used. Specially, merely the weight fractions were changed keeping the smallest and largest particle size similar to original. However, a considerable reduction of particle circulation, about 32%, was observed with monodisperse particles. This is a clear illustration of the force exerted by smaller particles on larger particles and

highlights the percentage error related to using mean size rather than size distribution. The geometry and the particle mass were equal for all cases and further, the loopseal operates at fluidizing regime (i.e. size distribution can affect the pressure drop at packed bed conditions), which can be the reason behind the similar pressure results for different size distributions.

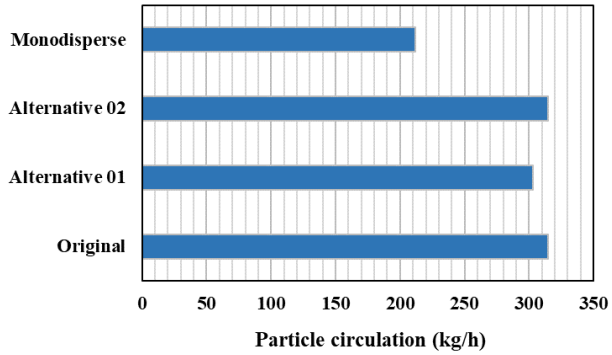

Figure 9: Change of particle circulation with size distribution

5 Conclusion

This work was carried out to analyze the effect of selected uncertainties related to geometrical lengths and particle size distribution in a circulating fluidized bed system. If the experiments are deliberately designed to generate data for CFD model validation, all the necessary parameters are available. However, whenever the existing experimental data from the literature are used in validation, certain uncertainties can be existed and therefore, adequate illustrations should be presented to compensate. The uncertainties related to physical reality and all accurately measurable parameters should be minimized (avoided) prior to the sensitivity analysis of models and model constants.

The loopseal pipe diameter displayed a great influence over particle circulation rate. The system pressure prediction was lower than experimental data in all the sections of the domain. Prediction error of the pressure at the recycle pipe was comparatively high, which might originate from incorrect height of computational geometry used or deviated pressure at the riser bottom due to inaccurate particle holdup in the riser. Small changes in the particle size distribution within the same smallest and largest sizes did not cause much change in particle circulation rate. However, monodisperse particles with mean particle size gave a substantially reduced circulation rate, which was 32% lower.

More uncertainties can be prevailed related to geometrical lengths of other sections, particle mass in the system, particle properties such as sphericity and closed pack volume fraction, loopseal aeration velocity and location. Therefore, further analysis will be supportive to demonstrate the effect of mentioned uncertainties and it is highly recommended to perform specially designed experiments for CFD model validation with all the required data.

Acknowledgements

The authors like to forward their gratitude to Rajan Thapa for sharing his experimental data and University of South-eastern Norway for facilitating with computer resources and Barracuda VR CPFD software package.

References

M. J. Andrews and P. J. O'Rourke. The multiphase particle-in-cell (MP-PIC) method for dense particulate flows. International Journal of Multiphase Flow, 22: 379-402, 1996.

S. Bale, S. S. Tiwari, K. Nandakumar, and J. B. Joshi. Effect of Schmidt number and D/d ratio on mass transfer through gas-solid and liquid-solid packed beds: Direct numerical simulations. *Powder Technology,* 354: 529-39, 2019.

D. Gidapow. Multiphase Flow and Fluidization: Continuum and Kinetic Theory Descriptions. Boston: Americal Press, 1994.

H. Ma and Y. Zhao. Investigating the fluidization of disk-like particles in a fluidized bed using CFD-DEM simulation. Advanced Powder Technology, 29:2380-2393, 2018.

L. Mathelin, M. Y. Hussaini, and T. A. Zang. Stochastic approaches to uncertainty quantification in CFD simulations. Numerical Algorithms, 38: 209-236, 2005.

C. Moliner, F. Marchelli, N. Spanachi, A, Martinez-Felipe, B. Bosio, and E. Arato. CFD simulation of a spouted bed: Comparison between the Discrete Element Method (DEM) and the Two Fluid Model (TFM). Chemical Engineering Journal, 2018.

G. Olatunde and O. Fasina. Modified Ergun Equation for Airflow through Packed Bed of Loblolly Pine Grinds. *KONA Powder and Particle Journal,* advpub, 2019.

P. J. O'Rourke and D. M. Snider. Inclusion of collisional return-to-isotropy in the MP-PIC method. Chemical Engineering Science, 80: 39-54, 2012.

P. J. O'Rourke and D. M. Snider. A new blended acceleration model for the particle contact forces induced by an interstitial fluid in dense particle/fluid flows. Powder Technology, 256: 39-51, 2014.

P. J. O'Rourke and D. M. Snider. An improved collision damping time for MP-PIC calculations of dense particle flows with applications to polydisperse sedimenting beds and colliding particle jets. Chemical Engineering Science, 65: 6014-6028, 2010.

P. J. O'Rourke, P. Zhao, and D. M. Snider. A model for collisional exchange in gas/liquid/solid fluidized beds. Chemical Engineering Science, 64: 1784-1797, 2009.

P. Ostermeier, S. DeYoung, A. Vandersickel, S. Gleis, and H. Spliethoff, H. (2019). Comprehensive investigation and comparison of TFM, DenseDPM and CFD-DEM for dense fluidized beds. Chemical Engineering Science, 196: 291-309, 2019.

Pannala, S., Syamlal, M., & O'Brien, T. J. (2011). Computational Gas-Solids Flows and Reacting Systems: Theory, Methods and Practice. Hershey, USA: Engineering Science Reference.

Qi, Z., S. Kuang, and A. Yu. 2019. Lattice Boltzmann investigation of non-Newtonian fluid flow through a packed bed of uniform spheres. *Powder Technology 343*; 225-36.

Snider, D. M. (2001). An Incompressible Three-Dimensional Multiphase Particle-in-Cell Model for Dense Particle Flows. Journal of Computational Physics, 170, 523-549.

Tang, Y., Y. M. Lau, N. G. Deen, E. A. J. F. Peters, and J. A. M. Kuipers. 2016. Direct numerical simulations and experiments of a pseudo-2D gas-fluidized bed. *Chemical Engineering Science 143*; 166-80.

Thapa, R. K., Frohner, A., Tondl, G., Pfeifer, C., & Halvorsen, B. M. (2016). Circulating fluidized bed combustion reactor: Computational Particle Fluid Dynamic model validation and gas feed position optimization. Computers & Chemical Engineering, 92, 180-188.

Walters, R. W., & Huyse, L. (2002). Uncertainty Analysis for Fluid Mechanics with Applications. In. Hanover: NASA Center for AeroSpace Information (CASI).

State Estimation of a Thermal Model of Air-cooled Synchronous Generator

Madhusudhan Pandey, Thomas Øyvang, Bernt Lie

University of South-Eastern Norway, Porsgrunn, Norway, Bernt.Lie@usn.no

Abstract

In this paper, we extend a previous study on a totally enclosed thermal model of a synchronous generator, with temperature state estimation using experimental data. The extension includes a new formulation of the system model, with four different model variations with and without temperature dependence in the metal, air, and water heat capacities and the copper resistances, where temperature variation in water and/or air requires a non-standard heat exchanger model. In the former study, the Unscented Kalman Filter (UKF) was used for state estimation. Here, we include both the UKF as well as the Ensemble Kalman Filter (EnKF) in the comparison. UKF and EnKF are compared based on estimation accuracy and computational speed. Results show that EnKF exhibits lower RMSE for the innovation process and thus is more accurate than the UKF even with a "minimum" of 50 particles, but the UKF with 6 sigma points (3 states) is faster. It is too early to conclude which of 4 models is more accurate, as they need to be tuned individually wrt. parameter fitting.

Keywords: Air-cooled synchronous generator, dynamic model, state estimation, Unscented Kalman filter, Ensemble Kalman filter

1 Introduction

1.1 Background

Due to the increase in intermittent renewable energy resources, hydropower plants will become a key component to provide higher operational flexibility in the future power system. In European hydropower generation, the synchronous generator power factor is restricted to the range $[0.85, 0.95]$, (ENTSO-E, 2016); for Norway, the power factor should be less than 0.86, (Statnett, 2012).

The power factor is the ratio of active power to apparent (complex) power. A small power factor implies a reduced active power production compared to a higher power factor. High production of active power is desired by the plant owners, but an increased power factor may cause problems due to the thermal design limitation of the machine. An important question is: would it be acceptable to relax on the constraint on the power factor for a limited time period in order to take out unexploited power in critical situations? To allow for such a relaxation in the power factor, it is important to have a measure of the temperature evolution, and how this influences the lifetime of the generator.

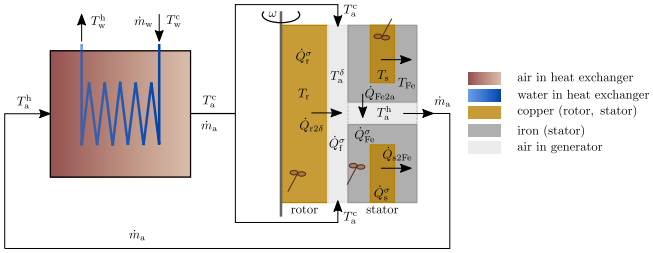

Figure 1. Thermal model of air-cooled synchronous generator, from (Lie, 2018).

In this paper, we consider how to obtain information about the temperature evolution.

A thermal model of a totally enclosed air-cooled hydro generator was developed in (Øyvang, 2018), using a closed-loop, water cooled heat exchanger for cooling heated air from the outlet of generator, and applied to a case study of a vertically mounted 103 MVA air-cooled hydro generator at Åbjøra, Norway. A similar model with more general structure and more efficient heat exchanger description was developed in (Lie, 2018).

It is of interest to extend the description in (Lie, 2018) with temperature dependent heat capacities (metals, air) and temperature dependent copper resistances. Furthermore, it is of interest to carry out a more extensive study on state estimation compared to (Øyvang, 2018), using several variations of the Unscented Kalman Filter (UKF) as well as introducing the Ensemble Kalman Filter (EnKF).

1.2 Organization of paper

The paper is organized as follows. The mathematical model is presented in Section 2. State estimation algorithms UKF and EnKF are presented in Section 3. Results are presented and discussed in Section 4. Finally, conclusions are drawn in Section 5, together with possible future work.

2 Mathematical model

Figure 1 shows the thermal operation of an air-cooled synchronous generator.

The cold air out of the heat exchanger is blown by a fan into the rotor/stator air gap. The air is heated by heat flow from rotor, air gap windage, and bearing friction. Next, air is forced into ducts through the stator iron core where it gets heated by heat flow from the iron. At the outlet

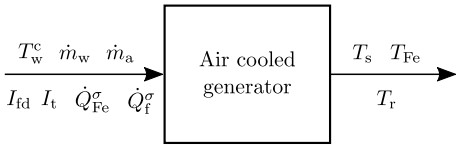

Figure 2. Functional diagram for air-cooled synchronous generator, from (Lie, 2018).

from the stator ducts, the heated air is collected and passed through a counter-current heat exchanger. The heated air is cooled down through the heat exchanger using continuous cold water circulation, before it is re-injected into the air gap in a continuous, closed loop process.

The water mass flow rate through the heat exchanger is $\dot{m}_w$, and it enters at temperature T_w^c and leaves the heat exchanger at temperature T_w^h. The air mass flow rate is $\dot{m}_a$ with temperature T_a^h at stator outlet and heat exchanger entry; through the heat exchanger, the air is cooled down to temperature T_a^c. The metal volumes are assumed to be homogeneous in temperature, with rotor copper at temperature T_r, stator copper at temperature T_s, and stator iron at temperature T_{Fe}. Rotor copper is heated by heat rate $\dot{Q}_r^{\sigma}$ due to resistive electric loss from the field current I_f. Similarly, the stator copper is heated by heat rate $\dot{Q}_s^{\sigma}$ due to stator terminal current I_t. The stator iron is heated by heat rate $\dot{Q}_{Fe}^{\sigma}$ due to eddy current losses and hysteresis losses, (Hargreaves et al., 2011). The air gap between rotor and stator is heated at heat rate $\dot{Q}_f^{\sigma}$ due to bearing and windage losses, (Øyvang, 2018). In addition, heat conduction/convection between the various volumes take place. It is of interest to consider how the inputs $\dot{m}_w$, $\dot{m}_a$, T_w^c, $\dot{Q}_{Fe}^{\sigma}$, $\dot{Q}_f^{\sigma}$, I_t and I_f influence the temperatures in the generator metals, T_r, T_s, and T_{Fe}. A functional diagram for the air-cooled synchronous generator is shown in Figure 2 relating inputs and outputs.

The mathematical model governing generator metal temperatures is taken from (Lie, 2018),

$$m_r \hat{c}_{p,Cu} \frac{dT_r}{dt} = 1.1 R_r I_f^2 - \mathscr{U} A_{r2\delta} \left(T_r - T_a^{\delta} \right) \quad (1)$$

$$m_s \hat{c}_{p,Cu} \frac{dT_s}{dt} = 3 R_s I_t^2 - \mathscr{U} A_{s2Fe} \left(T_s - T_{Fe} \right) \quad (2)$$

$$m_{Fe} \hat{c}_{p,Fe} \frac{dT_{Fe}}{dt} = \mathscr{U} A_{s2Fe} \left(T_s - T_{Fe} \right) - \mathscr{U} A_{Fe2a} \left(T_{Fe} - T_a^h \right) + \dot{Q}_{Fe}^{\sigma}. \quad (3)$$

Here, m_r, m_s, and m_{Fe} are the masses of the respective metal volumes. $\hat{c}_{p,Cu}$ and $\hat{c}_{p,Fe}$ are specific heat capacities of copper and iron, respectively. R_r and R_s are resistances of copper in the rotor and stator, respectively, $\mathscr{U} A_{r2\delta}$, $\mathscr{U} A_{s2Fe}$, and $\mathscr{U} A_{Fe2a}$ are heat transfer factors between rotor metal and rotor-stator air-gap, stator copper and stator iron, and stator iron and stator duct air gaps, respectively. T_a^{δ} and T_a^h are air temperatures in the rotor-stator air-gap and in the stator duct, respectively.

Similarly, for air inside the generator,

$$0 = \dot{m}_a \hat{c}_{p,a} \left(T_a^c - T_a^{\delta} \right) + \mathscr{U} A_{r2\delta} \left(T_r - T_a^{\delta} \right) + \dot{Q}_f^{\sigma} \quad (4)$$

$$0 = \dot{m}_a \hat{c}_{p,a} \left(T_a^{\delta} - T_a^h \right) + \mathscr{U} A_{Fe2a} \left(T_{Fe} - T_a^h \right). \quad (5)$$

Here, $\hat{c}_{p,a}$ is the specific heat capacity of air.

For the heat exchanger, we introduce *Stanton numbers* N_{St}^w and N_{St}^a,

$$N_{St}^w = \frac{\mathscr{U} A_x}{\hat{c}_{p,w} \dot{m}_w} \quad (6)$$

$$N_{St}^a = \frac{\mathscr{U} A_x}{\hat{c}_{p,a} \dot{m}_a} \quad (7)$$

$$N_{St}^{\Delta} = N_{St}^w - N_{St}^a. \quad (8)$$

Here, $\hat{c}_{p,w}$ is the specific heat capacity of water, and $\mathscr{U} A_x$ is the heat transfer factor between water and air in the heat exchanger. Provided that the Stanton numbers are constant and independent of (i) position, and (ii) temperatures, the counter-current heat exchanger model is

$$\left(N_{St}^w - N_{St}^a \exp\left(-N_{St}^{\Delta} \right) \right) T_a^c = N_{St}^{\Delta} T_a^h + N_{St}^a \left(1 - \exp\left(-N_{St}^{\Delta} \right) \right) T_w^c. \quad (9)$$

The heat exchanger model in 9 is the result of analytically solving a linear two point boundary value problem.

This model can be extended in several directions, by (a) introducing temperature dependence in the specific heat capacities $\hat{c}_{p,j}$, (b) introducing temperature dependence in the copper resistances R_r and R_s, and (c) in principle also in the heat transfer factors $\mathscr{U} A_j$. The only substantial change in the model is that if any of the Stanton numbers become temperature dependent, this will invalidate 9, and the involved two point boundary value problem must be solved numerically instead of analytically. Here, we assume constant Stanton numbers, even when the specific heat capacity of air is allowed to vary in 4–5.

To this end, four different models will be considered here:

- Model 1: constant values, $\hat{c}_p$, R
- Model 2: constant specific heat capacity, temperature dependent resistance, $\hat{c}_p$, $R(T)$
- Model 3: temperature dependent specific heat capacity, constant resistance, $\hat{c}_p(T)$, R
- Model 4: temperature dependence specific heat capacity and resistance, $\hat{c}_p(T)$, $R(T)$.

To simplify the discussion and avoid invalidating the heat exchanger model in 9, we will assume that specific heat capacity of air is constant in the heat exchanger but varies with temperature in the air gap/air duct, while we will introduce temperature dependence in copper and iron. To this end, for $\hat{c}_{p,j}(T)$, $j \in \{\mathrm{a,Cu,Fe}\}$, we will use a linear approximation given as,[1]

$$\hat{c}_{p,j}(T) = \frac{\mathscr{R}}{M_j}(a_j + b_j T), \tag{10}$$

where $\mathscr{R}$ is *universal gas constant* and M_j is the molecular mass. For the copper resistance,

$$R_j(T_j) = R_j^{\circ}(1 + \alpha_{\mathrm{Cu}}(T_j - T_{\mathrm{Cu}}^{\circ})), \quad j \in \{\mathrm{r,s}\} \tag{11}$$

where α_{Cu} is temperature coefficient of resistance for copper.

The parameters for the model of (Øyvang, 2018) are given in Table 1.

Operating conditions for the model are given in Table 2.

2.1 Overview of experimental data

A *heat-run test* of the synchronous hydro generator machine was performed for 600 min, (Øyvang, 2018). Table 3 lists measured quantities in the test.

Measurements were logged every minute for a supplied field current (I_{f}) from cold-start. The cold-run lasted 53 min, where the terminal voltage was built-up by residual flux in rotor windings. After the cold-run period, the supplied field current was increased leading to an increase in the measured stator copper and iron temperatures. The experimental results are displayed in Figure 3.

3 State Estimation

Notation used in the state estimation algorithms are given in Table 4.

A relatively general nonlinear system model can be represented as

$$x_{k+1} = f(x_k, u_k) + w_k \tag{12}$$

$$y_k = h(x_k) + v_k \tag{13}$$

with $w_k \sim \mathcal{N}(\bar{w}_k, \mathscr{W}_k)$ and $v_k \sim \mathcal{N}(\bar{v}_k, \mathscr{V}_k)$.

For our model, the state is $x = \begin{pmatrix} T_{\mathrm{r}} & T_{\mathrm{s}} & T_{\mathrm{Fe}} \end{pmatrix}$, while the measurements are $y = \begin{pmatrix} T_{\mathrm{s}} & T_{\mathrm{Fe}} \end{pmatrix}$. We wish to combine the measurements (y) with the state space model to estimate the unmeasured rotor copper temperature T_{r} and air gap temperature T_{a}^{δ}. To do that, we use two different Kalman Filter algorithms: the Unscented Kalman Filter (UKF) is presented in (Simon, 2006), while the Ensemble Kalman Filter (EnKF) is succinctly described in (Brastein et al., 2019). A summary of the UKF and EnKF algorithms are given in Tables 5 and 6, respectively.

[1] We will be considering linear approximation for temperature dependent specific heat capacity. The 7-coefficients, often called as NASA Lewis coefficients, power series form is given in (McBride et al., 2002; Zehe et al., 2002) which is converted to linear approximation for simplifying mathematical models.

Table 1. Parameters for air-cooled synchronous generator model. For the NASA Lewis coefficients, see 10.

Quantity	Symbol	Value
Atmospheric pressure	p_{a}	$1.01 \cdot 10^5\,\mathrm{N/m^2}$
Specific heat capacity, air	$\hat{c}_{p,\mathrm{a}}$	$1.15\,\mathrm{kJ/kg/K}$
Specific heat capacity, water	$\hat{c}_{p,\mathrm{w}}$	$4.2\,\mathrm{kJ/kg/K}$
Specific heat capacity, copper	$\hat{c}_{p,\mathrm{Cu}}$	$385\,\mathrm{J/kg/K}$
Specific heat capacity, iron	$\hat{c}_{p,\mathrm{Fe}}$	$465\,\mathrm{J/kg/K}$
Universal gas constant	$\mathscr{R}$	$8.314\,\mathrm{J/K/mol}$
Molar mass, air	M_{a}	$28.97\,\mathrm{g/mol}$
Molar mass, water	M_{w}	$18.01\,\mathrm{g/mol}$
Molar mass, copper	M_{Cu}	$63.54\,\mathrm{g/mol}$
Molar mass, iron	M_{Fe}	$55.84\,\mathrm{g/mol}$
NASA Lewis coefficient-linear approx., air	a_{a}, b_{a}	$3.28,\ 6.72 \cdot 10^{-4}$
NASA Lewis coefficient-linear approx., copper	a_{Cu}, b_{Cu}	$2.56,\ 1.2 \cdot 10^{-3}$
NASA Lewis coefficient-linear approx., iron	a_{Fe}, b_{Fe}	$0.19,\ 6.76 \cdot 10^{-3}$
Copper mass, rotor	m_{r}	$9260\,\mathrm{kg}$
Copper mass, stator	m_{s}	$6827\,\mathrm{kg}$
Iron mass, stator	m_{Fe}	$71.2 \cdot 10^3\,\mathrm{kg}$
Heat transfer, rotor to air gap	$\mathscr{U}A_{\mathrm{r2}\delta}$	$2.7\,\mathrm{kW/K}$
Heat transfer, stator copper to iron	$\mathscr{U}A_{\mathrm{s2Fe}}$	$20\,\mathrm{kW/K}$
Heat transfer, stator iron to air	$\mathscr{U}A_{\mathrm{Fe2a}}$	$14.3\,\mathrm{kW/K}$
Heat transfer, solid to air	$h_{\mathrm{a}}A_{\mathrm{x}}$	$55.6\,\mathrm{kW/K}$
Heat transfer, solid to water	$h_{\mathrm{w}}A_{\mathrm{x}}$	$222\,\mathrm{kW/K}$
Heat transfer, air to water	$\mathscr{U}A_{\mathrm{x}}$	$1/\left(\frac{1}{h_{\mathrm{a}}A_{\mathrm{x}}} + \frac{1}{h_{\mathrm{w}}A_{\mathrm{x}}}\right)$
Reference temperature air	T_{a}°	$25\,^{\circ}\mathrm{C}$
Rotor copper ohmic resistance, $T_{\mathrm{r}}^{\circ} = 15.7\,^{\circ}\mathrm{C}$	R_{r}°	$0.127\,\Omega$
Stator copper ohmic resistance, $T_{\mathrm{s}}^{\circ} = 20\,^{\circ}\mathrm{C}$	R_{s}°	$1.95\,\mathrm{m}\Omega$
Resistance nominal temperature	T_{Cu}°	$25\,^{\circ}\mathrm{C}$
Resistance temperature coeff.	α_{Cu}	$4.04 \cdot 10^{-3}\,^{\circ}\mathrm{C}^{-1}$

Table 2. Operating conditions for air cooled synchronous generator model.

Quantity	Symbol	Value
Initial value, rotor temperature	$T_\mathrm{r}\,(t=0)$	28 °C
Initial value, stator copper temperature	$T_\mathrm{s}\,(t=0)$	28 °C
Initial value, stator iron temperature	$T_\mathrm{Fe}\,(t=0)$	28 °C
Influent water temperature	T_w^c	3.8 °C
Water mass flow rate	$\dot{m}_\mathrm{w}$	53.9 kg/s
Air mass flow rate	$\dot{m}_\mathrm{a}$	49.2 kg/s
Rated rotor field current	I_f	1055 A
Rated stator terminal current, rated	I_t	5360 A
Stator iron generated heat	$\dot{Q}_\mathrm{Fe}^\sigma$	212 kW
Friction work	$\dot{W}_\mathrm{f}$	528 kW
Friction heating	$\dot{Q}_\mathrm{f}^\sigma$	$0.8\cdot\dot{W}_\mathrm{f}$

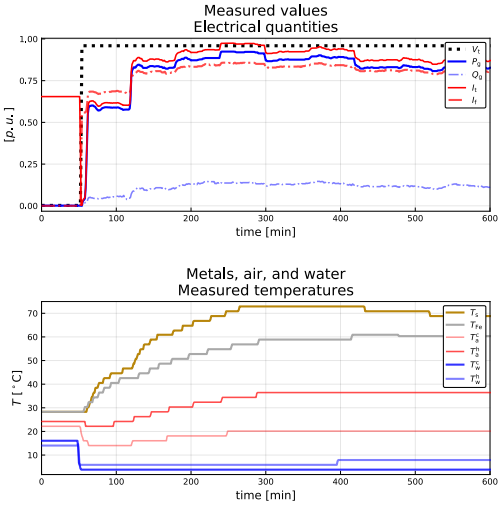

Figure 3. Experimental data for generator model from a 600 min heat-run test.

Table 3. Measured quantities.

Quantity	Symbol	Units	Sensor	#
Generator terminal voltage	V_t	kV	–	–
Active power of generator	P_g	MW	–	–
Reactive power of generator	Q_g	MVar	–	–
Rotor field current	I_f	A	–	–
Temperature of stator copper	T_s	°C	PT100	15
Temperature of stator iron	T_Fe	°C	PT100	4
Hot air temperature	T_a^h	°C	PT100 /CTD	2/2
Cold air temperature	T_a^c	°C	PT100 /CTD	2/2
Cold water temperature	T_w^c	°C	Analog	–
Hot water temperature	T_w^h	°C	Analog	–
Terminal current	$I_\mathrm{t}=\frac{P_g^2+Q_g^2}{\sqrt{3}\cdot V_\mathrm{t}}$	A	–	–

Table 4. Notations for the UKF and EnKF algorithms.

Symbol	Description
$x, \bar{x}, \hat{x}$	State vector, its mean, its estimate
x_k	Vector x at time instance k
$\hat{x}_{k\|k-1}$	*a priori* estimate of x_k based on measurements up to time t_{k-1}
$\hat{x}_{k\|k}$	*a posteriori* estimate of x_k based on measurements up to time t_k
X	State co-variance
w	Process noise
v	Measurement noise
$\mathscr{W}$	Process noise co-variance
$\mathscr{V}$	Measurement noise co-variance
K	Kalman gain
$\mathscr{E}$	Innovation co-variance
Z	Cross co-variance
ε	Error between measurement and estimate

Table 5. Algorithm: UKF.

Initialization, $k = 1$:

$\hat{x}_{1|1} = \mathbb{E}(x_1) = \bar{x}_1$

$X_{1|1} = X_1$

for $k = 2,\ 3, ...$

Propagation step:

1. Generate *sigma points* using *unscented transformation*

$x^{(i)}_{k-1|k-1} = \hat{x}_{k-1|k-1} + \tilde{x}^{(i)}, \quad i \in \{1,2,...2n\}$

where, with Cholesky root R: $R^T R = n \cdot X_{k-1|k-1}$,

$\tilde{x}^{(i)} = R_{:,i}, \quad i \in \{1,2,...n\}$

$\tilde{x}^{(n+i)} = -R_{:,i}, \quad i \in \{1,2,...n\}$

2. Propagate sigma points through process model

$x^{(i)}_{k|k-1} = f\left(x^{(i)}_{k-1|k-1}, u_{k-1}, \bar{w}_k\right), \quad i \in \{1,2,...2n\}$

3. *a priori* state and co-variance estimate

$\hat{x}_{k|k-1} = \frac{1}{2n}\sum_{i=1}^{2n} x^{(i)}_{k|k-1}$

$X_{k|k-1} =$

$\frac{1}{2n}\sum_{i=1}^{2n}\left(x^{(i)}_{k|k-1} - \hat{x}_{k|k-1}\right)\left(x^{(i)}_{k|k-1} - \hat{x}_{k|k-1}\right)^T + \mathscr{W}_k$

Information update:

1. Propagate sigma points through measurement equation

$y^{(i)}_{k|k-1} = h\left(x^{(i)}_{k-1|k-1}, u_{k-1}, \bar{v}_k\right), \quad i \in \{1,2,...2n\}$

2. Predicted measurements

$\hat{y}_{k|k-1} = \frac{1}{2n}\sum_{i=1}^{2n} y^{(i)}_{k|k-1}$

3. Innovation and cross co-variance

$\mathscr{E}_{k|k-1} =$

$\frac{1}{2n}\sum_{i=1}^{2n}\left(y^{(i)}_{k|k-1} - \hat{y}_{k|k-1}\right)\left(y^{(i)}_{k|k-1} - \hat{y}_{k|k-1}\right)^T + \mathscr{V}_k$

$Z_{k|k-1} = \frac{1}{2n}\sum_{i=1}^{2n}\left(x^{(i)}_{k|k-1} - \hat{x}_{k|k-1}\right)\left(y^{(i)}_{k|k-1} - \hat{y}_{k|k-1}\right)^T$

4. Kalman gain

$K_k = Z_{k|k-1}\mathscr{E}^{-1}_{k|k-1}$

5. *a posteriori* update

$\varepsilon_{k|k-1} = y_k - \hat{y}_{k|k-1}$

$\hat{x}_{k|k} = \hat{x}_{k|k-1} + K_k\varepsilon_{k|k-1}$

$X_{k|k} = X_{k|k-1} - K_k\mathscr{E}_{k|k-1}K_k^T$

Table 6. Algorithm: EnKF

Initialization, $k = 1$:

$x^i_{1|1} \sim \mathscr{N}(\bar{x}_1, X_1),\ i \in \{1,2,...,n_p\}$

$w^i_k \sim \mathscr{N}(\bar{w}_1, \mathscr{W}_k),\ i \in \{1,2,...,n_p\}$

$v^i_k \sim \mathscr{N}(\bar{v}_1, \mathscr{V}_k),\ i \in \{1,2,...,n_p\}$

$\hat{x}_{1|1} = \frac{1}{n_p}\sum_{i=1}^{n_p} x^{(i)}_{1|1}$

$X_{1|1} = \frac{1}{n_p - 1}\sum_{i=1}^{n_p}\left(x^{(i)}_{1|1} - \hat{x}_{1|1}\right)\left(x^{(i)}_{1|1} - \hat{x}_{1|1}\right)^T$

for $k = 2,\ 3, ...$

Propagation step:

1. Propagate particles through process model

$x^{(i)}_{k|k-1} = f\left(x^{(i)}_{k-1|k-1}, u_{k-1}, w^{(i)}_{k-1}\right)\ i \in \{1,2,...,n_p\}$

2. *a priori* state and co-variance estimates

$\hat{x}_{k|k-1} = \frac{1}{n_p}\sum_{i=1}^{n_p} x^{(i)}_{k|k-1}$

$X_{k|k-1} =$

$\frac{1}{n_p - 1}\sum_{i=1}^{n_p}\left(x^{(i)}_{k|k-1} - \hat{x}_{k|k-1}\right)\left(x^{(i)}_{k|k-1} - \hat{x}_{k|k-1}\right)^T$

Information update:

1. Propagate particles through measurement equation

$y^{(i)}_{k|k-1} = h\left(x^{(i)}_{k-1|k-1}, u_{k-1}, v^{(i)}_{k-1}\right)\ i \in \{1,2,...,n_p\}$

2. Predicted measurements

$\hat{y}_{k|k-1} = \frac{1}{n_p - 1}\sum_{i=1}^{n_p} y^{(i)}_{k|k-1}$

3. Innovation and cross co-variance

$\mathscr{E}_{k|k-1} =$

$\frac{1}{n_p - 1}\sum_{i=1}^{n_p}\left(y^{(i)}_{k|k-1} - \hat{y}_{k|k-1}\right)\left(y^{(i)}_{k|k-1} - \hat{y}_{k|k-1}\right)^T$

$Z_{k|k-1} =$

$\frac{1}{n_p - 1}\sum_{i=1}^{n_p}\left(x^{(i)}_{k|k-1} - \hat{x}_{k|k-1}\right)\left(y^{(i)}_{k|k-1} - \hat{y}_{k|k-1}\right)^T$

4. Kalman gain

$K_k = Z_{k|k-1}\mathscr{E}^{-1}_{k|k-1}$

5. *a posteriori* update of state and co-variance

$\varepsilon^{(i)}_{k|k-1} = y_k - y^{(i)}_{k|k-1}$

$x^{(i)}_{k|k} = x^{(i)}_{k|k-1} + K_k\varepsilon^{(i)}_{k|k-1}$

$\hat{x}_{k|k} = \frac{1}{n_p - 1}\sum_{i=1}^{n_p} x^{(i)}_{k|k}$

$X_{k|k} = \frac{1}{n_p - 1}\sum_{i=1}^{n_p}\left(x^{(i)}_{k|k} - \hat{x}_{k|k}\right)\left(x^{(i)}_{k|k} - \hat{x}_{k|k}\right)^T$

The UKF and EnKF are initialized with $\mathscr{W} = \text{diag}(4,4,4)$, $\mathscr{V} = \text{diag}(1,1)$ and $X = 10 \cdot \mathscr{W}$. Both the process noise w and measurement noise v are considered to be *white Gaussian noise* with zero-mean. The simulation time step Δt is set to 1 min and the total time of simulation is 584 min.

The simulation environment is the Julia programming language[2]. UKF and EnKF are compared based on root mean square error (RMSE) of innovation residuals, $\varepsilon = y_k - \hat{y}_{k|k-1}$, and computational speed[3].

4 Results and Discussion

The result for air and metals temperature estimation for Model 1 ($\hat{c}_p$, R) using UKF and EnKF for different particles is given in Figure 4.

Similarly, for four different models the estimates using UKF is given in Figure 5 and using EnKF with n_p=1000 is given in Figure 6.

The rotor copper temperature and air gap temperature estimates using EnKF, for Model 1, with different particles is given in Figure 7.

Figure 5 and 6 show a substantial difference in rotor copper and air gap temperature estimates for Model 3 and Model 4: models with temperature dependence in $\hat{c}_p$ tend to decrease the temperature of metals, but increase the air temperatures. In opposition to this, models with temperature dependence in R show an increase in both metal and air temperatures.

Figure 7 shows a comparison of EnKF depending on particle number n_p: with increased n_p, the estimates converge better and give a result similar to that of the UKF.

A comparison of UKF and EnKF with different number of particles, based on RMSE of innovation residuals and computational speed, is given in Table 7.

The results show that the RMSE of the UKF is larger than that of the EnKF. Furthermore, for EnKF the residuals decrease with increased number of particles n_p. The RMSE of residuals were lowest for Model 2 as compared to the other models. The computational time increases from UKF to EnKF and with n_p. The computational time also increases when the model complexity increases from Model 1 to 2 to 3 to 4 for EnKF with $n_p = 1000$.

5 Conclusions and future work

State estimation using UKF, and EnKF with different number of particles, have been studied for four different models. Results indicate that temperature dependent heat capacities increase air temperatures and reduce metal temperatures, while temperature dependent resistances increase all temperatures. EnKF shows better estimation accuracy than UKF, but with a penalty in computational speed. In the comparison, we have re-used the constant

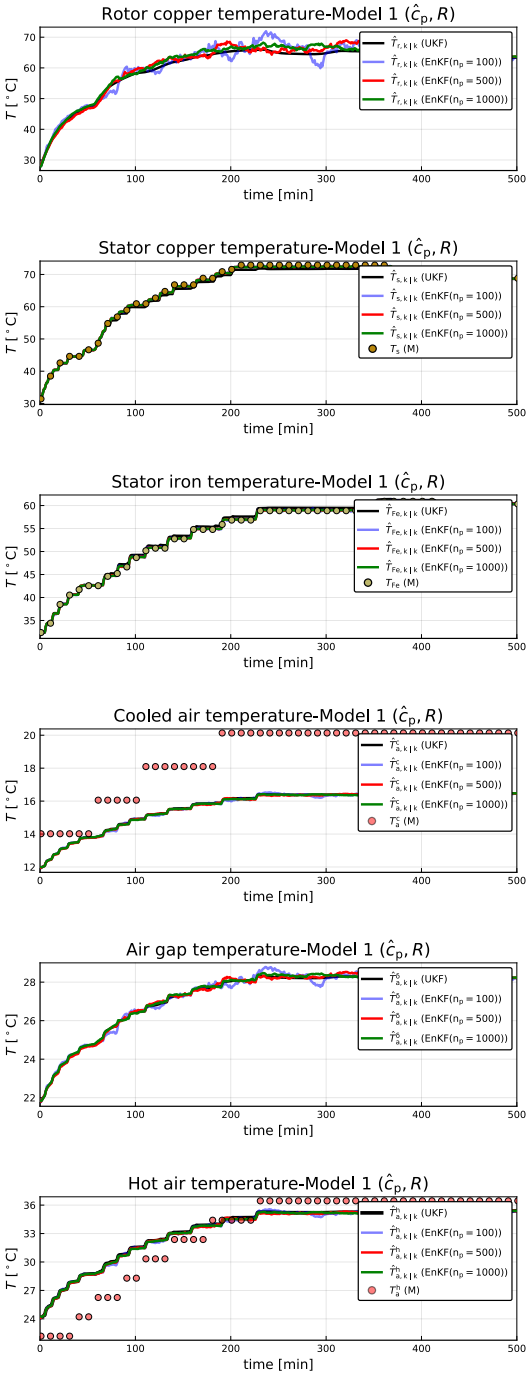

Figure 4. Air and metal temperature estimates using UKF and EnKF for Model 1 ($\hat{c}_p$, R). Subscript $k \mid k$ represents *a posteriori* estimate.

[2]Version 1.0.3 (2018-12-18)

[3]Processor: Intel(R) Core(TM) i7-7500U CPU @ 2.70GHz, 2901 Mhz, 2 Core(s), 4 Logical Processor(s)

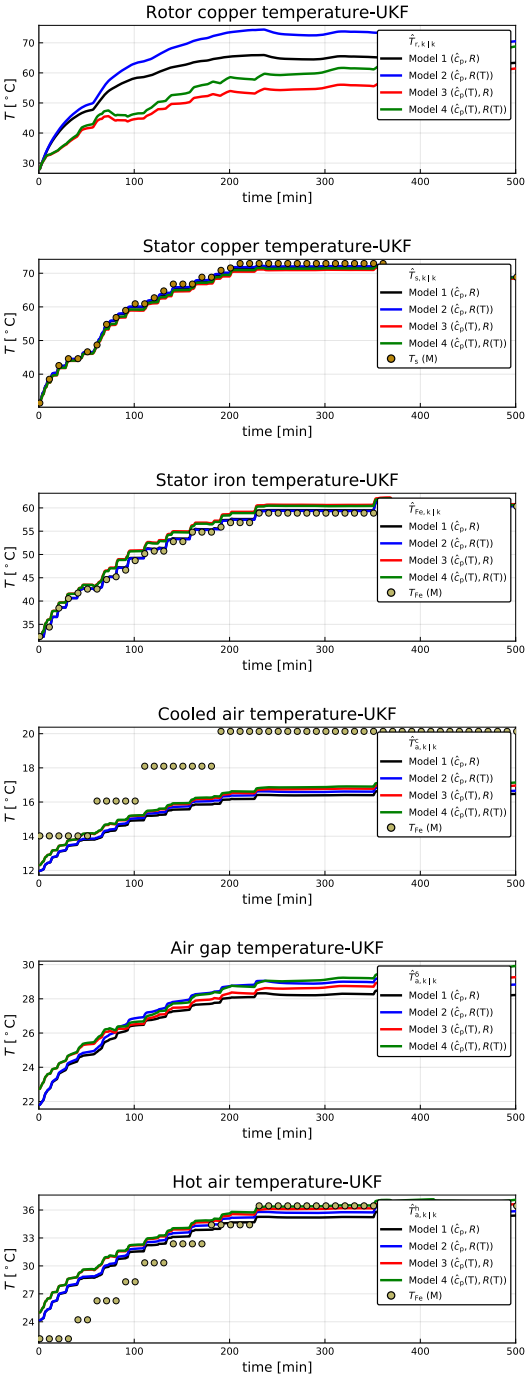

Figure 5. Air and metal temperature estimates using UKF for different models.

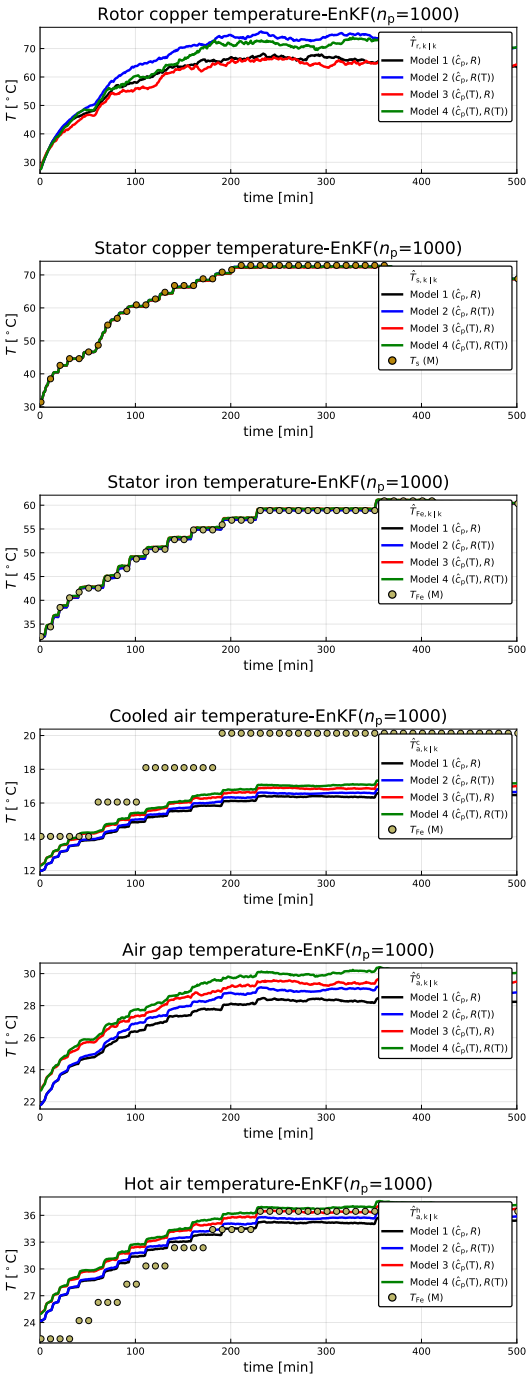

Figure 6. Air and metal temperature estimates using EnKF ($n_p = 1000$) for different models.

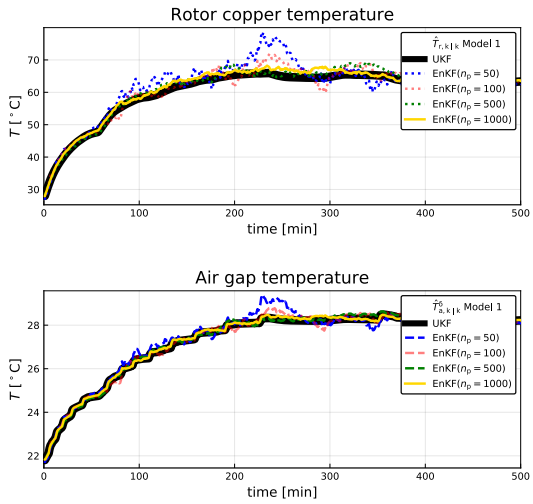

Figure 7. Rotor copper temperature and air gap temperature estimates using different number of particles for EnKF.

Table 7. Comparing Kalman filters with different models.

Model	KF	RMSE(ε)	Elapsed[s]
1	UKF	2.215	0.338
	EnKF($n_p = 50$)	2.066	1.088
	EnKF($n_p = 100$)	2.039	2.211
	EnKF($n_p = 500$)	2.010	10.860
	EnKF($n_p = 1000$)	2.012	26.343
2	UKF	1.652	0.744
	EnKF($n_p = 50$)	1.573	1.774
	EnKF($n_p = 100$)	1.524	3.414
	EnKF($n_p = 500$)	1.500	16.729
	EnKF($n_p = 1000$)	1.492	32.225
3	UKF	3.137	1.041
	EnKF($n_p = 50$)	2.735	3.238
	EnKF($n_p = 100$)	2.729	7.643
	EnKF($n_p = 500$)	2.705	36.663
	EnKF($n_p = 1000$)	2.701	58.595
4	UKF	2.730	0.798
	EnKF($n_p = 50$)	2.407	3.154
	EnKF($n_p = 100$)	2.342	5.287
	EnKF($n_p = 500$)	2.331	35.877
	EnKF($n_p = 1000$)	2.327	60.993

model parameters in all the models. Because these parameters essentially have been tuned for Model 1, it is difficult to draw strong conclusions on which model is best at this moment.

Future work will involve studies of (i) temperature dependent specific heat capacity for air and water with numeric solution of the resulting two point boundary value problem, (ii) extending the number of outputs from two (T_s, T_{Fe}) to four (T_s, T_{Fe}, T_a^c, and T_a^h), (iii) and a more formal model fitting for the various models.

References

Ole Magnus Brastein, Bernt Lie, Roshan Sharma, and Nils-Olav Skeie. Parameter estimation for externally simulated thermal network models. *Energy and Buildings*, 191:200–210, 2019. doi:10.1016/j.enbuild.2019.03.018.

ENTSO-E. Commission regulation (eu) 2016/631 of 14 april 2016 establishing a network code on requirements for grid connection of generators. Technical report, European Network of Transmission System Operators for Electricity, ENTSO-E Avenue de Cortenbergh 100 1000 Brussels Belgium, 2016.

Philip A. Hargreaves, B.C. Mecrow, and Ross Hall. Calculation of Iron Loss in Electrical Generators Using Finite-Element Analysis. *Industry Applications, IEEE Transactions on*, 48(5):1368–1373, May 2011. doi:10.1109/IEMDC.2011.5994805.

Bernt Lie. Solution, Project, FM1015 Modelling of Dynamic Systems. University of South-Eastern Norway, November 2018.

Bonnie J McBride, Michael J Zehe, and Sanford Gordon. Nasa glenn coefficients for calculating thermodynamic properties of individual species. Technical Report NASA/TP–2002-21155, NASA, NASA Center for Aerospace Information 7121 Standard Drive Hanover, MD 21076, 2002. URL `http://gltrs.grc.nasa.gov/GLTRS`.

Thomas Øyvang. *Enhanced power capability of generator unites for increased operational security*. PhD thesis, University of South-Eastern Norway, Faculty of Technology, Natural Sciences and Maritime Sciences University of South-Eastern Norway N-2018 Porsgrunn Norway, December 2018. ISBN: 978-82-7206-503-3 (print) ISBN: 978-82-7206-504-0 (online).

Dan Simon. *Optimal State Estimation: Kalman, H Infinity, and Nonlinear Approaches*. Wiley-Interscience, Hoboken, New Jersey, 2006.

Statnett. Fiks funksjonskrav i kraftsystemet [functional requirements in the power system]. Technical report, Statnett, 2012.

Michael J. Zehe, Sanford Gordon, and Bonnie J. McBride. CAP: A Computer Code for Generating Tabular Thermodynamic Functions from NASA Lewis Coefficients. Technical Report NASA/TP–2001-210959/REV1, NASA, NASA Center for Aerospace Information 7121 Standard Drive Hanover, MD 21076, 2002. URL `http://gltrs.grc.nasa.gov/GLTRS`.

Online Monitoring of a Synchronous Generator's Capability with MATLAB

Prabesh Khadka Dietmar Winkler Thomas Øyvang

University of South-Eastern Norway, corresponding author: thomas.oyvang@usn.no

Abstract

The future power systems are expected to operate closer to its security and stability limits mainly due to growth in variable renewable generation and the increase in load demand. In particular, voltage stability has been a major subject of discussion and concern in electric power system operation and planning worldwide. This evolution of the power system demands enhancement in ability from large synchronous generators to respond to change in demand and supply. In this contribution, a new visualization tool for online monitoring of a synchronous generator's capability is presented. In addition, the proposed tool is illustrated with a long-term voltage stability simulation carried out on a 10-bus benchmark power system. It is shown that the load models, load tap changing transformer and generator over-excitation limiter have a significant influence on voltage stability and collapse phenomena.

Keywords: generator capability diagram, visualization tool, long-term voltage stability, PSAT, MATLAB

1 Introduction

Voltage stability is becoming one of the major concern in power system operation and planning worldwide due to the increased power demand. Many incidents of voltage collapse have been reported at different corners of the world and few examples can be found in CIGRE report (CIGRE Task Force 38.02.10 1993). The inability of the power system to meet the reactive power demand in an electrical network is one of the causes of voltage instability. Generators are normally the sources of reactive power support during voltage insecurities. Thus, monitoring the voltage profiles, voltage regulation and the reactive power output of generators is one of the important countermeasures for voltage collapse.

In a recent Ph.D. study (Øyvang 2018), utilization of the thermal capacity of a synchronous generator to enhance the voltage stability of the power system was studied. The available voltage control capability depends upon the temperature rise of the machine during contingencies (Øyvang 2018). Furthermore, the normal limits of operation of generators without exceeding their thermal limitations are defined by the reactive capability curve. The method of determining the capability curves are described by various authors in different papers as in (Pejovski, Velkovski, and Najdenkoski 2016) and (I.Ili et al. 2007). However, the development of an automatic visualization tool which monitors the generator's operating conditions in real-time with sophisticated visualization adds quality to the usefulness of the PQ diagram.

This paper will primarily address the implementation of PQ capability diagram for online monitoring of the generator's capability in MATLAB through a visualization tool. In addition, long term voltage stability or the collapse phenomenon which includes the dynamics of slow acting components such as transformer under-load tap changer (ULTC), generator overexcitation limiter (OXL) and thermostat controlled loads, has been investigated in this research work along with the visualization of its result in the visualization tool. The dynamic simulation is carried out on Kundur 10-bus test system (Kundur 1994), in MATLAB based power system toolbox PSAT; a Free and Open Source Software (FOSS) which includes different static and dynamic power system component models. Moreover, the PQ capability diagram is implemented in the MATLAB programming language with the help of Graphical User Interface.

This paper is organized as follows. Section 2 gives a brief introduction to the generator PQ capability diagram. Section 3 presents the model formulation and the development of a automatic visualization tool. In Section 4, the dynamic voltage stability analysis of a test power system is demonstrated whereas the temperature visualization of a hydrogenerator in the visualization tool is shown in Section 5. The simulation results and the discussions are included in Section 6.

2 Generator capability curve

Synchronous generator is a primary source of reactive power in the network and plays an important role in maintaining the voltage stability in the network. The boundaries for supplying the reactive power at a given active power output is defined by the generator capability curve provided by the manufacturers (Dragosavac et al. 2012). Following operational constraints are the reasons for the limits in active and reactive power of the synchronous generator (Machowski, Bialek, and Bumby 2008).

1. Armature current limit.
2. Field current limit.
3. Steady-state stability limit.

4. Stator end region heating limit.

5. Generator active power limit.

Figure 1 shows the synchronous generator capability diagram where the area bounded by the curve *ABCDEFG* indicates the safe region of operation for salient-pole machine.

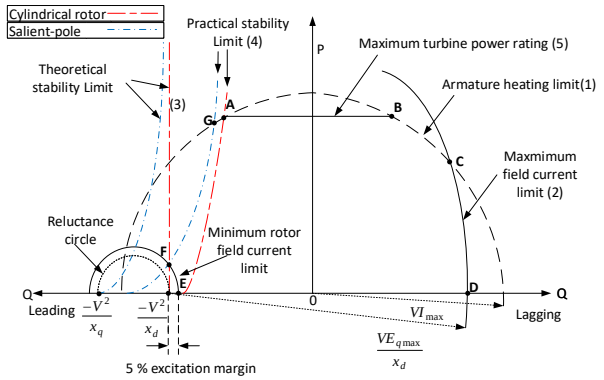

Figure 1. Capability diagram of synchronous generator (Walker 1953).

3 Model development

This paper presents the methodology for obtaining the PQ diagram for a cylindrical rotor synchronous generator with the following simplification during its modelling:

- The synchronous generator has been assumed to be connected to the infinite bus, i.e., with constant voltage.
- The machine saturation effect on the direct axis synchronous reactance has not been considered, i.e., x_d = constant.
- The effect of armature resistance has also been neglected.

The rated parameters of generator G3 in local area in the Kundur 10-bus system (Kundur 1994) is taken as reference for determining capability diagram with 10% stability margin.

The theoretical PQ diagram can be derived by dividing every phasor in the vector diagram by direct-axis synchronous reactance x_d and multiplying them with the armature voltage as shown in Figure 2. The figure so obtained, contains P and Q as the x-axis and y-axis respectively.

3.1 Rated turbine power limit

The maximum and the minimum turbine power limits are drawn according to the following two conditions (I.Ili et al. 2007):

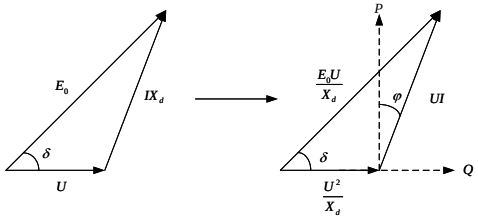

Figure 2. Derivation of a P-Q capability diagram from the phasor diagram (cylindrical rotor) (Vrazic, Viskovic, and Hanic 2014).

- If the power of the turbine (P_T) exceeds the rated power of the generator (P_n), i.e., if $P_T > P_n$, then $P_{max} = P_n$.
- If the power of the turbine is equal to or less than the rated power of the generator ($P_T \leq P_n$), then $P_{max} = P_T \cdot \eta_G$.

This limit is indicated in Figure 3 as P_{max}. The minimum power depends upon the turbine requirements regarding turbine efficiency. For example, in Kaplan and Francis turbine minimum power output is 5 % to 30% of rated output whereas in some turbines like Pelton turbine this limitation does not exists (I.Ili et al. 2007).

3.2 Rated stator current limit

The rated stator current limit is plotted as a constant semicircle with center at origin '0' and radius as the rated apparent power, S_n as shown in Figure 3. Point 'P' denotes the rated operating condition of the generator. The typical operating point is considered as $\cos\phi_n = 0.72$. So,

$$P_{\text{rated}} = S_n \cos\phi = 1 \cdot 0.72 = 0.72 \text{ p.u.}$$

$$Q_{\text{rated}} = S_n \sin\phi = 1\sqrt{1-(\cos\phi)^2} = 0.69 \text{ p.u.}$$

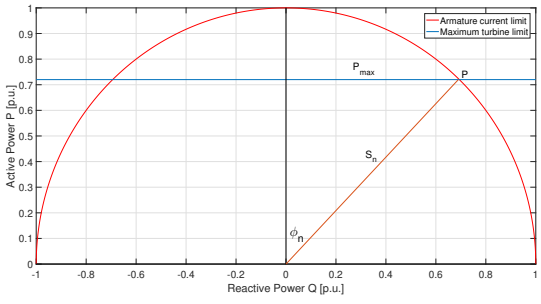

Figure 3. Rated stator current limit and maximum turbine limit plot.

3.3 Rated field current limit

For implementing the rated field current limit, an arc is drawn with the center at (0,-$\frac{V^2}{x_d}$) and radius $\frac{E_{qmax}\,V}{x_d}$ from

$\cos\phi = 0$ to $\cos\phi = 0.72$ (rated) where $E_{q_{max}}$ is calculated from the phasor diagram as shown in Figure 2 as:

$$E_{q_{max}} = \sqrt{(V + Ix_d \sin\phi)^2 + (Ix_d \cos\phi)^2} \quad (1)$$

The limit is drawn as curve PK in Figure 4.

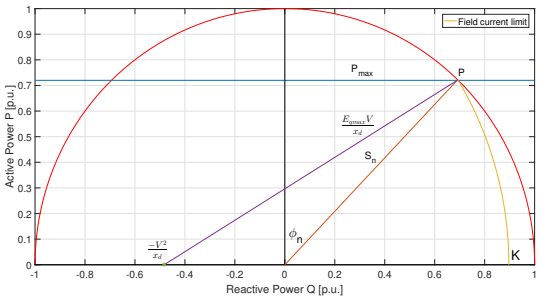

Figure 4. Rated field current limit plot.

3.4 Practical Stability limit

For round-rotor generators, theoretical stability limit is achieved at load angle δ=90°. However, the theoretical stability curve is reduced by a constant power value, for example by 10% of the rating of the machine as a safety margin and the corresponding curve so obtained is termed as practical stability margin (Walker 1953).

The theoretical stability curve is drawn as a straight line at point (0,-$\frac{V^2}{x_d}$)= (0,-$\frac{1}{2.07}$)= (0,-0.48) represented by dashed line in Figure 5. The practical stability limit is represented as curve AD in the same figure.

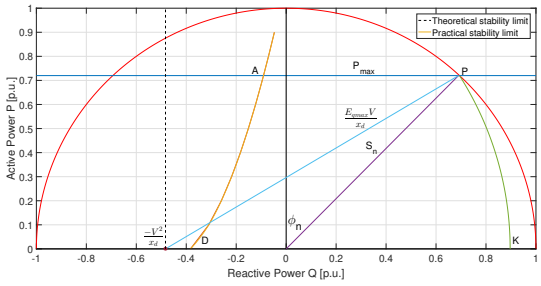

Figure 5. Theoretical and practical stability limit plot.

Hence, the safe region for the operation of a synchronous generator is represented by the area bounded by curve APKD in Figure 5.

3.5 Visualization tool

As discussed earlier in this section, various operational limits in PQ diagram was implemented in the MATLAB software environment. For improved visualization of the diagram, a visual App was created using MATLAB App designer. The App yields a more accurate approximation to test for conditions of instability as it provides enhanced online information of the system. A Graphical User Interface was created by using different components from the component library and specifying app's design and layout. For defining the App behavior, App designer allows an integrated version of the MATLAB Editor (*MATLAB App Designer* 2019). All the parameter values implemented, and the dynamics observed in the visualization tool is based upon the case study of Kundur 10-bus test system which is described further in Section 4.

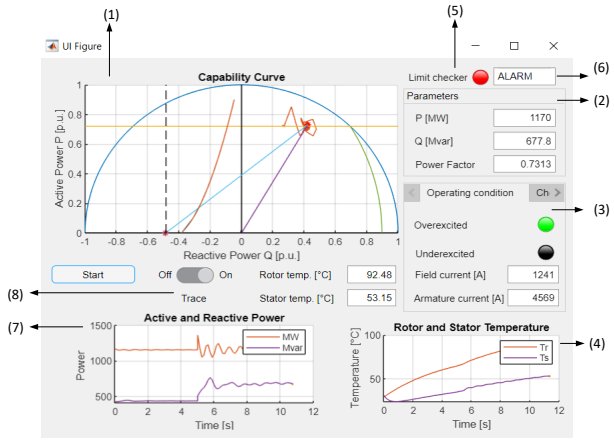

Figure 6. Graphical User Interface for generator capability diagram.

Figure 6 shows a GUI environment for the designed App in order to visualize the generator capability. The GUI consists of three figure windows and two main tabs. The upper figure (1) in the user interface shows the capability curve with the real-time operating point as indicated by 'red' asterisk symbol. The 'Parameters' tab (2) shows the operating point (P and Q) values in real time along with the operational power factor. The 'Operating conditions' tab (3) shows the actual operating condition, i.e., whether the generator is operating in over excitation mode or under excitation mode with current operation mode indicated by lamp glowing 'green'. The 'Machine Paramters' tab as shown in Figure 7 indicates the generator rated conditions which can be changed by changing the values in the respective fields. For example, the effect of change of direct axis synchronous reactance on the generator limits can be visualized in the figure section (1) by changing its value in the 'Machine rating' tab. The two lower figure windows (7) and (4) shows the plot of active and reactive power, and the plot of rotor and stator temperature of the synchronous machine respectively.

On top of the 'Parameters' tab resides a 'Limit checker' (5) as indicated by a lamp which glows 'red' when the defined operational limits on the capability curve are violated along with the actuation and information of 'ALARM' (6) to notify the operating personnel about the limit violation as shown in Figure 6. The lamp glows 'green' along with an information 'NORMAL' when the operating point lies within the defined boundaries as shown in Figure 7. The 'Trace' button (8) is used to turn on or turn off the trace of the operating point's path which

is as shown in Figure 6 and Figure 7 respectively.

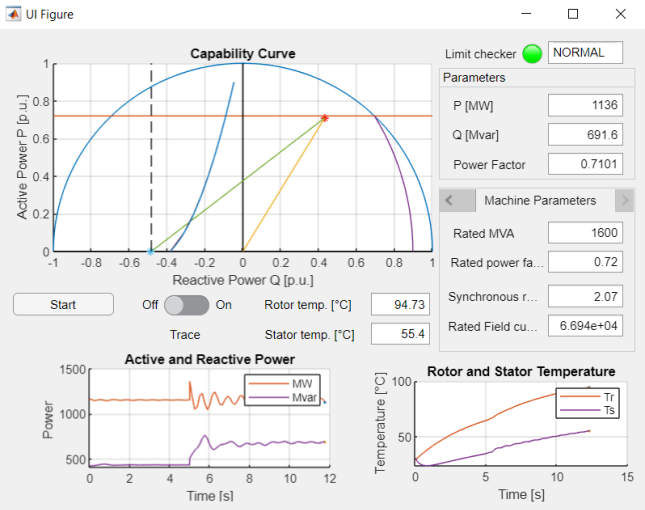

Figure 7. Graphical User Interface for Generator Capability Diagram showing 'NORMAL' condition.

4 Case study

As a case study, the long term voltage stability analysis is carried out on a 10-bus benchmark power system, and the dynamics involved during the simulation is visualized in the automatic visualization tool.

4.1 Description of a test system

The Kundur-10 bus test system (Kundur 1994) is chosen in order to analyze the performance and influence of different power system components in voltage stability. The test system used for the study is actually based on the system described in (CIGRE Task Force 38.02.08 1995) as BPA[1] test system, with some changes in load and compensating devices parameters. The necessary data used for the simulation of the system is provided in Appendix A.

Here the generators G1 and G2 in remote areas supply loads to the local area through five 500 kV transmission lines. The local generator G3 at bus 3 generates 1154 MW and the remaining power is supplied by two remote generators. Shunt capacitors are placed at various locations in the local area. Figure 8 shows the implementation of test system in PSAT.

4.2 Simulation results

The voltage at bus 11 and the reactive power output of the generator G3 is compared for the test system including and excluding the overexcitation limiter (OXL) with under-load tap changer (ULTC) in action for both cases, which are as presented in the Figure 9 and Figure 10 respectively.

The sequence of events triggered during the simulation in different time frames can be explained as follows.

[1]Bonneville Power Administration `https://www.bpa.gov`

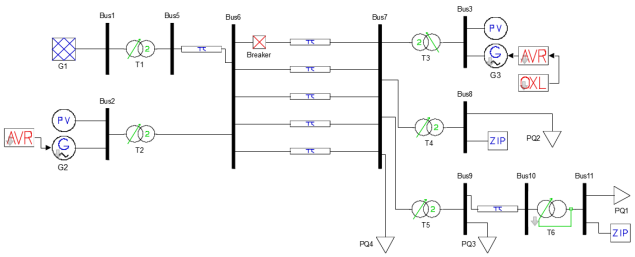

Figure 8. Single line diagram implementation of the test system in PSAT.

- One of the transmission lines is disconnected at time t=5 seconds. When the line has been disconnected, the apparent impedance and consequently the line losses and voltage drop of the transmission system is increased.

- The second time frame starts at around 10 seconds where the ULTC is activated as the voltage at the bus 11 is lower than the preset value. The ULTC tries to keep the voltage at the secondary bus (bus-11) at its original value by adjusting its tap ratio which demands more reactive power support from the generators present in the network. Thus, to meet the increased reactive power demand the excitation current is continuously increased until the maximum tap of transformer is reached or voltages at the buses are recovered. This time frame can be observed in Figure 9a and Figure 10a. The voltage at bus 11 is restored to nearly its reference value in about 90 seconds as shown in Figure 9.

- The third time frame begins with the actuation of overexcitation limiter as shown in Figure 9b at around t=150 seconds by ramping down the field current. The following chains of events occurs after the actuation of OXL.

  – As the field current of G3 is reduced, its terminal voltage drops.
  – Voltages at bus 11, 10 and 7 drops.
  – ULTC on T6 tries to restore the voltage at bus 11 back to its original value.
  – The reactive power demand on generators increases. Field current of machine 3 increases and continues to remain at its limit and the terminal voltage of G3 further decreases.
  – Voltage at bus 7 drops and causes a further reduction in terminal voltage of bus 10 and bus 11.
  – The ULTC operates again, repeating above mentioned chains of events.

Hence in response to each tap movement of ULTC, the voltage at bus 11 reduces rather than increased.

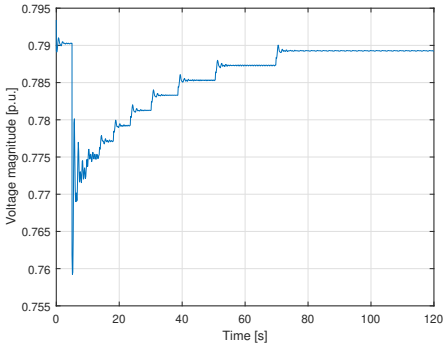

(a) With only ULTC

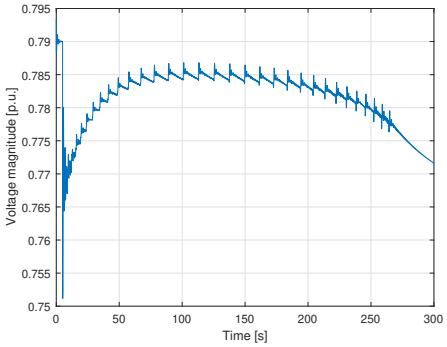

(b) With ULTC and OXL

Figure 9. Bus 11 voltage without and with OXL.

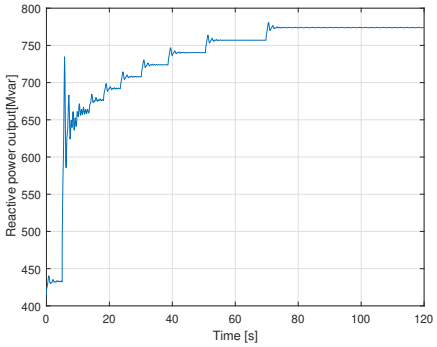

(a) With only ULTC

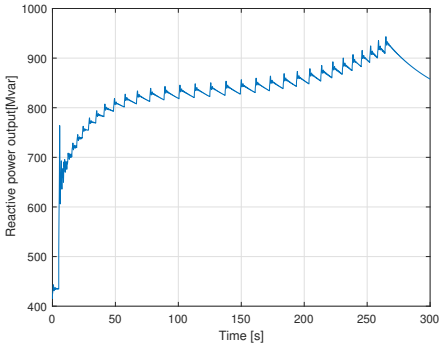

(b) With ULTC and OXL

Figure 10. Reactive power output of generator G3 without and with OXL.

This indicates that the system has entered into the voltage instability phase. The bus 11 voltage falls progressively as shown in Figure 9b until the ULTC reaches its maximum tap position at around 260 seconds. The voltage at bus 11 settles at around 0.77162 p.u.

Furthermore, the effect of static load models on long term voltage stability was studied for the test case considered. Figure 11 shows the voltage profile at bus 11 when the load at bus 8 is modelled as constant impedeance, constant current and constant power load keeping the load at bus 11 as constant impedeance. The ULTC and OXL were kept inactive during this condition and transformer T6 is implemented as a fixed tap transformer with tap ratio same as that of transformer T5.

It is observed that the constant power load stabilizes at a lower value as compared to constant impedance and constant power load because of its load restoring characteristics (Nguyen 2008). That means constant power load tries to consume the same power at a pre-disturbance level as consumed power is independent of voltage variations and hence the voltage drops even further. The dynamics of voltage profile obtained is comparable to the similar case study performed in Ph.D. thesis (Nguyen 2008) using PSS/E software.

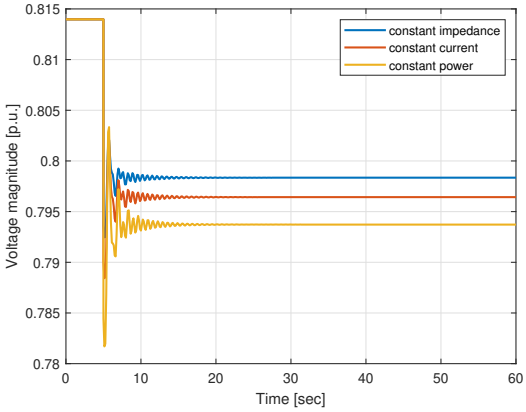

Figure 11. Voltage profile at bus 11 for different load types.

5 Temperature visualization

The temperature development in the stator and rotor windings of the synchronous generator was also observed in the same tool by using the thermal model as described in (Øyvang 2018). This is shown in Figure 13. Figure 12 shows the thermal model implemented in Simulink software environment. The output temperatures as seen in the figure is the result of input field current and armature current taken from the local generator G3 in Kundur 10-bus system when replaced by 103 MVA hydrogenerator at 'Åb-

jøra' in Norway. The machine data of hydrogenerator is provided in Table 6. The field and the stator currents in real time are observable in the tool. The initial temperature in the stator and rotor was taken as 28°C during the simulation.

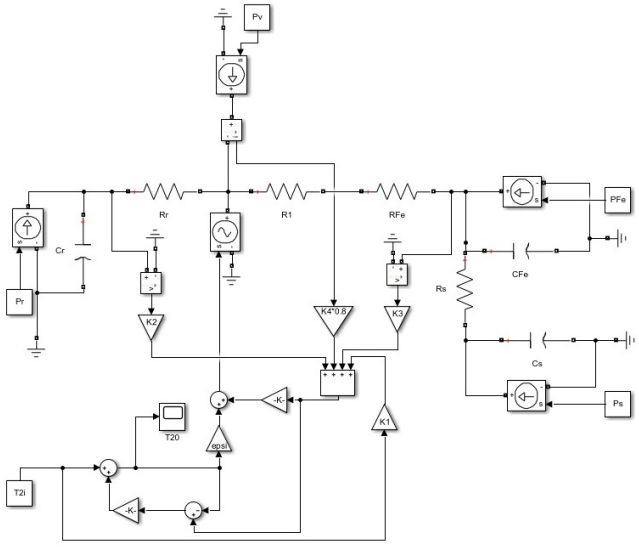

Figure 12. Simulink circuit for the thermal model proposed in (Øyvang 2018)

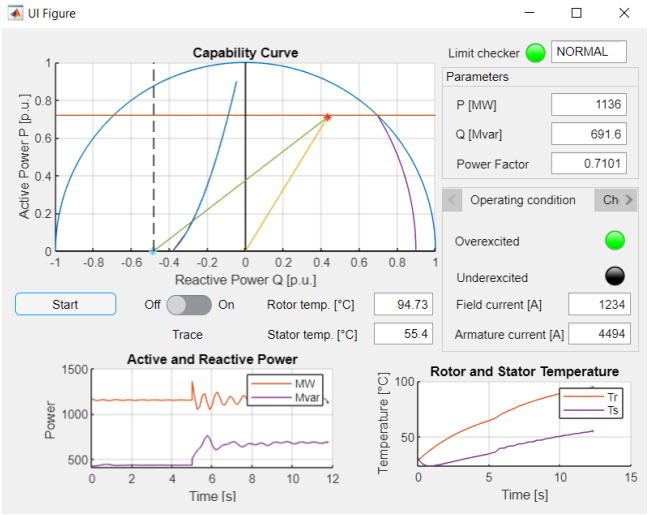

Figure 13. Temperature observation in the visualization tool.

6 Conclusion and further work

This paper proposes a visualization tool for the online monitoring and visualization of a generator's capability. The tool was developed using a MATLAB software environment with the help of Graphical User Interface which provides the user interaction with the visualization tool through graphical displays, inputs, and visual indicators. The tool provides power factor, active and reactive power in real-time along with an alarm signal in the case of limit violation. For the validation of the tool, a simulation regarding a long term voltage stability analysis is carried out and the dynamics involved are shown in the same tool.

Furthermore, the effect of ULTC, overexcitation limiter and the static loads on the voltage collapse scenario is presented in this paper. The severity of effect depends upon the type of load.

Future work will focus on the implementation of additional characteristics in the tool such as stator end region heating limit, the temperature dependence of the generator limits and the variable terminal voltage. In addition, the effect of dynamic load characteristics which has a significant influence on voltage stability can be analyzed further.

References

CIGRE Task Force 38.02.08. *Long Term Dynamics Phase II*. Tech. rep. CIGRE, 1995.

CIGRE Task Force 38.02.10 . *Modelling of Voltage Collapse Including Dynamic Phenomena*. Tech. rep., 1993.

J. Dragosavac et al. On-line Estimation of Available Generator Reactive Power for Network Voltage Support. In *8th Mediterranean Conference on Power Generation, Transmission, Distribution and Energy Conversion (MEDPOWER 2012)*. Institution of Engineering and Technology. DOI: 10.1049/cp.2012.2014, 2012

I. Ili et al. Methodology for Determining the Actual PQ Diagram of a Hydrogenerator. In *Journal of Energy* 56.2, pp. 144–181. URL: https://hrcak.srce.hr/13153, 2007

Prabha Kundur. *Power System Stability and Control*. McGraw-Hill, Inc., 1994.

Jan Machowski, Janusz W. Bialek, and James R. Bumby. *Power System Dynamics : Stability and Control*. 2nd ed., John Wiley & Sons Ltd, 2008.

MATLAB App Designer. URL: https://se.mathworks.com/products/matlab/app-designer.html (visited on 03/22/2019), 2019.

Dang Toan Nguyen. Contributions to analysis and prevention of power system blackouts. Theses. Institut National Polytechnique de Grenoble - INPG. URL: https://tel.archives-ouvertes.fr/tel-00352414, Nov. 2008.

Thomas Øyvang. Enhanced power capability of generator units for increased operational security. PhD thesis, 2018.

Dejan Pejovski, Bodan Velkovski, and Krste Najdenkoski. MATLAB Model for Visualization of PQ diagram of a Synchronous Generator. URL: https://www.researchgate.net/publication/312190893_MATLAB_Model_-for_Visualization_of_PQ_diagram_of_a_Synchronous_Generator, 2016.

M. Vrazic, A. Viskovic, and Z. Hanic. User P-Q Diagram as a Part of a Synchronous Generator Monitoring System. *Electronics and Electrical Engineering,* 20(4). DOI: 10.5755/j01.eee.20.4. 5333.

J. H. Walker. Operating characteristics of salient-pole machines. In: *Proceedings of the IEE -Part II: Power Engineering* 100.73, pages 13–24. DOI: 10.1049/pi-2.1953.0004, Feb. 1953.

A Data for Test System

S_{base} = 100 MVA

Table 1. Bus Data

Bus No	*Base [kV]*	$V_{scheduled}$ *[p.u.]*	*Phase [rad]*	Q_{shunt} *[Mvar]*	P_{load} *[MW]*	Q_{load} *[Mvar]*
1	13.8	0.98	0	0	0	0
2	13.8	0.96	0	0	0	0
3	13.8	1.04	0	0	0	0
5	500	1.00	0	0	0	0
6	500	1.00	0	0	0	0
7	500	1.00	0	750	0	0
8	13.8	0.94	0	1500	3000	1800
9	115	0.95	0	300	0	0
10	115	0.89	0	0	30	0
11	13.8	0.91	0	0	3100	90

Table 2. Generators load flow data

Bus No	*Gen Name*	*Base [kV]*	P_{gen} *[MW]*	Q_{gen} *[Mvar]*	S_{base} *[MVA]*	Q_{max} *[Mvar]*	Q_{min} *[Mvar]*
1	G1	13.8	3471.9	1129.03	5000	1600	-1000
2	G2	13.8	1736	712.53	2200	725	200
3	G3	13.8	1154	414.58	1600	700	-100

Table 3. Transmission lines data

From Bus	*To Bus*	*R [p.u.]*	*X [p.u.]*	*B [p.u.]*
5	6	0.0000	0.0040	0.0000
6	7	0.0015	0.0288	1.1730
9	10	0.0010	0.0030	0.0000

Table 4. Transformers data

Transformer	*R [p.u.]*	*X [p.u.]*	*Tap ratio*
T1	0.0000	0.0020	0.8857
T2	0.0000	0.0045	0.8857
T3	0.0000	0.0125	0.9024
T4	0.0000	0.0030	1.0664
T5	0.0000	0.0026	1.0800
T6	0.0000	0.0010	0.9750

Machine parameters:
Machine 1: Infinite bus
Machine 2: H = 2.09, MVA rating = 2200 MVA
Machine 3: H = 2.33, MVA rating = 1400 MVA

Following are the parameters for machine 2 and machine 3 on their respective MVA ratings:

Table 5. Thermal model data

Parameters	*Symbol*	*Value*	*Unit*
Thermal resistance, $T_{Fe} - T_{\delta}$	R_{Fe}	0.07	K/kW
Thermal resistance, $T_s - T_{Fe}$	R_s	0.05	K/kW
Thermal resistance, air	R_1	0.018	K/kW
Gain coefficient, $T_{2,i}$	K1	0.59	-
Gain coefficient rotor(Cu)	K2	0.5	-
Gain coefficient stator(Fe)	K3	0.36	-
Heat exchanger effieicency (epsi)	ε	0.595	-

Table 6. Machine data of Åbjøra (Øyvang 2018)

Description	*Parameters*	*Value*	*Unit*
Rated power	S_n	103	MVA
Rated voltage	V_{tn}	11	kV
Rated current	I_{tn}	5406	A
Rated field current	I_{fdn}	1064	A
Inertia constant	H	2.66	s
Number of polepairs	p	6	-
Synchronous reactance d-axis	x_d	1.09	[p.u.]
Synchronous reactance q-axis	x_q	0.67	[p.u.]
Transient reactance d-axis	x'_d	0.24	[p.u.]
Subtransient reactance d-axis	x''_d	0.15	[p.u.]
Subtransient reactance q-axis	x''_q	0.19	[p.u.]
Transient OC Time constant d-axis	T'_{do}	10	s
Transient OC Time constant q-axis	T'_{qo}	0.23	s
Subtransient OC Time constant d-axis	T''_{do}	0.086	s
Subransient OC Time constant q-axis	T''_{qo}	0.23	s
Stator leakage inductance	X_l	0.08	[p.u.]
Stator resistance	R_a	0.00182	[p.u.]

$$R_a = 0.0046 \quad X_d = 2.07 \quad X_q = 1.99$$
$$X_l = 0.155 \quad X'_d = 0.28 \quad X'_q = 0.49$$
$$X''_d = 0.215 \quad X''_q = 0.215$$
$$T'_{do} = 4.10 \quad T'_{qo} = 0.56$$
$$T''_{do} = 0.033 \quad T''_{qo} = 0.062$$

Exciters:
Both machine 2 and machine 3 uses thyristor exciters with a gain of 100 and the time delay of the measurement system as 0.02 seconds.

Overexcitation limiter for machine 3:
The OXL model used in the simulation is as described in Section 4.2 with integrator time constant (T_0)= 60 seconds, maximum field current i_{fd}^{lim}= 11.7 p.u. and maximum output signal $v_{OXL}^{\max}$= 5.02 p.u.

ULTC data for transformer T6 between bus 10 and bus 11:
Deadband: ± 1 % p.u. bus voltage
Tap range: ± 16 steps
Step size: 5/8 % (=0.00625 p.u.)

Current Use of Lighting Simulation Tools in Sweden

Anahita Davoodi[1] Peter Johansson[1] Thorbjörn Laike[2] Myriam Aries[1]

[1]Department of Construction Engineering and Lighting Science, Jönköping University, Sweden
[2]Department of Architecture and Built Environment, Environmental Psychology, Lund University, Lund, Sweden
Corresponding author Email: Anahita.davoodi@ju.se

Abstract

This paper presents the findings of a web-based survey on the current use of lighting simulation tools in Sweden. The objective was to understand which lighting simulation tools are currently used in Sweden and to understand the design practitioners' needs for future software development. The results showed that lighting simulation programs are widely used in Sweden. However, the respondents paid less attention to daylight than to artificial light. The respondents' principal training methods were university courses and self-study. Interior illuminance values, glare indexes, and the daylight factor were the most commonly calculated simulation outputs. "Ease of use" and "accuracy" were identified as the most important factors in the use of the software, while "the slowness of simulation processes" causes the most dissatisfaction. Dialux was the most popular software program used.

Keywords: lighting simulation tools, simulation programs, lighting design, Dialux

1 Introduction

Good lighting quality is one of the essential values that buildings provide. The effect of daylight on saving energy, occupant well-being, and productivity is demonstrated in various studies (Veitch and Newsham ,1997; Bodart and De Herde, 2002; Krarti *et al.*, 2005; Reinhart *et al.*, 2006; Aries and Newsham, 2008; Borisuit *et al.*, 2015; Yu and Su, 2015; Arif *et al.*, 2016; Tonello *et al.*, 2019). In addition, the right balance between daylighting and artificial lighting is necessary for providing good lighting (Boyce 2014).

Lighting simulation tools help designers to analyze different aspects of lighting quality and assess alternatives design solutions (Reinhart and Fitz, 2006). Using these tools provides a great opportunity to improve the quality of lighting in indoor environments as well as to save energy. Their applications and functions are growing rapidly, and currently more lighting designers, engineers, and architects increasingly tend to use these tools (Hien *et al.*, 2000; Reinhart and Fitz, 2006)

This survey investigated the current use of lighting simulation tools in Sweden. The aim of the survey was to understand which lighting design tools are currently used, and to understand the design practitioners' needs for future software development. The target audience was lighting designers, architects, engineers, and researchers who work in interior lighting design.

1.1 Previous studies

Reinhart and Fitz (2006) reviewed previous surveys on the use of lighting simulation tools covering the period from 1985 to 2002 and followed on with a web-based survey focused solely on the use of daylight simulation tools. The goals of the paper were to identify the most popular daylighting design tools, the top metrics measured and to investigate how these metrics influenced design decisions. They received responses from 193 participants from 27 countries. More than 50% of the simulation software used by the participants was based on Radiance (Larson, Shakespeare et al. 1998). Daylight factor and illuminance level were the most measured metric, and type and control of shading devices were the design aspect most influenced by the simulation results.

A paper authored by Attia et al. (2012) reviewed current trends in building simulation and outlined the major criteria for selection and evaluation of building performance simulation (BPS) tools, based on analyzing user's needs for tools capabilities and requirement specifications. The main criteria suggested for software evaluation included: usability and information management (UIM), integration of intelligent design knowledgebase (IIKB), accuracy of tools and ability to simulate detailed and complex building components (AADCC), interoperability of building modeling (IBM), and integration with building design process (IBDP). Four hundred and forty-five architects and 453 engineers responded to the survey, providing a snapshot of the preference for and current use of the ten BPS tools. The results of the survey confirmed the previous findings of architects' preference for better UIM of BPS interfaces (Attia 2009; Holm 1993; Mahdavi, 2003; Punjabi 2005; Van Dijk 2002). On the contrary, the engineers' top BPS tool selection criterion was the AADCC. The authors concluded that development of the next generation of BPS tools had to be directed within the gestalt of UIM interface, IIKB, AADCC, IBM, and IBDP (Attia *et al.*, 2012).

A state of the art literature review in lighting simulation for building science was conducted by

(Ochoa *et al.*, 2012). The study explored main aspects of a program (input, modelling, and output) and concluded that lighting simulation for building science has advanced rapidly within two decades. Aspects that have experienced development were: accuracy, number of parameters to calculate, computational times, scenario complexity and connection to whole building simulation. Radiance remains a widely accepted general purpose simulation engine.

2 Method

The method and questionnaire for the survey by Reinhart and Fitz (2006) was used as a base for this survey. The major differences were that this survey was geographically limited to Sweden with a special focus on lighting designers. In addition, the domain was extended beyond daylight to include electrical light.

2.1 Participants selection

For convenience and ease of reach, this survey was conducted remotely via an online surveying service from October 27 to December 8, 2014. Two resources were used to identify lighting designers: the first resource was the list of graduates from Lighting Design program at Jönköping University (Sweden), which accounted for about 43% of participants (N=54). The remaining (N=81) lighting designers were identified from the list of registered companies in the Ljuskultur database (www.ljuskultur.se), the magazine for lighting designers in Sweden. In total, emails were sent to 135 people to invite them to participate, out of which 15 emails were not delivered. One of the participants forwarded the questionnaire to four other lighting designers, so the target audience was 124 designers in total. Nine people responded saying they do not work in the area (anymore). Five people declined to participate. Thirty-one people took part and filled out the questionnaires, which was 28% of our target audience.

According to the Ljuskultur database, there are 75 registered companies in the lighting design field. Since the questionnaire spread over 25 unique companies, the results of this survey represent one-third of the Swedish lighting design companies.

2.2 Questionnaire procedure

The creation and administration of the questionnaire were done with Survey Gizmo (www.surveygizmo.com). The questionnaire contained four types of questions: multiple choice multiple selection (check box), multiple choice single selection (radio button), prioritizable selection list (Drag & Drop Ranking question), and open question (free text). Some of the multiple-choice questions had an additional textbox for custom input or clarification of answers. It was possible to leave some questions unanswered.

A draft version of the questionnaire was tested for clarity and integrity by lighting expert colleagues at Jönköping University. The questionnaire was revised according to the comments and feedback and approved for final distribution.

The questionnaire began with a welcome page and a short description of the survey. The first section collected the background information of the participants: age, gender, education, profession, and types of companies in which they worked and for how long. The second and third sections were dedicated to daylighting and electric light, respectively. There were two branching questions in each section and a final open-ended question as outlined below:

1. Do you consider daylighting/electric lighting in your design?
    a. If yes, answer more detailed questions
    b. If no, go to 3
2. Do you use simulation tools in your design?
    a. If yes, answer more questions about simulation tools and their pros and cons
    b. If no, why not?
3. Open-ended question:
    a. For daylighting section: “Do you think the use of daylight should be increased? If so, how?”
    b. For electric lighting section: “What do you think is the most important item to do to create better electric lighting design?”

Depending on the answers given, the questionnaire varied in length from 11 to 36 questions.

3 Results

3.1 Participants' background

The survey results on the participants' background showed that 46% of them were 25 to 34 years old and 35% were 35 to 54 years old; two-third of the participants were men. In terms of education, 55% had a bachelor's degree and 29% had a post-graduate degree (Figure 1.).

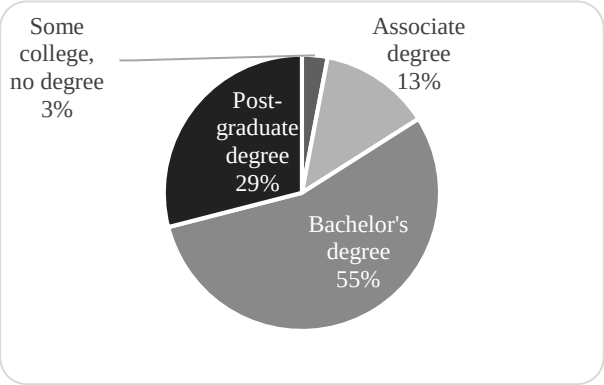

Figure 1. Participant´s education

As expected, most of the participants (85%) identified themselves as a lighting designer. In addition, there were two lighting consultants, an engineer, a technical manager, and outdoor lighting designer among the participants (Figure 2.)

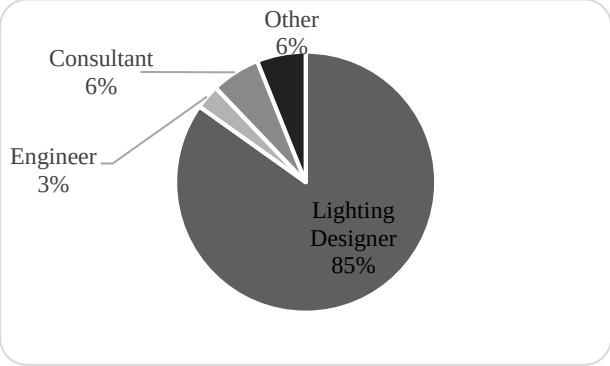

Figure 2. Participant´s profession

Forty-three percent of the participants had more than 10 years of work experience in lighting design, 30% had 3–5 years, and 17% had 5–10 years. Only three respondents had less than two years of work experience. The majority of participants (87%) said that they worked in a lighting design company. However, they also added other fields to their company's area of operation including luminaire manufacturing/trade, construction, infrastructure and urban design and planning, landscape architecture, environmental consulting, electrical design, heating ventilating/ventilation and air conditioning (HVAC) design, and telecommunications.

The participants were from companies of varying sizes: 23% of the people were from companies with 1–19 employees, 27% with 20–99, 13% with 100–499, 23% with 500–100,000, and 13% with 10,000+ employees.

3.2 Daylight

The aim of the daylight section was to investigate how and to what extent lighting designers considered aspects of daylight in their design. Twenty (65%) of the 31 individuals who completed the survey, said that they take daylighting into account in their designs.

Out of those who considered daylighting, 85% (17) used daylight simulation tools. The 15% who did not simulate daylight, mentioned two reasons for this: either their clients were not willing to pay for the service or the tools were not reliable. This group used their experience combined with lookup tables for estimating and calculating daylight metrics during the schematic design and design development phases.

The 17 participants who used simulation tools were asked to specify the primary simulation tool they were using. They could choose one item out of ten popular programs or enter a custom program name. As shown in Figure 3., Dialux was by far the most popular software, followed by Diva (12%), Relux (12%), and Ecotect/Radiance (6%).

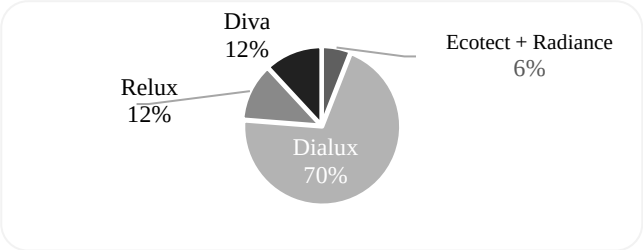

Figure 3. Software selection

The lighting designers then selected the type of outputs they calculated using simulation tools. They could choose from several predefined options and could append additional comments. The overall majority (88%) of designers calculated interior illuminance. Glare indices came second. Daylight factor and interior luminance were calculated with the same frequency at the third place. One person also mentioned the calculation of exposure time to UV. Figure 4. illustrates the answers.

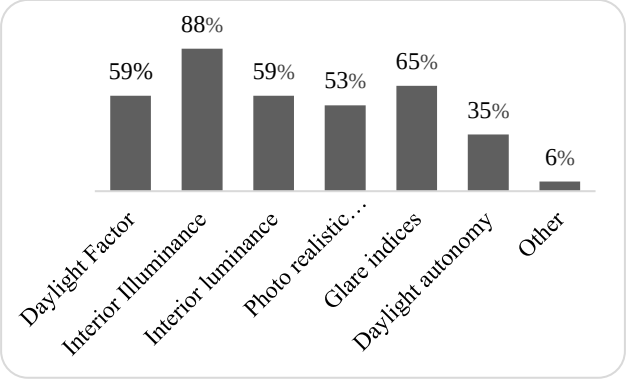

Figure 4. Type of outputs calculated using software

The next set of results was about the stages(s) of the lighting design process in which simulation tools were employed. The participants could choose among the following alternatives: schematic design, design development, detailed design, and others. Answers indicated that the use of simulation tools were highest during the design development stage (34%); however, a number of comments highlighted the importance using the simulation tools in all stages of the design. The choices for which of the eight design aspects most influenced daylighting analysis were weighted based on how the respondents had prioritized them (number of options minus the rank in the selection). The score computed for each answer option is the sum of all the weighted values. The results showed that "*size of windows*", "*room dimensions*", and "*building orientation*" were influenced the most by daylighting analysis. The results for how participants had learned to work with the software tools showed that 65% had university training, 53% trained themselves, and 18% were trained at a company (respondents could select more than one training method).

The results on the advantages of the simulation programs (including ease of use, accuracy, performance, simulation speed, sufficient program documentation, other) are shown in Figure 5. One designer expressed his/her satisfaction with the ability to reuse models from other disciplines by importing them into the chosen program.

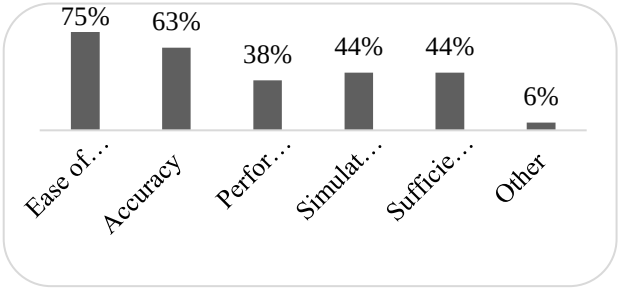

Figure 5. Advantages of simulation programs

Regarding disadvantages of simulation tools, one concerned poor quality of rendering and another concerned the incompatibility of Dialux with Mac OS. program. The results on the Disadvantages of the simulation programs (including slowness, inaccuracy complexity, insufficient documentation, performance problems, and other) are shown in Figure 6.

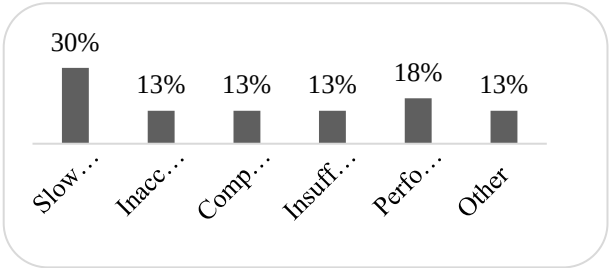

Figure 6. Disadvantages of simulation programs

Finally, eight participants said they used additional software for daylighting analysis. The secondary software programs were: 3DS max (+mental ray), DAYSIM, Ecotect, Ecotect + DAYSIM, Photoshop, andAGI32. One of the participants added a tertiary software, Velux Daylight Visualizer.

3.3 Electric light

The results for the section on electric light show that all the participants except one (97%) did consider electrical lighting. Of those who considered it, the majority (93%) used a simulation tool in their design process. One participant did not use any simulation tools because his/her clients were not willing to pay for the extra service. Another did not find simulation tools reliable. These two designed based on their knowledge and experience.

The17 participants who considered both daylighting and electrical lighting in their design were asked if they were using the same tools for both tasks. Seventy percent of them responded yes. Dialux stood out being 86% of participants' top choice. The type of outputs generated by designers using these tools are shown in Figure 7.

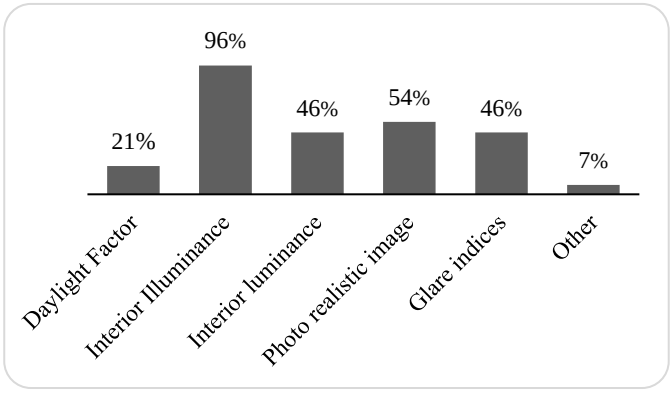

Figure 7. Type of outputs calculated by simulation tools

A comparison between the outputs generated for daylighting and electrical lighting is illustrated in Figure 8. By interpreting the answers, it can be observed that many designers used Dialux for calculating glare indexes produced by daylight. The method that Dialux used to calculate glare is recommended for electric light, but not for daylight (DiLaura, 2011; Jakubiec and Reinhart, 2012).

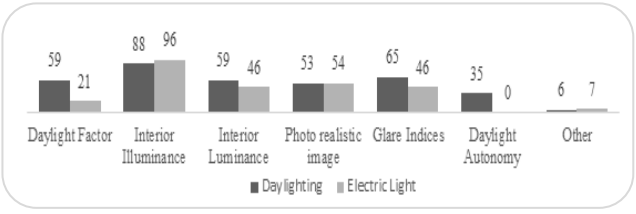

Figure 8. Comparison of outputs generated for daylighting and electric lighting

Similar to that in daylighting design, the use of simulation tools in the electrical lighting design was highest during the design development phase (43%). Some designers stated that they used simulations tools throughout all stages of design.

The results on building design aspects that were influenced by electric lighting analysis revealed that "*placement of fixtures*" was affected more than any other design aspect.

The results on the software training methods (from those who had not already answered the question show that self-training was the dominant training method among participants (91%), followed by university (27%), company (18%), and workshop (18%) training.

Those who had skipped the daylighting section (N=12) were asked about the advantages and disadvantages of the software tools in relation to electrical lighting. There were some complaints regarding the inconsistency of simulation and reality, poor performance, and lack of feature. The view of participants on the advantages of the software (including ease of use, accuracy, performance, simulation speed, sufficient program documentation, other) is illustrated in Figure 9.

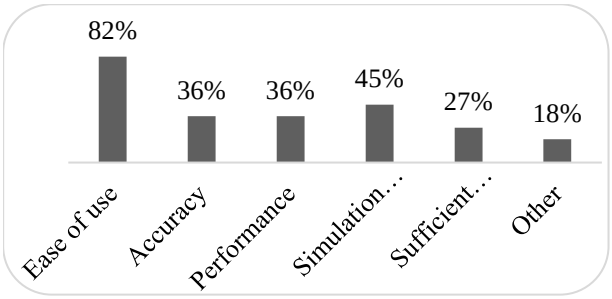

Figure 9. The view of participants on the advantages of the software

Thirty-six percent of the participants said they worked with other simulation programs, and mentioned using 3ds Max, DIAlux (+ evo), Photoshop, RELUX, AGi32, and HIlITE as their secondary software.

3.4 Qualitative Results (Content Analysis)

Fifty-five percent of participants provided answers to the questions, *"Do you think the use of daylight should be increased? If so, how?"* Most of them believe that it should be increased, although one person said "Not necessarily more daylight but the ability to control daylight should be increased in a way that benefits the sense of light (e.g., excessive daylight from uncontrolled large glass windows that let in plenty of natural light can also increase the feeling of darkness in inner spaces farther away from windows.)" [Translated from Swedish]. The answers to the questions were summarized in five categories including organizational, technical development, laws and rule and education of designers.

Forty-eight percent of participants answered the questions, *"What do you think is the most important thing to do to create better electrical lighting design?"* Some of their suggestions were '*better cooperation between different actors in the process'*, '*better use of simulation programs'*, and '*Take the human demands into consideration to a larger extent'.*

4 Discussion

Boundaries of this survey were limited in three aspects: geographically to Sweden, domain-wise to lighting design, and sample size to around 33% of the population of lighting designer's company in Sweden. Therefore, care must be taken when using the results for other studies.

As the results show, the majority of lighting designers tend to consider both daylight and artificial light in their design. Moreover, a high percentage use some type of simulation tools for analysis and/or rendering. Among the different factors mentioned, user friendliness (ease of use), accuracy, and speed, stood out as being key criteria for users' choice of software. Users were also reluctant to work with multiple software tools and preferred a one-size-fits-all type of software. The majority of participants ignored metrics such as daylight glare probability and dynamic daylight performance metrics, which are present only in relatively specialized software programs with relatively complicated user interfaces. If more attention was paid to these key user experience design factors in the development of new software programs or improvement of existing ones, it may result in greater use of the advanced metrics. If (very) specific lighting knowledge is needed to come up with proper results, it must be possible to bypass a sophisticated part of the software. The survey showed that the majority of the lighting designers has a bachelor's degree in lighting design and know about the existence of certain advanced metrics but have no sufficient training in using them. Nonetheless, fixing one issue should not come at the cost of another but an optimal trade-off should be achieved. One such example is sacrificing accuracy for speed. As reported by some designers, low accuracy and reliability were the main reasons why they did not use certain software tools. However, advancements in computer technology will have a positive effect in overcoming issues regarding simulation time.

Participants' comments in the open-ended questions imply that designers need a better understanding of software tools in terms of the features and limitations, accuracy, reliability, and the stage in which these tools should be employed. The results of this survey show that universities were the main training channel, which highlights the important role that universities can play in educating future lighting designers by offering specialized and advanced courses. This is especially true because of the ongoing paradigm shifts in building

modeling from document-based CAD models to objectbased Building Information Modeling (BIM) process. BIM's emphasis on collaboration is in line with collaborative nature of lighting design processes, and the new generation of software applications can provide new methods of design at different levels and stages in an integrated environment. Simulation tools could also be used as an effective educational tool for understanding physical concepts in an interactive environment (Feng 2003, Reinhart, Dogan et al. 2012).

5 Conclusions

The work in this study revealed that lighting simulation programs are widely used in Sweden. The most commonly calculated performance metrics were illuminance values, glare indexes, and the daylight factor. “Ease of use” and “accuracy” were identified as the most important factors in the use of the software, while “slowness of simulations process” causes the most dissatisfaction. Dialux was the most popular software program used.

Acknowledgements

The authors would like to acknowledge the financial support of the Swedish Energy Agency and the Bertil and Britt Svensson Foundation.

References

M. B. C. Aries and G. R. Newsham. Effect of daylight saving time on lighting energy use: A literature review. *Energy Policy*, 36(6): 1858-1866, 2008.

M. Arif, M. Katafygiotou, A. Mazroei, A. Kaushik, and E. Elsarrag. Impact of indoor environmental quality on occupant well-being and comfort: A review of the literature. *International Journal of Sustainable Built Environment*, 5(1): 1-11, 2016.

S. Attia, J. L. Hensen, L. Beltrán and A. De Herde. Selection criteria for building performance simulation tools: contrasting architects' and engineers' needs. *Journal of Building Performance Simulation*, 5(3): 155-169, 2012.

M. Bodart, and A. De Herde. Global energy savings in offices buildings by the use of daylighting. *Energy and Buildings*, 34(5): 421-429, 2002.

A. Borisuit, F. Linhart, J. L. Scartezzini, and M. Münch. Effects of realistic office daylighting and electric lighting conditions on visual comfort, alertness and mood. *Lighting Research and Technology*, 47(2): 192-209, 2015.

P. R. Boyce. *Human factors in lighting*, The Crc Press. 2014.

David DiLaura, Kevin Houser, Richard Mistrick, and Gary Steffy. *The IESNA lighting handbook: reference & ap plication*, Illuminating Engineering, 10 editions, 2011.

J. Feng. *Computer simulation technology and teaching and learning interior lighting design. ACM SIGGRAPH 2003 Educators Program*, ACM, 2003.

W. Hien, N., L. K. Poh, and H. Feriadi. The use of performance-based simulation tools for building design and evaluation-a Singapore perspective. *Building and Environment*, 35(8): 709-736, 2000.

J. A. Jakubiec and C. F. Reinhart. The ‘adaptive zone’–A concept for assessing discomfort glare throughout daylit spaces. *Lighting Research and Technology*, 44(2): 149-170, 2012.

M. Krarti, P. M. Erickson, and T. C. Hillman. A simplified method to estimate energy savings of artificial lighting use from daylighting. *Building and Environment*, 40(6): 747-754, 2005.

G. W.Larson, R. Shakespeare, C. Ehrlich, J. Mardaljevic, E. Phillips, and P. Apian-Bennewitz. *Rendering with radiance: the art and science of lighting visualization*, Morgan Kaufmann San Francisco, CA. 1998.

Morales Ochoa, C. E., M. Aries, and J. Hensen. State of the art in lighting simulation for building science: a literature review. *Journal of Building Performance Simulation*, 5(4): 209, 2012.

C. F. Reinhart and A. Fitz. Findings from a survey on the current use of daylight simulations in building design. *Energy and Buildings*, 38(7): 824-835, 2006.

C. F. Reinhart, T. Dogan, D. Ibarra, and H. W. Samuelson. Learning by playing - teaching energy simulation as a game. *Journal of Building Performance Simulation*, 5(6): 359-368, 2012.

C. F. Reinhart, J. Mardaljevic, and Z. Rogers. Dynamic daylight performance metrics for sustainable building design. *Leukos*, 3(1): 1-25, 2006.

G. Tonello, N. Hernández de Borsetti, H. Borsetti, L. Tereschuk, and S. López Zigarán. Perceived well-being and light-reactive hormones: An exploratory study. *Lighting Research and Technology*, 51(2): 184-205, 2019.

J. A. Veitch and G. R. Newsham. Lighting quality and energyefficiency effects on task performance, mood, health, satisfaction and comfort. In *Illuminating En gineering Society of North America (Iesna) Annual Conference Proceeding* 425-462, 1997.

X. Yu and Y. Su. Daylight availability assessment and its potential energy saving estimation - A literature review. *Renewable and Sustainable Energy Reviews*, 52: 494-503, 2015.

Uncertainty in Hourly Readings from District Heat Billing Meters

Lukas Lundström[1,2] Erik Dahlquist[1]

[1] Mälardalens University, Västerås, Sweden
[2] Eskilstuna Kommunfastighet, Eskilstuna, Sweden
lukas.lundstrom@mdh.se, erik.dahlquist@mdh.se

Abstract

Hourly energy readings from heat billing meters are valuable data source for the energy performance assessment of district heating substations and the buildings they serve. The quality of such analyses is bounded by the accuracy of the hourly readings. Thus, assessing the accuracy of the hourly heat meter readings is a necessary (but often overlooked) first step to ensure qualitative subsequent analyses.

Due to often limited bandwidth capacity hourly readings are quantized before transmission, which can cause severe information loss. In this paper we study 266 Swedish heat meters and assess the quantization effect by information entropy ranking. Further, a detailed comparison is conducted with three heat meters with typically occurring quantization errors. Uncertainty due to the quantization effect is compared with the uncertainty due to typical accuracy of the meter instrumentation. A method to conflate information from both energy readings and energy calculated from flow and temperature readings is developed.

The developed conflation method is shown to be able to decrease uncertainty for heat meters with severely quantized energy readings. However, it is concluded that a preferable approach is to work with the heat meter infrastructure to ensure the future recorded readings holds high enough quality to be useful for energy performance assessments with hourly or subhourly readings.

Keywords: heat meters, uncertainty, district heating, information entropy, EN 1434

Nonmenclature

Symbols	
Q	Energy/heat [kWh/h]
V	Volumetric flow rate [m^3/h]
θ	Temperature [°C]
$\Delta\theta$	Temperature difference [°C]
H	Information entropy [bits/sample]
c	Heat capacity [MJ/(K·m3)]
Δ	Quantization step size
L	Number of quantization levels
σ	Standard deviation
Subscripts	
0,1,2	Conflated, energy reading, calculated from flow and temperature readings
p	Permanent/nominal approved flow
i	Inferior/minimum approved flow
qe	Quantization error
met	Meter instrumentation error
f	Flow meter
t	Temperature sensor pair

1 Introduction

Many district heating operators gather hourly values to centralized databases from their heat billing meters (Gadd and Werner, 2015; Sandin et al., 2013). These hourly readings are a valuable information source for fault detection and energy performance assessment of the district heating substations and the buildings they serve (Gadd and Werner, 2015; Mansson et al., 2019; Sandin et al., 2013). In Sweden, district heating operators are required to share daily meter readings to their customers (EIFS 2014:2), while hourly values only must be provided if these are used for billing. Readings typically available in heat meter data management systems are hourly averages of energy and flow and hourly instantaneous samples of the primary side supply and return temperatures (Sandin et al., 2013). Because of bandwidth constraints, only a finite number of bits are available and recorded values are therefore quantized before transmission. Quantization can cause increased uncertainty, especially when the recorded value needs to be able to represent a large value range (e.g. cumulative values). Therefore, hourly values transmitted from the heat meters can have quantization error that is much larger than the accuracy of the measurement equipment. Such large quantization errors can severely deteriorate the quality of subsequent analyses.

In this paper we study 266 Swedish heat meters and assess the quantization effect by information entropy ranking (Section 2.1). Further, a detailed comparison is conducted with three heat meters. Uncertainty due to the quantization effect is compared with the uncertainty

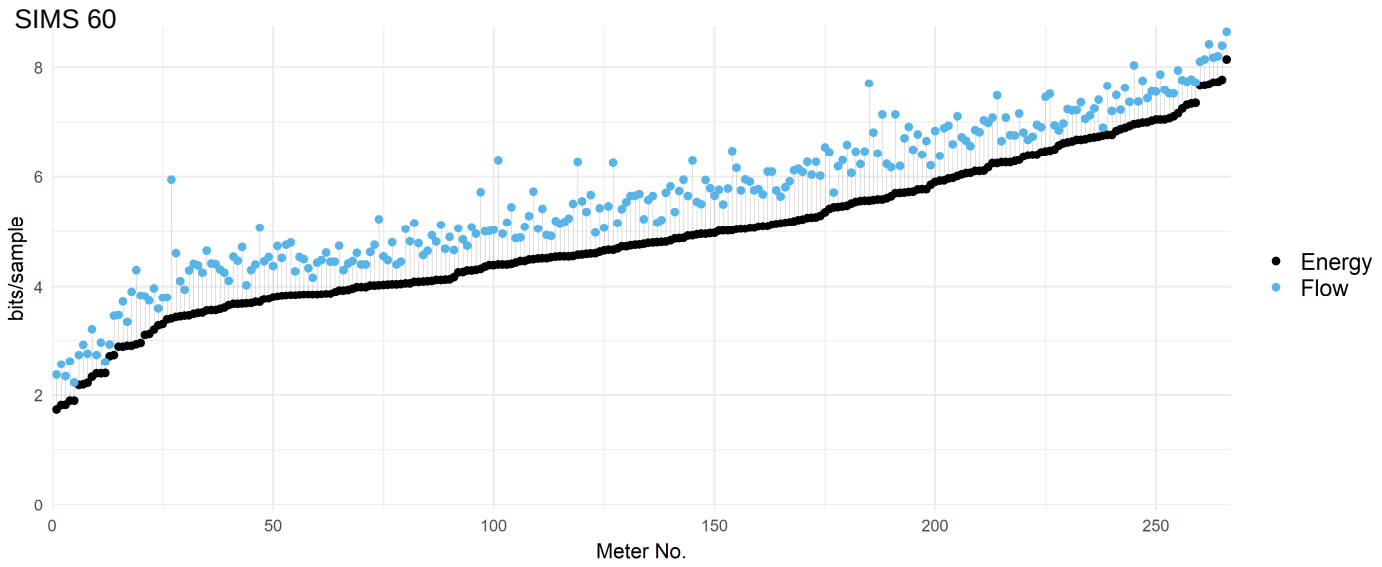

Figure 1. Entropy ranking of hourly energy and flow readings from 266 heat meters.

due to typical accuracy of the meter instrumentation (Section 2.2). A method to conflate information from both energy readings and energy calculated from flow and temperature readings is developed (Section 2.3-2.4).

2 Material and methods

Material consist of data from 266 district heating billing meters, serving multifamily buildings located in Eskilstuna, Sweden. Most of the heat meters are Kamstrup Multical 601 / 602 calculators equipped with Kamstrup Ultraflow 54 / 34 ultra sonic flow meters.

2.1 Information entropy

Sandin et al. (2013) suggested using information entropy ranking as a way of identifying heat meter readings with large quantization errors. Information entropy is defined as the sum of the negative binary logarithm log (·) of the probabilities p(·) for each value in the time series of length :

$$H = -\sum_{k=1}^{n} \mathrm{p}(x_k) \cdot \log_2\big(\mathrm{p}(x_k)\big) \qquad (1)$$

Two to the power of the entropy indicates the number of quantization levels (L) available in the meter readings: $\propto 2$ (provided that the observation period holds rich enough operation conditions). For example, H = 8 would indicate 256 levels and H = 4 would indicate 16 levels. However, information entropy depends on the actual operation conditions such as weather and the probability of an observation to occur (i.e. meters repeating same observation quantities, due design or even weather conditions, will get a lower information entropy value). Therefore, the 2 estimate, will generally result in fewer levels than what is available due to the meter configuration. Figure 1 shows the 266 heat meters ranked by their calculated entropy for energy readings and flow readings.

2.2 Uncertainty of the energy readings of the heat meter

The energy reading at time index k is denoted as $Q_{1;k}$. The time-varying uncertainty of the energy readings is estimated as

$$\sigma_{1;k} = \sqrt{\sigma_{met;k}^2 + \frac{\Delta_Q^2}{12}} \qquad (2)$$

where $\sigma_{met;k}$ is the standard deviation (SD) at time index *k* due to uncertainty of the meter equipment and Δ_Q denotes the quantization step size of the energy readings (i.e. the largest unit of measure, typically 1, 10 or 100 kWh). The $\Delta_Q^2/12$ is a commonly used approximation of the variance for the quantization effect used for noise modelling (Marco and Neuhoff, 2005).

The uncertainty calculations of the meter equipment is adopted from the European Standard EN 1434-1:2015:

$$\sigma_{met;k} = \sqrt{\sigma_{f;k}^2 + \sigma_{t;k}^2} \qquad (3)$$

where $\sigma_{f;k}$ is the standard deviations of the flow meter at time index *k* and $\sigma_{t;k}$ is the standard deviation of the temperature sensor pair and the calculator (where the temperature sensor pair is the dominating error source). Typical accuracy of Multical heat meters equipped with Ultraflow flow sensors (Kamstrup A/S, 2018) is used

$$\sigma_{f;k} = \begin{cases} Q_{1;k}(1 + 0.01V_p/V_k)/100, & if\ V_k > V_i \\ \Delta\theta_{1;k} V_i c(1 + 0.01V_p/V_i)/100, & if\ V_k \le V_i \end{cases} \qquad (4)$$

$$\sigma_{t;k} = \begin{cases} Q_{1;k}(0.6 + 6/\Delta\theta_{1;k})/100, & if\ \Delta\theta_{1;k} > 2 \\ 2V_k c(0.6 + 6/2)/100, & if\ \Delta\theta_{1;k} \le 2 \end{cases} \qquad (5)$$

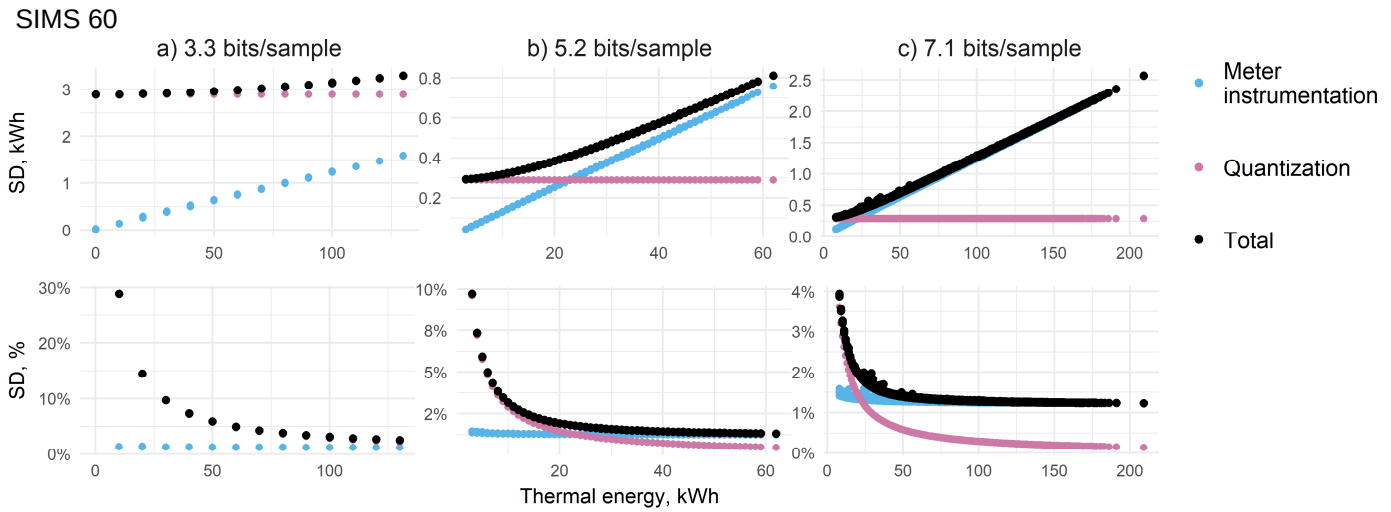

Figure 2. Uncertainty of hourly energy readings due to meter instrumentation accuracy and quantization effects for three example substations. Information entropy of the hourly energy readings are given in the subtitles.

where $Q_{1;k}$ [kWh] is the energy reading at time step *k* (accumulated heat use between *k-1* to *k*), V_k [m³/h] is the flow rate reading at time step *k* (flow rate between *k-1* to *k*), V_p is the permanent nominal flow rate , V_i is the inferior flow rate (where the meter shall function without exceeding the allowed accuracy), *c* is the heat capacity of the fluids (assumed as a constant of 4.12 MJ/(K·m³) (OIML R 75-1, 2002)), and $\Delta\theta_{1;k}$ is the average temperature difference between fluids calculated as

$$\Delta\theta_{1;k} = Q_{1;k}/(V_k c) \tag{6}$$

2.3 Energy calculated from flow and temperature readings

The quantization error of flow readings is generally lower than for the energy readings, especially during operation conditions when the temperature difference is low (see visualization in Figure 3). Therefore, in case of large quantization errors, it can be more accurate to estimated energy use from flow and temperature readings:

$$Q_{2;k} = c \cdot \Delta\theta_{2;k} V_k \tag{7}$$

$$Q_{2;k} = \max(Q_{1;k} - \Delta_Q, min(Q_{1;k} + \Delta_Q, Q_{2;k})) \tag{8}$$

where $\Delta\theta_{2;k}$ denotes the temperature difference estimated from the temperature readings. Due to the instantaneous nature of the temperature readings, the $\Delta\theta_{2;k}$ approximation can deviate much from the true average temperature difference. While, Eq. (6) can be assumed to calculate the true average $\Delta\theta$ when the quantization error is negligible.

Following equations are suggested to estimate the time-varying standard deviation for the energy use Q_2:

$$\sigma_{2;k} = \sqrt{\left(\sigma_{2;t;k}\right)^2 + \left(\sigma_{2;qe;k}\right)^2 + \left(\sigma_{met;k}\right)^2} \tag{9}$$

where $\sigma_{2;t;k}$ denotes the uncertainty due to instantaneous nature of the temperature readings and $\sigma_{2;qe;k}$ denotes the quantization error due to low resolution in the flow readings (see Eg (11)).

$$\sigma_{2;t;k} = Q_p/200 + 0.02 \cdot Q_{2;k} \tag{10}$$

$$\sigma_{2;qe;k} = \frac{\Delta\theta_{2;k}\Delta_V c}{\sqrt{12}} \tag{11}$$

where Q_p denotes the energy at nominal flow and Δ_V is the width of the quantization step size of the flow readings.

2.4 Conflation

The two energy variables Q_1 and Q_2 are not fully independent as they are derived from the same metering equipment. Therefore, the two quantities are weighted as two dependent normal variables (Winkler, 1981)

$$Q_0 = \frac{(\sigma_2^2 - \rho\sigma_1\sigma_2)Q_1 + (\sigma_1^2 - \rho\sigma_1\sigma_2)Q_2}{\sigma_1^2 + \sigma_2^2 - 2\rho\sigma_1\sigma_2} \tag{12}$$

$$\sigma_0^2 = \frac{(1-\rho^2)\sigma_1^2\sigma_2^2}{\sigma_1^2 + \sigma_2^2 - 2\rho\sigma_1\sigma_2} \tag{13}$$

where ρ denotes the correlation, which is assumed as $\rho = 0.5 \cdot \min(\sigma_1, \sigma_2)/\max(\sigma_1, \sigma_2)$. The practical impact of assuming a dependency between the variables is a more conservative conflated estimate (both on mean and uncertainty interval) than if the variables would be assumed fully independent.

3 Results

Figure 2 shows the estimated uncertainty of hourly energy readings due to meter instrumentation accuracy and quantization effects. For the heat meter (a) the quantization error is a much larger uncertainty source than the meter instrumentation accuracy – the quantization causes severe information loss. For heat

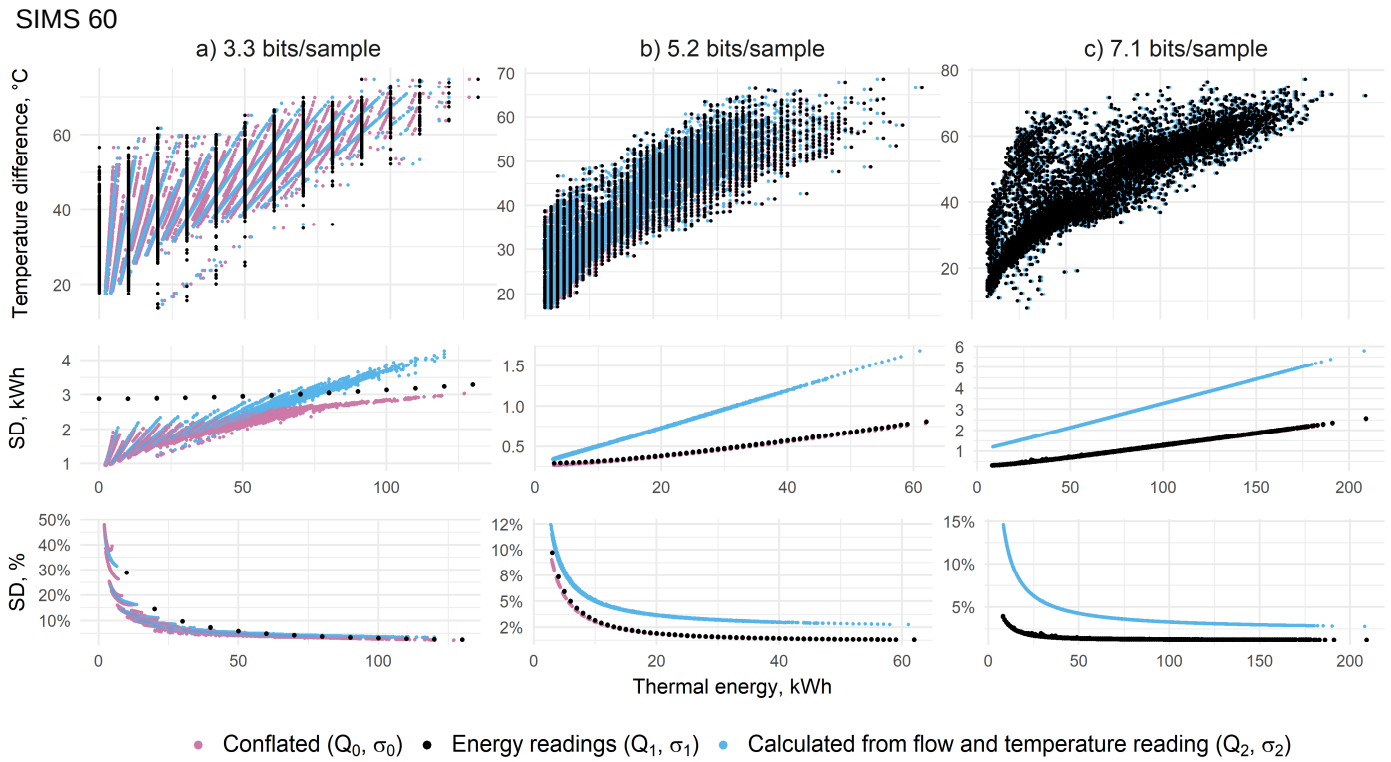

Figure 3. Three example heat meters (columns a, b and c) visualizing the impact of typically occurring quantization errors. Entropy of the hourly energy readings are given in the subtitles. Upper row: energy vs temperature difference between supply and return flows. Bottom row: energy vs standard deviation.

meter (b), the quantization does contribute to increased uncertainty, especially during low energy use conditions. For heat meter (c), the quantization only has effect during very low energy use conditions.

Figure 3 shows hourly energy readings with standard deviation for three example substations. As can be seen in the figure, the uncertainty of the calculated energy quantity (blue dots) dominates under most conditions (due to the high uncertainty in that the instantaneous temperature readings represent the average temperature difference for the whole integration step). However, when the quantization error is large, as in substation (a), the calculated energy quantity is a better estimate than the energy readings (black dots), especially during low energy use conditions. The conflated variable (purple dots) is a weighted estimate that weights the two variables according to their empirically estimated time-varying uncertainties.

4 Discussion

The information entropy ranking method, suggested by Sandin et al. (2013), is suitable for identifying meters with large quantization errors. The method is straightforward to conduct as the only required input are the readings themselves. However, it is dependent on the actual operation conditions, which makes it less suitable to compare meter readings from different time periods or different district heat operators.

There is no explicit regulation regarding the accuracy of the recorded energy readings. Flow meters have a maximum allowed error (1.96σ) of 5 % at $0.1 \cdot 3_4$ (SWEDAC, 2007) and district heat operators are required to provide their customer with daily energy readings (EIFS 2014:2). Using a 5 % error limit also for the quantization effect on daily energy readings would mean that hourly energy readings still could have entropy values as low as approximately 2.8-3.0 bits/sample.

The next generation of heat meters and data acquisition infrastructure (Kamstrup A/S, 2018) can provide data with higher resolution. However, it will take many years before all current infrastructure is upgraded. Therefore, the suggested conflation method can play a role in improving hourly readings for many years to come.

The proposed conflation method assumes normal distributions. The quantization error is however uniform and can also be biased (Marco and Neuhoff, 2005). The used additive noise approximation(Δ /12)is only valid if Δ is small compared to the quantization levels . Therefore, the proposed method is likely to have some discrepancies and can still be improved. The empirical uncertainty models, equations (4), (5) and (10), are however likely to be a larger error sources than the conflation method or the additive noise approximation. Notwithstanding, the proposed conflated energy quantity $_C$can be anticipated to be closer to the true mean values and have a tighter distribution than and would by themselves.

5 Conclusions

District heat operators should aim at information entropy at minimum of 5 bits/sample (approximately 32 observable quantization levels in a typical year) to ensure qualitative hourly readings.

To ensure high quality readings for the whole metering range and enable sub-hourly sampling, at least 7 bits per hourly sample information entropy is required.

For energy readings with entropy less than approximately 5 bits/sample, the suggested conflation method can counteract part of the quantization error by merging information from the flow and the instantaneous temperature readings, especially during low energy use conditions.

Acknowledgements

The work has been carried out under the auspices of the industrial post-graduate school Reesbe, and was funded by Eskilstuna Kommunfastigheter, Eskilstuna Energy and Environment, and the Knowledge Foundation (KK-stiftelsen).

References

EIFS 2014:2. *Energimarknadsinspektionens författningssamling*, Swedish Energy Markets Inspectorate regulatory code. EIFS, 2014.

EN 1434-1:2015. *Heat Meters - Part 1. European Standards*, Geneva, Switzerland, 2015.

H. Gadd and S. Werner. Fault detection in district heating substations. *Applied Energy*, 157: 51–59, 2015. https://doi.org/ 10.1016/j.apenergy.2015.07.061.

Kamstrup A/S. Technical description. Multical ® 603, 5512th– 2029_ ed. Kamstrup A/S, Skanderborg, Denmark, 2018.

S. Mansson, K. Davidsson, P. Lauenburg, and M. Thern. Automated statistical methods for fault detection in district heating customer installations. *Energies*, 12(1), 2019. https:/ /doi.org/10.3390/en12010113.

D. Marco and D. L. Neuhoff. The Validity of the Additive Noise Model for Uniform Scalar Quantizers. *IEEE Transactions on Information Theory*, 51: 1739–1755, 2005. https://doi.org/10.1109/TIT.2005.846397.

OIML R 75-1. *Heat meters Part 1: General requirements (OIML R 75-1)*. Paris, France, 2002.

F. Sandin, J. Gustafsson, J. Delsing. *Fault detection with hourly district data.* Stockholm, Sweden. 2013.

SWEDAC. STAFS 2007:2. Styrelsens för ackreditering och teknisk kontroll (SWEDAC) föreskrifter och allmänna råd om återkommande kontroll av vatten- och värmemätar, 2007.

R. L. Winkler. Combining Probability Distributions from Dependent Information Sources. *Management Science*, 27(4):479–488, 1981. https://doi.org/10.1287/mnsc.27.4.479.

The optimization of a distribution and over distribution line structure

S. Firouzifar E.Dahlquist

Malardalen University, Vasteras, Sweden, sfirouzifar@yahoo.com

Abstract

This paper discusses that the significant voltage drop under load condition is the big problem of distribution networks, because it limits the transfer capability of distribution lines. A utilization of the compact lines technology allows a significant increase in the transfer capability of distribution lines. Important developments for controlling over voltage and conductor resonances in recent decades gave the possibility to reduce the distances between phases. The modern distribution lines can be optimized with respect to their electric parameters in comparison with normal distribution lines, and by this increase the capacity in energy transmission.

Keywords: Natural power, transmitted power, capacity

Nomenclature

P_n = SIL	surge impedance loading
U_1	voltage at the start of line
U_2	voltage at the end of line
λ	line impedance $\lambda = wl/\upsilon$
J	current density, A/mm^2
ρ	conductor special resistance
ℓ_{cr}	length of line
X	inductive impedance
R	active resistance
P/Pn	transmitted power / surge impedance loading or natural power
$U_{2.nom}$	real value voltage
φ	shift angle between voltage and current
Dav	average geometrical distance between conductors
Z	surge impedance
r_0	radius of a conductor
Irc	reactive current end of line for consumed
I_2	loading current end of a line

1 Introduction

Voltage drops occur in transmission lines, sub transmission lines and distribution lines between the source and load. The voltage drop is very important when the impedance of transmission and sub-transmission line is high relative to the components of the circuit. By choosing suitable physical inductive reactive power and capacity power in exit line. Then we do not need to have extra equipment like capacitors and reactors. The high efficient transmission of electricity is depending on two important problems: voltage drop and power losses. Since alternating current (AC) depend on: (1) reactive power, and (2) characteristic impedance (inductance and capacitance).

Part of the capacity transmitted depends on reduced reactive power in the line. If we provide the right conditions, electrical energy can be transmitted without power losses. The reactive power can be compensated by extra equipment installed in the line as a parallel reactor or compensating capacitor, but we will have problems to provide equipment and we have to pay a lot of money for the purchase of the equipment. There are other methods for reducing reactive power by creating balance between reactive power, inductance and capacitance in the line. This will be discussed in this paper.

The effect cost for these equipment can be predicted, respectively. Transmission line design is discussed in (Clerci and Landonin, 1991; Heidari and Heidari, 2002; Doss, 2002). More details of technology is available e.g. in (Alcola Conduc tor Accessories, 2003; ACCR, 2003; 3M, 2003).

2 Designing modern lines in sub-transmission and distribution voltages

The equivalent scheme of a distribution lines is presented in Figure 1, Here X is the inductive impedance of a line, R is its active resistance. Let us present the loading current at the consuming end of a line in the symbolized form

$$I_2 = I_n \frac{P}{P_n}(1 - j.tg\varphi), \quad (1)$$

$$I_n = \frac{U_{2.nom}}{Z} \quad (2)$$

where Z is the surge impedance of a line, P_n is the natural power of this line or surge impedance loading, P is the transmitted power, φ is the shift angle between voltage and current. The reactive current, consumed (generated) by the line at its end is equal to

$$I_{r.c} = j\frac{U_{2.nom}}{2Z}\frac{X}{Z}\left[1-\left(\frac{P}{P_n}\right)^2\right] = jI_n\frac{\lambda}{2}\left[1-\left(\frac{P}{P_n}\right)^2\right], \quad (3)$$

where λ is the wave length of a line. By $P = P_n$, the line does not consume and does not generate reactive current. But when $P < P_n$ the line generates a reactive current, and when $P > P_n$, the line consumes reactive current. The sum of a current at the end of a consuming end of a line is equal to

$$\dot{I} = \frac{U_{2.nom}}{Z}\frac{P}{P_n}(1-j.tg\varphi) + j\frac{U_{2.nom}}{Z}\frac{\lambda}{2}\left[1-\left(\frac{P}{P_n}\right)^2\right], \quad (4)$$

The voltage at the sending end of a line is shown in Figure 2.

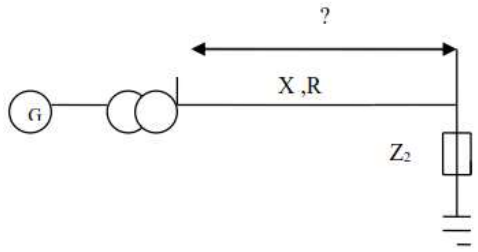

Figure 1. Inductive impedance (X) and active resistance (R) in distribution line.

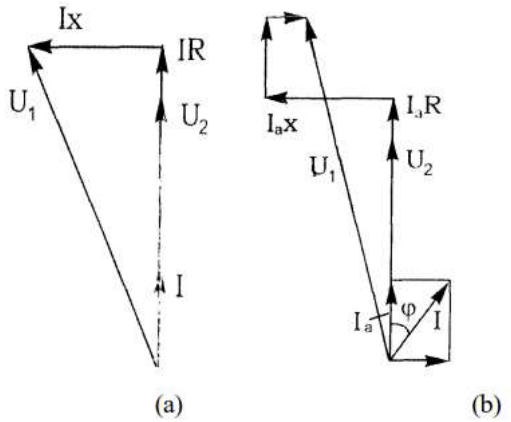

Figure 2. Vector diagram of voltages for transmission lines (a) for clean active loading and by presence of inductive component (b).

$$\dot{U} = U_2 + I(R + jX) =$$

$$= U_2 + U_{2.nom}\left\{\frac{P}{P_n}\left(\frac{R}{Z}+\frac{X}{Z}tg\varphi\right)+\left[\left(\frac{P}{P_n}\right)^2-1\right]\frac{X}{Z}\frac{\lambda}{2}+j\frac{P}{P_n}\left(\frac{X}{Z}-\frac{R}{Z}tg\varphi\right)\right\} = , \quad (5)$$

$$= U_2 + U_{2.nom}\left\{\frac{P}{P_n}\left(\frac{R}{Z}+\lambda.tg\varphi\right)+\left[\left(\frac{P}{P_n}\right)^2-1\right]\frac{\lambda^2}{2}+j\frac{P}{P_n}\left(\lambda-\frac{R}{Z}tg\varphi\right)\right\} =$$

where vector U_2 is combined with the axis of a real value and $X = \lambda Z$. By neglecting the unreal component, which influences on the value of U_1 practically negligible and by assuming that $U_2 = U_{2.nom}$ we obtain the value of voltage at the sending end of a line:

$$U_1 = U_2\left\{1+\frac{P}{P_n}\left(\frac{R}{Z}+\lambda.tg\varphi\right)+\left[\left(\frac{P}{P_n}\right)^2-1\right]\frac{\lambda^2}{2}\right\}, \quad (6)$$

where the assumption ($U_2 = U_{2.nom}$) is real, because by permissible voltage drop the voltage at the consuming end is to be not less then $U_{2.nom}$.

The ratio R / Z can be estimated by the next method. The active cross-section of the phase conductor is equal to

$$F_a = \frac{I}{J} = \frac{I_a}{J.\cos\varphi} = \frac{I_a}{J}\frac{P}{P_n}\frac{1}{\cos\varphi} = \frac{U_{2.nom}}{JZ}\frac{P}{P_n}\frac{1}{\cos\varphi}, \quad (7)$$

where J is the current density in a conductor. Hence the active resistance of the phase conductor is equal to

$$R = \frac{\rho.\ell}{F_a} = \frac{\rho.\ell.z.J}{U_2}\frac{P_n}{P}\cos\varphi, \quad (8)$$

where ρ is the specific resistance of a conductors and / is the length of a line. Therefore, the ratio

$$\frac{R}{Z} = \frac{\rho.\ell.z.J}{U_2}\frac{P_n}{P}\cos\varphi \quad (9)$$

Putting this ratio into the relation (6) we obtain

$$U_1 = U_2 + \rho.J.\ell.\cos\varphi + U_2\frac{P}{P_n}\lambda.tg\varphi + U_2\left[\left(\frac{P}{P_n}\right)^2-1\right]\frac{\lambda^2}{2}, \quad (10)$$

or the square equation in relation to the ratio P / P_n

$$\left(\frac{P}{P_n}\right)^2\lambda^2 + 2\frac{P}{P_n}\lambda.tg\varphi + 2 + \frac{2\rho.J.\ell.\cos\varphi}{U_2} - 2\frac{U_1}{U_2} - \lambda^2 = 0, \quad (11)$$

As a result of this equation solution the permissible ratio P / P_n by the given permissible ratio U_1/U_2 is equal to

$$\frac{P}{P_n} = \frac{1}{\lambda}\left[\sqrt{tg\varphi^2 + 2\left(\frac{U_1}{U_2} - 1 - \frac{\rho.J.\ell.\cos\varphi}{U_2} + \lambda^2\right)} - tg\varphi\right], \quad (12)$$

Inserting in the last formula we get a value of *SIL*

$$P_n = \frac{3U_{2.nom}^2}{Z}\ , \qquad (13)$$

We obtain another formula for the permissible transmitted power over a line

$$P = \frac{3U_2^2}{Z}\left[\sqrt{tg\varphi^2 + 2\left(\frac{U_1}{U_2} - 1 - \frac{\rho.J.\ell.\cos\varphi}{U_2} + \lambda^2\right)} - tg\varphi\right] \qquad (14)$$

It is possible to conclude from these last formulas, that it is impossible to transmit electrical energy over relatively short lines ($\lambda \leq 0.1$ rad), for which these formulas were obtained, without voltage drop. More over the voltage drop along the line is to be bigger than the voltage drops on the active resistance, which is determined by the item with the specific resistance ρ.

By the presence of an inductive load ($\varphi > 0$), the total voltage drop over the line is to be cover and increasing the reactive item, which is determined by the last item in (12) and (14). Therefore by nominal operating voltage at the consuming end of a line the voltage at the sending end of a line is to be bigger, however, not bigger than the maximum operating voltage. For this reason the bigger is the length of a line, the less is the permissible transmitted power. By the given permissible ratio U_1/U_2 and by the given length of a line, the permissible transmitted power *P* is inverse proportional to the surge impedance of a line.

3 Identification of surge impedance in modern distribution lines

This conclusion confines the efficiency of measures for compactization of a line structure and additional measures, caused the decrease of the surge impedance of a line. Really the surge impedance of lines with single conductors in a phase is equal to

$$Z = 60\ell n\frac{Dav.g}{r_0}\ , \qquad (15)$$

where *Dav.g* is the average geometrical distance between all three phases, r_0 is the radius of a conductor. By the decrease of *Dav.g*. The surge impedance *Z* decreases, but not so much. It is possible to decrease Z by using a conductor bundle instead of a single conductor with the same cross-section which is determined by the selected value of *J*. For double conductors in a phase the surge impedance of a line is equal to

$$Z = 60\ell n\frac{Dav.g}{\sqrt{r_0 d}} \qquad (16)$$

where *d* is the distance between two sub conductors. By triple conductors in a phase, the surge impedance of a line is equal to

$$Z = 60\ell n\frac{Dav.g}{\sqrt[3]{r_0 d^2}}\ . \qquad (17)$$

and by four sub conductors

$$Z = 60\ell n\frac{Dav.g}{\sqrt[4]{r_0 d^3.\sqrt{2}}} \qquad (18)$$

It is possible to see that the bigger the number of sub conductors the more effective is the splitting of the conductor. It is necessary to note that the efficiency of a conductor splitting increases by the decrease of Dav.g. The minimum Dav.g is by the triangle disposition of all phases.

By optimizing the distance between neighboring conductors *d=0,5 - 0,6* cm and by minimum possible distances between phases it is possible to decrease the surge impedance of a distribution line by two - three times compared to conventional lines (130 - 160 Ohm instead of 350 - 400 Ohm). Without interphases, the insulation spacers (compact lines) are two times and approximately three times less by the installation of interphase insulation spacers (super compact lines). This is in accordance with (14).

4 Ratio P/P_n versus length

The permissible ratio P/P_n , which was calculated by means of formula (12) with permissible voltage drop $U_1/U_2 = 1.1$ by current density J=1 A/mm^2, by different values of a power factor cosφ and by different operating voltages of lines are presented in Figure 4 versus their length.

Figure 3. Voltage line.

As it is possible to see for each level of operating voltage a decrease of the power factor cosφ leads to a significant decrease of permissible ratio P / P_n , if this ratio $P / P_n > 1$. On the contrary if this ratio $P / P_n < 1$ the decrease of *cosφ* leads to the increase of a permissible ratio P / P_n. A crossing of all curves takes

place by the same length of lines. This critical length of lines ℓ_{cr} increases when the operating voltage increases: The dependence $\ell_{cr} = f(U_{nom})$ is linear (Table 1) and can be estimated by means of the simple formula

$$\ell_{cr} = 1.9U_{nom} \quad , \qquad (19)$$

where ℓ_{cr} is in km and U_{nom} is in kV.

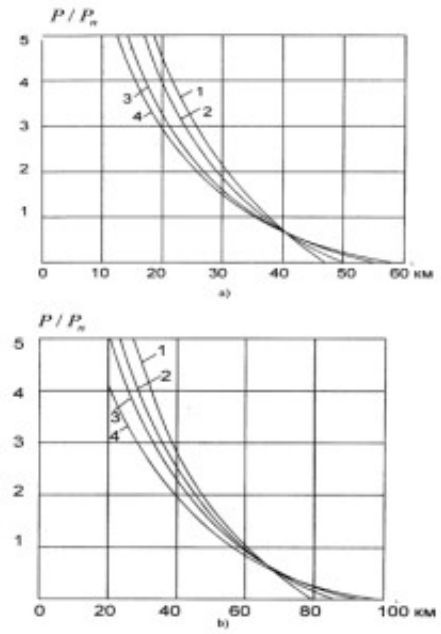

Figure 4. Ratio P/P_n versus length in kilometers.

An increase of the operating voltage leads to a significant increase of the permissible ratio *P / Pn* for the given length of a line. Respectively, the permissible length of a line for a transmission of the given ratio *P / Pn* increases significantly by an increase in the operating voltage. Table 1 shows the significant length of modern distribution line for different operating voltages

Table 1. Operating voltages.

U_{nom}, kV	20	35	63
ℓ_{cr}, km	39,5	65	120

5 Conclusions

Low power factor leads to the increase of voltage drop along the line and as the result limits the transmitted power and the possible length of electrical energy transmission. In order to decrease the influence of the power factor on the transfer capability of lines it is very useful to decrease inductive impedance of lines by using bundles of conductors and decreased distances between phases.

References

ACCR. *Power Conductor Accelerated Testing Facility (PCAT)*, ACCR Technology Description, November 2003.

Alcola Conductor Accessories. *Transmission Accessories*, 2003.

G. N. Alexandrov and H. Heidari. Equalization of overhead Ch. RI, "Heida" Increasing Lind Voltage.

Aluminum Conductor Composite Reinforced, Technical Notebook, 3M, March 2003.

A. Chakir and H. Koch. Thermal Calculation for Buried Gas –Insulated Transmission Lines (GIL) and XLPE-Cale, In *IEEE Winter Power Meeting 2001, Columbus*, 2001.

A. Chakir and H. Koch. Long Term Test of Buried Gas Insulated Transmission Lines (GIL). In *IEEEWPM 2002 New York*, 2002.

A. Clerci and M. Landonio. EHV Compact Lines – a new solution. In *CIGRE*, 1991.

CRIEPI, Report: Development of Make 66 to 154 kV Overhead Compact Transmission Lines (Part7) – Study on Mechanical Stresses to 154 kV Insulation Arms on Full-Scale Actual Test. CRIEPI Rep. W95037

Dennis Doss. Double your transmission capacity without changing existing towers. In *Electric light 7 and Cable*, August 2002.

Gh. Heidari. Equalization of overhead transmission line capacity different classes of voltage. In *PSC 95, Tehran*, Nov. 1995.

Gh. Heidari and G. N. Alexandrov, Increasing line voltage or sub conductors number each phases. In *CIGRE, Paris, France*, Sept. 1996.

Gh. Heidari and Maziar Heidari. Effect of land price on transmission line design. In *CIGRE*, Sept. 2002.

C. G. Heningen, G. Kaul, H. Koch, A. Scheuette, and R.Plath. Electrical and Mechanical Long-Time Behaviour of Gas – Insulated Transmission Lines. In *CIGRE*, 08/2000.

T. Hiller and H. Koch. Gas Insulated Transmission Lines (GIL): proven technology with new performance. In *Xiamen Switchgear Seminar*, China, 1997

T. Hiller and H. Koch. Gas–Insulated Transmission Lines for high power transmission over long distances. In *EMPT, Singapore*, 1998a.

T. Hiller and H. Koch. Gas –insulated Transmission Lines (GIL): A solution for the power supply of metropolitan areas. In *CEPSI, Thailand*, 1998b.

H. Koch and A. Schuette. Gas Insulated Transmission over long distances. In *EPSR, Hong Kong*, 1997.

Inventions & Innovations. *Development of a Composite–Reinforced Aluminum Conductor*, Project Fact Sheet, 1999.

H. B. Markus, P. Vestner, Diego F. Sologuren-Sanchez, Bodo A. Bruhl, and Paul F. Coventry. Dimensioning criteria and test result for a polymer enclosed gas insulted line. In *CIGRE*, 2000.

F. Sganzerla, J. A. A., Casagrande, and D. B. Galia. Electron are Brazila – 500 kV and 230 kV Compavr Lines: Design and 2. G or subconductors number in each phase, *CIGRE*, Paris, France, Sept.1996.

Biography

Sohrab Firouzifar was born in Damavand in Tehran, IRAN, on July 9, 1959. He graduated from The Institute of Technology of Tehran (M.Sc.) and is a PhD student at Malardalen University in Vasteras Sweden. He was the director of standard and quality control in the Mazandaran regional electrical company in the north of Iran and is a member IEEE in IRAN, and member of the board in IEEE north of Iran. He has published several papers in Iran for example: International Power system conference (PSC) and distribution system conference about expert systems in transmission substation & power transformer utilization. He was the director for the technical office for 10 years and was director R&D in M.R.E.C for 7 years.

Electrical characteristic of new calculation in sub-transmission line with simulation

S. Firouzifar E.Dahlquist

Malardalen University, Vasteras, Sweden, sfirouzifar@yahoo.com

Abstract

Important developments for controlling over voltage and conductor resonances in recent decades has given the possibility of reducing the phase distances in vast range. By this optimization can be made of some of the electric parameters in comparison with normal distribution lines, increasing the capacity in energy transmission. The reduction of the reactance of the line, increasing capacitance, increasing serge impedance loading (SIL) and reduction or increase of some of the other electrical parameters such as the geometric mean distance (GMD), will increase the capacity of this kind of modern distribution lines in comparison to normal distribution lines. By doing this, optimization can be made for different parts of the net. In this paper, a program in windows using Delphi software is presented for this optimization. The electrical specifications of modern and normal distribution lines are compared.

Keywords: SIL-GMD surge impedance, modern line, sub-transmission line

Nomenclature

GDM	Geometric Mean Distance
GMR	Geometric Mean Radius
X_l	Inductive reactance of distribution line
X_c	Capacitance reactance of distribution line
SIL	Serge Impedance Loading
L	Inductance
C	Capacitance
Z	Serge Impedance
ds	Distance between sub- conductors
ns	Number of extraneous
r	Radius in centimeter
μ	Respective permeability
λ	Wave length of line
υ	Velocity of wave propagation

1 Introduction

If we want to transmit energy in alternating current with acceptable efficiency, we must provide the minimum drop of voltage and energy. Alternating current is accompanied with reactive power and the transmission capacity of the line is determined by this. For suitable operation and using the maximum transmission capacity of the line, the reactive power should be minimized for any current load. If we provide these conditions, we can transmit energy without any loss due to reactive and capacitive characteristic. We can reduce the reactive power of the line by balancing between reactive power of line and additional equipment like capacitors or reactors. The effect cost for these equipment can be predicted, respectively. Transmission line design is discussed in (Clerci and Landonin, 1991; Heidari and Heidari, 2002; Doss, 2002). More details of technology is available e.g. in (Alcola Conduc tor Accessories, 2003; ACCR, 2003; 3M, 2003).

Another way to reduce the reactive power of lines is to balance between the inductive and capacitive reactive power of the line as such, whereby the total reactive power of the line will be minimum and about zero. The balancing between inductive reactive power and capacitive reactive power, can be possible by selecting the suitable physical shape of pilars and suitable placement of conductors. In this way, we don't need additional equipment such as classical lines. For modern compared to normal lines, a basic review in calculation and reduction of phase distance is required. Gas insulated transmission lines (GIL) are discussed in (Koch and Schuette, 1997; Hiller and Koch, 1997; Hiller and Koch, 1998a; Chakir and Koch, 2001; Chakir and Koch, 2002) and their applications in metropolitan areas (Hiller and Koch, 1998b), Heningen et al. (2000) focus on long-time electrical and mechanical behavior of GILs. Full scale tests are presented in (CRIEPI).

The advantage of this process is increasing the capacity, reducing the passing band width and reducing the line cost. The research shows that reducing the geometric mean distance (GMD) in a wide range is possible. (Markus et al., 2000; Inventions and Innovation, 1999).

2 Designing modern lines

2.1 Sub-transmission and distribution voltages

In Iran, the 10-20 kV voltages are considered as distribution voltages and the 63-132 kV voltages as sub transmission voltages. The length of these lines is several tens multiplied by the length of transmission lines. Distribution and sub transmission nets provide the required energy for consumers. For this reason all of the

cities, province centers, industrial centers and productive centers, agricultural and animals' installations, are connected to distribution 20 kV or sub-transmission 63 kV nets. For this voltage range, the classic approach is to not use groups of conductors. Lack of the conductor group and incremental capacitive properties, causes problems in the designing of modern lines. The other property of distribution lines is not the use of tall towers with wooden or concrete legs but our main discussion in this article, are the GMD variations for increasing natural power or the serge impedance loading (SIL) of the line (Alexandrov and Heidari; Koch and Schuette, 1997).

2.2 Geometric mean distance of phases

One of the most important parameters for defining the inductance and capacitance of distribution lines is the distance between line phases. By assuming transposed line on the way of it we use, the GMD to evaluate the transmission line parameters. As the distance between conductors in the tower arrangement is defined, the expression (1) is achieved.

$$X_l = 0.1447 \times Log\left(\frac{GMD}{GMR}\right) \quad (1)$$

where the quantity of GMR is the geometric mean radius of filled cylindrical conductors. Normally, if we replace the phases in towers, even for a specified distribution line, the GMD can have different quantities. As the erected shape of modern lines in the appendix of this article shows, according to the phase's arrangement, the GMD varies in a wide range. So, the electrical parameters of distribution lines have vast varieties according to the conductors' arrangement.

2.3 Inductive reactance

Inductive reactance is one of the most important parameters in voltage loss, stability limit and active and reactive losses and distribution line capacity too. Normally if we reduce the inductive reactance, we get some benefits for the lines. To calculate the inductance in a three-phase distribution line, we can use (1) for conductors of one kind that we get from

$$\mu/_4\, GMR = r.e \quad (2)$$

where r is the radius in centimeter and μ is the respective permeability of conductor that for copper and aluminum is equal to one. Most of the distribution lines are filamentary, and in some cases these filaments are of different kind like (ACSR). So the real quantity of GMR is a little different from the formula. By replacing the quantity of μ in (2), we can calculate GMR by

$$GMR = 0.7788 \times r \quad (3)$$

Above formulas are related to simple distribution lines with one conductor in every phase. If distribution lines are installed in the form of bundles (some conductors in each phase) the quantity of GMR must be corrected as

$$GMR_b = \sqrt[ns]{ns \times GMR \times A^{ns-1}} \quad (4)$$

$$A = \frac{ds}{2 \times \sin\frac{\pi}{ns}}) \quad (5)$$

In above formulas *ns* is the number of extraneous conductors in each phase, *ds* is the distance between extraneous conductors in centimeter and *A* is area of conductor. Above formulas show that if we reduce the phase distance, the quantity of line will decrease the variations of inductive reactance of lines in the GMD for several conductors compared to only one. In (3), the variation of inductive reactance of line according to the number of conductors in each phase for (curlew) conductors has been shown. It is shown in the fig that, if we compare the inductive reactance of simple and bundle lines in some cases, the inductive reactive reactance of simple modern lines (one conductor in each phase) is nearly equal to normal double bundle lines.

2.4 Capacitive reactance

Distribution lines are the consumers of reactive power and because of capacitive property, phases produce reactive power too. In a three-phase distribution line, the capacitance reactance X_c of the distribution line is as

$$X_C = 0.1318 \times Log\frac{GMD}{r.r_b} \quad (6)$$

where r_b is the radius of the group of conductors in centimeter. Other parameters are corresponding to former definitions. By designing modern distribution lines that have less phase distance than normal lines, the susceptance of line will increase too. For reduction of the amount of capacitive reactance or increasing the susceptance of line, we can use more numbers of extraneous conductors in each phase.

2.5 Surge impedance

Surge or natural impedance in distribution lines is the amount of consuming impedance when the generative and consuming VAR are equal

$$Q_C = CWV^2 \quad (7)$$

$$Q_L = L\,W\,V^2 \quad (8)$$

when the generative VAR (Q_C) and consuming VAR (Q_L) of distribution lines are equal (QC=QL) we have

$$\left(\frac{V}{I}\right)^2 = \frac{L \cdot W}{C \cdot W} \quad (9)$$

$$Z_S = \frac{V}{I} \quad (10)$$

$$Z_S = \sqrt{L/C} \quad (11)$$

2.6 Natural power of line

The other factor that is important in distribution lines is the natural power of line (surge impedance loading). This is the power needed to load with pure resistance and equal surge impedance. If the transmission power of the line is equal to the natural power of the line, the voltages at both ends of the line are nearly equal. So the power can be uses as an important index in loading distribution lines. The amount of natural power of distribution line depends on the amount of reactance and susceptance of the line. We can use the following formulas

$$SIL = \frac{U^2}{Z_s} \quad (12)$$

$$SIL = \frac{U^2}{\sqrt{L/C}} \quad (13)$$

to calculate them (Sganzerla et al., 1996; Alexandrov and Heidari; Heidari, 1995: Heidari and Alexandrov, 1996).

As you see in

$$V = 1/\sqrt{l.c} \quad (14)$$

this power is a function of the inductive and capacitive reactances of the line. As much as is reduced from reactance (or is increased to the capacitance of line), so much the surge impedance loading of the line will increase. Modern or bundle distribution lines that have low inductive reactance have more natural power inductance multiplied by the capacitance of the line. This is a function of the voltage of electromagnetic waves, that is expressed as below

As seen in (14), v or the velocity of electromagnetic waves is nearly constant. The amount of inductance multiplied by capacitance are constant too. It means that that whatever reactance decreases, capacitance increases and leads to an increase in the quality of distribution line. By combining formulas (12), (13) and (14), we can show the natural power of the line is a function of line voltage, the velocity of electromagnetic waves and inductive and/or capacitive reactance of the line:

$$SIL = C_{\bullet v \bullet U^2} \quad (15)$$

$$SIL = \frac{U^2}{L_{\bullet v}} \quad (16)$$

These formulas show that, because of constant amounts of a distribution line, natural power is a function of inductive or capacitive reactance of the lines. In other words, increasing or decreasing the amount of inductive and/or capacitive reactance of a line directly affects the natural power of the line.

3 Modern means voltage line

The 20 kV lines as distribution lines are usually forecasted and built as one or two circuits on cement or wooden tower (Figure 1). We need a distance about 1.5-2 meters between the phases, according to the tower distance or span. This decreases the capacitive property, but also increases the required right-of-way in the transmission line. In modern lines, the distance between phases in tower place and along the span is decreased by 0.4 - 0.5 meters. So the capacitive property of the line increases about 20-30%. By a suitable design of line, forecasting isolated insulators and using polymer insulators and assuming three phases in three vertexes of a triangle, the phase distance is limited to 0.5 meter. (Heidari and Alexandrov, 1996)

According to phase distance the amount of surge impedance in existed lines is 370 Ω and in modern lines 250 Ω. For case one, natural power of the line is

$$SIL = \frac{U^2}{Z_s} = 1.1\text{MW}$$

For modern line by installing three similar phases we will have

$$SIL = \frac{U^2}{Z_s} = 1.8\ \text{MW}$$

Figure 1. Voltage line.

As you see, the SIL or the natural power of 20 kV line increases about 0.7 MW. The reactive power for two kinds of above lines with 15 MW nominal power and 20 km length is calculated as below.

A) Line with GMD = 1.5 (existing line)

$$Q_1 = \omega CU^2 - \omega LI^2 = \omega CU^2\left(1-\frac{LI^2}{CU^2}\right)$$

$$= \omega CU^2\left(1-\frac{U^2I^2}{\left(\frac{U^2}{\sqrt{L/C}}\right)^2}\right)$$

$$= SIL.\lambda\left[1-\left[\frac{P}{SIL}\right]^2\right] = 1.15MVAR$$

B) Line with GMD=0.5 (modern line)

$$Q_L = SIL.\lambda\left[1-\left[\frac{P}{SIL}\right]^2\right] = 0.65MVAR$$

where λ is the wave length of line and υ is the velocity of wave propagation=300,000 km/sec.

As is seen, the consumed reactive power of the line has decreased about a half. As the load of 15 MW, was an industrial load and is maintained continuously and stable in 24 hours, decreasing reactive power to half, will accompany considerable economy from decreasing losses. By providing software we can do the calculations by computer easier and the results are analyzed faster and in for a wide range of data.

4 Program provided in Delphi

This program can do the electrical calculations of the line from the formulas in presented in this article. This capability means, according to the conditions, we can find the best situation by different inputs. The reports contain all electrical information of the line. As it was said in Section 2.7 about the GMD changes, the program can handle it.

By drawing two charts of the GMD changes according to SIL and P/SIL, we can observe the charts of changes by decreasing and increasing GMD and a boundle line or multicircuit lines that we show as examples. The page of reports contains all electrical data of the line. It is opened in the page of input data by specifications that are shown in Figure 2 and pressing the key of doing calculations.

Figure 2. Face plate for input data.

As you see in Figure 2, the phase distance of line is specified by assuming that the line is modern, the phase distances equal. The ambient or primary temperature and the temperature of the under load conductor are considered too.

The circuits' numbers of line can calculate up to three. As you see in (4) and (5), if the number of line bundles is one, the number of line for n boundles can be calculated. If the number of line boundle is one, the other data of the line like the line length, line current, line voltage, cosφ and the active power of line for accurate calculations are required. If the line is long, π model can be used for that.

The output data of the calculations are seen in Figure 3. This has all the required electrical data for line design as it is shown with the data in Figure 3: the losses of the line are 1.04.

Figure 3. Output data from the calculations.

Figure 4. Table with relationship between changes in GMD with different kind of conductor.

In Figure 4, the change in the SIL can be seen by changing the GMD and it is concluded that by increasing the GMD means increase in the phase distance and the SIL, the natural power of the line decreases (Figure 5).

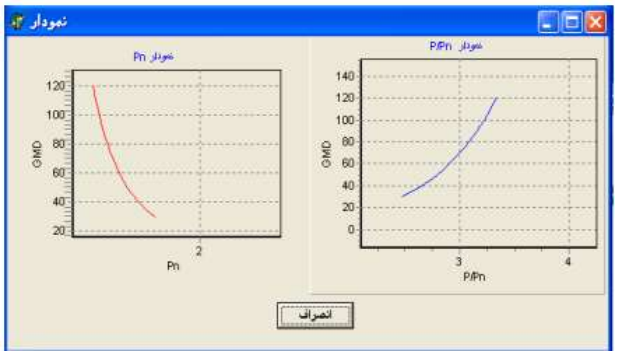

Figure 5. Curve GMD vs. SIL and GMD vs. P/SIL.

4.1 The ratio of transmitted power to natural power of line P/SIL

When the induced reactive power of a line is minimum, the ideal ratio of P/SIL is equal to one. To reach this amount P/SIL=1 we can not reduce P, because decreasing P and conductor's section is not economic. However, we can increase SIL and this is achieved by decreasing impedance Zs that increases the capacitive property of the line as below:

$$SIL = \frac{U^2}{Zs} \longrightarrow Zs = \sqrt{L/C} = \frac{1}{X.C} \text{V}$$

The propagation velocity of wave is equal to

$$\frac{1}{\sqrt{L.C}}$$

4.2 Surveying the GMD changes and its effects on the ratio of transmitted power to Surge Impedance Loading.

By changes in GMD, we can see the changes in C, L, Zs, and at last SIL that is the natural power of the line. The purpose of this program is decreasing the inductance of line (L). A comparison between the conventional and compact lines with consideration (GMD) is presented in the appendix, the difference between a normal 20 kV line and a modern 20 kV line shows that the natural power in modern lines is more than in normal lines. By increasing the natural power according to decreasing GMD and changes in phase arrangement, power is increased. Increasing transmitted power will decrease the ratio of transmitted power to the natural power of line SIL (Figure 5). By decreasing the GMD, this ratio is near to one now. In 20kV lines, the ratio of P/SIL is more than three, but we must make it near to 1 by changing the phase arrangement.

The provided software has this capability to decide how much we should change the GMD, and to find the optimum point of the GMD for every voltage. For example, the best status of phase's arrangement in 20 and 63, 33 kV voltages can be defined. At the same time, the difference between two circuits and two boundles or three circuits, can be specified pluralization and deduction: don't need to develop a bay at 63, 20 kV stations.

5 Conclusions

According to two basic theories in modern transmitting energy:

- For transmitting energy in modern lines, it is better to have two or three circuit lines as more energy can be transmitted.
- In the second theory, its better to transmit energy in two or more boundless, because in this situation we can in fact transmit more energy and don't need to pay anything for the development of the station bay.

However, regard to the above reasons, we have a new suggestion in this article. By using Delphi software and several experiments we concluded that for transmitting energy, if we want to use the number of circuits, construct the transmission lines with two circuits, and if we require to transmit more energy it is better to construct a modern line with three or four boundless, instead of three circuit line, because the natural power of a three-boundle line is more than a three-circuit line.

For increasing the SIL, the natural power, of 20, 33 and 63 kV lines, the major solution is an increasing capacitive property by nearing three-phase conductors to each other and providing the minimum distance of the phase to phase isolation. By this way, we conclude the following:

1) Increasing the capacitive property of line.
2) Reducing voltage and power loss.
3) Reducing the losses of line.
4) Reducing the surge impedance.
5) Reducing the inductive inductance.
6) Increasing the stability of line.

Our research shows that it is possible to reduce GMD in a wide range. By modern lines in 20, 33 and 63 kV voltages, we can reduce the GMD triply.

References

ACCR. *Power Conductor Accelerated Testing Facility (PCAT)*, ACCR Technology Description, November 2003.

Alcola Conductor Accessories. *Transmission Accessories*, 2003.

G. N. Alexandrov and H. Heidari. Equalization of overhead Ch. RI, "Heida" Increasing Lind Voltage.

Aluminum Conductor Composite Reinforced, Technical Notebook, 3M, March 2003.

A. Chakir and H. Koch. Thermal Calculation for Buried Gas –Insulated Transmission Lines (GIL) and XLPE-Cale, In *IEEE Winter Power Meeting 2001, Columbus*, 2001.

A. Chakir and H. Koch. Long Term Test of Buried Gas Insulated Transmission Lines (GIL). In *IEEEWPM 2002 New York*, 2002.

A. Clerci and M. Landonio. EHV Compact Lines – a new solution. In *CIGRE*, 1991.

CRIEPI, Report: Development of Make 66 to 154 kV Overhead Compact Transmission Lines (Part7) – Study on Mechanical Stresses to 154 kV Insulation Arms on Full-Scale Actual Test. CRIEPI Rep. W95037

Dennis Doss. Double your transmission capacity without changing existing towers. In *Electric light 7 and Cable*, August 2002.

Gh. Heidari. Equalization of overhead transmission line capacity different classes of voltage. In *PSC 95, Tehran*, Nov. 1995.

Gh. Heidari and G. N. Alexandrov, Increasing line voltage or sub conductors number each phases. In *CIGRE, Paris, France*, Sept. 1996.

Gh. Heidari and Maziar Heidari. Effect of land price on transmission line design. In *CIGRE*, Sept. 2002.

C. G. Heningen, G. Kaul, H. Koch, A. Scheuette, and R.Plath. Electrical and Mechanical Long-Time Behaviour of Gas – Insulated Transmission Lines. In *CIGRE*, 08/2000.

T. Hiller and H. Koch. Gas Insulated Transmission Lines (GIL): proven technology with new performance. In *Xiamen Switchgear Seminar*, China, 1997

T. Hiller and H. Koch. Gas–Insulated Transmission Lines for high power transmission over long distances. In *EMPT, Singapore*, 1998a.

T. Hiller and H. Koch. Gas –insulated Transmission Lines (GIL): A solution for the power supply of metropolitan areas. In *CEPSI, Thailand*, 1998b.

H. Koch and A. Schuette. Gas Insulated Transmission over long distances. In *EPSR, Hong Kong*, 1997.

Inventions & Innovations. *Development of a Composite–Reinforced Aluminum Conductor*, Project Fact Sheet, 1999.

H. B. Markus, P. Vestner, Diego F. Sologuren-Sanchez, Bodo A. Bruhl, and Paul F. Coventry. Dimensioning criteria and test result for a polymer enclosed gas insulted line. In *CIGRE*, 2000.

F. Sganzerla, J. A. A., Casagrande, and D. B. Galia. Electron are Brazila – 500 kV and 230 kV Compavr Lines: Design and 2. G or subconductors number in each phase, *CIGRE*, Paris, France, Sept.1996.

Biography

Sohrab Firouzifar was born in Damavand in Tehran, IRAN, on July 9, 1959. He graduated from The Institute of Technology of Tehran (M.Sc.), and is a PhD student at Malardalen University in Vasteras Sweden. He was the director of standard and quality control in Mazandaran regional electrical company in north of Iran, and is a member IEEE in IRAN, and member of the board in IEEE north of Iran. He has published several papers in Iran for example: International Power system conference (PSC) and distribution system conference about expert system in transmission substation & power transformers utilization. He was director for technical office for 10 years, and was director R&D in M.R.E.C for 7 years.

Appendix: Comparison between conventional and compact line with consideration (GMD)										
(Cm) GMD	circuit	Cub conductor	C	X_C	L	X_L	Z_1	$\Delta u\%$	$\frac{p}{SIL}$	$\frac{u_1}{u_2}$
70-70-140	1	1	0.0001	30.5	0.01066	33.5	319	30	4.8	1.44
20 KV	1	2	0.00018	17.5	0.0612	19.22	183.5	18	2.7	1.2
"	2	1	0.00023	14.06	0.04917	15.44	147	15	2.22	1.17
"	2	2	0.0004	7.85	0.02743	8.6	82.25	8.5	1.24	1.09
70-70-70	1	1	0.00011	29.18	0.10198	32.04	305	29	4.6	1.41
20 KV	1	2	0.0002	16.19	0.05658	17.78	169	17	2.5	1.19
"	2	1	0.00022	14.59	0.05099	16.01	152	15	2.3	1.17
"	2	2	0.00039	8.09	0.02829	8.88	84.88	8.7	1.28	1.09
140-140-280	1	1	0.0001	31.17	0.108	34.22	326	16	4.9	1.2
63 KV	1	2	0.00016	19.83	0.069	21.7	207	11	3.13	1.12
"	2	1	0.00022	14.3	0.0499	15.7	149	7.9	2.25	1.08
"	2	2	0.00036	8.63	0.03	9.47	90.4	4.9	1.36	1.05
140-140-140	1	1	0.00011	29.85	0.1043	32.77	312	16	4.7	1.19
63 KV	1	2	0.00017	18.51	0.0646	20.32	193	10	2.92	1.11
"	2	1	0.00021	14.92	0.05216	16.38	159	8.2	2.35	1.09
"	2	2	0.00034	9.25	0.03234	10.15	96.98	5.2	1.46	1.05

Operations Dynamics of Gas Centrifugal Compressor: Process, Health and Performance Indicators

Helge Nordal Idriss El-Thalji
University of Stavanger, Norway, {helge.nordal,idriss.el-thalji}@uis.no

Abstract

Emerging technologies of Industry 4.0 have introduced novel ways of perceiving maintenance management, which has developed from being perceived as a "necessary evil" to become proactive with a holistic focusing on entire systems rather than single machines from Maintenance 3.0. In this context, the industry has begun to really appreciate the unique opportunities followed by system dynamics and simulation tools capabilities of representing the real world. However, maintenance management and performance are complex aspects of asset's operation that is difficult to justify because of its multiple inherent trade-offs. Although the majority areunanimous when it comes to the expected impact maintenance plays on company profitability, this is in most cases challenging to determine and quantify. Moreover, relevant literature is considered as limited, especially with regards to impact simulation of Maintenance 4.0. Therefore, this paper focuses on the supportive function system dynamics, and modeling and simulation tools can be of help to assess behavior and predicting the future outcome of Maintenance 4.0 in the era of Industry 4.0. This includes developing a conceptualized model that enables simulating the future expected behavior i.e. (un)availability and cost by implementing such a maintenance system. In this context, a centrifugal compressor with the function of exporting gas to Europe is applied as a case study.

Keywords: Industry 4.0 Architecture, system dynamics, maintenance management, impact simulation

1 Introduction

The perception of maintenance management has been highly influenced by several technological developments and evolved in from being a "necessary evil", "technical matter", "cost-cutting contributor", "profit contributor" until it today is perceived as a "cooperative partnership" that can potentially add value to the business (Pintelon and Parodi-Herz, 2008). Moreover, maintenance strategies have developed rapidly over the last three industrial revolutions from being reactive, preventive, predictive and finally to become proactive and holistic (focus on entire system rather than single machine) (Alsyouf, 2007). Those strategic changes lead to several maintenance programs e.g. reliability centered maintenance (RCM), condition based maintenance (CBM), and total productive maintenance (TPM) (Pintelon and Parodi-Herz, 2008).

Maintenance is often associated with high cost allocated in the phase of an asset's operation and maintenance (O&M). In fact, the cost of maintenance is determined as sector dependent and varies all from 15 to 70 percent of total production cost (Bevilacqua and Braglia, 2000; Mobley, 2002; Gräber 2004). Moreover, several authors state that maintenance management is often attributed to poor planning and decision support resulting into inefficiency and waste of both cost and resources (Wireman, 1990; Noemi and William, 1994; Mobley, 2002; Wireman, 2004; Bardey, 2005). However, maintenance management and performance are complex aspects of asset's operation that is difficult to justify because of its multiple inherent trade-offs. Therefore, the expected or estimated impact of maintenance is often challenging to determine and quantify. Nevertheless, several literature are in fact unanimous when it comes to the expected impact maintenance plays on company profitability, supporting current perception of maintenance as a "cooperative partnership" (Komonen, 2002; Alsyouf, 2007; Maletič et al., 2012; Erguido et al., 2017; Colledani et al., 2018; Olde Keizer et al., 2018).

The importance of facilitating simulating the expected impacts of emerging technologies in the context of Industry 4.0 and its associated concepts has never been as important as it is today. It exists a great optimism of what the expected impact Industry 4.0 will bring to the oil and gas sector (O&G). (World Economic Forum, 2017) states that predictive maintenance and operations optimization are the two main technologies that will have the highest industrial and societal impacts in this specific sector, by e.g. reducing maintenance costs by 20% and operational downtime by 5% (mainly due to predictive maintenance). However, nowadays, only one single percent of data originating from 30 000 sensors located on a traditional oil rig is exploited. Moreover, this single percentage is in most cases utilized with regards to control and detection of operational anomalies (Manyika et al., 2015) and not for optimization and prediction in which World Economic Forum (2017) highlights as the most beneficial impact.

Moreover, as the cumulative maintenance expenditures concerning offshore installations with the design life of 30 years can reach up to £2 Billion, and often more, as life-extending measures are commonly adopted to enable operating such facilities over its designed lifetime (Register, 2017), there exist a great potential of reducing the associated cost by £400 Million, given that a 20% reduction in maintenance cost as presented by World Economic Forum (2017) is reasonable. Hence, the potential impacts of adopting an intelligent maintenance system in Industry 4.0 is considered as tremendous. However, estimating these specific impacts of predictive maintenance and operations optimization require techniques with growing complexity and capabilities. Therefore, simulation is considered as the key enabling technology as highlighted by (Oesterreich and Teuteberg, 2016) that may facilitate forecasting impacts of e.g. intelligent maintenance in Industry 4.0 in the context of predictive maintenance and operations optimization.

Several studies have adopted the methodology of system dynamics and investigated the opportunities of developing a model that enables simulating the impact of maintenance or internet of things (IoT) with respect to output variables such as e.g. companies' availability, cost and profit (Jokinen et al., 2011; Endrerud et al., 2014; Manyika et al., 2015; Hussain et al., 2016; Linnéusson et al., 2016; Qu et al., 2016; Linnéusson et al., 2018; McKee et al., 2017; Marshall, 2015; Jalali et al. 2017; Markus et al., 2018). Regardless, the authors identify two research gaps: (1) none of the existing models enables simulating the causal relationship that is present in the maintenance phase of a centrifugal compressor applied to export gas in the O&G industry and (2) none of existing literature facilitate simulation of intelligent maintenance architecture based on Industry 4.0 requirements. Hence, the purpose of this paper aims to develop a conceptualized model that enables simulating both the behavior of the associated compression system applied in gas export and the expected impacts introduced through the implementation of an intelligent maintenance system, by adopting the methodology of systems dynamics (SD) and simulation.

The remainder of this paper is organized as follows. Section 2 presents some relevant theory regarding process modeling and industrial simulation. Then, the case study of the centrifugal gas export compressors is investigated in Section 3. Section 4 is dedicated to the presentation of the conceptualized model developed in which enables simulating the behavior of the case study and the expected impact of implementing intelligent maintenance in the era of Industry 4.0. At last, Section 5 provides some concluding remarks.

2 Process Modeling and Industrial Simulation

Industry 4.0 and associated emerging technologies of cyber-physical systems (CPS), internet of things (IoT), big data, and cloud computing (including diagnosis and prognosis) are expected to play a vital role in companies future competitiveness and sustainability. However, determining the future benefits of adopting such technologies is of vital importance. Therefore, model-based representations i.e. process modeling and industrial simulation approaches e.g. system dynamics have become a highly embraced tool with its growing complexity and capabilities (McKee et al., 2017). This includes tools such as e.g. discrete event simulation (e.g. Arena), system dynamics (e.g. Vensim), and multi simulation methods (e.g. Anylogic and Numerus (Nova)), which all are frequently applied by industries to facilitate modeling and simulation of complex processes to perceive their nonlinear characteristics, either in the phase of early design, operation and maintenance, or late in decommissioning. The benefit of adopting process modeling and industrial simulation relates to its unique way of representing scenarios that are as close as possible to the real world. In this process, causal relationships are investigated and described in details, yielding an understanding of system behavior.

The literature describes the application of process modeling and industrial simulation in order to enhance asset operation. This is especially interesting i.e. maintenance and its impact on companies' availability, cost, and profit. In this context, some of the most well-known simulation models are presented in Table 1, considering their associated influencing variables, rates, and estimated benefits. Moreover, these well-known models constitute a supportive function when developing the conceptualized model presented in this paper. In fact, the model of (Jokinen et al., 2011) is especially interesting by its classification of failures (critical, degraded, and incipient) and its description of detection rate w.r.t sensor technology and maintenance management.

In this paper, the authors intend to adopt the approach of system dynamics to investigate and describe the case study and successively aid developing a model that enables simulating the causal relationship(s) associated with the operation of the case study.

Table 1. Summary of four of the most well-known simulation models.

	Influencing variables	Rates	Estimated benefits
(Linnéusson *et al.*, 2018)	- Number of repair workers and maintenance engineers - Goal and fraction of PM and CBM based on root cause analysis - Inspection interval - Scheduled and unscheduled repairs - Backlog of PM and CBM - Equipment health	- Take down and break down rate - Mean Time To Failure (MTTF)	- Availability - Maintenance cost - Acc. maintenance budget margin - Acc. company result
(Jambekar, 2000)	- Throughput pressure - Planned throughput - Preventive maintenance	- Equipment and labor force utilization - Breakdown	- Process quality - Process reliability
(Zuashkiani, *et al.*, 2011)	- Resource shift to reactive maintenance - Production - No. of repairmen allocated to reactive maintenance - No. of repairmen left to proactive maintenance - Reactive maintenance - Collateral damage	- Accumulated defects - Breakdown - Downtime due to proactive maintenance - Pressure on production - Take down rate for proactive maintenance - Downtime due to reactive maintenance - No equipment time for PM	- Plant OEE
(Honkanen, 2004)	- Working components - Components that are either failing soon, under repair, or have failed due to aging and infant life. - Working and failing components to be CBM maintained. - Components under maintenance	- (Net, Effective and Total) operating time - (Net) availability - (Scheduled) downtime - Speed and defect losses - Work start rates of repair, PM work, and CBM work.	- Availability - Performance - Quality
(Jokinen *et al.*, 2011)	- Spare part management - Maintenance management (e.g. target and active tasks related to preventive and corrective maintenance)	- Time - Increased degradation with time - New components and worn out components - Failures (incipient, degraded, and critical)	- Availability - Maintenance cost

3 Case Study

The case study in this investigation is a compression system with the primary function of enabling transporting sales gas (processed natural gas) through subsea pipelines by dynamically compressing it from 62 to 185 barg – thus, decisive as it determines whether the end users receive their booked gas or not. The compression system comprises four identical compressor trains, which each includes an electric motor, gearbox, and two centrifugal compressors arranged in series. In operation, only two out of the four compressor trains are in operation and sharing loads. Hence, two trains are at any time functioning as redundancy in cold standby (Wang, 2009; Tan, 2011). A cold standby system is a system that does not deteriorate or includes economic dependence of the operation.

Moreover, each compressor train includes 45 sensor signals related to condition monitoring: 26 sensor signals of single sensor signal that monitors vibration in terms of velocity. The data generated by the different sensors are in most cases exploited through trending. Therefore, it is of interest to investigate the behavior of the respective compression system (as a decisive part of the transportation system) and how a potential implementation of an intelligent maintenance system in the era of Industry 4.0 may impact the operation/ transportation in terms of availability and cost. To do so, the methodology of system dynamics and modeling and simulation is adopted. In order to manage to develop a simulation model that allows simulating the expected impacts, several processes must be studied at first:

1. Gas production/compression scenario (normal loading, seasonal demand): The need for gas compression is highly dependent on the season as the consumers mainly utilize the gas for heating and cooking at households (in addition to industrial consumption). Thus, end-user demand is peaking at winter-season when the need for heating is at its greatest. From a maintenance perspective, this will obviously play an important role when it comes to planning as a specific action will affect the operational (un)availability differently.

2. Planned maintenance scenario (planned schedule timeline): Equipment vendor usually provides customers with recommendations of preventive maintenance action throughout the equipment's life cycle. These are often based on either time in operation or numbers of cycles. Clearly, this will have an impact on planned unavailability and maintenance cost, and must, therefore, be considered in the context of intelligent maintenance and maintenance decision support (maintenance optimization).

3. Failure growth scenarios: The occurrence of symptoms of failure, or even failure, rises demand for necessary future action. The (symptom of) failure will

impact the operation differently based on its characteristics i.e. location, size, and severity. This is highly associated with maintenance management and the application of condition monitoring technologies including sensor technology, diagnosis, prognosis, which determines detection stage and thereby the criticality of the degradation and urgency for repair along with its cost.

4. Fault detection scenario: The introduction of Industry 4.0 has brought novel opportunities in maintenance management, especially considering cloud computing including diagnosis and prognosis. In more detail, maintenance 4.0 differentiates from maintenance 3.0 by moving its focus from the traditional enterprise level to become more holistic comprising the asset-level and between asset and enterprise-level. Therefore, it is of interest to simulate the difference between three monitoring scenarios in terms of impact: (1) compressor without CMS, (2) compressor with CMS (maintenance 3.0), and (3) compressor with maintenance 4.0. In this context, it is expected that the detection rate related to condition monitoring increases and the cost related to the level of repair is reducing, respectively.

5. Fault prevention scenario (by the control system): The objective of intelligent maintenance is to enhance right maintenance to be executed at the right time. This could e.g. include performing temporary maintenance actions that extend the remaining useful lifetime (RUL) estimate, which enables delaying the need for executing the required maintenance action from the diagnosis – thus, gaining opportunistic benefits. This comprises, for instance, the ability to plan the maintenance work for next opportunistic interval e.g. low production season or no-production days. Additionally, preventing the needs for corrective (maintenance) measures, which is commonly known as costly in comparison to other maintenance strategies.

6. Fault prevention scenario (by maintenance action): Accurate health assessments (diagnosis) and remaining useful life (RUL) estimations enable developing detailed work orders including spare part management, required human resources, and expected execution time. This improves the maintenance supportability and enhances the maintenance action's successfulness ensuring that the right maintenance action is conducted.

7. Maintenance performance: It is clear that execution of diagnosis will pose a beneficial impact of the maintenance performance since it enables assessing the current health status of the equipment and by this pinpoint the exact degradation mechanism. Thus, if the diagnosis e.g. reveals degradation of outer racing of a roller bearing, the maintenance personnel can plan down to the smallest details on how to maintain this in the best way. Hence, enhancing the improved performance of the maintenance action that is measurable through e.g. the mean-time-to-repair (MTTR).

8. Spare Part Management: The capabilities of prognostics is expected to impact the cost of inventory since it reduces the need for having spare parts in stock as it is possible to forecast at what time the different spare parts are required in advance.

Table 2. Summary of the related case study scenarios with associated potential estimated impact.

Scenarios Affecting Transportation	Potential Estimated impact
Gas production/compression scenario (normal loading, seasonal demand)	Availability, performance
Planned maintenance scenario	Planned Unavailability, planned maintenance cost
Failure growth scenario	Unplanned Unavailability, unplanned maintenance cost, equipment degradation
Fault detection scenario	Saving losses (unplanned maintenance cost, cost related to the level of repair (since the fault was detected before the whole system was damaged), etc.)
Fault prevention scenario	Gain opportunistic benefits e.g. able to plan the maintenance work for next opportunistic interval e.g. low production season or no-production days.
Maintenance performance scenario	Operational availability and unavailability (e.g. MTTR), cost of inventory, required human resources
Spare part management scenario	Cost of inventory

4 The Conceptualized Model

The prime objective of implementing intelligent maintenance architecture based on Industry 4.0 is to facilitate optimizing existing maintenance schedule. Although, the definition of "optimization" (Diwekar, 2008) can be interpreted ambiguously, it is in this context referred to as the mathematical concept that determines the optimal solution to a function comprising several different input and output variables such as e.g. gas price, cost, spare part management, operational (un)availability, and resources required and available. The most optimal solution based on the multiple variables is dependent on their weighting that may vary from time to time, under different circumstances. Resultantly, the optimization process shall ensure that the right maintenance takes place at the right time.

The conceptualized model developed to enable simulating this optimum maintenance action is based on maintenance theory from the literature review, systems dynamics (Vensim), the well-known simulation models presented in Table 1, and the scenarios extracted from the case study. As seen from the conceptualized model presented in Figure 1, it can be decomposed into four sub-models: (1) production, (2) maintenance management, (3) CBM, and (4) equipment degradation. In general, production (sub-model 1) is similar to any commodity, highly associated with the logic of supply and demand comprising variables such as e.g. politics, regulations, wealth, technology, population, and substitutes. Briefly, this is, in turn, determining the price of the commodity and thereby the revenue of the company. Moreover, the production is restricted by the availability of resources (hydrocarbons) and the associated overall equipment efficiency (OEE) that is governed by specific maintenance management (sub-model 2). The most important content of maintenance management is to optimize the existing maintenance schedule. This includes detecting failures (diagnosis), predicting the future development of the degradation and its impact on the system (prognosis), in which enables developing a detailed maintenance plan that identifies the best opportunistic window to perform the required action that improves availability and thus minimizes unavailability.

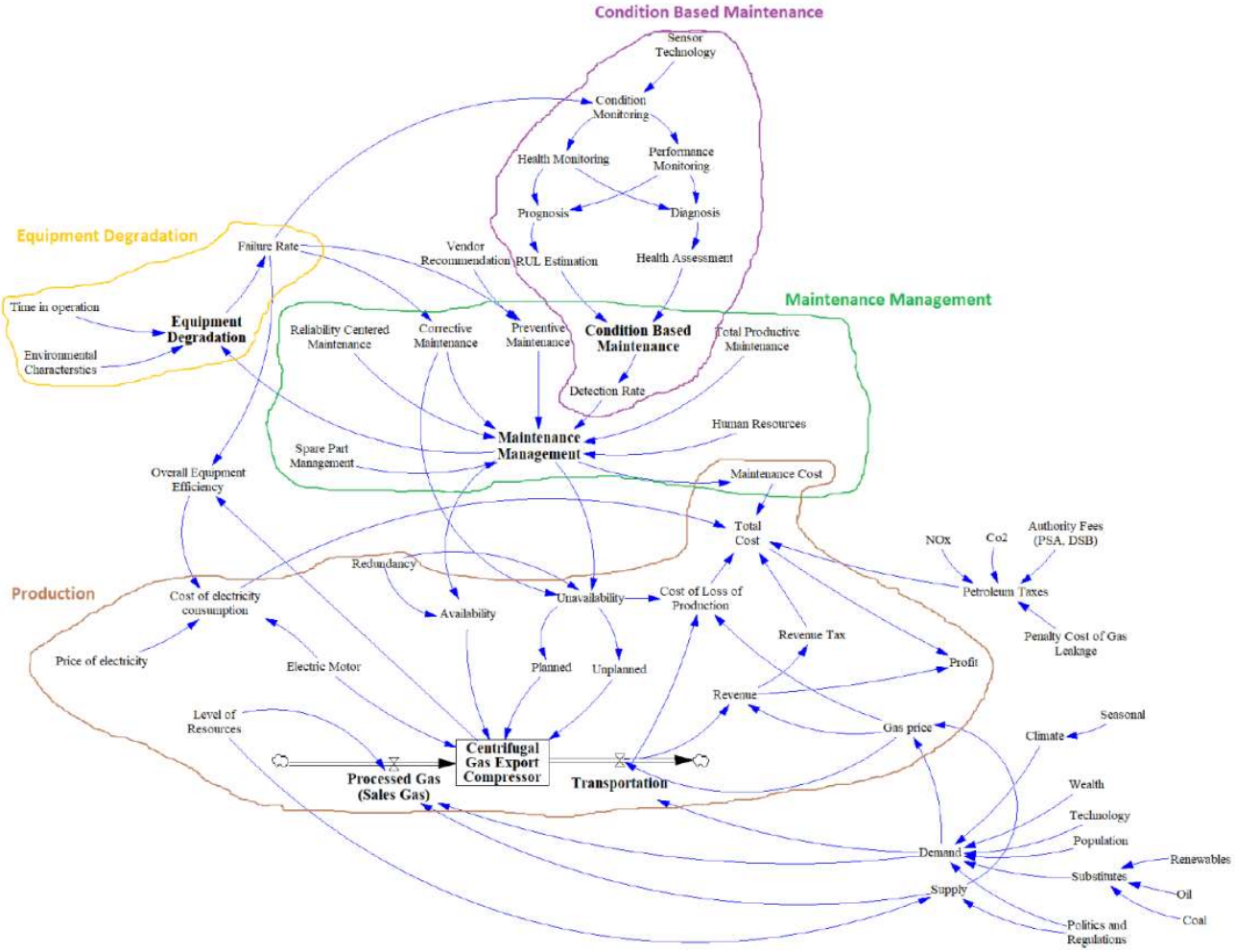

Figure 1. The conceptualized simulation model developed with associated sub-models.

CBM (sub-model 3) is all about monitoring performance and health data through sensor technology in order to detect (diagnosis), predict (prognosis), and extend the RUL estimate by prolonging the time to when the specific maintenance action is required. In this context, failure modes are classified into critical, degraded, and incipient failure modes. Traditionally, critical failure modes are detectable through performance monitoring (variables related to the process such e.g. pressure, temperature, and flow), while health parameters can improve the detection rate of critical failure modes and may even comprise certain degraded failure modes by combining performance and health parameters in terms of multivariate analyses of big data.

In order to detect degradation mechanisms early, awareness of equipment degradation (sub-model 4) affected by certain characteristics such as e.g.

environment (weather and climate) and operation (rpm and loading) is of high importance as it is connected with the equipment's failure rate. Moreover, such awareness supports achieving an understanding of equipment behavior along with responding to the results from the diagnosis and prognosis by e.g. prolonging the time to required maintenance action.

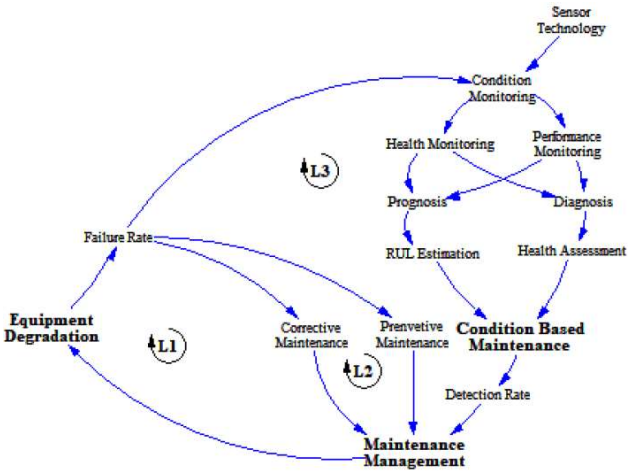

Figure 1. Three different causal loops identified by the conceptualized simulation model.

In final, Figure 2 shows the three causal loops identified in the conceptual model, which is the basic benefit of systems dynamic to manage (balancing or reinforcement). To summarize, the conceptualized simulation model shows the interaction between the different maintenance strategies affecting maintenance management. Furthermore, this plays a vital role for the estimated impacts i.e. availability and cost efficiency (as shown in Figure 1). It is clear from Figure 2 that the causal loop of CBM (L3) yields the greatest impacts and thus the objective of maintenance management, and vice versa for the causal loop regarding corrective maintenance (L1). However, in order to estimate the specific impacts, the capabilities of detecting the different failure modes associated with the system through sensor technology (parameter monitoring) and data analyses (diagnosis and prognosis) must be investigated.

5 Conclusions

Industry 4.0 and associated emerging technologies of CPS, IoT, big data, and cloud computing (including diagnosis and prognosis) are expected to play a key role in companies' future competitiveness and sustainability. However, determining these future benefits of adopting such technologies is of vital importance. Therefore, process modeling and industrial simulation approach e.g. system dynamics have become a highly embraced tool with its growing complexity and capabilities to facilitating perceiving nonlinear characteristics of complex processes.

Literature describes the importance of having a rigid maintenance management, which is reflected in associated impacts such as e.g. availability and cost estimations. Moreover, based on the growing complexities and capabilities of system dynamics, simulation is frequently adopted to estimate such impacts. However, maintenance management and performance are complex aspects of asset's operation that is difficult to justify because of its multiple inherent trade-offs. Although the majority are unanimous when it comes to the expected impact maintenance plays on company profitability, this is in most cases challenging to determine and quantify.

The conceptualized model developed in this paper demonstrates three causal relationships between different scenarios and its potential estimated impacts related to a case study concerning a centrifugal compressor that is applied to transport natural gas. The three causal loops (corrective maintenance, preventive maintenance, and CBM) shows the importance of having rigid maintenance management and its impact on company availability and cost. However, in order to quantify these specific impacts, the capabilities of detecting the different failuremodes associated with the system through sensor technology (parameter monitoring) and data analyses (diagnosis and prognosis) must be investigated. Moreover, it is expected that implementation of maintenance 4.0 will not only aid for improved operational impacts such as those two mentioned but also enhance the asset's HSE. This is described rather narrowly in the report. Nevertheless, HSE is of greatest importance but is excluded as it is challenging to quantify and simulate such intangible aspects of the operation.

References

I. Alsyouf. The role of maintenance in improving companies' productivity and profitability. *International Journal of Production Economics,* 105(1): 70-78, 2007.

D. Bardey. To maintain or not maintain? what should a risk-averse decision maker do?. *J Qual Maint Eng,* 11: 115-120, 2005.

M. Bevilacqua and M. Braglia. The analytic hierarchy process applied to maintenance strategy selection. *Reliab. Eng. Syst. Saf.*, 70(1): 71–83, 2000.

M. Colledani, M. C. Magnanini, and T. Tolio. Impact of opportunistic maintenance on manufacturing system performance. In *CIRP Annals*, 2018.

U. Diwekar. Introduction to Applied Optimization. In *Springer Science & Business Media*. Berlin, Germany. 22, 2008.

O.-E. V. Endrerud, J. P. Liyanage, and N. Keseric. Marine logistics decision support for operation and maintenance of offshore wind parks with a multi method simulation model. In *Proceedings of the 2014 Winter Simulation Conference*, 2014.

A. Erguido, A. Crespo Márquez, E. Castellano, and J. F. Gómez Fernández. A dynamic opportunistic mainte-

nance model to maximize energy-based availability while reducing the life cycle cost of wind farms. *Renewable Energy,* 114: 843-856, 2017.

U. Gräber. Advanced maintenance strategies for power plant operators - introducing inter-plant life cycle management. In 29th MPA Seminar in the series Safety and Reliability of Pressure Components Stuttgart, *Int. J. Press. Vessels Pip.,* 81 10–11: 861–865, 2004.

T. Honkanen. *Modelling Industrial Maintenance Systems and the Effects of Automatic Condition Monitoring.* Master of Science, Helsinki University of Technology Information and Computer Systems in Automation, 2004.

Y. M. Hussain, S. Burrow, L. Henson and P. Keogh. *Benefits Analysis of Prognostics & Health Monitoring to Aircraft*.

Maintenance using System Dynamics. In *EUROPEAN CONFERENCE OF THE PROGNOSTICS AND HEALTH MANAGEMENT SOCIETY*, 2016.

M. S. Jalali, J. P. Kaiser, M. Siegel, and S. Madnick. *The Internet of Things (IoT) Promises New Benefits – and Risks: A Systematic Analysis of Adoption Dynamics of IoT Products.* W. P. C. 2017-15, Cybersecurity Interdisciplinary Systems Laboratory (CISL), Sloan School of Management, Massachusetts Institute of Technology Cambridge, 2017.

A. B. Jambekar. A systems thinking perspective of maintenance, operations, and process quality. *Journal of Quality in Maintenance Engineering,* 6(2): 123-132, 2000.

T. Jokinen, P. Ylén, and J. Pyötsiä. *Dynamic Model for Estimating the Added Value of Maintenance Services*, Technical research centre of Finland, VTT, 2011.

K. Komonen. A cost model of industrial maintenance for profitability analysis and benchmarking. *Int. J. Production Economics,* 79: 15-31, 2002.

G. Linnéusson, A. Ng, and T. Aslam. Investigating Maintenance Performance: A Simulation Study. In *7th Swedish Production Symposium*, Lund, Sweden, October 25-27, 2016.

G., Linnéusson, A. H. C. Ng, and T. Aslam. Quantitative analysis of a conceptual system dynamics maintenance performance model using multi-objective optimisation. *Journal of Simulation,* 12(2): 171-189, 2018.

G. Linnéusson, H. C. A. Ng and T. Aslam. Towards strategic development of maintenance and its effects on production performance by using system dynamics in the automotive industry. *International Journal of Production Economics* 200: 151-169, 2018.

D. Maletič, M. Maletič, B. Al-Najjar and B. Gomišček. The role of maintenance regarding improving product quality and company's profitability: A case study. *IFAC Proceedings Volumes* 45(31): 7-12, 2012.

J. Manyika, M. Chui, P. Bisson, J. Woetzel, R. Dobbs, J. Bughin and D. Aharon. *THE INTERNET OF THINGS: MAPPING THE VALUE BEYOND THE HYPE EXECUTIVE SUMMARY,* McKinsey & Company, 2015.

A. Markus, A. Marques, G. Kecskemeti, and A. Kertesz. Efficient Simulation of IoT Cloud Use Cases. *Autonomous Control for a Reliable Internet of Services*, pages 313-336, 2018.

P. Marshall. System dynamics modeling of the impact of Internet-of-Things on intelligent urban transportation. In *Regional Conference of the International Telecommunications Society (ITS)*, Los Angeles, CA, 25-28 October, 2015, International Telecommunications Society, Los Angeles.

D. W. McKee, S. J. Clement, X. Ouyang, J. Xu, R. Romanoy and J. Davies. The Internet of Simulation, a Specialisation of the Internet of Things with Simulation and Workflow as a Service (SIM/WFaaS)). In *2017 IEEE Symposium on Service-Oriented System Engineering (SOSE)*: 47-56, 2017.

R. Mobley. *An Introduction to Predictive Maintenance*. 2002.

M. P. Noemi and L. William. Maintenance Scheduling: Issues, Results and Research Needs. *International Journal of Operations & Production Management* 14: 47-69, 1994.

T. D. Oesterreich and F. Teuteberg. Understanding the implications of digitisation and automation in the context of Industry 4.0: A triangulation approach and elements of a research agenda for the construction industry. *Computers in Industry,* 83: 121-139, 2016.

M. C. A. Olde Keizer, R. H. Teunter, J. Veldman and M. Z. Babai. Condition-based maintenance for systems with economic dependence and load sharing. *International Journal of Production Economics*, 195: 319-327, 2018.

L. Pintelon and A. Parodi-Herz. Maintenance: An Evolutionary Perspective. In *Complex System Maintenance Handbook.* Springer, London, Springer Series in Reliability Engineering, 2008.

T. Qu, M. Thürer, J. Wang, Z. Wang, H. Fu, C. Li and G. Q. Huang. System dynamics analysis for an Internet-of-Things-enabled production logistics system. *International Journal of Production Research* 55(9): 2622-2649, 2016.

L. S. Register. *Reducing the maintenance burden*, 2017. Retrieved 20th of March, 2019, from https://www.offshoreenergytoday.com/reducing-the-maintenance-burden.

L. Tan, J. Yang, Z. Cheng and B. Guo. Optimal replacement policy for cold standby system. *Chin. J. Mech. Eng* 24 (2): 316–322, 2011.

L. Wang, E. Zheng, Y. Li, B. Wang, J. Wu. Maintenance optimization of generating equipment based on a conditionbased maintenance policy for multi-unit systems. In Chinese Control and Decision Conference (CCDC 2009), IEEE: 2440–2445, 2009.

T. Wireman. *World class maintenance management*, 1990.

T. Wireman. *Benchmarking best practices in maintenance management.* In Industrial Press, 2004. World Economic Forum. Digital Transformation Initiative Oil and Gas Industry, 2017.

A. Zuashkiani, H. Rahmandad and A. K. S. Jardine. Mapping the dynamics of overall equipment effectiveness to enhance asset management practices. *Journal of Quality in Maintenance Engineering,* 17(1): 74-92, 2011.